Planetary Exploration Using Biomimetics

An Entomopter for Flight on Mars

Phase II Project NAS5-98051

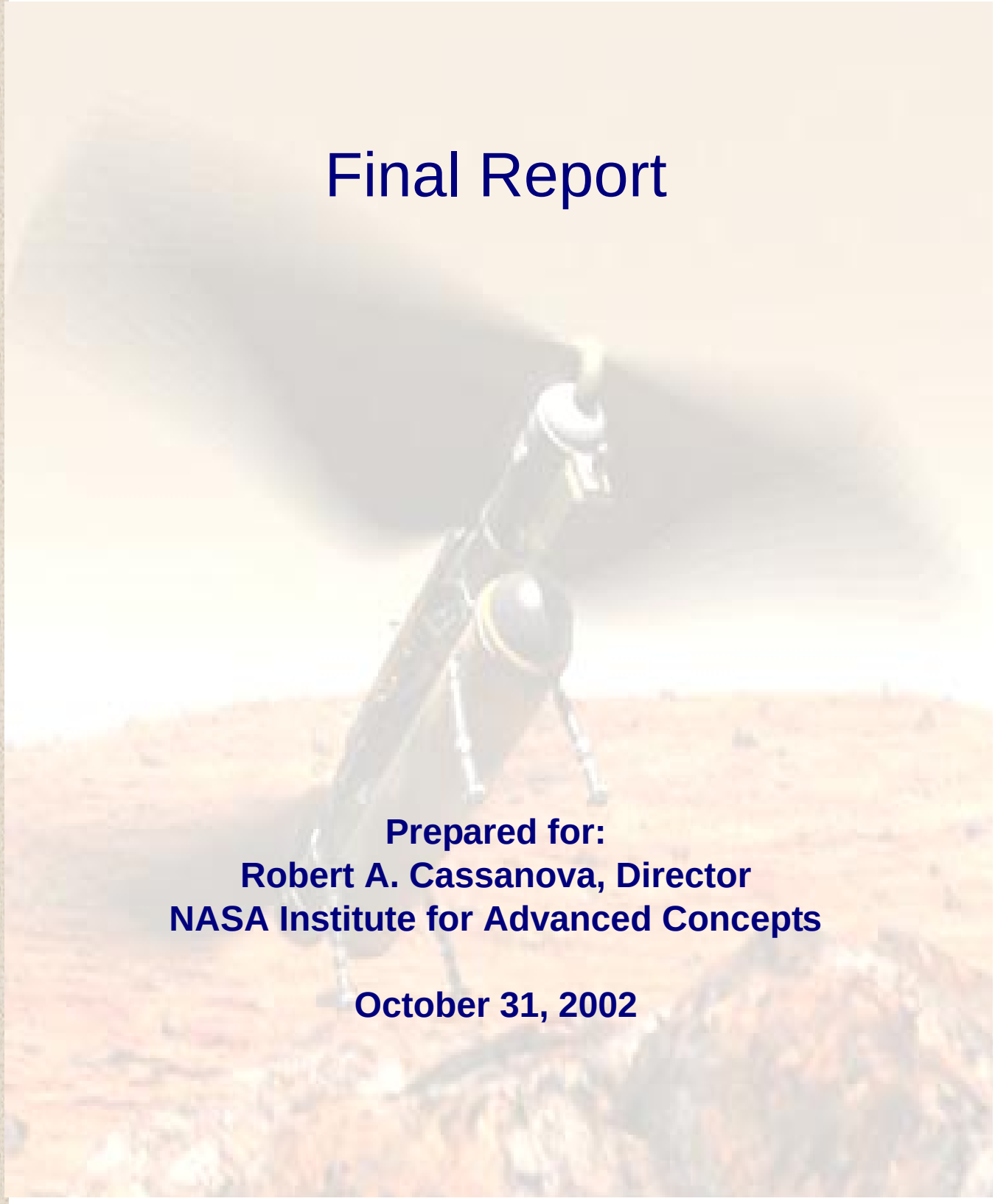

Final Report

Prepared for:
Robert A. Cassanova, Director
NASA Institute for Advanced Concepts

October 31, 2002

OAI

Table of Contents

List of Tables iii
List of Figures v
List of Contributors xiii
Executive Summary xv
Chapter 1.0 Introduction 1
1.1 History of Mars Flight 4
1.2 Origins of the Entomopter Concept 7
1.2.1 Why Flapping Wing Flight? 10
1.3 Mission 12
1.3.1 Mission Introduction 12
1.3.2 Mission Architecture 13
1.3.3 Science Application 16
Chapter 2.0 Entomopter Configuration and Operation 25
2.1 Introduction 25
2.2 Entomopter Morphology and Function 25
2.3 Baseline Mars Survey Flight Scenario for System Sizing 29
2.4 Environmental Conditions for Flight on Mars 31
2.4.1 Physical Properties 33
2.4.2 Atmospheric Conditions 33
2.4.3 Dust Storms and Wind 36
2.4.4 Soil Composition 38
Chapter 3.0 Vehicle Design 41
3.1 Wing Sizing 41
3.1.1 Engine Energy Production Requirements 41
3.1.2 Energy Required Due to Motion 41
3.2 Wing Motion and Structure Analysis 50
3.3 Wing Aerodynamics 65
3.3.1 Computational Fluid Dynamics 65
3.3.2 Angle of Attack Analysis 112
3.3.3 Analytical Analysis of Mars Entomopter Aerodynamics 116
3.3.4 Active Flow Control (“Blowing” of the Wings) 151
3.4 Reciprocating Chemical Muscle 154
3.4.1 Fourth-generation Design Goals 157
3.4.2 Fourth-generation Concept 158
3.4.3 Sizing of the Entomopter-based Aerial Mars Surveyor 163
3.5 Fuel Storage and Production 169
3.5.1 Introduction 169
3.5.2 Propellant Selection 170
3.5.3 Propellant Production and Storage 179
3.5.4 Fuel Storage System 203
3.5.5 Fuel Systems Comparison 205
3.6 Power System 206
3.6.1 Communications 207
3.6.2 Science Instruments 208
3.6.3 Internal Systems 208
3.6.4 Photovoltaic/Battery 209
3.6.5 Thin-film Photovoltaics 210
3.6.6 Lithium Batteries 216
3.6.7 Thermoelectric Power Generation 220
3.6.8 Linear Alternator System 223

Chapter 4.0 Entomopter Flight Operations 225
4.1 Entomopter Navigation and Communications on Mars 225
4.2 Rover-centric Entomopter Navigation 225
4.2.1 Minimum Energy Short Range Obstacle Avoidance System 227
4.2.2 Navigation Under the Baseline Mars Scenario 231
4.3 Entomopter-borne Active Emitters for Navigation and Communication 236
4.3.1 Assumptions and Performance Goals 236
4.3.2 Propogation Losses 240
4.3.3 Frequency of Operation 241
4.3.4 Antennas 242
4.3.5 Link Budget Analysis 248
4.3.6 Link Budget Results 252
4.3.7 Future Development Path for the Active Communications Option 257
Chapter 5.0 Potential Payload Functions Using a Communication/Control Subsystem 259
5.1 General Science Objectives 259
5.2 Imaging and Terrain Mapping 260
5.3 Digital Terrain System 262
5.4 Scatterometers and Spectrometers 264
Chapter 6.0 Media Exposure 267
6.1 Introduction 267
6.2 Print Media 268
6.3 Online Media 269
6.4 Television Science Programming, News, and Video Archives 270
6.5 CD Distribution and Live Performances 270
6.6 Special Recognition and Awards 271
Chapter 7.0 Conclusion 273
Appendix A: Mars Atmosphere Data A-1
Appendix B: Sizing Results B-1
Appendix C: List of References C-1

List of Tables

Table 2-1: Physical Properties of Mars 33
Table 2-2: Mars Atmospheric Composition 33
Table 2-3: Mineral Composition of Mars Soil 38
Table 2-4: Element Composition of Mars Soil 39
Table 3-1: Entomopter Parameters and Design Space Ranges 49
Table 3-2: Design Point Operational Characteristics 49
Table 3-3: Baseline Operating Conditions 52
Table 3-4: Wing Geometry and Mass 59
Table 3-5: Simulation Conditions 73
Table 3-6: Lift and Drag Coefficient Values 86
Table 3-7: Lift and Drag Summary for Reynolds Number = 510-5,100 Range 92
Table 3-8: List of Symbols 126
Table 3-9: Design of Experiment Array 142
Table 3-10: Fuels and Their Phase-change Temperatures 171
Table 3-11: Oxidizers and Their Phase-change Temperatures 171
Table 3-12: Monopropellants and Their Phase-change Temperatures 172
Table 3-13: Characteristics of Fuel Candidates 172
Table 3-14: Characteristics of Oxidizer Candidates 173
Table 3-15: Characteristics of Monopropellant Candidates 174
Table 3-16: Propellant Candidates based on Temperature and Operational State Req'ts 176
Table 3-17: Percent of Hydrogen by Weight for the Various Candidate Propellants 177
Table 3-18: Combustion of Various Metals with CO_2 178
Table 3-19: Metal Hydrides and Hydrogen-density Capability 186
Table 3-20: Commercially Available Metal Hydride Hydrogen-storage Specifications 186
Table 3-21: Tank-insulation Properties 190
Table 3-22: Fuel System Mass for Various Mission Durations 205
Table 3-23: Thin-film Solar Cell Types and Their Characteristics 212
Table 3-24: Environmental Properties for Solar Power Generation 212
Table 3-25: Specifications for Lithium Polymer Batteries, Ultralife Battery 219
Table 3-26: PV/Battery System Mass Estimate 220
Table 3-27: Thermoelectric System Mass Estimate 222
Table 3-28: Specifications for Radioisotope Heater Unit 222
Table 4-1: Parameters for Obstacle-detection Analysis 252
Table 4-2: Parameters for Altimetry Analysis 253
Table 4-3: Parameters for Communications Analysis 255
JPL Reference Mars Atmosphere for -20° Latitude A-1
General Mars Atmosphere Model (NASA Langley) A-3
Mars-GRAM Generated Atmosphere Profile for -25° Latitude, 11° Longitude A-7
Mars-GRAM Generated Atmosphere Profile for 57° Latitude, 2.35^{o} Longitude A-10

List of Figures

Figure 1-1: Conventional Airfoil and Insect Wing Lift-Generation Mechanisms 2
Figure 1-2: Flapping Insect Wing Leading Edge Vortex Formation 3
Figure 1-3: Insect Wing Lift-generation 4
Figure 1-4: Mini-Sniffer High Altitude Aircraft 6
Figure 1-5: Solar-Powered Mars Aircraft 6
Figure 1-6: JPL "Kitty Hawk" Glider 7
Figure 1-7: Ames "MAGE" Aircraft 7
Figure 1-8: Generations of the Reciprocating Chemical Muscle Actuator and the Biologically-inspired Wing that it Drives for Applications on Earth and Mars 8
Figure 1-9: Stereolithographic Kinematically-correct Model of the Terrestrial Entomopter ... 12
Figure 1-10: Animation of Entomopter Mission (Take off, Flight, Sample Gathering, and Return to the Lander) 15
Figure 1-11: Mission Flight Profile for Multiple Entomopters in Conjunction with a Rover ... 16
Figure 1-12: High Resolution Image of Mars Surface Taken by Pathfinder Lander 17
Figure 1-13: Example of a Wide-Angle Context Camera-type Image 18
Figure 1-14: Magnetic Field Shape on Earth and Mars 19
Figure 1-15: Radar Sounding for Investigating Surface and Subsurface Features 21
Figure 1-16: Atmospheric Sampling and Data Collection Over Grid 22
Figure 1-17: Artist's Concept of the Entomopter Taking a Surface Sample 23
Figure 2-1: Entomopter-based Mars Flyer Configuration 25
Figure 2-2: ABS Plastic Wing Ribs from Fused Deposition Modeling Machine 26
Figure 2-3: Lift Vectors on the Upthrust and Down Thrust Wing Halves 27
Figure 2-4: Integral Propulsion-ultrasonic Obstacle Avoidance and Altimetry System 28
Figure 2-5: Baseline Mission 30
Figure 2-6: Image of Mars Atmosphere Taken From Pathfinder Lander 31
Figure 2-7: Orbital Image of Surface Features on Mars 32
Figure 2-8: Image of Mars Surface from Pathfinder Lander 32
Figure 2-9: Daily Pressure Variation (Pathfinder Data) 35
Figure 2-10: Pressure Variation Over a One-month Period (Pathfinder Data) 35
Figure 2-11: Atmospheric Temperature Variation Throughout a Day (Pathfinder Data) 36
Figure 2-12: Wind Direction Throughout the Day (Pathfinder Data) 37
Figure 2-13: Measurements Taken During a Dust Devil (Pathfinder Data) 38
Figure 3-1: Parameters for Power Consumption Optimization 41
Figure 3-2: Mass and Corresponding Force Distribution Along Wing Section 42
Figure 3-3: Acceleration Force Diagram 43
Figure 3-4: Wing Motion and Energy Usage, Velocity and Acceleration Profiles 43
Figure 3-5: Examples of the Effect of Wing Length, Flapping Rate and Flap Angle on the Work Performed by the Engine 44
Figure 3-6: Resultant Force and Velocity for the Flapping Wing 45
Figure 3-7: Lift Distribution for Various Operational Conditions 46
Figure 3-8: Total Wing Mass as a Function of Wing Length 48
Figure 3-9: Entomopter Landing Approach 50
Figure 3-10: Forces Acting on a Given Point Along the Way 51
Figure 3-11: Wing Motion Represented by Angle Change with Time 52

Figure 3-12: Plan-view of Entomopter Wing 53
Figure 3-13: Mass Distribution Along the Wing Length 54
Figure 3-14: Load Diagram and Coordinate System for Wing Loading 55
Figure 3-15: Entomopter Wing Structural Geometry 57
Figure 3-16: Total Mass for Various Wing Structural Configurations 58
Figure 3-17: Mass Distribution for Various Structural Geometries 58
Figure 3-18: Loading Profile at Various Radial Stations Along the Wing for a Hollow Tapered Wing 60
Figure 3-19: Radial Loading Profile at Various Locations Along the Wing for a Hollow Tapered Wing 61
Figure 3-20: Loading, Shear, and Bending Moment for a Hollow Tapered Wing 61
Figure 3-21: Effect of Hollow Elliptical Core Dimensions on Wing-section Mass 62
Figure 3-22: Effect of Hollow Elliptical Core Dimensions on Wing-tip Deflection 62
Figure 3-23: Effect of Wing-root Thickness on Wing-tip Deflection & Wing-section Mass ... 63
Figure 3-24: Effect of Wing-tip Thickness on Wing-tip Deflection & Wing-section Mass 63
Figure 3-25: CAD Wing Section for the Hollow, Tapered Baseline Geometry--Root to Tip from Wing Top 64
Figure 3-26: CAD Wing Section for the Hollow, Tapered Baseline Geometry - Top View 64
Figure 3-27: CAD Wing Section for the Hollow, Tapered Baseline Geometry--Leading Edge View 65
Figure 3-28: Computational Grid 67
Figure 3-29: Surface Grid 67
Figure 3-32: Wing Outline and Trailing Edge Mass Ejection Used for Circulation Control 69
Figure 3-33: Dynamic Stall Vortex Highlighted Using Streamlines 69
Figure 3-30: Dynamic Stall Vortex Highlighted by Massless Particles 69
Figure 3-31: Cambered Airfoil Surface with 30° Ejection from Bottom Rear of the Airfoil 69
Figure 3-34: Airfoil Surface Grid Highlighting Tangential Blowing and LEV Development .. 70
Figure 3-35: Airfoil Surface Highlighting Tangential Blowing and LEV Development 70
Figure 3-36: Drag Coefficient vs. Time with Blowing/Oscillation 70
Figure 3-37: Lift Coefficient vs. Time with Blowing/Oscillation 71
Figure 3-38: Pressure Contours for Blowing (Left) and No Blowing (Right) 72
Figure 3-39: Airfoil with Elliptic Leading Edge 72
Figure 3-40: Airfoil with the Mesh 73
Figure 3-41: Lift Coefficient vs. Angle of Attack 74
Figure 3-42: Drag Coefficient vs. Angle of Attack 75
Figure 3-43: Velocity Vectors for a = -3° 76
Figure 3-44: Pressure Contours for a = -3° 76
Figure 3-45: Velocity Vectors for a = 0° 77
Figure 3-46: Pressure Contours for a = 0° 77
Figure 3-47: Velocity Vectors for a = 2.31^o 78
Figure 3-48: Pressure Contours for a = 2.31^o 78
Figure 3-49: Velocity Vectors for a = 5.31^o 79
Figure 3-50: Pressure Contours for a = 5.31^o 79
Figure 3-51: Velocity Vectors for a = 8.31^o 80
Figure 3-52: Pressure Contours for a = 8.31^o 80
Figure 3-53: Velocity Vectors for a = 11.31^o 81

Figure 3-54: Pressure Contours for a = 11.31^o 81
Figure 3-55: Velocity Vectors for a = 14.31^o 82
Figure 3-56: Pressure Contours for a = 14.31^o 82
Figure 3-57: Velocity Vectors for a = 17.31^o 83
Figure 3-58: Pressure Contours for a = 17.31^o 83
Figure 3-59: Airfoil with New, Finer Triangular Mesh 84
Figure 3-60: Cambered, Zero-thickness Airfoil 84
Figure 3-61: CL Values for the Thick and Thin Airfoils 85
Figure 3-62: Cd Values of the Thick and Thin Airfoils 85
Figure 3-63: Lift Coefficient Variation, a = 8.31^o, Reynolds Number = 9,600 87
Figure 3-64: Drag Coefficient Variation, a = 8.31^o, Reynolds Number = 9,600 87
Figure 3-65: Velocity Vectors, a = 8.31^o, Reynolds Number = 9,600 88
Figure 3-66: Pressure Contours, a = 8.31^o, Reynolds Number = 9,600 88
Figure 3-67: Pressure Contours, a = 45.79^o, Reynolds Number = 5,100, Time = 3.5648 s 89
Figure 3-68: Pressure Contours, a = 45.79^o, Reynolds Number = 5,100, Time = 3.5948 s 89
Figure 3-69: Pressure Contours, a = 45.79^o, Reynolds Number = 5,100, Time = 3.6248 s 90
Figure 3-70: Pressure Contours, a = 45.79^o, Reynolds Number = 5,100, Time = 3.6548 s 90
Figure 3-71: Pressure Contours, a = 45.79^o, Reynolds Number = 5,100, Time = 3.6848 s 91
Figure 3-72: Lift Convergence History. U=1.4 m/s. a = 34.8^o. 93
Figure 3-73: Drag Convergence History. U=1.4 m/s. a = 34.8^o 93
Figure 3-74: Lift Convergence History. U=14 m/s. a = 34.8^o. 94
Figure 3-75: Drag Convergence History. U=14 m/s. a = 34.8^o. 94
Figure 3-76: Top View of Entomopter Wing 95
Figure 3-77: Side View of Entomopter Wing 95
Figure 3-78: Lift Coefficient for the Oscillating Wing Case 96
Figure 3-79: Drag Coefficient for the Oscillating Wing Case 96
Figure 3-80: North American Cicada Forewings and Right Hind Wing 97
Figure 3-81: Elliptic Wing Modeled After North American Cicada Wing 97
Figure 3-82: Dimensions Used for Entomopter Wing Mesh Generation 98
Figure 3-83: Mesh View 1 99
Figure 3-84: Mesh View 2 100
Figure 3-85: Mesh View 3 100
Figure 3-86: Mesh View 4 100
Figure 3-87: Mesh View 5 101
Figure 3-88: Mesh View 6 101
Figure 3-89: Residual Convergence Plot 102
Figure 3-90: Force Convergence Plot 102
Figure 3-91: U Velocity Contours on Symmetry Plane 103
Figure 3-92: U Velocity Contours at Span Location z = -0.26 103
Figure 3-93: U Velocity Contours at Span Location z = -0.5 104
Figure 3-94: Residual Convergence Plot 105
Figure 3-95: Force Convergence Plot 105
Figure 3-96: U Velocity Contours on Symmetry Plane 106
Figure 3-97: U Velocity Contours at Span Location z = -0.26 107
Figure 3-98: U Velocity Contours at Span Location z = -0.5 107
Figure 3-99: Forces (Newtons) Time History for Simulation with Blowing 109

Figure 3-100: Force (Newtons) Time History for Simulation Without Blowing 110
Figure 3-101: Force (Newtons) Time History for Case with Continuous Blowing Velocity of 1 m/s 111
Figure 3-102: Wind Tunnel Flow Visualization Image of Flow Over a Thin Wing at High a. Flow is from Bottom to Top and Light Sheet Illumination from Left to Right. Trailing Edge Vortex is Clearly Visible. 112
Figure 3-103: Wing-velocity Profile Due to Wing Motion Through One-flap Cycle 113
Figure 3-104: Angle of Attack for a Maximum Flap Angle of 65° and Flight Speed of 2 m/s 114
Figure 3-105: Angle of Attack for a Maximum Flap Angle of 65° and Flight Speed of 14 m/s 115
Figure 3-106: Angle of Attack for a Maximum Flap Angle of 85° and Flight Speed of 2 m/s 115
Figure 3-107: Angle of Attack for a Maximum Flap Angle of 85° and Flight Speed of 14 m/s 116
Figure 3-109: Typical Low Reynolds Number Airfoil 117
Figure 3-108: Hawk Moth Lift and Drag vs. Angle of Attack 117
Figure 3-110: Pressure Distribution for Optimized Airfoil vs. That of Conventional Airfoil . 118
Figure 3-111: Flapping Wing Micro Air Vehicle Test Model 119
Figure 3-112: Parameter Definitions for the Jones Model 119
Figure 3-113: Flapping Airfoil Combinations 120
Figure 3-114: CFD and Empirical Thrust Coefficient Results for the Jones Model 120
Figure 3-115: LEV Formation (View 1) 122
Figure 3-116: LEV Formation (View 2) 122
Figure 3-117: Thin Flat Plate Airfoil 126
Figure 3-118: Flapping Motion 130
Figure 3-119: Pitching Motion 131
Figure 3-120: Chord vs. Span Location 132
Figure 3-121: Lift Coefficient vs. Time 139
Figure 3-122: Moment Coefficient vs. Time 140
Figure 3-123: Power Coefficient vs. Time 140
Figure 3-124: CFD Results of the Unblown Case 141
Figure 3-125: Coefficient of Lift 144
Figure 3-126: Coefficient of Moment 144
Figure 3-127: Coefficient of Power 145
Figure 3-128: Variation of Lift Coefficient with Span 146
Figure 3-129: Variation of Lift Coefficient with Forward Velocity 147
Figure 3-130: Variation of Lift Coefficient with Flapping Frequency 148
Figure 3-131: Variation of Lift Coefficient with Flapping Amplitude 149
Figure 3-132: Variation of Lift Coefficient with Pitching Amplitude 150
Figure 3-133: GTRI Kinematically-correct Full-scale Wind Tunnel Flapping Simulator 151
Figure 3-134: Flight Speed at Mars Surface vs. Required C_L 154
Figure 3-135: Wing Structures Grown in Georgia Tech's Stereolithography and Fused Deposition Modeling Machines. 155
Figure 3-136: First-generation Reciprocating Chemical Muscle 156
Figure 3-137: Second-generation Reciprocating Chemical Muscle 156

Figure 3-138: Stereolithographic Scale Model of the Terrestrial Flight-sized Reciprocating Chemical Muscle 156
Figure 3-139: Third-generation Reciprocating Chemical Muscle 157
Figure 3-140: Initial Fourth-generation RCM Actuator Design Using a Pressure-activated Spool 159
Figure 3-141: Acrylic Kinematic Visualization Testbed 160
Figure 3-142: Coordinated Piston Extension 162
Figure 3-143: Fourth-generation RCM Dual Opposing Piston Shaft and Spur Gear Shown in Place 162
Figure 3-144: X-Wing Flapping as Viewed Along the Torsional Axis. 164
Figure 3-145: Mars Entomopter RCM Actuator (Side View, Actual Size) 167
Figure 3-146: Mars Entomopter RCM Actuator (End View) 168
Figure 3-147: Hydrogen Density at Various Pressures and Temperatures 182
Figure 3-148: Spherical Pressure Tank Mass Constructed of Carbon and Titanium at Various Storage Pressures 183
Figure 3-149: Tank Radius as a Function of Storage Pressure for Various Hydrogen Mass .. 184
Figure 3-150: Effect of Conformal Tanks on Available Space Utilization 185
Figure 3-151: Glass Microsphere Hydrogen Storage: Mass Fraction and Density for Various Storage Pressures 188
Figure 3-152: One-dimensional Heat Transfer for Liquid Hydrogen Tank 191
Figure 3-153: Effect of Insulation Thickness on Overall Storage Tank Mass 193
Figure 3-154: Effect of Insulation Thickness on Overall Tank Mass 193
Figure 3-155: Theoretical Increase in Density with the Addition of Methane Gelling Agent 194
Figure 3-156: Single-stage 20° K Cryocooler 195
Figure 3-157: Rate of Energy Loss Due to Boil-off of the Liquid Hydrogen 196
Figure 3-158: Cryocooler Power Requirement to Meet Boil-off Demand 197
Figure 3-159: Cryogenic Tank System Mass as a Function of Insulation Thickness 198
Figure 3-160: Hydrogen Gas Storage System 199
Figure 3-161: Liquid Hydrogen Storage System 200
Figure 3-162: Hydrogen Peroxide Generation Method 201
Figure 3-163: Dynamic Heat Engine Power System Diagram 202
Figure 3-164: PV Battery Power System Diagram 203
Figure 3-165: Monopropellant Fuel Storage System 204
Figure 3-166: Mass of Fuel Storage System Versus Amount of Hydrogen Peroxide Stored . 204
Figure 3-167: Total Fuel System Mass as a Function of Mission Duration 206
Figure 3-168: Typical Communication Power Profile for One Mission Segment 208
Figure 3-169: Typical Science Instrument Power Profile for One Mission Segment 208
Figure 3-170: Typical Internal Systems Power Profile for One Mission Segment 209
Figure 3-171: PV Array/Battery System Layout 210
Figure 3-172: Historical Progress of Thin-film Solar Cell Efficiency. Experimentally Achieved Efficiencies (Extrapolated to Air Mass Zero Spectrum, in Percent) 211
Figure 3-173: Mars: Available Power Throughout the Day at 0° Latitude 213
Figure 3-174: Mars: Available Power Throughout the Day at 20° Latitude 214
Figure 3-175: Mars: Available Power Throughout the Day at 40° Latitude 214
Figure 3-176: Mars: Available Power Throughout the Day at 60° Latitude 215
Figure 3-177: Mars: Available Power Throughout the Day at 80° Latitude 215

Figure 3-178: Output per Array at the Equator During the Summer Solstice 218
Figure 3-179: Output per Array at 80° North Latitude During the Summer Solstice 218
Figure 3-180: Solar Array Average Output Power for the Equator and 85o North Latitude at Day 170 (Summer Solstice, Northern Hemisphere) 219
Figure 3-181: Operational Diagram of a Thermoelectric Generator 221
Figure 3-182: Photo of a Thin Film Thermoelectric Device 221
Figure 4-1: Acoustically Excited Tuned Resonant Cavity 228
Figure 4-2: Measured Response Data of a Mechanically-modulated FMCW Source Sized for the Terrestrial Entomopter. (Data acquired under GTRI's DARPA/DSO-funded Mesoscaled Aerial Robot Program.) 229
Figure 4-3: Multiplexing of Waste Gas-driven FMCW Ultrasonic Acoustic Ranging Source 230
Figure 4-4: Rover-centric Information Paths Used in Navigation 233
Figure 4-5: Conceptual View of Communications/Control Subsystem Functionality 236
Figure 4-6: Side View of Entomopter Illustrating Assumed Coordinate System 237
Figure 4-7: Atmospheric Absorption Attenuation by Water Vapor and Oxygen at Earth and Mars Surface 242
Figure 4-8: Linearly Tapered Slot Antenna (LTSA) Circular Array (Sunflower Antenna) 245
Figure 4-9: Measured Radiation Pattern at 19.8 GHz. H-Plane, and E-Plane at Elevation Angles of 0 = 25° and 40° 246
Figure 4-10: Measured Radiation Pattern at 19 GHz With and Without Ground Plane. (a) H-Plane and (b) E-Plane 247
Figure 4-11: Potential Antenna-mounting Scenario for Front and Rear of Entomopter 247
Figure 4-12: Top View of Entomopter Body Showing Illustrative Antenna Patterns from Mounting Scenario of Figure 4-11 248
Figure 4-13: Side View of Entomopter Body Showing Illustrative Antenna Patterns from Mounting Scenario of Figure 4-11 248
Figure 4-14: Time-domain Plot of Modulated Gaussian Waveform (MGW) Centered at 18 GHz 249
Figure 4-15: Peak and Average Transmitter Power Required for Obstacle Detection at 18 GHz as a Function of Range 252
Figure 4-16: Peak Transmitter Power Required for Obstacle Detection at 15 m and 200 m as a Function of Frequency 253
Figure 4-17: Average Transmitter Power Required for Obstacle Detection at 15 m and 200 m as a Function of Frequency 253
Figure 4-18: Peak and Average Transmitter Power Required for Altimetry at 18 GHz as a function of Altitude 254
Figure 4-19: Peak Transmitter Power Required for Altimetry at 10 m and 200 m as a Function of Frequency 255
Figure 4-20: Average Transmitter Power Required for Altimetry at 10 m and 200 m as a Function of Frequency 255
Figure 4-21: Peak and Average Transmitter Power Required for Communications at 18 GHz as a Function of Range 256
Figure 4-22: Peak Transmitter Power Required for Communications at 200 m and 1,000 m as a Function of Frequency 256
Figure 4-23: Average Transmitter Power Required for Communications at 200 and 1,000 m as a function of Frequency 257

Figure 4-24: Average Transmitter Power Required for Communications at 200-m and 1,000-m as a Function of Data Rate 257
Figure 5-1: Geometry for a Scanning Imaging Radar Altimeter 261
Figure 5-2: Possible Flight Configuration for 3D Mapping 262
Figure B-1: Relative Lifting Capacity for Various Engine Powers and Wing Lengths at 15 m/s Flight Speed B-1
Figure B-2: Flapping Frequency vs. Pwr. Consumption (Watts) for a Wing Length of 0.3 m B-1
Figure B-3: Flapping Frequency vs. Pwr. Consumption (Watts) for a Wing Length of 0.4 m B-2
Figure B-4: Flapping Frequency vs. Pwr. Consumption (Watts) for a Wing Length of 0.5 m B-2
Figure B-5: Flapping Frequency vs. Pwr. Consumption (Watts) for a Wing Length of 0.6 m B-3
Figure B-6: Flapping Frequency vs. Pwr. Consumption (Watts) for a Wing Length of 0.7 m B-3
Figure B-7: Flapping Frequency vs. Pwr. Consumption (Watts) for a Wing Length of 0.8 m B-4
Figure B-8: Flapping Frequency vs. Pwr. Consumption (Watts) for a Wing Length of 0.9 m B-4
Figure B-9: Flapping Frequency vs. Pwr. Consumption (Watts) for a Wing Length of 1.0 m B-5
Figure B-10: Flight Power vs. Velocity for a Wing Length of 0.3 m and Relative Lift Capacity of 0.5 kg B-5
Figure B-11: Flight Power vs. Velocity for a Wing Length of 0.3 m and Relative Lift Capacity of 1.0 kg B-6
Figure B-12: Flight Power vs. Velocity for a Wing Length of 0.3 m and Relative Lift Capacity of 1.5 kg B-6
Figure B-13: Flight Power vs. Velocity for a Wing Length of 0.3 m and Relative Lift Capacity of 2.0 kg B-7
Figure B-14: Flight Power vs. Velocity for a Wing Length of 0.4 m and Relative Lift Capacity of 0.5 kg B-7
Figure B-15: Flight Power vs. Velocity for a Wing Length of 0.4 m and Relative Lift Capacity of 1.0 kg B-8
Figure B-16: Flight Power vs. Velocity for a Wing Length of 0.4 m and Relative Lift Capacity of 1.5 kg B-8
Figure B-17: Flight Power vs. Velocity for a Wing Length of 0.4 m and Relative Lift Capacity of 2.0 kg B-9
Figure B-18: Flight Power vs. Velocity for a Wing Length of 0.5 m and Relative Lift Capacity of 0.5 kg B-9
Figure B-19: Flight Power vs. Velocity for a Wing Length of 0.5 m and Relative Lift Capacity of 1.0 kg B-10
Figure B-20: Flight Power vs. Velocity for a Wing Length of 0.5 m and Relative Lift Capacity of 1.5 kg B-10
Figure B-21: Flight Power vs. Velocity for a Wing Length of 0.5 m and Relative Lift Capacity of 2.0 kg B-11
Figure B-22: Flight Power vs. Velocity for a Wing Length of 0.6 m and Relative Lift Capacity of 0.5 kg B-11
Figure B-23: Flight Power vs. Velocity for a Wing Length of 0.6 m and Relative Lift Capacity of 1.0 kg B-12
Figure B-24: Flight Power vs. Velocity for a Wing Length of 0.6 m and Relative Lift Capacity of 1.5 kg B-12
Figure B-25: Flight Power vs. Velocity for a Wing Length of 0.6 m and Relative Lift Capacity of 2.0 kg B-13

Figure B-26: Flight Power vs. Velocity for a Wing Length of 0.7 m and Relative Lift Capacity of 0.5 kg B-13
Figure B-27: Flight Power vs. Velocity for a Wing Length of 0.7 m and Relative Lift Capacity of 1.0 kg B-14
Figure B-28: Flight Power vs. Velocity for a Wing Length of 0.7 m and Relative Lift Capacity of 1.5 kg B-14
Figure B-29: Flight Power vs. Velocity for a Wing Length of 0.7 m and Relative Lift Capacity of 2.0 kg B-15
Figure B-30: Flight Power vs. Velocity for a Wing Length of 0.8 m and Relative Lift Capacity of 0.5 kg B-15
Figure B-31: Flight Power vs. Velocity for a Wing Length of 0.8 m and Relative Lift Capacity of 1.0 kg B-16
Figure B-32: Flight Power vs. Velocity for a Wing Length of 0.8 m and Relative Lift Capacity of 1.5 kg B-16
Figure B-33: Flight Power vs. Velocity for a Wing Length of 0.8 m and Relative Lift Capacity of 2.0 kg B-17
Figure B-34: Flight Power vs. Velocity for a Wing Length of 0.9 m and Relative Lift Capacity of 0.5 kg B-17
Figure B-35: Flight Power vs. Velocity for a Wing Length of 0.9 m and Relative Lift Capacity of 1.0 kg B-18
Figure B-36: Flight Power vs. Velocity for a Wing Length of 0.9 m and Relative Lift Capacity of 1.5 kg B-18
Figure B-37: Flight Power vs. Velocity for a Wing Length of 0.9 m and Relative Lift Capacity of 2.0 kg B-19
Figure B-38: Flight Power vs. Velocity for a Wing Length of 1.0 m and Relative Lift Capacity of 0.5 kg B-19
Figure B-39: Flight Power vs. Velocity for a Wing Length of 1.0 m and Relative Lift Capacity of 1.0 kg B-20
Figure B-40: Flight Power vs. Velocity for a Wing Length of 1.0 m and Relative Lift Capacity of 1.5 kg B-20
Figure B-41: Flight Power vs. Velocity for a Wing Length of 1.0 m and Relative Lift Capacity of 2.0 kg B-21

List of Contributors

Georgia Tech Research Institute

Mr. Robert J. Englar
Prof. Robert C. Michelson
Maj. Messam A. Naqvi

Northland Scientific

Mr. Anthony Colozza (PI)

OAI

Ms. Laurie Beringer
Ms. Terri Deacey
Mr. Franklin Porath
Mr. Curtis Smith

University of Missouri-Rolla

Dr. Raja Banerjee
Dr. Kakkattukuzhy Isaac
Mr. Pavan Shivaram

Independent Consultants

Mr. Teryn DalBello
Dr. Carol Kory
Dr. Thomas Scott

Acknowledgements

We would like to thank Marc Seibert of NASA John H. Glenn Research Center (GRC) for his contributions to this project, and Rainee N. Simons of NASA GRC for his helpful discussions regarding the LTSA antenna. We would also like to acknowledge Daniel Maas of Maas Digital for his outstanding work on the video animation for this project.

Executive Summary

The first serious look at flying on Mars was done in the mid 1970s. Since then there have been numerous studies and designs for flying aircraft on Mars. Because of the very low atmospheric density on Mars all of these conventional aircraft designs have come across the same limitation, in order to generate sufficient lift the aircraft must fly fast. That fact and the rough rock strewn surface of Mars makes it almost impossible to produce a conventional aircraft that can safely land and take off again. Therefore all previously proposed aircraft missions have been limited in duration to the amount of fuel the aircraft could carry for one flight.

The Entomopter concept is a potential way around this problem of having to fly very fast within the atmosphere of Mars. The Entomopter doesn't generate lift in the same fashion as a conventional aircraft. The Entomopter concept uses the same lift generating means that insects do here on Earth to generate lift within the Mars environment. Unlike aircraft or birds, insects generate lift by the continuous formation and shedding of vortices on their wings. This vortex formation and shedding produces very high wing lift coefficients on the order of 5 compared to maximum lift coefficients of 1 to 1.2 for conventional airfoils. This very high lift generating capability is what allows insects to fly, hover and maneuver as they do. The investigation of the aerodynamics of insect flight is still a new science and the mechanisms for how they fly are not completely understood. However, it is believed that their ability to generate these large amounts of lift is a Reynolds number based phenomena. As Reynolds number increases the ability is diminished.

This high lift generating capability under low Reynolds number flight conditions poses an interesting solution to flight on Mars. Because of the low atmospheric density on Mars, a vehicle with a wing-span on the order of 1m would be in the same flight Reynolds number regime as most insects are here on Earth. Because of this it is conceivable to construct a vehicle that can fly near the surface of Mars (up to 100s of m in altitude) and generate sufficient lift to allow it to fly slow, maneuver easily and land. This realization is the genesis for the Entomopter concept for Mars. The Entomopter consists of a central fuselage which houses the propulsion system, fuel and all instrumentation. On top to the tubular fuselage are two sets of wings that oscillate 180° out of phase. These wings provide the flapping motion that generates the lift for the vehicle. Beneath the vehicle are spring loaded legs that absorb energy during landing, assist in take-offs and stabilize the vehicle while on the ground.

For the Entomopter to fly it will need to flap its wings at a specified rate, thereby producing and shedding the vortices that will generate the lift. The motion of the wings is a fairly power intensive process so a given flight mission for the Entomopter will be short (on the order of 10 to 15 minutes). These short flight times are due to the amount of fuel it is estimated the Entomopter can carry. Because of these short flight times the Entomopter would need to be operated as part of a system. It is envisioned that this system would consist of one or more Entomopter vehicles that operate in conjunction with a base vehicle such as a lander or rover. This base vehicle would provide refueling capability to the Entomopters as well as act as a data relay for the science data and samples the Entomopters collect.

The most promising scenario is to utilize the Entomopter in conjunction with a rover. The rover would be capable of slowly moving over the Mars surface, while the Entomopters fly off to

investigate areas inaccessible to the rover. The Entomopters could also be used to guide the rover from the air, indicating the best path to traverse of scope out interesting terrain or objects for the rover to further investigate. In addition to acting as a scout for the rover the Entomopter could perform a number of science data gathering tasks on its own. These tasks could include surface imaging in the visible, infrared or other wavelengths, magnetic field mapping, atmospheric science, surface sample collection and searching for the chemical signs for life.

For the Entomopter to work within the Mars environment it will need to be as lightweight and efficient as possible. This means that systems and devices on the vehicle will need to perform more the one task if possible. This multiple use philosophy has been integral to the design effort. It begins with the propulsion system. The engine will decompose hydrazine (a monpropellant) to provide the power to move the wings. After a thorough evaluation of a number of potential fuels, hydrazine was chosen as the best candidate because of its high energy density and the fact that it was a monopropellant. Utilizing a monopropellant simplifies the fuel delivery and refueling systems by requiring one tank and filling nozzle. Also, hydrazine decomposes when passed over a catalyst allowing for a low risk combustion scheme. The gas produced during the decomposition of Hydrazine will be used to produce the wing motion through the reciprocating chemical muscle engine. Once the exhaust leaves the engine it is used for several other functions before being blown out the trailing edge and tips of the wings. This gas entrainment into the flow field over the wing enables vortex stabilization and greatly enhances the lifting capacity of the wing. Wind tunnel experiments on fixed wings have shown that with the trailing edge blowing wing lift coefficients of 10 or greater are achievable. CFD runs corroborate the lift enhancement of the blown wing in both fixed and flapping modes. In addition to lift enhancement the trailing edge blowing will be used as a means of control for the Entomopter. The gas flow to each of the individual wings will be controlled to enable differential lift to be generated between the wings. To steer the Entomopter lift variation through control of the trailing edge blowing will be utilized to provide banking and pitching moments.

The communications system is another example of the implementation of the multiple use philosophy. The communications system will utilize an ultra wide band (UWB) signal for sending signals to and receiving signals from the base vehicle. The type of signal provides large data transfer rates with very low power consumption. In addition to communications, the UWB signal can also be used for obstacle detection, establishing positioning between the Entomopters and the base vehicle and altimetry. Instead of using the communications system, a passive navigation and obstacle avoidance scheme has been devised that utilizes signals sent from the base vehicle to the Entomopter.

This report describes the analytical and computational analyses that have been performed under the NIAC Phase II program to extend the terrestrial Entomopter design foundations begun as GTRI IRAD, DARPA feasibility, and AFRL propulsion developments, into a parallel development scaled and modified for flight in the lower Mars atmosphere.

Chapter 1.0 Introduction

The 1997 Mars vehicle Pathfinder progressed only 52 meters in 30 days because it had to await instructions from Earth 190 million km away. Each command took 11 minutes to travel between the two planets. It couldn't move any faster without risking collision with obstacles. A flying surveyor would serve to expand the area of regard for a ground-limited rover which cannot negotiate large obstacles nor can it venture out into canyons.

During the mid 1990s the Defense Advanced Research Projects Agency began considering the feasibility and uses for tiny terrestrial flying vehicles on the scale of small birds and insects. In response to this interest, the notion of the 'Entomopter' (*entomo* as in entomology + *pteron* meaning wing, or a “winged insect machine”) was borne as an internal research and development (IRAD) program within the Georgia Tech Research Institute (GTRI). The Entomopter will extend a rover's eyes and will allow the rover to choose its path ahead more intelligently. The rover will be able to move more rapidly with less risk. The result will be a greater science return per unit time. With Entomopter augmentation, the field of regard for the rover will be swaths of hundreds of meters for close inspection/sampling, and to the horizon for high perspective line-of-sight remote inspections. In addition, the Entomopters will be able to perform scientific investigations that otherwise could not be attempted by a rover (e.g., cliff side inspections or magnetic profiling), or which would be too time consuming (e.g., wide area geologic characterization such as the mapping fault lines or strata).

The environment on Mars makes the ability to fly conventional aircraft much more difficult than on Earth. The main obstacle is the very low atmospheric density. This low density requires an aircraft to fly within a very low Reynolds number/high Mach number regime unlike any experienced by present day aircraft. This low-density atmosphere translates into flight Reynolds numbers for the wing of around 50,000 and for a propeller of around 15,000. The Reynolds number is a ratio of the inertia forces to the viscous forces for a fluid flow. As a practical matter, if the Reynolds number of two vehicles is similar then the aerodynamics of the vehicles should be similar.

Reynolds Number = (Density)*(Characteristic Length)*(Velocity) / (Viscosity)

With a low flight Reynolds number, a conventional aircraft has a number of aerodynamic issues that severely limit its performance. The main issue is laminar separation of the boundary layer. This separation can cause loss of lift resulting in a catastrophic loss of the aircraft. To avoid this flow separation, the boundary layer must be transitioned from laminar to turbulent. Within low Reynolds number flow it is very difficult (if possible at all) to transition to a turbulent boundary layer. This flow restriction is a major factor that severely limits the flight envelope and capabilities of a conventional aircraft.

Although conventional flight may be difficult under such low Reynolds numbers, insects have succeeded in efficiently exploiting the low Reynolds number flight regime. The mechanisms in insect flight are significantly different of conventional aircraft and are not completely understood. First investigated in 1994 by Charles Ellington at the University of Cambridge, the main mechanism for lift generation on an insect wing was determined to be vortex interaction caused

by the flapping motion. This interaction is dependent on the Reynolds number. As the Reynolds number increases, this lift-producing mechanism diminishes. Experiments have shown that flow on an insect wing at Reynolds numbers greater than 10^6 there is a crisis of flow over the wing caused by early boundary layer separation. As the Reynolds number decreases around 10^4 this crisis is greatly reduced and the flow displays a smoother shape. At Reynolds numbers of 10 to 10^3 flow separation is absent. As the Reynolds number decreases, other lift-producing mechanisms such as differential velocity and drag, and other boundary layer effects may come into play. These Reynolds number effects are a main reason for the difference in the flight characteristics between birds and insects. A diagram of this vortex generation is shown in Figure 1-1. This vortex generation is not completely explained by present theory. However, it is believed that it is caused by the separation of flow over the leading edge of the insect wing. A diagram of the vortex formation is shown in Figure 1-2. [69, 110]]

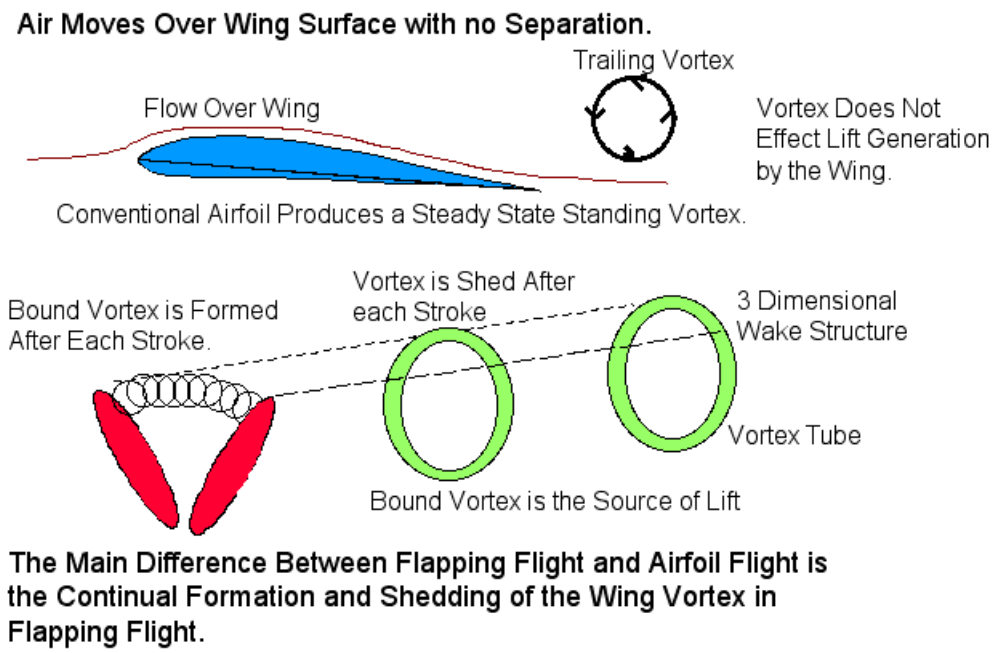

Figure 1-1: Conventional Airfoil and Insect Wing Lift-Generation Mechanisms

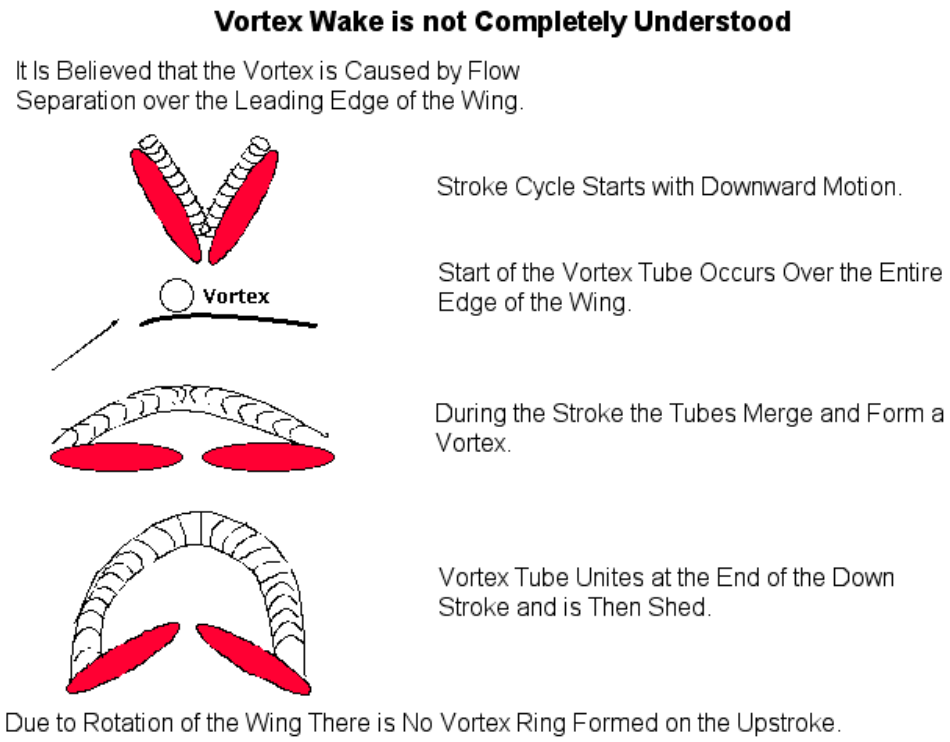

Figure 1-2: Flapping Insect Wing Leading Edge Vortex Formation

Flapping alone is not sufficient to generate the maximum vortex circulation possible for achieving maximum lift. This limit on reaching the maximum circulation levels is due to the flapping rate of the wings and the time delay required for the growth of the vortex circulation. It is believed that insects overcome this issue by the interaction of the insect wing with the vortex as it is shed. Unlike conventional airfoils, there is no dramatic reduction in lift after the wing achieves super critical angles of attack. This suggests that flow separation prior to the vortex formation does not occur. It is believed that this resistance to flow separation during vortex formation is due to the low flight Reynolds number and the high wing flap rate of 10^{-1} to 10^{-2} seconds. An additional lift producing mechanism that insects take advantage of is the Magnus force. This is the force generated due to the rotational motion of the wing during each flap. This force is most widely known for its effect in producing a curveball in baseball. Insect flight control is achieved by controlling these lift-producing mechanisms from wing to wing. Based on these mechanisms insects are capable of achieving lift coefficients on the order of 5. This high lift coefficient and the forces that are used to generate it are what allows them to fly in a manner that is different from conventional aircraft or birds. It also gives them the ability to hover, rise vertically and change direction instantly. A diagram of the lift produced through a stroke of an insect's wings is shown in Figure 1-3.[69, 110]

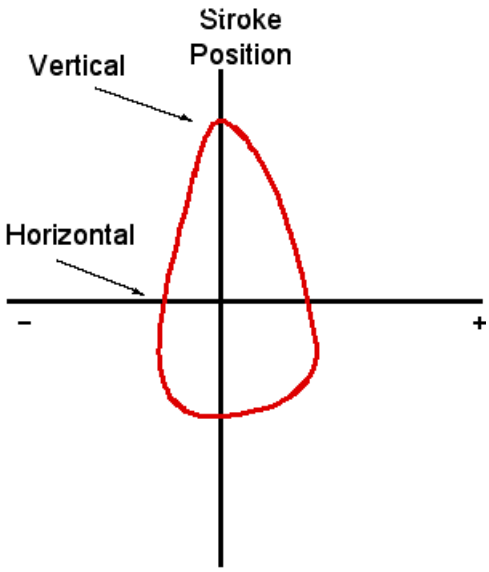

Lift is 0 at the beginning of the stroke.

Increases and achieves its extreme value in the second half of the downstroke.

Begins to lessen at the end of the down-stroke.

Becomes negative throughout the upstroke.

Figure 1-3: Insect Wing Lift-generation

An Entomopter on Mars, with an approximate 1-meter wingspan, would be operating with a Reynolds number similar to that of terrestrial insects. Flight within the Mars environment can take advantage of the lift-producing mechanisms of insects with a vehicle of significant size and operating close to the surface. This combination of physics and environmental conditions may lead to an elegant way of producing an aircraft to fly on Mars. Mars has an additional advantage in that the gravitational force is a third of that on Earth. This reduced gravity enables thinner, lighter structures to be used, which can be an important factor in the feasibility of this concept.

If achievable, an Entomopter on Mars would have the ability to take off, land, and hover--a significant mission enhancement over conventional aircraft. This flight capability is a consequence of the flapping wing flight mode and the ability to control the enormous lift-generating capacity of the vortex described above.

1.1 History of Mars Flight

Mars has been a target of scientific exploration for more than twenty-five years. Most of this exploration has taken place using orbiting spacecraft or landers. Orbiters offer the ability to image large areas over an extended period of time, but are limited in their resolution. Landers can handle surface and atmospheric sampling, but are limited to the immediate landing site. Mobility is the key to expanding the scientific knowledge of Mars. The Pathfinder/Sojourner mission offered a new opportunity in that it was the first time that an autonomous mobile platform could be used for exploration. This allowed scientists the freedom to explore the surrounding terrain, maneuver to interesting sites, and perform an analysis of soil and rock composition over a broader area. In short, the scientific community has many more options. However, the

surface rover is limited by the terrain it is traversing: large rocks and canyons are obstacles which are difficult for a surface rover to overcome.

Airborne platforms can achieve science objectives that are difficult to achieve from orbit or from surface rovers. They can cover much larger distances in a single mission than a rover and are not limited by the terrain, much more easily providing imaging of very rocky or steep terrain. Airborne platforms can return images of a magnitude higher resolution than state-of-the-art orbiting spacecraft. Near infrared spectrometry, which is crucial to analyzing mineralogy on the planet, and high spatial resolution magnetometry, which may provide clues as to the origin of high crustal magnetism seen from orbit, require moving platforms. The resolution and sensitivity of these instruments is further increased by being close to the surface. Finally, atmospheric sampling can be accomplished over a far greater space, allowing scientists to study variations over a broad area.

The notion of flight on Mars has been a subject of NASA contemplation since Werner von Braun conceived a rocket plane as a means of Mars exploration in 1953. In the 1950s, Mars flight was purely fancy, but in the 1970s it was revisited more seriously, being spurred on by the successes of the Viking Program.

One of the most studied airborne platforms for Mars is the airplane, with initial concepts dating back to the late 1970's. Flying an airplane on Mars represents a significant challenge, mainly because of the constraints posed by the Mars environment. The lift on a wing is proportional to the atmospheric density, velocity, and wing area. The Mars atmospheric density is extremely low, approximately 1/70th that at the Earth's surface. In order to compensate for this, the wing area and/or the velocity must be increased to generate sufficient lift. Wing area, however, is limited by packing, volume, and deployment constraints. Therefore, in order for flight to be feasible on Mars, the plane must travel at higher velocities to compensate for the lack of density and the constrained wing area. Also, the speed of sound on Mars is approximately 20% less than on Earth. Both of these factors combine to put the plane in a low Reynolds number, high Mach number flight regime which is rarely encountered here on Earth. The high velocities limit imaging camera stability and resolution. Also, given the rocky Mars terrain, it is virtually impossible for a plane to land and take-off again, thus limiting a mission to a single flight.

The NASA Dryden Research Center, Developmental Sciences, Inc., and the Jet Propulsion Laboratory (JPL) proposed unmanned aircraft designs for Mars exploration in 1977 and 1978. Their concept was a propeller-driven fixed wing aircraft fueled by hydrazine. This aircraft was based on the Mini-Sniffer high altitude aircraft shown in Figure 1-4. A prototype of this aircraft was constructed and some testing was performed (Figure 1-5).

Examples of Aircraft Concepts for Mars Flight

Figure 1-4: Mini-Sniffer High Altitude Aircraft

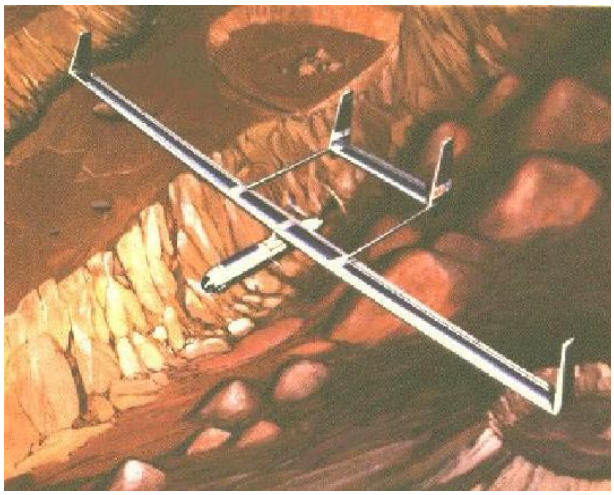

Figure 1-5: Solar-Powered Mars Aircraft

A decade later, JPL sponsored a Mars airplane study in which Aurora Flight Sciences proposed the electrically propelled “Jason” aircraft. About the same time, Ames Research Center and Sandia National Labs conceived a high speed aerospace plane named AEROLUS. Unlike the earlier attempts to make a slow speed aircraft that would be deployed from an aeroshell after touchdown on the Mars surface, AEROLUS would make a direct atmospheric entry and then fly through the Mars atmosphere at hypersonic speeds. To date, neither the Jason nor the AEROLUS projects have been embraced by NASA's Mars exploration program.

Throughout the 1980's and early 1990's, a number of studies were conducted looking at various approaches to flight on Mars. These studies were conducted by NASA and various universities. An example of some of this work was the solar powered Mars aircraft studied by NASA. (Artist's concept Figure 1-5.)

Successes with the Mars Pathfinder and Global Surveyor programs renewed interest in Mars flyers for exploration. In 1995 NASA Dryden and Ames Research Centers once again considered unmanned aerial vehicles to extend the reconnaissance range of Mars landers. The new concept was to launch a small unmanned aerial vehicle (UAV) from the lander after it had stabilized on the surface. The UAV would provide video of the immediate vicinity of the lander (within several thousand meters) to provide feedback as to the most interesting areas for investigation by ground-based rovers. The expendable, one-flight UAV would be electrically powered with rocket assisted takeoff.

The following year in 1996, the Ames Research Center proposed an unmanned Mars aircraft in response to a NASA Announcement of Opportunity for Discovery Exploration Missions. Ames' approach was to use a propeller driven, sailplane configuration which they called “Airplane for Mars Exploration” (AME). It was not, however, selected for the Discovery mission.

On the following NASA Announcement of Opportunity for Discovery Exploration Missions in 1998, JPL submitted a proposal for a multiple glider system (dubbed “Kitty Hawk”) wherein several areas could be investigated during a single mission (Figure 1-6). Being gliders, the vehicles were obviously limited in endurance, but benefited from the lack of weight and complexity associated with a propulsion system in return for redundancy of numbers. NASA Ames also submitted a proposal to the 1998 Announcement for a motorized UAV named “MAGE” (Figure 1-7). This aircraft was based on a similar hydrazine propulsion system as the Mini-Sniffer concept. Both concepts deployed from an aeroshell once it had become subsonic, approximately 12,000 meters above the Mars surface. Again, neither concept was selected for the Discovery mission.

Recently Proposed Mars Aircraft

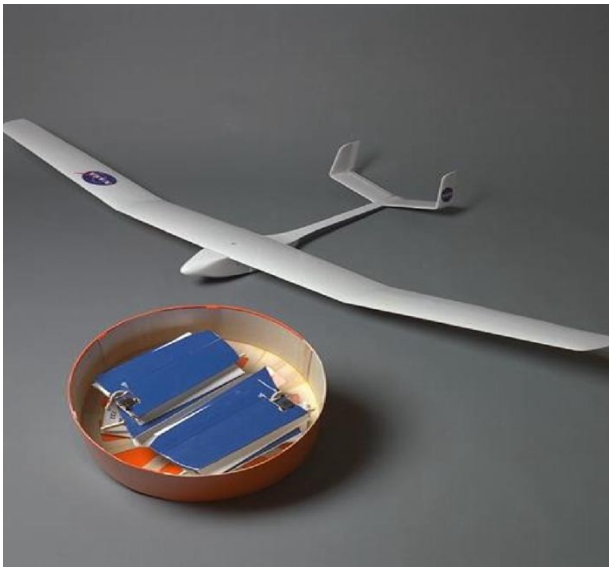

Figure 1-6: JPL “Kitty Hawk” Glider

Figure 1-7: Ames “MAGE” Aircraft

On February 1, 1999, NASA Director Daniel Goldin announced the “Mars Airplane Micromission,” which would have been the first NASA micromission program to launch on an Ariane 5 rocket. The flight would have had the first Mars airplane arriving on the Red Planet around December of 2003, coincidentally close to the hundredth anniversary of the Wright Brothers' first flight. Although conceptual designs of the plane were completed, the project was cancelled due to funding constraints.

1.2 Origins of the Entomopter Concept

The terrestrial Entomopter is a multimode autonomous robot capable of flight, ambulatory locomotion, and swimming behaviors in a single vehicle. Autonomous navigation is based on a combination of attraction and avoidance behaviors deriving input from both an integrated optic-olfactory sensor for detection of chemical species (or, alternatively, a sensor for a specific type of radiation), and an ultrasonic swept beam ranging device.

Designed as the answer to indoor flight operations, the flapping wing was chosen as the best approach. Other modes of locomotion (crawling or swimming) are based on the same actuation

system as that used for flapping wing flight, but they do not involve the complexity, precision, or energy expenditure associated with flight.

Terrestrial Entomopter feasibility was established under contract to the DARPA Defense Sciences Office Mesomachines Program, where it is referred to as a Mesoscaled Aerial Robot (MAR). The Air Force (AFRL) then issued a contract under its Revolutionary Technology Program to extend the flight muscle into the fourth generation of size reduction and performance enhancement. Of particular interest to the Air Force and others is the potential for swarms of Entomopter vehicles to rapidly penetrate denied areas, such as deeply buried underground facilities. This is possible because of the Entomopter's size, multimode locomotion, and anaerobic propulsion system, which allows covert ingress through sewer pipes, ducts, or electrical conduits.

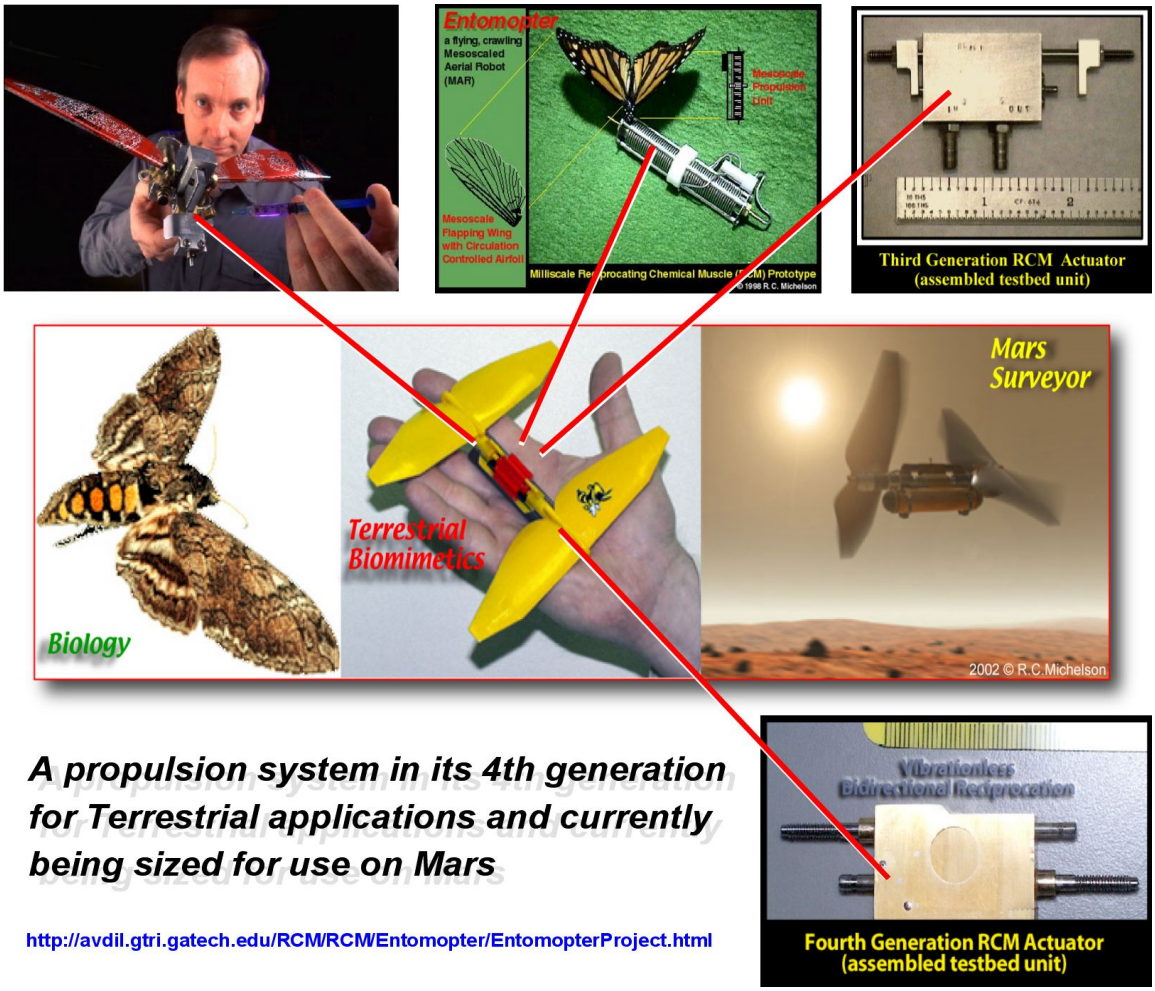

A propulsion system in its 4th generation for Terrestrial applications and currently being sized for use on Mars

http://avdil.gtri.gatech.edu/RCM/RCM/Entomopter/EntomopterProject.html

Figure 1-8: Generations of the Reciprocating Chemical Muscle Actuator and the Biologically-inspired Wing that it Drives for Applications on Earth and Mars

Interestingly, the terrestrial Entomopter would find potential in other applications beyond Earth. Present planetary surface rovers were found to have shortcomings that could be addressed by a slow flying aerial platform... but flight on Mars is complicated by the fact that the atmosphere is

rarefied, thereby making it difficult to generate lift with conventional wings. In fact, fixed wing vehicles must have enormous wings and travel at significant speeds to stay aloft in the Mars atmosphere. Fixed wing Mars flyers must traverse the surface at speeds in excess of 300 mph, making it difficult to land on the unprepared surface for sampling, or refueling.[44] Turn radii are on the order of kilometers, making it inefficient to return to points of interest, and high speed traverse across the surface at lower altitudes causes smearing of sensor data, thereby negating any beneficial increase in resolution that may have otherwise been gained.

The NASA Institute for Advanced Concepts (NIAC) funded a Phase I program in 1999 to study the Entomopter for use as an aerial Mars surveyor for exploration. This was expanded into a more detailed Phase II study in 2001. NASA personnel recognized the Entomopter's ability to fly in low Reynolds number conditions without the need for air-breathing propulsion made it a natural candidate for flight in Mars' rarefied atmosphere, albeit in a larger incarnation. Unlike fixed wing flyers, an entomopter-based Mars surveyor would be able to cover a wide area while still being able to fly slowly, land, crawl, obtain surface samples for analysis, and return to a refueling rover. As of this writing, two patents have been issued for the Entomopter concept, and the reciprocating chemical muscle that is integral to the Entomopter's operation.

The Entomopter began as a biologically inspired design, but rather than attempting to replicate biological kinematics and aerodynamics, improved systems have been devised to leverage what is observed in biological systems to produce a machine that is manufacturable, controllable, and able to generate the power necessary to fly from onboard energy sources. Just as wheels are superior locomotors under certain circumstances but are not a common form of locomotion for biological systems, so the Entomopter has extended its design beyond the biological baseline in some areas.

The Hawk Moth (Manduca *sexta*) was chosen as a baseline model for the wing aerodynamics. The University of Cambridge in England was part of the initial Entomopter design team because it had studied Hawk Moth wing aerodynamics for more than a quarter of a century and had produced seminal works describing the Leading Edge Vortex (LEV) and its effects on the flapping wing [78, 265, 281, 280, 166] The flapping mechanism for the Entomopter has been extended beyond that of the Hawk Moth to provide a resonant single-piece construction that takes advantage of torsional resonance in the Entomopter fuselage to recover flapping energy common to flying insects that temporarily store potential energy in either muscles or exoskeletal parts (resilin).

In the terrestrial version, the same structure that provides wing flapping also scans a frequency modulated continuous wave (FMCW) ultrasonic beam to provide front, side, and down-looking range measurements for obstacle avoidance and altimetry. It also has the potential to track and follow free-moving agents in a fashion similar to that employed by bats.

Stability and control in flight as well as navigation are achieved by actively modifying the lift of each wing on a beat-to-beat basis using pneumatic control of the air circulating over the beating wing. Also, as demonstrated in GTRI's wind tunnels, where pneumatically controlled wings have been shown to develop positive lift at negative angles of attack (α) as great as -70° [83,

84], Entomopter wings (unlike those of the Hawk Moth) should be able to generate positive lift not only the downbeat but the upbeat as well.

These wind tunnel tests have shown that coefficients of lift exceeding the theoretical maximum by 500% for the given wing shape can be achieved without the complexity of active angle-of-attack modulating mechanisms.

A chemically fueled reciprocating chemical muscle has been designed and is in its fourth generation of development at the time of this writing. This actuator system has demonstrated 70 Hz reciprocation rates with throws and evolved power levels necessary to support flight, crawling, or swimming of a self-contained fully autonomous Entomopter system [187]. The reciprocating chemical muscle uses the energy locked in various chemical fuels to produce reciprocating motion for propulsion as well as waste gas products for the operation of gas bearings, an ultrasonic obstacle avoidance ranging system, and full flight control of the vehicle.

1.2.1 Why Flapping Wing Flight?

Rotary wing vehicles have been proposed as a method for achieving slow controlled flight in the Mars atmosphere while allowing takeoff and landing. Unfortunately, the rarefied atmosphere brings with it a lower speed of sound. Rotor tips rapidly exceed the speed of sound at rotational speeds that are insufficient to lift the vehicle. This has forced those considering such an approach to use multiple smaller diameter articulated rotors or variable speed propellers. The redundancy of transmissions, motor casings, control mechanisms, and the structure to support the multiple rotor system are at the expense of performance (added weight). In addition, those techniques that rely on pitch changes in the rotor or the vehicle's fixed propeller's angle of attack, result in unwanted blade stall conditions due to the sensitivity of the low Reynolds number flow over these critical airfoils. This makes horizontal translation of the vehicle difficult. Tests of a small unarticulated propeller in JPL's Mars atmosphere simulation chamber produced lift, but performance was disappointing compared to that which was originally predicted.[146]

Another way to move air over a wing without fuselage translation is to move the wing relative to the fuselage and the surrounding air in a flapping motion rather than a rotary one. It could be argued that a flapping wing implementation is an inherently lower bandwidth system than one using a helicopter rotor or fixed pitch fans. Both systems require cyclic (once-per-flap or once-per-revolution) control inputs to maintain vertical lift and stability, but the frequencies at which these inputs must be generated can be much lower for comparably sized flapping implementations. Because of the lower flapping frequencies required of a lower aspect ratio wider chord wing as opposed to a narrow high aspect ratio rotor, the tips do not approach supersonic speeds.

The lift of a flapping wing can be superior to that of a fixed or rotary wing, however it is still not optimal based on any conventional wing shape when operating in the atmosphere of Mars. Techniques such as active flow control of blown wing surfaces offer the potential to create significant added lift, thereby making a blown flapping wing plausible as a method for achieving relatively slow controlled flight in the lower Mars atmosphere. This can be done by "blowing" the surfaces of the wing to keep flow attached and to increase lift in an intelligent manner by using an internally-generated pressure source. This has been demonstrated in manned aircraft and certain

experimental unmanned vehicles, but is typically inefficient unless there is a source of gas pressure already available (such as bleed air from a gas turbine engine).

Flapping wings are more survivable and robust in the presence of foreign object damage (FOD) and grazing impacts than rotary wings. The flapping wing operates over a range of energies from zero at the top and bottom of the stroke, to maximum at mid-flap. Rotors and propellers on the other hand, concentrate all of their energy at their rotational frequency and tend to explode when coming in contact with objects. It is a well documented fact that birds and insects are able to sustain collisions with walls (or one another) without major damage when they become trapped indoors.

Further, the reciprocating nature of flapping wings lends itself to resonant operation with its accompanying energy efficiencies. Rotors can not be resonant in rotation and rotary wing designs tend to avoid resonance rather than capitalizing upon it. It should be noted that all insects store energy in a substance called “resilin” to recapture flapping energy in a resonant fashion. [188]

There is another reason to consider flapping wing flight, and that is due to the leading edge vortex phenomenon. Recently, flow visualization studies on the Hawk Moth Manduca *sexta* and a 10x scale mechanical model have identified dynamic stall as the high-lift mechanism used by most insects [281]. During the downstroke, air swirls around the leading edge of the airfoil and rolls up into an intense leading-edge vortex (LEV). The direction of circulation in the LEV augments the bound vortex and hence the lift. LEV grows until it becomes unstable at a distance of three to four chord lengths at which time it breaks away from the wing causing deep stall. Ellington and associates have shown that a strong axial (spanwise) flow in the LEV, when coupled with the swirling motion of the vortex, results in a spiral LEV with a pitch angle of 46 degrees across the surface of the flapping wing [78, 265, 266, 281]. The axial flow convects vorticity out toward the wing tip, where it joins with the tip vortex and prevents the LEV from growing so large that it breaks away. Thus stabilized, the LEV prolongs the benefits of dynamic stall for the entire downstroke. Helicopter rotors also experience spanwise pressure gradients, but these beneficial large-scale axial flows have not been observed [53], leading one to surmise that resonant flapping wing solutions in the rarefied Mars atmosphere will be more successful in producing required lift than nonresonant rotary wing attempts.

During the mid 1990s the Defense Advanced Research Projects Agency began considering the feasibility and uses for tiny terrestrial flying vehicles on the scale of small birds and insects. In response to this interest, the notion of the 'Entomopter' (*entomo* as in entomology + *pteron* meaning wing, or a “winged insect machine”) was borne as an internal research and development (IRAD) program within the Georgia Tech Research Institute (GTRI).

Nothing in creation exhibits fixed wing flight behavior or propeller-driven thrust. Everything that maintains sustained flight, uses flapping wings. Even though there has been considerable analysis in the literature of mechanisms for bird flight [73] and insect flight [13, 29], and ornithopter-based (bird flight) machines have been demonstrated, the unsteady aerodynamics of blown flapping wings is an absolutely new area of research and the work performed to date by GTRI's terrestrial Entomopter design team has been pioneering (Figure 1-9)

The unique potential of the terrestrial Entomopter with its high lift mechanisms were recognized to have use in slow speed controlled flight through the lower Mars atmosphere, and the NASA Institute for Advanced Concepts subsequently funded both a Phase I and Phase II study to explore the Mars application further.

Figure 1-9: Stereolithographic Kinematically-correct Model of the Terrestrial Entomopter

The Entomopter will extend the rover's eyes and will allow the rover to choose its path ahead more intelligently. The rover will be able to move more rapidly with less risk. The result will be a greater science return per unit time. With Entomopter augmentation, the field of regard for the rover will be swaths of hundreds of meters for close inspection/sampling, and to the horizon for high perspective line-of-sight remote inspections. In addition, the Entomopters will be able to perform scientific investigations that otherwise could not be attempted by a rover (e.g., cliff side inspections or magnetic profiling), or which would be too time consuming (e.g., wide area geologic characterization such as the mapping fault lines or strata).

1.3 Mission

1.3.1 Mission Introduction

Mars has been a target of scientific exploration for more than 25 years. Most of this exploration has taken place using orbiting spacecraft or landers. Orbiters offer the ability to image large areas over an extended period of time but are limited in their resolution. Landers can handle surface and atmospheric sampling but are limited to the immediate landing site. Mobility is the key to expanding the scientific knowledge of Mars. The Pathfinder/Sojourner mission offered a new opportunity to scientists; it was the first time an autonomous mobile platform could be used for exploration. This allowed scientists the freedom to explore the surrounding terrain, maneuver to scientifically interesting sites, and perform an analysis of soil and rock composition over a broader area. In short, it offered many more options to the scientific community. However, the terrain it is traversing limits the rover: Large rocks and canyons are difficult obstacles for a surface rover to overcome. [245, 246]

Airborne platforms can achieve science objectives difficult to reach from orbit or from surface rovers. Platforms can cover much larger distances in a single mission than a rover and are not limited by the terrain; much more easily providing images of very rocky or steep terrain. Air-

borne platforms can return images of more than a magnitude higher resolution than state-of-the-art orbiting spacecraft. Near infrared spectrometry, crucial to detecting mineralogy on the planet, and high spatial resolution magnetometry, which may provide clues as to the origin of high crustal magnetism seen from orbit, require moving platforms. Being close to the surface also increases the resolution and sensitivity of these instruments. Finally, atmospheric sampling can reveal variations over a much greater area. [182,49,175]

The Entomopter concept provides a unique means of achieving flight on Mars without the constraints imposed by the environment on conventional aircraft. The Entomopter can fly slowly near the surface, land, and take off. This capability enables the Entomopter to accomplish missions that are not possible with fixed wing aircraft. The ability to land on the rocky surface of Mars enables the Entomopter to refuel, which greatly extends mission duration over that of conventional aircraft. The slow flight of an Entomopter with ground locomotion affords the possibility of landing on the surface of Mars to inspect objects and take samples, to rest during periods of communication blackout and adverse weather, and to harvest energy from the environment.

Because of these unique flight capabilities a number of mission scenarios can be conceived for an Entomopter vehicle system. Utilizing these capabilities with a variety of instruments, scientists can collect significant science data that would be impossible to acquire with any type of present-day exploration vehicle.

1.3.2 Mission Architecture

Based on the analysis done under the Phase I portion of the program, it was determined that utilizing the Entomopter in conjunction with a rover would return the most science date and provide the greatest flexibility. Therefore, this architecture was established as the baseline mission profile.

In this scenario, a rover containing two or more Entomopters lands on the surface. The rover and Entomopters leave the aeroshell-lander and begin to explore. The aeroshell-lander is a transport capsule and has no additional capabilities. The Entomopters communicate with the rover, which in turn relays the data to an orbiting communication system. The Entomopters can assist the rover in terrain navigation as the group slowly moves across the surface. The Entomopters would be able to dock with the rover for recharging; their range would be limited to the round trip distance to and back from the rover. This mission sequence is shown in Figure 1-10.

The main advantage of this type of system is that new territory can be explored each day by the Entomopters as their home base, the rover, slowly moves along the surface. The rover would carry fuel to refuel the Entomopters after each flight. The mission would continue until the fuel within the rover is exhausted.

A diagram of a potential mission scenario is shown in Figure 1-11. This figure represents four Entomopter flight vehicles flying to and from a rover. The flight-duration profile represents the flight and ground time for the Entomopter throughout the return trip to and from the rover. This is one example of the flight profile. The combination of ground and flight segments can be

altered and distributed differently to account for investigating varying points of interest along the flight path.

The science instruments the Entomopter can carry will depend on their weight and volume. However, each Entomopter can carry a different science instrument payload. This adds overall versatility to the mission. There is also the potential that the science payloads can be changed out while the Entomopter is on the rover. This would enable the science-gathering capability to be tailored to a specific geographic location or objective and to adjust as the mission progresses and new data is gathered.

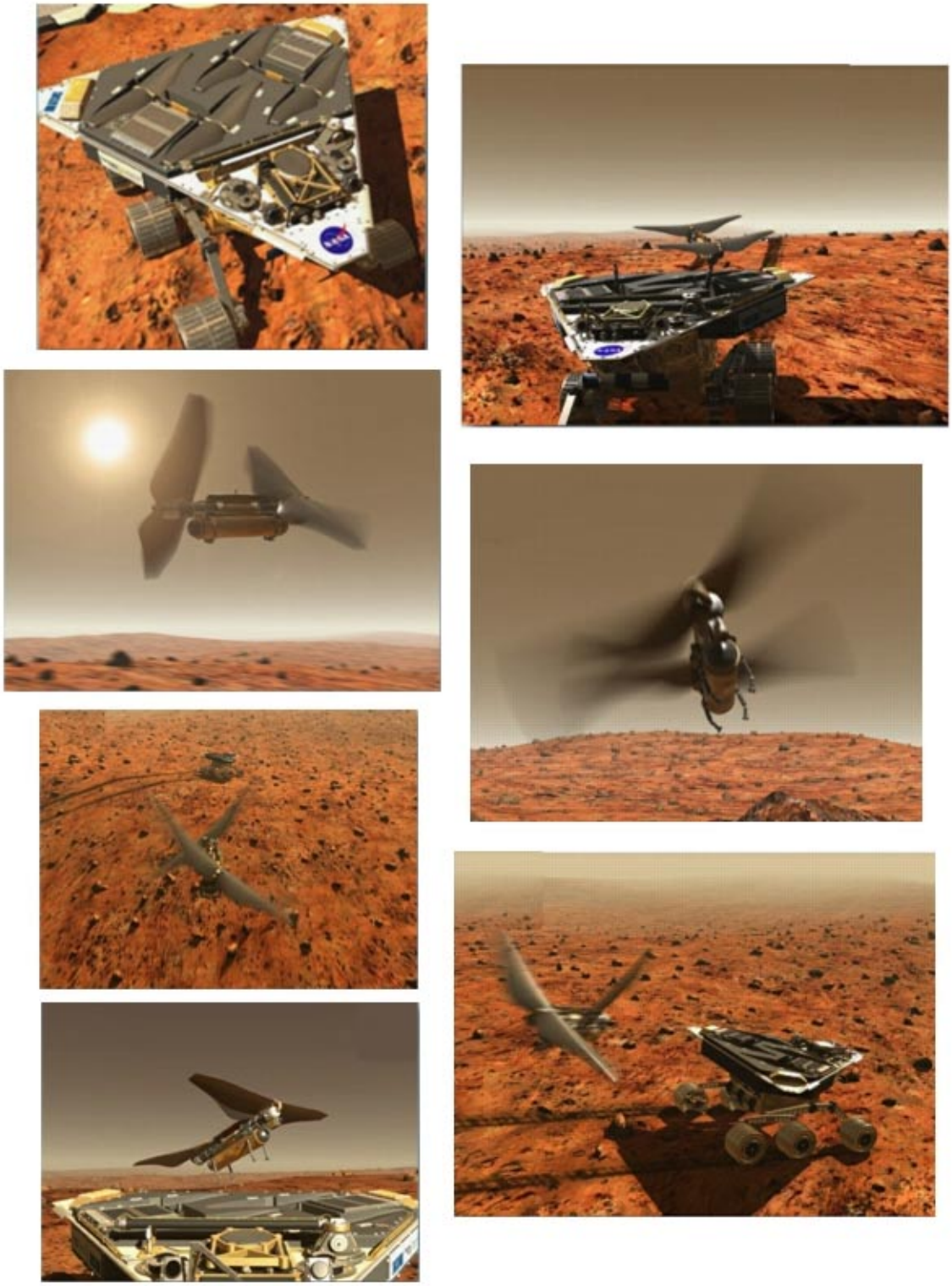

Figure 1-10: Animation of Entomopter Mission (Take off, Flight, Sample Gathering, and Return to the Lander)
[87]

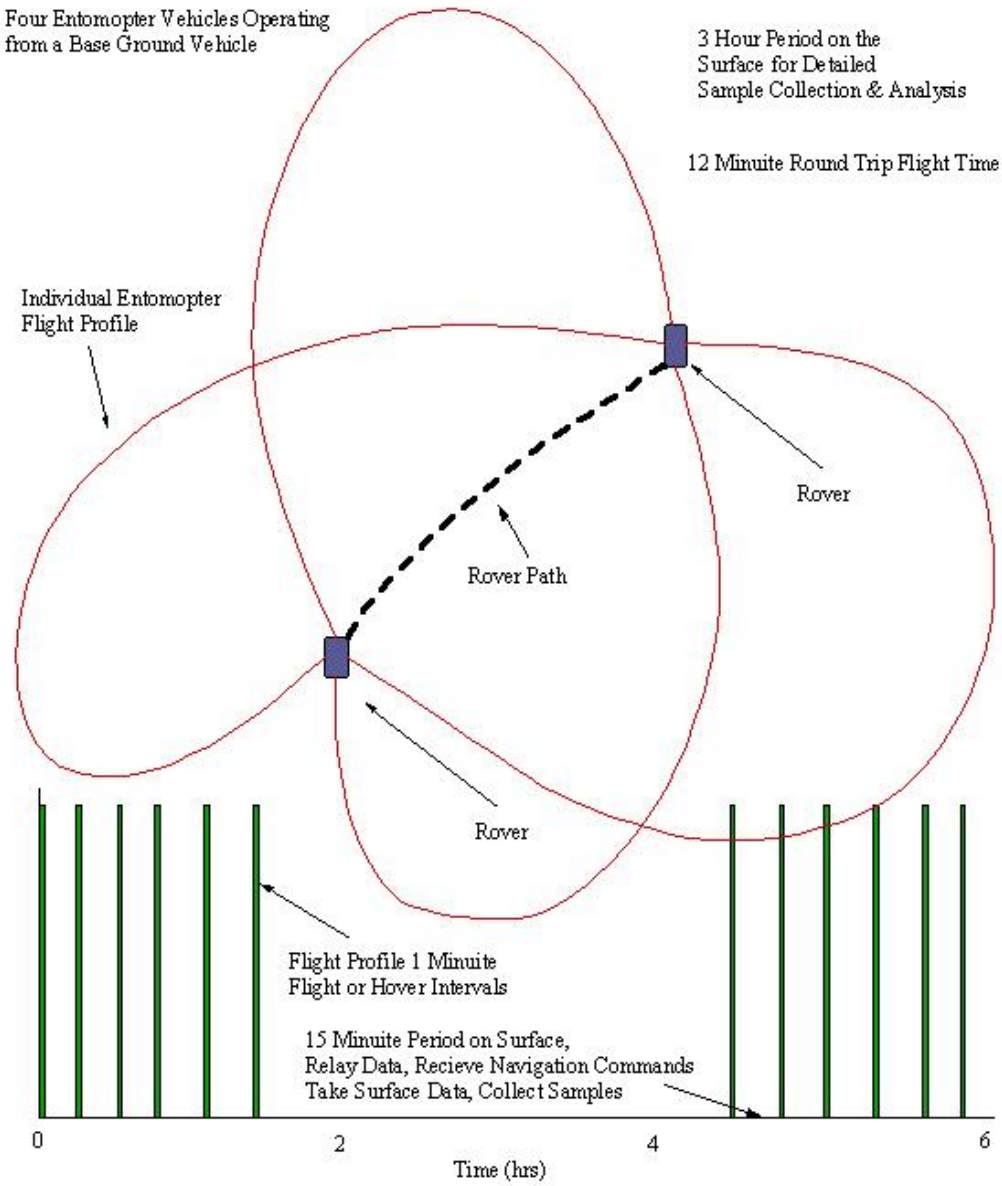

Figure 1-11: Mission Flight Profile for Multiple Entomopters in Conjunction with a Rover

1.3.3 Science Application

Probably the most obvious and potentially useful science application for the Entomopter is as an airborne observational platform. The types of imagery that can be taken from the Entomopter include high-resolution imagery, global surveillance imagery, and multi-spectrum imagery.

1.3.3.1 Surface Imaging

Figure 1-12: High Resolution Image of Mars Surface Taken by Pathfinder Lander

The Entomopter vehicles can enable ultra-high resolution imaging (on the order of centimeters resolution) over extensive areas, similar to the type of images acquired by landers or rovers. An example of a high resolution surface image is shown in Figure 1-12. This type of data can make possible recognition of individual rocks and specific land features. It can also aid the identification of areas for further examination by the rover. High resolution imaging is also valuable for interpreting the geologic history of a region and examining Aeolian, hydrothermal, aqueous, volcanic, cratering, tectonic, and other processes based on their geomorphology. High resolution imagery can also be valuable in examining layers in crater walls and hydrothermal system associated with volcanoes and impact craters. In addition, data collected by other science instruments, such as magnetic and neutron observations, can be correlated with local geologic features.

The Entomopter can enable the acquisition of high resolution compositional information on surface rocks using infrared spectroscopy and other techniques that can take advantage of observation elevations from a few hundred meters to a few kilometers and collect measurements at the meter-spatial resolution. Mineralogy is directly related to the formation environment of rocks. Thus locating key mineral deposits is central to locating sites that may have allowed life to thrive on early Mars and to understanding the chemical evolution of the Mars surface and atmosphere.

In past science missions, imaging has provided the most beneficial planetary science and contributed to the most planetary science discoveries that have been made. Based on previous results of exploration missions, it can be inferred that the higher the resolution of the imagery the greater the science value and discoveries that are made. The Entomopter vehicle is ideally suited for producing high resolution imagery. Its flight speed is slow, and it can fly near the surface, enabling very high resolution and very good perspective of the terrain.

The Mars Orbiter Camera on the Mars Global Surveyor spacecraft can achieve 1.5 m/pixel images of the surface. This compares to the Viking Orbiter resolution of 200 m/pixel. This 100-fold increase in resolution has greatly increased our understanding of Mars. With the Entomopter, we can achieve resolutions on the order of 0.01 m/pixel, a 100-fold improvement over

the Global Surveyor. This type of resolution will allow the study of weathering processes, erosion, surface material composition, and a number of other environmental and geological processes on Mars.

The complete range of surface imaging can be achieved with two separate cameras:

- A camera can take images of the surface at high resolution.
- A lower resolution, wide angle camera can provide context for these images so that they can be related to observations from orbiters. An example of this type of image is shown in Figure 1-13.

Figure 1-13: Example of a Wide-Angle Context Camera-type Image

The purpose of the low resolution, wide angle camera (context camera) is to provide a context for which low resolution orbital imagery can identify where the Entomopter is taking data and pictures. Also, the picture has to be of a high enough resolution so that the high resolution camera images can be found within the picture. This staging of picture resolutions from orbital to wide angel context imagery to high resolution imagery enables the detailed high resolution images to be referencable to a global view of the terrain. Orbital imagery of Mars can presently achieve about 1 m/pixel to 3 m/pixel. Based on this, the context camera with a resolution of 0.15 m/pixel (6:1 ratio) should be sufficient to place the high resolution imagery (at 0.01 m/pixel) within the context of the orbital spacecraft pictures. For very closeup imagery (such as imaging a specific rock or the strata on a cliff), the ability to place the high resolution image into the global imagery may not be possible. However, the context camera can at a minimum place the detailed image in the general area in which it was taken. This ability to reference the imagery to a global scale is vital to having the Entomopter data aid in the overall understanding of the planet.

1.3.3.2 Magnetic Field Mapping and Investigation

Strong remnant fields have been identified from orbital observations of the Mars surface. The Entomopter provides an ideal platform to investigate these fields. Because of its flight altitude on the order of 10s of meters, the Entomopter can provide both the spatial resolution and the signal strength for detailed magnetic field mapping. The information gathered by studying impact

craters' magnetic signatures, can lead to a greater understanding of the early history of magnetism on Mars. Also, by identify young craters in older terrain and mapping the magnetic fields around these craters, information relevant to the thermal evolution of the planet can be obtained. The history of Mars' magnetic field may be an important link for understanding the radiation environment due to the early sun's solar wind.

From previous scientific investigation, it is know that the magnetism of Mars varies greatly over the planet's surface. It is very highly magnetized at certain locations (an order of magnitude greater than the magnetic field strength on Earth, and at altitudes an order of magnitude higher than on Earth, greater than 1,500 nT at 100 km altitude, and greater than 250 nT at 400 km altitude), and weakly magnetized at others. The locations of the strong magnetic fields correspond with some of the older and highly cratered areas of Mars.

Presently there is no active mechanism for forming a uniform magnetic field (as on Earth). Because of this lack of a planetary magnetic field, it is much easier to measure the crustal magnetization directly. This crustal magnetization can exceed several Gauss (200,000 nT). The magnetic landscape of Mars was first discovered by the Mars Global Surveyor spacecraft. This spacecraft measured many large scale, highly magnetic locations on the surface of Mars, many extending over hundreds of kilometers. However, due to the distance from the surface, small scale variations in the magnetic fields, which are believed to exist could not be discerned. The Entomopter can be used to investigate these magnetic field regions and provide high resolution data on the magnetic field strength variations within these regions. An example of the differences between the magnetic fields on Mars and Earth are shown in Figure 1-14.

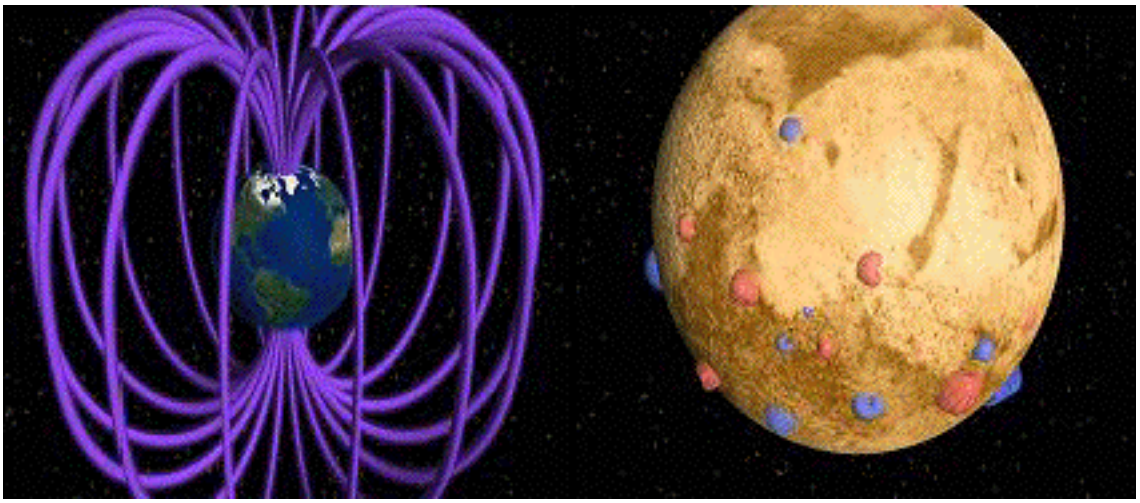

Earth Magnetic Field Mars Magnetic Field

Figure 1-14: Magnetic Field Shape on Earth and Mars

The magnetic field mapping done by the Entomopter would enable a greater understanding of the crustal magnetism on Mars. For this to be accomplished, it would require that measurements of the magnetic field be performed with enough spatial resolution to relate magnetism to specific geologic features and structures. With the Entomopter, the spatial resolution on these measurements would be less than 1 m, orders of magnitude greater than what is achievable from orbit.

The magnetic field mapping requires use of a three-axis magnetometer. The magnetic field sensor would need to be mounted in a location that minimizes magnetic field contamination from other systems or instruments on the Entomopter. To minimize the magnetic signature of the Entomopter, it should have as little magnetic materials within it as possible. Also, any magnetic field-inducing devices (such as the power generation system) will have to be shielded and/or properly grounded to minimize the magnetic field effects. The mass and power of this type of device is on the order of 0.2 kg and 150 mW, respectively.

1.3.3.3 Near Infrared and Neutron Spectroscopy

The distribution of water (ice or liquid) is vital to the search for life. Neutron spectroscopy is a powerful technique for detecting an excess of hydrogen to a depth of about a meter. Such a technique can be implemented from orbit but has a resolution of several hundred kilometers. From the Entomopter platform, the spatial resolution is several orders of magnitude better, so the potential exists for locating kilometer-sized bodies or much smaller.

Mineralogy is a key tool for investigating the formation and geologic history of Mars. Near infrared spectroscopy can be used to provide data on the mineralogy of Mars. This includes measuring the pH, abundance and phase of water, atmospheric chemistry, temperature, and surface pressure. It can also be useful in examining the geologic processes of the planet, such as sedimentation, volcanism, and hydrothermal alteration.

Mineral makeup can be determined through near infrared absorption and spectroscopic evaluation. This technique has been widely used in the past both on Earth and for planetary exploration. (It was used on Phobos to determine surface-mineral composition.) Near infrared spectroscopy (at the wavelengths between 0.7 mm and 2.5 mm) can provide information on soil makeup and identify materials such as iron oxides, iron oxyhydroxides, carbonates, clays, olivines, and pyroxenes, as well as establish their degree of crystallinity. This type of science will allow the detection of these minerals and their abundance in the soil.

The objective of any near infrared spectroscopy investigation should be to link the mineralogy with specific geologic formations on the planet (imagery), thereby providing a more detailed understanding of the geologic processes of the planet.

The ability to perform imaging spectroscopy from the Entomopter vehicle probably will not be possible (unless there are significant advances in sensor technology). Therefore, non-imaging spectroscopy would be the applicable choice for this type of data collection. However, to get useful data from a non-imaging spectroscopy system, it would need to be closely integrated with the camera imaging.

1.3.3.4 Radar Sounding

Radar sounding can investigate subsurface structure and search for buried ground ice and subsurface water. This type of exploration from orbiting space craft has been proposed, but by performing this from 100 m or so above the surface, increased spatial and depth resolution can be achieved. Aerial radar sounders have a proven capability to detect subsurface water beneath glacial ice at a depth of up to 4 km with more than 100 subglacial lakes identified in Antarctica.

Significant miniaturization will be needed for radar sounders to be compatible with the Entomopter vehicle; however, because of its close proximity to the surface, the power required by this device will be minimized. This type of sounding is similar to what is proposed for the European Space Agency's Mars Express orbiter. This type of data collected in this manner is shown in Figure 1-15.

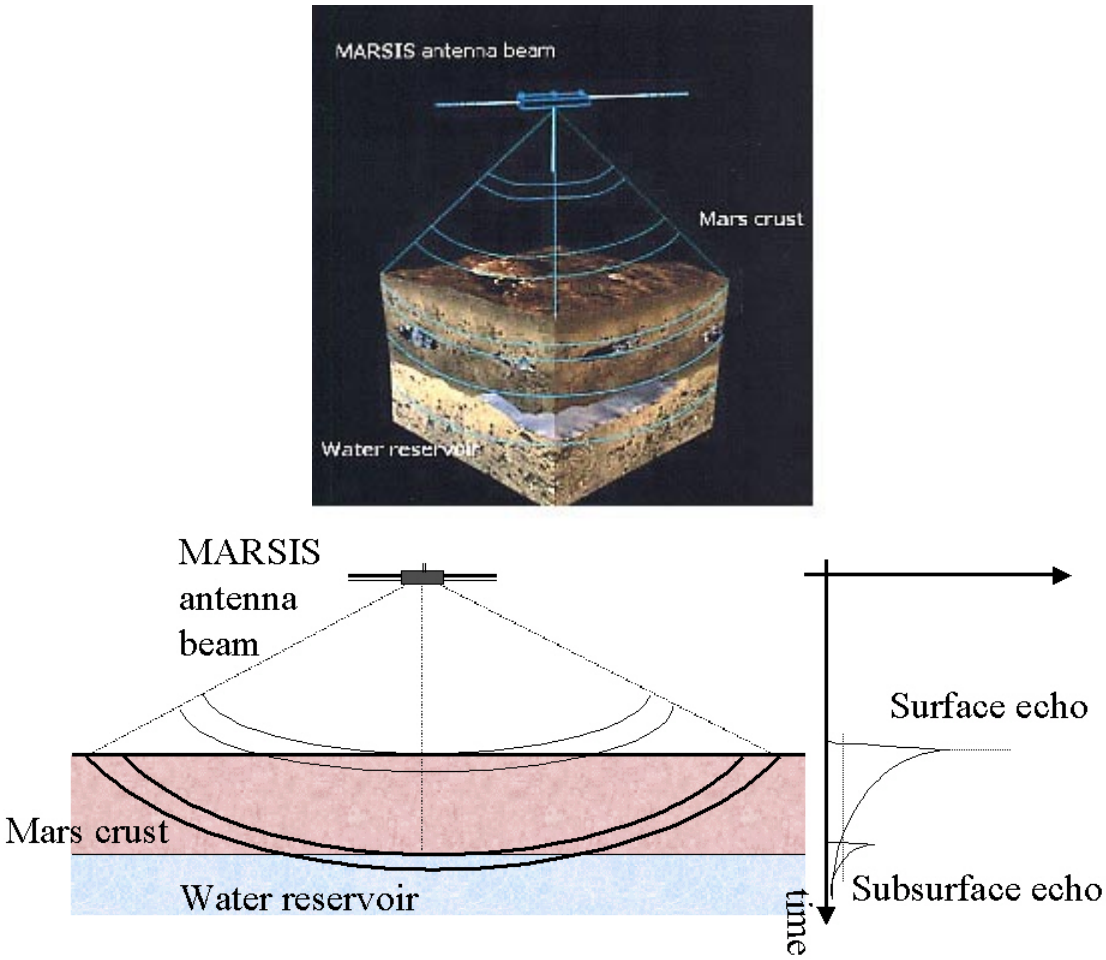

Figure 1-15: Radar Sounding for Investigating Surface and Subsurface Features

1.3.3.5 In Situ Atmospheric Science

The Entomopter can take atmospheric samples over a range of altitudes from the surface up to hundreds of meters. It can also take these samples in a controlled grid fashion, providing a comprehensive view of the atmosphere near the surface. These samples can be used to validate global remote sensing data from orbiting spacecraft, which can reflect signals off of the Mars atmosphere (sound) to gather information. The atmospheric samples either can be captured and returned to the base vehicle for analysis or, potentially, some basic analysis could be done on them in flight. This analysis could include ultra-sensitive compositional observations using mass spectrometric and tunable diode laser techniques developed for stratospheric research. In addition to sampling the atmosphere, basic atmospheric meteorology can be performed that would include wind velocity, temperature, and pressure measurements. The meteorological data can be taken at different vertical altitudes at various points above the surface. This data can provide a

comprehensive survey of the atmospheric conditions from the surface up to 100 m or so in altitude over a large surface region. This type of grid sampling is demonstrated in Figure 1-16. Each node or line intersection would be a data collection point.

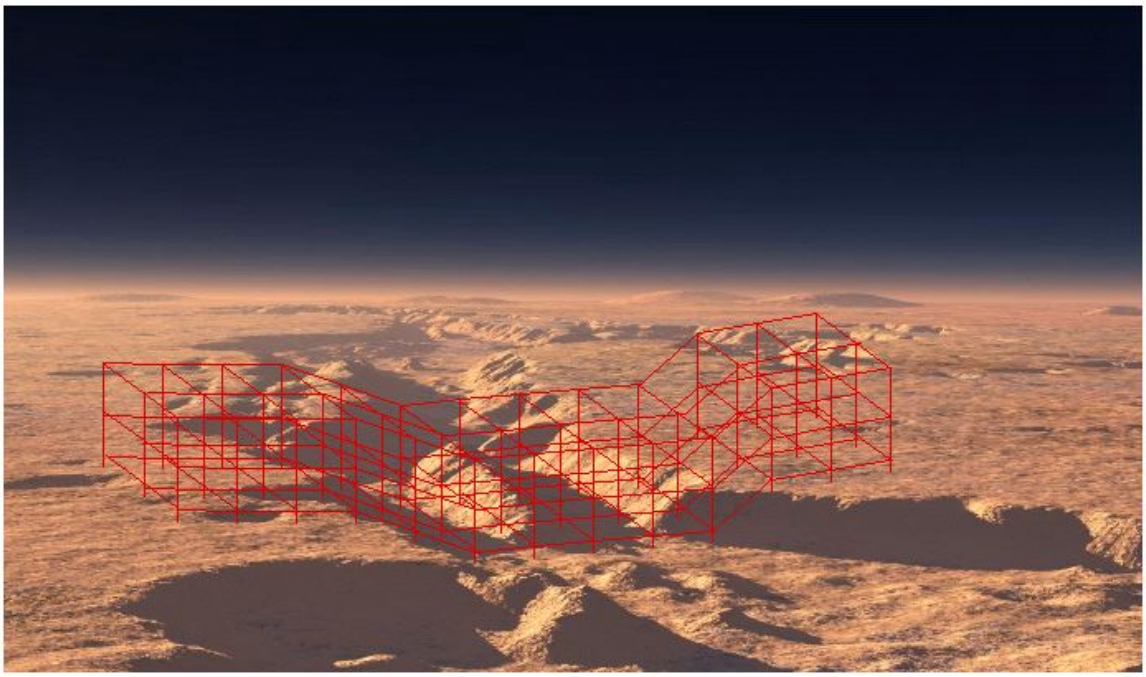

Figure 1-16: Atmospheric Sampling and Data Collection Over Grid

The dust on Mars is one of the unique features of its atmosphere. Because there is no rain, any dust particles lifted into the atmosphere tend to remain within the atmosphere for extended periods of time. This causes the optical depth of the planet to remain above 0.5, based on Viking lander data. (In this regard, optical depth is a measure of how opaque the atmosphere is to visible light passing through it. It is defined as zero for no effect on light transmission; atmosphere is perfectly clear.) Dust storms can be global in size and last for months before dying down. Therefore, the Entomopter can expect to fly with an optical depth of between 0.5 and 1.0 throughout its mission.

Mars dust is a major influence on the transfer of heat to and from the planet's surface. Presently, only particle size and optical properties are know about the dust on Mars.

The Entomopter, flying above the surface, can sample the long-lived airborne dust. Key science objectives in understanding the effects of the dust on the Mars environment include direct measurements of the radiation field, direct determination of the size distribution of the airborne dust, and determination of the electrostatic charging of the dust.

The photochemistry and trace gases in the Mars atmosphere are not well understood. The chemistry of primary interest is the photodissociation of H_2O, O_2, and CO_2, which can result in the production of a variety of reactive oxidizing species, such as O_3, H_2O_2, O, H, OH, HO_2, and possibly others. The concentration of these species can tell us about atmospheric photochemistry as well as provide insight into the nature of the oxidative processes responsible for the absence of organics in Mars soil, which may be a key piece of evidence in looking for life. The search for

trace gases such as CH_4, H_2S, NH_3, N_2O, C_2H_6, etc., which are reducing agents, would be of particular interest if detected on Mars. The presence of any of these reduced gases in the oxidizing environment of Mars would indicate the possibility of life on the surface or subsurface.

1.3.3.6 Payload Delivery

Because of its ability to land and take off again, the Entomopter can be used to deliver payloads to various locations on the surface. The payloads would be small micro-packages that can be placed at desired locations on the surface or on top of hills or cliffs. The packages can contain equipment for weather observing, seismic monitoring, solar intensity monitoring, dust monitoring, or atmospheric adsorption observation. If the packages are intended to collect samples over an extended period of time, the Entomopter can be used to retrieve the package once the sampling period has ended.

1.3.3.7 Surface Sample Collection

The acquisition of surface samples over a region of the surface can be used for morphological, mineralogical, and topographic data. As with the atmospheric samples, these surface samples can be returned to the base vehicle for analysis. The physical characteristics and composition of the samples can be determined. In addition to using the samples to characterize the surface material, the samples also can be used for assessing a given location for various applications. For example:

Soil and rock samples taken over a regional scale (500 m to 1,000 m) can be used to select landing sites for potential future Mars missions.

Soil and rock samples taken over a local scale (10 m to 100 m) can be used to guide rovers or the base vehicle and get to sampling areas that cannot be reached from other ground vehicles.

Samples taken over a concentrated range (1 m to 10 m) can be used to develop a detailed evaluation of a specific location. These samples can be taken from areas inaccessible by ground rover, such as up a steep incline or on the edge of a cliff. An artist's concept of the Entomopter vehicle taking a sample from a rock surface is shown in Figure 1-17.

Figure 1-17: Artist's Concept of the Entomopter Taking a Surface Sample

1.3.3.8 Searching for Subsurface Life

Possibly one of the most exciting applications of the Entomopter is the search for life on Mars. Aside from the identification of the surface morphology and near surface mineralogy, there are other ways in which the Entomopter vehicle can be used in the search for Mars life (both past and present).

The use of magnetic and radar sounding can provide data on the past environment and, more importantly, on the identification of subsurface water. If subsurface water is found, this would be a prime location for a vehicle that can penetrate the surface in search of life.

The atmospheric sampling capability allows for the investigation of chemical components that may signal a location where life may be present. The trace gasses that would indicate life will be highly localized, making them difficult to detect from the ground due to the amount of territory that would need to be covered. The Entomopter can be highly efficient in searching for these trace compounds and then bring back soil samples from any location in which they may be found. The potential for microenvironments on Mars that may harbor life is believed to be very high, and a flight vehicle that can cover large amounts of territory as well as investigate specific locations in detail would be invaluable.

Payload packages that can be used for the detection of life can be deployed at places that could not be reached by a ground vehicle. These sites may be on steep terrain or across a gully or valley not traversable by the rover.

The Entomopter can be used to simply guide the rover to areas of interest where life may be present. This simple application may have the largest impact on the overall capability to discover life on Mars. From the surface, the rover only has at best a 10m view of its surroundings. This limited view means that exploration must be done on a trial-and-error basis. And in searching for life, this may mean the probability of chancing upon it would be slim. However by guiding the rover to locations that have the greatest probability of finding life, the effectiveness of the mission is increased greatly. Once at an area of interest, the rover can perform a detailed survey for life both surface and subsurface, and investigations can be performed.

Chapter 2.0 Entomopter Configuration and Operation

2.1 Introduction

The basic terrestrial Entomopter configuration is applicable to Mars flight if properly scaled. The terrestrial Entomopter having a wing-span of approximately 15 cm operates in the same Reynolds number regime in the lower Mars atmosphere as a scaled up Entomopter with wing span of approximately 92 cm. In both cases, the Entomopter has a twin wing configuration in which the wings flap 180° out of phase at a constant autonomic rate. On Earth, this flapping frequency ranges between 25 and 30 Hz.

The Entomopter-based Mars Flyer is assumed to scale proportionately for the purpose of this analysis. The basic Entomopter is shown in Figure 2-1.

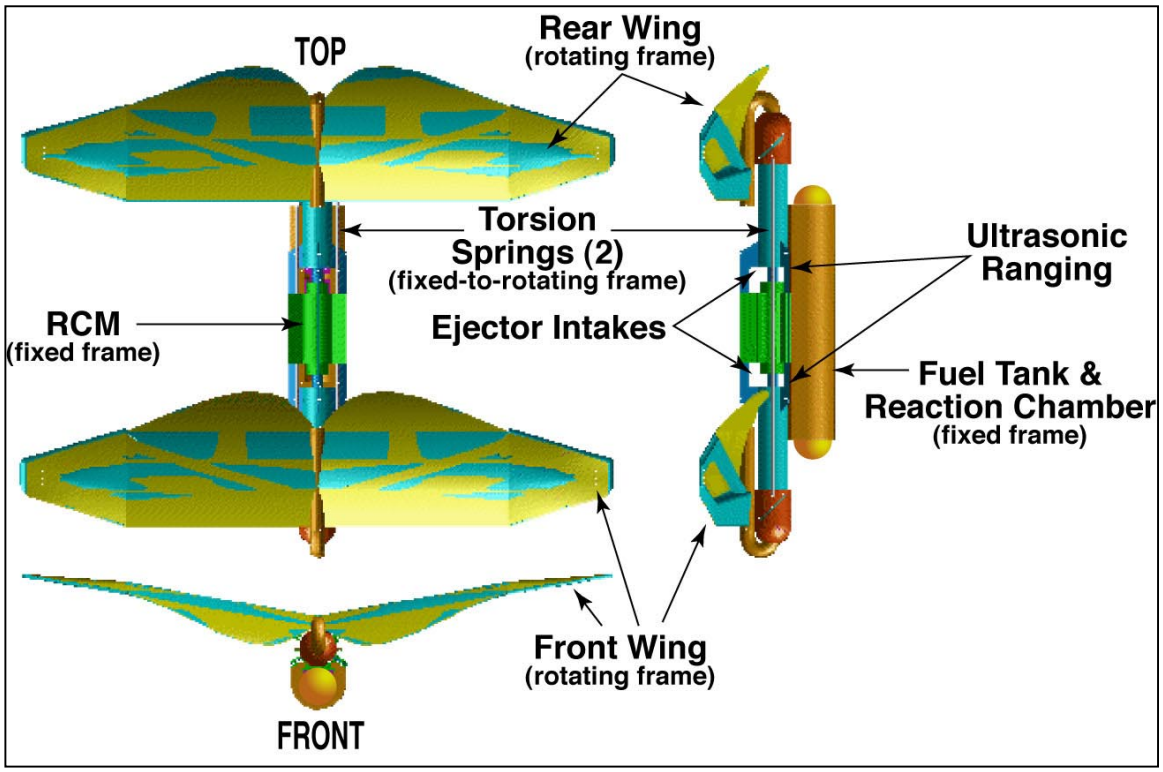

Figure 2-1: Entomopter-based Mars Flyer Configuration

2.2 Entomopter Morphology and Function

Currently several leg configurations exist for the terrestrial Entomopter, depending upon its mission. Long unjointed legs have been designed for positioning of sensors after landing, whereas short cilia-like legs are envisioned for locomotion through highly restricted areas, such as conduits and pipes. The use of longer legs for the Mars Flyer is expected; however this is a subject

for future study. The purpose of legs on Mars would be to position sensors after landing, reposition the Entomopter for a more favorable launch, and grapple with ground-based rovers during refueling operations. The primary form of locomotion is intended to be flight; the legs are for limited surface mobility, not extended ambulation.

The Entomopter wing is a thin air foil with a sharp leading edge and moderate camber. The leading edge of the wing is sharp to improve creation of the lift-enhancing leading edge vortex during flapping. The separation location for this leading edge vortex is controllable and is used to modulate the lift of the wing on a beat-to-beat basis. Because the coefficient of lift of each wing section is thus controllable, the wings need not beat at varying rates or angles of attack to maintain attitude and heading of the vehicle. Thus, the Entomopter is designed to flap its wings autonomically at a single optimal wing beat frequency. This feature facilitates the incorporation of resonance into the wing beating kinematics. In fact, this resonance is essential for any flapping wing device to operate efficiently. The flapping mechanism for the Entomopter provides a resonant single-piece construction that takes advantage of torsional resonance in the Entomopter fuselage to recover flapping energy as is common to flying insects that temporarily store potential energy in either muscles or resilin.

The Entomopter wing will be designed to produce lift on both the downstroke and the upstroke. Instead of relying on wing twist under muscular control (a complex action requiring an extra degree of freedom in the wing hinge), the wings will be stiffened with materials that react differently to opposite aerodynamic loads. Flexure of the wing structure will cause it to deform relative to the leading edge spar (which drives the wing up and down) such that it maintains an angle of attack and camber that provides positive lift on the downstroke.

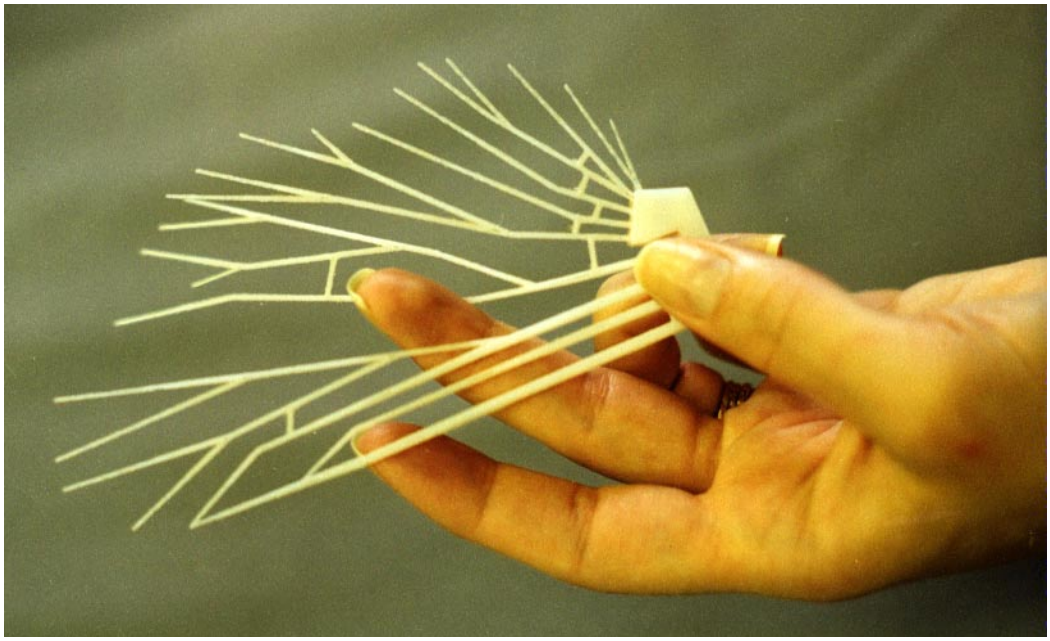

Figure 2-2: ABS Plastic Wing Ribs from Fused Deposition Modeling Machine

Upon the upstroke, the wing structure will deform under an opposite aerodynamic load to create an angle of attack and camber relative to the leading edge spar, which also has an upward lift

vector on the inboard section of the wing for at least a portion of the upbeat. The interstitial material between the wing spars serves as the aerodynamic lifting surface and the wing relies on the compliance of this material to give it a specific form under load. This is depicted in Figure 2-3.

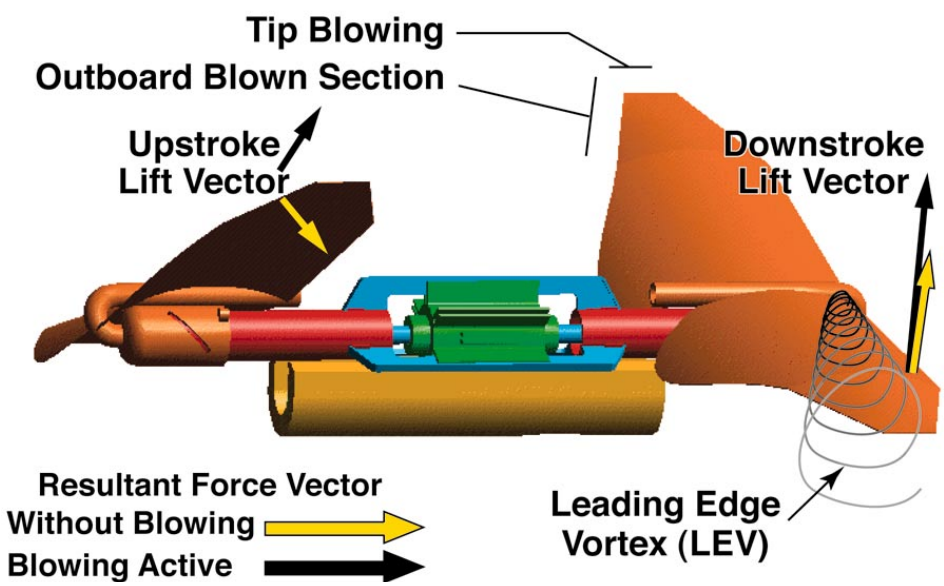

Figure 2-3: Lift Vectors on the Upthrust and Down Thrust Wing Halves

Circulation-controlled airfoil development work conducted for NASA generated positive lift measured at very large negative angles of attack (approaching -70°) and produced by very high supercirculation caused by the trailing edge circulation controlled blowing.

Coupling the deformation of the wing on the upstroke with intelligent application of circulation control will allow lift to be generated not only on the entire downbeat but on the upbeat as well, resulting in an efficiency greater than that of a conventional insect wing. Beyond the upbeat lift that can be created, the overall coefficient of lift (C_L) of the wings can be augmented by pneumatic blowing to achieve values that are five to eight times higher than the theoretical maximum achievable by a typical wing platform and camber (which for most fixed wings has a C_L of one or less).

Because of the latency in transmissions between Mars and Earth, teleoperation of an aerial Mars surveyor is impractical. Even supervised autonomy is of limited value. A an aerial Mars surveyor will have to be able to carry out its science mission without human intervention while being ever cognizant of its environment to assure that it avoids obstacles, hazards, and situations that would result in starvation.

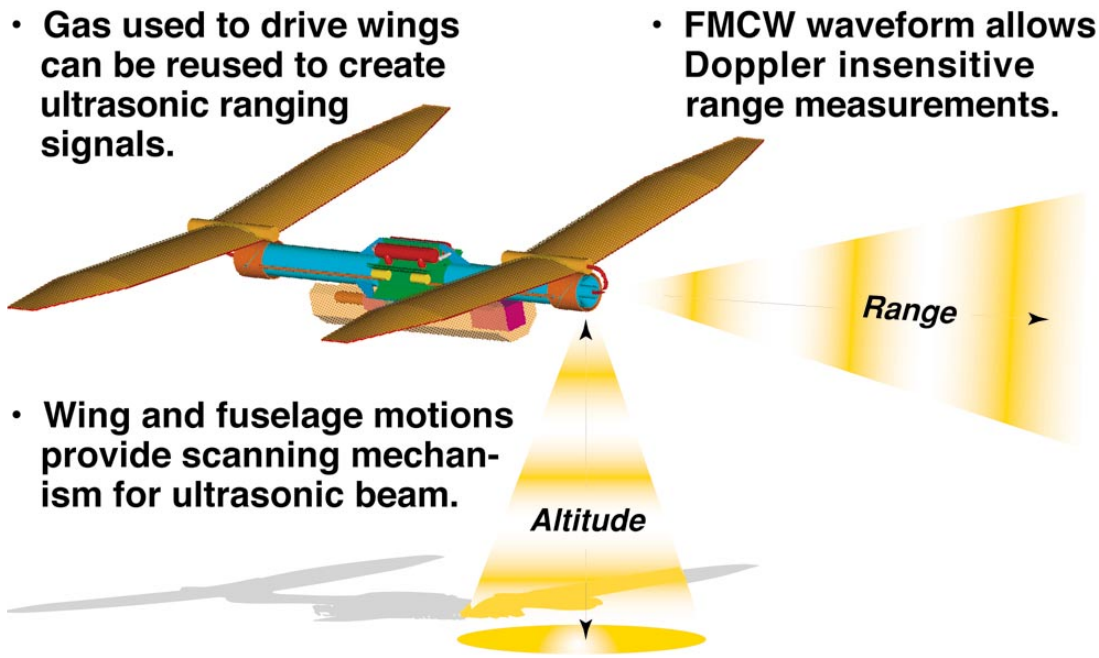

Figure 2-4: Integral Propulsion-ultrasonic Obstacle Avoidance and Altimetry System

Motivation for navigation would be based on various remote sensors that will be dictated by the type of science experiments to be performed by each Entomopter. For example, the search for life might entail sensors that can detect traces of water or fossil-bearing rock. Other Mars Flyers could measure atmospheric species or perform reconnaissance for later close inspection by ground-based rovers. In each case, the Mars Flyers would use preprogrammed search patterns initially. When measuring a volume, as in the case of atmospheric sampling, the entire flight might be preprogrammed. When searching for life, a preprogrammed search pattern would be abandoned in favor of following gradients based on the frequency of occurrence of evidence (motivational behavior). During the landing process, obstacles on the surface must be negotiated (avoidance behavior), and the Entomopter must select a spot from which it can launch itself back into the air as it transitions from ground locomotion to flight.

Due to the occurrence of storms on Mars, the Entomopter-based Mars Flyers might have to seek shelter on the surface by landing in a self preservation behavior. In all cases however, the Mars Flyers would have to be able to find their way back to the lander or rover in order to replenish depleted fuel supplies as they exhibit a feeding behavior also driven by a self preservation motivation.

The ability to fly autonomously is possible because of the ability of the Entomopter to modulate its coefficient of lift for each wing section on a beat-to-beat basis, thereby controlling attitude. This feature also permits the vehicle to change heading for navigation. Implicit is the presence of an onboard inertial system having stability that is either of duration commensurate with the flight mission length, or that is updated by an external reference analogous to GPS.

2.3 Baseline Mars Survey Flight Scenario for System Sizing

The sizing and flight performance proofs for the Entomopter-based aerial Mars surveyor will be based on the following minimal scenario:

1. Entomopter launches from refueling rover and proceeds at an angle between 80° and 90° from the rover's direction of travel. Launch is to the right side of the rover.
2. The rover will move at about 1 m/s.
3. The flight path will go out to nearly 200 m in a straight line, and then a circular 180° turn to the left will be initiated. At no time will the Entomopter be at a range of greater than 200 m from the rover.
4. The Entomopter will then fly in a straight line back to the rover, which will have progressed along its initial path at a rate of 1 m/s. The diameter of the 180° turn will roughly equal the distance traveled by the rover during the entire flight out and back.
5. The rover launch platform is assumed to be 1 m above the surface.
6. The flight altitude is 5 m AGL.
7. Flight speed is not fixed, but will be an output from the analysis. Therefore, we might find that the most efficient flight speed is too fast or too slow to make the Entomopter meet the rover upon return. We will adjust the rover speed to accommodate whatever outcome is desired to keep the baseline problem simple.
8. The Mars surface is assumed to be flat, so obstacle avoidance does not enter into this initial scenario.
9. Mars atmosphere is assumed to be at rest (no wind, no thermals).
10. This will be a daytime mission, and the atmospheric temperature will be over 10° C.
11. Altitude of flight will be based on terrain-following (flat terrain). Navigation is based upon relative position cues received from the rover's tracking system.

This is depicted schematically in Figure 2-5.

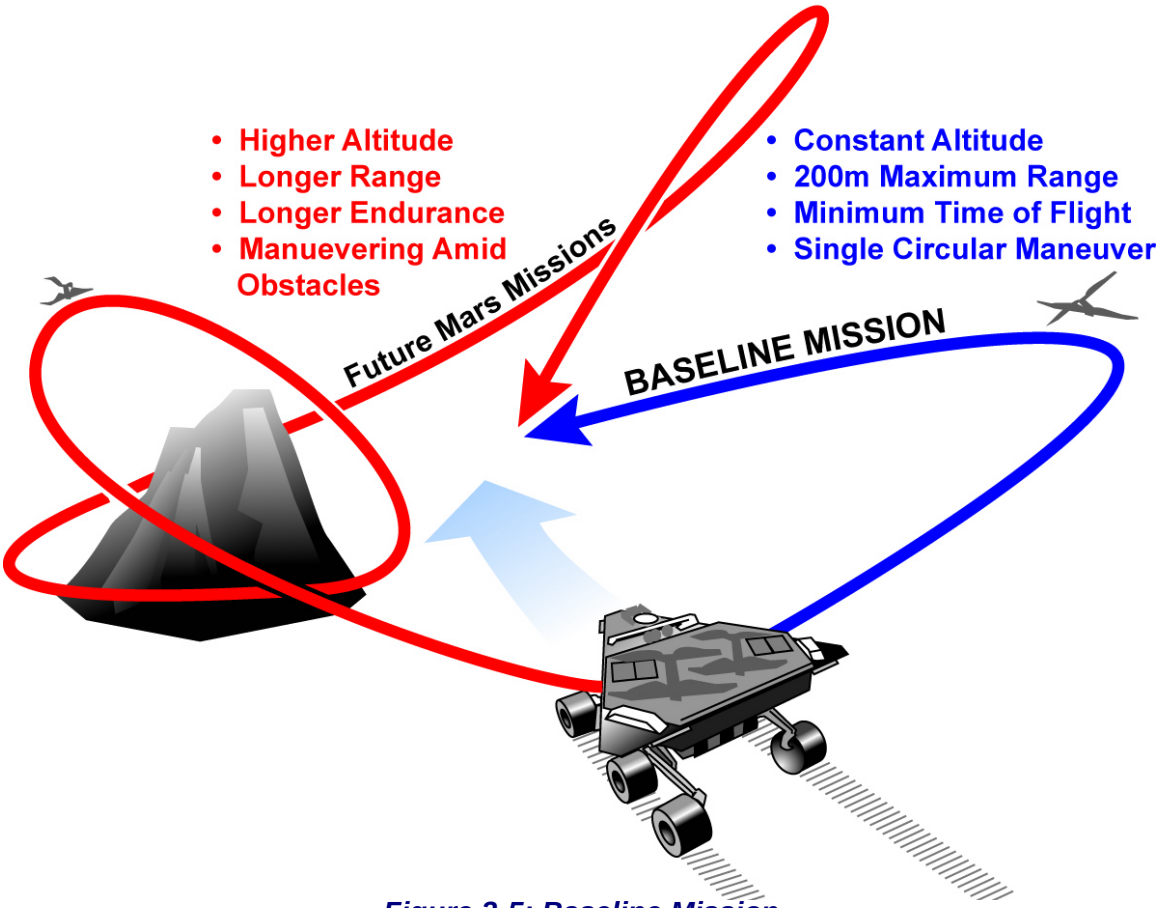

Figure 2-5: Baseline Mission

This baseline scenario is not intended to be a bound on Entomopter performance but rather a starting point for sizing of the vehicle. Due to realistic energy requirements for Mars flight in general, it is not expected that Entomopters (or any powered flight vehicle) will perform long-endurance, slow flight over vast distances. Rather, the Entomopter will serve to expand the area of regard for its ground-limited refueling rover, which cannot negotiate large obstacles or venture out into canyons.

The 1997, Mars vehicle Pathfinder progressed only 52 meters in 30 days because it had to await instructions from Earth 190 million km away. Each command took 11 minutes to travel between the two planets. It couldn't move any faster without risking collision with obstacles. The Entomopter will extend the rover's eyes and will allow it to choose its path ahead more intelligently. The rover will be able to move more rapidly with less risk. The result will be a greater science return per unit time. With Entomopter augmentation, the field of regard for the rover will be swaths of hundreds of meters for close inspection/sampling, and to the horizon for high-perspective line-of-sight remote inspections. In addition, the Entomopters will be able to perform scientific investigations that otherwise could not be attempted by a rover (e.g., cliffside inspections or magnetic profiling) or would be too time-consuming (e.g., wide area geologic characterization, such as mapping fault lines or strata). Even the baseline scenario is supportive of these science missions.

2.4 Environmental Conditions for Flight on Mars

The Mars environment is very different form that here on Earth. Therefore, there are issues and concerns associated with operating a vehicle in this environment that are not encountered on Earth. Mars has an atmosphere (Figure 2-6), but it is very thin. Near the surface of Mars, the atmospheric density is similar to the density of Earth's atmosphere at 30 km. The atmosphere is made up almost entirely of carbon dioxide. The temperature on Mars is on average much colder than on Earth. Although at certain times of the year and at certain locations the temperature will rise above freezing, temperatures are well below the freezing point of water most of the time.

Figure 2-6: Image of Mars Atmosphere Taken From Pathfinder Lander

The Entomopter and its accompanying system design will in a large part be dictated by environmental conditions on Mars. In fact, the viability of the concept is based on the thin atmosphere: Because of this thin atmosphere, the Entomopter can take advantage of the lift-generating mechanisms that insects use to fly here on Earth. The ability to generate lift in this fashion is Reynolds number based. Therefore, having a very low atmospheric density enables a vehicle with an approximate 1 m wingspan to fly in within the same Reynolds number regime (and therefore generate lift in the same manner) as small insects on Earth. Also, the lower gravity on Mars means that the amount of lift needed to pick up a given amount of mass is less than it would be on Earth. This combination of low atmospheric density (near the surface) and lower gravity is what makes this concept feasible.

Other environmental characteristics important to the system design include surface temperature, atmospheric dust, solar intensity, soil and atmospheric composition, and terrain characteristics (Figure 2-7 and Figure 2-8). These factors influence just about every aspect of the Entomopter and its associated system design. Examples include what type of fuel the Entomopter will use, whether it will be manufactured on site or brought from Earth, what type of power system is

used to power the electronics and other systems, the type and capabilities of the communications system, the type and approach of the navigation and control system, the construction materials used in the vehicle, and the landing and sampling approach.

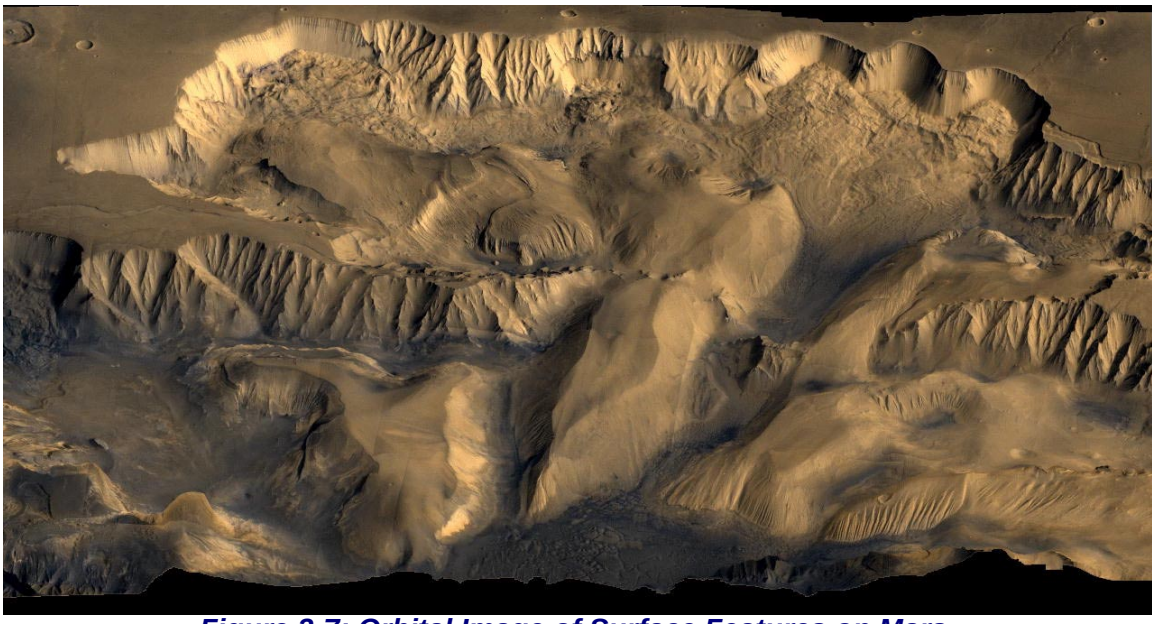

Figure 2-7: Orbital Image of Surface Features on Mars

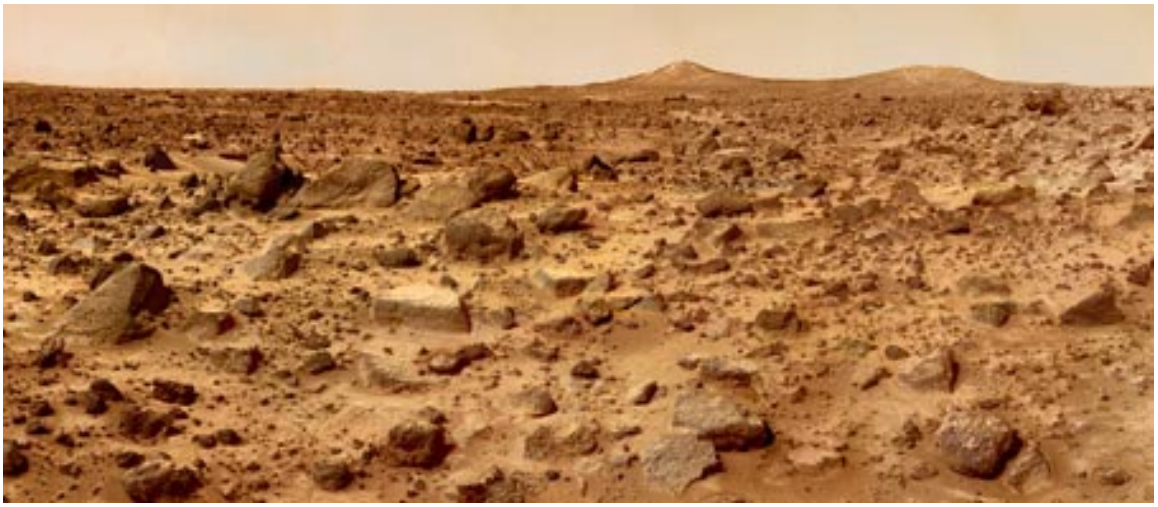

Figure 2-8: Image of Mars Surface from Pathfinder Lander

As a basis for the Entomopter design and analysis, a concise summary of the Mars environmental conditions was assembled. Some of the more recent Mars science missions (particularly the Pathfinder mission) have provided detailed information on various aspects of the Mars environment. However, many aspects of that environment are still not well understood, so the information provided in the following tables and figures represents the present state of knowledge. This

information and the influence it has on the Entomopter design may be subject to change as our understanding of the Mars environment increases.

2.4.1 Physical Properties

Table 2-1: Physical Properties of Mars

Inclination of Equator to Orbit	25.2^{o}
Day Period	24 hours, 39 minutes
Solar Radiation Intensity	Mean: 590 W/m^2 Parihelion: 718 W/m^2 Apehelion: 493 W/m^2
Gravitational Constant	3.73 m/s^2
Sidereal Year	687 days (Mars)
Surface Temperature Extremes	130 ^{o}K to 300 ^{o}K

2.4.2 Atmospheric Conditions

Table 2-2: Mars Atmospheric Composition
[243]

Gas	Percent Volume
Carbon Dioxide (CO_2)	95.32
Nitrogen (N_2)	2.7
Argon (Ar)	1.6
Oxygen (O_2)	0.13
Carbon Monoxide (CO)	0.07
Water Vapor (H_2O)	0.03
Neon (Ne)	2.5 ppm
Krypton (Kr)	0.3 ppm
Xenon (Xe)	0.08 ppm

Mars atmospheric profiles are listed in Appendix A. This appendix consists of four atmospheric profiles generated by different sources and for different locations on Mars. The data available with each profile is not necessarily the same.

The first profile is a reference atmosphere supplied by JPL. This data was generated for a latitude of -20°. It provides data on temperature, pressure, viscosity, and density from just above the surface to nearly 10 km [142].

The second profile is a general atmospheric model, not specific to any location, generated to provide a rough estimate of the atmospheric conditions at any location on the planet. It provides density, temperature, pressure, and speed-of-sound data for elevations of -5 km (below the mean surface level) to 120 km above the surface [27].

The third profile was generated using the Mars-GRAM atmospheric simulation tool. This profile was generated for a specific location on Mars, Parana Valles (-25°, 11°). It contains information on density, temperature, pressure, speed of sound, and viscosity for altitudes of 2.38 km to 20 km [48].

The fourth and last profile was also generated using the Mars-GRAM atmospheric simulation tool. This profile was generated for a specific location on Mars, Utopia Planitia (57°, 235°). It contains information on density, temperature, pressure, speed of sound, and viscosity for altitudes of -1.74 km to 20 km [48].

Significant data was also collected on the Mars atmosphere during the recent Pathfinder mission. For the first 30 days, surface pressure at the landing site underwent substantial daily variations of 0.2 to 0.3 mbar, which were associated primarily with the large thermal tides in the thin Mars atmosphere. Daily pressure cycles were characterized by a significant pressure change throughout the day period. This is shown in Figure 2-12, and the pressure change over a 30-day period is shown in Figure 2-13.

The near-surface temperature on Mars is greatly influenced by the surface temperature cycle (surface heating during the day and radiative cooling at night due to the low density of the Mars atmosphere). At sunrise, the atmosphere is typically stable, and cool, dense air lies near the surface. As the surface warms the air mass is heated, and by early morning begins to rise. As the heating continues the atmosphere becomes unstable. This causes temperature fluctuations on the order of 15 °K to 20 °K, during the remainder of the morning and early afternoon. Later in the afternoon the surface cools, the atmospheric stability increases, and the temperature fluctuations decrease.

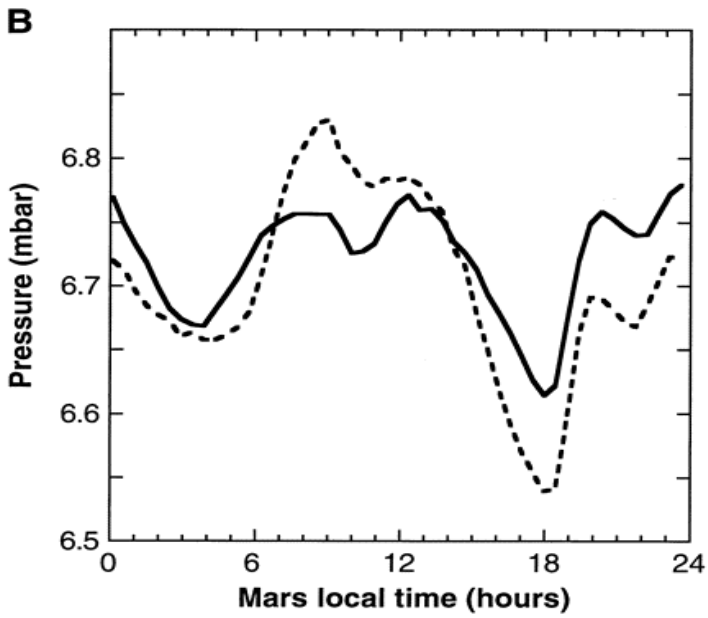

Figure 2-9: Daily Pressure Variation (Pathfinder Data)
[227]

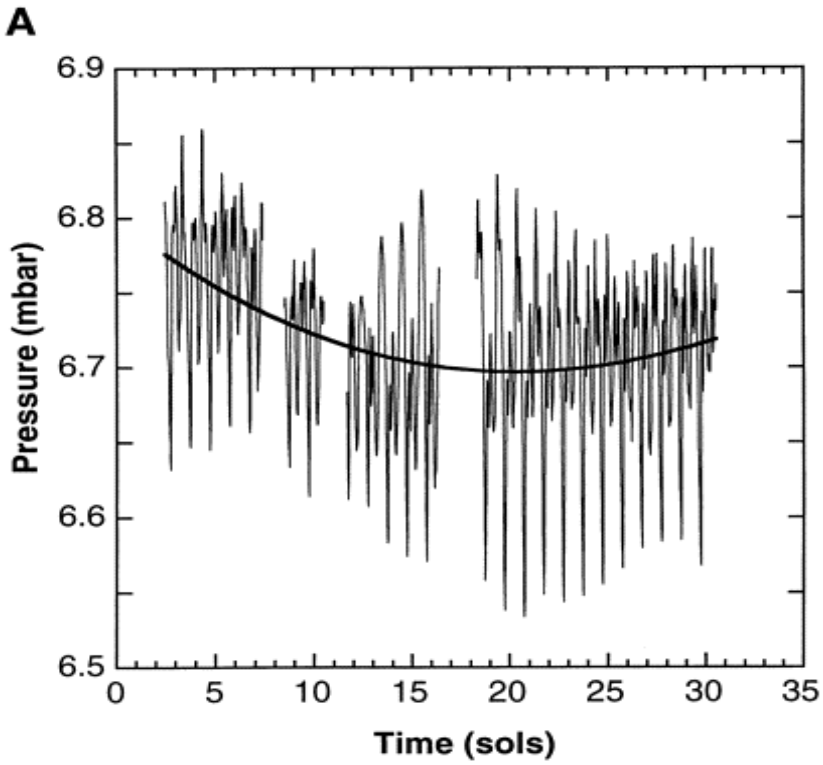

Figure 2-10: Pressure Variation Over a One-month Period (Pathfinder Data)
[227]

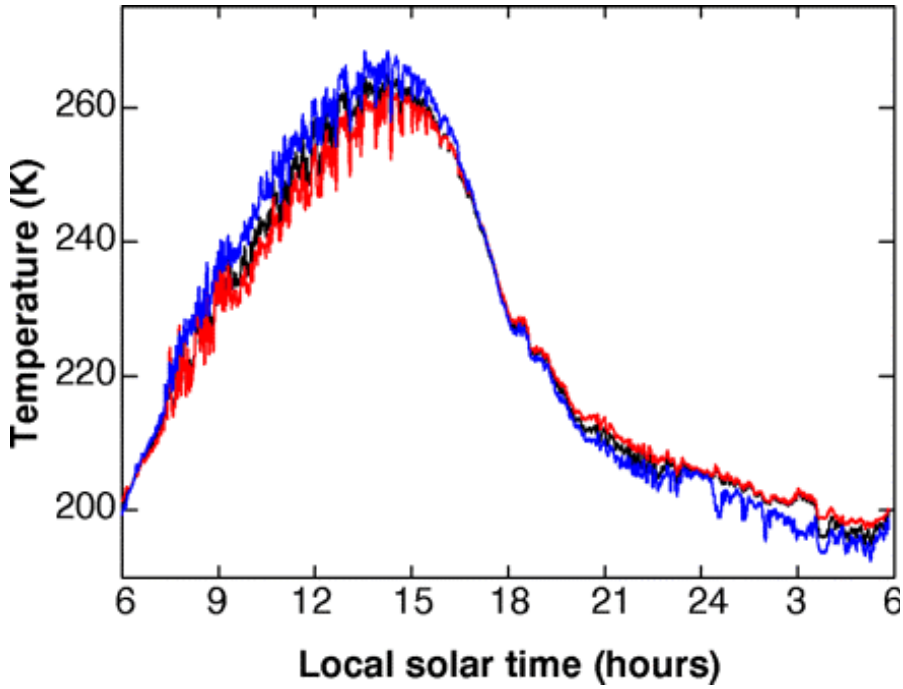

Figure 2-11: Atmospheric Temperature Variation Throughout a Day (Pathfinder Data) [227]

By evening, the thermal convection subsides and the instability in the atmosphere is diminished. The atmosphere becomes stable again due to surface cooling during the night. Any major night-time temperature fluctuations are caused by downslope winds that disturb the surface boundary layer.

2.4.3 Dust Storms and Wind

The wind at or near the surface can range from 2 to 7 m/s, (based on Viking Lander data). These winds have a strong diurnal and seasonal variation in both direction and magnitude. Wind speeds of up to and possibly greater than 50 m/s will occur above the surface boundary layer; this surface boundary layer is estimated to extend tens of meters above the surface. Preliminary estimates of the Pathfinder wind data suggest that wind speeds were comparable with or lower than those measured by Viking Lander-1 at the same time of year. Speeds were generally less than 5 to 10 m/s, except during the passage of dust devils, and were often less than 1 m/s in the morning hours. This may be consistent with the lower slope at the Pathfinder site. [227]

For a one-month period, pathfinder data shows that wind direction generally rotated in a clockwise manner through a full 360°. Winds were consistently from the south in the late and early morning and then rotated steadily through west, north and east during the day. The wind direction at night was very consistent but became more variable throughout the day. The wind direction is shown in Figure 2-12.

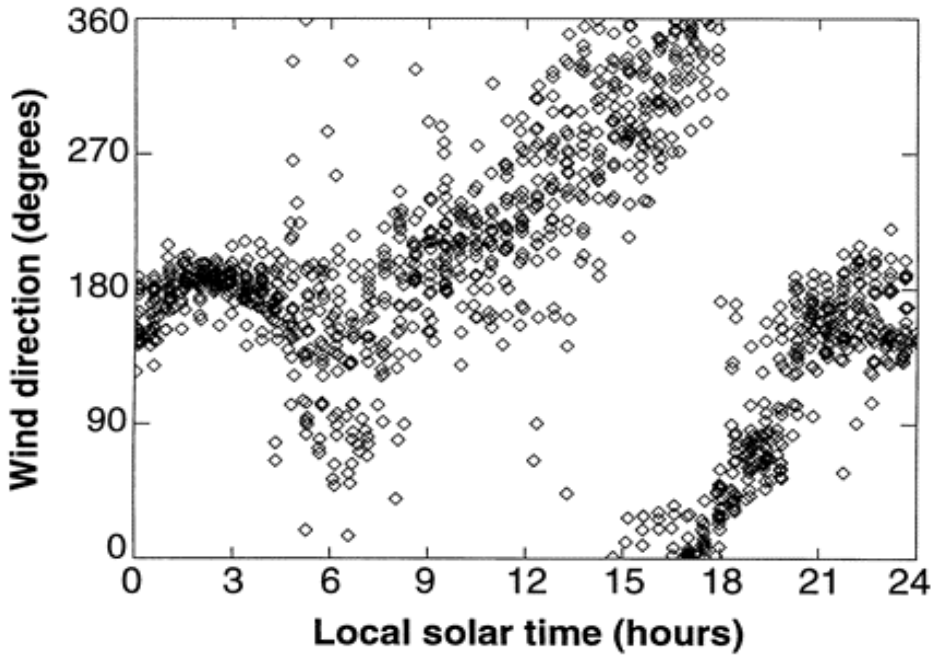

Figure 2-12: Wind Direction Throughout the Day (Pathfinder Data)
[227]

Dust storms tend to occur when Mars is near perihelion, when the solar intensity is the greatest. It is believed that the greater intensity of solar radiation, coupled with variations in the topology of Mars, triggers the dust storms. The storms can last up to several months, and the opacity of the storms can be quite high. Due to the low atmospheric density, these dust storms result in only minimal distribution and accumulation of debris. More information on dust storms, gathered for the Mars micromission aircraft program is given in [47].

Dust devils are short-term variations in measured surface pressure, wind velocity, and air temperature over periods of tens of seconds to minutes, shown in Figure 2-13. Dust devils, about 2 km wide and a few kilometers high, have been observed in the tropics by the Viking orbiters.

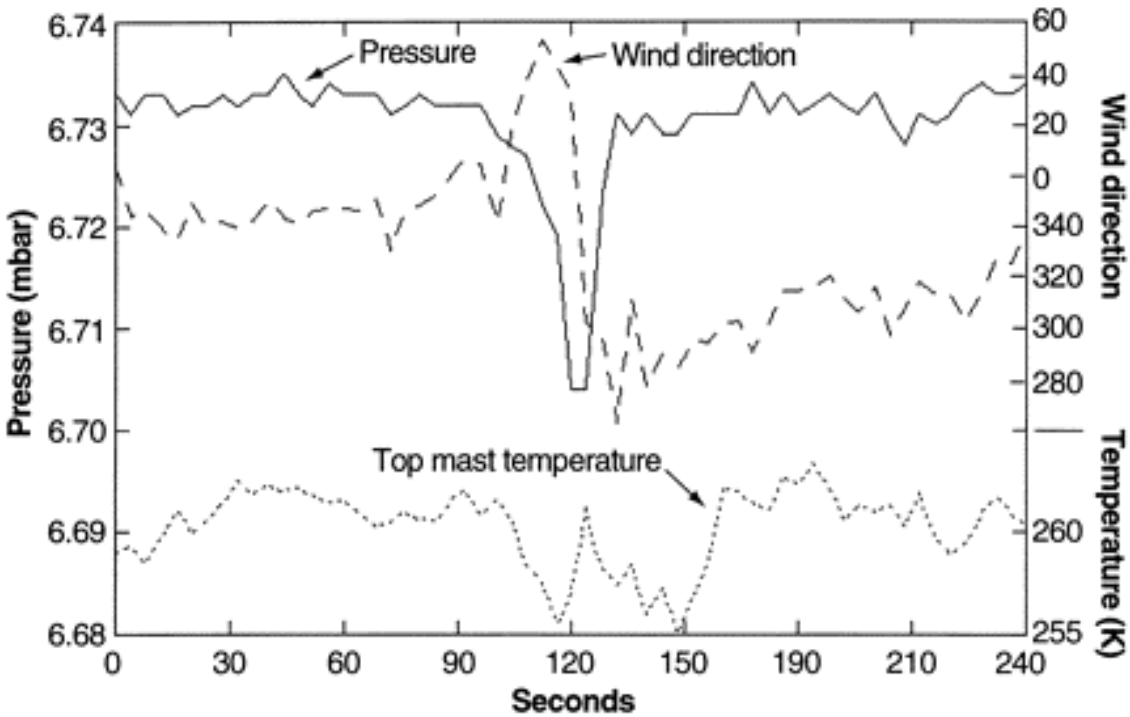

Figure 2-13: Measurements Taken During a Dust Devil (Pathfinder Data)
[227]

2.4.4 Soil Composition

Mars soil composition is an important factor in the potential of utilizing in-situ resources for propellant production. Soil composition data was generated by the Mars Pathfinder mission.

Table 2-3: Mineral Composition of Mars Soil
[222]

Mineral	Percent Composition by Weight
Na_2O	2.4
MgO	7.8
Al_2O_3	8.6
SiO_2	48.6
SO_3	5.9
C_L	0.6
K_2O	0.3
CaO	6.1
TiO_2	1.2

Table 2-3: Mineral Composition of Mars Soil (Continued)
[222]

Mineral	Percent Composition by Weight
FeO	16.5

Table 2-4: Element Composition of Mars Soil
[222]

Element	Percent of Soil Composition by Weight
Oxygen (O)	43.9
Sodium (Na)	3.8
Magnesium (Mg)	5.5
Aluminum (Al)	5.5
Silicon (Si)	20.2
Phosphorus (P)	1.5
Sulfur (S)	2.5
Chlorine (C_L)	0.6
Potassium (K)	0.6
Calcium (Ca)	3.4
Titanium (Ti)	0.7
Chromium (Cr)	0.3
Manganese (Mn)	0.4
Iron (Fe)	11.2
Nickel (Ni)	

Chapter 3.0 Vehicle Design

3.1 Wing Sizing

3.1.1 Engine Energy Production Requirements

The energy consumed by the wing motion during each flap can be broken down into two main components: The energy needed to move the wing mass, acceleration and deceleration, at the desired flapping rate, and the energy needed to overcome the drag on the wing due to the lift produced during flapping. The energy due to motion is much greater than that due to lift generation. Initially, therefore, only the energy due to motion will be evaluated.

3.1.2 Energy Required Due to Motion

The energy required to move the mass of the wing can be easily calculated based on the geometry of the wing, mass distribution along the wing, and the flapping rate. These parameters, which include wing length, flapping frequency, and the angle through which the wing moves during the flap cycle, are shown in Figure 3-1. They can be varied to try to optimize wing design and operation. The optimization consists of maximizing lift while minimizing the power required. From the structural analysis the mass distribution along a wing section length was determined. Utilizing this mass distribution. Loading on the wing due to its acceleration can be determined using the mass distribution. The mass distribution and corresponding loading are shown in Figure 3-2.

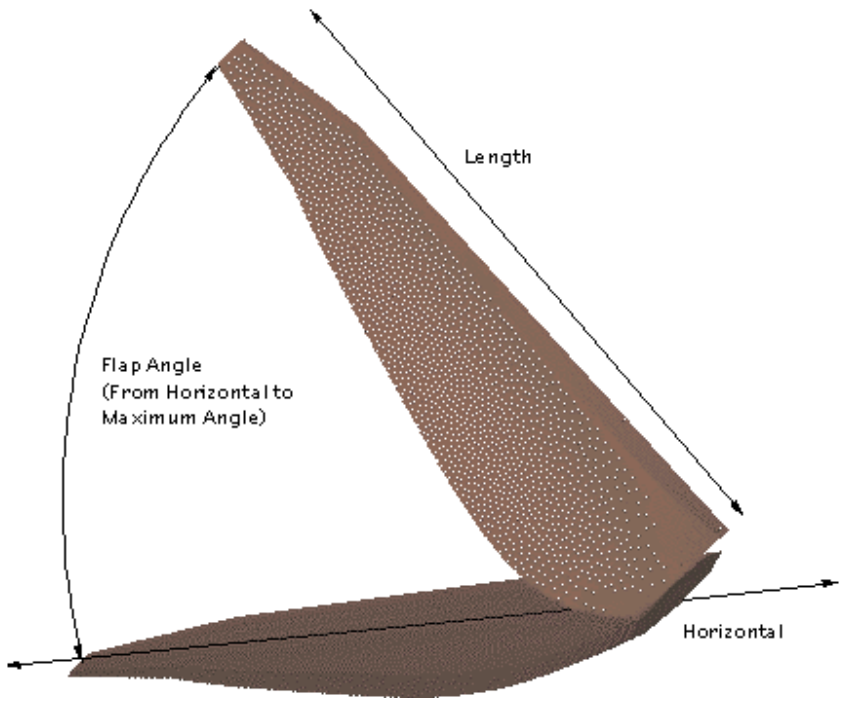

Figure 3-1: Parameters for Power Consumption Optimization

The wing loading shown in Figure 3-2 is due to the acceleration of the wing mass; aerodynamics and other loads are not included at this point. The force (F) was based on Equation 3-1, where mi is the mass of an incremental piece of the wing corresponding to a mean radial distance of ri, q is the angle through which the wing will move during the acceleration (this is equal to the maximum deflection angle used during the structural analysis), and f is the flapping frequency in cycles per second. Wing acceleration was assumed to be a constant from the beginning of the stroke where the wing is in its full upward position to the wing in a horizontal position. The

curves shown in Figure 3-2 show the force and mass distributions for a generic case. The curve profiles should be the same for all operating conditions and wing sizes; only the absolute values should be affected by a change in these parameters. From this figure it can be seen that the maximum force occurs about midway along the wing section. Further toward the wing tip, the force is reduced. Although wing acceleration increases towards the tip the mass is decreasing and produces a net reduction in force. The opposite occurs toward the root, where there is greater mass but less acceleration, thereby reducing the total force.

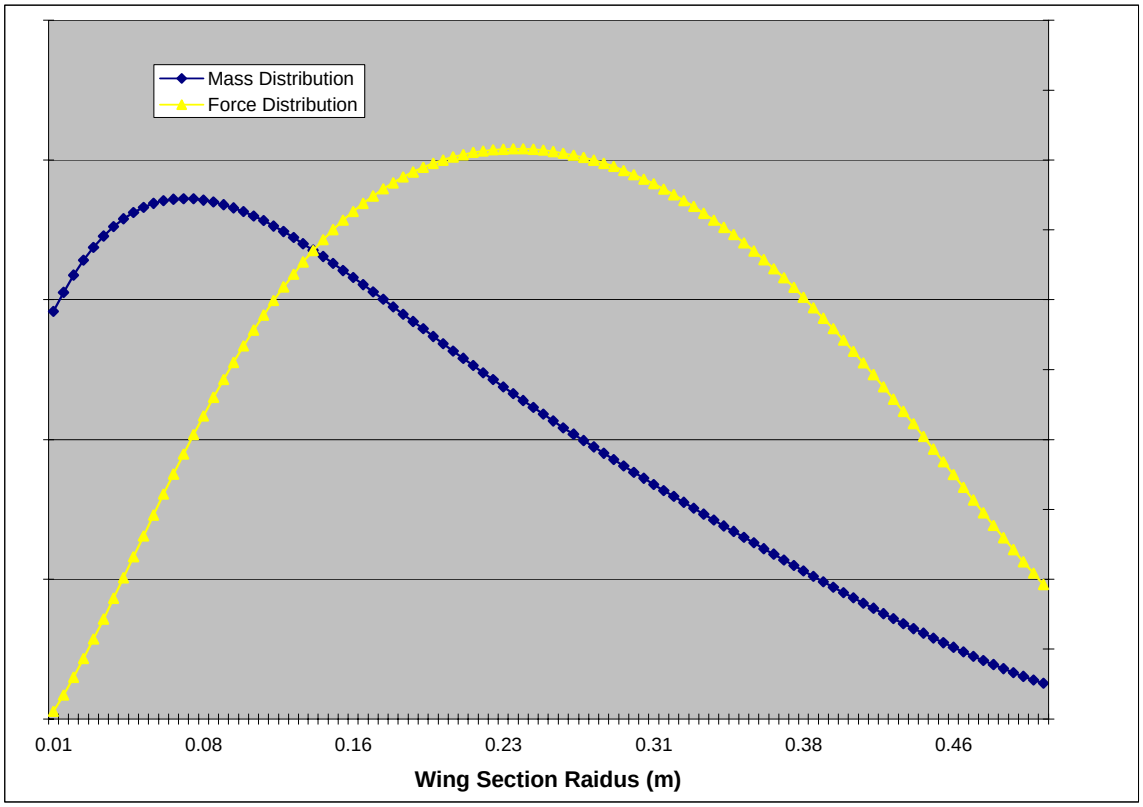

Figure 3-2: Mass and Corresponding Force Distribution Along Wing Section

$$F = \sum_{i=0}^{i=R} m_i \frac{2\theta r_i}{(\frac{1}{4f})^2}$$

Equation 3-1

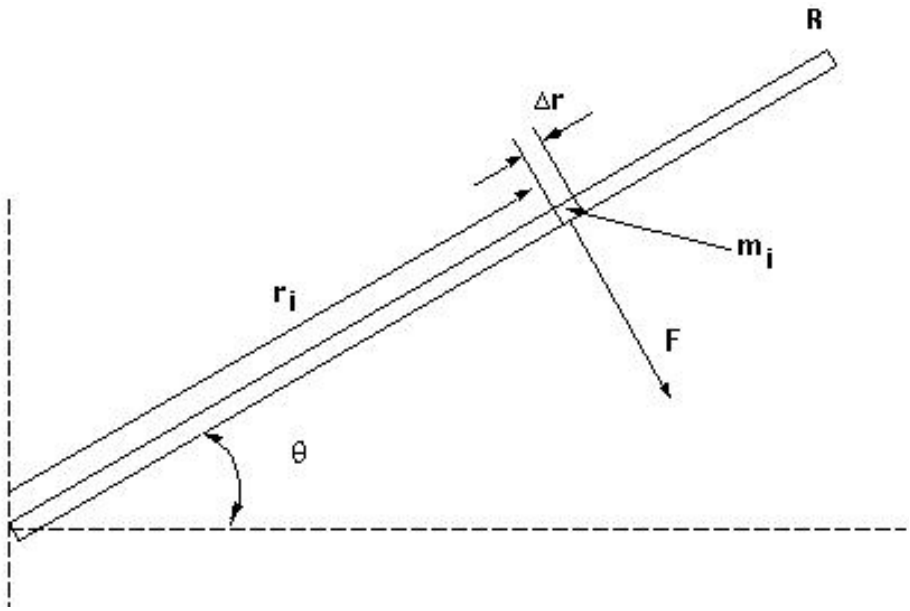

Figure 3-3: Acceleration Force Diagram

The absolute values associated with the curves given in Figure 3-2 are dependent on the size of the wing, flapping rate, and maximum angle through which the wing will move. The combination of these variables must be optimized to maximize the amount of lift generated by the wing while operating at a power level that is achievable by the propulsion system. Figure 3-4 shows the energy utilized by the wing throughout the motion of one flap cycle, as well as the velocity and acceleration profiles assumed for the wing motion.

The total work performed by the engine to provide the acceleration during the segments shown in Figure 3-4 is given by Equation 3-2. For this initial analysis the energy recapture portion of the stroke is not being taken into account. The initial sizing will utilize no energy capture, which will build margin into the sizing as well as account for some of the forces, such as drag, that are presently not being taken into account.

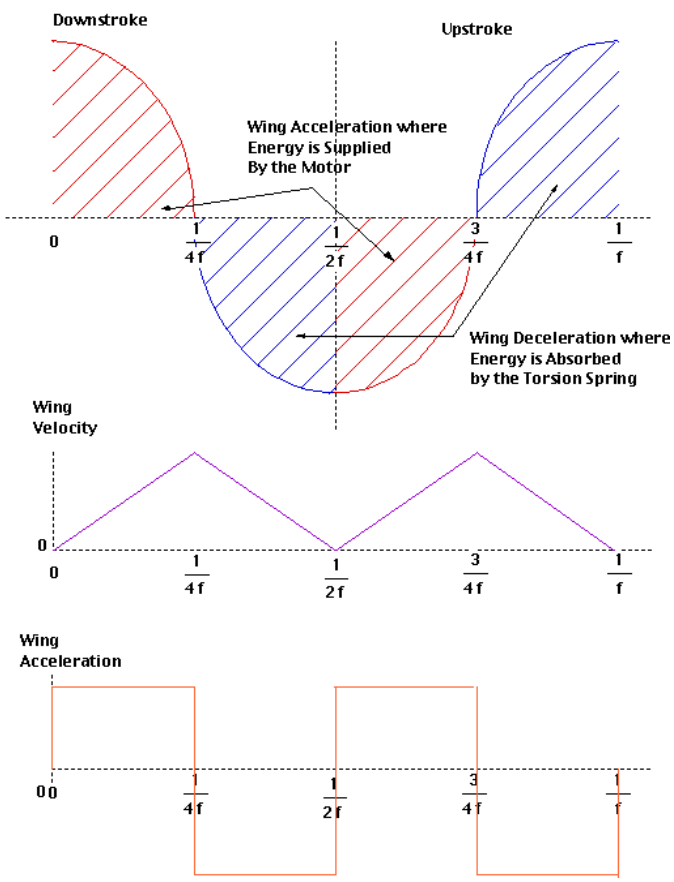

Figure 3-4: Wing Motion and Energy Usage, Velocity and Acceleration Profiles

$$W = \int_0^R F(r)\theta r\,dr \qquad \textbf{Equation 3-2}$$

The total work performed, under a given operational condition and wing geometry, by the engine per flap (represented by the red-shaded areas in Figure 3-4) is the area under the force-distance traveled curve. Examples are shown in Figure 3-5 for various flapping frequencies, wing lengths, and flapping angle.

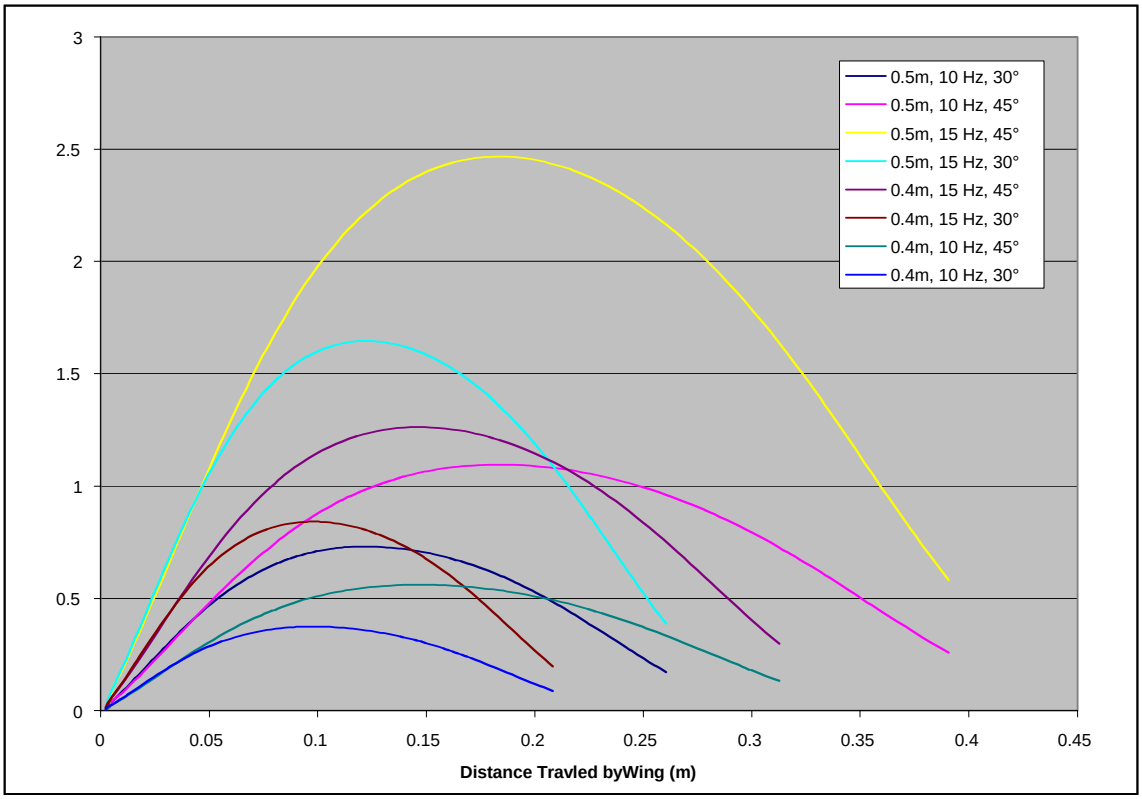

Figure 3-5: Examples of the Effect of Wing Length, Flapping Rate and Flap Angle on the Work Performed by the Engine

An optimization of the vehicle geometry and operational characteristics was performed. To determine the combination of flapping frequency, wing length, and flap angle that maximized lift and minimized wing weight for a given amount of engine power. The effect of engine power on the maximum lifting capacity of the vehicle was also examined.

The lift generated (L) by the wing can be estimated from Equation 3-3 below, where ρ is the atmospheric density of Mars near the surface, C_L is the lift coefficient of the wing, A_w is the wing area, and V_{res} is the resultant velocity due to the forward motion of the Entomopter and the flapping of the wings. The resultant velocity is shown in Figure 3-6.

$$L = \frac{1}{2}\rho V_{res}^2 C_l A_w$$ **Equation 3-3**

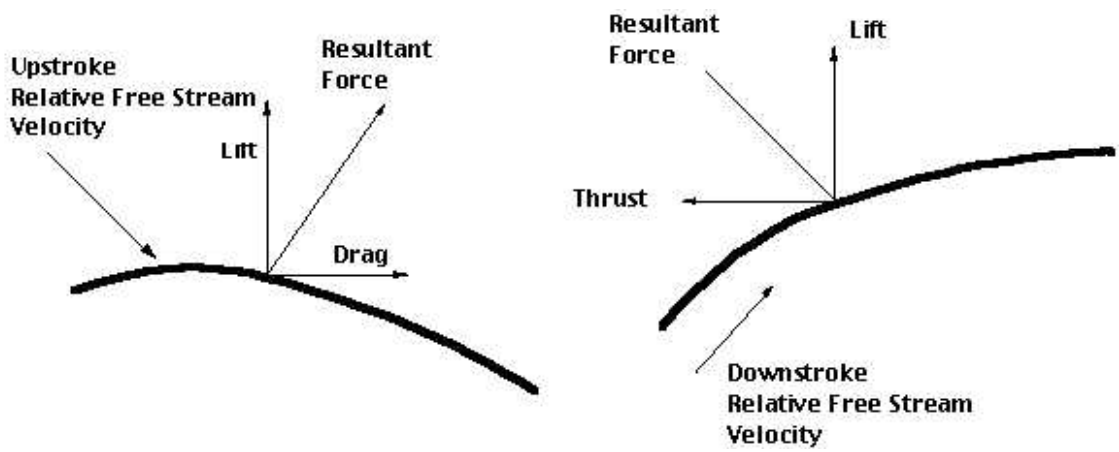

Figure 3-6: Resultant Force and Velocity for the Flapping Wing

The resultant velocity will vary along the wing length, so the lift will not be constant along the wing. The resultant velocity can be expressed by Equation 3-4, where θ is the maximum angle the wing moves through, r_i is the incremental distance along the wing, f is the flapping frequency, and V is the free-stream (or flight) velocity. The flight velocity was chosen to be 15 m/s for this initial analysis. This equation represents the average velocity throughout one flap of a section of wing a distance r from the root.

$$V_{res} = \sqrt{(\theta r_i 4 f)^2 + V^2}$$ **Equation 3-4**

From the environmental section the density of the atmosphere near the surface is approximately 0.0145 kg/m^3. The lift coefficient is based on the vortex formation and shedding that occurs on each flap as well as the vented gas blowing along slots in the trailing edge of the wing. Lift coefficients generated by insects due to flapping are on the order of 5. By adding blowing it is estimated these lift coefficients can be increased two to three times that. For this analysis a lift coefficient of 10 was used which represents the lower end of this estimate. The wing chord also varies along the wing length. Therefore, the wing area of an incremental section of wing will not be constant along the wing length and will vary based on the chord variation. From the structures section the chord (c) as a function of wing location is given by Equation 3-5.

$$c = 0.32814 + 2.61643\,r - 9.1414\,r^2 + 15.642\,r^3 - 12.951\,r^4 + 4.0584\,r^5$$ **Equation 3-5**

The total lift generated by one of the wing segments can be approximated by the summation shown in Equation 3-6.

$$L = \frac{1}{2}\rho c_l \sum_{0}^{R}((4 f\theta r_i)^2 + V^2)(0.328 + 2.616 r_i - 9.141 r_i^2 + 15.642 r_i^3 - 12.951 r_i^4 + 4.058 r_i^5)$$

Equation 3-6

Lift distribution along the wing is shown in Figure 3-7. This figure compares the lift distribution along the wing section for flapping angles of 30° and 45° at engine power levels of 700 W and 800 W. The engine power represents what is needed to move all four wing segments at the frequency and maximum flap angle specified. From this figure it can be seen that the shape of the lift profile is consistent for all the cases tried. Greater lift is achieved by increasing the maximum flapping angle then increasing the flapping rate (power level). This figure demonstrates that to maximize lift for a given power level, the largest flapping angle achievable should be used.

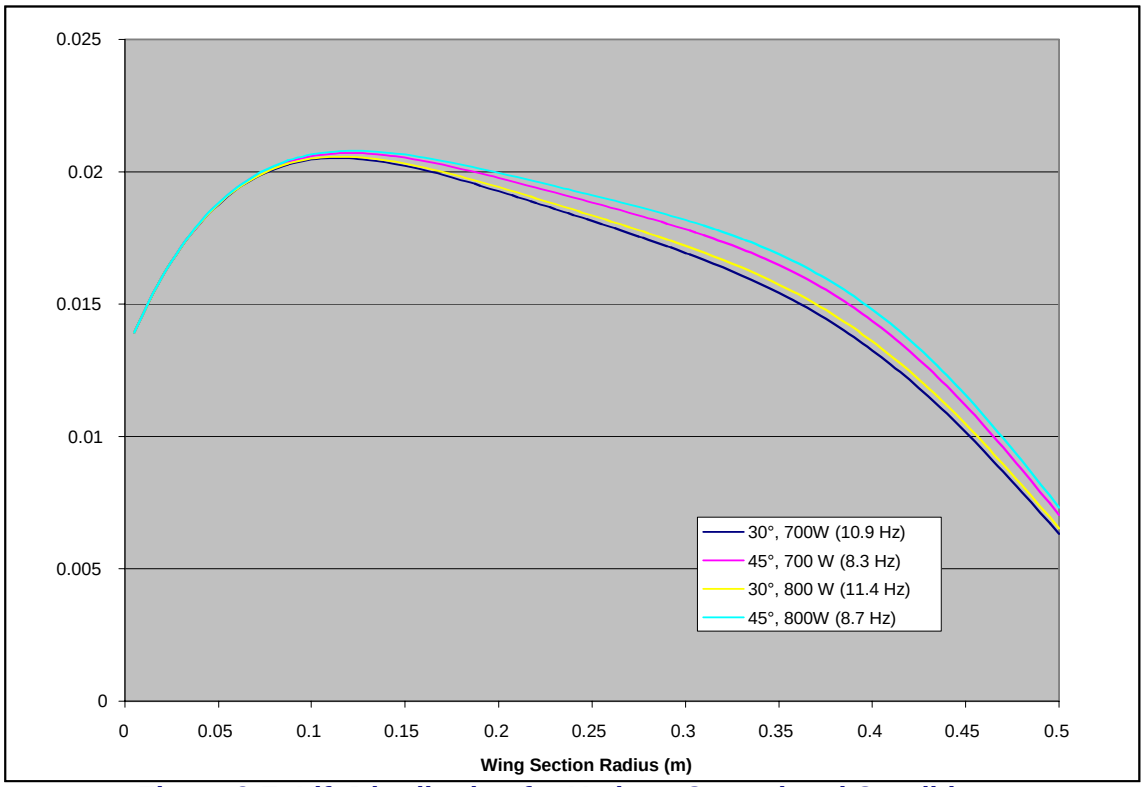

Figure 3-7: Lift Distribution for Various Operational Conditions

As shown in the above equations, the lift generated and power required by the Entomopter will be dependent on the flapping rate of the wings, degree of motion, or flapping angle, of the wings; the length or area of the wing; and the speed at which the Entomopter is traveling. All of these factors have varying but direct impacts on the lifting capacity of the wing and its power consumption. To optimize the Entomopter design, vehicle geometry and operational conditions would need to maximize lifting capacity while minimizing required power. The number of factors that can influence both lift generation and power consumption make this optimization process complex. Therefore, the analysis will examine each of the variables individually to

determine the individual effect on lift and power. With the insight provided by this single-variable analysis, a multivariable analysis will be performed to produce an optimized vehicle configuration.

As shown in Figure 3-5, the loading on the wing will vary depending on the wing geometry and operational conditions. Because the wing structure mass is based on the loading experienced by the wing, the mass of the wing structure will also change. This will affect the relative lifting capacity of the vehicle. Relative lifting capacity (m_r) is defined as the total mass the Entomopter can lift (m_t) minus the mass of the wings (m_w).

$$mr = mt - mw \qquad \textbf{Equation 3-7}$$

The mass the Entomopter can lift is the vertical lift component of the resultant lift shown in Figure 3-5. The lift generated by the wings is also used as the means of forward propulsion for the Entomopter. Therefore, when calculating the total lift generated by the Entomopter based on the resultant velocity, given by Equation 3-6, the drag-force vector must be subtracted to calculate the portion of lift used to maintain the vehicle in flight. The drag on the vehicle due to forward motion (D) is given by Equation 3-8.

$$D = \frac{1}{2}\rho V^2 c_d S_w \qquad \textbf{Equation 3-8}$$

The total vehicle wetted surface area (S_w) is given by Equation 3-9, where the area of the Entomopter body was assumed to be 0.5 m^2. The total drag coefficient (c_d) for the vehicle was assumed to be 0.3. Based on this drag calculation the effective lift (L_e) of the Entomopter is given by Equation 3-10.

$$S_w = 2A_w(4) + 0.05 \qquad \textbf{Equation 3-9}$$

$$L_e = \sqrt{L^2 - D^2} \qquad \textbf{Equation 3-10}$$

A relative lifting capacity is a much more useful characteristic of Entomopter performance than the total lift generated by the wings. By factoring out the wing mass a truer representation of the vehicle's relative performance under various operating conditions is achieved. Wing mass is dependent on the structural analysis described in the Entomopter wing structure section. The biggest effect on wing mass is the size of the wing. The relation between wing mass and size is shown in Figure 3-8.

To examine the effect of the various operational parameters on the lift and power requirement for the Entomopter, a base operating configuration must be established. From this base operating point the variables, such as flapping rate, flapping angle, and wing length will be individually varied. Initially in-flight cruise conditions were examined. This assumed a flight speed (V) for the vehicle of 15 m/s and a C_L generated by the wings of 10. This lift coefficient was based on the baseline lift coefficient of 5 for the flapping wing and the estimated doubling or tripling enhancement due to active boundary layer blowing at the trailing edge of the wing. The analysis

was performed on the lower end of the potential lift coefficient range to provide some margin and conservatism.

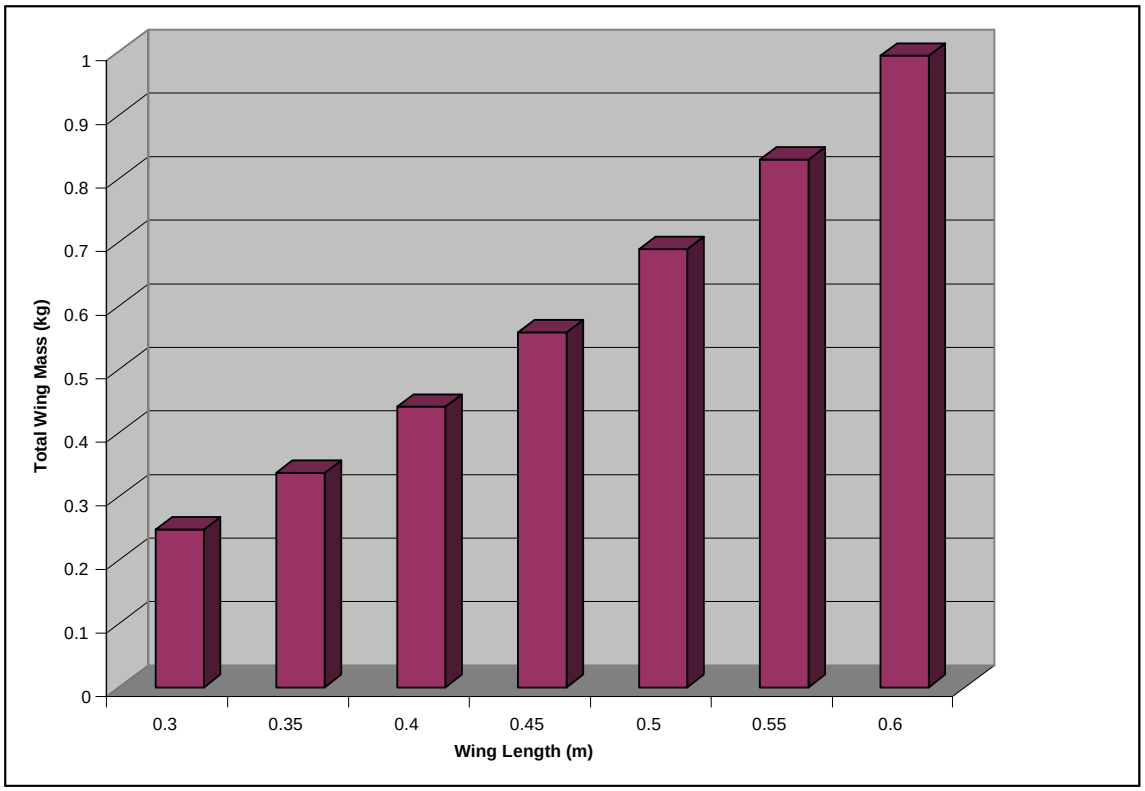

Figure 3-8: Total Wing Mass as a Function of Wing Length

The relative lifting capacity for various wing lengths and engine power levels is shown in Figure 3-8. From this figure it can be seen that wing length has a fairly large effect on the lifting capacity of the vehicle, but an increase in engine power produced only a modest increase in lifting. It can be inferred that increasing wing length has a much greater benefit then increasing engine power. Increasing the flap angle for a given power level, has a benefit for increasing relative lifting capacity. By increasing the wing length and or flapping frequency and maintaining the same power level the flapping frequency must decrease. Although the absolute relative lifting capacity values shown in these curves are specific to the flight speed and operational configuration specified, the trends shown should be consistent for all vehicle configurations and flight speeds. This figure demonstrates that the Entomopter wing and flapping angle should be as large as possible to maximize the relative lifting capacity of the vehicle for a given power level.

The complete design space for the Entomopter is quite large. Changing any of the parameters can affect power required and relative lifting capacity. To determine the best configuration for the proposed Mars mission, power required and relative lifting capacity were plotted over a

range of wing lengths, flapping frequencies, flapping angles, and flight velocities. The ranges of these values used to generate this design space are given in Table 3-1.

Table 3-1: Entomopter Parameters and Design Space Ranges

Parameter	Range
Flight Velocity	2 to 30 m/s
Flapping Frequency	1 to 30 Hz
Wing Length	0.3 to 1.0 m
Maximum Flapping Angle	35° to 85°
Relative Lifting Capacity	0.5 to 2.0 kg

Figures B-1 through B-41 in Appendix B show the power required and relative lifting capacity of the Entomopter over this complete design space. The first eight of these figures in Appendix B (Figures B-1 through B-8) correlate the power required by the Entomopter to a flapping frequency for various wing lengths and flapping angles. These first eight figures are meant to be used as a means of determining the flapping frequency for Figures B-9 through B-41 in Appendix B for the various conditions presented in these graphs. From the data shown in these figures a design point was chosen. (see Figure B-23 in Appendix B.) This design point represents a realistic operating configuration for the Entomopter. The specifications for the design point are shown in Table 3-2.

Table 3-2: Design Point Operational Characteristics

Parameter	Value
Flight Velocity	14 m/s
Flapping Frequency	6 Hz
Wing Length	0.6 m
Maximum Flapping Angle	75°
Relative Lifting Capacity	1.5 kg
Power Required	883 W
Fuel Consumption Rate	0.011 kg / min.

These figures show that to fly slower power must increase exponentially. Therefore, to slow down to a near stop and land the Entomopter would require a significant increase in power. Producing these high power levels is not a practical approach to landing the Entomopter. Additional techniques can be used to reduce speed and get the Entomopter on the ground without such a dramatic increase in power. A potential landing sequence is shown in Figure 3-9.

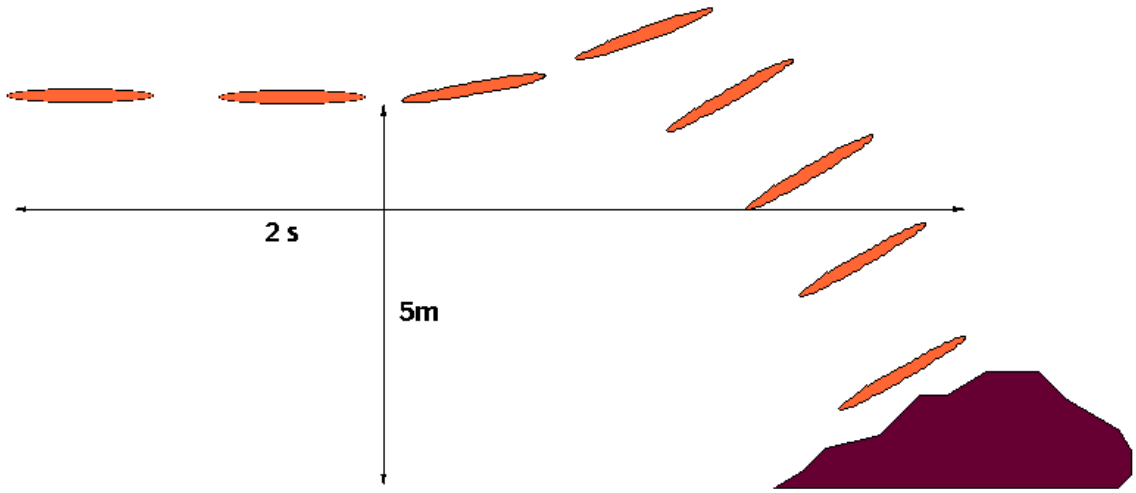

Figure 3-9: Entomopter Landing Approach

In this landing sequence the Entomopter would slow by flaring upward as it approaches the landing site. This would cause the vehicle to slow as well as lose lift. The Entomopter would then descend to the landing site. To ease the descent the engine would be overpowered for a short period of time to increase the flapping frequency of the wings as much as possible. This would produce extra lift and help slow the vehicle's descent. The over-speeding of the engine would occur for a very short amount of time (1 to 2 seconds) and therefore should have little effect on the engine. The main effect on the engine from running at these increased output power levels would be an increase in temperature. Because the engine would run in this condition only for a short period of time, the temperature rise would be absorbed by the thermal mass of the engine. While the Entomopter is on the surface the engine would need to cool down to its normal operational temperature before the Entomopter could take off again. In addition to providing increased power, over-speeding the engine will also consume more fuel, which will produce more exhaust gases. This increase in exhaust gas can be used to further augment the vortex formation and attachment to the wing, thereby temporarily increasing the lift coefficient of the wing. Some additional flight energy can be absorbed by spring mechanisms in the legs of the Entomopter. These springs act as shock absorbers and to lock into a compressed state upon landing. Releasing the leg springs can be used to push the Entomopter into the air and assist with takeoff. The combination of the over-speeding of the engine, increased gas production, and leg spring energy absorption should be sufficient to allow the Entomopter to safely land on the surface.

3.2 Wing Motion and Structure Analysis

The structural analysis for the Entomopter wing is an important part of the overall vehicle design. Even though the gravitational force on Mars is only roughly a third of Earth's, significant forces can still affect the wing structure. The bulk of the force the wing will see comes from the motion of the wing. The operation of the Entomopter entails the rapid motion of the wings. Caused by the acceleration and deceleration of the wing on each beat, this motion imparts a significant loading on the wing structure.

This initial analysis looks at the loading on the wing due to its motion and the gravitational force on Mars. For the time, the lifting loads on the wings have been ignored. A simplified two dimensional analysis can be performed based on the wing platform geometry. It is initially assumed that the wing thickness is uniform over the entire wing. As the analysis progresses more detail will be added to accurately represent the wing geometry and extend the analysis to three dimensions.

The forces exerted on a uniform two-dimensional wing are shown in Figure 3-10, where F_g is the force due to gravity, F_t is the tangential force at a point a distance r along the wing, and F_r is the radial force at that same point. These forces can be represented by the following equations:

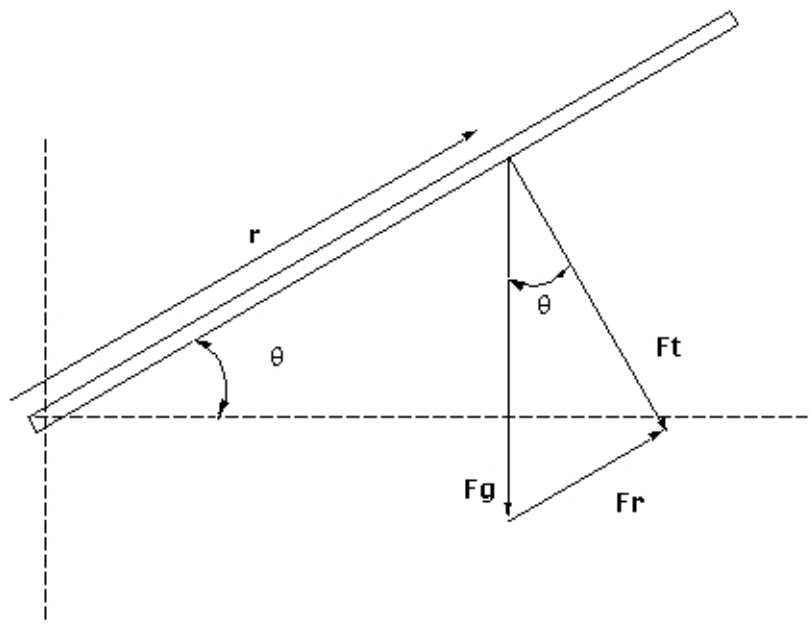

Figure 3-10: Forces Acting on a Given Point Along the Way

$$F_t = m\,(r\,(d^2\theta / dt^2) + 2\,(dr / dt)\,\theta) + m\,g\,\mathrm{Cos}\,(\theta)$$ ***Equation 3-11***

$$F_r = m\,(\,(d^2 r / dt^2) - 2\,r\,(\,d\theta / dt)^2\,) + m\,g\,\mathrm{Sin}\,(\theta)$$ ***Equation 3-12***

In these equations θ represents the angle of the wing with respect to the horizontal at a given point in time, r is the radius along the wing where the forces being calculated act, m is the mass of the wing section at r, t is the time, and g is the gravitational force on Mars (-3.75 m/s^2). Because the wing cannot change length the derivatives of radius with respect to time (dr/dt and d^2r/dt^2) are zero.

The forces generated are dependent on the operational conditions and geometry of the Entomopter wing. From the subsequent sizing analysis a baseline set of conditions was established representing the most desired operating conditions. These are listed in Table 3-3.

Table 3-3: Baseline Operating Conditions

Flapping Frequency	6 Hz
Maximum Wing Motion Angle	$\pm 75^{o}$
Wing Section Length	0.6 m

It was assumed that the change in θ, or wing position, with respect to time follows a cosine function. This motion is shown in Figure 3-11. This curve is for a 6 Hz wing flapping frequency and a ±75° wing motion. The cycle starts with the wing in the maximum upward position.

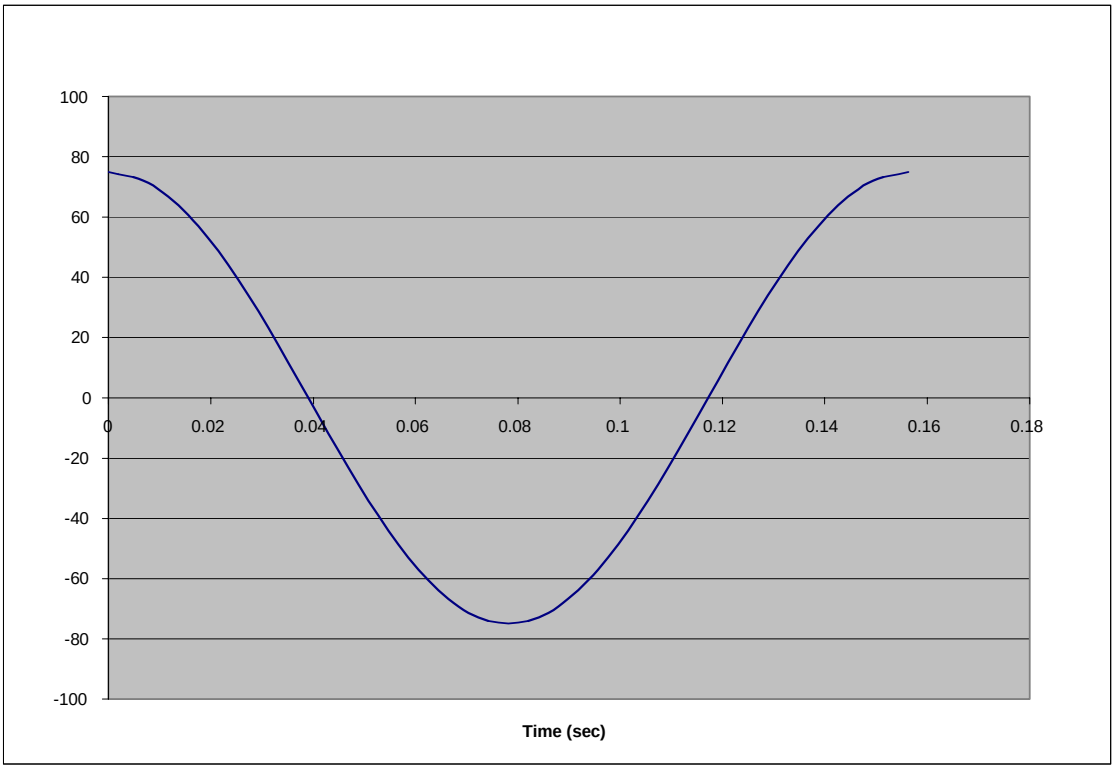

Figure 3-11: Wing Motion Represented by Angle Change with Time

In general the equation for θ (shown in Figure 3-11) can be represented by Equations 3-13 and 3-14. Where a is the absolute value of θ at its maximum point, the constant b is set by the wing flapping frequency (f) given by Equation 3-14 and c sets the starting point for the cycle (c is 0 in this case). By changing c the curve will shift to the left or right. For this analysis the wing starts at the maximum upward position at time 0 and begins its flap with a downward stroke.

$$\theta = a \cos(bt + c)$$ ***Equation 3-13***

$$b = 2\pi / (1/f)$$ ***Equation 3-14***

Subsequently the derivatives of θ with respect to time are given in Equations 3-15 and 3-16.

$$d\theta / dt = -a [\sin(b t + c)] b$$ ***Equation 3-15***

$$d^2\theta / dt^2 = -a [\cos(b t + c)] b^2$$ ***Equation 3-16***

For this initial 2D case it was assumed that the wing had a thickness of 1 cm and a wing section mass (one half of a full wing) of 0.75 kg. This is based on a wing material density of 1000 kg/ m^3. Since with wings are symmetrical the loading on each wing section will be the same. Therefore the analysis is for only one wing section.

The chord of the wing varies along the wing length This variation in chord length with radius is shown in Figure 3-12. Based on this figure the chord change as a function of radial station can be calculated. A regression was performed to determine an expression for the chord length as a function of radial location along the wing section. Equation 3-17 represents this curve fit normalized to a wing section length of 1.

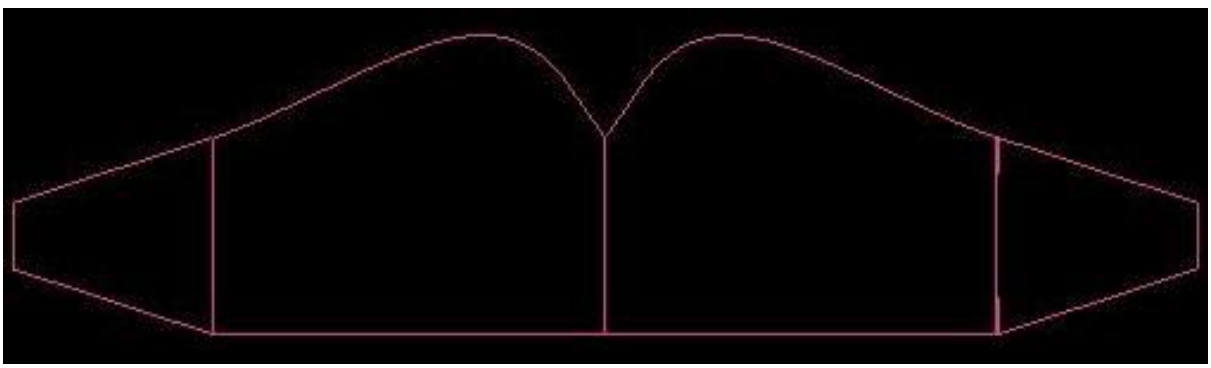

Figure 3-12: Plan-view of Entomopter Wing

$$c = 0.32814 + 2.61643 r - 9.1414 r^2 + 15.642 r^3 - 12.951 r^4 + 4.0584 r^5$$ ***Equation 3-17***

The effect of this variable chord geometry on the mass distribution along the wing is shown in Figure 3-13. This mass was calculated for a solid wing which is not the optimal structural design. However this was done to demonstrate how the mass distribution is affected by the variable chord length of the wing. The mass was calculated in ten equal increments along a 0.5m long wing section. The figure shows the comparison in wing mass at sections along the wing length between the variable chord wing shown in Figure 3-20 and a fixed chord wing with an aspect ratio of 2.5. The total mass of both wing types are similar (1.0 kg for the fixed chord wing section and 0.9 kg for the variable chord wing section). The reduction in mass on the outer portion of the wing has a significant effect in lowering the loading on the wing. Since the acceleration loads increase along the wing length, mass reduction on the outer portion of the wing will have the greatest effect in reducing the overall wing loading.

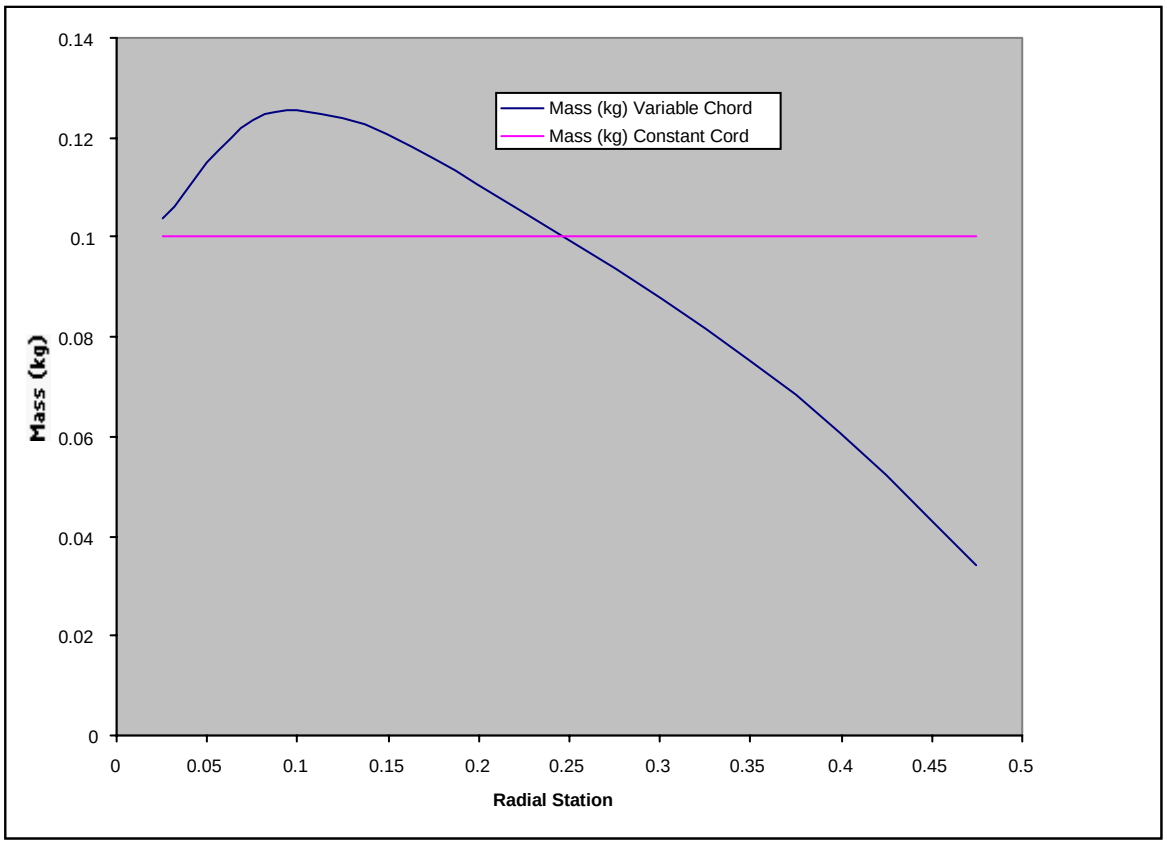

Figure 3-13: Mass Distribution Along the Wing Length (Based on 10 Incremental Mass Sections)

By using Equations 3-11 through 3-17 the loading on the wing was determined at 10 radial stations. Flapping frequency, wing length and maximum wing angle were varied to see what effect these had on the loading. The following figures show what effect these variables have on the wing loading. The tangential loading in N/m is at various times throughout the complete stroke cycle. This tangential load will vary from positive (upward away from the surface) to negative (downward toward the surface) depending on the direction the wing is moving.

Based on the sizing analysis the wing angle will need to be as great as possible (on the order of ±75°). It is worth noting that the increase in wing angle has a greater effect on the radial loading then on the normal (tangential) or bending loads.

The maximum loading at each point along the wing occurs when the wing is at its maximum downward position. It this position the wing sees both a maximum acceleration load as well as a gravitational load both working in the downward direction.

Utilizing the wing loading profile (W(r) given in Equation 3-19 and shown in Figure 3-14) the shear force, bending moment and deflection of the wing can be calculated. The shear loading is calculated by integrating the wing loading profile. This integration can be done numerically or analytically, utilizing an equation for the loading profile. For example using the wing loading for

the base operating conditions of 6 Hz, 75° Maximum angle and a 0.6 m wing section length (shown in Equation 3-19) the shear loading can be calculated as follows.

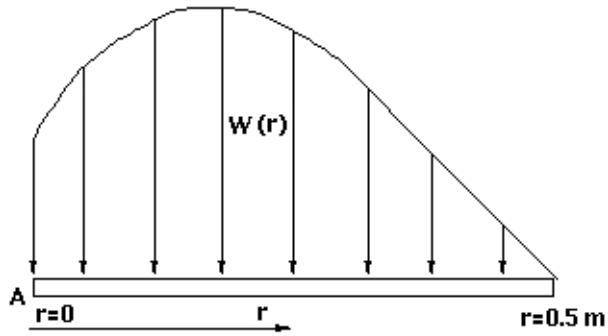

Figure 3-14: Load Diagram and Coordinate System for Wing Loading

$$V(r) = \int W(r)dr$$ ***Equation 3-18***

$$W(r) = -554.63+1.0608E5\ r - 60373\ r^2 - 2.2389E5\ r^3$$ ***Equation 3-19***

Integrating yields

$$V(r) = -554.63\ r + 53040\ r^2 - 20124.33\ r^3 - 55972.5\ r^4 + C_1$$ ***Equation 3-20***

The boundary conditions used to determine C_1 are; r = 0. 5 (the wing tip) the shear must be equal to; V = 0.

$$_1 = -6968.86$$ ***Equation 3-21***

The bending moment along the wing is the integral of the shear load given by Equations 3-20 and 3-21. This is represented by the following equations.

$$M(r) = \int V(r)dr$$ ***Equation 3-22***

$$M(r) = -277.315\ r^2 + 17680\ r^3 - 5031.08\ r^4 - 11194.5\ r^5 - 6968.66\ r + C_2$$ ***Equation 3-23***

Where C_2 is determined from the boundary conditions; M = 0 at r = 0.5.

$$C_2 = -2007.93$$ ***Equation 3-24***

Based on this analysis the shear loading and bending moment for the various flight conditions is shown in Figure 3-18.

The tangent angle to the bending curve (q) is the next quantity that can be calculated by integrating the moment (Equation 3-23). This angle can be represented by the following equation. Since the wing geometry changes from the root to the tip the moment of inertia (I) is not a constant and therefore varies along the wing length. This integral can be approximated by an infinite series

from 0 to i. Where I(r) is the moment of inertia of the wing section and E is the modulus of elasticity.

$$\theta = \int \frac{M(r)}{I(r)E} dr = \sum_{0}^{i} \frac{\overline{M}_i \Delta r}{\overline{I}_i E}$$ **Equation 3-25**

Lastly the deflection of the wing can be calculated by integrating the tangent angle (θ). This integration is given below.

$$y = \int \theta(r) dr = \sum_{0}^{i} \overline{\theta}_i \Delta r$$ **Equation 3-26**

Utilizing the above analysis the geometry of the wing structure was examined to determine what geometry would provide the greatest stiffness with a minimum amount of weight for the base line operating conditions given in Table 3-3. The initial structural design was a solid wing with an elliptical cross section of uniform thickness from the root to the tip. Variations from this geometry were then tried in order to reduce mass while maintaining the same amount of deflection. To reduce structural mass a hollow ellipse for the wing cross section was used. Since the majority of the strength in the wing comes from the material furthest form the center (core) of the wing, this type of structure enabled the wing to be light-weight while providing sufficient structural rigidity. The reasoning behind this type of cross section can be seen in the moment of inertia (I) equation for an ellipse, given in Equation 3-27. To minimize deflection the moment of inertia has to be as large as possible. This can be accomplished by increasing the thickness of the wing (b). However you also want to minimize mass. This is accomplished by utilizing the smallest cross sectional area (of material) as possible. The cross sectional area for the wing section (A) is given in Equation 3-28. To accommodate these two somewhat contradictory requirements mass is moved from the center of the ellipse to the edges by making it hollow and thicker. Since the moment of inertia for the ellipse is proportional to the thickness cubed, any small increase in thickness can have a large increase in wing strength.

To further optimize the wing geometry the thickness was tapered from the root to the tip. This allowed more mass to be utilized near the root where the bending and shear loads are the greatest. This geometry is shown in Figure 3-15. The effect of utilizing a hollow wing and tapering it toward the tip has a substantial effect on the overall mass of the wing and therefore the structural loading.

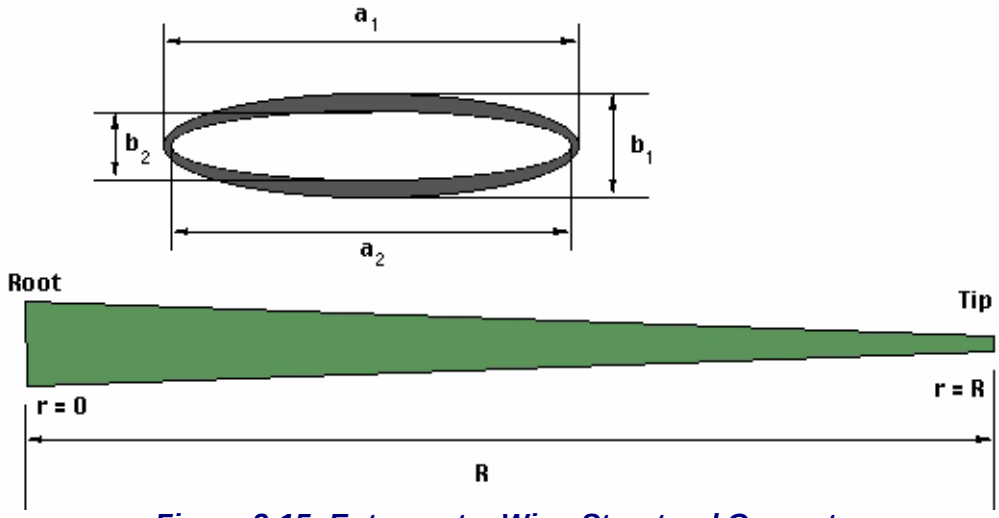

Figure 3-15: Entomopter Wing Structural Geometry

The inner ellipse, that represents the empty area, is of slightly different proportions then the outer ellipse. This provides for increased mass on the upper and lower wing surfaces to increase the structural rigidity and minimizes the mass at the front and trailing edges where it is needed the least. The thickness taper for the wing was assumed to be a linear function from the root to the tip.

$$I = (\pi / 64)\,(a_1\, b_1^3 - a_2\, b_2^3)$$ *Equation 3-27*

$$A = (\pi / 4)\,(a_1\, b_1 - a_2\, b_2)$$ *Equation 3-28*

To quantify the benefit of using a hollow wing and taper, the above analysis was performed for four different structural designs. The maximum tip bending of each case was held constant and the mass of the wing section was determined based on a configuration that would not exceed the set bending limit. The results of this are shown in Figure 3-16. This bending limit was chosen for comparison between the different geometries and may not represent the actual bending limit required by the Entomopter. Because of the aerodynamics of the wing operation it may be desirable to actually have a greater tip bending then what was used in this analysis. If this is the case then this will reduce the wing section mass from what is presented here. However the trends regarding the geometry impacts on the wing mass will still be valid regardless of the desired wing bending limit.

The mass distribution curves are generated by plotting the mass of wing sections, each 1/100 of the total wing section length. Each curve in Figure 3-16 represents the mass distribution necessary to maintain a maximum wing tip deflection of 0.015 m. Depending on the case the taper ratio, inner hollow ellipse or both were varied until the wing was able to achieve the minimum deflection required. The details of the wing geometry and total mass are shown in Table 3-4.

From Figures 3-16 and 3-17, and Table 3-4 it can be seen that the greatest benefit in reducing the wing mass while maintaining the desired deflection is by utilizing a hollow wing.

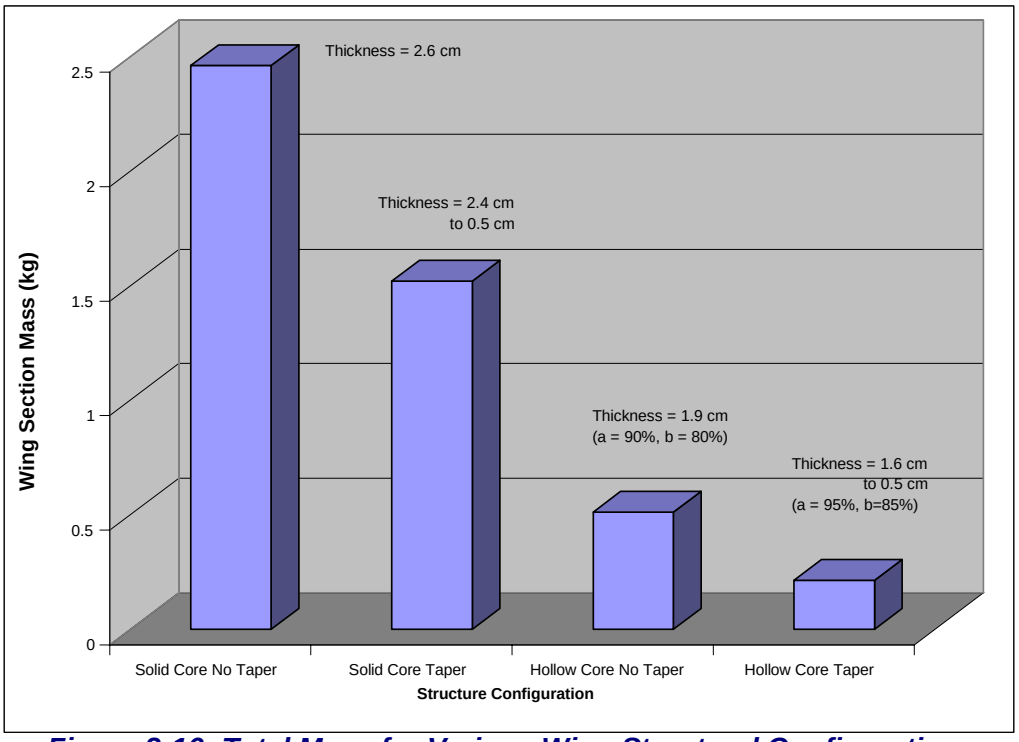

Figure 3-16: Total Mass for Various Wing Structural Configurations

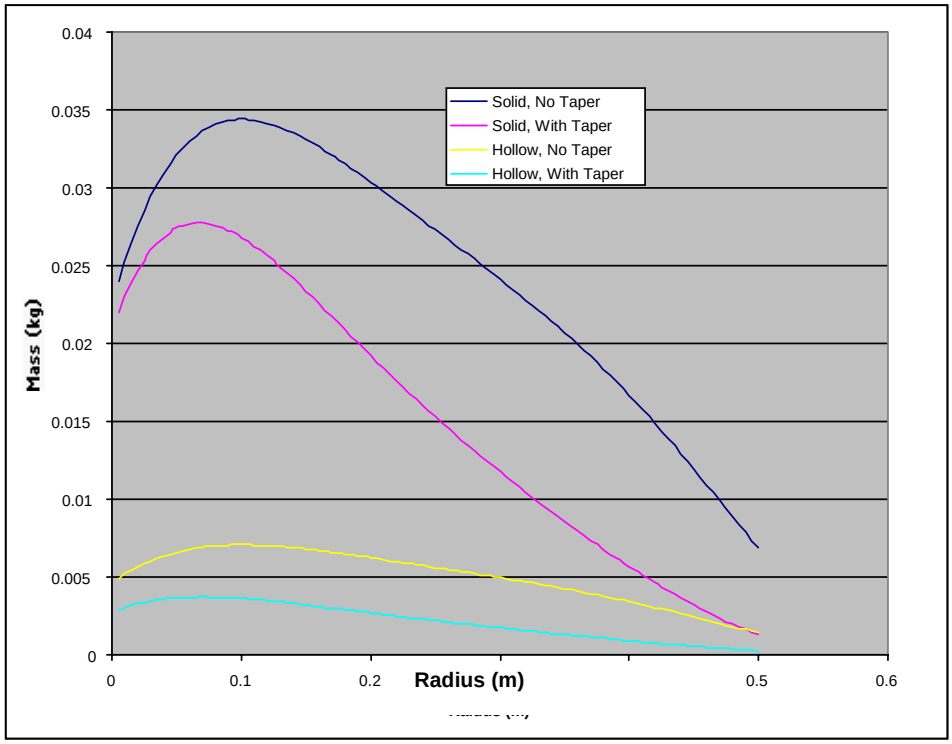

Figure 3-17: Mass Distribution for Various Structural Geometries

Table 3-4: Wing Geometry and Mass

Thickness (m) (Root to Tip)	0.026 to 0.026	0.024 to 0.005	0.019 to 0.019	0.0165 to 0.005
Interior Ellipse as a Percent of Outer Wing Dimensions	Solid: a = 0%, b = 0%	Solid: a - 0%, b = 0%	a = 90% b = 80%	a = 95% b = 85%
Total Wing Section Mass (kg)	2.46	1.52	0.51	0.214
Maximum Tip Deflection (m)	0.015	0.015	0.015	0.015

The tapering of the wing also had an effect but it wasn't as dramatic. The maximum loading point on the wing, used to generate the results given above, occurs when the wing is at its maximum downward position. In this position the wing sees both a maximum acceleration load as well as the gravitational load both working in the downward direction. This maximum loading profile along the wing is shown in Figure 3-18 for the base flight conditions given in Table 3-3 and the hollow tapered wing geometry shown in Table 3-4. The radial loading profile is shown in Figure 3-19. Structurally the radial loading is not significant and does not affect the wing structural design. The structural geometry will not effect the maximum loading point for the wing. It will however have an effect on the absolute value of the loading experienced. Therefore the loading profile and point of maximum loading will be consistent for each structural geometry considered.

The hollow tapered geometry produced the lightest wing for a given amount of deflection. Based on these results this geometry configuration will be the baseline geometry for the wing. This baseline, as listed in Table 3-4, consists of a wing taper from 0.0165 m at the root to 0.005 m at the tip and an inner ellipse length “a” equal to 95% and thickness “b” equal to 85% of the outer ellipse dimensions respectively. For this hollow tapered geometry, the loading profile along the wing length is shown in Figure 3-20. Also shown in this figure are the subsequent shear loading and bending moment curves for this wing geometry.

Variations in the wing structural geometry from the baseline values were also examined. This was done to determine what effect each of the parameters had on the wing mass and tip deflection. The results of these variations are shown in Figures 3-21 through 3-24. Figures 3-21 and 3-22 show the effect changing the dimensions of the hollow elliptical core of the wing has on the wing section mass and wing tip deflection. As the hollow core dimensions are increased the wing section mass decreases linearly with both dimensions (a and b) as should be expected. The tip deflection is greatly effected by variations in the thickness (b) of the core ellipse. This is because the moment of inertia for the wing is greatly dependent on the ellipse thickness. From this curve it can be seen that a minimum tip deflection occurs at a hollow core thickness of approximately 85% of the overall wing thickness. This is consistent with the design point that was chosen.

The reduction in the wing-tip deflection is influenced most by the wing-root thickness, as shown in Figure 3-22. As the root thickness increases, the mass of the wing section increases and tip deflection decreases. This large benefit in reducing the tip bending by increasing the root thickness occurs because the added mass, hence wing strength, is added at a location with the minimum amount of structural loading. Therefore, the increase in mass does not add much to the bending load on the wing but does contribute to its strength. Conversely, reducing wing thickness and hence structural mass at the wing tip reduces maximum bending seen at the tip. This is shown in Figure 3-24.

Based on this analysis, the geometry of a hollow-core wing with a tapered thickness from the root to the tip produces the most efficient structural design. This design is capable of withstanding structural loading applied under baseline operating conditions with minimal wing flexing and a fairly light weight.

A CAD drawing of the wing structure was produced based on the hollow, tapered geometry established as the base wing geometry through this analysis. This geometry is show in Figures 3-25 through 3-27.

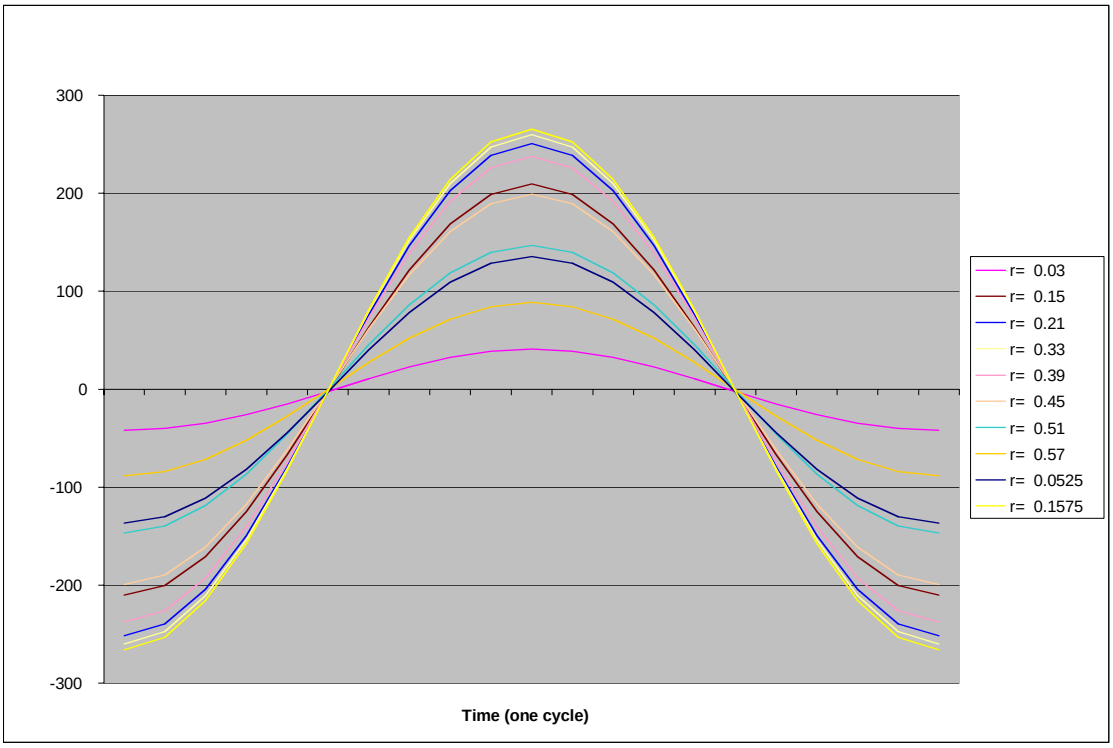

Figure 3-18: Loading Profile at Various Radial Stations Along the Wing for a Hollow Tapered Wing

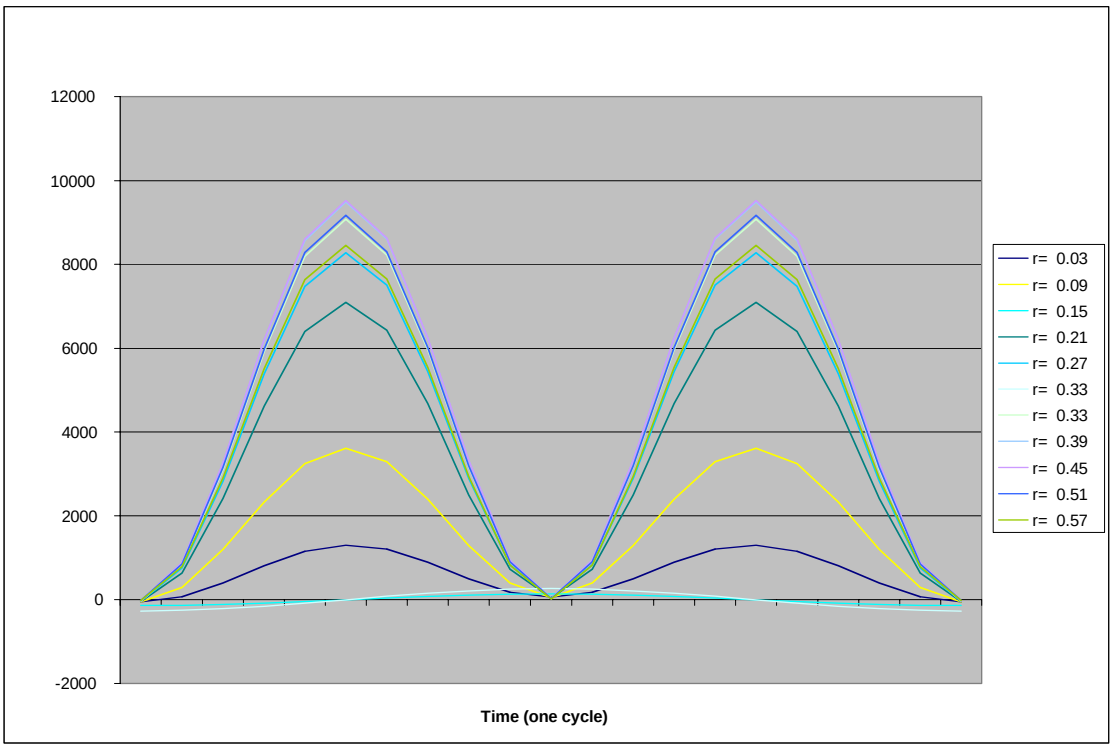

Figure 3-19: Radial Loading Profile at Various Locations Along the Wing for a Hollow Tapered Wing

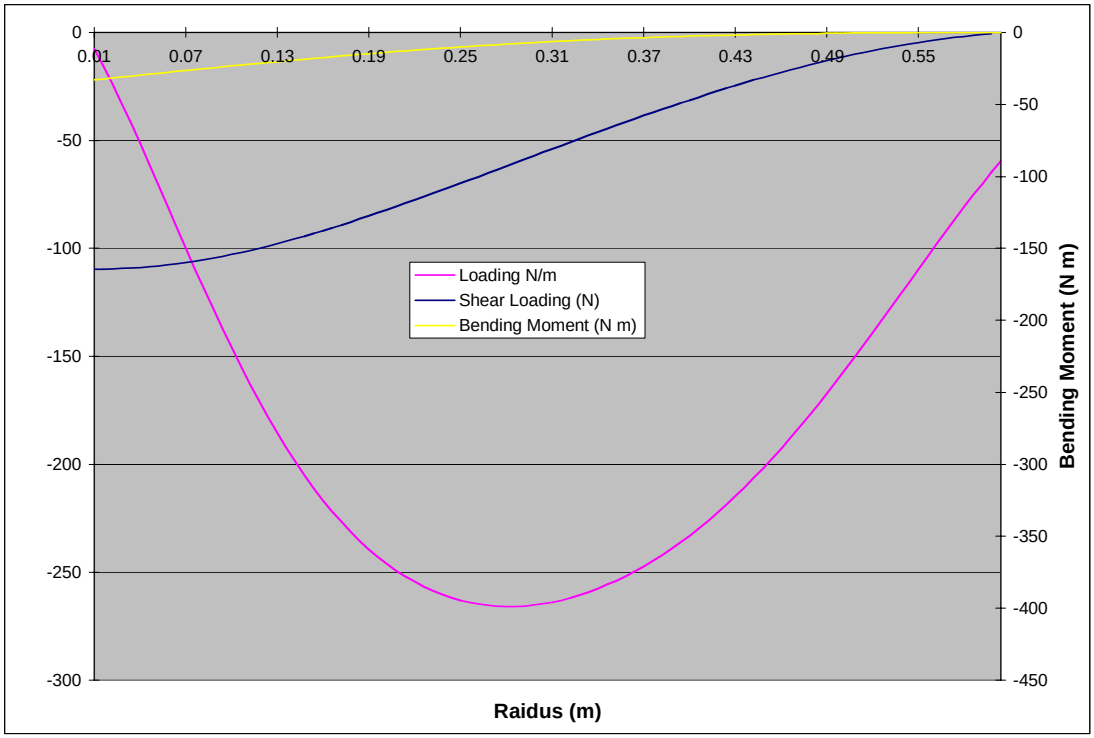

Figure 3-20: Loading, Shear, and Bending Moment for a Hollow Tapered Wing

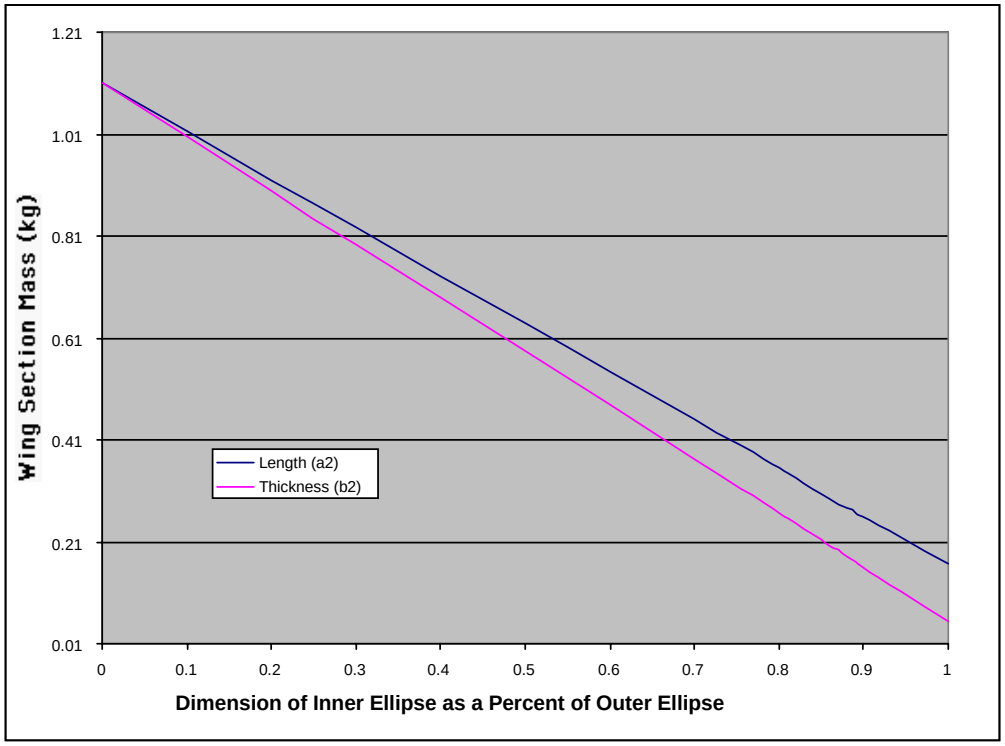

Figure 3-21: Effect of Hollow Elliptical Core Dimensions on Wing-section Mass

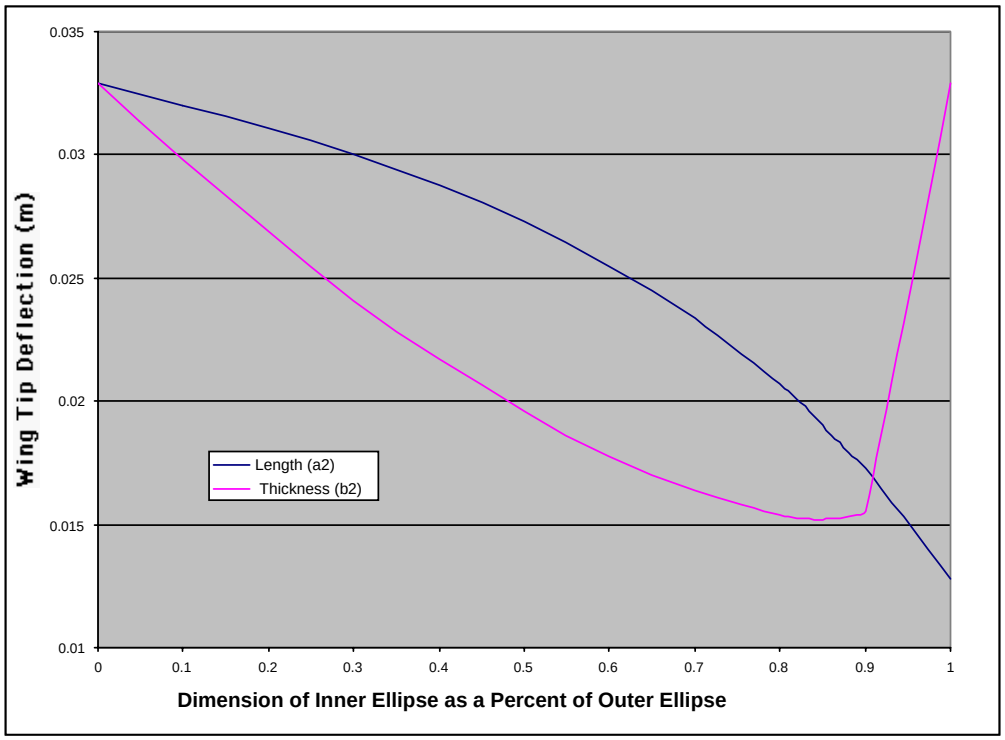

Figure 3-22: Effect of Hollow Elliptical Core Dimensions on Wing-tip Deflection

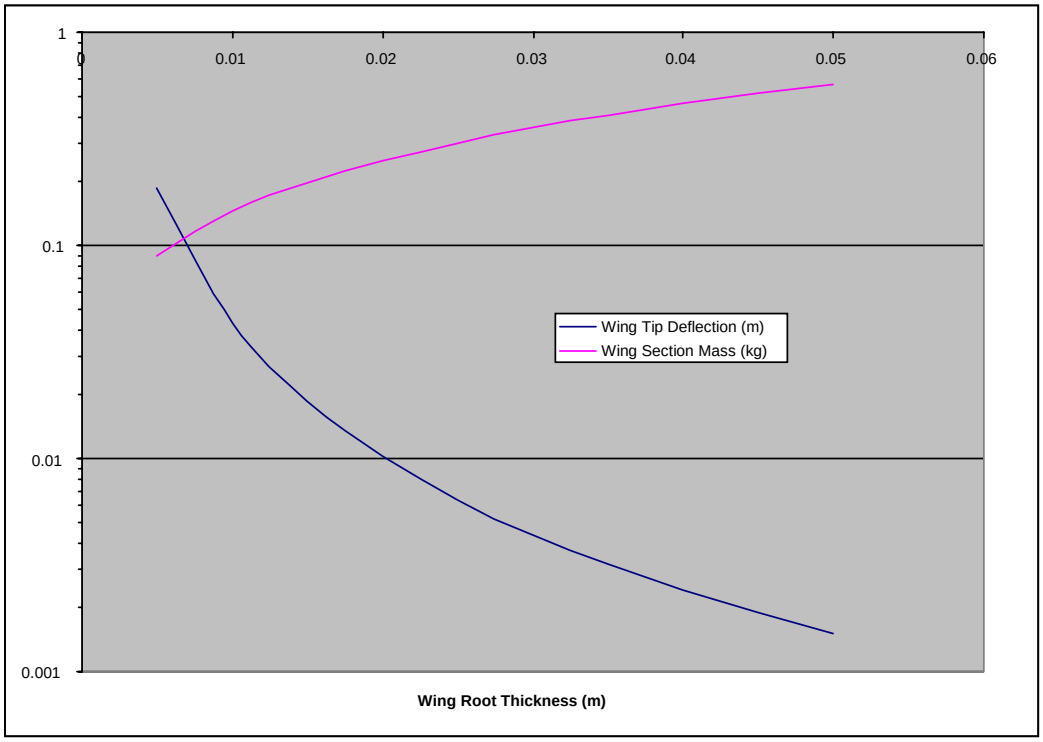

Figure 3-23: Effect of Wing-root Thickness on Wing-tip Deflection & Wing-section Mass

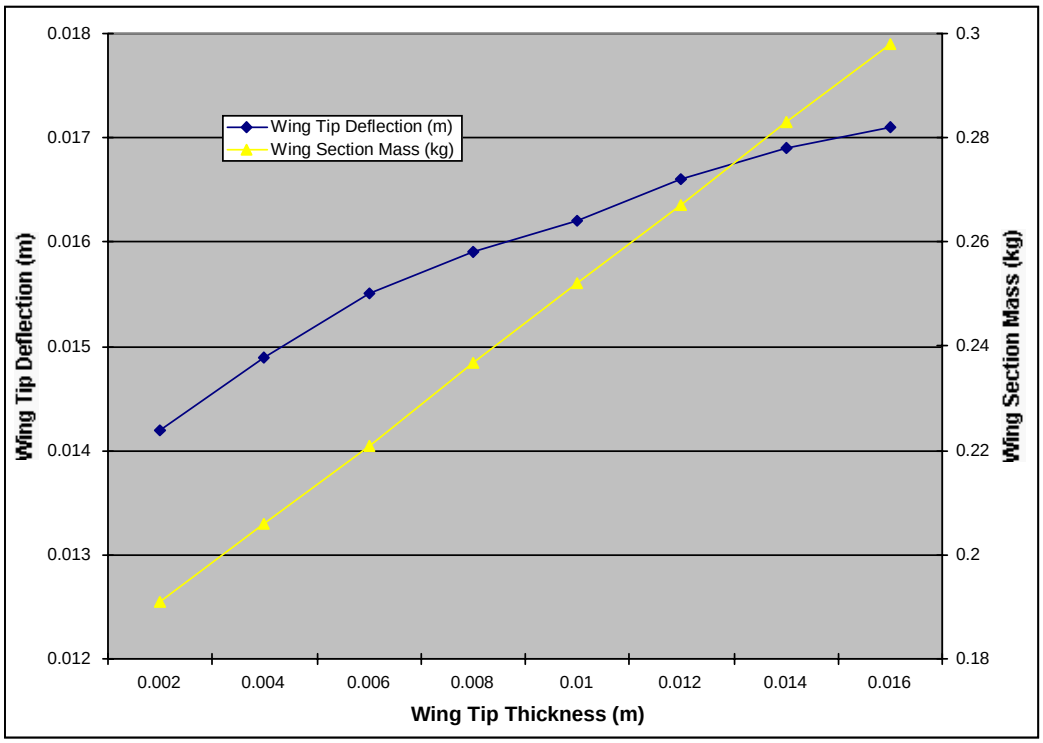

Figure 3-24: Effect of Wing-tip Thickness on Wing-tip Deflection & Wing-section Mass

Figure 3-25: CAD Wing Section for the Hollow, Tapered Baseline Geometry--Root to Tip from Wing Top

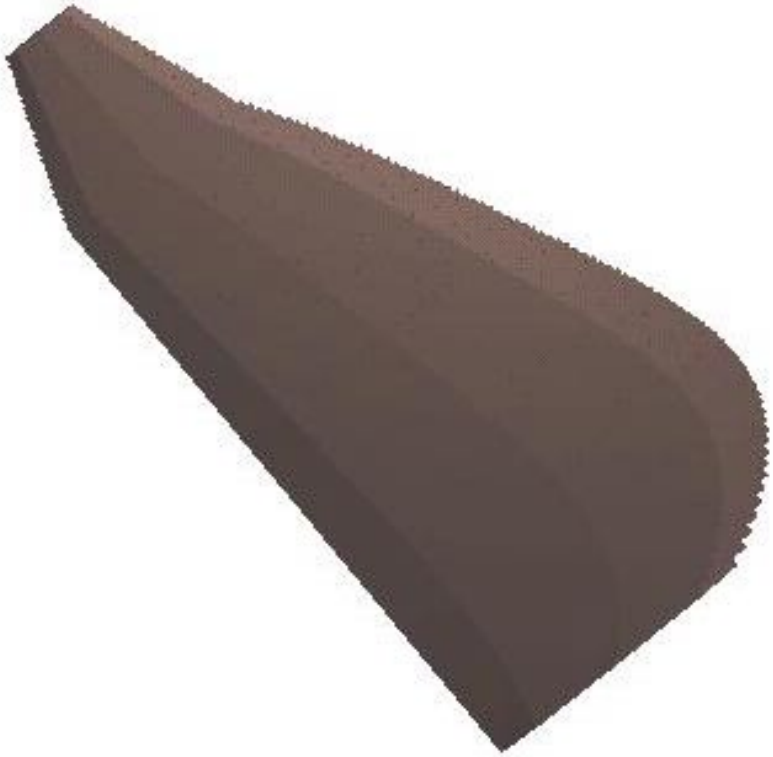

Figure 3-26: CAD Wing Section for the Hollow, Tapered Baseline Geometry - Top View

Figure 3-27: CAD Wing Section for the Hollow, Tapered Baseline Geometry--Leading Edge View

3.3 Wing Aerodynamics

3.3.1 Computational Fluid Dynamics

3.3.1.1 Introduction

Low Reynolds number, unsteady aerodynamics of thin cambered wings is of current interest because of technological applications such as micro air vehicles (MAV). High lift associated with insect flight, not predicted by conventional quasi-steady aerodynamics, has been a fascinating subject for many researchers. Several mechanisms, such as the “clap-and-fling” (Weis-Fogh mechanism) and the “delayed-stall-rotational-lift-wake-capture” (Dickinson mechanism), have been proposed to explain how lift is generated during the cyclic motion of the insect wing. Forward flight, requiring both lift and thrust, has been more easily analyzed than hovering flight. Studies on tethered live animals have been conducted to measure forces and visualize flow patterns. Experimental studies using models with basic wing kinematics, such as heaving, flapping, and pitching, have also been undertaken [115, 129]. Gaining a thorough understanding of insect wing aerodynamics and incorporating their desirable features into MAV design have become one of the critical technologies of MAV development.

In this work, we use computational fluid dynamics (CFD) tools to simulate low Reynolds number, unsteady aerodynamics that incorporate geometries and kinematics representative of insect wings. Leading edge vortex (LEV) dynamics, span-wise flow features, and dynamic camber variation during the wingbeat are of particular interest. CFD is an extremely powerful tool for flow field visualization and provides a tremendous amount of data on the flow field (e.g., lift, drag). It is especially useful for simulating environments that are either too dangerous or too

expensive to simulate on Earth. Additionally, the fundamental basis of the Navier-Stokes equations (Reynolds-averaged) tightly couples CFD to physics.

The ability to acquire the data from the time history of unsteady forces and vortex formation on the wing is extremely important and has been demonstrated in this report. The Entomopter vehicle design hinges on whether or not the wings can generate sufficient lift and have an acceptable lift-to-drag ratio.

This section will address computations with the CFD codes WIND and FLUENT, as well as codes from Metacomp Technologies, Inc., presented in chronological order. Three-dimensional cases with blowing were simulated initially using WIND to determine if aerodynamic performance can be enhanced by surface blowing. Cases showing the effect of blowing tangential to the trailing edge surface are presented. Animations of the resulting flow fields show the effect of blowing. A major part of the effort at the University of Missouri-Rolla (UMR) with FLUENT has been to design the airfoil section and the 3D planform to mimic the aerodynamic attributes of a typical insect wing. A cicada wing was analyzed for its aerodynamic parameters, such as camber, thickness, planform, structural attributes, and role of the hind wing. Extensive literature review was conducted on the aerodynamic aspects of insect flight and the current status of insect-derived MAV design. A series of two-dimensional studies was conducted using FLUENT to optimize airfoil section parameters, such as thickness and camber, and to establish leading edge vortex (LEV) behavior. Reynolds number was varied by a factor of 10, and the resulting flow fields have been analyzed. A small thickness, cambered three-dimensional wing was designed for the work in progress on flapping wing simulations. Understanding low Reynolds unsteady aerodynamics and controlling wing kinematics during the stroke cycle have been identified as key topics for the continuing Entomopter CFD work.

3.3.1.2 Entomopter Wing CFD Analysis: WIND

Preliminary CFD calculations were conducted with WIND Version 3 Code [283], a product of the NPARC Alliance, a partnership between NASA Glenn Research Center (GRC) and Arnold Engineering Development Center (AEDC) dedicated to the establishment of a national, applications-oriented flow-simulation capability. WIND solves the Reynolds-averaged Navier-Stokes equations, along with supporting equation sets governing turbulent and chemically reactive flows.

Calculations with WIND were completed early in the project to get some idea of the complexity and physics associated with a sinusoidally oscillating airfoil with tangential blowing. Although the sinusoidal flapping motion did not physically represent the actual motion of the Entomopter wing, purely sinusoidal flapping runs were important in understanding basic vortex creation and convection over the airfoil, which ultimately drives the aerodynamics and wing lift.

Both steady and unsteady computations with an oscillating inflow and blowing (mass ejection at the wing tips) were completed to assess the code's ability to handle this very demanding flow field, which includes a very low Mach number inflow, with sinusoidal oscillation to simulate flapping motion, and mass ejection on the outer wing panels to simulate blowing. Blowing is used to entrain lower energy boundary-layer air and reenergize it with higher energy air, decreasing the tendency for the flow to separate and thereby increasing circulation. This, along

with vortex action, leads to very high lift coefficients despite the very low dynamic pressure of the Mars atmosphere.

The final computational grid, created with GRIDGEN [109] software, consisting of 495,824 points (fairly coarse), is shown in Figure 3-28. Details of the grid on the wing surface can be seen in Figure 3-29. The wing is an untapered, unswept, viscous, cambered flat plate representing a generic low speed airfoil. The Navier-Stokes equations were solved at the grid points, simulating the flow over the Entomopter wing.

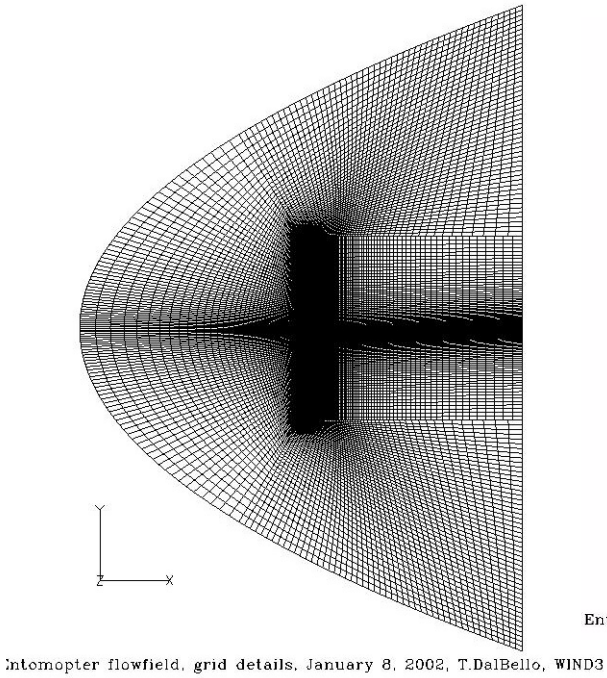

Figure 3-28: Computational Grid

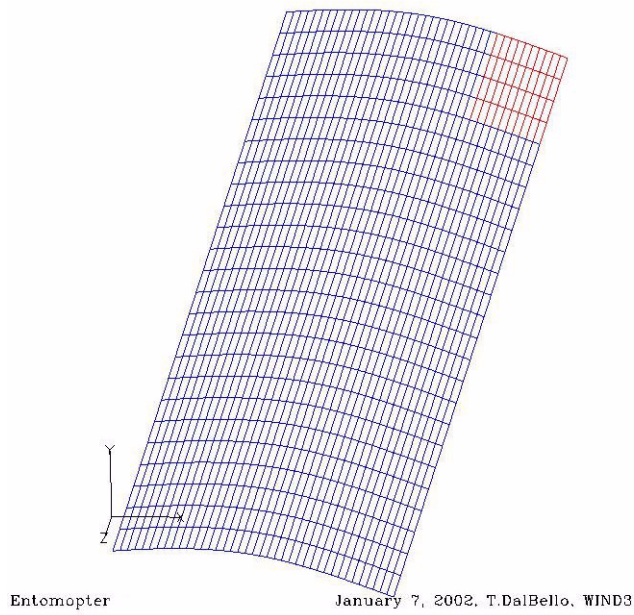

Figure 3-29: Surface Grid

WIND Version 3 Simulation Conditions:

- Mars atmosphere: Treated as 100% CO_2
- Mach number = 0.09 (~30 mph)
- Total pressure = 0.11 psi
- Total temperature = -207° F (252 Rankine)
- angle of attack = 5°
- Laminar viscosity = 2.235e-7 slug/foot-second
- Oscillation rate, amplitude: 15 cycles/second, 20°
- Blowing parameters: Pressure = 0.14 psi, temperature = 700° R
- Spalart-Allmaras turbulence model
- Reynolds number: About 6,000
- Wing span = 39.4"
- Wing chord = 6.38 inches (constant chord)
- Blowing region area = 10.74 in^2 (2.1% of wetted area)

The flow conditions used in the WIND simulations represented the Mars environment. These conditions are shown in the list above. Qualitative results from these simulations can be seen in Figures 3-30 through 3-35. Figure 3-30 shows the complexity of the flowfield and dynamic stall vortex using massless particles released ahead of the wing. Figure 3-32 shows the outline of the wing (black lines) with a Mach number cut and velocity vectors depicted near the wing tip. A dynamic stall vortex and flow ejection off the trailing edge can be seen. Figure 3-33 shows the dynamic stall vortex using streamlines. Figures 3-34 and 3-35 show the airfoil surface and LEV development. Animation of time-dependent calculations showed the familiar repeated shedding of dynamic stall vortices from the leading edge across the airfoil. This interaction of vortices with the upper wing surface at this Reynolds number results in higher lift coefficients over the case without oscillation (a static airfoil such as on a fixed wing airplane).

Quantitative results were also obtained, as shown in Figures 3-36 and 3-37. Figure 3-36 shows the drag coefficient vs. time with blowing and oscillation. Figure 3-37 shows the lift coefficient vs. time with blowing and oscillation. Similar lift and drag results were found for the case without blowing. It is expected that blowing should increase circulation above and beyond the contributions to oscillation alone.

However, in all figures except Figure 3-31, the blowing was ejected tangential to the top wing surface (which is essentially horizontal). However, blowing horizontally off of the flat trailing edge just acts as a jet of air, and does not add to circulation of the airfoil. Thus, the WIND flapping (or oscillating) results show similar lift and drag for the case with and without blowing when a zero-degree jet angle is used. This combination of blowing and flapping gave a maximum lift coefficient of 4 and maximum drag coefficient of 0.85 at a total pressure ratio of 1.27. Figure 3-38 shows the pressure contour field for the case with blowing (left) and no blowing (right). As a side study, a few calculations were completed with mass ejection at a 30 deg angle down (Figure 3-31) from the bottom rear of the airfoil (jet flap), in hopes that it would help induce circulation over the top of the airfoil. It turned out it did not, agreeing with the limited lift augementation benefit of the jet flap concept seen in literature. It should be mentioned that the high lift augmentation characteristics of blowing over a curved trailing edge [81] which we envision for use on this vehicle have not yet been investigated here.

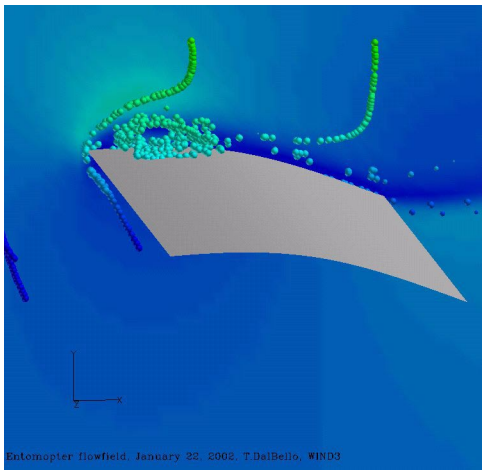

Figure 3-30: Dynamic Stall Vortex Highlighted by Massless Particles

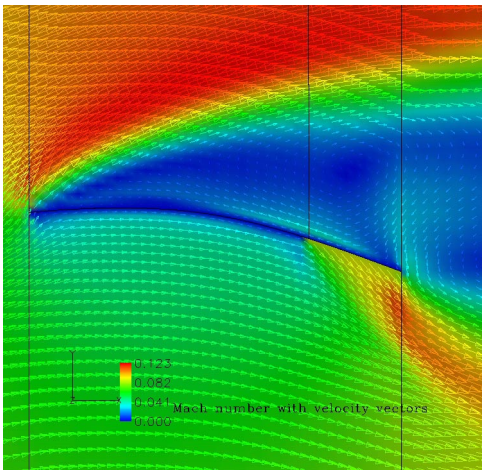

Figure 3-31: Cambered Airfoil Surface with 30° Ejection from the Bottom Rear of the Airfoil

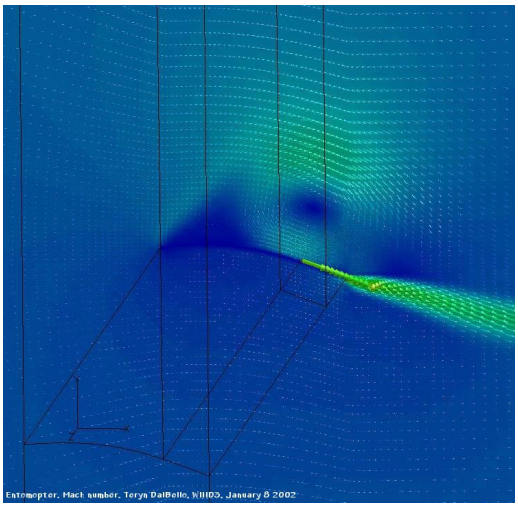

Figure 3-32: Wing Outline and Trailing Edge Mass Ejection Used for Circulation Control

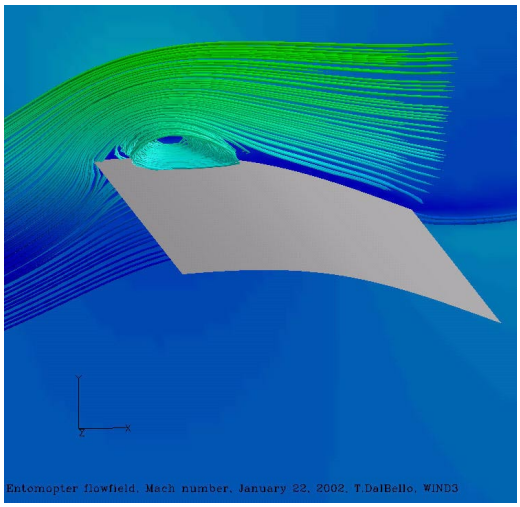

Figure 3-33: Dynamic Stall Vortex Highlighted Using Streamlines

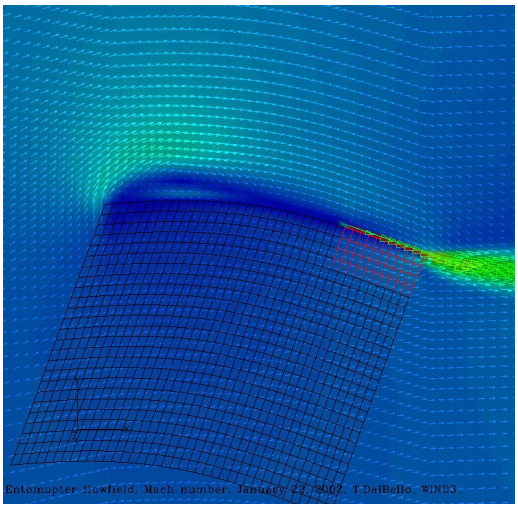

Figure 3-34: Airfoil Surface Grid Highlighting Tangential Blowing and LEV Development

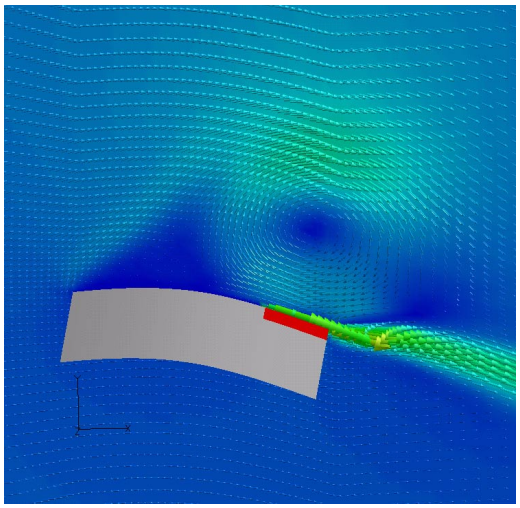

Figure 3-35: Airfoil Surface Highlighting Tangential Blowing and LEV Development

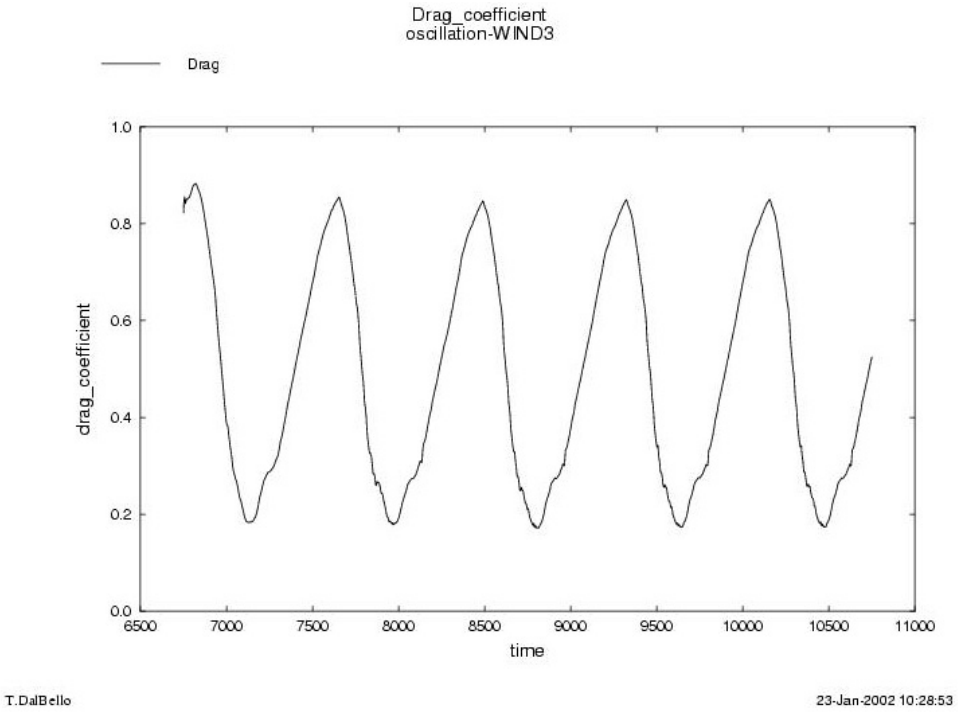

Figure 3-36: Drag Coefficient vs. Time with Blowing/Oscillation

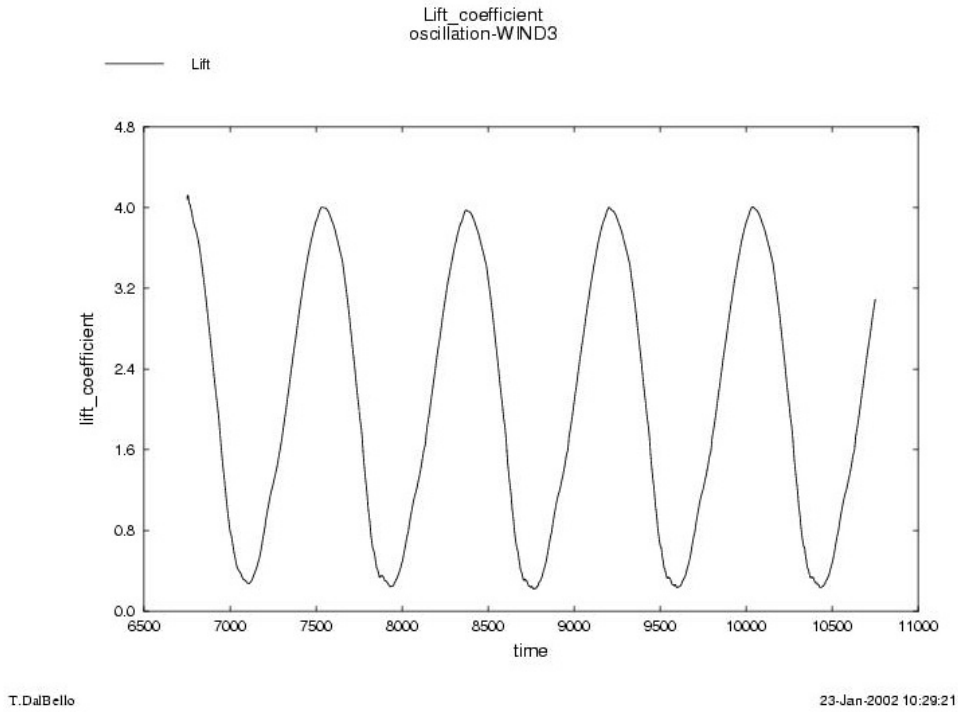

Figure 3-37: Lift Coefficient vs. Time with Blowing/Oscillation

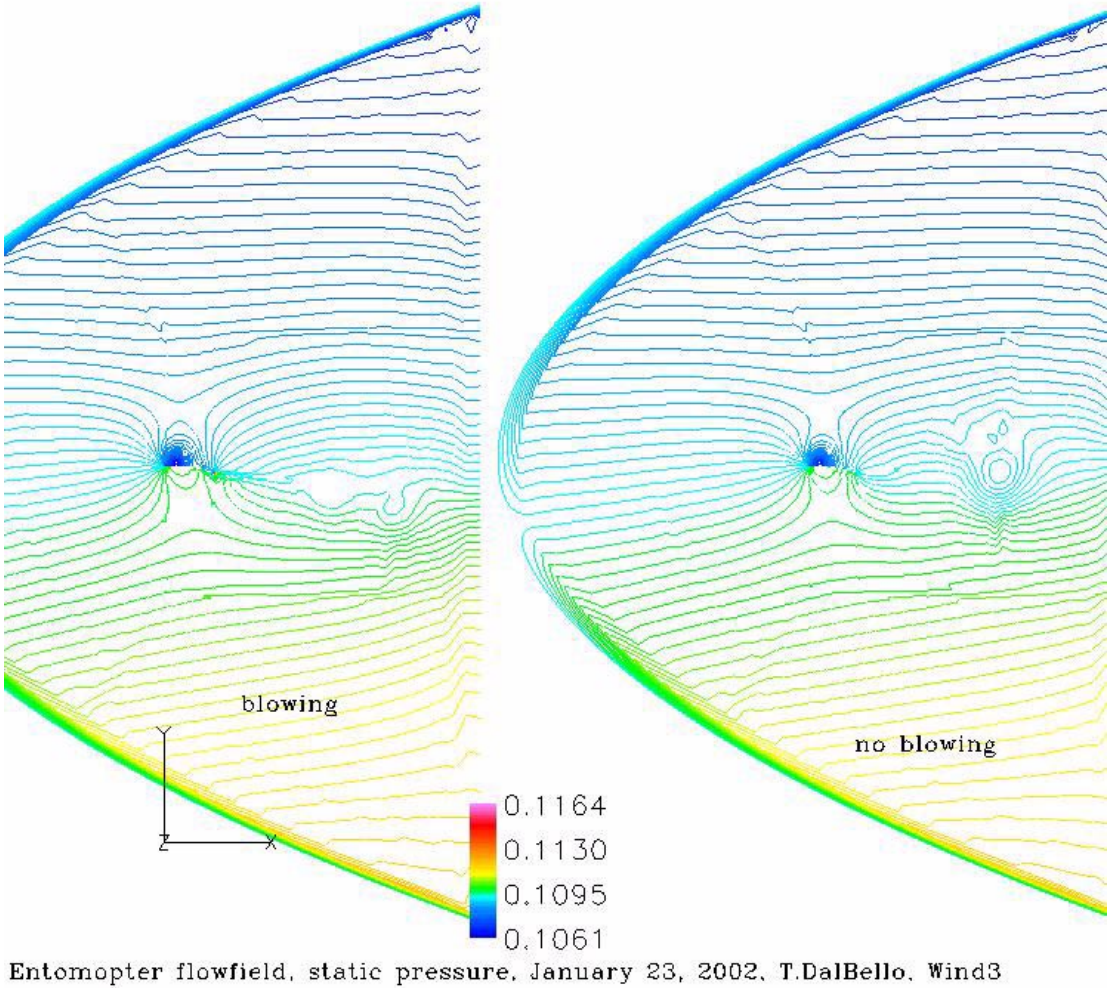

Figure 3-38: Pressure Contours for Blowing (Left) and No Blowing (Right)

3.3.1.3 Entomopter Wing CFD Analysis: FLUENT

The first step in the CFD analysis of the Entomopter wing was to model the wing cross-section. The geometry of the airfoil was modified from the one used for the previous cases, as the results obtained were far from those expected. In the new design, an airfoil with an elliptic leading edge and a gradually tapering trailing edge was modeled. Figure 3-39 shows the airfoil section. GAMBIT, a grid generation package, was used for modeling the geometry and for grid generation. FLUENT 5 was used for the CFD simulations.

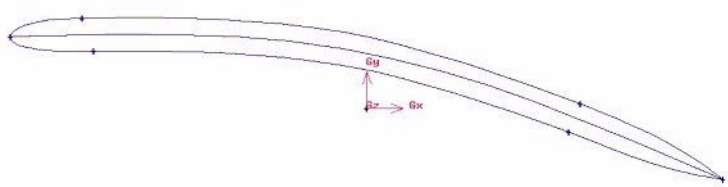

Figure 3-39: Airfoil with Elliptic Leading Edge

The airfoil chord length, C, was 30 cm, and the maximum thickness was 1.4 cm, which is approximately 5% of C. When the free stream-flow direction was tangential to the camber line at the leading edge, the angle between the chord line and the free stream-flow direction (angle of attack) was 11.310.

3.3.1.3.1 Preliminary Case Studies

For the first set of cases, a parabolic flow domain was meshed using the pave scheme of meshing, with quadrilateral cells. The total number of cells in the mesh was 42,026. A larger number of cells close to the airfoil surface and fewer away from it were used. Eight cases were run for angles of attack ranging from -3° to 17°, in increments of about 3°. Figure 3-40 shows the airfoil with the mesh used for the analysis.

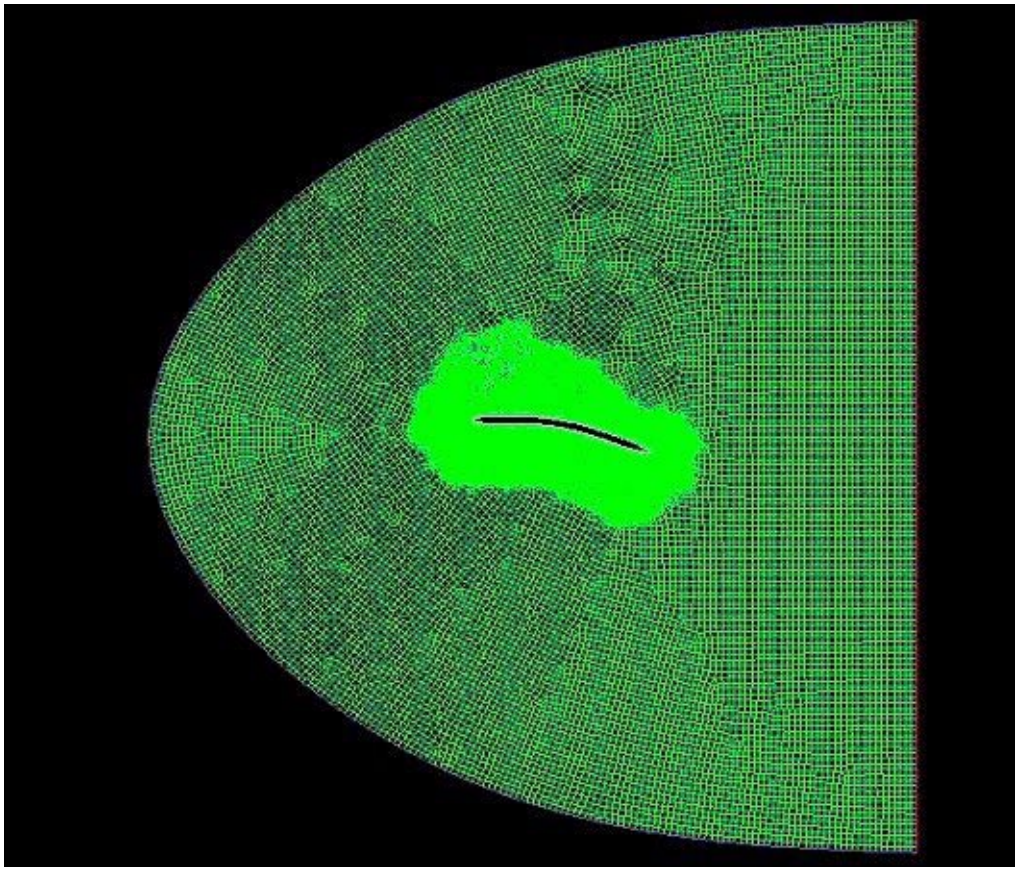

Figure 3-40: Airfoil with the Mesh

The conditions used were those on Mars, given in Table 3-5 below.

Table 3-5: Simulation Conditions

Density	0.176 kg/m^3
Dynamic Viscosity	1.0705e-05 kg/m-s
Operating Pressure	709 Pa
Free Stream Velocity	30 m/s

Table 3-5: Simulation Conditions (Continued)

Free Stream Temperature	210 K
Solver	Segregated-Implicit, Steady

In the CFD analysis, the values of lift and drag coefficients were to be determined. The lift coefficient and the drag coefficient are given by Equations 3-29 and 3-30, respectively.

$$c_l = L/(0.5\rho V_\infty^2 S)$$ ***Equation 3-29***

$$c_d = D/(0.5\rho V_\infty^2 S)$$ ***Equation 3-30***

L and D are the lift and drag forces, respectively, *p* is the density of the fluid, V is the free stream velocity, and S is the wing planform area.

All the cases were run for turbulent conditions with the Spalart-Allmaras model and the conditions shown in Table 3-5. After the solutions converged, the C_L and c_d values were noted. According to the "lifting-line theory," C_L - = $2\pi\alpha$, where α is the angle of attack in radians. The theoretical values of C_L obtained from the lifting line theory, and those obtained from the CFD simulations were compared. Figure 3-40 shows the comparison.

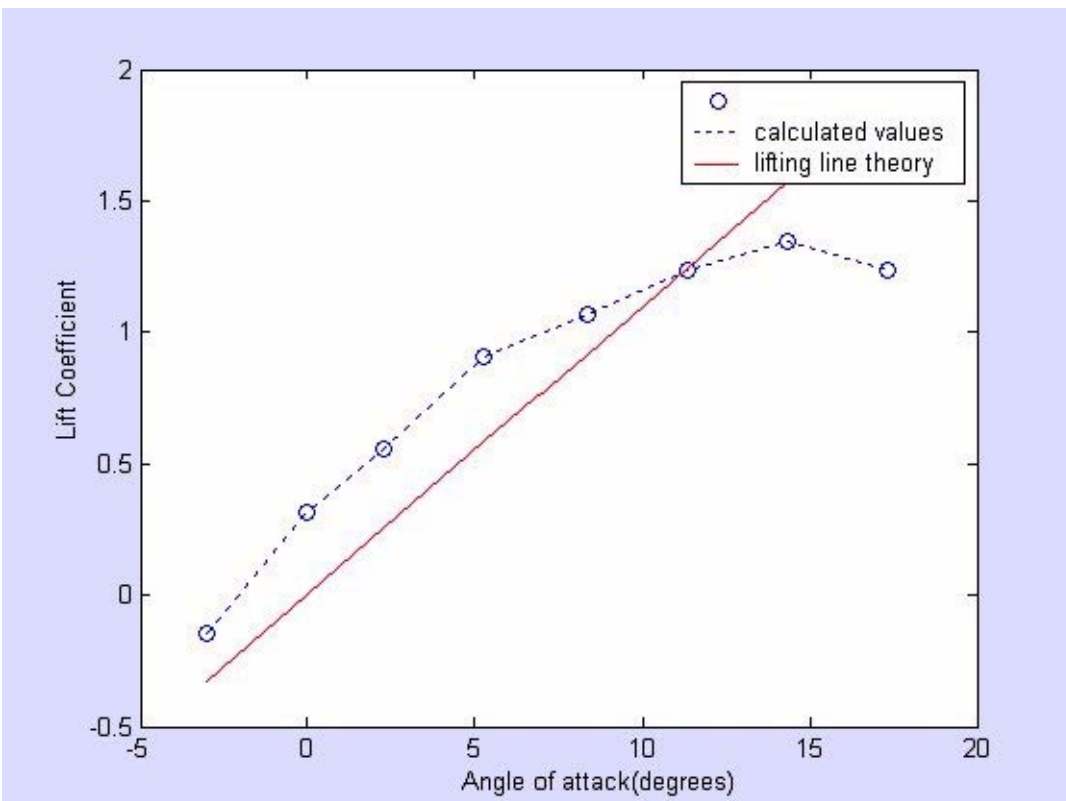

Figure 3-41: Lift Coefficient vs. Angle of Attack

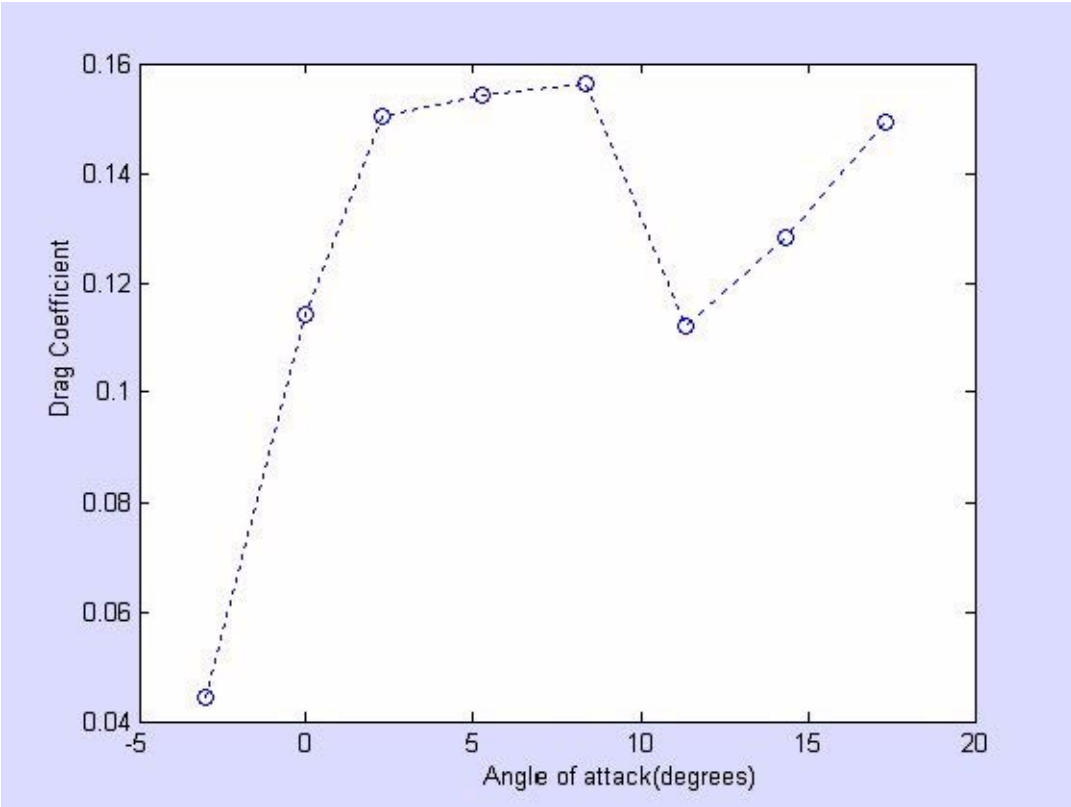

Figure 3-42: Drag Coefficient vs. Angle of Attack

For angles of attack higher than about 100°, C_L plateaus and then decreases, probably indicating the beginning of stall.

The velocity vectors show that there is some separation at the trailing edge in the form of a small bubble, but the flow reattaches itself ahead of the trailing edge. The velocity vectors and pressure contours for various angles of attack and the conditions in Table 3-5 are shown in Figures 3-43 through 3-58.

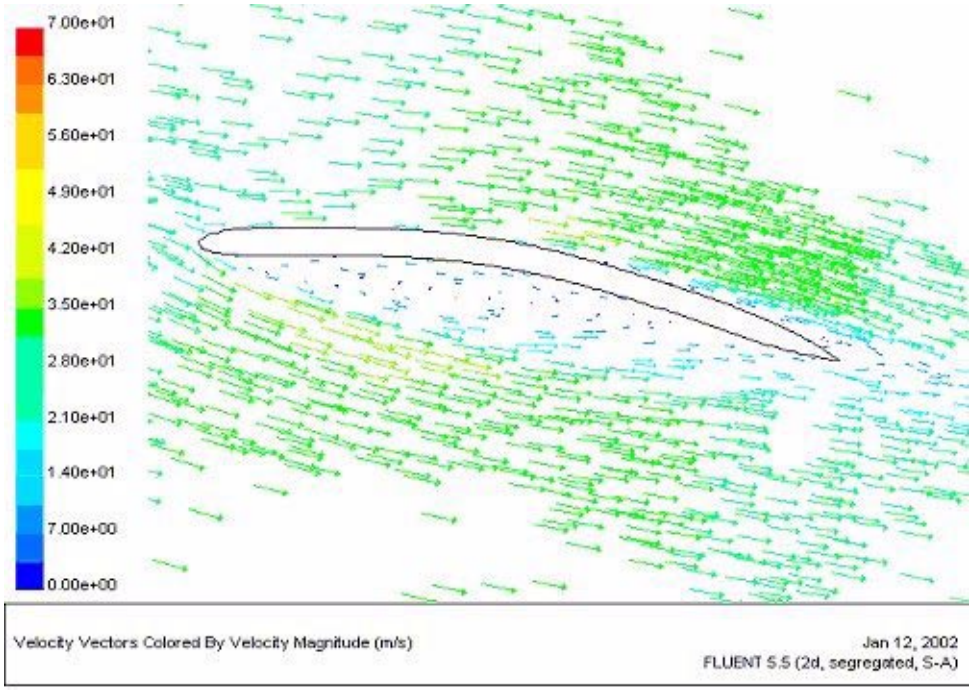

Figure 3-43: Velocity Vectors for $\alpha = -3^o$

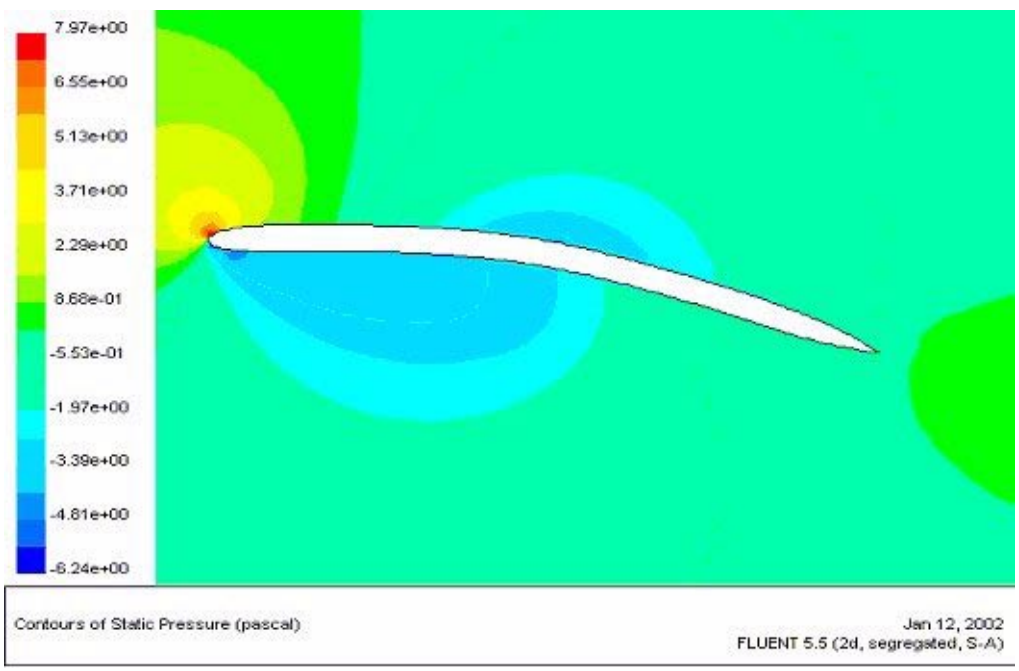

Figure 3-44: Pressure Contours for $\alpha = -3^o$

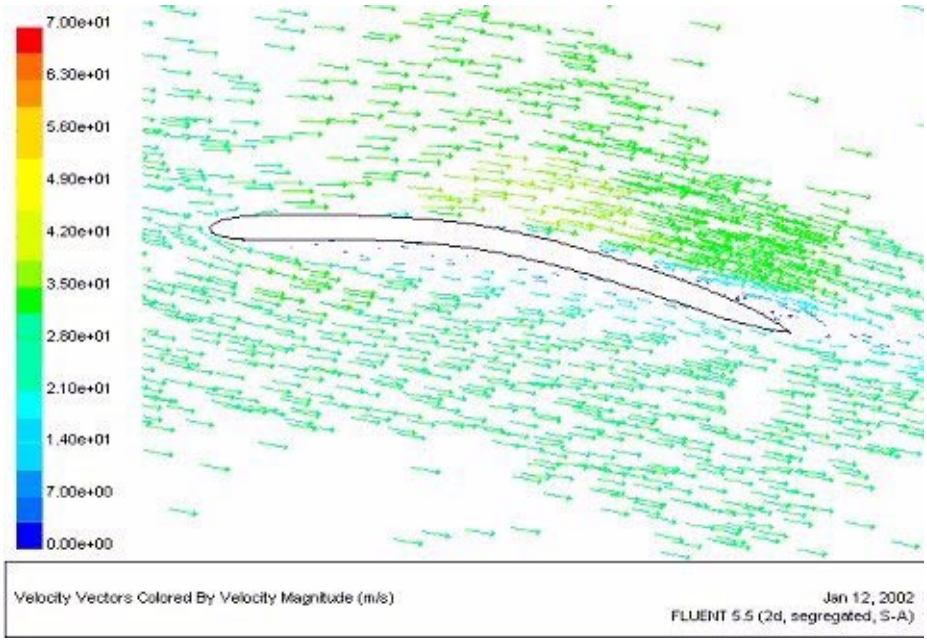

Figure 3-45: Velocity Vectors for $\alpha = 0^o$

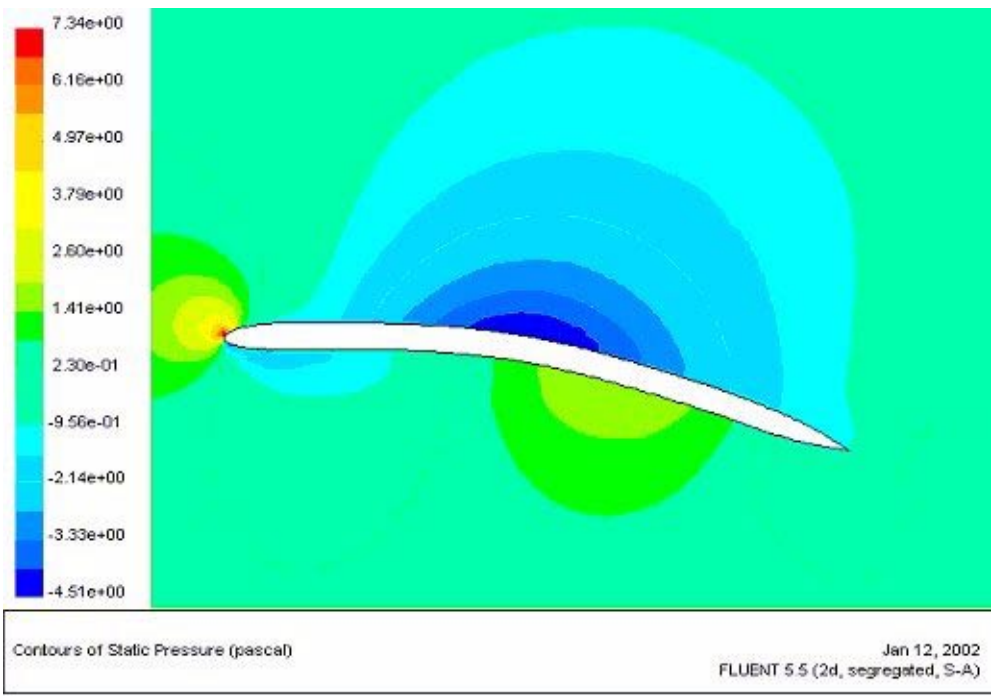

Figure 3-46: Pressure Contours for $\alpha = 0^o$

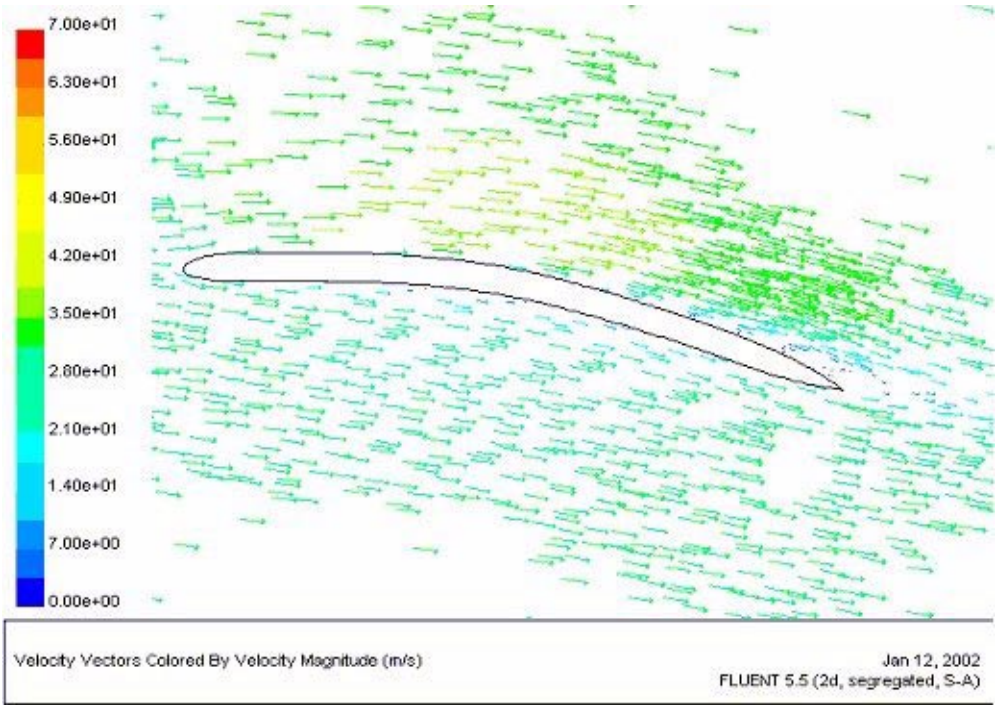

Figure 3-47: Velocity Vectors for $\alpha = 2.31^{o}$

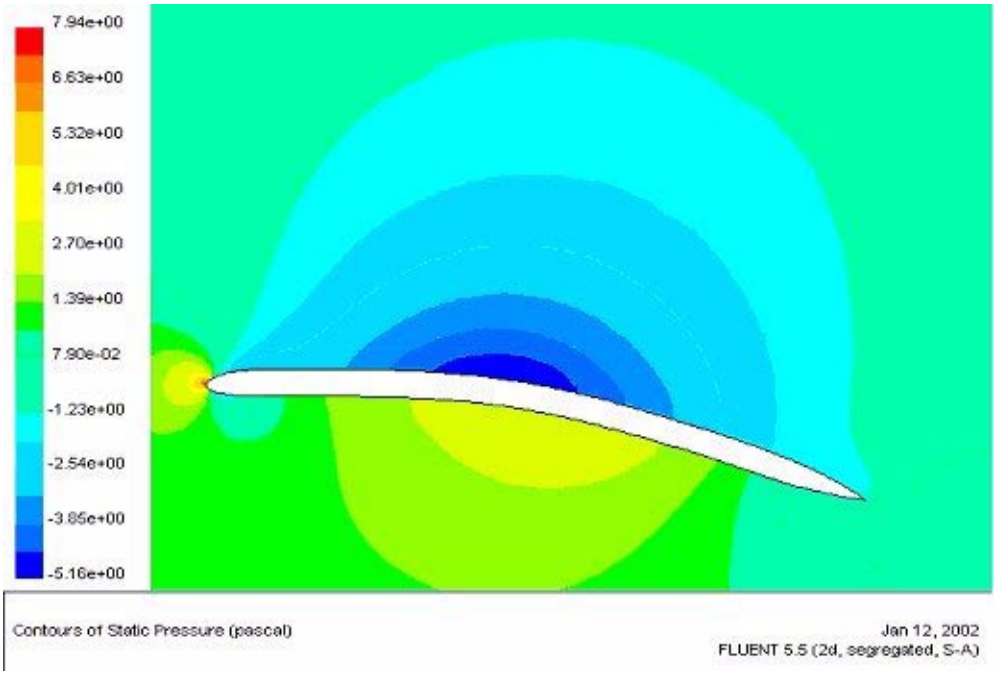

Figure 3-48: Pressure Contours for $\alpha = 2.31^{o}$

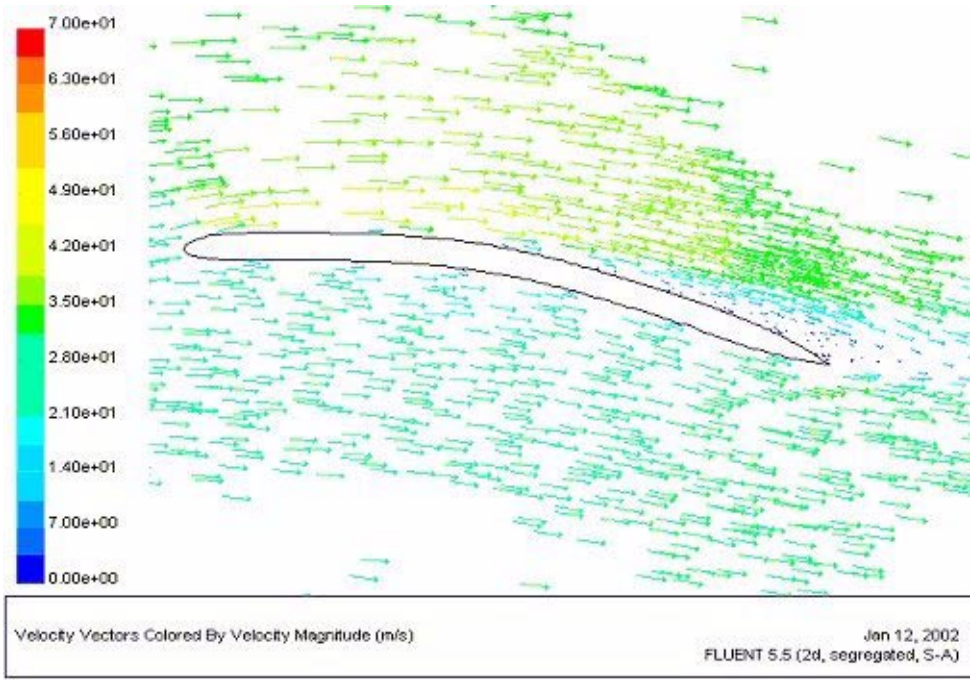

Figure 3-49: Velocity Vectors for $\alpha = 5.31^{o}$

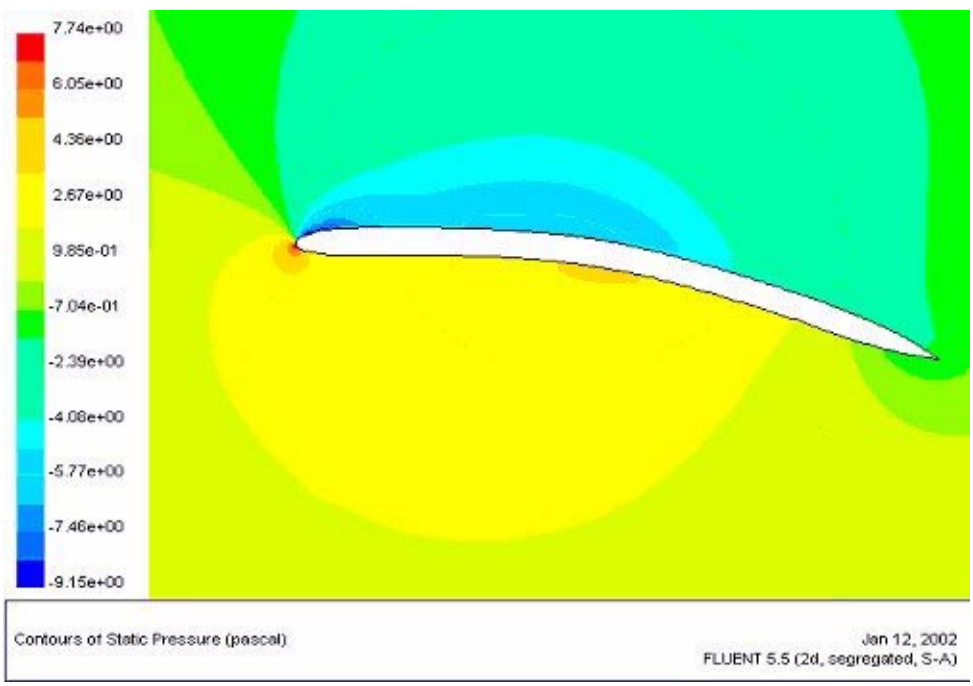

Figure 3-50: Pressure Contours for $\alpha = 5.31^{o}$

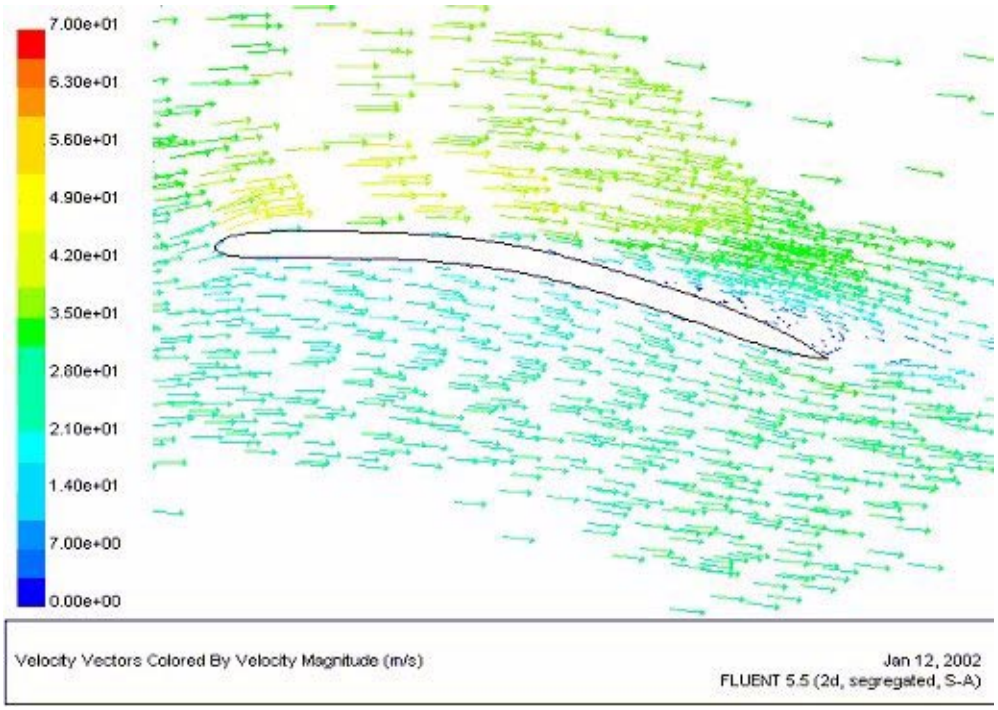

Figure 3-51: Velocity Vectors for $\alpha = 8.31^{o}$

Figure 3-52: Pressure Contours for $\alpha = 8.31^{o}$

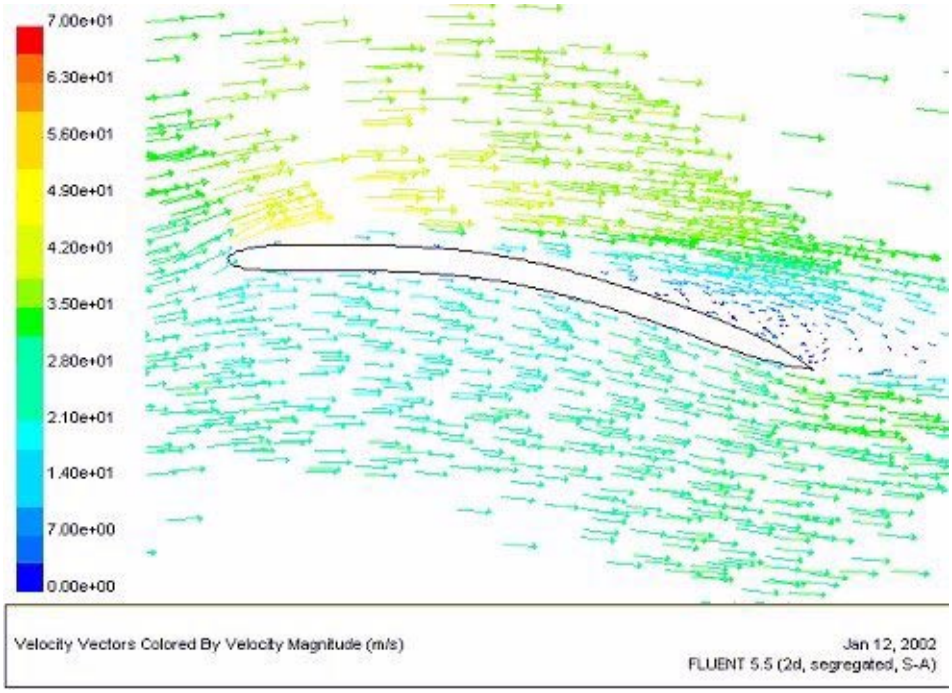

Figure 3-53: Velocity Vectors for $\alpha = 11.31^{o}$

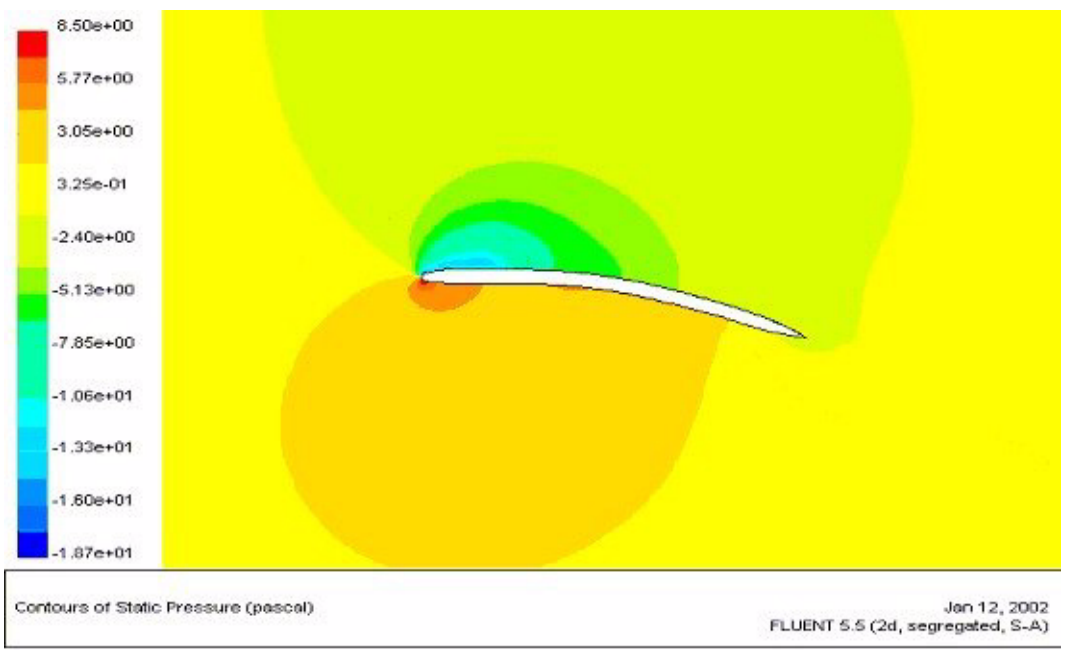

Figure 3-54: Pressure Contours for $\alpha = 11.31^{o}$

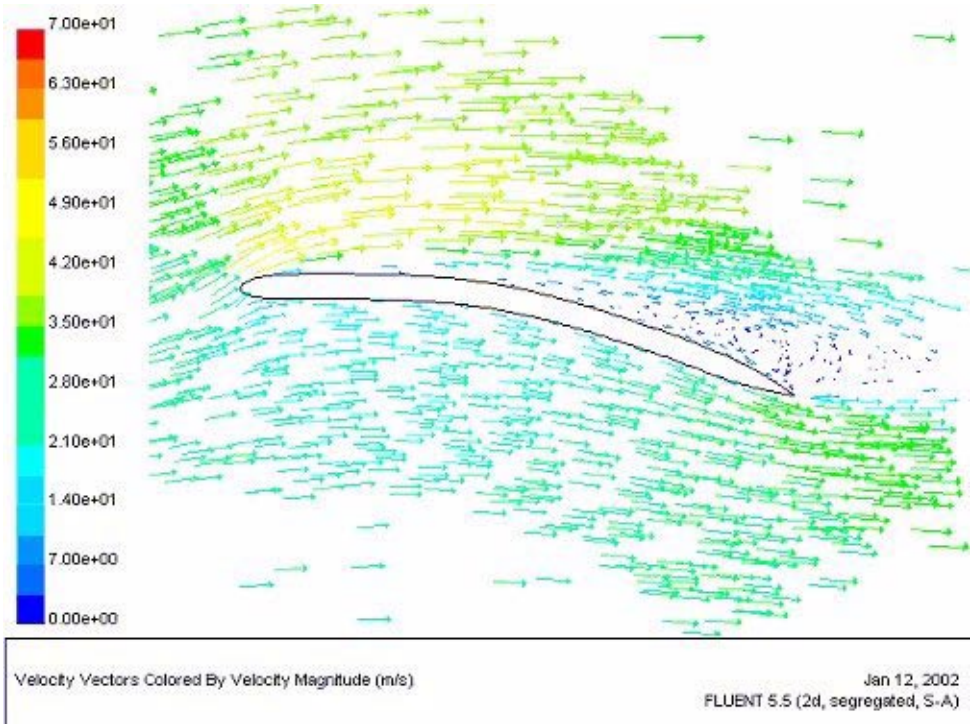

Figure 3-55: Velocity Vectors for $\alpha = 14.31^{o}$

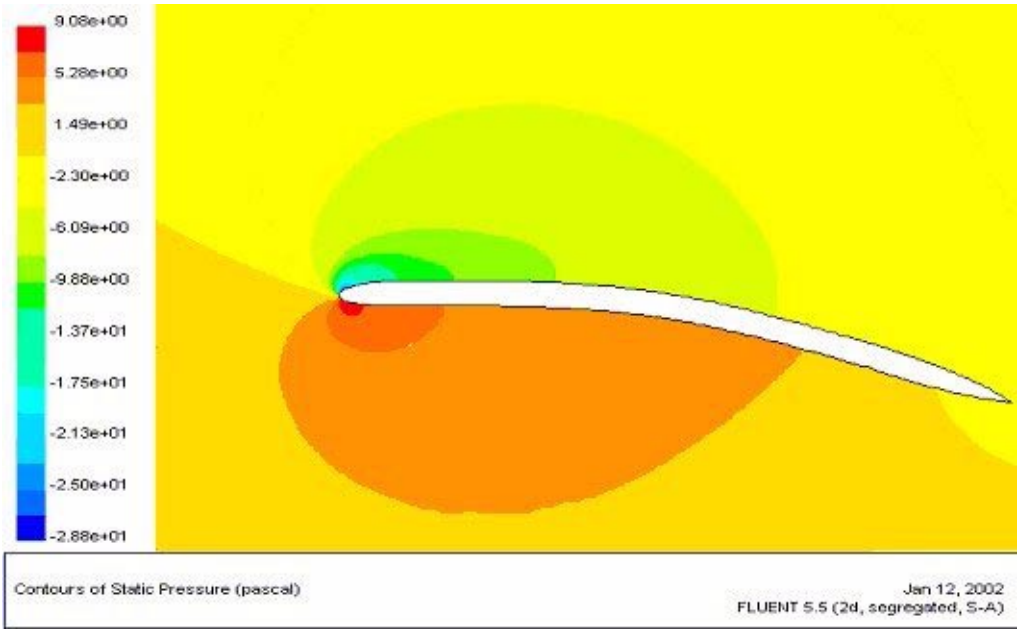

Figure 3-56: Pressure Contours for $\alpha = 14.31^{o}$

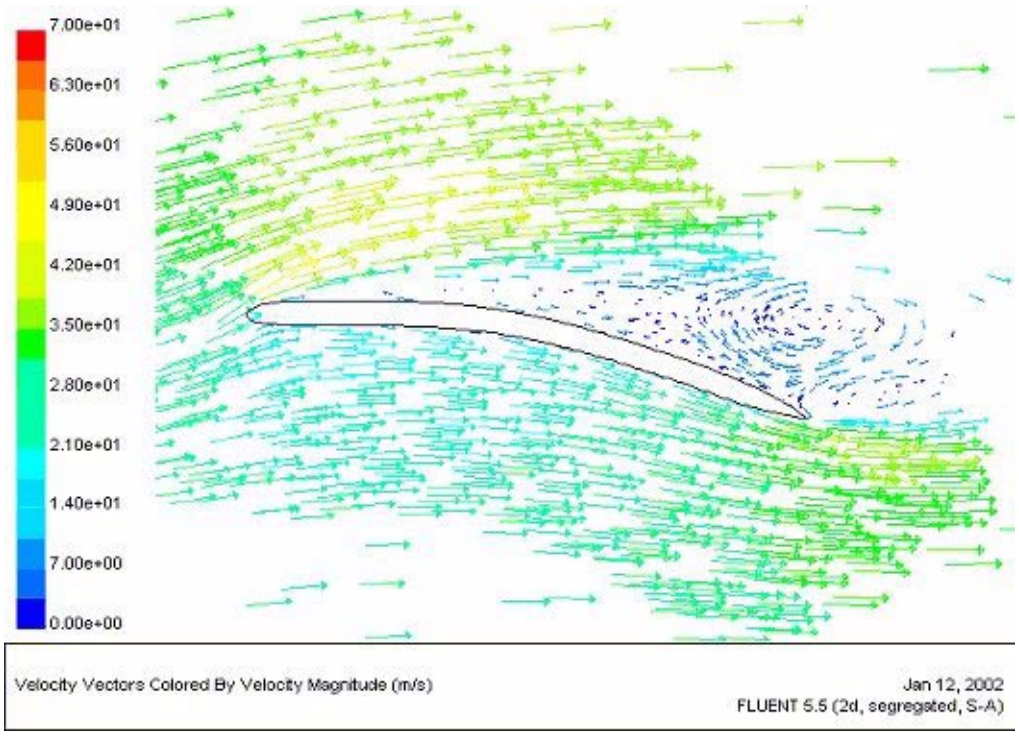

Figure 3-57: Velocity Vectors for $\alpha = 17.31^{o}$

Figure 3-58: Pressure Contours for $\alpha = 17.31^{o}$

A set of 3D cases was run with the same conditions as of the 2D case, and for the same angles of attack. A triangular mesh with 119,105 cells was used. The meshing was much denser near the airfoil surface than in the previous mesh. Figure 3-59 shows the airfoil with the new grid.

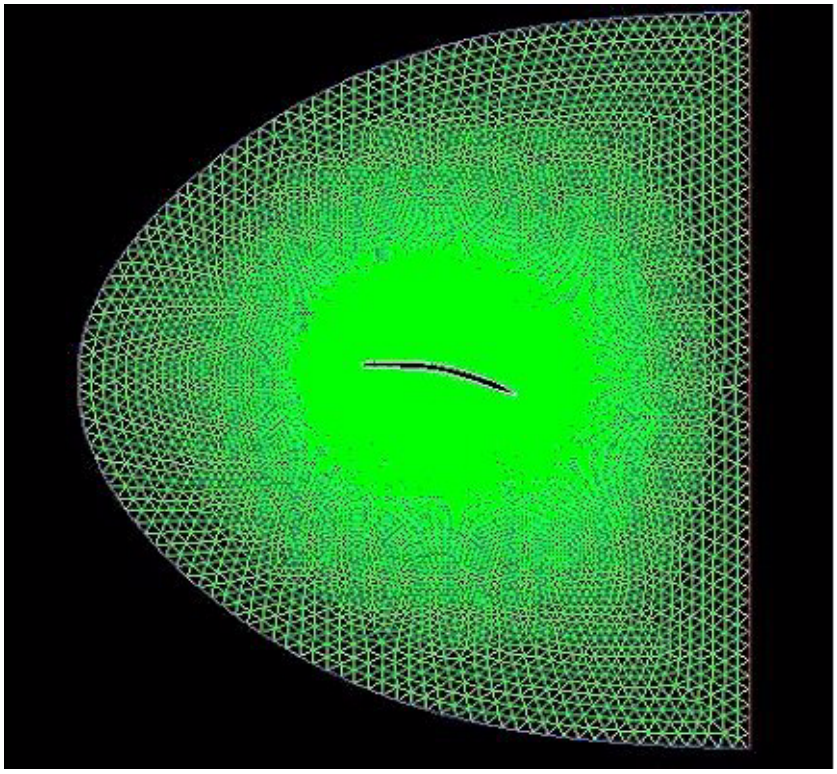

Figure 3-59: Airfoil with New, Finer Triangular Mesh

To determine the effect of thickness on the lift and drag coefficients, another set of cases was run for an infinitesimally thin airfoil. Figure 3-60 shows the airfoil used for these cases. Eight cases were run with the same conditions as used previously and given in Table 3-5.

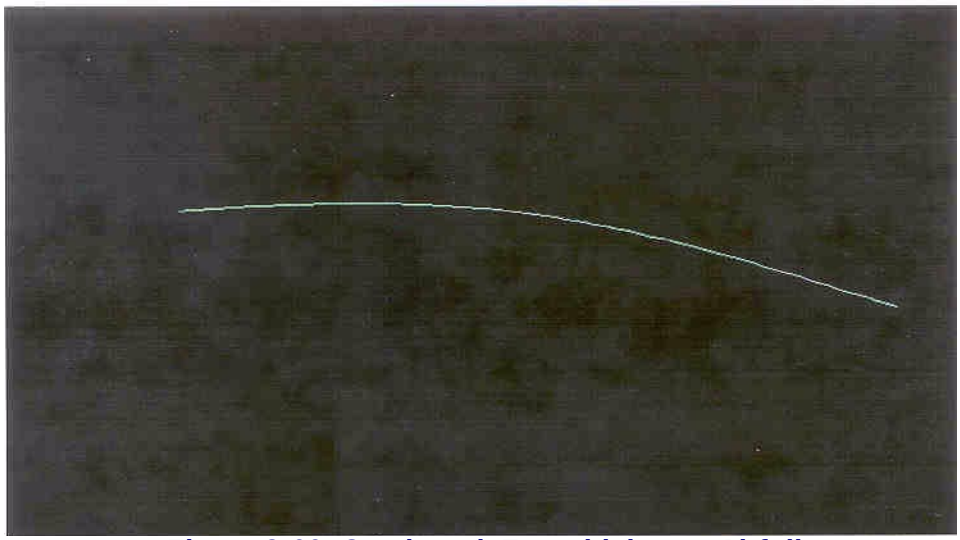

Figure 3-60: Cambered, Zero-thickness Airfoil

The lift and drag coefficients obtained for the thick and thin airfoils were compared. Figure 3-61 shows a comparison of the C_L values and Figure 3-62 shows a comparison of the c_d values.

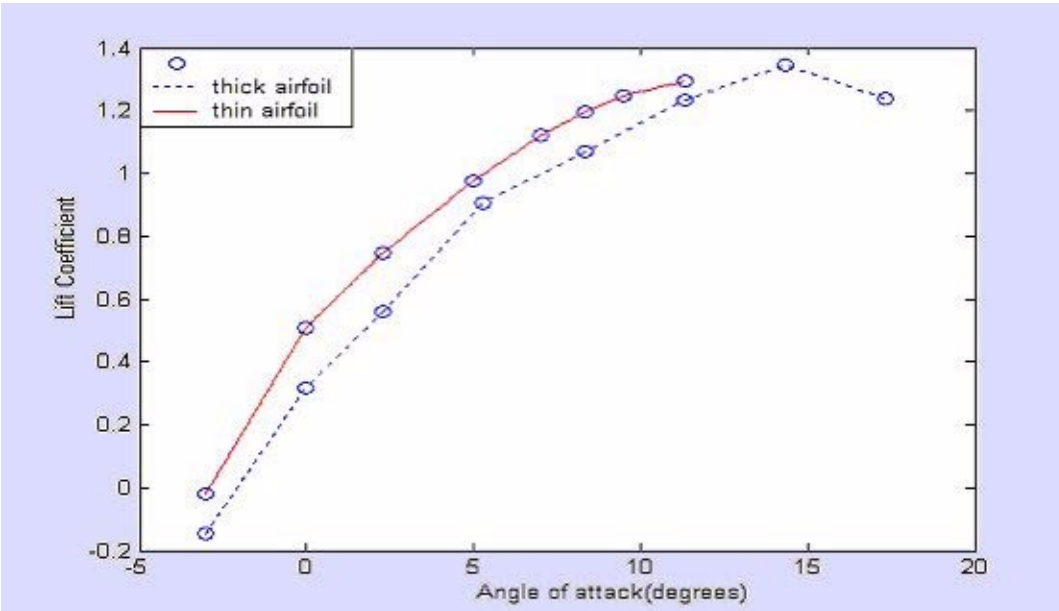

Figure 3-61: C_L Values for the Thick and Thin Airfoils

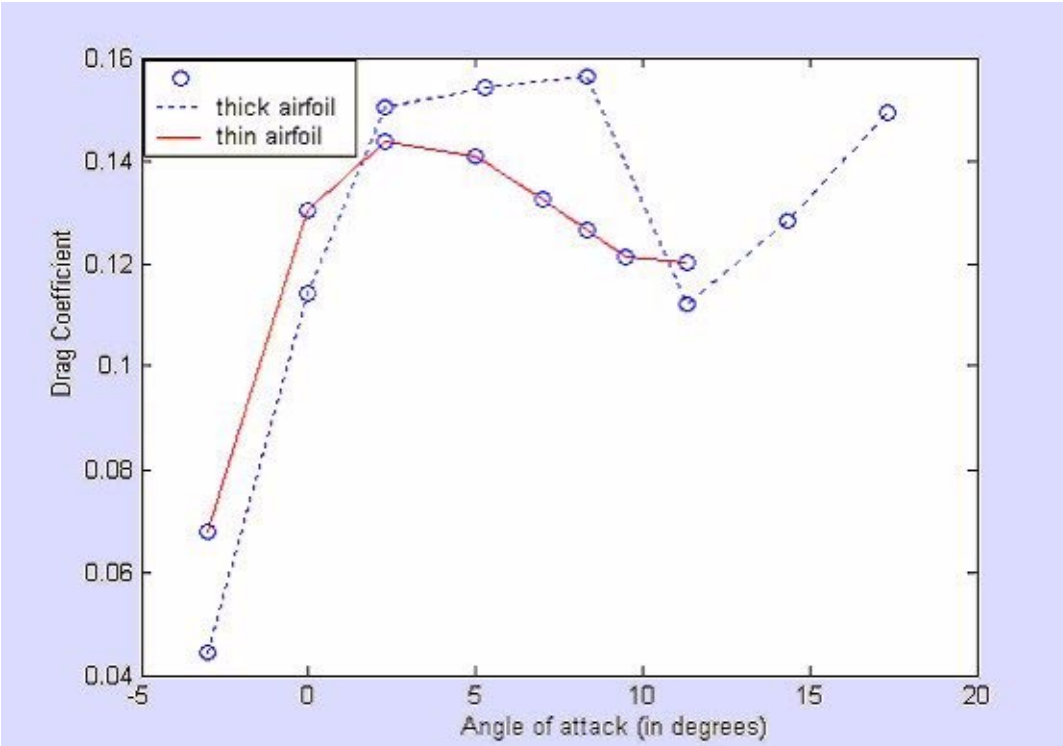

Figure 3-62: C_d Values of the Thick and Thin Airfoils

From the plots, we notice that the thin airfoil generates a higher lift coefficient than the thick airfoil. Also, beyond an angle of attack of about 2°, the drag coefficient begins to reduce.

3.3.1.4 Refined Case Studies

With the knowledge gained from the previous case studies, a new airfoil section was created for further simulations. A thin cambered airfoil has the necessary low Reynolds number characteristics that can be used to advantage in MAVs. A circular arc airfoil with negligible thickness and a thin airfoil with an elliptical leading edge and a gradually tapering trailing edge, having the same camber as the first airfoil, were modeled. The choice of these two airfoil shapes, differing in thickness but identical in other respects, provided a means to evaluating further the effect of thickness on the low Reynolds number, unsteady flow field. The chord length (C) of the airfoils is 36.5 cm, and the maximum thickness of Airfoil 1 is 1.825 cm (0.05C).

Seven cases were run with angle of attack ranging from 8.3^o to 45.79^o. CFD simulations were done at the conditions of the Mars environment, assumed to consist of CO_2 as given in Table 3-5.

Lift and drag coefficients were determined from the simulations. C_L values from the small-α simulations were compared to those from "lifting-line theory." The close agreement between the C_L values from the steady state simulations and the "lifting-line theory" served to validate the CFD procedure.

Figures 3-63 and 3-64 show results from $\alpha = 8.31^o$ and Reynolds number = 9,600 simulations. Figures 3-63 and 3-64 show C_L and c_d variations, respectively, vs. time. The present-time accurate simulations, using a fine grid optimized for the geometry and flow conditions, capture the cyclical nature of lift and drag. The frequency of the force oscillations is related to the frequency of the LEV dynamics.

Figure 3-65 shows velocity vector plot, and Figure 3-66 shows the static pressure contours. These results are based on a time-accurate solution with a step size of 0.001 s. Several interesting features were observed for this case. At regular intervals, the vortex formed at the leading edge stayed attached to the top surface, grew, and convected downstream. The lift showed a cyclical variation depending on the phase of the LEV. Results from several other cases not included in this report showed that the behavior of the LEV depends strongly on the Reynolds number.

Table 3-6: Lift and Drag Coefficient Values

Case	Flow Time(s)	C_L	C_d
1	1.5	2.44	0.486
2	1.6	2.55	0.366
3	1.7	2.80	0.360
4	1.8	4.01	0.560

Table 3-6: Lift and Drag Coefficient Values (Continued)

Case	Flow Time(s)	C_L	C_d
5	1.9	4.27	0.468

Figures 3-67 through 3-71 show pressure contours at 0.03-s intervals for $\alpha = 45.79^o$ and Reynolds number = 5,100. The corresponding C_L and c_d values are shown in Table 3-6. Several important features can be observed from these results. At this high angle of attack, the wing generates, a large amount of lift, indicating that extrapolation of high Reynolds number results would be erroneous, especially because the catastrophic stall pattern of conventional high Reynolds number airfoils is not present in these cases. The other feature is the large variation of lift with time. Table 3-6 shows only part of a complete cycle in which the lift varies as shown in Figure 3-63, the frequency and amplitude differing due to differences in angle-of-attack and Reynolds number. Note that these large values of lift coefficient are obtained without any wing kinematics included. The challenge is to establish the relationship between the flow velocity and the vortex-shedding frequency so that, by choosing appropriate flapping frequency, the wing would operate in the high C_L mode during the entire beat cycle. A detailed review of literature indicates that similar cyclical variation of C_L has been observed experimentally [272].

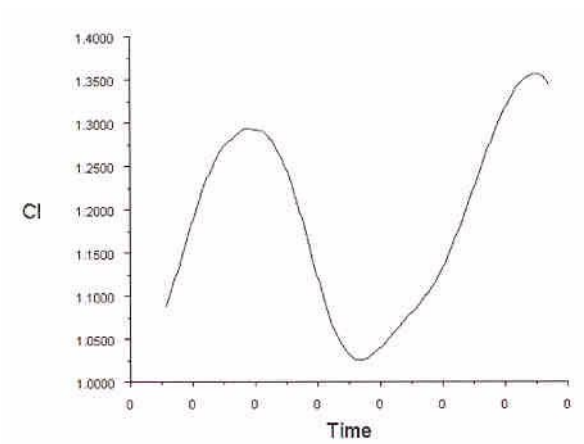

Figure 3-63: Lift Coefficient Variation, $\alpha = 8.31^o$, Reynolds Number = 9,600

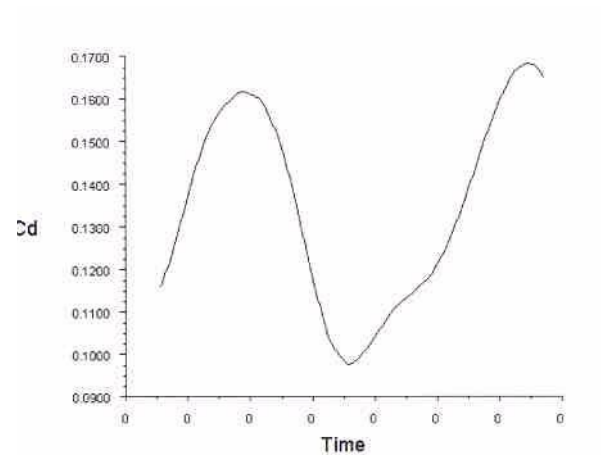

Figure 3-64: Drag Coefficient Variation, $\alpha = 8.31^o$, Reynolds Number = 9,600

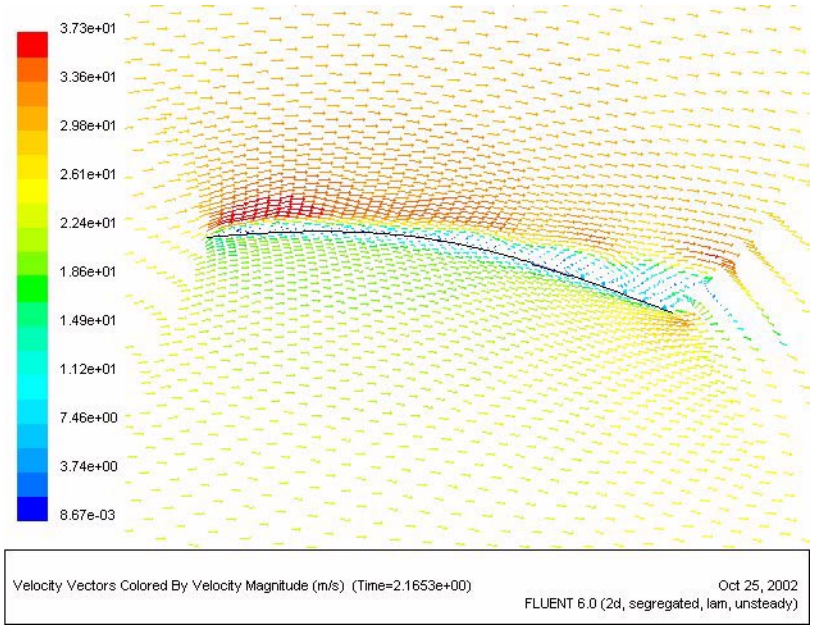

Figure 3-65: Velocity Vectors, α = 8.31^{o}, Reynolds Number = 9,600

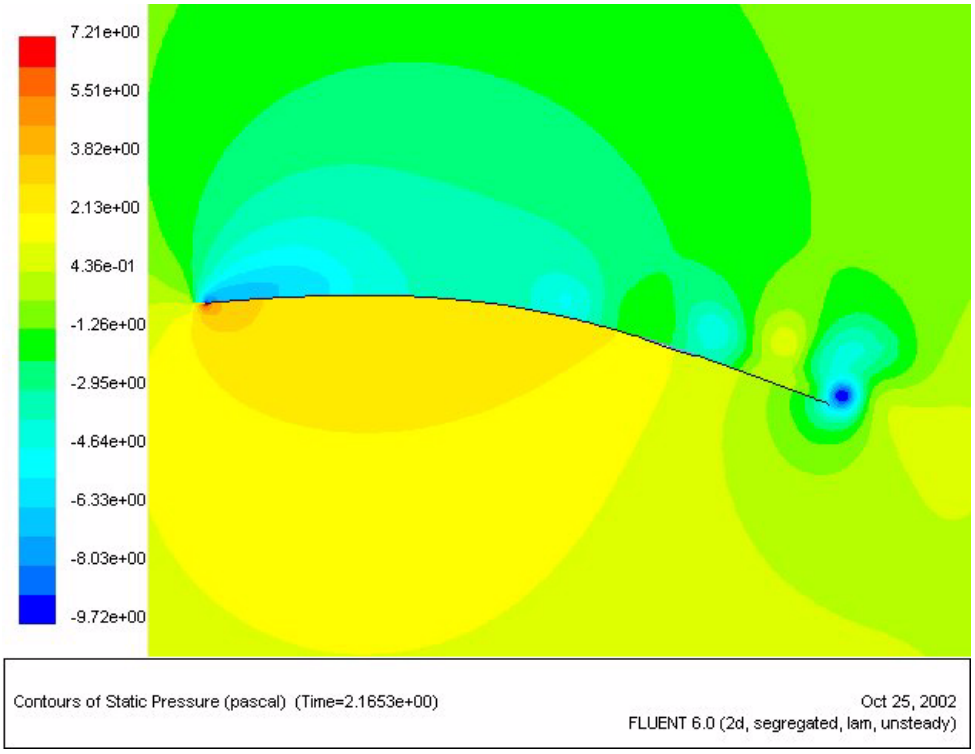

Figure 3-66: Pressure Contours, α = 8.31^{o}, Reynolds Number = 9,600

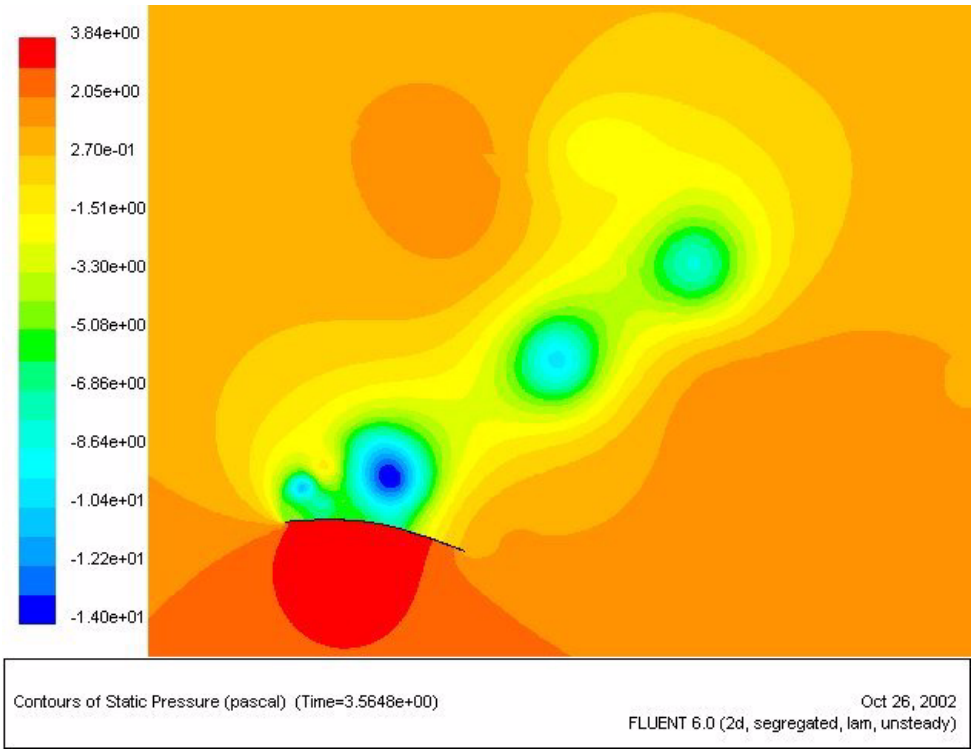

Figure 3-67: Pressure Contours, α = 45.79^{o}, Reynolds Number = 5,100, Time = 3.5648 s

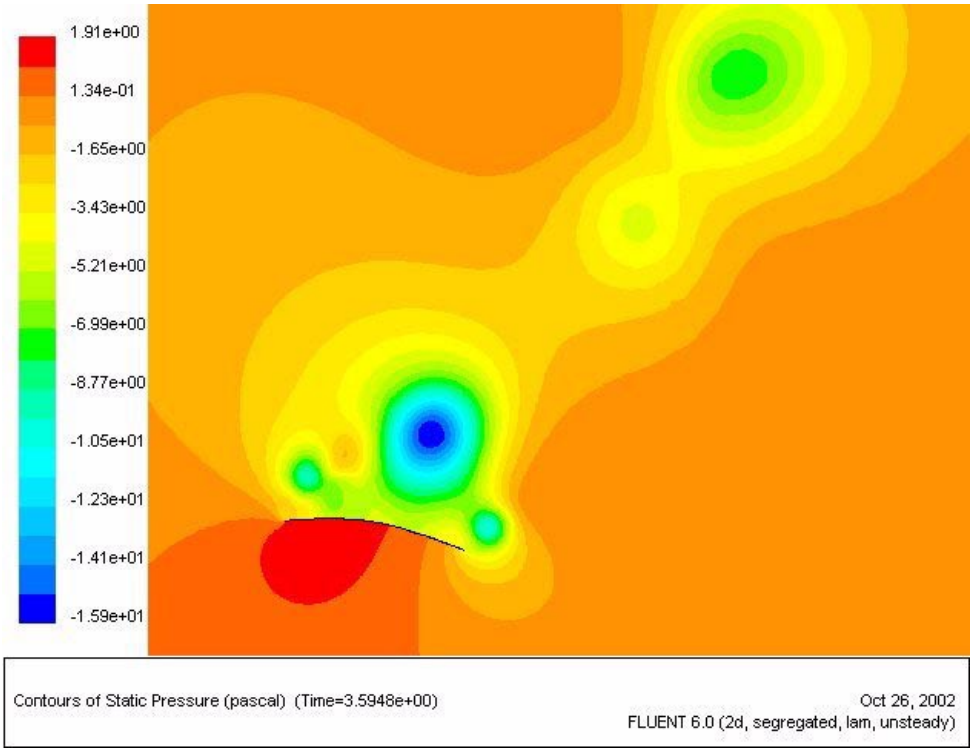

Figure 3-68: Pressure Contours, α = 45.79^{o}, Reynolds Number = 5,100, Time = 3.5948 s

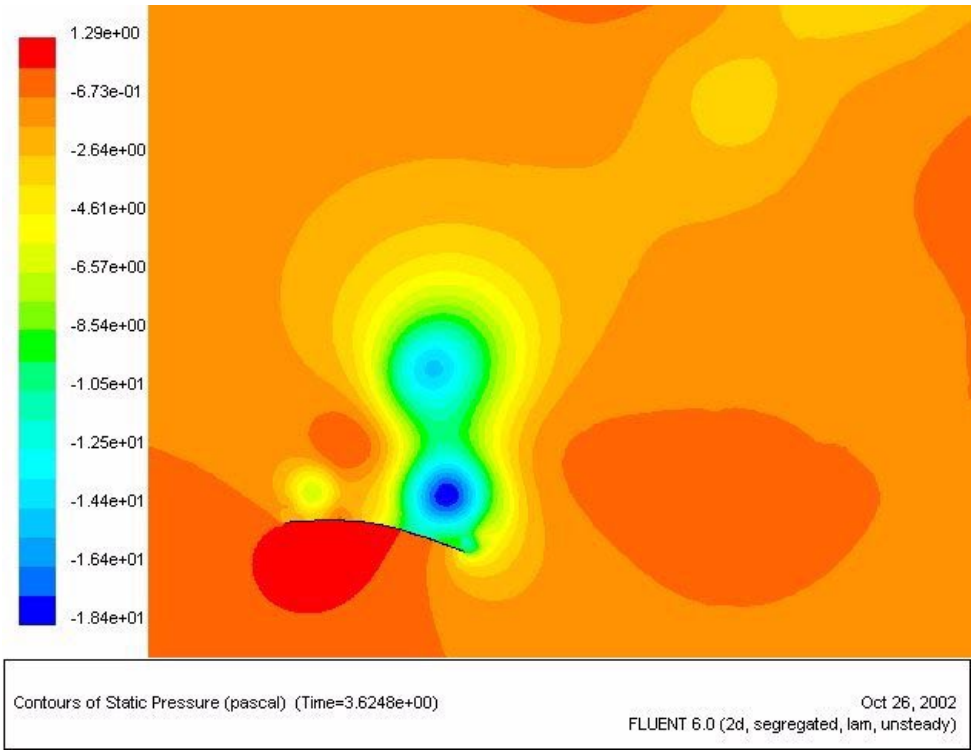

Figure 3-69: Pressure Contours, $\alpha = 45.79^{o}$, Reynolds Number = 5,100, Time = 3.6248 s

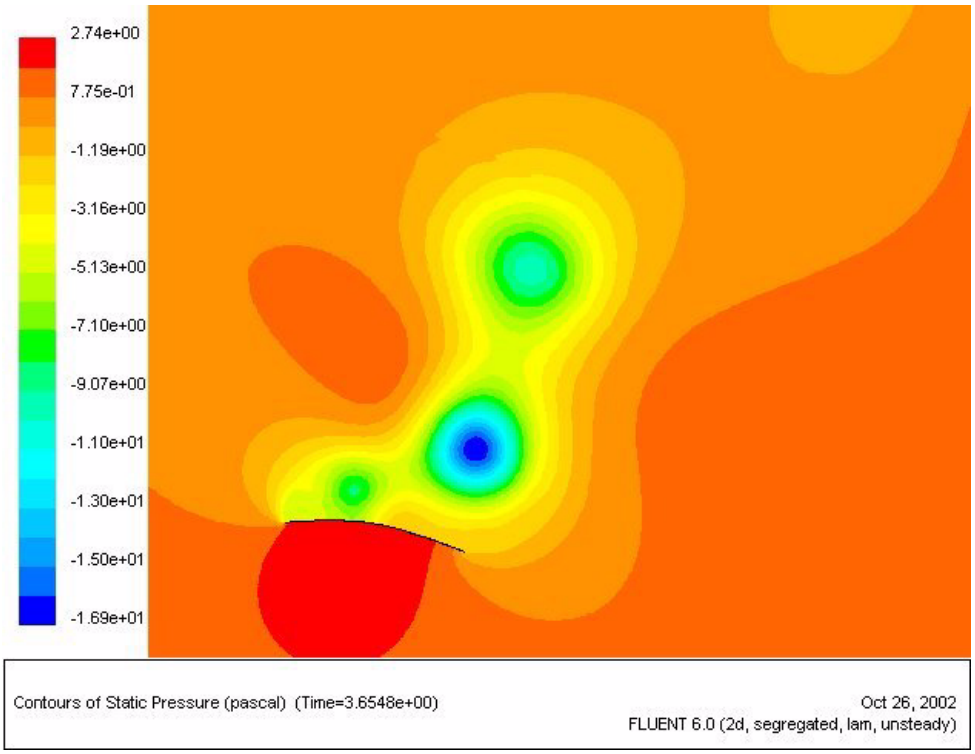

Figure 3-70: Pressure Contours, $\alpha = 45.79^{o}$, Reynolds Number = 5,100, Time = 3.6548 s

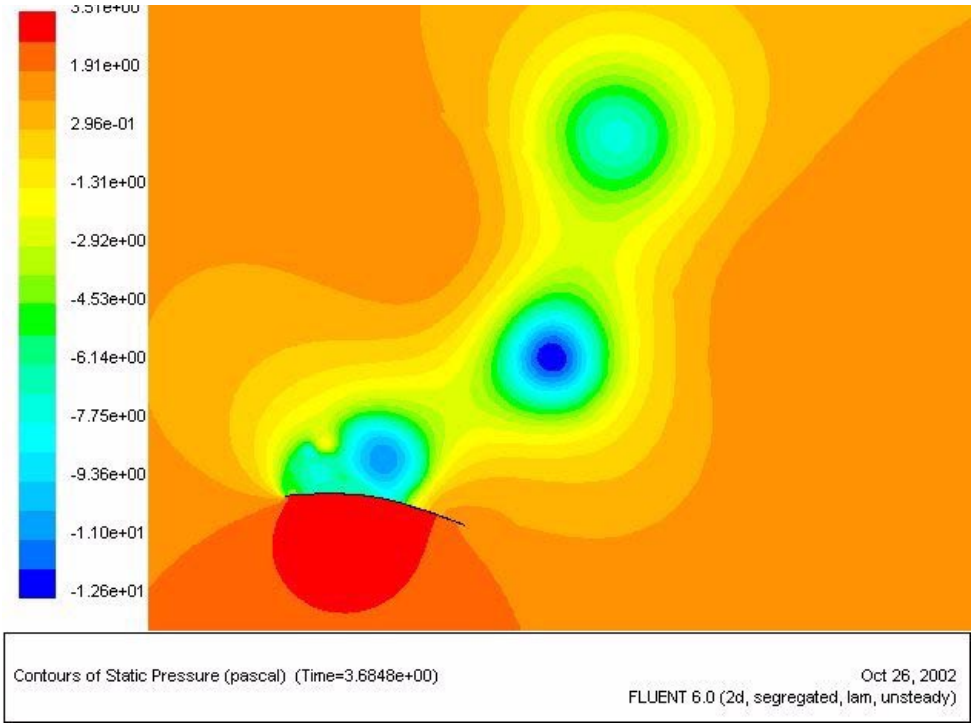

Figure 3-71: Pressure Contours, α = 45.79^o, Reynolds Number = 5,100, Time = 3.6848 s

3.3.1.4.1 Low Reynolds Number, High-α Results

A new cambered, thin wing modeled after the North American cicada wing was used in this series of simulations. Chord Reynolds number was varied in the range 510-5,100. A high angle of attack value was used to characterize the formation and evolution of the LEV. These time-accurate simulations were done using a very fine mesh and small integration time step. Both the mesh size and the time step were varied and the corresponding simulation results compared to ensure the results can be treated as independent of mesh size and time step.

Figures 3-72 and 3-73 show, respectively, the lift and drag coefficient variations for U = 1.4 m/s (Reynolds number = 510, Case A) and α = 34.8^o. The corresponding plots for U = 14 m/s (Reynolds number = 5,100, Case D) are shown in Figures 3-74 and 3-75. These four plots reveal several interesting characteristics not emphasized in previous work by other investigators of low Reynolds number, high angle of attack flow. Both cases show that there are distinct frequencies associated with each, and both the lift and drag variations have fairly large amplitudes. The salient features are summarized in Table 3-7. These results indicate that the flow is dominated by the formation and shedding of the LEV. The LEV forms at the leading edge, stays attached to the top surface and grows as it convects downstream. During this phase, the airfoil has a high C_L value, and then it drops as the vortex detaches from the surface, leading to the low C_L phase of the cycle. The c_d variation has a phase difference of approximately 180° from the C_L variation. From the summary results given in Table 3-7, several useful design guidelines can be drawn. For example, for Case D (Reynolds number = 5,100) the dominant frequency is f ~ 7.23 Hz. To investigate the relationship to the well known Karman vortex shedding from bluff bodies, the Strouhal number, defined as

$$St = \frac{fC}{U}$$ **Equation 3-31**

where C is the airfoil chord length and U is the free stream velocity, has been calculated. For Karman vortex shedding, the established value of St ~ 0.2 and the Strouhal numbers shown for Cases A and D in Table 3-7 are close to this value. Therefore, the flow in the present low Reynolds number high-α simulations is closely related to flow over bluff bodies at low Reynolds numbers. Some questions remain as to the characteristic length to be used in Equation 3-31. Depending on the value of α the thickness or the chord length may be appropriate, or projected length normal to the free stream might provide a better correlation. Due to the exploratory nature of the current work, we plan to address such details in the future. Another important observation is that the cases in the Reynolds number range above do not yield a steady state solution, indicating that such a solution will violate the flow physics. A similar observation has also been made by Kunz and Kroo [146, 149].

If the wing were to flap at the LEV-shedding frequency, the low C_L phase can be avoided, and the airfoil can always stay in the high C_L (and high C_L/c_d) phase. Note that the C_L/c_d ratio varies over the range ~3.273-20.8, indicating the benefits of tailoring the flapping frequency to the LEV-shedding frequency.

Table 3-7: Lift and Drag Summary for Reynolds Number = 510-5,100 Range

	Case A (Rec = 510)	Case B (Rec = 5100)
C_L (max)	4.5	5.2
C_L (min)	2.7	1.95
Δcl	1.8	3.25
C_L (average)	3.6	3.575
cd (max)	0.825	0.77
cd (min)	0.45	0.25
Δcd	0.375	0.52
cd (average)	0.636	0.51
C_L (max)/cd (min)	10	20.8
C_L (min)/cd (max)	3.273	2.53
Strouhal number (St)	0.237	0.2

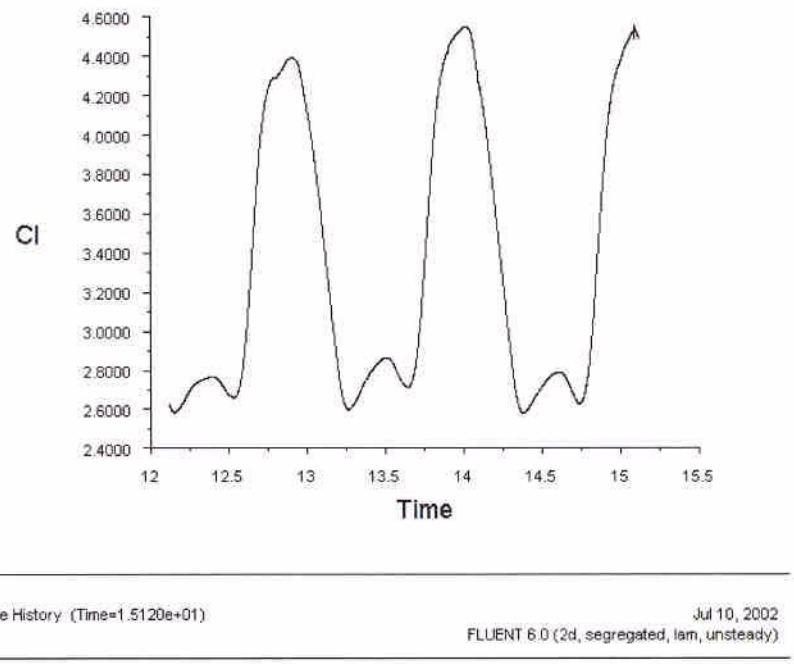

Figure 3-72: Lift Convergence History. U=1.4 m/s. α = 34.8^{o}.

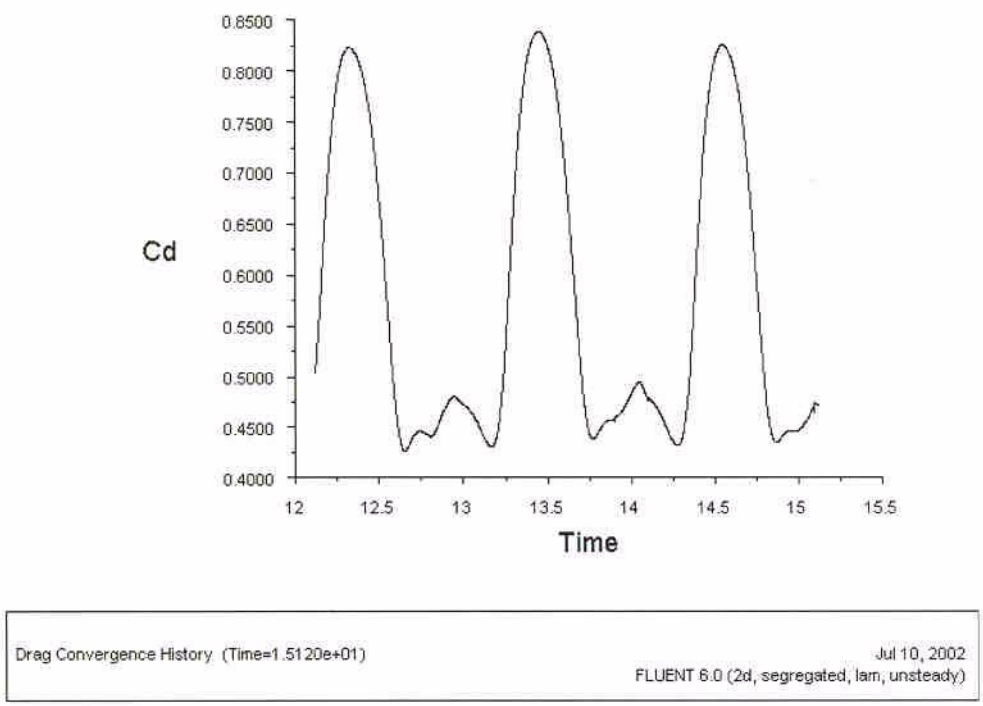

Figure 3-73: Drag Convergence History. U=1.4 m/s. α = 34.8^{o}

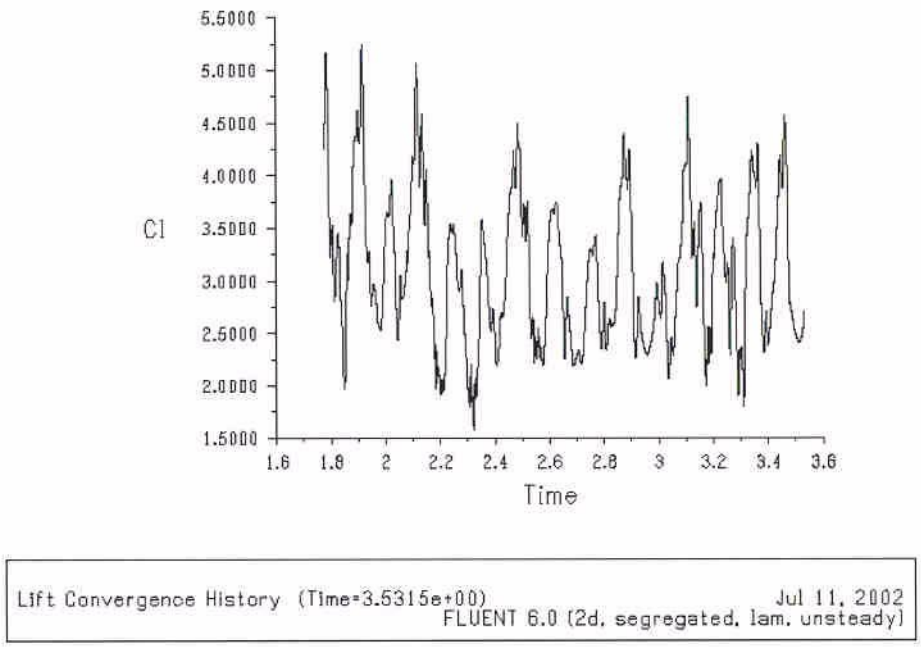

Figure 3-74: Lift Convergence History. U=14 m/s. α = 34.8^{o}.

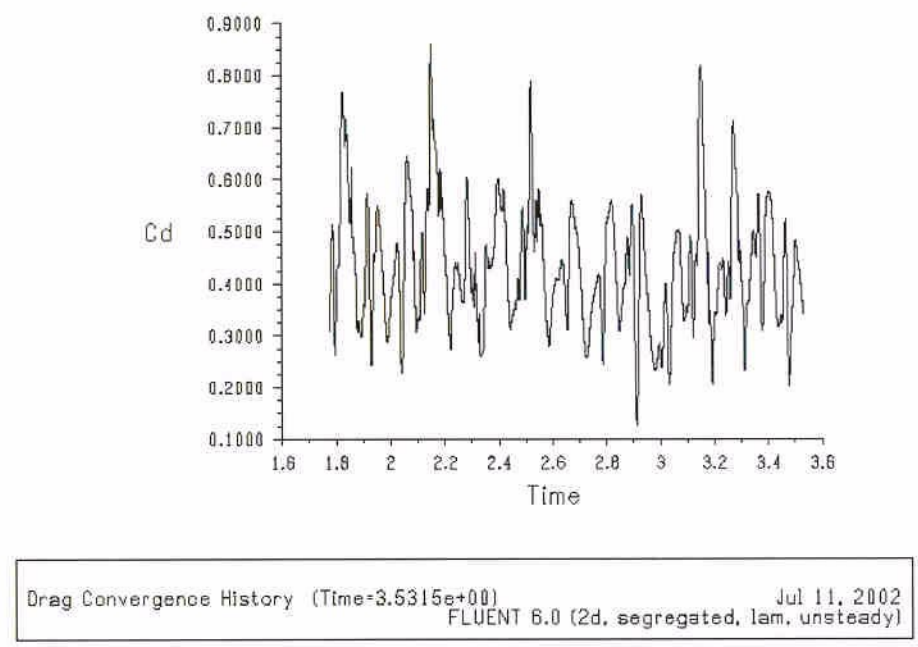

Figure 3-75: Drag Convergence History. U=14 m/s. α = 34.8^{o}.

3.3.1.4.2 Additional Three-dimensional Cases

3.3.1.4.2.1 Entomopter Wing (Current Design)

Next a preliminary 3D simulation was run with heaving. The top and side views of the wing are shown in Figures 3-76 and 3-77, respectively.

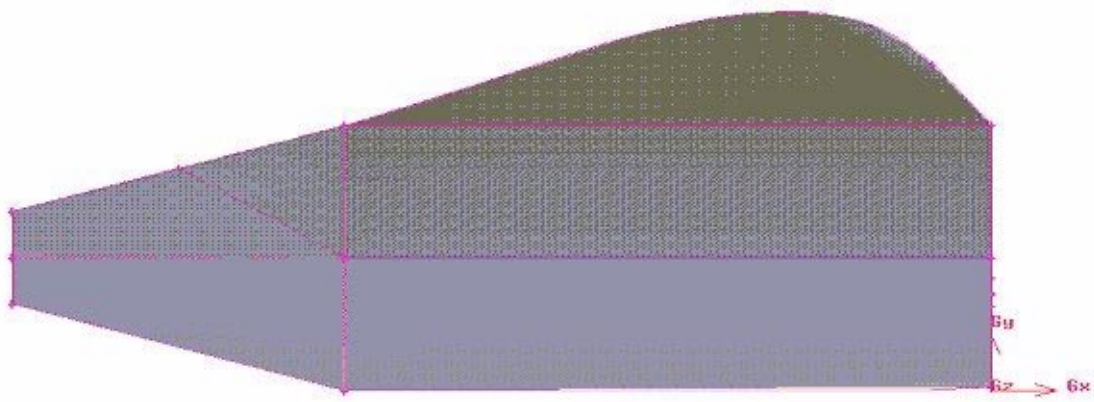

Figure 3-76: Top View of Entomopter Wing

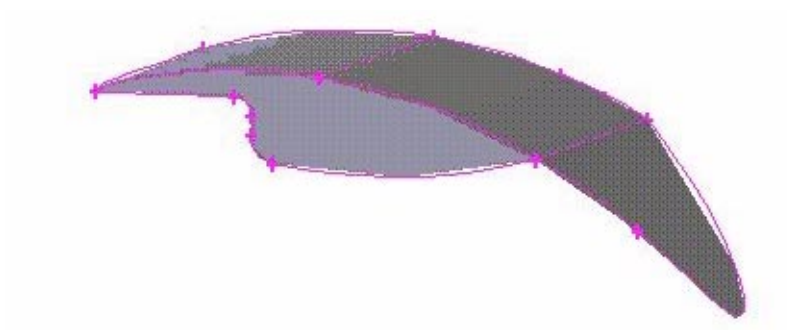

Figure 3-77: Side View of Entomopter Wing

The conditions used to run the case were the same as those for the 2D cases given in Table 3-5. The oscillating conditions used were: maximum velocity = 10 m/s, frequency = 20 rad/s.

This case was with the wing heaving up and down. The lift and drag coefficients obtained for the heaving case are shown in Figures 3-78 and 3-79.

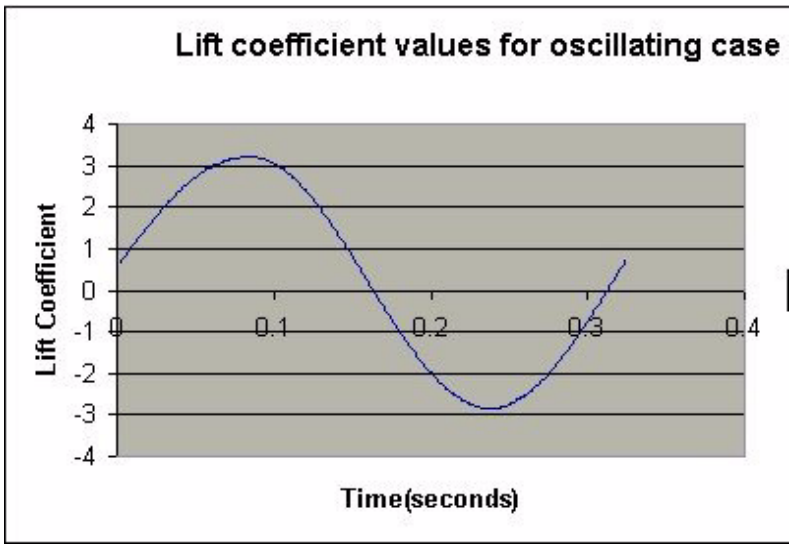

Figure 3-78: Lift Coefficient for the Oscillating Wing Case

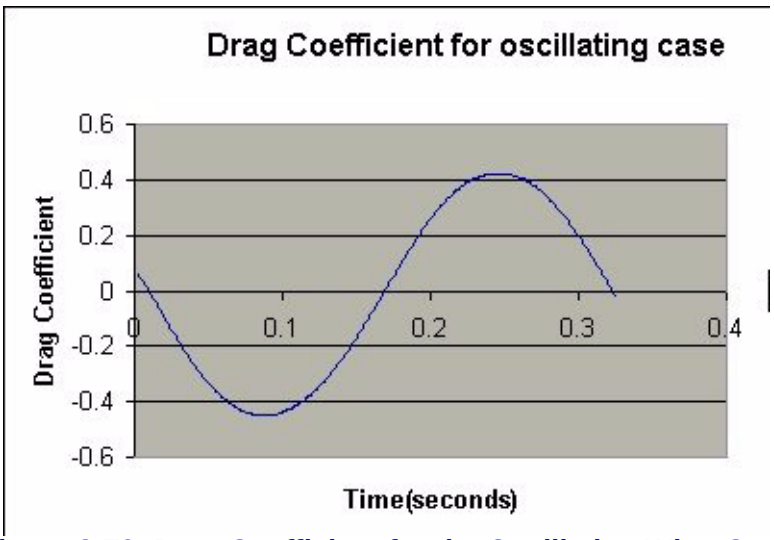

Figure 3-79: Drag Coefficient for the Oscillating Wing Case

3.3.1.4.2.2 Thin 3D Wing Geometry

To further investigate the low Reynolds number high-α behavior, a thin 3D wing was modeled after the North American cicada wing (Figure 3-80). The planform was approximated as a semi-ellipse with an aspect ratio of 3. Even though the cicada has hind wings (the right one is shown in Figure 3-80), the CFD model used only the forewing. The wing is thin (thickness-to-maximum chord ratio ~ 0.02), has a slight camber, and a slight curvature in the span wise direction. The hind wing can rotate about the leading edge, which forms a common line of contact with the forewing trailing edge. It appears that one of the functions of the hind wing is to act as a control surface to control camber during the stroke cycle. As discussed by Dickinson, et al. [57, 58, 56], the wing undergoes large changes in orientation during pronation and supination in order to provided optimum lift and thrust during the entire stroke cycle. The other interesting feature to note

about the cicada wing is the layout of the spar-and-rib structure. Unlike aircraft wing, it appears that the natural wing lends itself to large flexure, which has been observed in experiments with live insects.

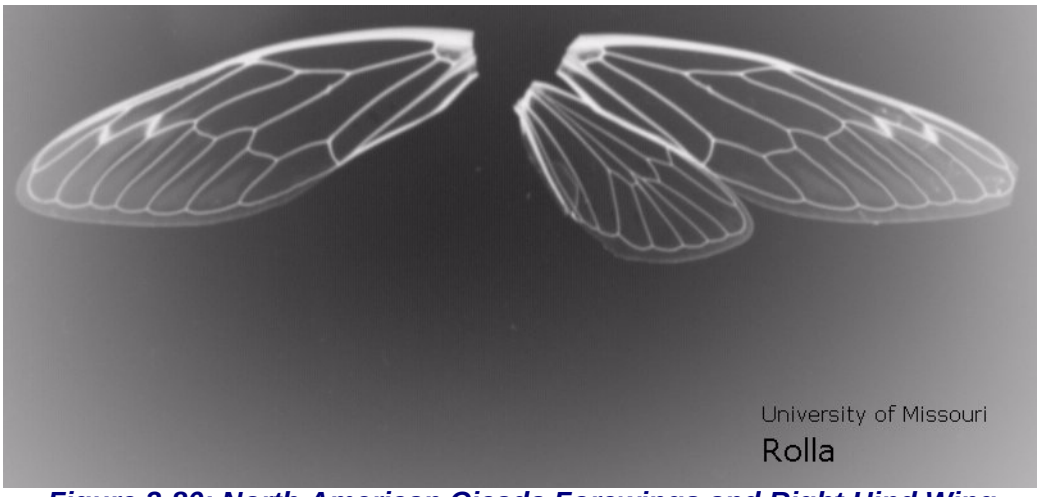

Figure 3-80: North American Cicada Forewings and Right Hind Wing

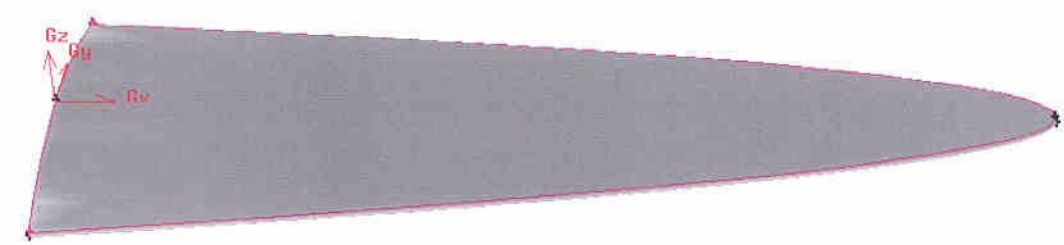

Figure 3-81: Elliptic Wing Modeled After North American Cicada Wing

3.3.1.5 CFD Analysis: Metacomp Technologies

Metacomp Technologies Inc. was subcontracted to perform (CFD) analyses on the Entomopter wing. The nature of this very complex problem resulted in a need for more sophisticated techniques than what was used in the FLUENT and WIND analyses. The goal here was to do more refined and accurate simulations of the wing motion, with flapping, and with blowing around a curved trailing edge. This CFD analysis was performed using Mars atmospheric data and flapping parameters found to be within the design space for a Mars Entomopter. Four cases were run:

1. No Flapping steady forward velocity, NO BLOWING
2. No Flapping steady forward velocity, BLOWN
3. Flapping with steady forward velocity, NO BLOWING
4. Flapping with steady forward velocity, BLOWN

The purpose of the non-flapping cases was to determine the degree to which the CFD could accurately simulate the Coanda effect due to the blowing over a trailing edge surface (curved flap). This known, one could then segregate the effects of blowing in the flapping cases from those created by the flapping itself.

The wing planform provided by GTRI to Metacomp Technologies for conversion to a CFD mesh included a "blown flap" with a radius that was 4% of the maximum chord value as shown in Figure 3-82. For the 0.6m winglet span, the max chord of the blown part is about 0.2m. This leads to a 4% radius of about 8mm. Due to various constraints the blowing slot, tangential to the blown flaps at the outer trailing edge and wing tip, was simulated to be about twice as large as it would be were it to be implemented physically. This could result in a higher mass flow than necessary to achieve a given degree of pneumatic control.

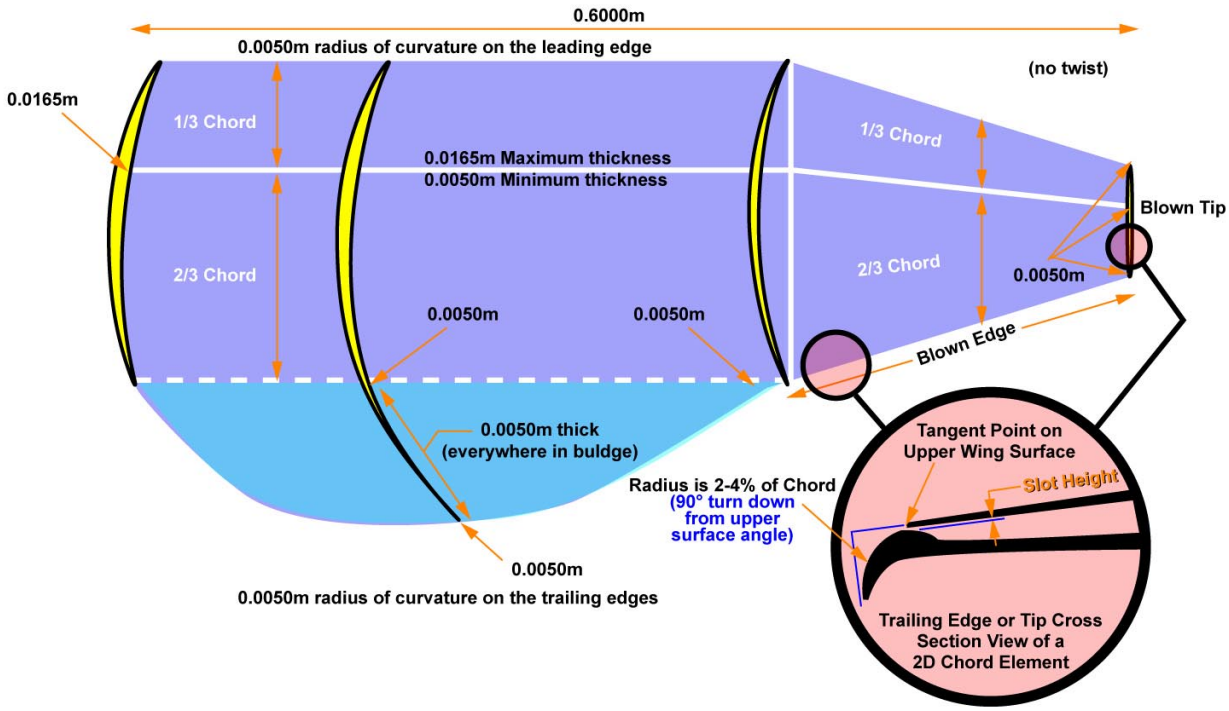

Figure 3-82: Dimensions Used for Entomopter Wing Mesh Generation

The Entomopter wing is designed to change its angle of attack at the top and bottom of the flapping cycle based on the compliance of the wing material so that an optimum angle of attack (α) is achieved without the use of actuators. The wing angle of attack changes throughout each wing beat due to the absolute velocity change of each point along the wing as well as the flexing motion of the wing itself. For the purposes of the Metacomp Technologies CFD wing design, this change of wing α occurs rapidly near the top and bottom of the flap (rather than continuously). Specifically, the angle of attack was chosen to be -8° for the down beat, and $+8^o$ for the upbeat. Since most of the lift is expected to come from the wing beating and not the forward flight, the wing makes its flip from -8° to $+8^o$ (and vice versa) in the first 10° of wing flapping after reaching the maximum excursion at the top/bottom of the flap. The rate of change in the angle is modeled to be linear over this 10° (going from -8° to $+8^o$ and vice versa) with the $\pm 8^o$ being held constant over the remainder of the flap.

Input parameters and boundary conditions used in this CFD analysis were:

1. Mars atmospheric parameters (STP within 3m of Mars equatorial surface)
2. Altitude: near surface (under 3m above mean planetary ground level)

3. Density: 1.40E-2 kg/m^3
4. Pressure: 750 Pa
5. Temperature: 263° K
6. Speed of sound: 265 m/s
7. Viscosity: 1.35E-5 kg/m s
8. Kinematic viscosity: 9.65E-4 m^2/s
9. Flapping frequency: 6 Hz
10. Inflow (forward flight) speed: 14 m/s
11. Wing flapping angle: ±75 degrees from horizontal

3.3.1.5.1 Mesh Topology

In the earlier computational studies, which focused on the flapping motion, Metacomp Technologies had used a relatively crude mesh. Also, they had not included the full details of the geometry of the blown flap. Subsequent studies modeled the blown flap region geometry, and developed a more dense mesh. On this mesh, Metacomp Technologies first studied the non-flapping case, with and without blowing. This section describes the overall mesh system topology.

In the following, “x” is the freestream direction, “y” is the vertical and “z” is the spanwise direction. The wing extends along the negative z direction.

Figures 3-83 through 3-88 present several views of the mesh used. For the simulations with blowing, the mesh has been further refined in the blown flap region. But the overall topology is similar to the figures shown below.

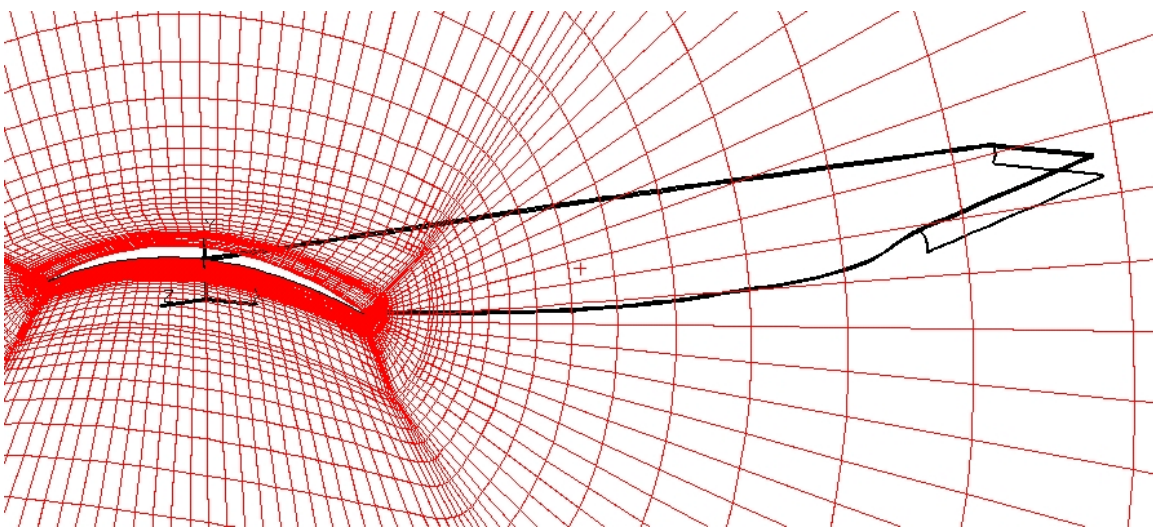

Figure 3-83: Mesh View 1

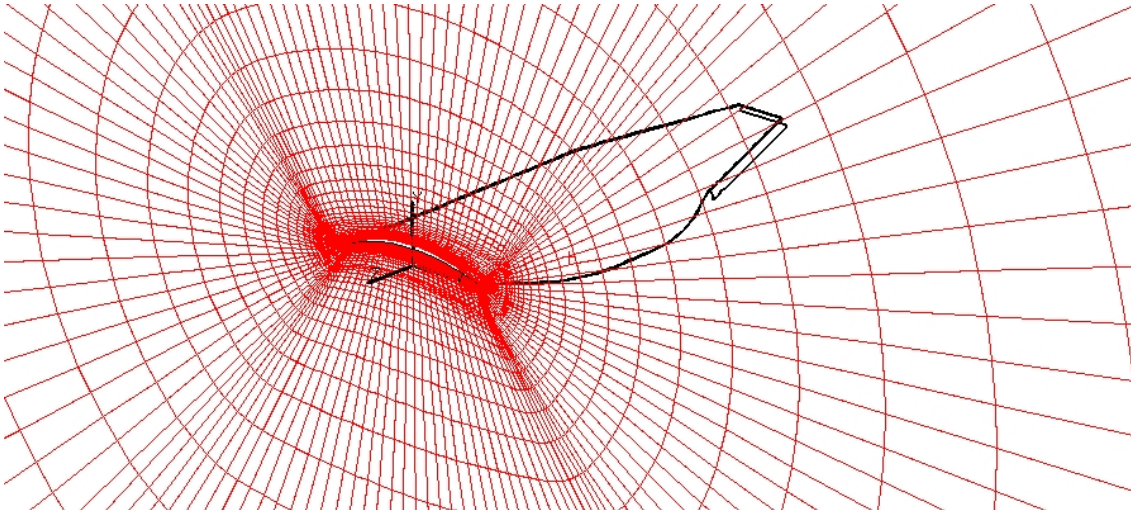

Figure 3-84: Mesh View 2

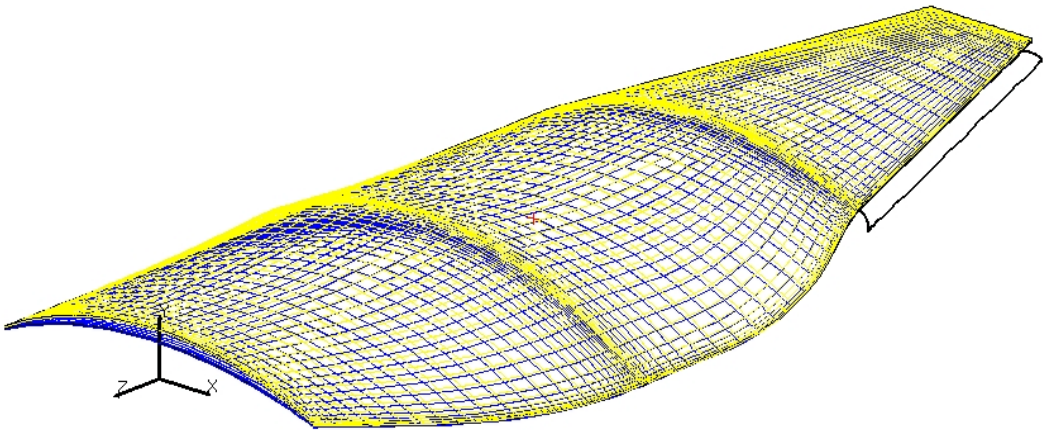

Figure 3-85: Mesh View 3

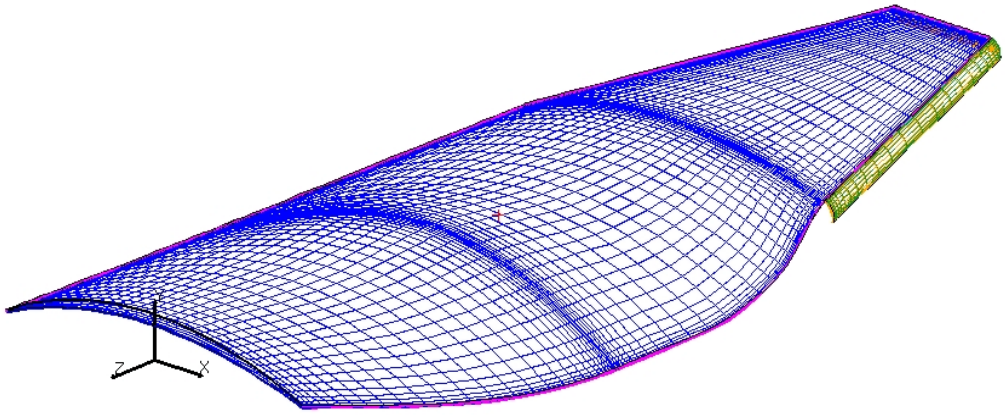

Figure 3-86: Mesh View 4

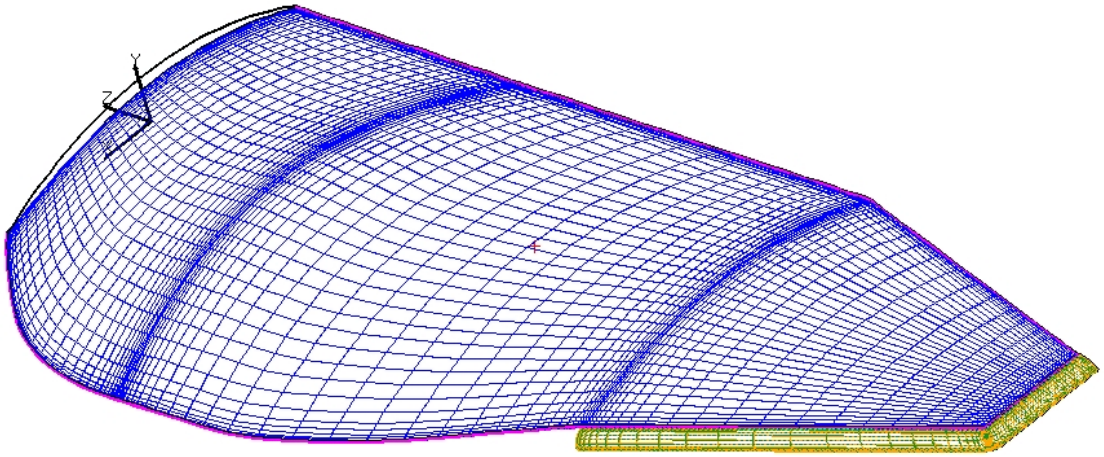

Figure 3-87: Mesh View 5

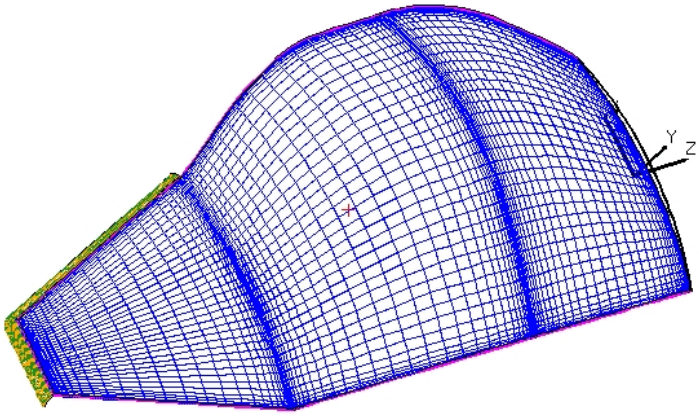

Figure 3-88: Mesh View 6

Figure 3-89 shows the residual convergence plot for the steady state wing in unflapping flight.

3.3.1.5.2 Unblown Steady State Case

This section presents results obtained for the case without blowing. Mars atmospheric conditions were used along with 14 m/s free stream velocity. The wing was assumed to be at “neutral” position. Figure 3-89 shows the residual convergence plot.

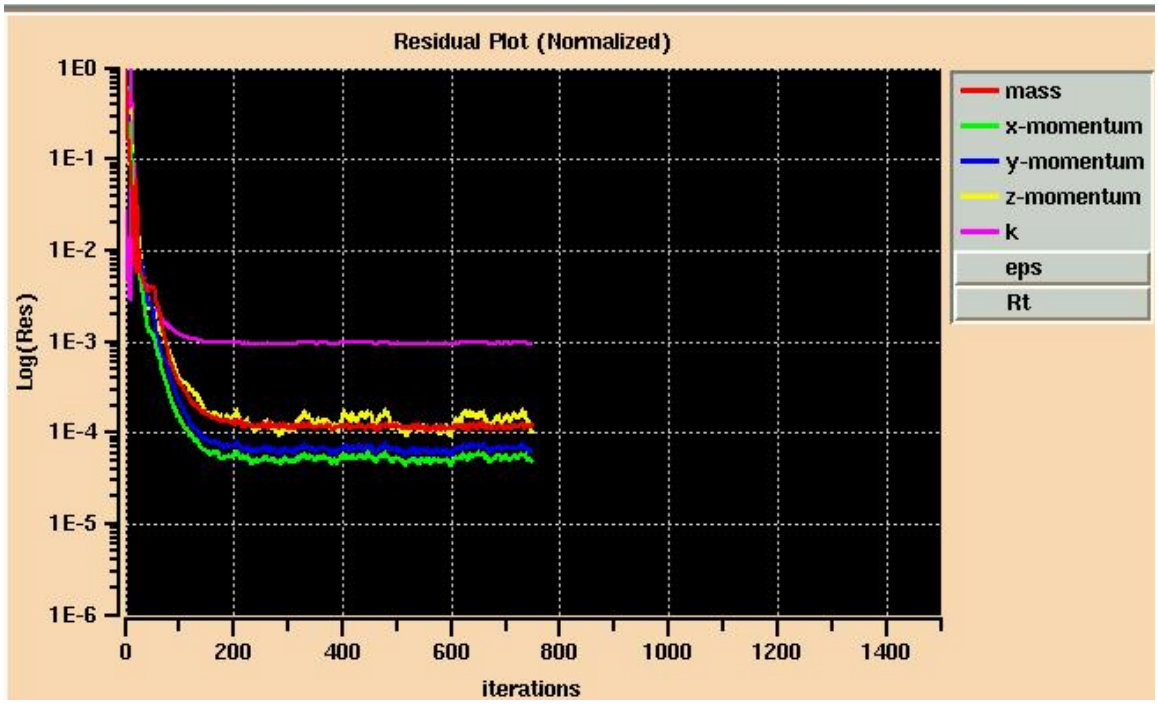

Figure 3-89: Residual Convergence Plot

Figure 3-90 shows the force convergence plot where the forces are portrayed in Newtons. The level of the forces can be compared with the blown case to determine the effectiveness of the CFD simulation. Empirical data for steady state (unflapping) wings has shown the effectiveness of blown airfoils to be as much as ten times that of the same airfoil if unblown. [80]

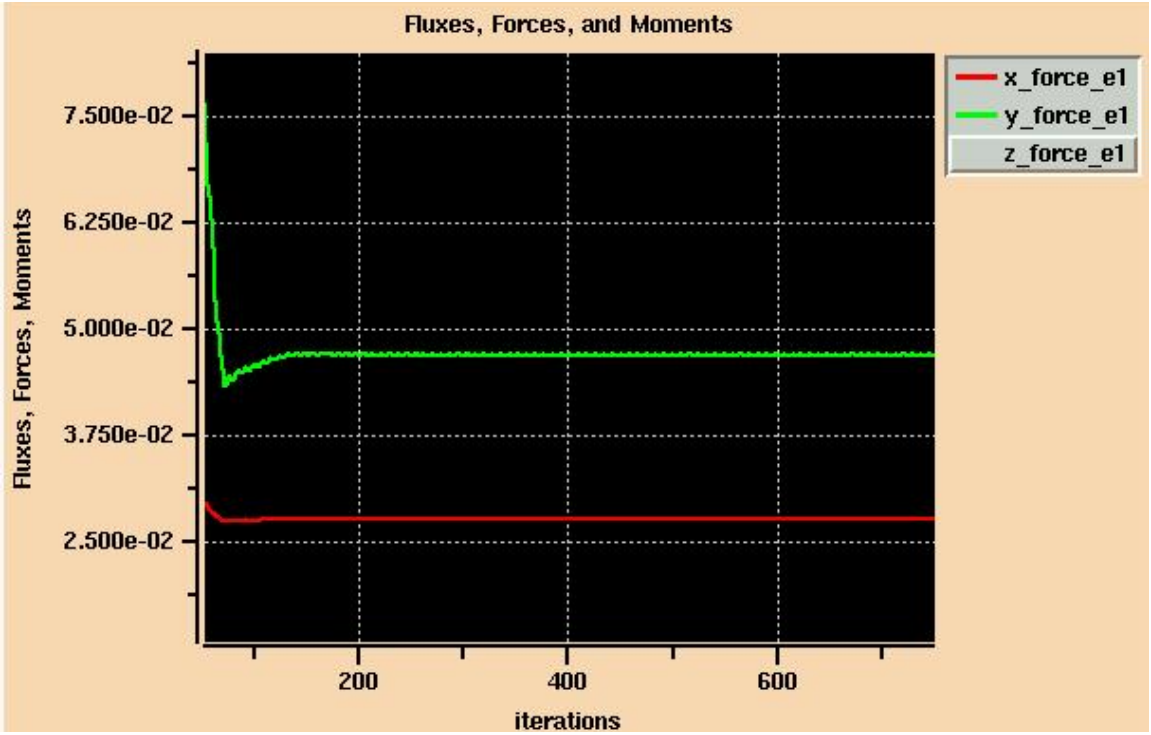

Figure 3-90: Force Convergence Plot

Figures 3-91 through 3-93 show the streamwise velocity contour at three spanwise stations. The last location (z= -0.5m) is approximately at the center of the blown flap. The streamwise separation is clearly evident and these figures must be compared with the corresponding figures for the blown flap case. These three views along the wing show stagnation points and regions where lift is being produced.

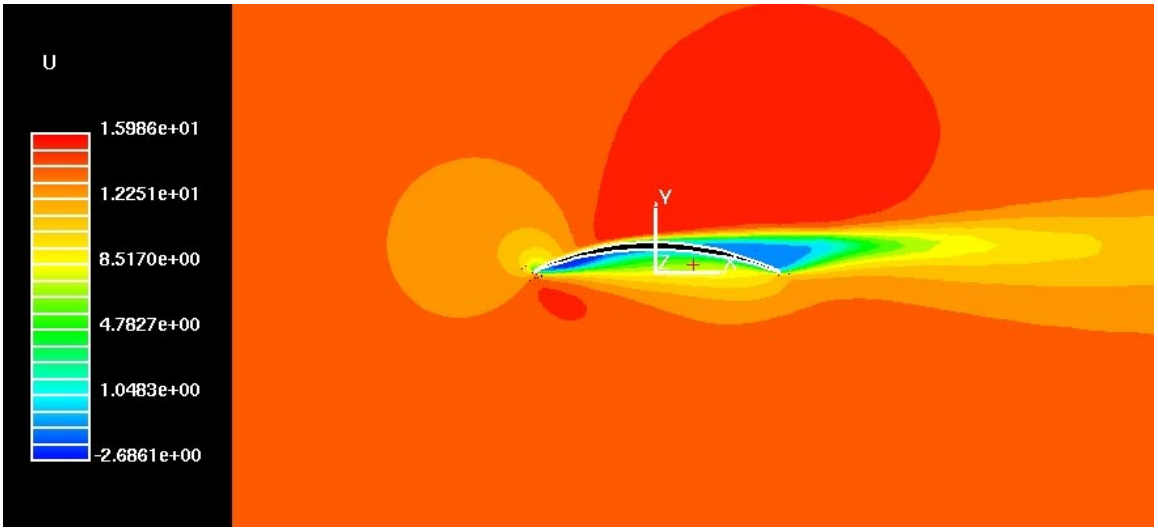

Figure 3-91: U Velocity Contours on Symmetry Plane

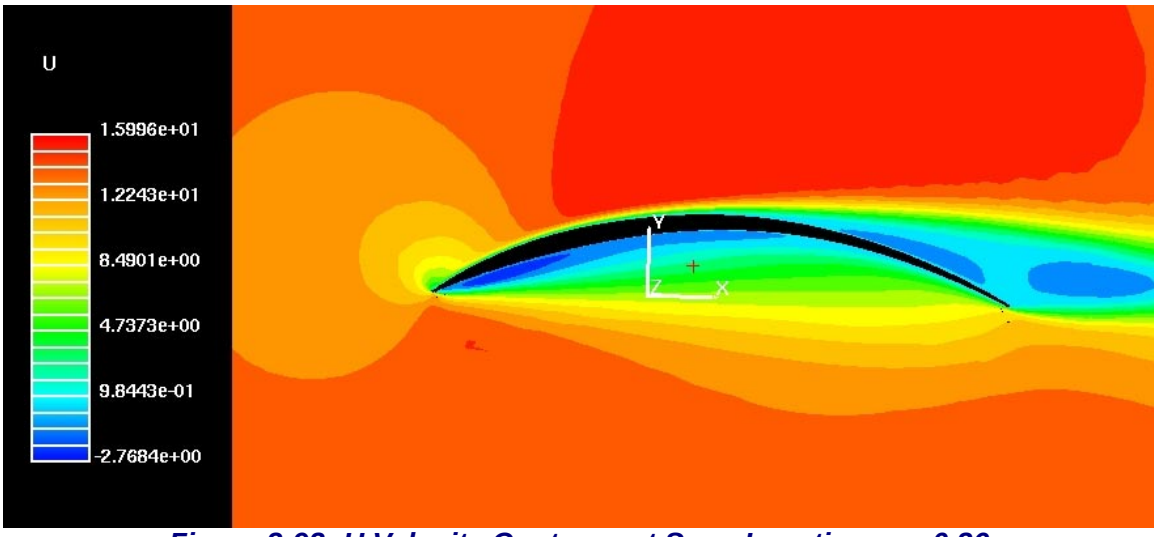

Figure 3-92: U Velocity Contours at Span Location z = -0.26

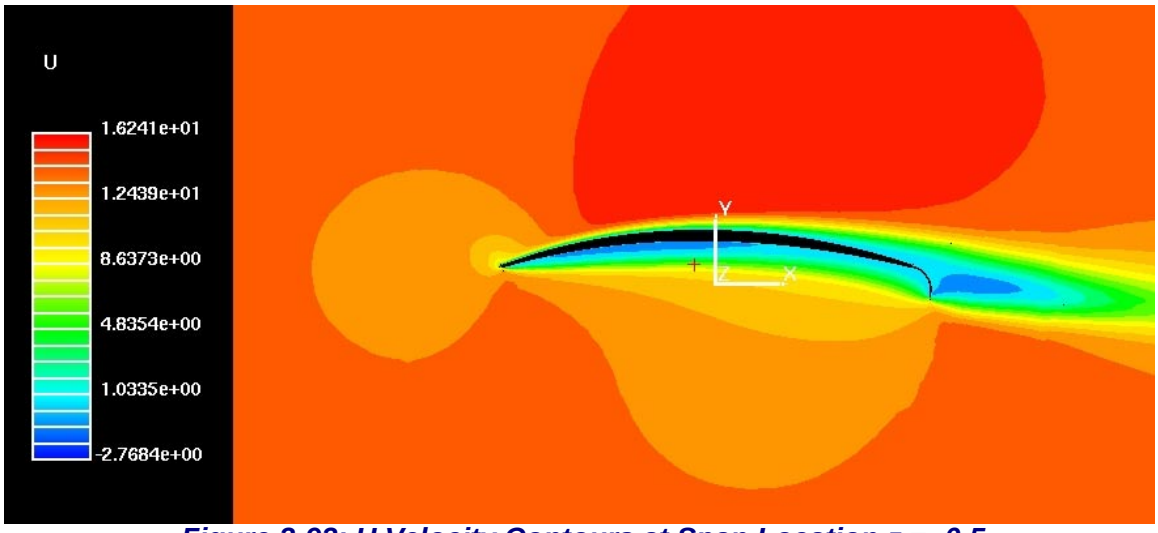

Figure 3-93: U Velocity Contours at Span Location z = -0.5

3.3.1.5.3 Blown Steady State Case

In this section, the results for the blown flap case are presented for comparison. The blowing velocity used is 100m/s. Normally the blowing velocity is 4 to 7 times that of the forward velocity, however the low density of the Mars atmosphere may change this rule of thumb. Currently the Mars Entomopter design team has not performed parametric studies to determine the optimum blowing velocity under Mars conditions, however this is a topic for planned follow-on efforts.

Once again, in the following figures, “x” is the freestream direction, “y” is the vertical and “z” is the spanwise direction. The wing extends along the negative z direction. Figure 3-94 shows the residual convergence plot for the blown case. As with the unblown steady state case, rapid convergence is reached. Even though the computations were performed in “steady state” mode, the oscillations in the time history are indicative that the flow “wants” to be unsteady.

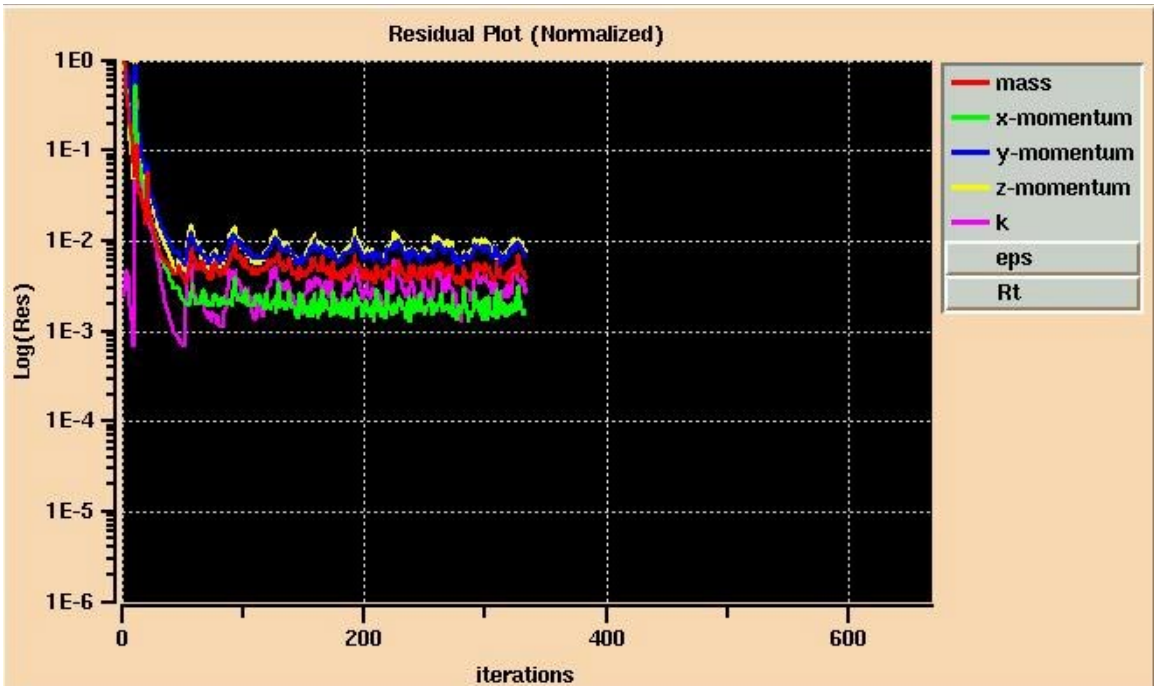

Figure 3-94: Residual Convergence Plot

Figure 3-95 shows the forces in Newtons. The drag does not appear to be affected by the number of computational iterations. The lift, however, is affected.

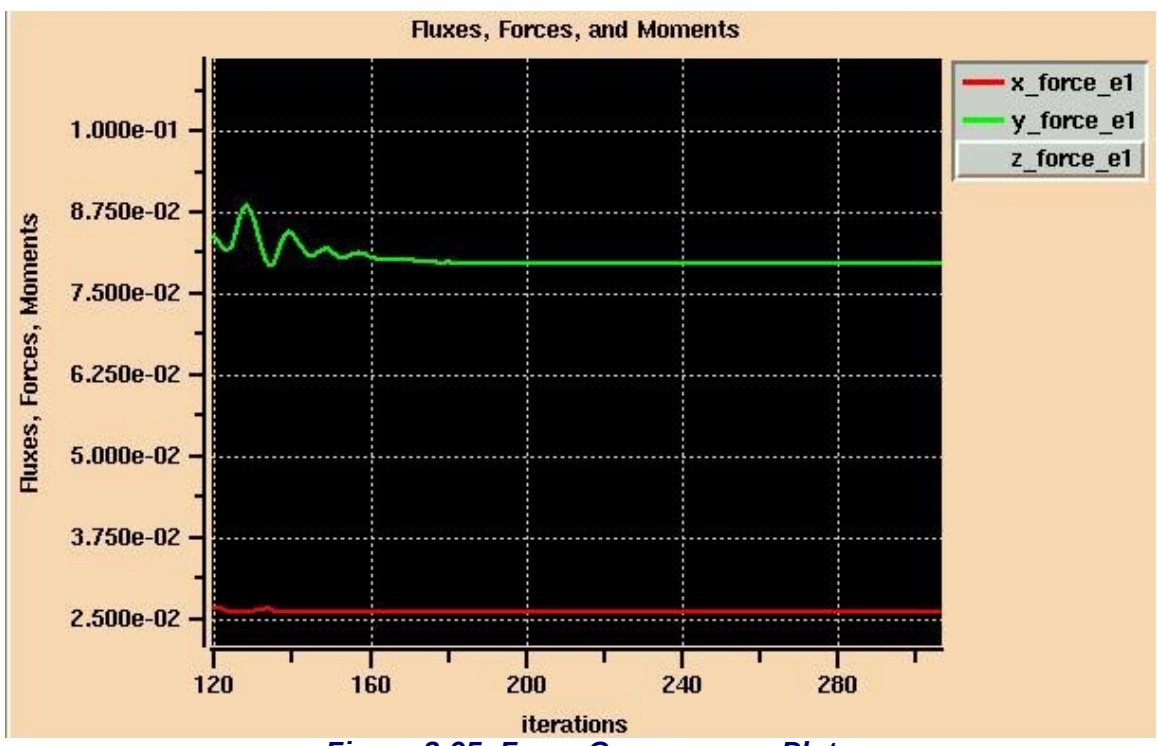

Figure 3-95: Force Convergence Plot

Figures 3-96 through 3-98 show the streamwise velocity contours. The z = -0.5m station shows a marked difference from the unblown case. The blowing and the resulting Coanda effect have resulted in the absence of flow separation on the top wing. This is the desired effect.

Note that in Figure 3-98, the trailing edge blowing at this station turns the flow down as desired (perhaps 30°), however downward turning of 90 degrees is possible, producing a corresponding increase in lift (in fact, wind tunnel tests have demonstrated that the local flow can be turned 180° using blown surfaces under correct circumstances). Within the time and funding allocated to the CFD analyses performed on this NIAC Phase II study, it was not possible to identify an optimal point in the design space where slot velocities and blown flap geometries would result in optimum lift while the airfoil is being blown under Mars atmospheric conditions. The CFD results shown demonstrate that increases in lift can be attained for the Entomopter wing on Mars, but by no means indicate the maximum potential to be gained in doing so. For the design point chosen (14 m/s forward flight and 6 m/s wing flapping over a 150° angle) a 100 m/s blowing velocity yields forces on the order of 0.08125 Newtons with blowing whereas the unblown wing only exhibits 0.046875 Newtons according to this single point CFD analysis (as shown in Figures 3-90 and 3-95). Empirical wind tunnel data have shown analogous test set ups to produce improvements in the range of 5 to 10 times this. [80, 82]

It is clear that the point in the design space is not optimum and while the present CFD model can to be refined, the choice of better operating parameters is also necessary. This parametric analysis will be conducted with the help of the analytical formulations developed during this study to define the “sweet spots” for operation within the overall design space. This work (for the unsteady blown flapping case) is being carried out as a Ph.D. research topic and will be further pursued in follow-on research efforts.

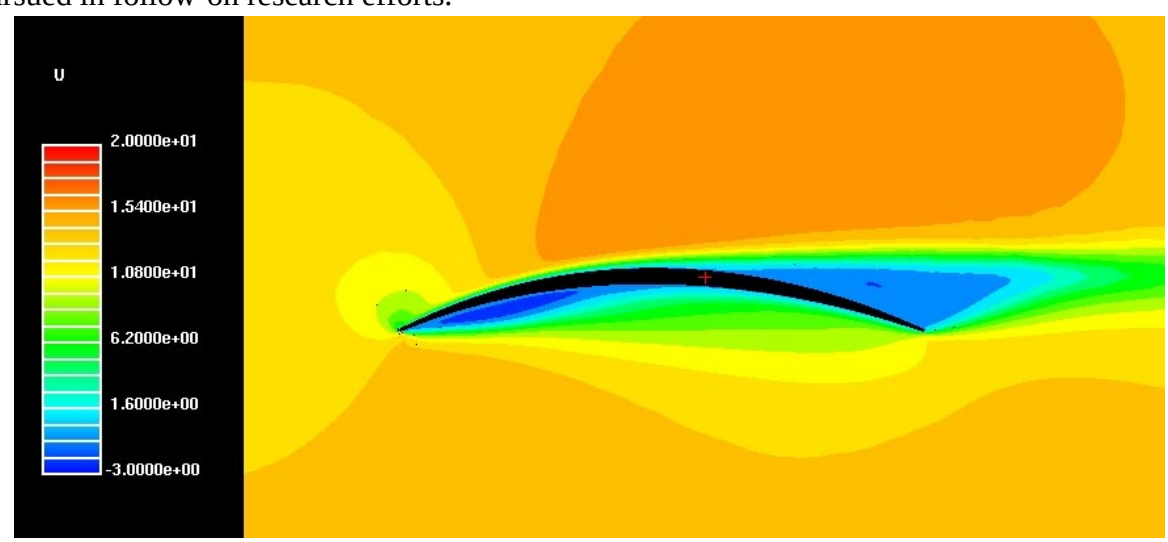

Figure 3-96: U Velocity Contours on Symmetry Plane

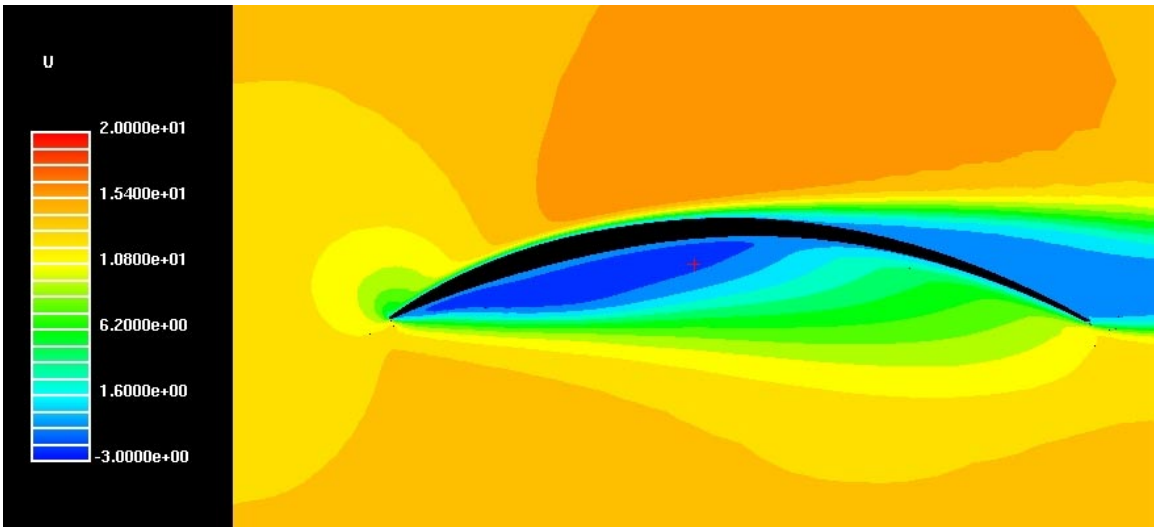

Figure 3-97: U Velocity Contours at Span Location z = -0.26

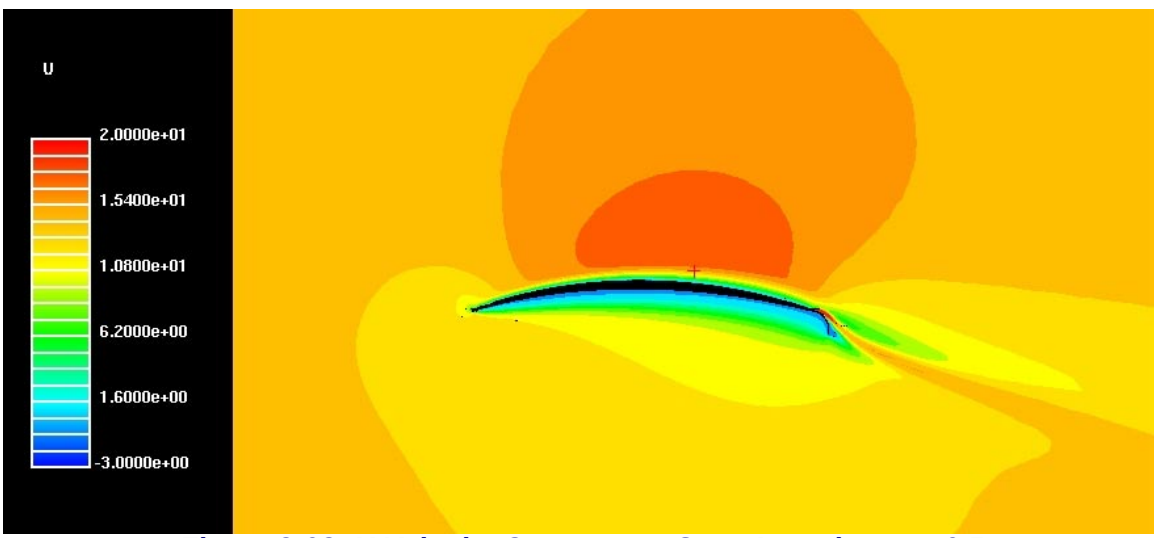

Figure 3-98: U Velocity Contours at Span Location z = -0.5

3.3.1.5.4

Having demonstrated the steady state case performance expected for the point solution, this section provides a summary of the approach and results achieved when the dimension of flapping is added to the CFD analysis.

All parameters remain the same as the steady state case except that the wing is now modeled as flapping over a 150° angle at a rate of 6 Hz. The wing also undergoes pitching motions as per the parameters presented in the introduction to the CDF analyses. In earlier simulations, Metacomp Technology's approach was to construct two meshes. The inner mesh enclosed the wing and had a spherical outer boundary. The outer boundary was a full sphere even though the wing was situated only on one side. In the current simulation, a single mesh has been used. This single mesh was subjected to flapping and pitching motions in its entirety. The computational region of inter-

est was only in one half of the domain using the assumption of symmetry in the flow-field that corresponds to symmetric flapping motion. During every time step, the entire mesh rotated along with the wing; and the part of this mesh that was outside the symmetry plane was "chopped off" with appropriate symmetry boundary conditions being applied to the newly created boundary between the chopped off mesh cells and the remaining mesh cells.

Forward flight was represented by assigning the corresponding velocity to the oncoming free stream (14m/s). This far-field velocity was held stationary in the inflow regions of the boundary. Only one half of the entire wing was used in the simulation, assuming symmetric flapping. The actual mesh was comprised of both wings on either side of the symmetry plane. This mesh was subjected to the rotations prescribed above. One side of the mesh was sliced off. This slicing was done during each time step to remove mesh cells from the "wrong" side of the symmetry plane. This approach is rather unique and extremely effective.

Two simulations were performed. One was with flapping (and pitching) but no blowing. The other was with continuous blowing with a jet velocity of 100 m/s.

The unsteady simulations use 80 time steps per flap cycle. Periodic behavior in time is reached almost from the first cycle, but several cycles were carried out to confirm this behavior. Each "iteration" represents a time step.

The x-force is along the free stream (along the horizontal from front to back of the wing).

The y-force is the vertical force.

The z-force is the force in the direction of the span. This is not significant because in a symmetric wing configuration this force will be opposed by a similar force acting on the other wing leading to zero net force in this direction when considering both wings as a system

In earlier coarse grid studies, cyclic behavior was reached very rapidly, essentially after one cycle of flapping. Figure 3-99 plots forces for the flapping case using the finer grid, blown flap geometry definition, and 100 m/sec blowing velocity. Two cycles were performed. Comparison of animations between the blown flap and the non-blown flap case shows that the blown flap has similar beneficial effects at the trailing edge as observed in the stationary wing cases, however the most significant effects appear to come directly from the dynamic movement of the wing itself. The subjective comparison of 2D slices of the flapping wing in the animations does not capture the leading edge vortex (LEV) activity except for the brief time that it exists at that station.

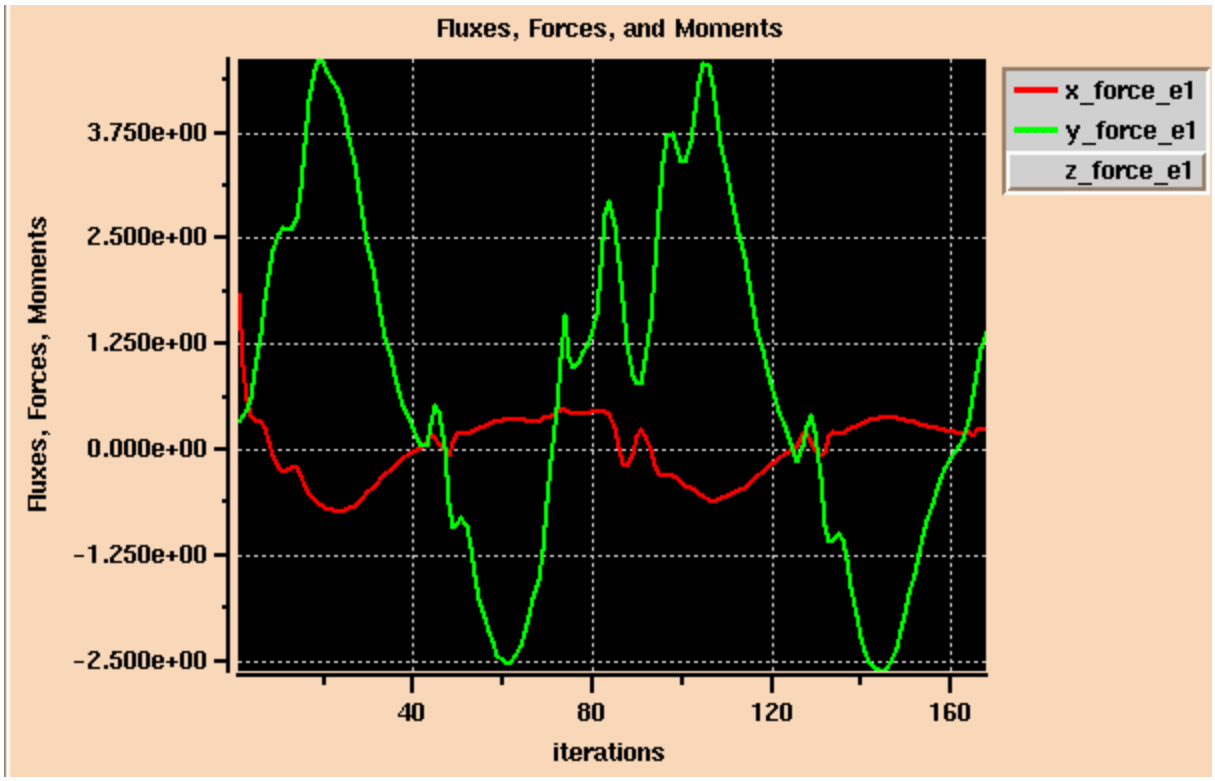

Figure 3-99: Forces (Newtons) Time History for Simulation with Blowing

3.3.1.5.5 Conclusions Stemming from CFD Analysis

The overall lift of the flapping wing has contributions from the physical wing shape, the virtual camber created by the leading edge vortex, and the extended flow attachment due to the blowing of the trailing edge plus the additional circulation and lift caused by blowing. The CFD simulation is not accounting fully for the effects of the blowing at this point in its development. Also, while the LEV is seen to form in animations, it is fleeting, either disassociating at the particular station simulated along the wing, or existing dynamically at different stations at different points in time during the flapping cycle. This too is a subject for further empirical investigation in the wind tunnel using a particle imaging velocimeter (PIV). Such measurement will provide an actual 3-D view of the LEV and will be used to update and validate both the CFD models and the analytical model that presently accounts for the flapping aerodynamics based on physical wing shape, but does not yet consider LEV effects or blowing effects.

Without flapping, the use of the blown flap is observed to reduce the upper surface separation and increases the lift by a substantial factor. In cases with flapping, the CFD model shows a major portion of the lift being supplied by the flapping process itself. The blown flap continues to be helpful in directing the trailing edge flow in a more downward direction when compared to corresponding case without blowing, however the overall effect on lift is relatively small since the most significant portion of the lift is coming from the flapping. This is consistent with the CFD model operating at a suboptimal point in the design space relative to both blowing and perhaps LEV formation. All of the indicators are favorable however the point of best performance

in the Mars atmosphere must be determined through a parametric analysis that more fully explores the entire design space over which the Entomopter can function.

Empirical results can be generated on a newly constructed flapping wing simulator in the GTRI wind tunnels. This hardware simulator, developed on another government-funded project, is capable of operating with a full scale blown winglet of the exact planform used by the Mars Entomopter and at speeds comparable to those used in the CFD simulations. These wind tunnel tests are beyond the scope of work originally proposed under this NIAC Phase II effort, but will be conducted as follow-on work to advance and refine the CFD and analytical models developed here.

3.3.1.6 Forces on the Entomopter Wing

Time histories of forces on the Entomopter wing for Case 1 (without blowing) are shown next.

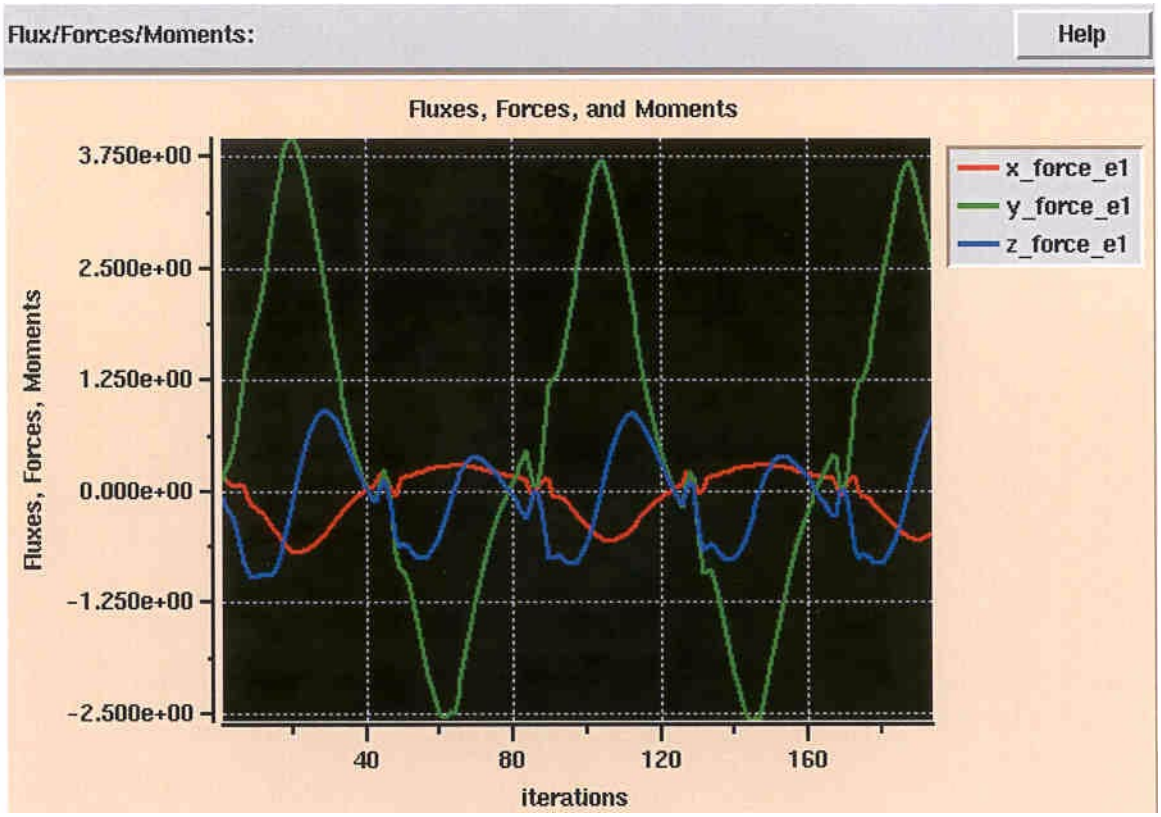

Figure 3-100: Force (Newtons) Time History for Simulation Without Blowing

The unsteady simulations started from time step 1. One flap cycle consisted of 80 time steps. Periodic behavior in time is reached almost from the first cycle, but several cycles were carried out to confirm this behavior. Each iteration represents a time step.

The x-force is along the free stream (along the horizontal from front to back of the wing), and the y-force is the vertical force.

The z-force is the force in the direction of the span. This is not worth a great deal of attention because in a symmetric wing configuration, this force will be opposed by a similar force acting

on the other wing leading to a net-zero force in this direction when taking both wings as a system.

We now present the force's time history for the case with continuous blowing with blowing velocity of 1 m/s. No noticeable difference was seen in the results, probably due to the fact that the blowing speed is so low and the blowing angle was not optimized to take advantage of the Coanda effect.

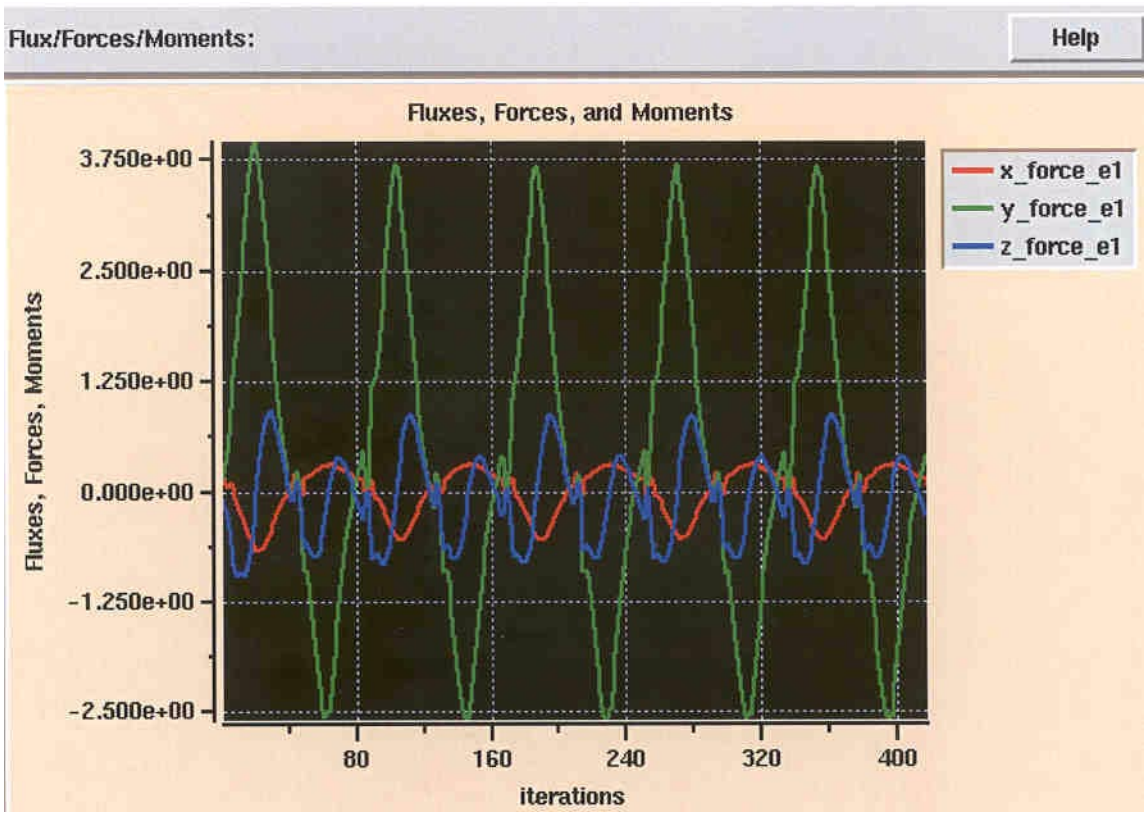

Figure 3-101: Force (Newtons) Time History for Case with Continuous Blowing Velocity of 1 m/s

Additional cycles of results were obtained for this case to confirm periodicity in time.

The wing-flapping motion is of sufficient strength, and the presence of the free stream velocity (corresponding to forward motion of the wing) carries the wing vortices downstream so that reasonable periodicity of the motion seems to be achieved essentially from the end of the first cycle.

3.3.1.7 Conclusions

The results presented in this section represent the first attempts to advance the solution of a very difficult flapping-wing problem. The plots show that the maximum lift coefficient was around 4 or 5, and with further refinements to blowing techniques, it can be augmented. The present results reveal several features of low Reynolds aerodynamics that haven't been systematically

investigated in previous works. The formation of the LEV and its downstream convection have been investigated for α and Reynolds variations over a wide range. Results from the cases considered in this report indicate that by carefully choosing the Reynolds number regime and the wing kinematics during the wingbeat cycle, lift can be increased to meet the demands of a flapping-wing MAV design for operating in the Mars environment.

3.3.1.8 Future CFD Work

Future work on the CFD portion of Entomopter analysis could focus on improving the current model and comparing these results to experiments. Understanding low Reynolds number, high angle-of-attack aerodynamics by conducting a coordinated CFD/experimental effort should be an important objective of future work. Improving the model would include a more detailed wing shape with thickness, wing bending, and more accurate flow conditions. The parameter space could be expanded to include larger ranges of flight speeds, flapping angles, flapping rates, and mass flow ejection rates. Experimental work would include PIV wind tunnel analysis of a flapping and/or pitching wing with CFD simulation results.

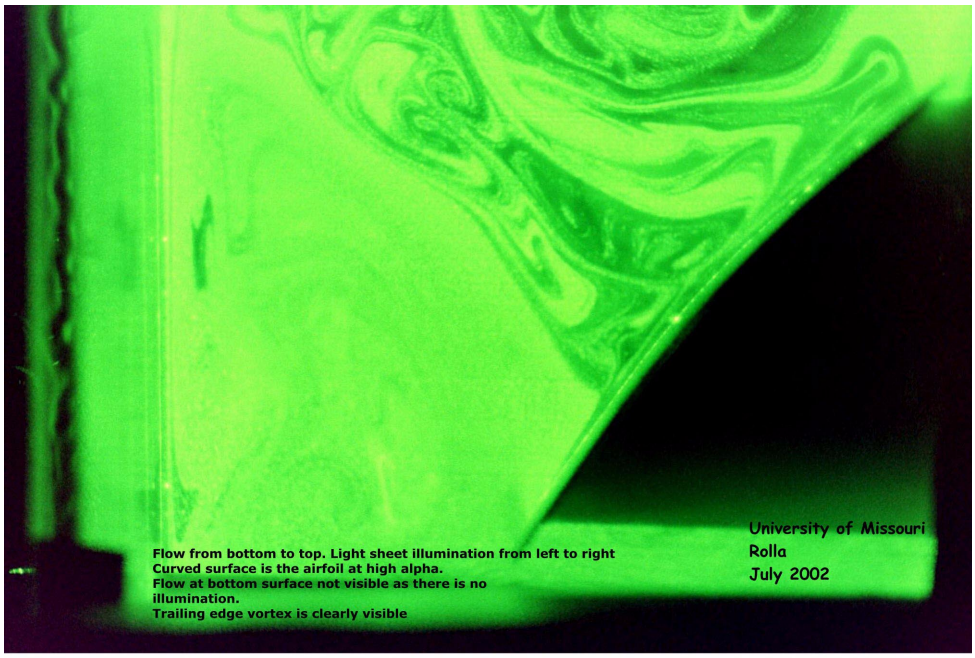

Figure 3-102: Wind Tunnel Flow Visualization Image of Flow Over a Thin Wing at High α. Flow is from Bottom to Top and Light Sheet Illumination from Left to Right. Trailing Edge Vortex is Clearly Visible.

3.3.2 Angle of Attack Analysis

A key factor calculating the wing lift for the Entomopter is the angle of attack of the atmosphere relative to the wing. Because of the unsteady environment in which the wings operate, this angle of attack is not constant and will vary throughout each wing beat. The angle of attack is also affected by wing geometry and operating conditions, such as wing-beat frequency, wing length, maximum wing-flap angle, and forward velocity of the vehicle.

For this analysis an operating point was chosen based on the power-required analysis. The wing section length was chosen to be 0.6 m and the relative lifting capacity was chosen to be 1.5 kg (This is the amount of mass that can be lifted by the wings minus the wing mass). The wing velocity through one flap cycle is shown in Figure 3-103.

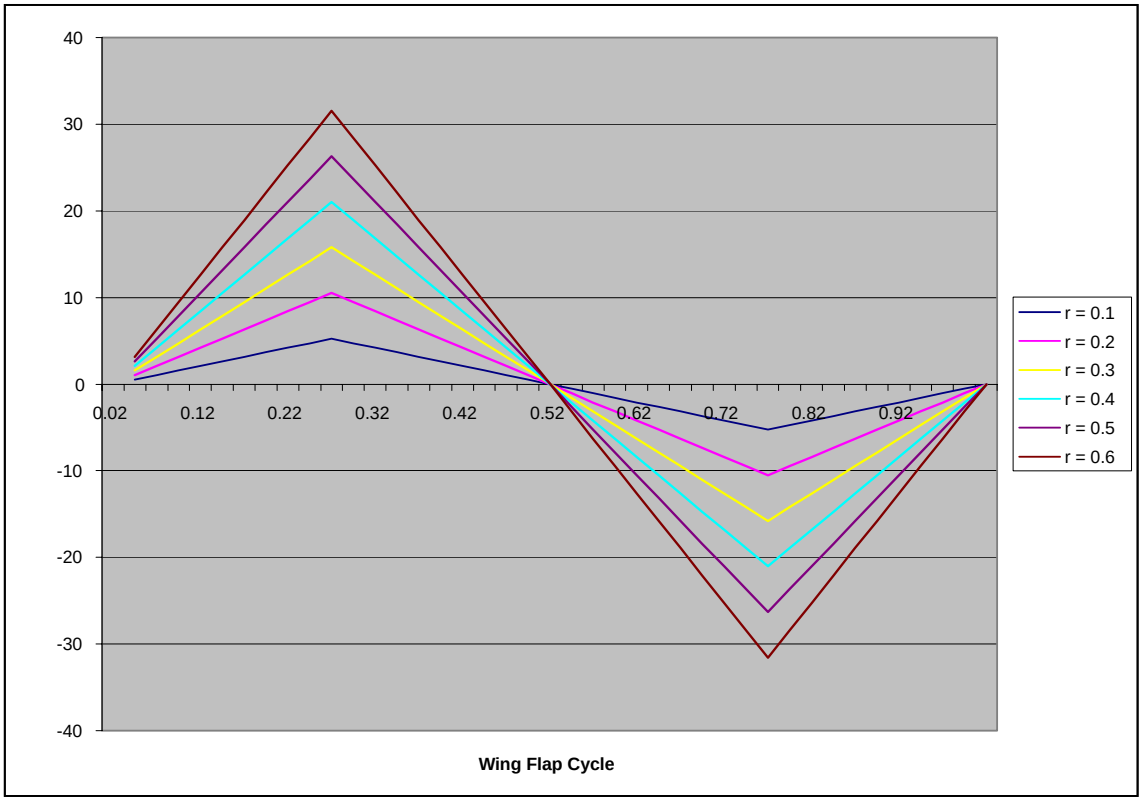

Figure 3-103: Wing-velocity Profile Due to Wing Motion Through One-flap Cycle

This figure shows the velocity profile throughout one flap cycle at various points along the radius of the wing. Wing-velocity profiles were generated for a flapping rate of 5.79 Hz and maximum flap angle of 65°. As these parameters vary, the absolute values of the curves will change, but the relative shape of the profiles will remain the same.

The equations for generating these velocity profiles are given below. The velocity calculation is broken up into three segments. The velocity profiles (V_{w1}, V_{w2}, and V_{w3}) for the three segments are given in Equations 3-32 through 3-34, where r is the length along the wing where the velocity is calculated, θ is the maximum flap angle for the wing, t is the time from the beginning of the cycle in seconds, and f is the flapping frequency of the wing in Hz.

$$V_{w1}=32\,\theta\,rtf$$ ***Equation 3-32***

$$V_{w2} = 16\,\theta\,rf - 32\,\theta\,rtf^2$$ ***Equation 3-33***

$$V_{w3} = -32\,\theta\,rf + 32\,\theta\,rtf^2$$ ***Equation 3-34***

This wing-velocity profile coupled with the free stream-air velocity produces the relative air velocity and angle of attack the wing sees during flight. The angle of attack (a) is given by Equation 3-35. Figures 3-104 through 3-107 show the angle of attack along the wing length

throughout a flap cycle. It should be noted the angle is for a horizontal wing. By twisting the wing we can adjust the absolute angle to one better suited for generating lift.

$$\alpha = Tan^{-1}\left(\frac{V_w}{V_f}\right)$$

Equation 3-35

As can be seen from these figures, changing the flight speed (V_f) has a significant effect on the wing angle. Changing the maximum flap angle, along with the corresponding change in frequency, did not have much effect on the wing angle of attack profile.

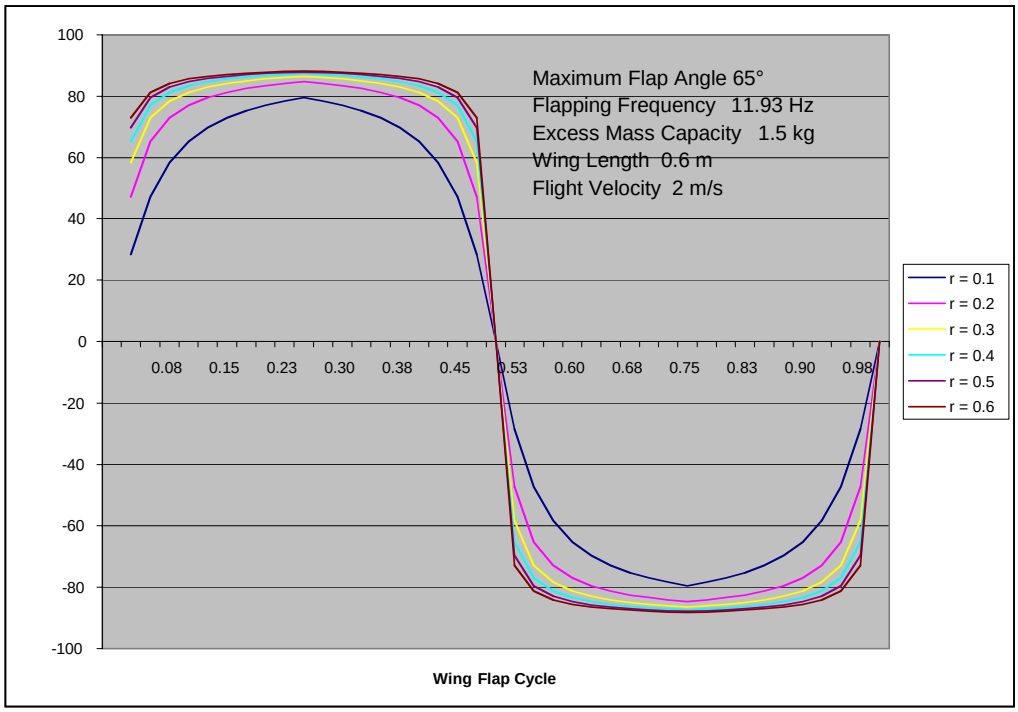

Figure 3-104: Angle of Attack for a Maximum Flap Angle of 65° and Flight Speed of 2 m/s

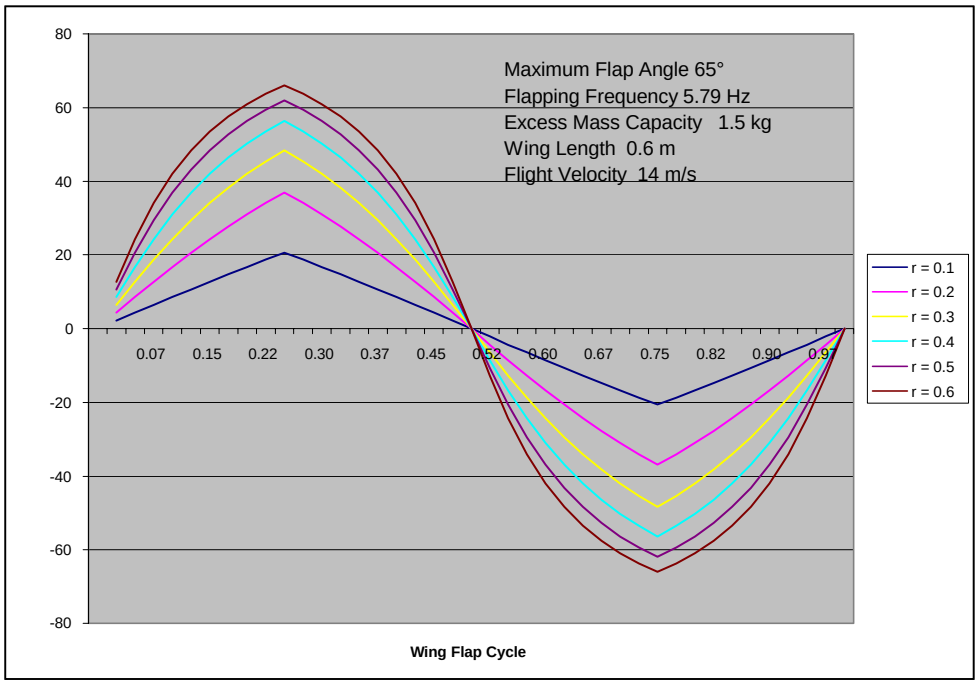

Figure 3-105: Angle of Attack for a Maximum Flap Angle of 65° and Flight Speed of 14 m/s

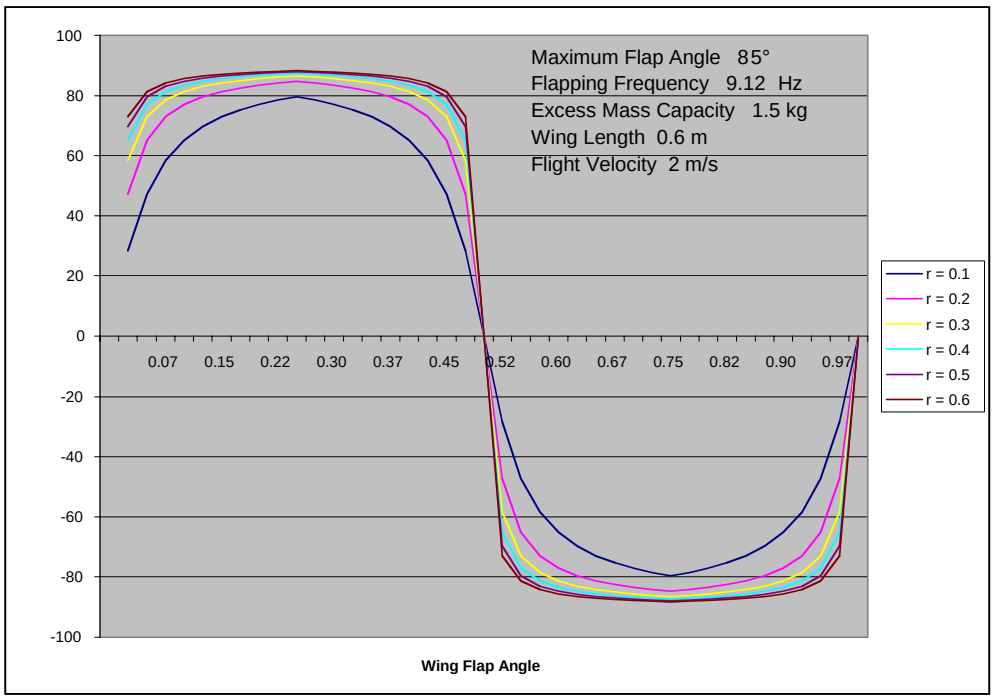

Figure 3-106: Angle of Attack for a Maximum Flap Angle of 85° and Flight Speed of 2 m/s

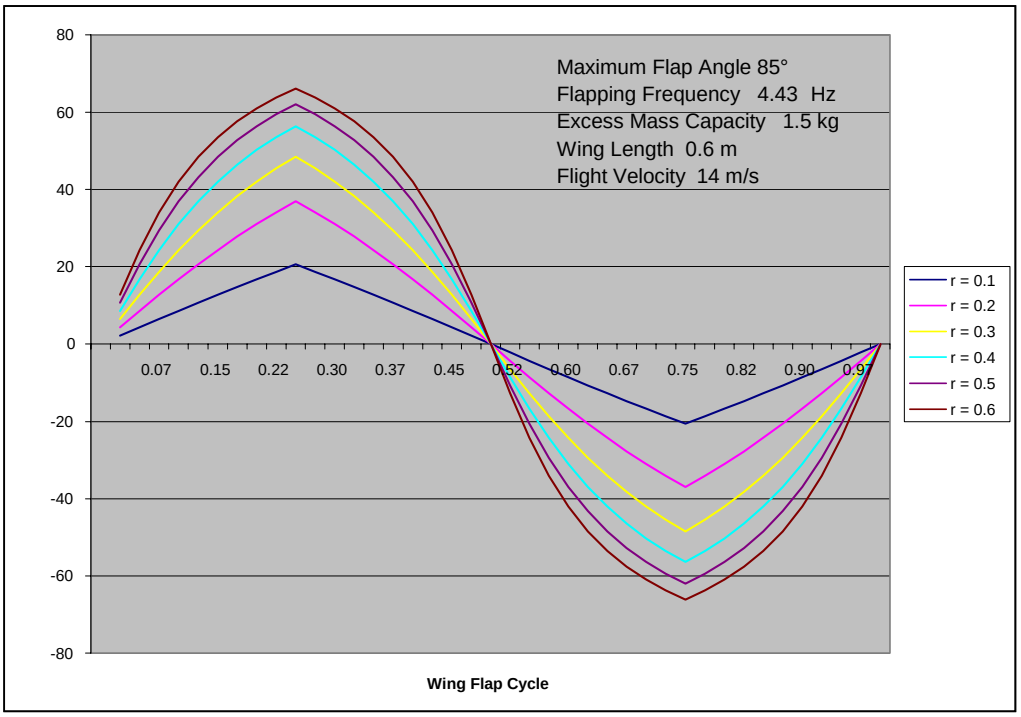

Figure 3-107: Angle of Attack for a Maximum Flap Angle of 85° and Flight Speed of 14 m/s

3.3.3 Analytical Analysis of Mars Entomopter Aerodynamics

3.3.3.1 Introduction

The aerodynamic analysis of the Entomopter for the Mars exploration should be able to take into account the complete mission profile of Entomopter in the Mars environment. The optimal design should satisfy the lift and thrust requirements over the entire flight regime. In order to assess the performance of an Entomopter designed for Mars, it must first be proved that flapping wing chosen for its low speed flight capability, provides enough lift and thrust to make the Entomopter fly robustly. This requires an analytical model that gives satisfactory estimates for lift and thrust values for different flight conditions. The mission includes different phases of flight (takeoff, steady level flight, turning performance, maneuvers, and landing) that must be analyzed in depth for if accurate performance predictions are to be obtained. As a first step, only steady level flight has been considered, because that constitutes the major part of the mission. Another important requirement is the validation of the analytical results against corroborating results derived from CFD and ultimately experimental tests in a wind tunnel.

Even though flapping wing flight is the major mode of locomotion used by birds and insects, no analytical model available has so far has been able to estimate the true performance of birds and insects. Many have studied flapping wing locomotion, but the complex modes of flight in nature still need to be addressed in much more detail and it will be some time before these complex motions and phenomena are completely understood. Based on prior work conducted by different researchers in this area, and taking into account the peculiar design of Entomopter, a physics

based model was created, which though approximate, can predict the actual performance of the Entomopter over a reasonable range. These results will ultimately be validated by experimental work.

3.3.3.2 Different Approaches

Various approaches were considered which could help formulate an aerodynamic model for analysis and design of Entomopter. The following summarize a number of these.

3.3.3.2.1 Historical Database

The simplest approach was to take the past results presented by different researchers and transform those results to create an empirical model by linear regression of statistical data. Most of the research on the kinetics of birds has been performed by biologists. The research performed by C.P. Ellington [77] reveals that a Hawk Moth wing (similar planform used by the Entomopter) produces the following values for coefficients of lift and drag for different the angles of attack as shown in Figure 3-108.

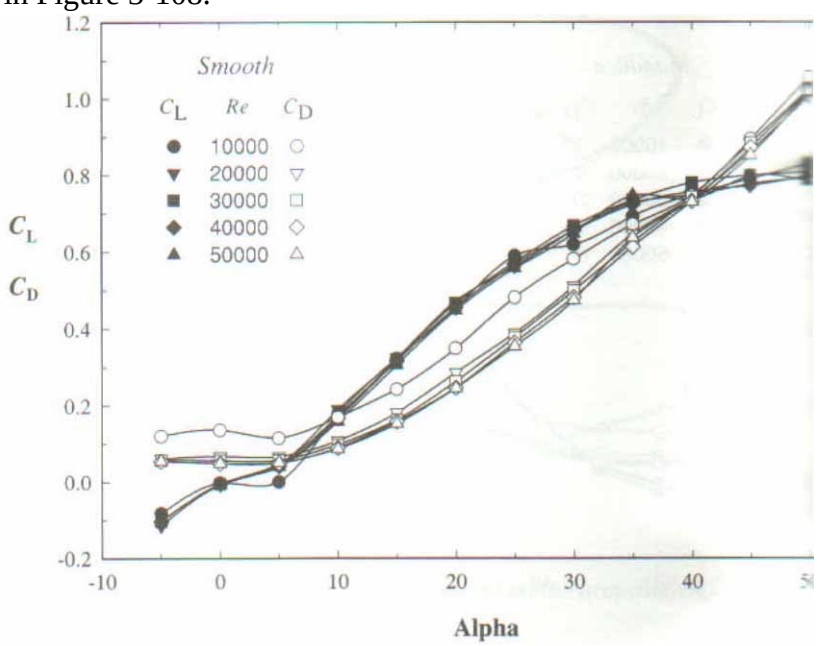

Figure 3-108: Hawk Moth Lift and Drag vs. Angle of Attack

Since kinematically correct flapping mimicking that of the Hawk Moth is not practical in a manufacturable vehicle, the flapping mode needs to be augmented with some other technology in order to extract the same amount of lift and thrust. Furthermore, these values of lift coefficient meet the requirement for flight on Earth, but are not sufficient for flight on Mars. Hence, one is faced with a challenge to find another contributor to lift along with flapping. One way to achieve the required values of lift is optimization of aerodynamic parameters. As per [149], the airfoil shape can be optimized for low Reynolds number flight. This can be as effective as increasing the lift coefficient by 50% in the case of conven-

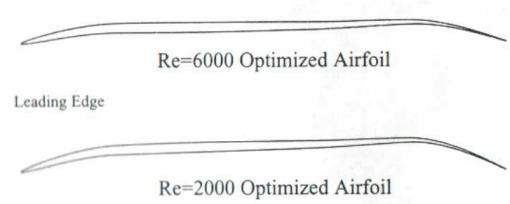

Figure 3-109: Typical Low Reynolds Number Airfoil

tional fixed wing flight. Similar advantage can be extracted in the case of flapping wing flight. The optimum airfoil suggested for low Reynolds number flight should have maximum camber and minimum thickness. Some of the suggested airfoils are shown in Figure 3-109. The pressure distribution on an optimized airfoil as compared to a conventional airfoil is shown in Figure 3-110.

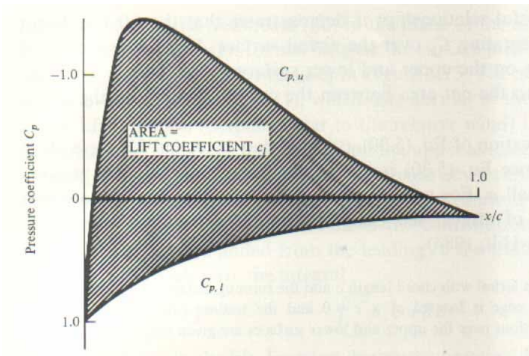

Conventional

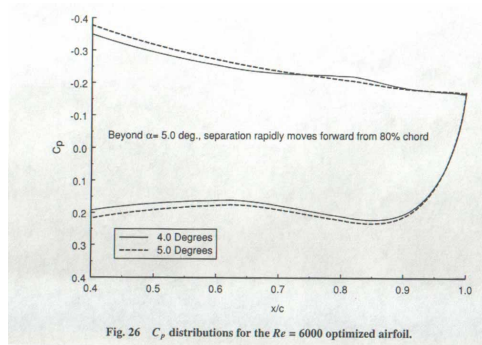

Optimum

Figure 3-110: Pressure Distribution for an Optimized Airfoil vs. That of a Conventional Airfoil

However, with regard to the requirements of the Mars environment, this optimal airfoil shape in a flapping mode would still not be able to sustain steady flight as the lift coefficient values required for Mars are much higher than those in the Earth's atmosphere. To achieve efficient and controllable Mars flight at slow speeds, it was decided that active flow control of the airfoils would be used along with flapping to increase the lift values. This will be discussed in more detail below.

After taking into consideration the lift requirement, another important aspect is the minimum value of thrust required for forward flight. In fact, in flapping motion, the resultant force produced has two components: lift and thrust, which should as a minimum, equal the weight and drag respectively for a steady flight. Unlike the conventional fixed wing airplane, where thrust is provided by engines, the sole contributor of thrust is the flapping motion. Many researchers in the past have addressed the thrust produced as a result of flapping. Kevin D. Jones has provided some experimental data for thrust produced by flapping motion of a 15 cm micro air vehicle in Earth's atmosphere [133]. His experimental model used is shown below as Figure 3-111. The experimental results are not generic and are only true for the current point solution problem, but can be extrapolated in the close vicinity of design points for thrust predictions. The model is fully capable of generating sufficient thrust to overcome drag values and produce forward flight for flapping frequencies of more than 25 Hz. Although the experimental data is only available for lower flapping frequencies (less than 12 Hz), values predicted by panel methods and CFD analysis can be taken for the purpose of estimation.

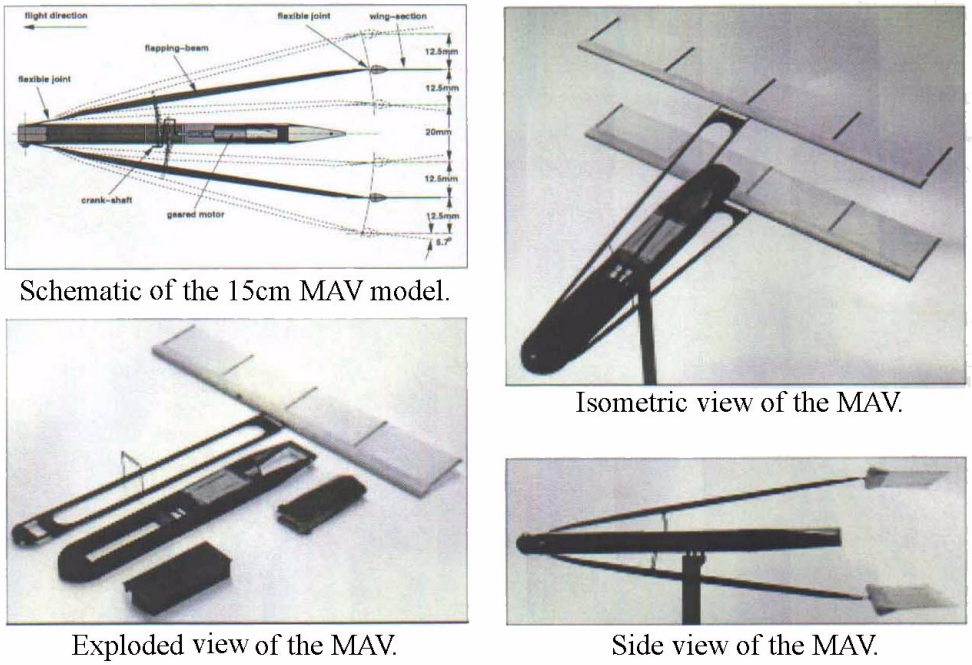

Schematic of the 15cm MAV model.

Isometric view of the MAV.

Exploded view of the MAV.

Side view of the MAV.

Figure 3-111: Flapping Wing Micro Air Vehicle Test Model

The equations of motion have been derived from the schematic given in Figure 3-112.

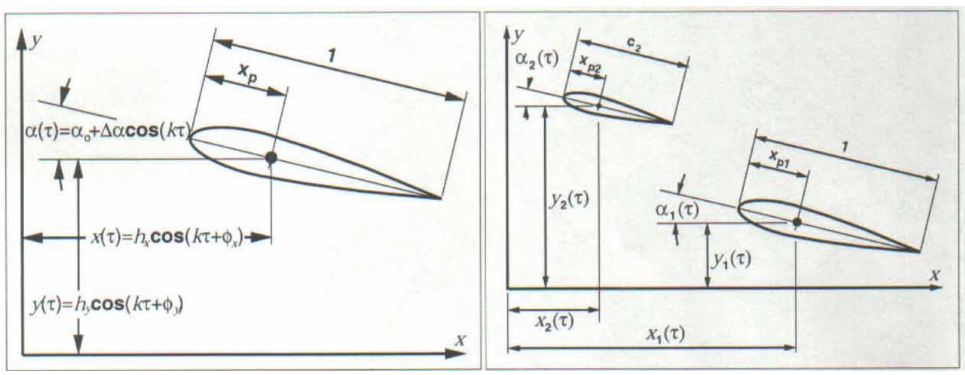

Figure 3-112: Parameter Definitions for the Jones Model

For the purpose of analysis, Dr. Jones has selected different combinations of airfoils, and then studied their combined effects. These studied combinations are given in Figure 3-113.

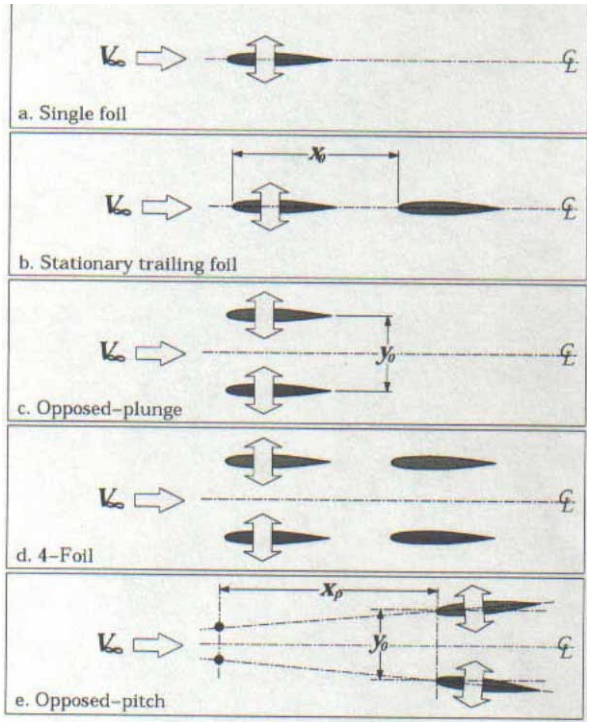

Figure 3-113: Flapping Airfoil Combinations

The values of thrust coefficient obtained from experimental results and those predicted by CFD are given in Figure 3-114.

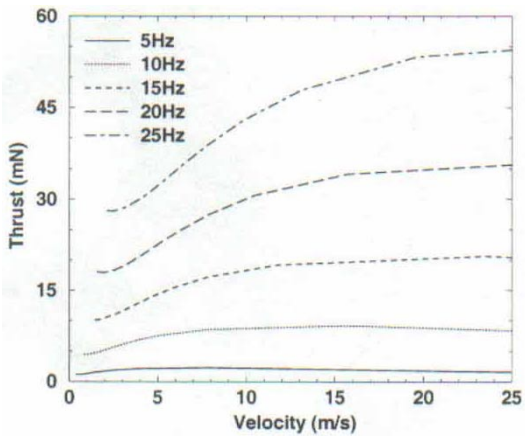

Panel-code predictions for MAV

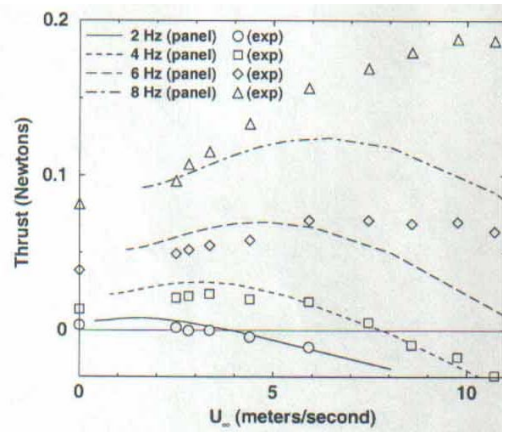

Thrust for pitch/plunge motion of (c)

Figure 3-114: CFD and Empirical Thrust Coefficient Results for the Jones Model

The results indicate that flapping flight is capable of producing values of lift and thrust required for a steady forward flight. But the values given above are the net average values of thrust and lift produced in a cycle. However, for true prediction, flapping needs to be considered as an

unsteady phenomenon, and the forces will vary at every point in a flapping cycle. The thrust and lift values will vary all along the flapping cycle, and time dependant results must be calculated. Furthermore, these results of past research can only act as a guideline, but in no way can be used to predict the result for Entomopter due to its peculiar design and environment.

3.3.3.2.2 Experimental/Computational Results

Since the historical data cannot be used directly for the Entomopter, the best approach for prediction of results could be obtained from CFD simulations or physical experiments for different configurations within the design space, and then extrapolate these results for Mars Environment. For this approach, complete design space exploration would require a huge array of experiments or CFD runs. A "design-of-experiments" could be performed within the reasonable ranges of design characteristics/variables to limit the number of experiments/runs required, but this would still require many experiments in wind tunnel or an enormous CFD effort which was not achievable within the scope of this NIAC Phase II study. However, a limited amount of CFD effort was used for this project which can only serve to validate the analytical model, but in no way was sufficient to help create an empirical model by itself.

3.3.3.2.3 Physics-based Model

Lifting line theory by Prandtl and boundary layer theory explain the physics of conventional fixed wing flight, and Navier Stokes equations explain the balance of aerodynamic forces. But these models cannot be directly applied to flapping wing flight, due to the peculiarities of flapping aerodynamics which remain unaccounted for in fixed wing models. It is pertinent to note that when relying only upon the principles of conventional fixed wing aerodynamics, an insect cannot produce sufficient lift to support its weight in Earth's atmosphere, despite using three degrees of freedom in flight. Hence, an endeavor was made to comprehend the peculiarities of low Reynolds number flapping wing flight. The following flapping wing peculiarities have been observed by many researchers, notably C.P Ellington of Cambridge University (who was part of the original GTRI-DARPA Entomopter team) [77]:

- Formation of a Leading Edge Vortex (LEV)
- Unsteady flow
- Deviation from normal boundary layer theory at much lower angles of attack
- Separation and Wake deformations

Mainly, the leading edge vortex is responsible for much higher lift values and cannot be accommodated in the domain of conventional aerodynamics. No parametric definition for these leading edge vortices exists and just the flow visualizations and experimental data by research for different point solutions is available- but that does not provide any deep insight to these lift generating phenomenon. Figures 3-115 and 3-116 given below illustrates the formation of leading edge vortices for flapping wings.

.

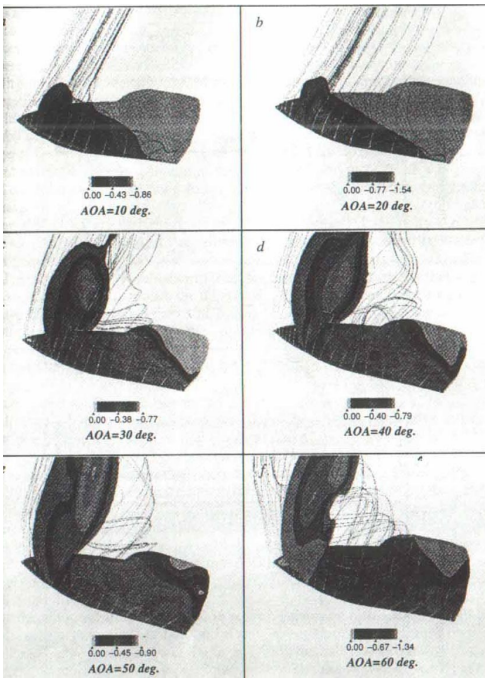

Figure 3-115: LEV Formation (View 1)

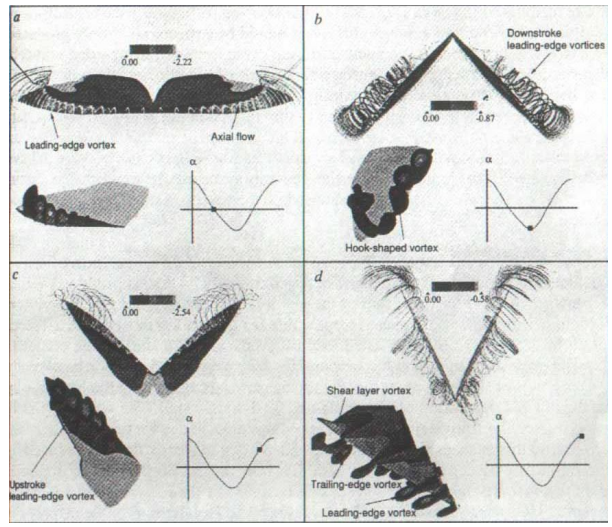

Figure 3-116: LEV Formation (View 2)

The wake deformations also play a major role in thrust characteristics of the vehicle at these low Reynolds numbers. Many researchers have tried to visualize the flow patterns of these wakes and have suggested that these tend to augment the thrust tremendously. These unsteady wakes also cannot be modeled using the conventional fixed wing aerodynamics.

Another approach is to model flapping wing as a propeller as suggested by Theodore Theoderson [255]. Azuma [12] has also used this approach to predict flapping wing performance. Rotorcraft aerodynamics has different approaches for computation of forces, which are as follows:

3.3.3.2.4 Momentum Theory

This is a very basic back-of-the-envelope type calculation approach which considers the propeller or rotor as a rotating disc and then computes forces based on mass and momentum conservation. This cannot be used as for case of flapping because the wing is not covering the entire 360° or 2π radians, and also direction of rotation is changing twice within each cycle during the upbeat and downbeat.

3.3.3.2.5 Blade Element Theory

This approach divides each propeller blade into different equal-length small strips/segments and then each strip/segment is analyzed separately taking into account the incoming flow velocity as well as angular velocity. The forces on the entire blade are then computed by summation of forces on all the segments. This approach considers the effective angle of attack at different segments, but still assumes a uniform inflow. This model has been modified to account for the non uniform flow by blade element momentum theory. Still these models do not consider the leading

edge vortices, which contribute significantly to the forces in the case of flapping wing flight. Hence, blade element theory also cannot be used.

3.3.3.2.6 Vortex Theory

This approach is probably the most applicable for use with the flapping wing, but here again no physics based modeling for vorticity and wakes exist, and empirical data provided by Robin Gray, Landgrebe in accordance with the Biot Savart Law and the Kutta Jowkousky Theorem is the basis for implementation of this model. The data on free wake modeling is all experimental and is specific to the point solutions by different researchers. Hence, here again experimental data is required for the case of Entomopter. Also, this model only considers the trailing edge vortices (mainly strong tip vortices), but leading edge vortex is still not included in this model.

3.3.3.2.7 Aeroelasticity Theory

Finally, the theory of aeroelasticity was considered to model the flapping wing aerodynamics. Most of the researchers in the past have used this theory to predict the flapping wing performance. Mainly Theodore Theoderson [254] has given closed form time-dependant expressions for two dimensional flat plate lift and moment. I. E. Garrick [99] has given a closed form expression based on the Theoderson work for average thrust computation, and Azuma [255] has given closed form time dependant expression for lift, moment, thrust and power based on this theory. The theory mainly addresses the mechanism of flutter instability and is used to find the structural deformations and loads in conventional fixed wing flight. Even though the aeroelastic deformations are generally smaller in nature under normal aerodynamic loads, this theory provides reasonable estimates for larger deformations as suggested by above referenced researchers. This theory takes into account four degrees of freedom, which are as follows:

1. Flapping or bending
2. Pitching or torsion
3. Aileron deflection
4. Tab deflection

For the Entomopter we need only consider two degrees of freedom: flapping and pitching. This approach takes into account the trailing edge vortices and forces produced by flapping and pitching in time domain, but still falls short of taking into account the strong leading edge vortex effect. Also, this approach can only calculate forces in two dimensions and also does not depend on the airfoil shape, instead assuming a thin flat plate. So, this model needs to be modified to account for three dimensional finite wing effects. Many researchers in the past have tried to arrest the finite wing effects based on this model, and more than twenty treatments exist for the same. Some have given solutions for an elliptic wing, while others have assumed a uniform rectangular wing. The treatment given by Eric Reissner [222] is geared toward a variable planform shape and can help simulate the wing of Entomopter. This approach was selected to create an analytical model for Entomopter.

3.3.3.3 Basic Methodology

The aerodynamic model proposed by Theodore Theoderson and I. E. Garrick for flutter analysis (aeroelasticity) was taken as the baseline model [254]. But this model is only applicable for two dimensional analysis, hence the three dimensional planform effects of the Entomopter will be

superimposed onto the model proposed by Eric Reissner [222]. Since the model proposed by Theoderson involves a harmonic motion analysis with real and imaginary parts, it was decided that motion in two degrees of freedom would be modeled as real parts and equations provided by Azuma [12] would be used. The formulation was initially done for a baseline configuration, and once the model was formulated and validated by CFD results, the analytical model was used to explore the design space based on a parametric analysis.

This model does not account for the airfoil shape, instead being considered as a thin flat plate, which is close to the actual case as the proposed wing design is very thin, however, camber effects are also not taken into account. The three dimensional effects for wing planform shape, sweep, and change of chord length with span is modeled in terms of correction factors for both flapping and pitch motion. These correction factors are then added to the results of the two dimensional model to complete the analysis.

Having considered the nature of the modeling, the next step was to select the engineering metrics which should comprise evaluation criteria for analysis and design. Basically lift and thrust are the main factors, and the net lift should be able to support the weight of the vehicle and net thrust should provide the forward flight capability. In addition to these two, the moment and power required are the other key metrics. All these things in non dimensional form for their respective coefficients were selected as the key responses, in order to assess the flight worthiness of the flapping wing Entomopter on Mars.

After having selected the key responses, the next step is selection of key variables that are sensitive to the variability of these responses. The variables are:

- Wing span
- Chord length
- Flapping frequency in Hertz
- Flapping amplitude
- Pivot location from leading edge
- Angle of attack
- Pitch amplitude
- Phase between pitch and plunge
- Free stream density
- Free stream velocity
- Free stream kinematic viscosity

The model is unsteady and the responses are varying within each time period of motion, however, motion is harmonic and is the same for each time period. To simplify the model, flow is assumed inviscid, thereby eliminating the viscosity variable. Also the density of Mars lower atmosphere is assumed constant for nap-of-the-planet flight.

3.3.3.4 Detailed Aerodynamic Analysis

The problem of determining the aerodynamic forces on an airfoil moving in simple harmonic motion about an equilibrium position is very detailed, and is fully derived in Reference [254]. At this point, a qualitative explanation of basic concepts is attempted.

Consider the forces acting on a thin airfoil, of infinite aspect ratio, moving with constant velocity in a perfect fluid and with constant angle of attack. From elementary aerodynamics it is deduced that the net forces acting on such an airfoil are those associated with the circulation of the fluid around the airfoil. The circulation for the steady state condition is proportional to the velocity, angle of attack, and chord length.

However, for the case of unsteady motion the lift on the airfoil section is no longer a simple function of the circulation. For one thing, it can be easily shown that any plate accelerated in a fluid exerts forces and moments even in the absence of circulation. Thus, even at zero forward velocity for an airfoil performing simple harmonic motion, the fluid will exert forces and moments on the airfoil section due to the acceleration and deceleration of the fluid moving with the airfoil. These can be considered aerodynamic inertia forces. A second important contribution to the lift for the case of unsteady motion is known as the quasi steady lift. This is the lift which would be produced by the motion of the airfoil if the circulation pattern behind it (i.e., the wake) had no effect. It represents the force that would be produced if the instantaneous velocity and angle of attack of the airfoil were permanently maintained. The lift can then be considered to vary and to be a function of the instantaneous configuration of the system.

In general, every change of the state of motion of the airfoil is accompanied by a change in circulation around it. Furthermore, every change in circulation about an airfoil section is accompanied by a vortex shed from the trailing edge of the airfoil. For the change of a continuously changing circulation, such as for a simple harmonic motion, a continuous band of shed vortices develop behind the airfoil section. These shed vortices (or the vortex sheet) produce vertical velocities in the neighborhood of the airfoil. The periodic force is a function of this vortex sheet, the distributed vortex strength of which is another periodic function in terms of reduced frequency parameter (k). This will be explained in more detail below.

Thus from the qualitative discussion above, it can be deduced that lift on a flapping airfoil is a function of free stream velocity and periodic functions of plunge and pitching motion. Now after having discussed the problem qualitatively, the different assumptions made to simplify the model and equations formulated as a result of this analytical model, will be explained. This will be followed by the results thus obtained.

3.3.3.5 Assumptions

1. The flow is assumed to be by a perfect gas, which behaves in accordance with a perfect gas law, with constant specific heat values over a reasonable range of temperature and pressure.
2. No friction is considered internally or externally; so for the required power analysis, a factor must be added to account for frictional losses.
3. Irrotational flow such that all fluid particles have zero angular momentum about the center of gravity axis.
4. The basic model only encompasses the two dimensional airfoil effects with infinite span. This will be modified to include the three dimensional finite span effects and planform shape by inclusion of Reissner's correction factors.
5. The model is based on non stationery potential flow theory, and no deviations from potential flow are being considered.

6. Actual deformations which could develop as a result of aerodynamic loads are not considered.

3.3.3.6 Coordinate System

The coordinate system defined for the formulation is shown below in Figure 3-117.

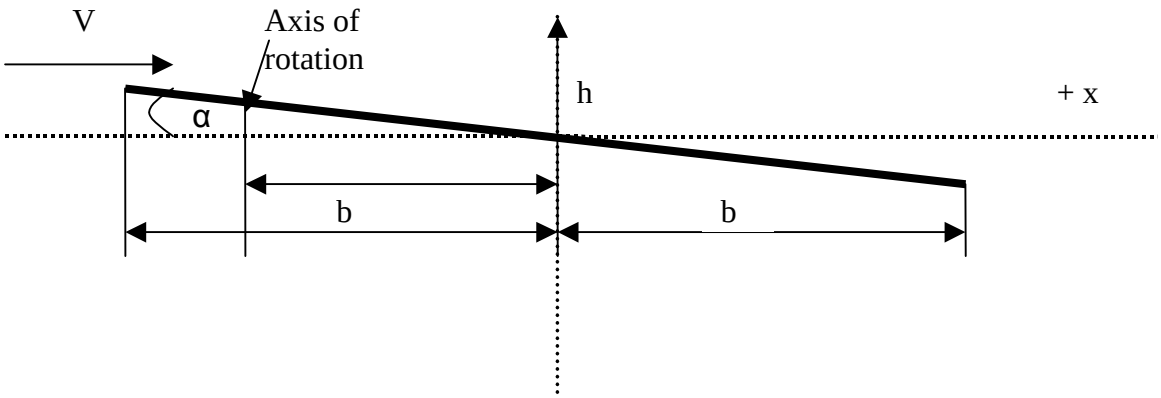

Figure 3-117: Thin Flat Plate Airfoil

h = vertical coordinate at zero center of airfoil, considered positive downwards
α = angle of attack, considered positive right hand clockwise
V = wind velocity positive towards right
a = axis of rotation from center of airfoil (dimensionless, with reference to semichord b
b = semichord = chord/2

Leading edge and trailing edge also normalized at +1 and -1 respectively.

Table 3-8: List of Symbols

Span = Span of the entire wing (both sides), in ft
V = velocity of air in ft/sec
freq = Flapping frequency in Hertz
Plamp = Flapping amplitude in degrees
Pitamp = Pitch amplitude in degrees
sspan = semi span (half span)
a = axis of rotation fixed at -0.25
ω = angular velocity in radians/sec
hamp = Flapping amplitude in ft, based on span
α**amp** = Pitching amplitude in radians
t = time within the cycle, a cycle has been divided into 100 equal parts, and **t** varies as a function of frequency

Table 3-8: List of Symbols (Continued)

h(t) = Instantaneous flapping height, or plunge as a function of time. It is defined as a cosine wave function of angular velocity and time, with h0x as the intercept, h1x as the coefficient of cosine function and ωhx as phase angle. x corresponds to different phases in the cycle. This has been explained in the model formulation.
α(t) = Instantaneous pitch angle, it is defined on the same lines as h(t)
ϕ = span location, span has been divided into 20 sub parts.
b(ϕ) = semichord as a function of span location ϕ
rchord = chord at semi span = root chord
U(ϕ) = Effective velocity at a span location ϕ (Euclidean of V, and angular velocity)
b1(ϕ) = semichord normalized by semi root chord
xt(ϕ) = location of trailing edge at span location ϕ
xl(ϕ) = location of leading edge at span location ϕ
k(ϕ) = Reduced Frequency at span location ϕ
zm(ϕ) = dimensionless coordinate of midchord line
k0 = reduced frequency at semispan
s = ratio of semispan to rootchord
F(ϕ) = Real part of Theoderson Lift Deficiency Factor as a function of reduced frequency at span location ϕ. It is a combination of first and second kind of Bessel functions of first and second order. J and Y represent Bessel function of first and second kind.
G(ϕ) = Imaginary part of Theoderson Lift Deficiency Factor as a function of reduced frequency at span location ϕ.
C(ϕ) = Theoderson Lift Deficiency factor
μ(ϕ) = Function of Bessel Functions
Ωh2(ϕ) = Amplitude of two dimensional circulation function due to flapping
Ωα2(ϕ) = Amplitude of two dimensional circulation function due to pitching
Ωη(ϕ) = Amplitude of three dimensional circulation function due to flapping
Ωα(ϕ) = Amplitude of three dimensional circulation function due to pitching
σh(ϕ) = Finite span and planform correction factor for flapping
σα(ϕ) = Finite span and planform correction factor for pitching
Ctxxx, Clxxx, Cmxxx, Cpxxx = Different coefficients used to simplify the solution of equations for coefficients of thrust, lift moment, and power calculation respectively [12]
ψθh(ϕ) = Phase angle between pitching and flapping.
Ct = Coefficeint of Thrust
C_L = Coefficient of Lift

Table 3-8: List of Symbols (Continued)

Cm = Coefficient of Moment
Cp = Coefficient of Power Required.

3.3.3.7 Model Formulation for Baseline Case

It was assumed that the planform shape of the Entomopter wing is fixed in three dimensions and for parametric analysis, as we change the span of the wing, the chord length will vary all along the wing, so the shape of the planform is just defined by one parameter: span. Also it is assumed that the axis of rotation ("a") is constant. Hence, the total number of variables considered reduce to five: span, velocity, flapping frequency, flapping amplitude, and pitch amplitude. A cycle is defined as one complete upbeat and one downbeat, starting with h = 0 at t = 0, and then it moves (upwards) to -hamp at 1/4 time period, and then starts the down beat, continuing until the 3/4 time period. In the final 1/4 time period, it comes back to the zero position. The angle of attack stays constant during the upbeat and downbeat and it flips during the 1/20th portion of time period at the extremes of the upbeat and down beat. A computer code was written in Mathcad 2000 to evaluate these results. The values and equations used for baseline case are as follows: (NOTE: the notation used below ":=" means "defined as".)

$V := 14 \quad freq := 16 \quad Plamp := 75 \quad Pitamp := 8$

$$sspan := \frac{span}{2}$$

$$a := -0.25$$

$$\omega := 4 \cdot freq \cdot Plamp \cdot \frac{\pi}{180}$$

$$hamp := sspan \cdot \sin\left(Plamp \cdot \frac{\pi}{180}\right)$$

$$\alpha amp := Pitamp \cdot \frac{\pi}{180}$$

$$t := \frac{0}{100 \cdot freq}, \frac{1}{100 \cdot freq} .. \frac{1}{freq}$$

Since the instantaneous flapping height changes linearly, it was decided that different coefficients would be calculated for the first quarter cycle, then from 1/4 until 3/4 and finally for the last quarter of the cycle. This will give close to linear change effects. A similar approach was adopted for pitching motion coefficients and different coefficients were evaluated for flipping from positive to negative and vice versa. These coefficients were determined by solving a system of nonlinear simultaneous equations.

$$h01 + h11 \cdot \cos(\phi h1) = 0$$

$$h01 + h11 \cdot \cos\left(\frac{\omega}{8 \cdot freq} + \phi h1\right) = \frac{-hamp}{2}$$

$$h01 + h11 \cdot \cos\left(\frac{\omega}{4 \cdot freq} + \phi h1\right) = -hamp$$

$$Coeff1 := Find(h11, \phi h1, h01)$$

$$h02 + h12 \cdot \cos\left(\frac{\omega}{4 \cdot freq} + \phi h2\right) = -hamp$$

$$h02 + h12 \cdot \cos\left(\frac{\omega}{2 \cdot freq} + \phi h2\right) = 0$$

$$h02 + h12 \cdot \cos\left(\frac{3 \cdot \omega}{4 \cdot freq} + \phi h2\right) = hamp$$

$$Coeff2 := Find(h12, \phi h2, h02)$$

$$h03 + h13 \cdot \cos\left(\frac{3 \cdot \omega}{4 \cdot freq} + \phi h3\right) = hamp$$

$$h03 + h13 \cdot \cos\left(\frac{7 \cdot \omega}{8 \cdot freq} + \phi h3\right) = \frac{hamp}{2}$$

$$h03 + h13 \cdot \cos\left(\frac{\omega}{freq} + \phi h3\right) = 0$$

$$Coeff5 := Find(h13, \phi h3, h03)$$

$$h0(t) := if\left(t \le \frac{1}{4 \cdot freq}, Coeff1_2, if\left(t > \frac{1}{4 \cdot freq} \wedge t \le \frac{3}{4 \cdot freq}, Coeff2_2, Coeff5_2\right)\right)$$

$$h1(t) := if\left(t \le \frac{1}{4 \cdot freq}, Coeff1_0, if\left(t > \frac{1}{4 \cdot freq} \wedge t \le \frac{3}{4 \cdot freq}, Coeff2_0, Coeff5_0\right)\right)$$

$$\phi h(t) := if\left(t \le \frac{1}{4 \cdot freq}, Coeff1_1, if\left(t > \frac{1}{4 \cdot freq} \wedge t \le \frac{3}{4 \cdot freq}, Coeff2_1, Coeff5_1\right)\right)$$

$$h(t) := h0(t) + h1(t) \cdot \cos(\omega \cdot t + \phi h(t))$$

The flapping motion produced is shown in Figure 3-118.

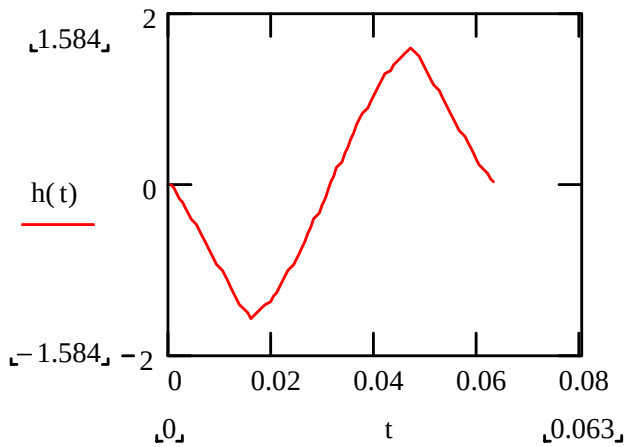

Figure 3-118: Flapping Motion

$$\alpha 01 + \alpha 11 \cdot \cos\left(\frac{\omega}{4 \cdot freq} + \phi\alpha 1\right) = \alpha amp$$

$$\alpha 01 + \alpha 11 \cdot \cos\left(\omega \cdot \frac{30}{100 \cdot freq} + \phi\alpha 1\right) = -\alpha amp$$

$$\alpha 01 + \alpha 11 \cdot \cos\left(\frac{\omega \cdot 27.5}{100 \cdot freq} + \phi\alpha 1\right) = 0$$

$$Coeff3 := Find(\alpha 11, \phi\alpha 1, \alpha 01)$$

$$\alpha 12 \cdot \cos\left(\frac{\omega \cdot 3}{4 \cdot freq} + \phi\alpha 2\right) = -\alpha amp$$

$$\alpha 12 \cdot \cos\left(\frac{\omega \cdot 80}{freq \cdot 100} + \phi\alpha 2\right) = \alpha amp$$

$$Coeff4 := Find(\alpha 12, \phi\alpha 2)$$

$$\alpha 1(t) := if\left(t \le \frac{1}{4 \cdot freq}, 0, if\left(t > \frac{1}{4 \cdot freq} \wedge t \le \frac{30}{100 \cdot freq}, Coeff3_0, if\left(t > \frac{30}{100 \cdot freq} \wedge t \le \frac{75}{100 \cdot freq}, 0, if\left(t > \frac{75}{100 \cdot freq} \wedge t \le \frac{80}{100 \cdot freq}, Coeff4_0, 0\right)\right)\right)\right)$$

$$\alpha 0(t) := if\left(t \le \frac{1}{4 \cdot freq}, \alpha amp, if\left(t > \frac{1}{4 \cdot freq} \wedge t \le \frac{30}{100 \cdot freq}, 0, if\left(t > \frac{30}{100 \cdot freq} \wedge t \le \frac{75}{100 \cdot freq}, -\alpha amp, if\left(t > \frac{75}{100 \cdot freq} \wedge t \le \frac{80}{100 \cdot freq}, 0, \alpha amp\right)\right)\right)\right)$$

$$\phi\alpha(t) := \text{if}\left(t \le \frac{1}{4\cdot freq}, 0, \text{if}\left(t > \frac{1}{4\cdot freq} \wedge t \le \frac{30}{100\cdot freq}, Coeff3_1, \text{if}\left(t > \frac{30}{100\cdot freq} \wedge t \le \frac{75}{100\cdot freq}, 0, \text{if}\left(t > \frac{75}{100\cdot freq} \wedge t \le \frac{80}{100\cdot freq}, Coeff4_1, 0\right)\right)\right)\right)$$

$$\alpha(t) := \alpha0(t) + \alpha1(t)\cdot\cos(\omega\cdot t + \phi\alpha(t))$$

The pitching motion produced is shown in Figure 3-119.

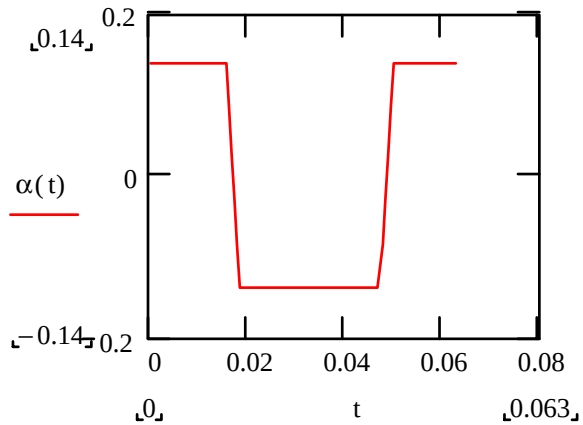

Figure 3-119: Pitching Motion

The planform shape of Entomopter wing was defined as a five-degree polynomial to evaluate chord in terms of span location, similarly five degree polynomials were formulated for leading edge and trailing edge locations. Chord as a function of span location is shown in Figure 3-120.

$$\phi := acos(0), acos(0.05) .. acos(1.0)$$

$$b(\phi) := \begin{bmatrix} 6.9105\cdot(\cos(\phi))^5 - 19.883\cdot(\cos(\phi))^4 \ldots \\ +21.551\cdot(\cos(\phi))^3 - 11.177\cdot(\cos(\phi))^2 + 2.3791\cdot(\cos(\phi)) + 0.3395 \end{bmatrix}\cdot\frac{sspan}{2}$$

$$U(\phi) := \sqrt{V^2 + (\cos(\phi)\cdot\omega\cdot sspan)^2}$$

rchord = 0.339 • sspan

$$b1(\phi) := \frac{2\cdot b(\phi)}{rchord}$$

$$xt(\phi) := \begin{pmatrix} 1.9534\cdot\cos(\phi)^5 - 7.7057\cdot\cos(\phi)^4 \ldots \\ +11.407\cdot\cos(\phi)^3 - 7.7318\cdot\cos(\phi)^2 + 1.9612\cdot\cos(\phi) + 0.1714 \end{pmatrix}\cdot sspan$$

$$xl(\phi) := \left(\begin{array}{l} 5.2883 \cdot \cos(\phi)^6 - 13.172 \cdot \cos(\phi)^5 \ldots \\ + 11.387 \cdot \cos(\phi)^4 - 4.248 \cdot \cos(\phi)^3 + 0.6663 \cdot \cos(\phi)^2 - 0.0336 \cdot \cos(\phi) + 0.1698 \end{array} \right) \cdot sspan$$

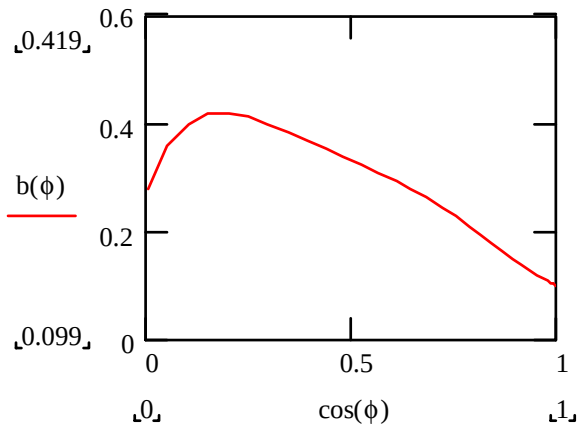

Figure 3-120: Chord vs. Span Location

$$k(\phi) := b(\phi) \cdot \frac{\omega}{U(\phi)}$$

$$zm(\phi) := \frac{xl(\phi) + xt(\phi)}{2 \cdot b(\phi)}$$

$$k0 := rchord \cdot \frac{\omega}{2 \cdot U(acos(0.5))}$$

$$km(\phi) := k0 \cdot zm(\phi)$$

$$s := \frac{sspan}{rchord}$$

$$F(\phi) := \frac{J1(k(\phi)) \cdot (J1(k(\phi)) - Y0(k(\phi))) + Y1(k(\phi)) \cdot (Y1(k(\phi)) - J0(k(\phi)))}{(J1(k(\phi)) + Y0(k(\phi)))^2 + (Y1(k(\phi)) - J0(k(\phi)))^2}$$

$$G(\phi) := \frac{Y1(k(\phi)) \cdot Y0(k(\phi)) + J1(k(\phi)) \cdot J0(k(\phi))}{(J1(k(\phi)) + Y0(k(\phi)))^2 + (Y1(k(\phi)) - J0(k(\phi)))^2}$$

$$C(\phi) := \frac{J1(k(\phi)) \cdot (J1(k(\phi)) - Y0(k(\phi))) + Y1(k(\phi)) \cdot (Y1(k(\phi)) - J0(k(\phi)))}{(J1(k(\phi)) + Y0(k(\phi)))^2 + (Y1(k(\phi)) - J0(k(\phi)))^2} \ldots$$
$$+ 1i \cdot \frac{Y1(k(\phi)) \cdot Y0(k(\phi)) + J1(k(\phi)) \cdot J0(k(\phi))}{(J1(k(\phi)) + Y0(k(\phi)))^2 + (Y1(k(\phi)) - J0(k(\phi)))^2}$$

For determination of finite wing correction factors, the following methodology is adopted:

a. Choose span locations where the correction factors and amplitude of the three dimensional circulation function is to be determined. This span has been divided into twenty one segments in units of semispan.

   Cos(ϕ) = 0, 0.05, 0.10, ……, 1.0

b. Calculate values of normalized chord lengths, reduced frequencies, at these stations, and then calculate the two dimensional circulation function at these span locations.
c. Calculate the coefficients A(n,ϕ), where n is like the harmonic number. Note that if the wing flapping is symmetrical about the midspan, only odd values of n occur, while for the asymmetrical case, even values of n will occur. Our case is symmetric, so odd values of n have been taken as 1,3,5,7,9.
d. Solve the system of equations with complex coefficients to find Knj. Since there are twenty span locations, and only five Knj values need to be found, only five span locations will be used. This procedure has been solved by using Crout's Method for solution of equations with complex numbers.
e. Calculate the values of the three dimensional circulation function at all span locations.
f. Calculate the values of correction factors for flapping and pitching.
g. Add the real part of the correction term to F(ϕ) and imaginary part to G(ϕ) to get the solution with finite span and planform correction
h. To get the total forces on the wing, the forces of all segments (span locations) must be integrated and then divided by span. The solution obtained is asymptotic near the wing root, so an assumption has been made based on propeller theory that the force coefficients at the 75% span location are representative of the entire wing.

$$\mu(\phi) := \frac{J0(k(\phi)) - 1i \cdot J1(k(\phi))}{\pi \cdot k(\phi) \cdot \left[(J0(k(\phi)) - Y1(k(\phi))) - 1i \cdot (J1(k(\phi)) + Y0(k(\phi))) \right]}$$

$$\Omega h2(\phi) := \frac{4 \cdot 1i \cdot C(\phi)}{k(\phi) \cdot (J1(k(\phi)) - Y1(k(\phi)))} \cdot e^{1i \cdot km(\phi)} \cdot 1i \cdot k(\phi) \cdot \cos(\phi) \cdot hamp$$

$$\Omega\alpha 2(\phi) := \frac{4 \cdot 1i \cdot C(\phi)}{k(\phi) \cdot (J1(k(\phi)) - Y1(k(\phi)))} \cdot e^{1i \cdot km(\phi)} \cdot \left[1 + 1i \cdot k(\phi) \cdot \left(\frac{1}{2} - a \right) \right] \cdot b1(\phi) \cdot \alpha amp$$

n = 1,3,5,7,9

$$Sn(n,\phi) := \frac{\sin(n \cdot \phi)}{\sin(\phi)} \ldots + \frac{1i \cdot k0 \cdot s}{\pi} \cdot \int_0^{\pi} \frac{\cos(\phi) - \cos(\theta)}{|\cos(\phi) - \cos(\theta)|} \cdot \left[\begin{array}{l} \left[\begin{array}{l} -\ln(k0 \cdot s \cdot |\cos(\phi) - \cos(\theta)|) - 0.270 \ldots \\ + 0.764 \cdot (k0 \cdot s \cdot |\cos(\phi) - \cos(\theta)|) - 0.129 \cdot (k0 \cdot s \cdot |\cos(\phi) - \cos(\theta)|)^2 \ldots \\ + 0.011 \cdot (k0 \cdot s \cdot |\cos(\phi) - \cos(\theta)|)^3 \end{array} \right] \ldots \\ + 1i \cdot \left[\begin{array}{l} 1.319 - 0.757 \cdot (k0 \cdot s \cdot |\cos(\phi) - \cos(\theta)|) \ldots \\ + 0.202 \cdot (k0 \cdot s \cdot |\cos(\phi) - \cos(\theta)|)^2 - 0.020 \cdot (k0 \cdot s \cdot |\cos(\phi) - \cos(\theta)|)^3 \end{array} \right] \end{array} \right] \cdot \cos(n \cdot \theta)\, d\theta$$

$$A(n,\phi) := \frac{\sin(n \cdot \phi)}{n} + \frac{\pi}{s} \cdot b1(\phi) \cdot \mu(\phi) \cdot Sn(n,\phi)$$

$$Kh1 \cdot A(1,1.369) + Kh3 \cdot A(3,1.369) + Kh5 \cdot A(5,1.369) \ldots = \Omega h2(1.369) + Kh7 \cdot A(7,1.369) + Kh9 \cdot A(9,1.369)$$

$$Kh1 \cdot A(1,1.159) + Kh3 \cdot A(3,1.159) + Kh5 \cdot A(5,1.159) \ldots = \Omega h2(1.159) + Kh7 \cdot A(7,1.159) + Kh9 \cdot A(9,1.159)$$

$$Kh1 \cdot A(1,0.927) + Kh3 \cdot A(3,0.927) + Kh5 \cdot A(5,0.927) \ldots = \Omega h2(0.927) + Kh7 \cdot A(7,0.927) + Kh9 \cdot A(9,0.927)$$

$$Kh1 \cdot A(1,0.644) + Kh3 \cdot A(3,0.644) + Kh5 \cdot A(5,0.644) \ldots = \Omega h2(0.644) + Kh7 \cdot A(7,0.644) + Kh9 \cdot A(9,0.644)$$

$$Kh1 \cdot A(1,0.451) + Kh3 \cdot A(3,0.451) + Kh5 \cdot A(5,0.451) \ldots = \Omega h2(0.451) + Kh7 \cdot A(7,0.451) + Kh9 \cdot A(9,0.451)$$

$$Kh := Find(Kh1, Kh3, Kh5, Kh7, Kh9)$$

$$\Omega h(\phi) := Kh_0 \cdot \sin(\phi) + Kh_1 \cdot \frac{\sin(3 \cdot \phi)}{3} + Kh_2 \cdot \frac{\sin(5 \cdot \phi)}{5} + Kh_3 \cdot \frac{\sin(7 \cdot \phi)}{7} + Kh_4 \cdot \frac{\sin(9 \cdot \phi)}{9}$$

$$K\alpha 1 \cdot A(1,1.369) + K\alpha 3 \cdot A(3,1.369) + K\alpha 5 \cdot A(5,1.369) \ldots = \Omega\alpha 2(1.369) + K\alpha 7 \cdot A(7,1.369) + K\alpha 9 \cdot A(9,1.369)$$

$$K\alpha 1 \cdot A(1, 1.159) + K\alpha 3 \cdot A(3, 1.159) + K\alpha 5 \cdot A(5, 1.159) \ldots = \Omega\alpha 2(1.159) + K\alpha 7 \cdot A(7, 1.159) + K\alpha 9 \cdot A(9, 1.159)$$

$$K\alpha 1 \cdot A(1, 0.927) + K\alpha 3 \cdot A(3, 0.927) + K\alpha 5 \cdot A(5, 0.927) \ldots = \Omega\alpha 2(0.927) + K\alpha 7 \cdot A(7, 0.927) + K\alpha 9 \cdot A(9, 0.927)$$

$$K\alpha 1 \cdot A(1, 0.644) + K\alpha 3 \cdot A(3, 0.644) + K\alpha 5 \cdot A(5, 0.644) \ldots = \Omega\alpha 2(0.644) + K\alpha 7 \cdot A(7, 0.644) + K\alpha 9 \cdot A(9, 0.644)$$

$$K\alpha 1 \cdot A(1, 0.451) + K\alpha 3 \cdot A(3, 0.451) + K\alpha 5 \cdot A(5, 0.451) \ldots = \Omega\alpha 2(0.451) + K\alpha 7 \cdot A(7, 0.451) + K\alpha 9 \cdot A(9, 0.451)$$

$$K\alpha := \mathrm{Find}(K\alpha 1, K\alpha 3, K\alpha 5, K\alpha 7, K\alpha 9)$$

$$\Omega\alpha(\phi) := K\alpha_0 \cdot \sin(\phi) + K\alpha_1 \cdot \frac{\sin(3 \cdot \phi)}{3} + K\alpha_2 \cdot \frac{\sin(5 \cdot \phi)}{5} + K\alpha_3 \cdot \frac{\sin(7 \cdot \phi)}{7} + K\alpha_4 \cdot \frac{\sin(9 \cdot \phi)}{9}$$

$$\sigma h(\phi) := \left(C(\phi) + \frac{1i \cdot J1(k(\phi))}{J0(k(\phi)) - 1i \cdot J1(k(\phi))} \right) \cdot \left(\frac{\Omega h(\phi)}{\Omega h2(\phi)} - 1 \right)$$

$$\sigma\alpha(\phi) := \left(C(\phi) + \frac{1i \cdot J1(k(\phi))}{J0(k(\phi)) - 1i \cdot J1(k(\phi))} \right) \cdot \left(\frac{\Omega\alpha(\phi)}{\Omega\alpha 2(\phi)} - 1 \right)$$

$$Fh(\phi) := F(\phi) + \mathrm{Re}(\sigma h(\phi))$$

$$F\alpha(\phi) := F(\phi) + \mathrm{Re}(\sigma\alpha(\phi))$$

$$Gh(\phi) := G(\phi) + \mathrm{Im}(\sigma h(\phi))$$

$$G\alpha(\phi) := G(\phi) + \mathrm{Im}(\sigma\alpha(\phi))$$

$$Ct\theta 0(\phi) := \pi \cdot \left[F\alpha(\phi) + G\alpha(\phi)^2 - F\alpha(\phi) + k(\phi)^2 \cdot \left(F\alpha(\phi)^2 + G\alpha(\phi)^2 - F\alpha(\phi) + \frac{1}{2} \right) \right]$$

$$Ct\theta\theta c(\phi) := \pi \cdot \left[\begin{array}{l} k(\phi)^2 \cdot \left(G\alpha(\phi)^2 - F\alpha(\phi)^2 + F\alpha(\phi)\right) + F\alpha(\phi)^2 - G\alpha(\phi)^2 - F\alpha(\phi) \ldots \\ + \left[\left(2 \cdot k(\phi) \cdot G\alpha(\phi)\right) \cdot \left(1 - 2 \cdot F\alpha(\phi)\right)\right] \end{array} \right]$$

$$Ct\theta\theta s(\phi) := \pi \cdot \left[\begin{array}{l} G\alpha(\phi) \cdot \left(1 - 2 \cdot F\alpha(\phi)\right) \ldots \\ + k(\phi) \cdot \left(\begin{array}{l} 2 \cdot G\alpha(\phi)^2 - 2 \cdot F\alpha(\phi)^2 \ldots \\ + 2 \cdot F\alpha(\phi) + \frac{1}{2} \end{array} \right) + k(\phi)^2 \cdot G\alpha(\phi) \cdot \left(2 \cdot F\alpha(\phi) - 1\right) \end{array} \right]$$

$$Ct\theta h0(\phi) := 2 \cdot \pi \cdot \sqrt{\left[Gh(\phi) + k(\phi) \cdot \left(2 \cdot Fh(\phi)^2 + 2 \cdot Gh(\phi)^2 - Fh(\phi) + \frac{1}{2}\right)\right]^2 \ldots + \left(2 \cdot Fh(\phi)^2 + 2 \cdot Gh(\phi)^2 - Fh(\phi) - k(\phi) \cdot Gh(\phi)\right)^2}$$

$$Ct\theta hc(\phi) := 2 \cdot \pi \cdot \left[Gh(\phi) \cdot \left(1 - 4 \cdot Fh(\phi)\right) + k(\phi) \cdot \left(2 \cdot Gh(\phi)^2 - 2 \cdot Fh(\phi)^2 + Fh(\phi) + \frac{1}{2}\right)\right]$$

$$Ct\theta hs(\phi) := 2 \cdot \pi \cdot \left[2 \cdot Gh(\phi)^2 - 2 \cdot Fh(\phi)^2 + Fh(\phi) + k(\phi) \cdot Gh(\phi) \cdot \left(4 \cdot Fh(\phi) - 1\right)\right]$$

$$Cthh0(\phi) := 4 \cdot \pi \cdot \left(F\alpha(\phi)^2 - G\alpha(\phi)^2\right)$$

$$Cthhc(\phi) := 4 \cdot \pi \cdot \left(G\alpha(\phi)^2 - F\alpha(\phi)^2\right)$$

$$Cthhs(\phi) := 8 \cdot \pi \cdot F\alpha(\phi) \cdot G\alpha(\phi)$$

$$Ct\theta 0hc(\phi) := 2 \cdot \pi \cdot \left(k(\phi) - 2 \cdot Gh(\phi)\right)$$

$$Ct\theta 0hs(\phi) := -4 \cdot \pi \cdot Fh(\phi)$$

$$\phi h\theta(\phi) := \operatorname{atan}\left[\frac{\left(Fh(\phi) - 2 \cdot Fh(\phi)^2 - 2 \cdot Gh(\phi)^2 + k(\phi) \cdot Gh(\phi)\right)}{Gh(\phi) + k(\phi) \cdot \left(2 \cdot Fh(\phi)^2 + 2 \cdot Gh(\phi)^2 - Fh(\phi) + \frac{1}{2}\right)} \right]$$

$$Cl\theta 0(\phi) := 2 \cdot \pi$$

$$Cl\theta c(\phi) := 2 \cdot \pi \cdot \left[F\alpha(\phi) - k(\phi) \cdot G\alpha(\phi) - \left(\frac{k(\phi)}{2} \right)^2 \right]$$

$$Cl\theta s(\phi) := -2 \cdot \pi \cdot \left(G\alpha(\phi) + k(\phi) \cdot F\alpha(\phi) + \frac{k(\phi)}{2} \right)$$

$$Clhc(\phi) := -2 \cdot \pi \cdot (k(\phi) + 2 \cdot Gh(\phi))$$

$$Clhs(\phi) := -2 \cdot \pi \cdot 2 \cdot Fh(\phi)$$

$$Cm\theta c(\phi) := \frac{3}{16} \cdot \pi \cdot k(\phi)$$

$$Cm\theta s(\phi) := \frac{\pi}{2}$$

$$Cmh(\phi) := k(\phi) \cdot \frac{\pi}{2}$$

$$Cp\theta\theta 0(\phi) := \frac{1}{2} \cdot \pi \cdot k(\phi)^2$$

$$Cp\theta\theta c(\phi) := \frac{-1}{2} \cdot \pi \cdot k(\phi)^2$$

$$Cp\theta\theta s(\phi) := \frac{3}{16} \cdot \pi \cdot k(\phi)^3$$

$$Cp\theta h0(\phi) := 2 \cdot \pi \cdot \sqrt{(-F\alpha(\phi) + k(\phi) \cdot G\alpha(\phi))^2 + \left[G\alpha(\phi) + k(\phi) \cdot \left(F\alpha(\phi) + \frac{1}{2} \right) \right]^2}$$

$$Cp\theta hc(\phi) := -2 \cdot \pi \cdot \left[G\alpha(\phi) + k(\phi) \cdot \left(F\alpha(\phi) + \frac{1}{2} \right) \right]$$

$$Cp\theta hs(\phi) := 2 \cdot \pi \cdot \left[-F\alpha(\phi) + k(\phi) \cdot G\alpha(\phi) + \left(\frac{k(\phi)^2}{2} \right) \right]$$

$$Cphh0(\phi) := 4 \cdot \pi \cdot Fh(\phi)$$

$$Cphhc(\phi) := -4 \cdot \pi \cdot Fh(\phi)$$

$$Cphhs(\phi) := 2 \cdot \pi \cdot (k(\phi) + 2 \cdot Gh(\phi))$$

$$Cp\theta 0hs(\phi) := -4 \cdot \pi$$

$$\psi\theta h(\phi) := \operatorname{atan}\left[\frac{-F\alpha(\phi) + k(\phi) \cdot G\alpha(\phi)}{G\alpha(\phi) + k(\phi) \cdot \left(F\alpha(\phi) + \frac{1}{2} \right)} \right]$$

$$\begin{aligned} Cl(\phi, t) := {} & Cl\theta 0(\phi) \cdot \alpha 0(t) + \left(Cl\theta c(\phi) \cdot \cos(\omega \cdot t + \phi\alpha(t)) + Cl\theta s(\phi) \cdot \sin(\omega \cdot t + \phi\alpha(t)) \right) \cdot \alpha 1(t) \ldots \\ & + \left(Clhc(\phi) \cdot \cos(\omega \cdot t + \phi h(t)) + Clhs(\phi) \cdot \sin(\omega \cdot t + \phi h(t)) \right) \cdot \frac{k(\phi)}{2 \cdot b(\phi)} \cdot h1(t) \end{aligned}$$

$$\begin{aligned} Cm(\phi, t) := {} & \left(Cm\theta c(\phi) \cdot \cos(\omega \cdot t + \phi\alpha(t)) + Cm\theta s(\phi) \cdot \sin(\omega \cdot t + \phi\alpha(t)) \right) \cdot k(\phi) \cdot \alpha 1(t) \ldots \\ & + Cmh(\phi) \cdot \cos(\omega \cdot t + \phi h(t)) \cdot k(\phi) \cdot \frac{h1(t)}{2 \cdot b(\phi)} \end{aligned}$$

$$\begin{aligned} Ct(\phi, t) := {} & \left(Ct\theta\theta 0(\phi) + Ct\theta\theta c(\phi) \cdot \cos(2 \cdot \omega \cdot t + 2 \cdot \phi\alpha(t)) + Ct\theta\theta s(\phi) \cdot \sin(2 \cdot \omega \cdot t + 2 \cdot \phi\alpha(t)) \right) \cdot \alpha 1(t)^2 \ldots \\ & + \left(\begin{array}{l} Ct\theta h0(\phi) \cdot \cos(\phi h(t) - \phi\alpha(t) - \phi h\theta(\phi)) \ldots \\ + Ct\theta hc(\phi) \cdot \cos(2 \cdot \omega \cdot t + \phi\alpha(t) + \phi h(t)) \ldots \\ + Ct\theta hs(\phi) \cdot \sin(2 \cdot \omega \cdot t + \phi\alpha(t) + \phi h(t)) \end{array} \right) \cdot \alpha 0(t) \cdot \left(\frac{k(\phi) \cdot h1(t)}{2 \cdot b(\phi)} \right)^2 \ldots \\ & + \left(Cthh0(\phi) + Cthhc(\phi) \cdot \cos(2 \cdot \omega \cdot t + \phi\alpha(t)) + Cthhs(\phi) \cdot \sin(\omega \cdot t + \phi\alpha(t)) \right) \cdot \alpha 0(t) \cdot \alpha 1(t) \ldots \\ & + \left(Ct\theta 0hc(\phi) \cdot \cos(\omega \cdot t + \phi h(t)) + Ct\theta 0hs(\phi) \cdot \sin(\omega \cdot t + \phi h(t)) \right) \cdot \alpha 0(t) \cdot k(\phi) \cdot \frac{h1(t)}{2 \cdot b(\phi)} \end{aligned}$$

$$
\begin{aligned}
Cp(\phi,t) := & \begin{bmatrix} Cp\theta\theta0(\phi) + Cp\theta\theta c(\phi)\cdot\cos\left[(2)\cdot\omega\cdot t + 2\cdot\phi\alpha(t)\right] \ldots \\ + Cp\theta\theta s(\phi)\cdot\sin\left(2\cdot\omega\cdot t + 2\cdot\phi\alpha(t)\right) \end{bmatrix}\cdot\alpha1(t)^2 \ldots \\
& + \begin{bmatrix} Cp\theta h0(\phi)\cdot\cos\left(\phi h(t) - \phi\alpha(t) - \psi\theta h(\phi)\right) \ldots \\ + \left(Cp\theta hc(\phi)\cdot\cos\left(2\cdot\omega\cdot t + \phi h(t) + \phi\alpha(t)\right)\right) \ldots \\ + Cp\theta hs(\phi)\cdot\sin\left(2\cdot\omega\cdot t + \phi h(t) + \phi\alpha(t)\right) \end{bmatrix}\cdot\alpha1(t)\cdot k(\phi)\cdot\frac{h1(t)}{2\cdot b(\phi)} \ldots \\
& + \begin{bmatrix} Cphh0(\phi) + Cphhc(\phi)\cdot\cos\left(2\cdot\omega\cdot t + \phi h(t)\right) \ldots \\ + \left(Cphhs(\phi)\cdot\sin\left(2\cdot\omega\cdot t + \phi h(t)\right)\right) \end{bmatrix}\cdot\left(k(\phi)\cdot\frac{h1(t)}{2\cdot b(\phi)}\right)^2 \ldots \\
& + \alpha0(t)\cdot k(\phi)\cdot\frac{h1(t)}{2\cdot b(\phi)}\cdot Cp\theta hs(\phi)\cdot\sin\left(\omega\cdot t + \phi h(t) + \phi\alpha(t)\right)
\end{aligned}
$$

3.3.3.8 Results for the Baseline Case

The coefficient of lift is given in Figure 3-121.

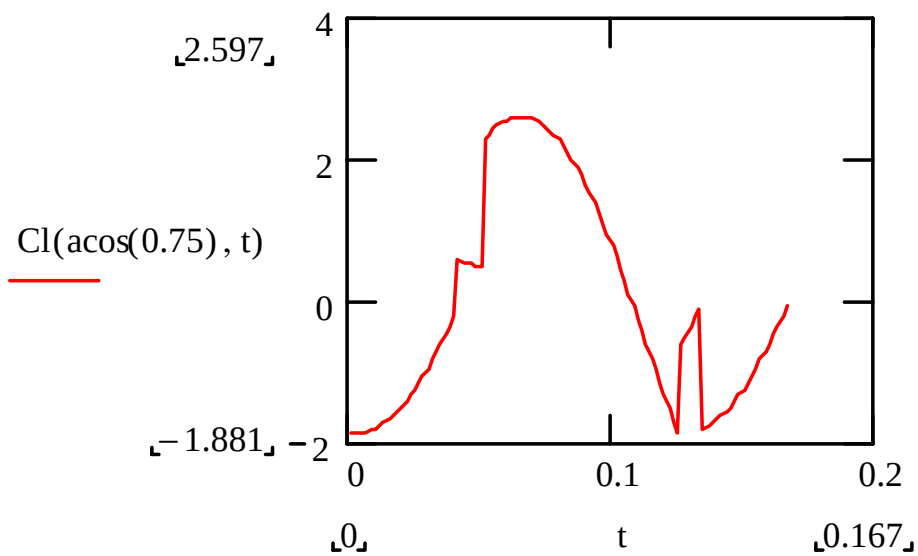

Figure 3-121: Lift Coefficient vs. Time

The values of thrust coefficient are of the same shape and scale as that of the lift. The moment produced in the upbeat is going to be neutralized by that produced by the downbeat, and is not significant. It has high values once the angle of attack changes and that comports with the physics of the problem. The graphs for moment and power coefficients are given in Figures 3-122 and 3-123.

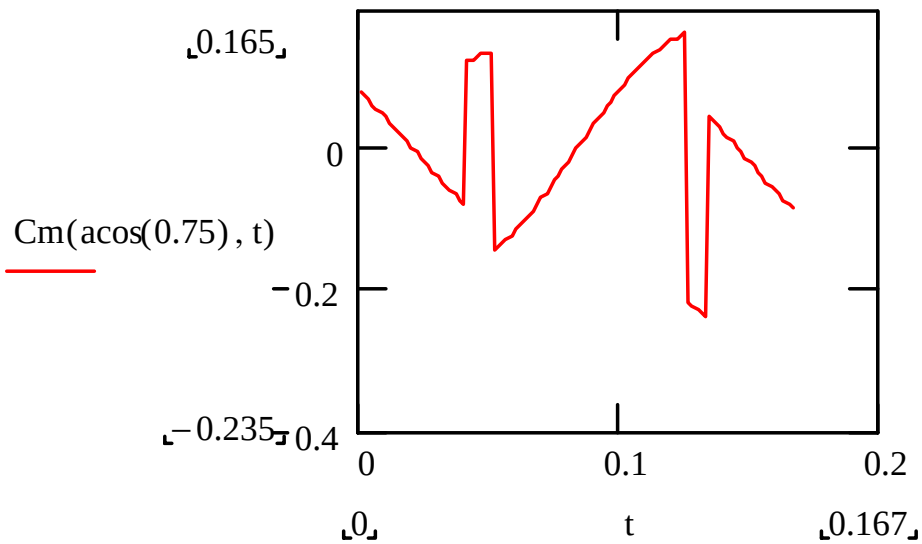

Figure 3-122: Moment Coefficient vs. Time

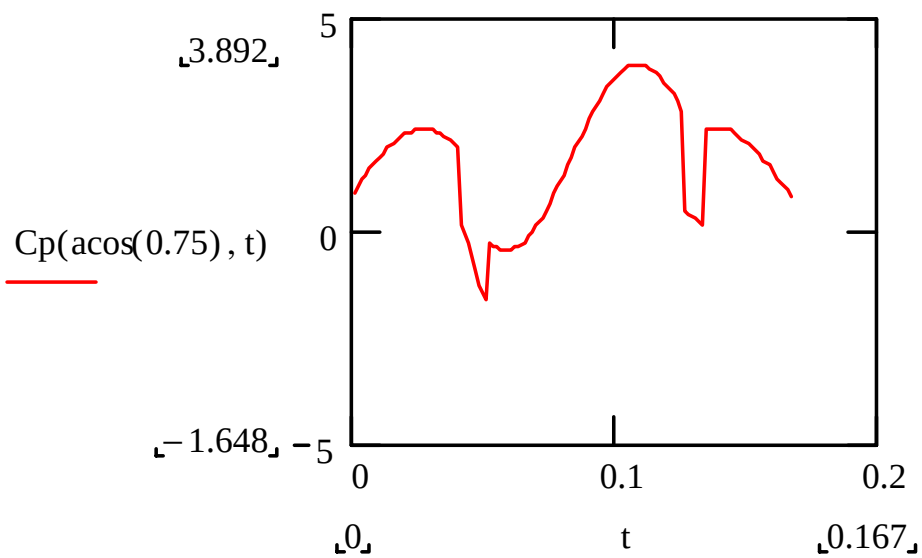

Figure 3-123: Power Coefficient vs. Time

3.3.3.9 Validation of Results

Figure 3-124 gives the CFD results of the unblown case for the same baseline configuration. Although the curve depicts the total value of lift and thrust force as a function of time, if normalized, the C_L values vary from approximately -2 to +4, which are bit higher than those obtained by the analytical model. This is because the leading edge vortex has not been modeled in the analytical model. Second, camber effects have been neglected, which will contribute to increase the lift coefficient value, but it can be deduced that the analytical model though approximate, gives the same shape of curve and the results are in the same range.

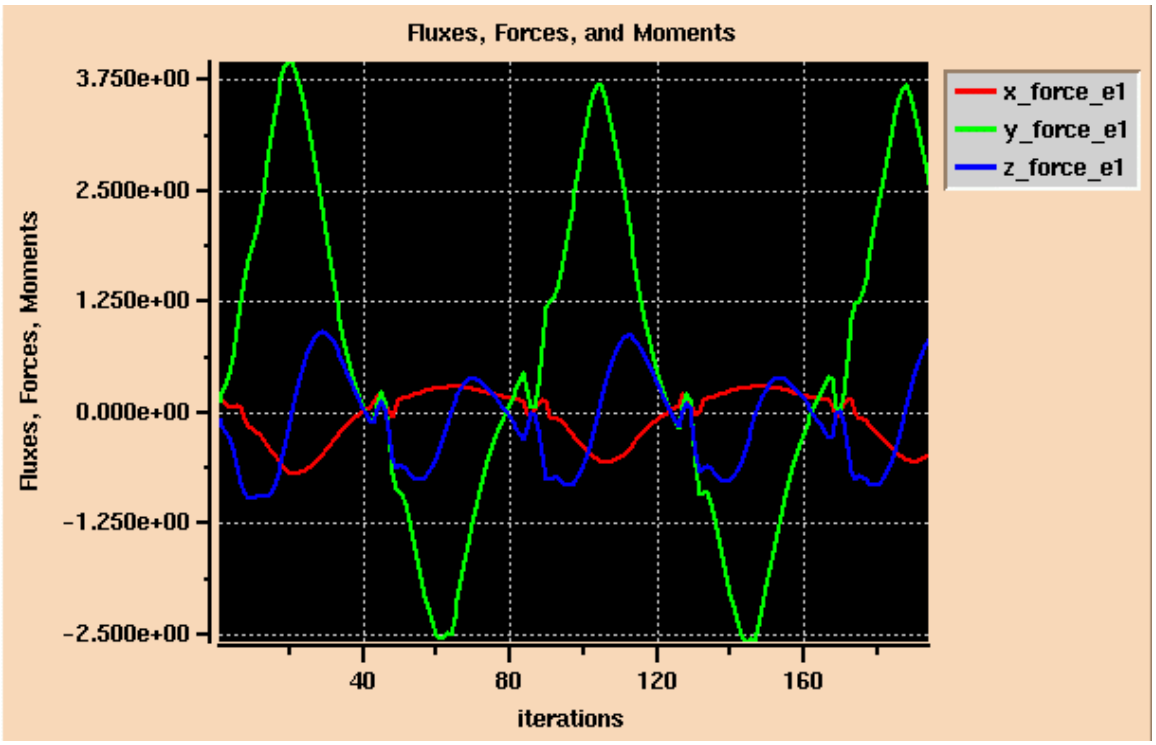

Figure 3-124: CFD Results of the Unblown Case

3.3.3.10 Design of Experiments and Parametric Analysis

After having evaluated the results of baseline case, and validating the analytical model with the values obtained by CFD analysis, the next step was to explore the design space parametrically. As explained earlier, there are five control variables: span, forward velocity, flapping frequency, flapping amplitude, and pitching amplitude. The sensitivity of key responses lift, thrust, moment, and power coefficients with the variability of control variables was assessed parametrically. A complete parametric exploration of the design space would require selection of adequate ranges for these control variables and then the sensitivity of each response variable must be determined in the five dimensional space. The existence of a feasible design space must also be calculated based on constraints being imposed by other disciplines such as structural integrity, the flapping frequency, etc. Similarly, forward speed will have a limitation based on the exploration requirements, and the shape parameters may also be confined as per the communication and avionics payload. Keeping all these aspects in mind, the following ranges were selected to make an initial estimation of the design space:

a. Span: 2.6ft to 4ft
b. Forward velocity: 14ft/sec to 26 ft/sec
c. Flapping frequency: 6Hz to 16Hz
d. Flapping amplitude: 45degrees to 75 degrees
e. Pitching amplitude: 8 degrees to 12 degrees

Based on the ranges of these variables defined above, the five dimensional design space has been defined. The key responses at different points within the design space must then be evalu-

ated. Innumerable combinations of these variables are possible and would require an extensive effort for exploration (beyond the scope of the NIAC Phase II study resources), so an assumption was made that within each dimension of design space the key response will have a quadratic relation with the dimension variable. Hence, based on this assumption, each variable will have three values: a minimum within the range, a maximum within the range, and the center point. For example, velocity will be taken as 14, 20, and 26ft./sec. After having made this assumption, a full factorial design space array would require 35 or 243 runs for evaluation of responses at all points. This can be mitigated by taking a fractional factorial orthogonal array for design space exploration. A face-centered composite design orthogonal array with 28 runs was formulated for the purpose of this analysis. The array is given in Table 3-9.

Table 3-9: Design of Experiment Array

Run No.	Span	Velocity	Frequency	Plunge Amplitude	Pitch Amplitude
1	2.6	14	6	45	12
2	2.6	14	6	75	8
3	2.6	14	16	45	8
4	2.6	14	16	75	12
5	2.6	26	6	45	8
6	2.6	26	6	75	12
7	2.6	26	16	45	12
8	2.6	26	16	75	8
9	4	14	6	45	8
10	4	14	6	75	12
11	4	14	16	45	12
12	4	14	16	75	8
13	4	26	6	45	12
14	4	26	6	75	8
15	4	26	16	45	8
16	4	26	16	75	12
17	3.3	20	11	60	10
18	3.3	20	11	60	10
19	2.6	20	11	60	10
20	4	20	11	60	10
21	3.3	14	11	60	10

Table 3-9: Design of Experiment Array (Continued)

Run No.	Span	Velocity	Frequency	Plunge Amplitude	Pitch Amplitude
22	3.3	26	11	60	10
23	3.3	20	6	60	10
24	3.3	20	16	60	10
25	3.3	20	11	45	10
26	3.3	20	11	75	10
27	3.3	20	11	60	8
28	3.3	20	11	60	12

The code written for analysis was executed for all 28 combinations to evaluate the response variables. The results for lift, moment and power are given in Figures 3-125, 3-126, and 3-127, respectively. These results can be used in many a ways. For example, keeping all the variables at fixed level for each dimension and just varying one variable can help determine the relation of a specific variable with the response variable. Also these results can be used to assess the optimum configuration in the design space. Also, a Multiple Analysis of Variance (MANOVA) can be performed to evaluate the response variables as response surface equations (RSE) in terms of the control variables. Because a quadratic relation was assumed in each dimension, and a fractional factorial array was used, only first and second order main effects and first order interactions can be included in the RSEs. These RSEs, in addition to having these five variables, would still be time-dependant within each time period.

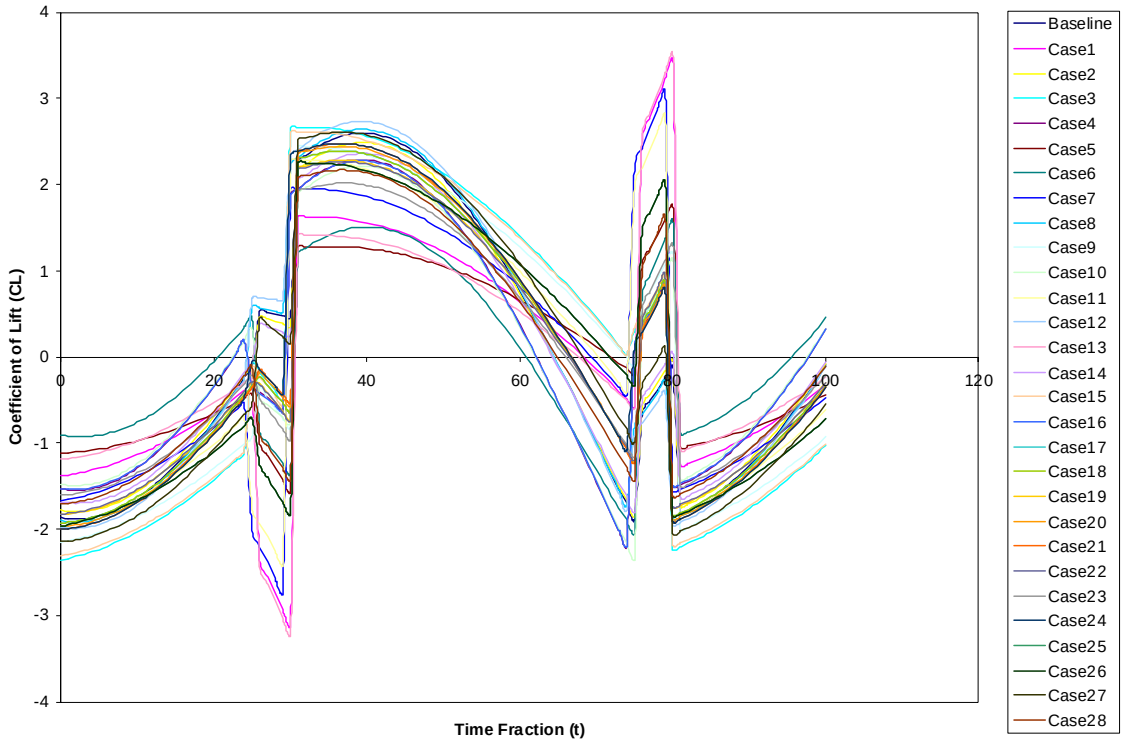

Figure 3-125: Coefficient of Lift

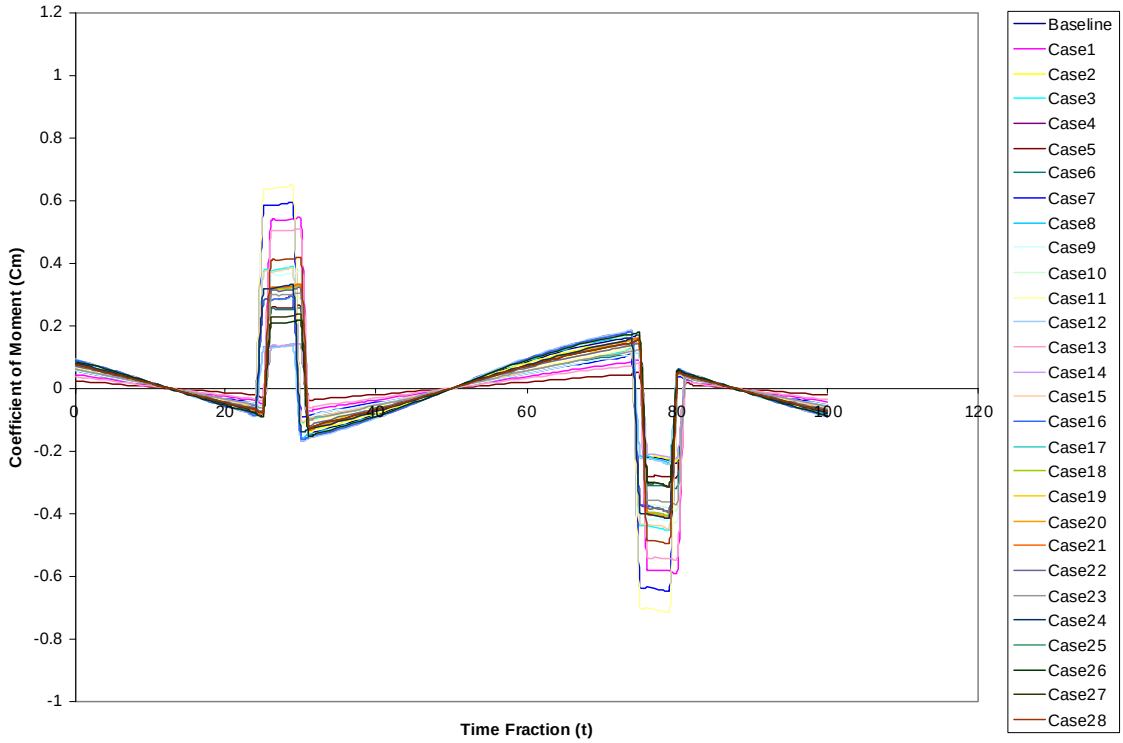

Figure 3-126: Coefficient of Moment

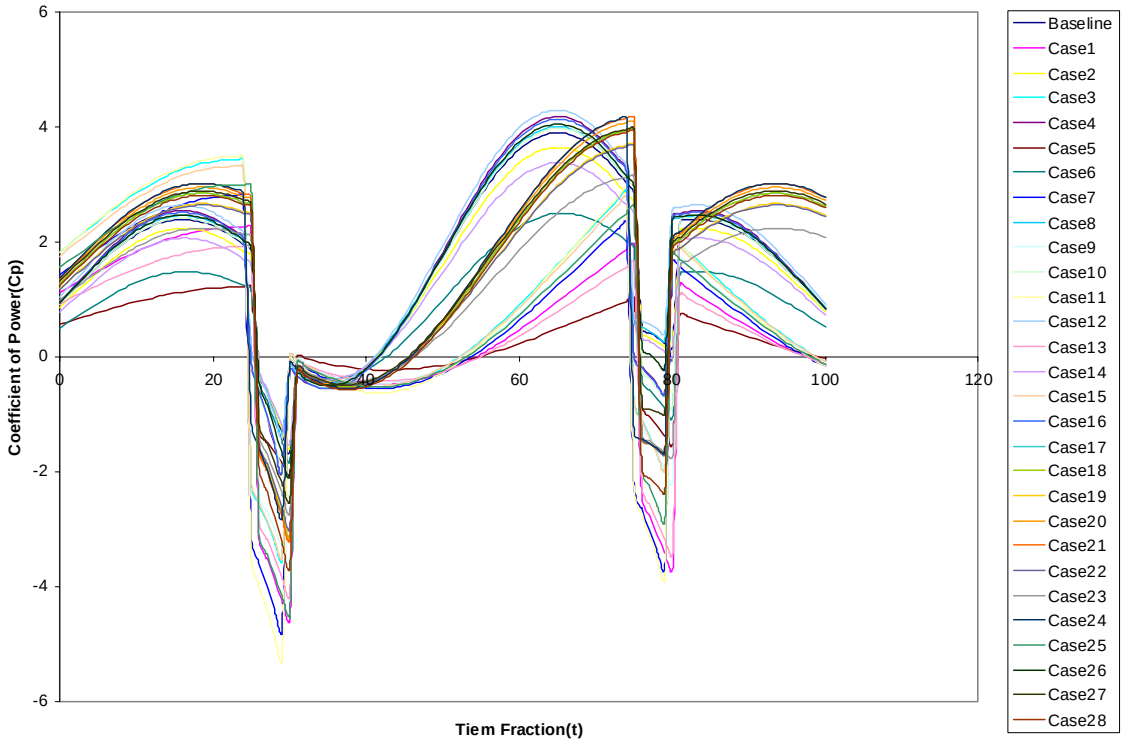

Figure 3-127: Coefficient of Power

Now the results produced above can be used to determine the variability of each response with each variable. Some of the relations determined for C_L with variables are as follows:

a. Keeping everything the same, and just changing the span of Entomopter, Case 19 and Case 20 of the design-of-experiments array depicts the change shown in Figure 3-128 below:

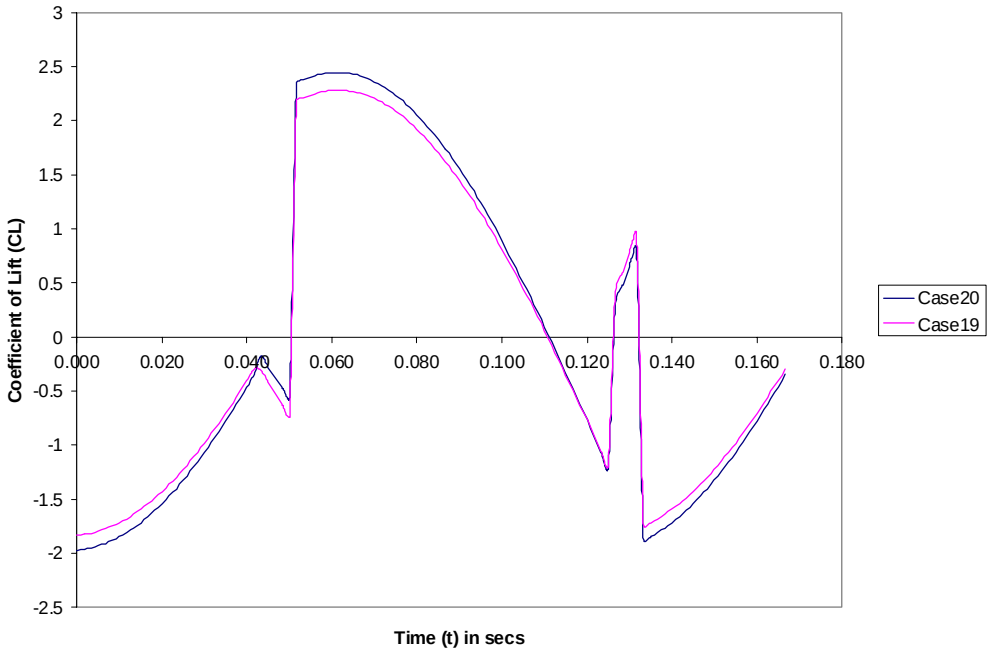

Figure 3-128: Variation of Lift Coefficient with Span

The chart shows that there will be very little effect on the lift coefficient value over the range of spans selected, and as such net lift coefficient will stay relatively constant with increase in span. This makes sense because the non dimensional lift coefficient will not change, however the lift force will change as a function of wing area.

b. Keeping all variables fixed and just changing the forward velocity results in that which is depicted in Case 21 and Case 22 of the design-of-experiments array shown in Figure 3-129.

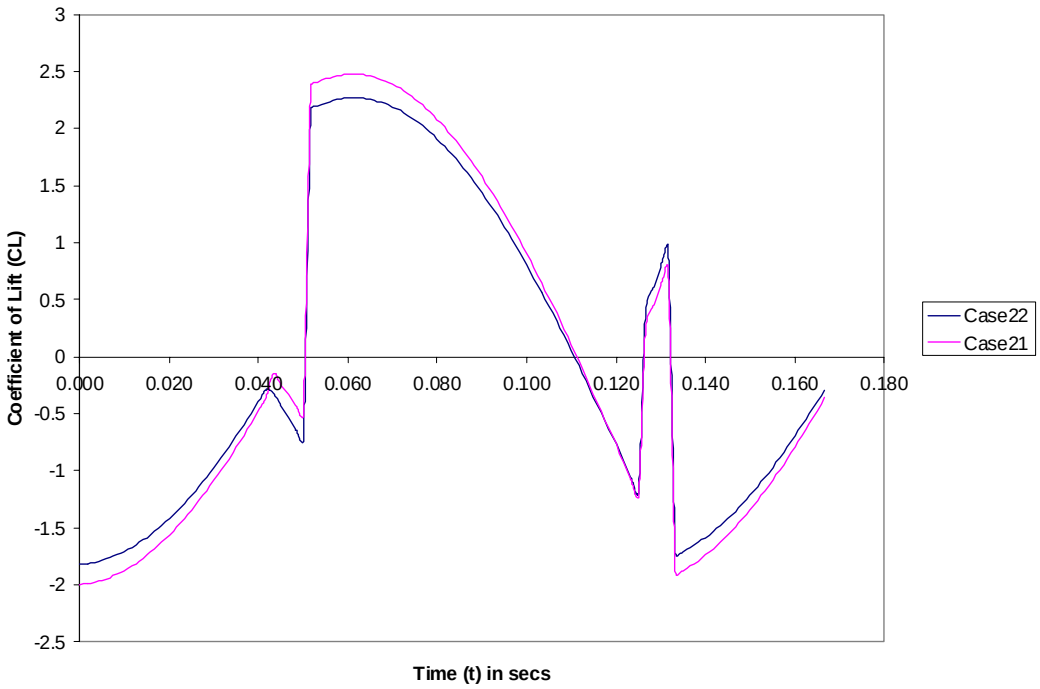

Figure 3-129: Variation of Lift Coefficient with Forward Velocity

Figure 3-129 shows that the net lift coefficient will stay almost the same, for variation in velocity; however, the lift force will increase proportional to the square of velocity.

c. Keeping all variables the same and just changing the flapping frequency results in that which is depicted in Case 23 and Case 24 of the design-of-experiments array. The results are shown in Figure 3-130.

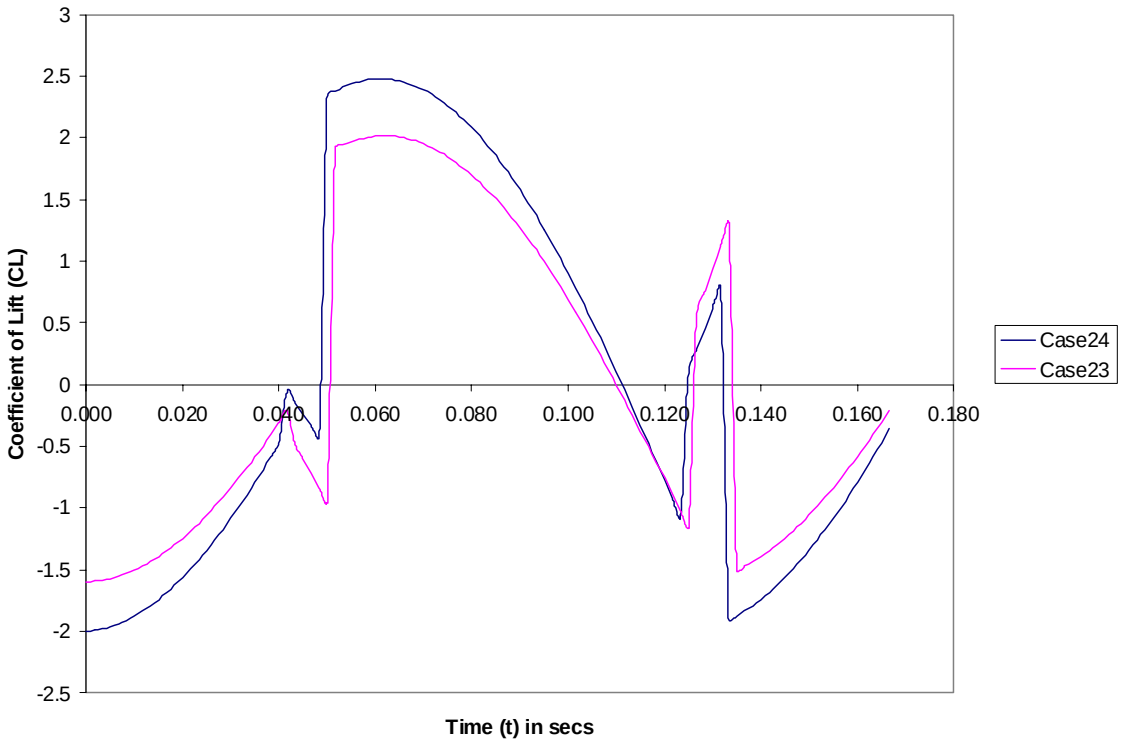

Figure 3-130: Variation of Lift Coefficient with Flapping Frequency

It can be seen that by increasing the flapping frequency the net lift coefficient has increased, although in the down beat, it reduces the lift coefficient, but the overall effect is still positive.

d. Keeping all variables constant and just changing the flapping amplitude results in that which is depicted in Case 25 and Case 26 of design-of-experiments array. The results are shown in Figure 3-131

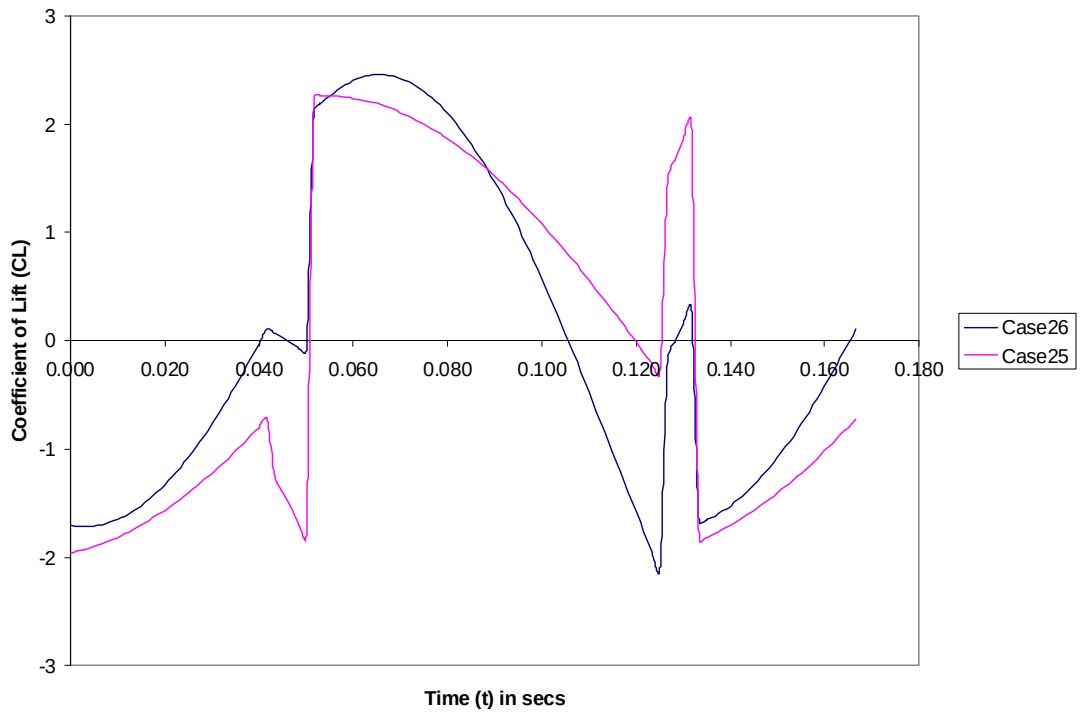

Figure 3-131: Variation of Lift Coefficient with Flapping Amplitude

It can be seen that by increasing the flapping amplitude, the results improve for the upbeat, but this has a negative influence for the down beat. The effect on thrust is just the opposite, with increased thrust being realized on the down beat.

e. Changing Pitching amplitude alone while keeping the rest of the variables fixed results in that which is depicted in Case 27 and Case 28 of design-of-experiments array. The results are shown in Figure 3-132.

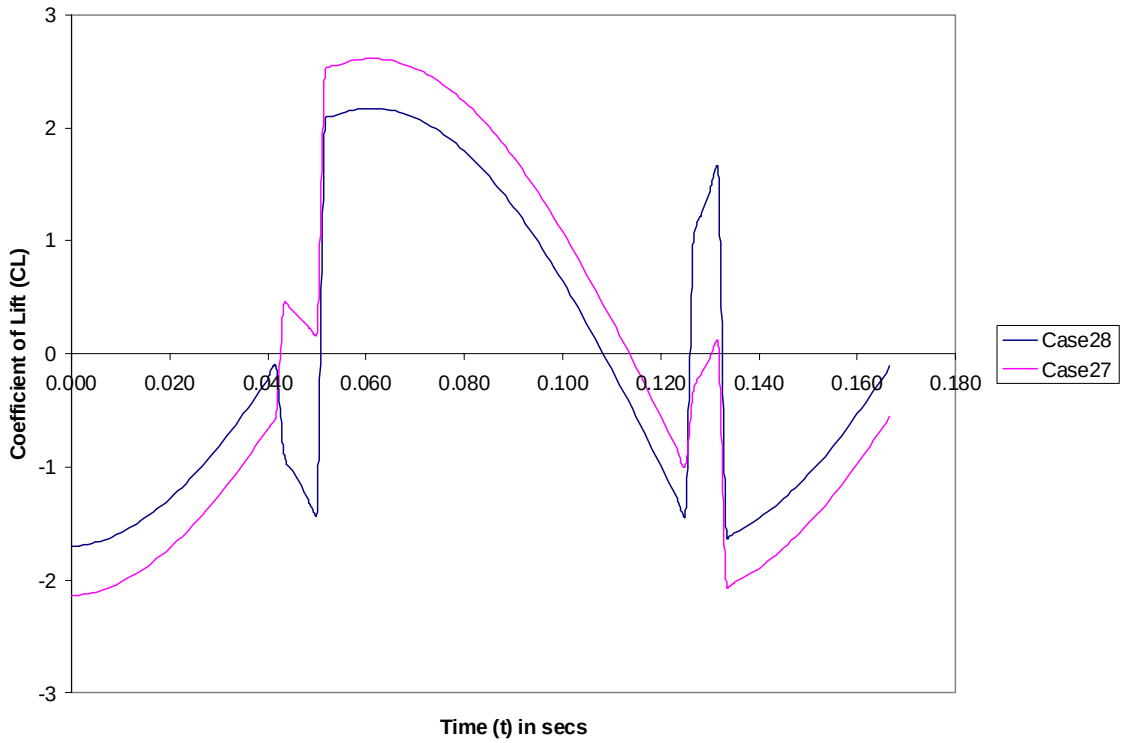

Figure 3-132: Variation of Lift Coefficient with Pitching Amplitude

The results depict a similar trend for lift coefficient as that of flapping amplitude, except that in addition to influencing the thrust, it has a tremendous effect on the moment values.

3.3.3.11 Recommendations and Conclusion

The results produced above are based on a simple analytical model defined to perform aeroelastic analysis. Although the results comport with the physics of the problem, the model is still not accurate enough to account for all the effects of flapping wing flight. To model the aerodynamics of Entomopter for true prediction of results in the lower Mars atmosphere, experimental results or more extensive CFD results must be calculated for all the cases defined in the design-of-experiments array. Then, based on MANOVA analysis of the experimental results, the model can be refined to give better estimations. Also, the model used here can be rebased on vortex theory for propellers to accommodate the strong leading edge vortex effects.

In addition to this modeling for the unblown wing, the main challenge will be to include the effects of circulation control into the analysis that can be modeled by addition of few more variables like:

a. Temperature of blown gases
b. Velocity of blown gases
c. Blown area
d. Direction of blown gases

This will further increase the number of cases required to be evaluated. The best option would be to perform CFD analyses for all these cases, and validating by experimental runs in the wind tunnel, to account for the unsteady effects of flapping wing flight. The experimental runs can be compensated for the Earth's environment and then based on Reynolds Number, the results could be extrapolated for the Mars Environment.

Empirical results can be generated on a newly constructed flapping wing simulator in the GTRI wind tunnels (See Figure 3-133.). This hardware simulator, developed under a DARPA-funded project, is capable of operating with a full scale blown winglet of the exact planform used by the Mars Entomopter and at speeds comparable to those used in the CFD simulations. These wind tunnel tests are beyond the scope of work originally proposed under this NIAC Phase II effort, but will be conducted as follow-on work to advance and refine the CFD and analytical models developed here.

Figure 3-133: GTRI Kinematically-correct Full-scale Wind Tunnel Wing Flapping Simulator

3.3.4 Active Flow Control ("Blowing" of the Wings)

Even though positive net lift is obtained from both the CFD and analytical solutions, the force is not sufficient for flight in Mars' lower atmosphere. Hence, active flow control technology will be used to augment the lift, and thrust along with reducing the drag of the Entomopter. The reciprocating chemical muscle-based propulsion of Entomopter provides exhaust that can be used as a supply of gas for circulation control. Blowing of the wing in a proper way is critical not only to the stability and control of the Entomopter, but in the Mars application, its ability to fly. Experiments on Earth in the wind tunnel have shown that blowing can achieve phenomenal results, with increases in lift by a factor of ten [83, 84]. Under the NIAC Phase II study, incorporation of the affects of blowing within the analytical formulation were not possible, though this has been identified as a follow-on effort. Similarly, the optimal computational description of the

effects of blowing as demonstrated in the wind tunnel has yet to be achieved through the study team's CFD efforts, though this too is an area slated for follow-on work.

Consider a baseline conventional fixed wing vehicle (one wing set) with a one meter wing span and having aspect ratio of 5.874 (similar to that of the Hawk Moth-based Entomopter wing) flying near the surface at a speed of 100 meters per second. Its wing area is 0.142m^2 (1.532ft^2). Reference atmospheric conditions on the Mars surface are: density = 0.0000279 slugs/ft^3, atmospheric pressure = 0.11475psia, and temperature = -20.4F. At a typical fixed wing lift coefficient of 1.0, that vehicle can carry 1.04kg (2.3lbs.) gross weight (approximately 2.8 Earth kg (6.2lbs.)) if Mars gravity is taken as 37% that of Earth's). That represents a wing loading of only 7.3kg/m^2 (1.5lb/ft^2) due to the low density and pressure compared to aircraft flying on Earth at perhaps 342kg/m^2 (70lb/ ft^2) to more than 488kg/m^2 (100lb/ft^2).

Based on the same pneumatic aerodynamic data used for the terrestrial pneumatic Entomopter (previous wind tunnel data for a GTRI circulation controlled wing model with the same aspect ratio), a C_L of 5.3 is attainable (this is steady-state data, not flapping, which will be larger, as discussed below). Assuming that the two-winged Entomopter has the same total wing area and aspect ratio as the one meter conventional wing, giving it a reduced wing span of only 0.646m (2.12ft) per wing. At the same high flight speed (100m/s), this blown Entomopter can lift 5.53kg (12.2lbs.) on Mars (15 Earth kg (33lbs.)). Or, if one assumes the two aircraft have the same wing area and a gross weight of 1.04kg (2.3lbs.) from above, the blown Entomopter can reduce the required flight speed from 100m/s to 43.4m/s, i.e. the dynamic pressure is reduced from 7.3kg/m^2 (1.5 lb/ft^2) to 1.387kg/m^2 (0.284lb/ft^2). Lastly, if we assume that both aircraft (aspect ratio = 5.874) fly the same flight speed (perhaps a lower value of 50m/s speed) with 1.04kg (2.3lbs.) gross weight, the blown Entomopter can do it with a total wing area of only 0.107m^2 (1.156ft^2) or a wing span of 0.56m (1.84ft) per wing set, compared to the span of 1.83m (6.0ft) and area of 0.569m^2 (6.126ft^2) for the conventional wing. The size reduction possibility is clear, however this also has implications in that were the wing to remain the same length, it could be flapped at a slower speed, thereby accommodating the effects of inertia and strength of materials.

Finally, using a slot height geometry of such a size as to obtain the blown C_L = 5.3 requires a C_L= 0.40. At the flight speed of 100m/s, q = 7.333kg/m^2 (1.502lb/ft^2), and the required total slot blowing weight flow = 0.0076kg/s (0.0168lb/s), jet velocity = 538m/s (1765ft/s) and blowing pressure is 0.18kg/cm^{2}g (2.5 psig), mainly due to the very low external atmospheric pressure and temperature on Mars.

An additional valuable comparison can be made if appropriate wing loadings are considered along with the required flight speeds. The terrestrial pneumatically-blown Entomopter design with two wing sets (i.e., 4 wing panels: 2 front, 2 aft) has a wing loading of 3.554kg/m^2 (0.728lb/ft^2). For a 1m span Mars Entomopter with 2 wing sets scaled to that wing loading and an aspect ratio of 5.874, a flight weight of 1.01kg (2.24lb) can be achieved. The conventional aircraft with the same weight and aspect ratio and one wing set has a wing loading of twice that, or 7.13kg/m^2 (1.46lb/ft^2). Figure 3-134 shows the flight speeds required for each aircraft at those wing loadings, as well as double the wing loading for each vehicle. The conventional aircraft with C_L=1.0 requires a speed of 98.4m/s to support that weight in level flight, while the same weight pneumatically blown Entomopter with attainable C_L = 5.3 can fly at 30.2m/s. C.P.

Ellington of the University of Cambridge in his paper entitled, “The Aerodynamics of Insect-Based Flying Machines” [75] states that flapping-wing unsteady aerodynamics of insects can increase the attainable lift by a factor of 2 to 3 times the steady-state value. Unsteady data for leading-edge shed vortices of pitching helicopter rotor blades show similar trends but somewhat smaller values. So, assuming a more conservative factor of 1.5 to 2, then the pneumatically blown Entomopter can yield a C_L of 7.95 to 10.6 and the resulting reduced flight speeds are 24.7 and 21.4m/s respectively. Note that since the curves are power functions of C_L, doubling a large C_L has lesser effect on the required speed than doubling a smaller value; in this case, doubling the Entomopter higher lift coefficient for unsteady effects reduces speed by only 9m/s. Thus the exact lift value achieved by the flapping Entomopter with its unsteady aerodynamics has a relatively lesser effect compared to the base steady value, but does serve to produce a favorable effect. However, going from the fixed wing aircraft’s lift coefficient of 1.0 to even the steady-state pneumatic value of 5.3 reduces the required speed by 68.2m/s or more than 2/3. Figure 3-134 also shows the effect on required speed for either aircraft by doubling the weight or the wing loading, and once again, the high lift attainable by the pneumatic configuration produces a significant effect.

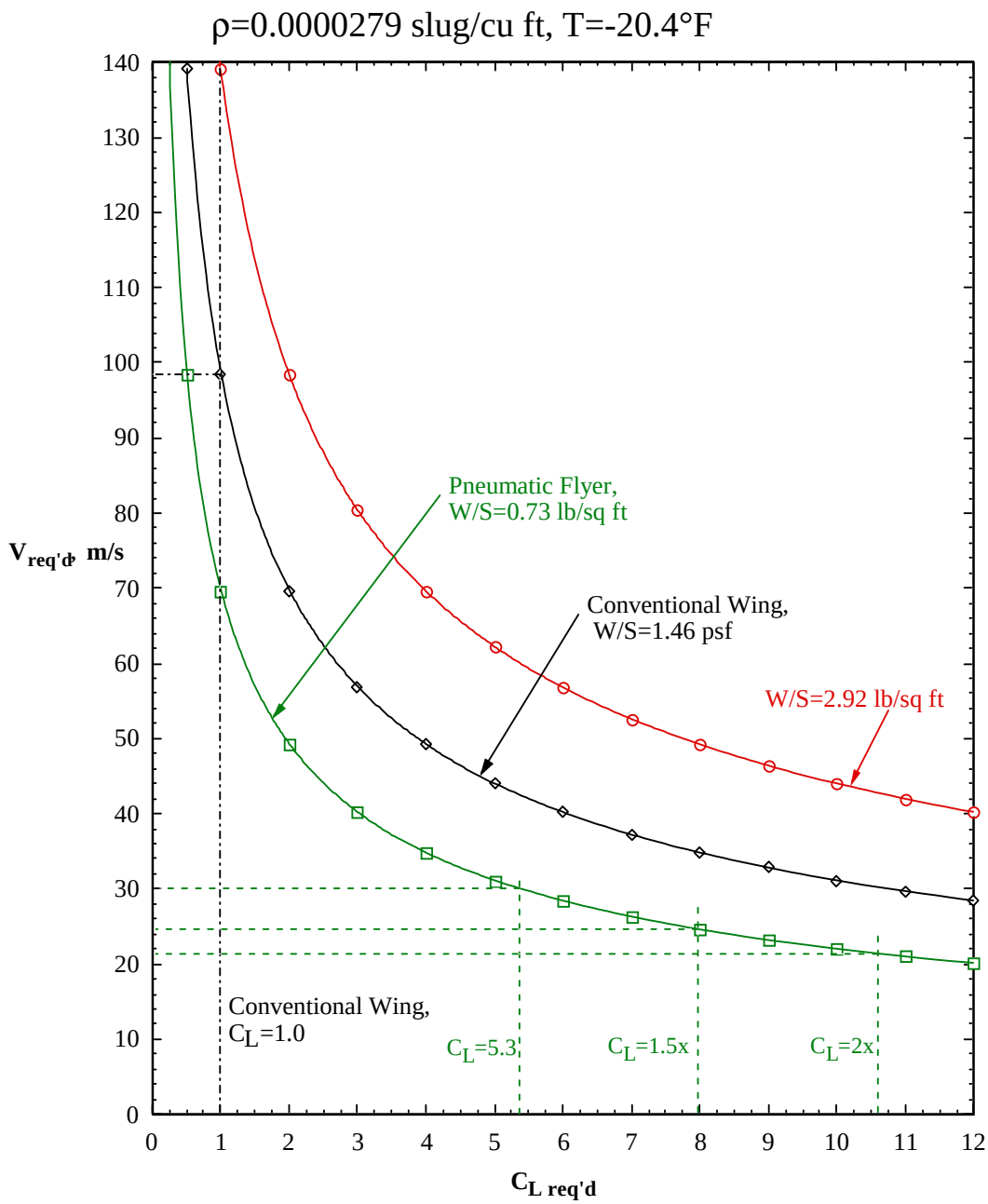

Figure 3-134: Flight Speed at Mars Surface vs. Required C_L

3.4 Reciprocating Chemical Muscle

The heart of the proposed Mars Entomopter is a reciprocating chemical muscle (RCM). Internally-funded efforts at the Georgia Tech Research Institute were conducted to develop a proof of principal RCM. The RCM is an anaerobic, ignitionless, catalytic device that can operate from a number of chemical fuel sources. While under funding from DARPA/DSO to show feasibility of an Entomopter-based MAR, the RCM was refined, reduced in size, and demonstrated to develop the power and speed necessary for flight.

The RCM is a regenerative device that converts chemical energy into motion through a direct noncombustive chemical reaction. Hence, the concept of a “muscle” as opposed to an engine. There is no combustion taking place nor is there an ignition system required. The RCM is not only capable of producing autonomic wing flapping as well as small amounts of electricity for control of MEMS devices and the “nervous system” of the Entomopter, but it creates enough gas to energize circulation-controlled airfoils. This means that simple autonomic (involuntary, uncontrolled) wing flapping of constant frequency and equal amplitude can result in directional control of the Entomopter by varying the coefficient of lift (CL) on each of the wings, thereby inducing a roll moment about the body of the Entomopter while in flight. Figure 3-135 shows 'milli-scaled' wing structures grown in the Institute's stereolithography and fused deposition modeling machines. Wings like these will not only act as smart structures to create a proper angles of attack under opposite aerodynamic loads during the up beat and down beat, but the hollow micro-channels in the ribs provide circulation control gas from the RCM to “blow” the wings for directional control in flight as well as lift when the wing is at negative angles of attack during the up beat.

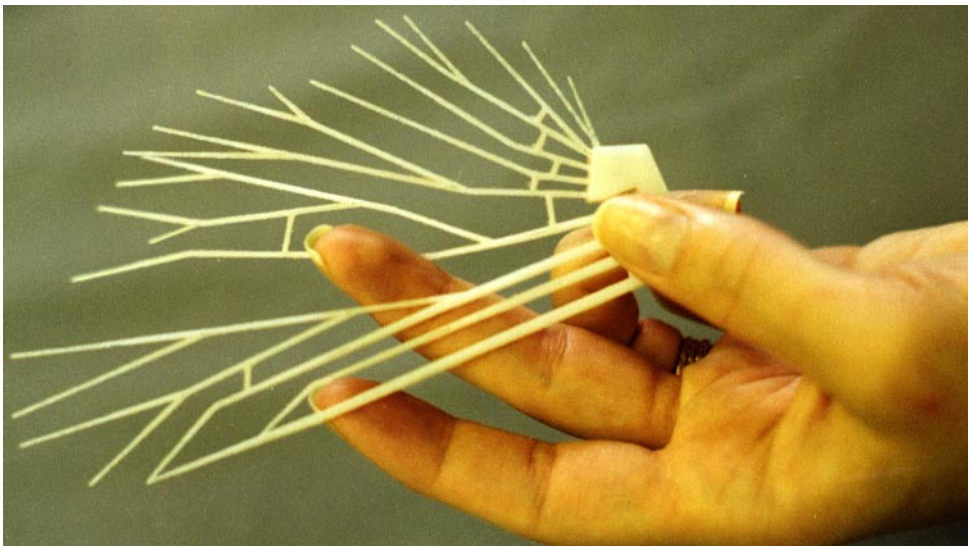

Figure 3-135: Wing Structures Grown in Georgia Tech’s Stereolithography and Fused Deposition Modeling Machines.

The implementation of a RCM is motivated chiefly by the basic necessity for very high rate of energy release from compact energy sources. Electrically-driven systems suffer from the poor energy density of batteries, while electrical actuators are typically dense (heavy), or suffer from insufficient force and motion as in the case of electrostatic or piezoelectric propulsors. To increase motion, piezoelectric ceramics can be stacked, but this leads to greater weight, stiffness, and often higher required voltages. Rheological fluids can be slow to respond and will therefore be difficult to use with flapping wing implementations requiring beat frequencies of 20 to 50 Hz. Faster acting polymeric muscles have been demonstrated, but require high actuation voltages, dictating the need for power conversion circuits which add weight and loss to the already heavy onboard battery pack. Actuators of NITINOL wire are totally out of the question due to the significant current requirements and variable performance under environmental extremes.

The RCM was originally conceived as an actuator for the flapping wing of a small insect-like terrestrial entomopter. (See Figure 3-136.) It had a reciprocation rate limited by inertia and fric-

tion to about 10 Hz when using a simple hydrogen peroxide-fueled gas generator without optimized fuel injection.

Figure 3-136: First-generation Reciprocating Chemical Muscle

Figure 3-137: Second-generation Reciprocating Chemical Muscle

The second generation was approximately a quarter the volume of generation one, but was able to demonstrate up to 20 Hz reciprocation rates while exhibiting pounds of force. (See Figure 3-137)

Figure 3-138: Stereolithographic Scale Model of the Terrestrial Flight-sized Reciprocating Chemical Muscle

The terrestrial Entomopter application called for a 50 gram vehicle with a wing flapping frequency of between 25 and 30 Hz, thus the third generation RCM was developed and demonstrated in coordination with the DARPA/DSO Mesomachines study to investigate the viability of the Entomopter concept for indoor military applications. This third generation RCM was constructed at a scale that was about 2.5 times larger than the flyable version (see Figure 3-138) required for the 50 gram Entomopter, but used internal porting that was at the 1:1 flyable scale. Not only did this generation perform with force necessary for wing actuation of the Entomopter, it was demonstrated to reciprocate at 70 Hz, more than twice the required speed, while producing a mechanical throw of 12.7 mm (0.5 inches).

As shown in Figure 3-139, the third generation RCM used external mechanical spool valve actuation and could be throttled by pressure regulation (either through fuel decomposition rate at the input, or by modulating back pressure on the exhaust port). The single piston design of the third generation device also produced a longitudinal vibration (in the direction of the piston motion) at the fundamental reciprocation rate. Although not appreciable in the 2.5X version, this vibration would become significant as the RCM cylinder housing was sculpted to remove mass as downsizing continued in latter generations.

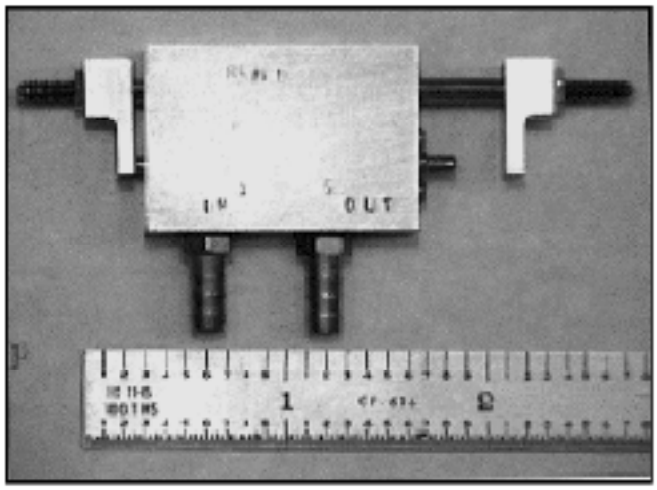

Figure 3-139: Third-generation Reciprocating Chemical Muscle

The vibration of the RCM along its longitudinal axis might not have been a significant problem in the Entomopter while in flight, (especially at a 30 Hz reciprocation rate), but it was realized that there are many other applications for the RCM for which vibration might not be acceptable, especially were a number of RCM devices used simultaneously in the same platform. Non-coherent actuation of numerous RCM actuators would result in random canceling vibration, but were free running units to drift in phase, coherent operation might momentarily result in the vibrational forces adding constructively. The solution was to make changes in the fourth generation RCM to eliminate vibration altogether while making other performance improvements.

As it turns out, this is also an important consideration for the Mars Entomopter too. The size of the RCM for the Mars Entomopter will be scaled up from the first generation unit in order to provide enough power to flap the longer wing (approximately 1m) that will be used for flight in the lower Mars atmosphere. The larger the RCM, the greater the inertias developed internally. It is therefore even more advantageous to design the RCM to be reactionless, that is, to have canceling inertias and no vibration.

3.4.1 Fourth-generation Design Goals

The fourth-generation RCM development began with an analysis of methods by which the mechanism could be simplified as it is reduced in size. Of principal concern was the vibration inherent in the third generation design. It was felt that the features of the RCM contributing to vibration must be eliminated prior to further size reduction. A new concept using pneumatic shuttle valve actuation was considered because this would eliminate all external components such as the strike plates shown in the third generation RCM depicted in Figure 3-139. Also, this new concept offered the possibility of eliminating any mechanical spool valve actuation internally (thereby reducing parts count and complexity. The new concept employed gas pressure increase during static end-of-stroke conditions to actuate a reversing spool valve.

3.4.2 Fourth-generation Concept

Figure 3-140 shows how this concept works. A split piston that moves in opposite directions under the influence equal pressures from the same source provides a reactionless opposing motion. The mass of the spool is negligible compared to the overall mass of the entire assembly and its vibrational contribution will be of little effect. The concept relies upon the fact that pressure cannot build up as long as there is gas flow into an expanding volume. As soon as the volume becomes a fixed value, continued flow will result in a pressure rise. This pressure rise can then act upon a pressure-triggered spool valve to redirect the flow into a different (expanding) volume. The process is regenerative.

In Frame 1 of Figure 3-140, the split pistons are located at their innermost positions and gas flow is directed toward the inner faces of each piston, inducing them to move away from the center as shown in progress during Frame 2. In Frame 3 the pistons have reached their outer limit and the volume between the inner piston faces can no longer expand. As a result, the pressure at point A begins to rise and the slight flow-restricted pressure at point B drops to zero when all expulsion flow ceases.

Frame 4 shows static motion of the internal pistons and spool valve as the pressure continues to increase. In Frame 5 the pressure at point A has risen to a point that is sufficient to overcome the spool valve holding force (represented in these frames by a spring-loaded ball detent). When this pressure is reached, the spool valve will begin to move as shown in Frame 5. The intent is that the force be “explosive” such that when the holding force is suddenly overcome, he spool is driven to the right. Inertia of the spool carries it past the all-ports-closed dead point.

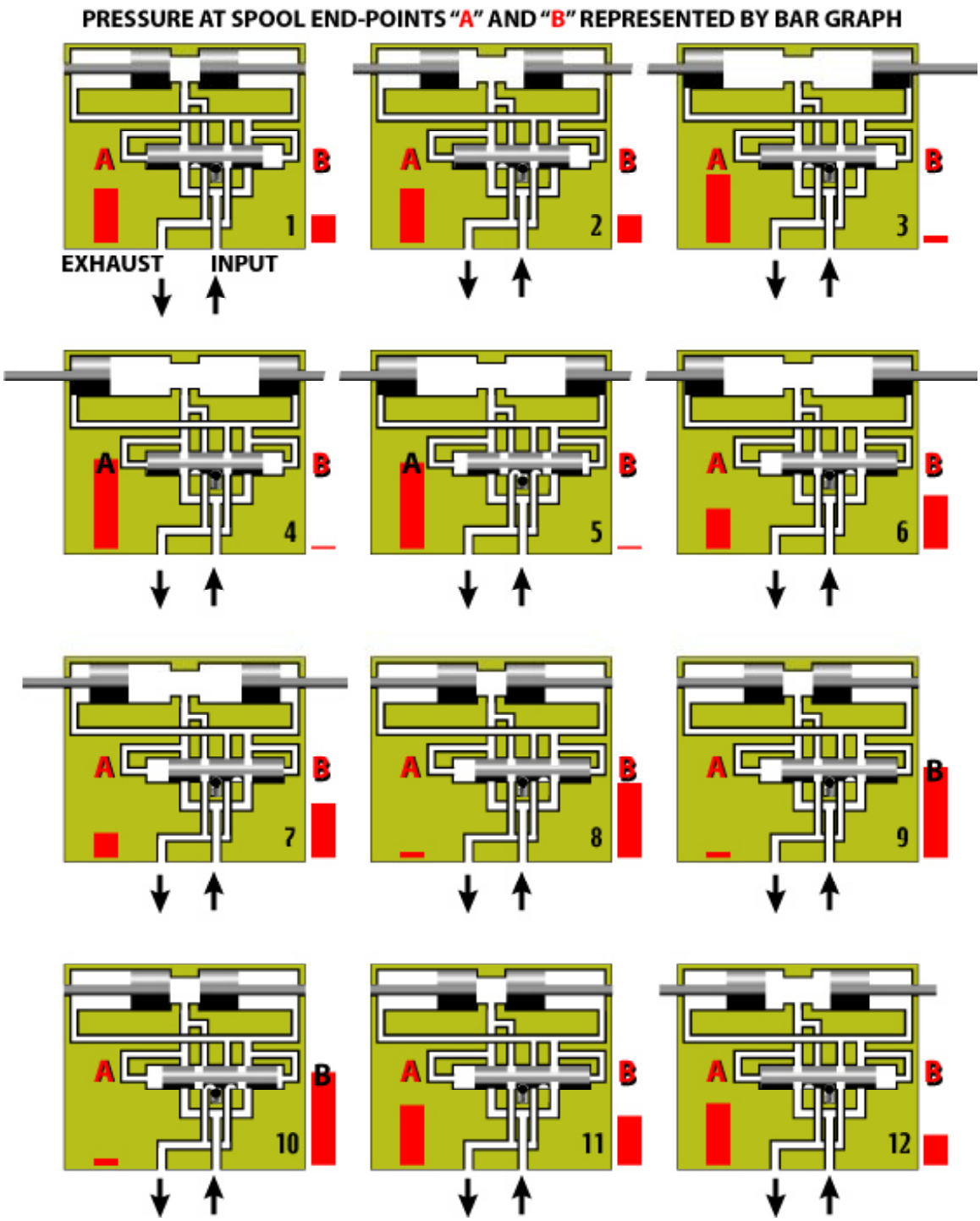

Figure 3-140: Initial Fourth-generation RCM Actuator Design Using a Pressure-activated Spool

With the spool valve in the right hand position of Frame 6, the dual pistons are now pressurized on their outer faces, forcing them back toward the center of the mechanism. As they move, the volume increases, so the pressure at point B reaches an equilibrium value that is dictated by the flow restriction of the internal porting (Frame 7). At the same time, the pressure at point A is

now very low, itself being a function of the expulsion of gases in front of each piston as they pass through the restrictions of the internal porting.

Frame 8 shows the split pistons in a static position at the end of their fully contracted throws. Once again the volume is unchanging and the pressure will rise (this time at point B) as gas mass continues to flow into the mechanism (see Frame 9). When the pressure exceeds the holding force of the spool, the spool will move suddenly to the left and the process starts over (Frames 10 - 12).

An oversized working model was constructed with a polycarbonate housing to allow inspection of the internal kinematics. This is shown in Figure 3-141. Although this system functioned, it was not consistent, requiring tuning of the spool holding force/friction at different pressures. Reliable operation was improved with the addition of poppet valves keyed to piston position (shown externally in Figure 3-141). In this configuration both single-ended and double-ended operation were demonstrated.

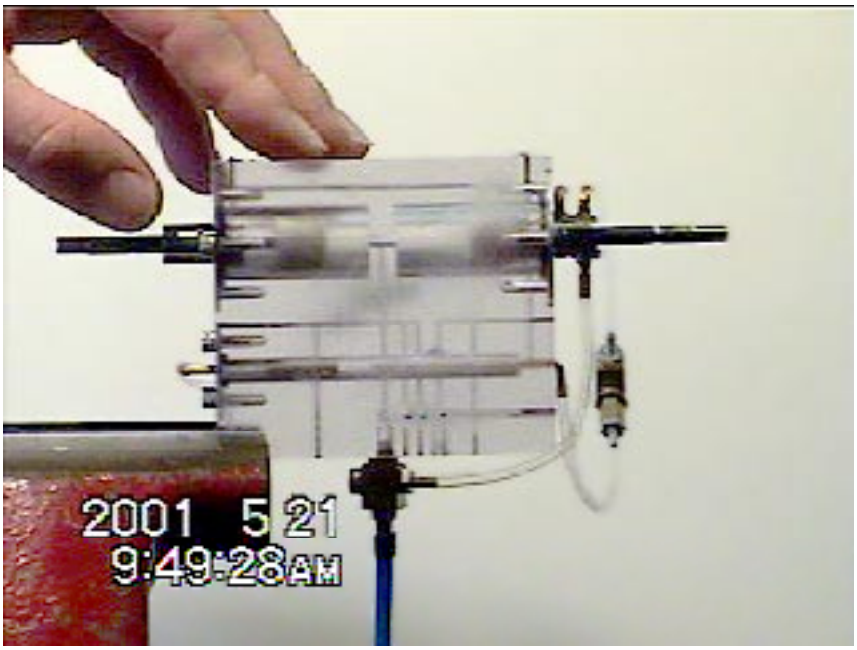

Figure 3-141: Acrylic Kinematic Visualization Testbed

Further examination of the timing revealed that in spite of the symmetrical design, differences in piston-bore friction caused the pistons to reach full extension/retraction at slightly different times. This could be tuned and controlled through friction reduction techniques (diamond coatings, etc.) and higher levels of fabrication precision but a desired goal was to make the RCM inexpensive and robust in the face of varying fabrication tolerances and environmental conditions (principally temperature variations). Effort was therefore begun to make a third iteration that would guarantee symmetrically equal and opposite motion of the split pistons at any pressure over a range of pressures, and at any operational speed.

3.4.2.1 Improved Design for Guaranteed Low-tolerance Symmetry

The fourth generation RCM evolved from the original third generation base mechanism consisting of two lower pair slider joints (piston and valve spool) which had a single degree of freedom,

providing low friction by spreading the wear over the bearing contact surfaces with narrow clearances which facilitated good conditions for lubrication and tight constraint of the motion. As stated above, initial efforts under the present grant focused on the development of a scaled up model manufactured with transparent polycarbonate and larger tolerances to intentionally magnify effects of manufacturing out-of-tolerance, large temperature changes, and prolonged wear. The clear polycarbonate body allowed for quick and precise understanding of performance since the movements of the internal components could be monitored visually in real time.

The original third generation configuration had only two lower pair joints (piston and valve spool) without fixed joints in between, and allowed for a minimal control loop. One of the major improvements over the previous third generation design is the fourth generation RCM valving control having two separate pistons for the extend and retract motions. This was a large departure from the original generations of RCM, and it was done in order to minimize or almost totally eliminate the moments of inertia of action and reaction between the RCM body and the rest of the RCM actuator system. In the third generation RCM the valve actuation was directly (and externally) coupled to the piston pair and cycle speed was directly proportional to gas volume/pressure and the natural harmonics of the kinematic system.

To assure positive action that has timing independent of piston friction, a pneumatic control valve actuation gated by a pilot valve directly machined on the pistons shaft was used. In this manner the actual shifting of the control (spool) valve is directly linked to piston shaft position, however (unlike the third generation devices) no mechanical linkages exist between the piston shaft and control valve, other than pneumatic pilot pressure. The result is positive valve control with no external parts or physical internal linkages. Vibration is eliminated and the resulting RCM is a single piece unit with equal and opposite-acting piston actuators, a single input pressure port, and a single waste gas exhaust port.

In order to avoid out-of-timing scenarios, the two piston shafts were internally mechanically linked in their extend/retract trajectories by a spur gear mounted in a rack and pinion fashion between both (rack portions of the) shafts as shown in Figure 3-142. This new design architecture controls speed by modulating inlet pressure or exhaust volume. Regardless of the speed of reciprocation (even when transitioning between different reciprocation speeds) the actuator extension is equal and opposite from each end of the RCM. Forces are balanced between the two actuator pistons because they share a common pressure source. Axial vibration is eliminated for all operating conditions.

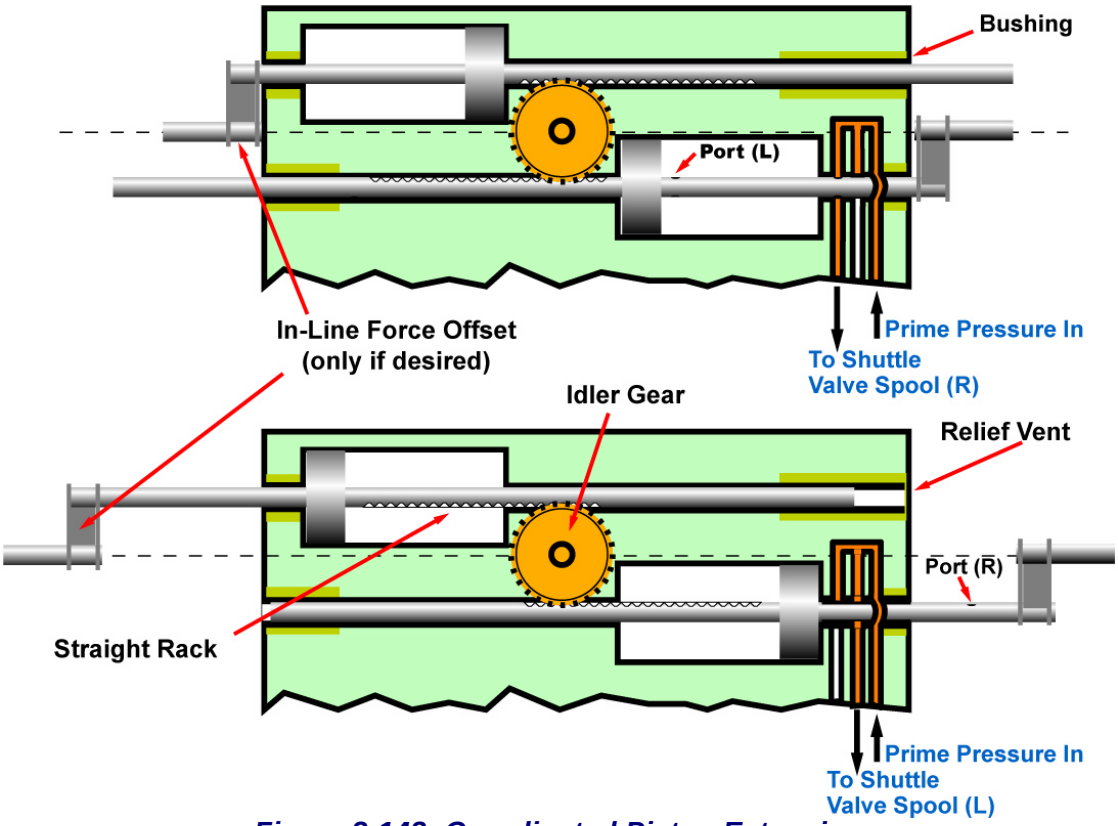

Figure 3-142: Coordinated Piston Extension

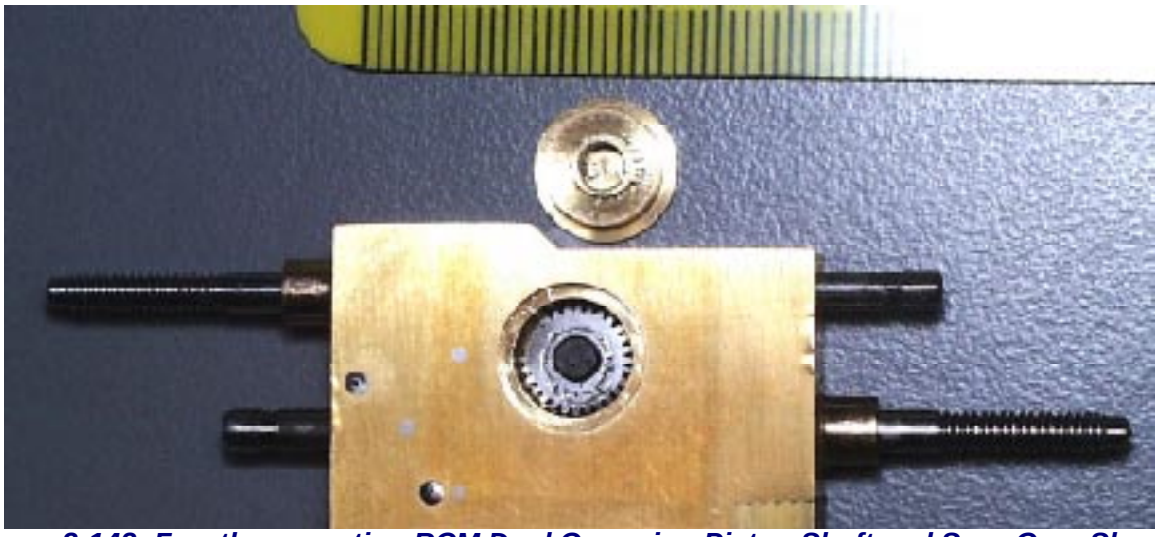

Figure 3-143: Fourth-generation RCM Dual Opposing Piston Shaft and Spur Gear Shown in Place

Advantages of this version of the fourth generation RCM can be summarized as:

1. Vibrationless
2. Internal porting
3. Guaranteed extension synchronization
4. Idler Gear sees low force and has low inertia
5. Force applied along central axis with offset arms
6. Straight rack and idler gear teeth easier to machine
7. Piston shafts can't rotate (due to idler gear)

In addition, by blocking one of the actuator pistons and removing the spur gear, the RCM can be made operate in a single ended mode. It can also be made to function in a “one-shot” mode. In addition the entire system has been manufactured of materials similar in coefficient of thermal expansion, in order to minimize seizures of close tolerance components. Special perfluoro organic and diamond like coatings will be used for high wear areas and gasketing material in a production version.

3.4.3 Sizing of the Entomopter-based Aerial Mars Surveyor

Many of the problems associated with the miniaturization of the terrestrial RCM actuator are relaxed when considering the scaled up Mars version. Further, the reciprocation rate required of the Mars RCM actuator will be less than half that required for the terrestrial version, so although the inertias of the larger component masses will be greater, the forces will be mitigated due to the smaller accelerations of those masses.

The sizing of the Entomopter for aerial Mars survey is driven by the constraints of the Mars environment and choices made regarding the RCM, fuel type, wing parameters, and the baseline mission. Variables to be considered in a first order sizing analysis include the following:

RCM Actuator:

- Single Cylinder Volume (liter)
- Piston Diameter (cm)
- Piston Area (typ) (square cm)
- Single Cylinder Throw (cm)
- Cylinder Pressure (N/m2)
- Temperature of Fuel Decomposition (°K)
- Reciprocation Frequency (Hz)
- Fuel Expansion Ratio (liquid-to-gas)
- Moles of Gas required per cycle (n=PV/RT)
- Liquid Fuel Expended per flap (both cylinders) (liters)
- Liquid Fuel Capacity per min of flight (liters/min)
- Liquid Fuel Weight consumed per minute of flight (kg)
- Linear Force of both Cylinders at full pressure (N)
- Linear-to-Rotational Cam-Follower Ratio
- Combined Rotational Force available (at wing root) (N)

The magnitude of above parameters is a function of the Entomopter sizing, in particular the that of the wings. The power necessary to fly must be evolved in the actuator, and that power depends aerodynamically on wing length, chord, and angle of attack, and camber. Aerodynamic considerations are not the only ones however. Since the wings flap, they must be accelerated and decelerated repetitively. Therefore the inertia of the wing becomes quite important to the peak powers that must be evolved. In fact, inertial forces will typically be much larger than the aerodynamic ones. When considering the power required to flap the wing from an inertial standpoint, wing length, chord, and mass distribution are the primary factors. Wing variables to be considered in a first order sizing analysis for the RCM include the following:

Entomopter Wing Parameters:

- Wing length (two winglet span) (m)
- Center of winglet mass from root (m)
- Average Winglet mass (normalized across span) (kg)
- Max Velocity of winglet at frequency of reciprocation (m/s)
- Peak Acceleration of winglet at frequency of reciprocation (m/s2)
- Peak Force to flap winglet at frequency of reciprocating (N)
- Peak Force to flap 4 winglets (N)
- RMS Force to flap 4 winglets (N)
- RMS Force to flap wing against gas resistance (N)
- Total RMS Force to flap wings (N)

The reason for considering the root mean square (RMS) forces to flap the wing come from the fact that the Entomopter flapping mechanism is resonant, so peak forces are not evolved continuously by the RCM actuator once the flapping angle and rate have been achieved. To do otherwise would be inefficient 'brute-force' flapping which would consume fuel at too high a rate.

3.4.3.1 The Importance of Resonance

An innovation incorporated into the Entomopter design is the use of an “X-wing” flapping mechanism instead of the classical opposed “clapping” wing flap. The X-wing relies on twin wings, one fore and one aft, that pivot like “seesaws” across the central fuselage. If operated 180 degrees out of phase with one another, there will always be two rising wings and two descending wings during the flapping cycle as depicted in Figure 3-144.

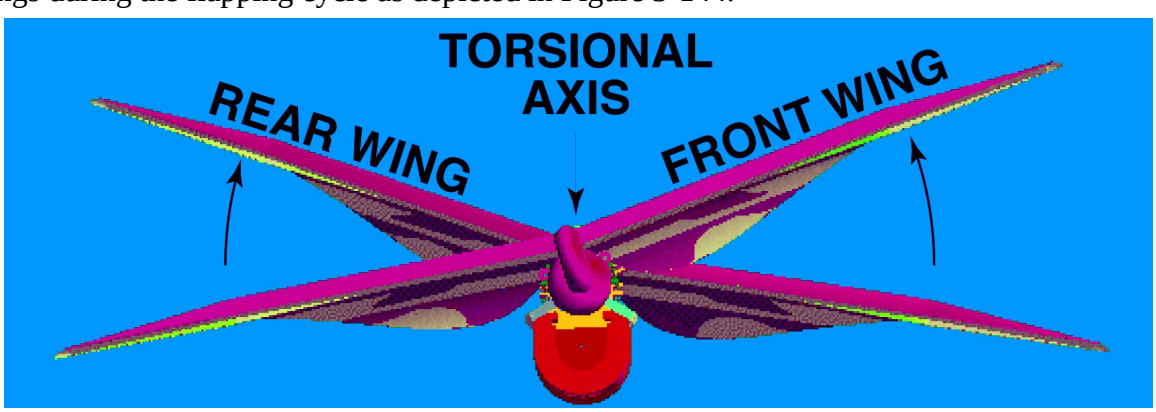

Figure 3-144: X-Wing Flapping as Viewed Along the Torsional Axis.

The forces from each wing pair are resolved across the fuselage. If each wing is producing an upward lift vector on both the down- and upstrokes, then a net lift for the entire vehicle will be realized. By separating the pair of wings at either end of a fuselage, longitudinal (pitch) stability is increased over a single flapping wing pair.

Now, if the fuselage separating the fore and aft wing spars is made of a material with a torsional memory, then the wing spars can become integral to the fuselage and can be torqued out of phase such that the fuselage acts as a torsional spring with a resonant frequency depending on the inertia of the wing spars, the flapping drag of the wings (damping), and the spring constant (K) of the torsional fuselage [185].

This implementation achieves two important things. First, it allows the entire system of fuselage, wing spars, and wing ribs to be constructed as a single piece with no hinged parts. This greatly simplifies the construction of the Entomopter and facilitates it mass production. If further guarantees a higher level of consistency of performance.

More importantly, this construction forms a totally resonant structure. The torsional resonance is essential to make a flapping wing vehicle viable. All insects have resonant structures that store potential energy in either the muscles themselves, or in their exoskeletal parts. Many insects use a substance called resilin to store mechanical potential energy. In order to flap wings, energy must be added incrementally in order make flight viable. Any attempt to flap wings using brute force without a tuned resonant structure will require too much energy. This is particularly obvious when one considers that actual insect muscles (wasp) have been shown to expand and contract only 2% of the overall muscle length during each full beat of the wing [104], while the muscle efficiency and level of resonant energy storage has been estimated for the fruit fly *Drosophila hydei* to be only 10%, with the energy stored elastically for resonant release estimated to be somewhere between 35% and 85% [59].

When first started, the RCM will drive the wings, but if it is sized for autonomic flapping cruise, it will be underpowered for start up. The result will be that the wings flap more slowly at first and with less than the designed flap angle. Since the system is tuned for resonant flapping and the torsional fuselage can release energy back into the wing system upon each flapping cycle, the speed of flapping will increase as will the flap angle until the full range of motion is achieved. Upon starting, the Entomopter will not attempt to lift off (nor will it be able) until the wings have had a chance to reach optimum (resonant) flapping frequency. What this means is that the RCM can be sized for autonomic cruise speeds (resulting in weight savings and optimized fuel consumption for maximum endurance) rather than blindly sizing it for the maximum force required to instantaneously flap the wing over its maximum excursion on the first flap.

3.4.3.2 RCM for the Mars Entomopter

The RCM is comprised of a fuel tank, reaction chamber, actuator, fuel metering, and control circuitry. The actuator is the primary component of the RCM system that affects the vehicle sizing, then to a lesser degree the reaction chamber with its fuel-specific catalyst bed. Of course the fuel tank size affects endurance and overall vehicle weight (when full). The reaction chamber is contained within the fuel tank to preheat the fuel since the highest system temperatures are evolved at this point in the RCM system. Gas generated within the reaction chamber, the quantity of

which is determined and controlled by a fuel metering valve, is directed to the RCM actuator. The surface area of the actuator piston and its range and speed of throw, coupled with the pressure of the gas generated in the reaction chamber, ultimately determine the horsepower or wattage of the RCM system.

The design point offered in Table 3-2 represents a realistic operating configuration for Entomopter on Mars. Here, a flapping frequency of 6 Hz over 75° will evolve 883W of power to nominally allow 14m/s flight in the lower atmosphere when using 1.2 m wings. In addition, this affords a useful lifting capacity of 1.5kg.

Using the 883W power output as a goal (about 1 HP), an RCM can be designed with the following physical parameters:

- 5.08 cm (2 in) Piston Diameter
- 5.08 cm (2 in) Piston Throw
- 3.5 kg/cm2 (50 psi) working pressure (maintained constant by the fuel metering through the reaction chamber)

Working in units of pounds and inches, this results in a piston force of 157 lbs/sec at 6 Hz, or 0.29 HP. Since the fourth generation RCM actuator uses a split piston that is double-acting, the surface area is actually twice that of the single 2 inch face. This results in a power output of 852W. Variations due to friction losses and loading are easily accommodated by adjusting the working pressure. 50 psi is a low value relative to the thousands of pounds of pressure that can be evolved in a correctly designed RCM system. In fact, for the power output by the RCM actuator, its weight is quite modest.

The RCM reaction chamber and actuator are the components that must withstand temperature and pressure extremes. These extremes will be dictated by the fuels used and the design pressure necessary to produce sufficient power for flight. Materials such as columbium coated titanium or Inconel steel are suitable candidates for the design of these components. Titanium alloys such as 6AL-V-2Sn exhibit 150,000 psi yield strength while Inconel-718X yields at 100,000 psi. The density of these materials is 0.164 lbs/in3 and 0.296 lbs/in3 respectively. Since RCM operation as defined above requires only 50 psi, the strength of a cylinder made from materials such as these is immense even with very thin walls. The addition of radial heat rejection fins adds significantly to the strength of the pressure vessels while not contributing greatly to the weight. In the final analysis, the thickness of the material will be dictated more by the desire for dimensional stability than pressure containment.

For a split piston RCM actuator with a 2 inch diameter piston and 2 inch throw (per piston), the overall actuator size would be approximately 4 inches (10.16 cm) in length (excluding actuation shafts), and 2 inches in diameter plus the cylinder wall thickness and cooling fin diameter. Because the Mars atmosphere lack density, larger cooling fins will be desirable, perhaps on the order of 2 inches (5.08 cm) in radial length. To the 4 inch length of the actuator, one must add the length of the plena at each end to accommodate ejectors as shown in Figure 2-1, and the gas bearings with cam-follower wing cuffs to define the total length of the fuselage.

For the Mars Entomopter, the RCM actuator will have a volume of approximately 50.3 in3 (824 cm3), which is slightly larger than the volume of two cola cans. Figure 3-145 is a one-to-one representation of the RCM actuator when printed.

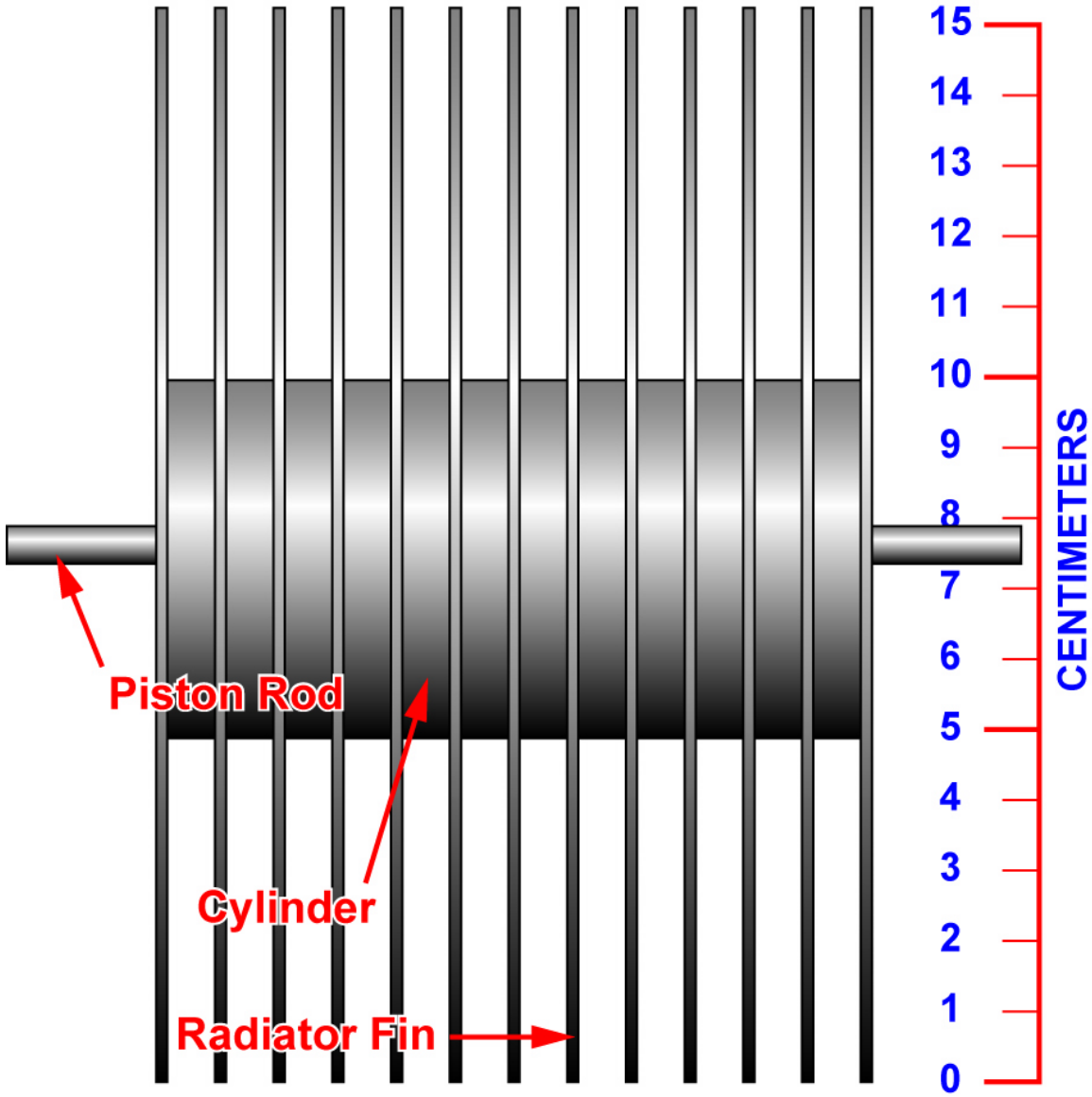

Figure 3-145: Mars Entomopter RCM Actuator (Side View, Actual Size)

The cooling fins will be designed to maximize mixing in the thin Mars atmosphere to create the maximum temperature differential and to prevent hot spots. Applied to the surface of these fins may be surface area-increasing treatments as well as heat-scavenging thermoelectric generator elements. The fins themselves act as strengthening bands like the hoops on a wooden barrel while avoiding unnecessary cylinder wall thickness and weight. As shown in Figure 3-146, the RCM actuator is mounted adjacent to its fuel tank that also contains the reaction chamber. Notional holes are shown in the cooling fins represent a mechanism to enhance mixing while reducing flat plate drag in forward flight.

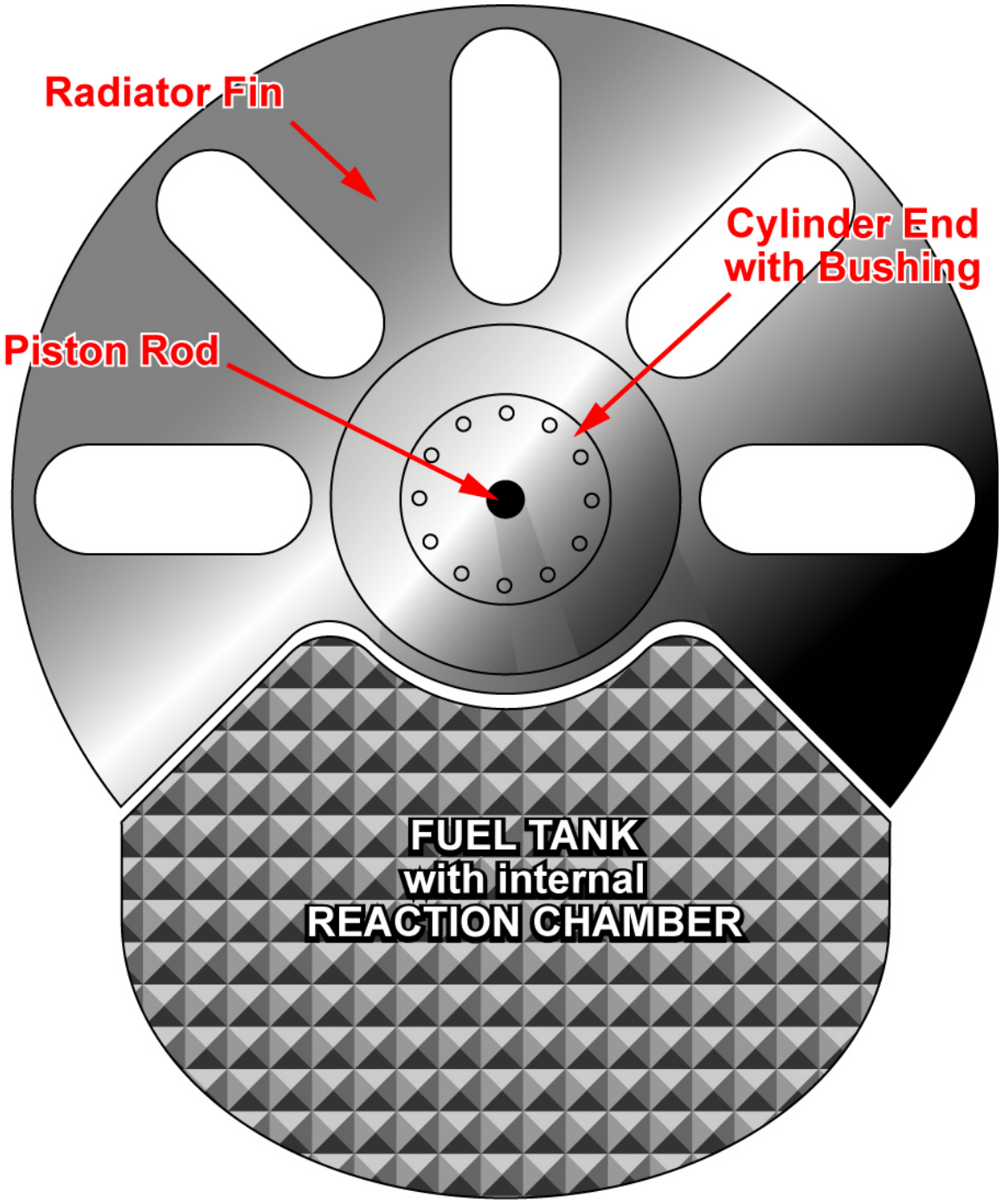

Figure 3-146: Mars Entomopter RCM Actuator (End View)

Internal surfaces between the pistons, and cylinder will be CVD Diamond coated to act as a durable high temperature, low friction interface. Sputtered diamond coatings of only 0.001-10 µm thick can provide friction coefficients of <0.010 with Vickers hardness of up to 3,000. This is in keeping with the philosophy of having no wetted lubricants in the Entomopter system. All surfaces moving relative to each other are either gas bearings (using waste gas from the RCM) or for hot surfaces, diamond coatings.

Based on the density of Inconel-718X (worst case), the RCM actuator with its internal components, plus the reaction chamber and fuel tank is estimated to weigh 0.3 kg. From Table 3-2, a reasonable fuel consumption rate is shown to be 0.011 kg/min. A ten minute flight with a 10% fuel reserve would thus require 0.12 kg of fuel, or 120 ml if the fuel were Hydrazine. This would therefore occupy 120 cm3 of fuel tank volume (about one quarter that of a cola can).

The weight of the RCM system plus a 10 minute fuel charge is on the order of 0.42 kg. Based on Table 3-2, this would leave 1.08 kg for mission payload equipment.

The design space identified by Table 3-2 is not believed to be optimum, but instead is only an example of one combination of flapping frequency, forward speed, fuel type, etc. A parametric study to identify the boundaries of the design space is required before any determination of optimum performance can be assessed. Table 3-2 serves to show that Mars Entomopter operation is indeed possible with useful endurance and payload capacity. Nonetheless, it is still imperative that as much weight as possible be removed from the Entomopter frame of reference and placed on the refueling rover without loss of functionality.

3.5 Fuel Storage and Production

3.5.1 Introduction

A number of mission scenarios have been proposed as a means to establish how to best utilize the capabilities of the Entomopter. From the evaluation of these missions, it became obvious that to maximize the potential of the Entomopter, it would need to be used in conjunction with either a lander or rover vehicle that would act as its base for communications, data and sample storage, and refueling. The ability to refuel the Entomopter is a critical element of the overall capability of the Entomopter and in providing a viable mission architecture. Without this capability the Entomopter would provide very little science return, because it would not be capable of flight for an extended period of time. There are two main approaches that can be taken to provide fuel for the Entomopter during its mission. The fuel can be carried from Earth and stored on the base vehicle or hydrogen can be brought from Earth, stored on the vehicle, and combined with elements gathered from the environment to produce fuel. Ideally, it would be possible to collect all the materials necessary to produce fuel on Mars from the soil or atmosphere. This would enable us to essentially have an infinite mission duration limited only by mechanical failure. However, based on the fuel and environmental survey, all practical fuels that can be used by the Entomopter require hydrogen (which is not available on Mars). Therefore, the fuel chosen to be produced on the surface is hydrogen peroxide, which is simple to make and can be constructed out of the atmospheric gases with the addition of hydrogen.

Because either producing the fuel on the surface or transporting it from Earth requires a finite supply of material from Earth (fuel or hydrogen), the determination of which method to utilize will be based on which one provides the longest mission duration for a given amount of weight. This is a critical determination because it will greatly affect vehicle propulsion system development by dictating the type of fuel that can be utilized. If it is determined that carrying hydrogen is more beneficial than a simple fuel such as hydrogen peroxide will be used. If it is determined that carrying the fuel from Earth is more beneficial, then a more complex energetic fuel can be

considered. The main restriction is that the fuel needs to be a monopropellant. This requirement is based on reducing the complexity of the engine and fuel storage/feed system on the Entomopter. Minimizing wing loading on the Entomopter is critical, so a fuel system with only one tank and associated piping is highly beneficial.

3.5.2 Propellant Selection

The design of the Entomopter requires the generation and expansion of gas for the vehicle to operate. This gas can be generated either by combustion, a catalytic reaction, or sublimation of a material. The gas is necessary to drive the reciprocating piston that drives the wing motion. However, it is also needed for various other aspects of the vehicle's design, including ultrasonic emissions for altimetry and obstacle avoidance, air bearings supply, and lift-augmentation blowing. Because gas generation is an integral part of the operation of the vehicle, the power source must be a fuel-based system.

Fuel selection will be based on the following criteria:

1. Ability of the fuel to meet the environmental conditions of the mission,
2. Ability of the fuel to provide the required amount of gas for the operation of the Entomopter,
3. and ability to make fuel on the Mars surface out of the indigenous materials present in the atmosphere and soil.

The ideal fuel will be a liquid monopropellant. A monopropellant is desirable because it reduces the complexity of storage and delivery systems for the fuel. Liquid form minimizes the storage volume and provides for easier containment.

The operational constraints on the fuel require it to be capable of being stored for extended periods of time (up to 2 years) with little or no degradation, and to be capable of withstanding the deep space environment during transit as well as the environment on the surface of Mars. The main environmental issue during transit and on the Mars surface is the temperature. Assuming that there is no active thermal control or heating available, the fuel must be capable of withstanding temperatures down to -40° C for extended periods of time. If the fuel can remain liquid at these temperatures, this greatly simplifies the propellant delivery system as well as eliminates the need for power- and weight-consuming heaters. This also reduces the overall risk of the mission by eliminating a failure source occurring from improperly thawed fuel or a failed heater.

An overall list of potential fuels (and fuel oxidizer combinations) is listed in Table 3-10 [119, 45]. The ability to meet the requirements listed above will be evaluated, and each will be ranked regarding their applicability for the mission.

Table 3-10: Fuels and Their Phase-change Temperatures

Fuel	Boiling Point (^oC)	Freezing Point (^oC)	Potential Oxidizers	Density (gm/cm^3 at 20° C)
Hydrogen (H2)	-253	-259	Oxygen, Fluorine	0.071(at -253°C)
Ammonia (NH3)	-33.4	-77.7	Oxygen, Fluorine, Nitrogen Tetroxide, Chlorine Trifluoride	0.611
Hydrazine (N2H4)	113.4	1.5	Oxygen, Fluorine, Nitrogen Tetroxide, Chlorine Trifluoride	1.008
Monomethyl Hydrazine (N2H6C)	89.2	-52.5	Nitrogen Tetroxide, Chlorine Trifluoride, Inhibited Red Fuming Nitric Acid	0.874
Unsymmetrical Dimethyl Hydrazine (N2H8C2)	63.8	-57.2	Oxygen, Fluorine, Nitrogen Tetroxide, Chlorine Trifluoride	0.792
RP-1 (C11.74H21.83)	185	-40	Oxygen, Inhibited Red Fuming Nitric Acid	0.801
Methane (CH4)	-161	-183.9	Oxygen, Fluorine	0.415 (at -164°C)
Propane (C3H8)	-42.2	-187.1	Oxygen, Fluorine	0.585(at -44°C)
Diborane (B2H6)	-92.6	-164.8	Difluoride	0.435(at -92.6°C)

Table 3-11: Oxidizers and Their Phase-change Temperatures

Oxidizer	Boiling Point (^oC)	Freezing Point (^oC)	Density (gm/cm^3)
Oxygen (O_2)	-183	-218.8	1.143
Fluorine (F_2)	-188.1	-219.6	1.505
Nitrogen Tetroxide (MON3) (N_2O_4)	21.2	-11.2	1.45
Chlorine Trifluoride (CLF_3)	11.8	-76.6	1.825
Inhibited Red Fuming Nitric Acid (IRFNA) ($0.835HNO_3 0.140NO_2 0.020H_2O 0.005HF$)	~ 60	~ -62.2	1.56
Oxygen Difluoride (OF_2)	-145	-223.9	1.521
Nitrogen Tetroxide (MON25) (N_2O_4)	-9	-54	1.45

Table 3-12: Monopropellants and Their Phase-change Temperatures

Monopropellant	Boiling Point (^oC)	Freezing Point (^oC)	Density (gm/cm^3)	Combustion Temperature (^oC)	Specific Impulse (Isp)
Hydrogen Peroxide ($0.9H_2O_20.1H_2O$)	141.1	-11.5	1.39	757	148
Ethylene Oxide (C_2H_4O)	10.6	-112.8	0.87	1004	199
Nitromethane (CH_3NO_2)	101.2	-29	1.14	2193	245
n-Propyl Nitrate ($C_3H_7NO_3$)	110.5	-101.1	1.057	1078	210
Hydrazine (N_2H_4)	113.4	1.5	1.008	633	199
Hydrazine Propellant Blend (HPB) HPB-1808 (18% HN, 8% water)	100	-20	na		230
61% Hydroxylammonium Nitrate ($(NH_3OH)NO_3$ (HAN) 14% Glycine (H_2NCH_2 CO OH)	100	-35	na		190

Table 3-13: Characteristics of Fuel Candidates

Fuel	Characteristics
Hydrogen	Hydrogen is a stable, noncorrosive, nontoxic material. However, in order to be usable for this mission it must be kept in a liquid state. This requires cryogenic storage which would significantly increase the complexity of the mission.
Ammonia	Ammonia is a stable compound that can be stored in Teflon, 18-8 stainless steel, aluminum or polyethylene. It is mildly toxic but can be fatal in concentrated exposure. The main issue with its use for this mission is that it is in the gaseous state under mission conditions.
Hydrazine	Although its most common use is as a monopropellant, hydrazine can also be used as a bipropellant. It has the same general properties as the monopropellant version; however, its performance is significantly improved when utilized in combination with an oxidizer.
Monomethyl Hydrazine	Monomethyl hydrazine is fairly stable at lower temperatures; however, it becomes unstable above 260°C (500°F). It can be stored in 18-8 stainless steel, aluminum, or Teflon. It is toxic. Its liquid temperature range is well within the requirements for the mission environment.
Unsymmetrical dimethyl-hydrazine (UDMH)	Unsymmetrical dimethyl-hydrazine is stable at low temperatures but becomes violently unstable at temperatures above 260°C (500°F). It can be stored in most materials including mild steel, 18-8 stainless steel, aluminum, Teflon, and polyethylene. It has a lower level of toxicity then hydrazine but more then that of ammonia. Its liquid-state temperature range is well within that of the mission requirements.

Table 3-13: Characteristics of Fuel Candidates (Continued)

Fuel	Characteristics
RP-1	RP-1 is a stable fuel developed for space applications. It is stable up to 370°C (700°F) and is compatible with all common metals, as well as meoprene, asbestos, fluorocarbons and epoxies. Its toxicity is comparable to that of kerosene. The liquid temperature range for RP-1 is within the operating range for the mission. However, the freezing point is at the estimated low temperature for the mission. To insure that RP-1 doesn't freeze during the mission, some active thermal control would probably be required.
Methane	Methane is stable and compatible with all common metals as well as neoprene, asbestos, fluorocarbon, and epoxies. It is essentially nontoxic. The main issue with it is its low boiling point. This would require it to be used as a gas or stored cryogenically. Due to the small volume of the proposed Entomopter, storing the fuel as a gas would significantly limit the flight duration. Also using it as a cryogenic liquid would greatly increase the mission complexity.
Propane	Propane essentially has the same properties as methane. It is stable and compatible with all common metals, as well as neoprene, asbestos, fluorocarbons, and epoxies. The issues with its use are the same as those of methane.
Diborane	Diborane is a gas at room temperatures and will slowly decompose. At higher temperatures it decomposes rapidly. It is compatible with most metals and some organic materials. It has moderate toxicity. The issues with using diborane are significant. It would need to be stored as a cryogenic liquid in order to provide for sufficient mission duration as well as minimize the decomposition rate. Because of these issues it would not be suitable for the proposed Entomopter mission.

Table 3-14: Characteristics of Oxidizer Candidates

Oxidizer	Characteristics
Oxygen	Oxygen is highly reactive and nontoxic. It is noncorrosive and is very stable in storage. The main issue with its use is that it would be in the gaseous form under the mission conditions. This will significantly limit the volume of oxygen which can be stored. Liquid oxygen can be used; however, this brings up significant issues regarding the storage and manufacture of a cryogenic liquid.
Fluorine	Fluorine is highly reactive with almost any material. It can be stored in 18-8 stainless steel or copper but monel is preferred. It is very important that all materials that come into contact with fluorine are thoroughly cleaned so that there are no contaminating particles for the fluorine to react with. There are no nonmetallic materials which are completely unreactive with fluorine. It is also highly toxic and corrosive to body tissue. Like oxygen, it is a gas at mission temperatures. Therefore, it would need to be stored cryogenically in order to be used in the mission.

Table 3-14: Characteristics of Oxidizer Candidates (Continued)

Oxidizer	Characteristics
Nitrogen Tetroxide	Nitrogen tetroxide is a stable compound. It is not highly reactive and can be stored in mild steel, stainless steel, aluminum, Teflon, and polyethylene. Its toxicity is comparable to that of chlorine. Various formulations of nitrogen tetroxide are available. These formulations vary the percent of nitric oxide in the formulation. This change in the nitric oxide content can affect the freezing point for the propellant. The mixtures of nitrogen tetroxide shown in the table above have varying amounts of nitric oxide. MON 25 (25% mixed NO) has a significantly decreased freezing point over MON 3 (3% mixed NO). This ability to lower the freezing point of nitrogen tetroxide makes it applicable to the mission environment and would eliminate the need for thermal control of the propellant.
Chlorine Trifluoride	Chlorine trifluoride is a stable oxidizer that can be stored in 18-8 stainless steel, nickel and monel. However, most common metals can be used if they are free of contaminants. It is highly toxic with a toxicity comparable to fluorine. Its liquid-state temperature range is more than sufficient to meet the mission requirements.
Inhibited Red Fuming Nitric Acid (IRFNA)	IRFNA is subject to decomposition at elevated temperatures, and its decomposition rate is directly related to temperature. It can be stored in 18-8 Stainless steel, polyethylene, and Teflon. It is toxic and corrosive to body tissue. The liquid-temperature range of IRFNA is sufficient to keep the oxidizer in a liquid state throughout the proposed mission duration.
Oxygen Difluoride	Oxygen difluoride is stable at normal room temperature but becomes increasingly unstable at elevated temperatures. It can be stored in 18-8 stainless steel, copper, aluminum, monel, and nickel. Nonmetallic materials are generally not compatible. It is highly toxic and corrosive to body tissue. The main issue is that it is a gas at mission temperatures. In order to be usable it would need to be stored cryogenically in order to be used in the mission. This would add significant risk and complexity to the overall mission.

Table 3-15: Characteristics of Monopropellant Candidates

Monopropellant	Characteristics
Hydrogen Peroxide	Hydrogen peroxide has a flight heritage dating back to the 1930s, although until recently, the technology has been dormant. It is seeing a revival of sorts, primarily as an oxidizer in a bipropellant combination, but also as a monopropellant. The main advantage of hydrogen peroxide is that it is nontoxic. However, the freezing point is higher then what is necessary to perform the mission without thermal control. There are a few options for dealing with this freezing issue. A passive thermal system may be used to maintain the temperature above freezing. This may be possible since its freezing point is within 30° C of the expected environmental conditions. Another advantage of this propellant is that it is the fuel presently used by GTRI in their Entomopter designs. Therefore, there is significant experience and history with its use in this type of vehicle. Hydrogen peroxide decomposes in the presence of a catalyst, such as carbon, steel or copper. For storage it doesn't react with certain materials, such as aluminum, tin, glass, polyethylene or Teflon.

Table 3-15: Characteristics of Monopropellant Candidates (Continued)

Monopropellant	Characteristics
Ethylene Oxide	Ethylene oxide remains liquid over a temperature range that is more than adequate to meet the mission requirements. It is generally stable, but the polymerization rate is increased in the presence of some materials. Storage materials it is compatible with include 18-8 stainless steel, aluminum, mild steels, copper, nylon, and Teflon. This material is relatively toxic and must be handled with caution.
Nitromethane	Nitromethane's temperature range is nearly within the range required by the mission. It would require some insulation or thermal control to assure it would not freeze. It doesn't react with 18-8 stainless steel, aluminum or polyethylene. These materials can be used for storage. The main issue with its use is that it may detonate under conditions of confinement, heating, and mechanical impact, any of which can possibly be experienced during this mission. Also, it is relatively toxic and must be handled with caution.
n-Propyl Nitrate	n-propyl nitrate is capable of remaining liquid well within the temperature range of the mission. It is relatively stable and insensitive to mechanical or thermal shock. It can be stored in containers made of either 18-8 stainless steel, aluminum, polyethylene, Teflon, nylon, Orlon, Dacron or Mylar. This material has no serious toxicity problems, which allows for easy handling.
Hydrazine	Hydrazine monopropellant has been used in spacecraft for the last 30 years. These have been mainly for low thrust applications like satellite station keeping. Decomposition is achieved by a catalyzed reaction with a metal oxide. Materials that are compatible with hydrazine and will not react include Teflon, 18-8 stainless steel, polyethylene, and aluminum. The main issues with using hydrazine are that it is highly toxic and has a high freezing point (approximately 1.5° C). Because of this high freezing point, significant heating would be required throughout the mission in order to maintain the propellant in its liquid state.
Hydrazine Propellant Blend (HPB)	HPB represents a family of monopropellant formulations composed of hydrazine, hydrazinium nitrate (HN), and water. The addition of NH and water serves to depress the freezing point and increase the performance of plain hydrazine. Several HPBs were developed and tested in the 1960s and 1970s primarily for military applications. HPBs are receiving renewed attention as a low freezing point monopropellant. Presently NASA is sponsoring HPB development work at Primex Aerospace.
HAN	HAN is a family of monopropellants composed of an oxidizer-rich salt, a fuel component and water. These types of propellants have been under development by NASA over the last decade. HAN-based monopropellants offer a high density, low freezing point, nontoxic alternative to hydrazine.

3.5.2.1 Propellant Candidates

One of the main requirements in propellant selection is that it must be in liquid form during storage. If possible, this would mean that the propellant be maintained in this state throughout the mission with a minimum amount of thermal control. This minimizes the complexity of storing, transporting, and manufacturing the propellant and greatly simplifies the Entomopter and support-vehicle design. Therefore, based on this requirement, most of the propellants listed and described in the previous section are not applicable to the Entomopter mission.

Table 3-16 lists the potential bipropellant combinations and monopropellants that would be applicable. Also given is the Isp of each propellant. This can be used to gauge the energy contained within the propellant. The higher the Isp the greater the energy released during combustion.

Table 3-16: Propellant Candidates based on Temperature and Operational State Requirements

Propellant	Oxidizer/Fuel Ratio	Isp	Combustion Temperature (^{o}C)
Fuel: Monomethyl Hydrazine Oxidizer: Nitrogen Tetroxide	2.20	288	3,122
Fuel: Monomethyl Hydrazine Oxidizer: Chlorine Trifluoride	3.00	283	3,318
Fuel: Monomethyl Hydrazine Oxidizer: IRFNA	2.50	274	2,848
Fuel: UDMH Oxidizer: Nitrogen Tetroxide	2.70	286	3,162
Fuel: UDMH Oxidizer: Chlorine Trifluoride	2.85	278	3,306
Fuel: RP-1 Oxidizer: IRFNA	4.90	263	2,881
Monopropellant: Hydrogen Peroxide	na	148	757
Monopropellant: Ethylene Oxide	na	199	1,004
Monopropellant: Nitromethane	na	245	2,192
Monopropellant: n-Propyl Nitrate	na	209	1,077
Monopropellant: HPB	na	200	----
Monopropellant: HAN	na	---	----

3.5.2.2 Fuel Production

A key Entomopter capability is our ability to refuel it while it is on the Mars surface. One potential method for achieving this is to produce the fuel from resources found within the Mars environment. A list of the elements and compounds is given in the environmental section for both the soil and atmosphere. From the listing of elements and compounds available, it can be seen that there is very little hydrogen available on Mars. The only compound containing hydrogen is the trace water vapor within the Mars atmosphere, and this constitutes only 0.03% of the atmosphere makeup. However all the propellants listed in Table 3-13 require hydrogen. Therefore it will need to be assumed that unless a water source is found on Mars, the hydrogen needed to produce the selected fuel will need to be brought from Earth. As of this writing, data from the Mars Odyssey spacecraft has indicated that there may be large quantities of subsurface water on

Mars [199]. However, insufficient information is available to determine if the potential water could be extracted and utilized by the Entomopter system for fuel production. Therefore, the fuel selection and analysis will be based on the need to provide hydrogen from Earth. As more information is obtained on the potential of utilizing the subsurface water on Mars, the results of this selection process may change.

The remaining elements that make up the fuels listed in Table 3-16 are present on Mars with the exception of fluorine. The lack of fluorine, as well as the scarcity of chlorine, eliminates the following four propellants as potential candidates for fueling the Entomopter: Monomethyl hydrazine and chlorine trifluoride, monomethyl hydrazine and IRFNA, UDMH and chlorine trifluoride, RPI and IRFNA. Also HAN and the HPB monopropellants were eliminated due the complexity in their chemical makeup, which would be very difficult to manufacture.

Because the remaining propellants all require hydrogen (which must be brought from Earth) the next step is to determine which of these propellants minimize this hydrogen requirement. Table 3-17 shows the percentage of hydrogen on a weight basis for the candidate fuels.

Table 3-17: Percent of Hydrogen by Weight for the Various Candidate Propellants

Fuel/Oxidizer	Chemical Makeup	Percent Hydrogen by Weight
Monomethyl Hydrazine and Nitrogen Tetroxide	(N2H6C)+2(N2O4)	2.61%
UDMH and Nitrogen Tetroxide	(N2H6C)+2.7(N2O4)	1.96%
Hydrogen Peroxide	(0.9H2O20.1H2O)	5.38%
Ethylene Oxide	(C2H4O)	9.09%
NitroMethane	(CH3NO2)	4.92%
n-Propyl Nitrate	(C3H7NO3)	6.66%

Based on Table 3-17, the primary choice to minimize the need for hydrogen is the bipropellant UDMH with nitrogen tetroxide. However, a bipropellant system will increase the complexity of the overall mission. It will require two separate production plants, one for the fuel and one for the oxidizer, as well as separate storage and fueling ports. Unless engine performance becomes a significant issue, the primary choice for the propellant will be a monopropellant that significantly reduces the complexity of the production system.

Overall, the propellant selection can be narrowed to four potential candidates, two bipropellants and two monopropellants: monomethyl hydrazine fuel and nitrogen tetroxide oxidizer, UDMH fuel and nitrogen tetroxide oxidizer, hydrogen peroxide and nitromethane. Ethylene oxide and n-propyl nitrate were eliminated as potential fuels due to the relatively higher percentage of hydrogen content. Of these remaining four fuels, hydrogen peroxide is the primary candidate for production on Mars.

The production of these fuels will require the ability to produce nitrogen, carbon and oxygen from the atmosphere present on Mars. The composition of the atmosphere and soil is listed under the environmental section. For the most part, these elements can be extracted from the atmosphere. The carbon and oxygen can be obtained by breaking apart the CO_2 within the atmosphere, and the nitrogen can be obtained by separating it out directly from the atmosphere.

The oxygen and carbon can be produced in a fashion similar to that planned for the Mars 2003 Surveyor Lander. [137]. In this scheme, the atmosphere will be initially compressed using a sorption compressor. This type of compressor contains no moving parts. It achieves its compression by alternately cooling and heating a sorbent bed of materials. These materials adsorb CO_2 at low temperatures and release them at high temperatures. If the correct material can be found, this same process can be used to separate out nitrogen from the atmosphere.

Once the CO_2 is removed from the atmosphere, the carbon and oxygen will then need to be separated. This can be accomplished by using a zirconia solid-oxide generator. The zirconia acts as an electrolyzer at elevated temperatures. At temperatures in excess of 750° C it will strip off oxygen ions from the CO_2. If a current is applied to the zirconia material it will also act as an oxygen pump and pass the oxygen atoms through its crystal lattice thereby separating the oxygen out of the CO_2.

Based on these processes, it should be possible to generate the main constituents of the propellants. The next step would be to produce a reactor and process that can recombine these elements into the proper compounds to construct the desired propellant.

It is also worth mentioning an additional nonconventional propellant concept that can potentially be used as fuel for the Entomopter. This concept is to utilize the atmosphere CO_2 directly as an oxidizer. CO_2 can react with various metals and act as the oxidizer for these reactions. The potential reactions that can utilize CO_2 as an oxidizer are listed in Table 3-18.

Table 3-18: Combustion of Various Metals with CO_2
[289]

Metal	Reaction	Ignition Temperature
Mg	$Mg + CO_2 = MgO + CO$	340°C
Li	$2Li + CO_2 = Li_2O + CO$	851°C
Al	$2AL + 3CO_2 = AL2O_3 + CO$	>2000°C

The experimental work outlined in reference 4 demonstrated that CO_2 would combust with the metals listed in Table 3-18. In this experimental work, the CO_2 pressure was kept at 1 atmosphere (Earth) with a flow rate of 0.5 m/s. On Mars this would require a 100:1 compression ratio of the atmosphere to provide the same combustion environment. Additional work would need to be performed to determine the burning properties at lower CO_2 pressures. If lower pressures could be used, this would significantly reduce the compression ratio. Even if significant compression is required, it may be possible to achieve this through the motion of the drive engine

piston, similar to that of a conventional internal combustion engine. However, there are a number of issues associated with the used of this type of fuel. Mainly, the solid metal oxides will condense within the combustion cylinder and potentially clog the engine and be a source of wear on the piston.

The main products of the combustion reactions listed in Table 3-18 are condensed metal oxide and CO. Of these, Mg is the easiest to ignite and has the highest burn rate, which is necessary to produce the required gas pressure for operation of the vehicle.

Magnesium oxide, which makes up about 7.8% of the soil on Mars, is present in significant enough quantities to potentially mine the soil for the magnesium that is needed. If the magnesium can be effectively separated out of the soil, it will probably need to be dissolved in solution to make it usable as a propellant [278, 279]. One potential candidate would be methanol (CH_3OH). However, the use of this type of fluid would require a supply of hydrogen as well as the ability to separate out carbon and oxygen from the atmosphere. This diminishes the attractiveness of a system that utilizes the CO_2 directly out of the Mars atmosphere. Based on results given in References 278 and 279, there are other significant issues with using methanol or any other fluid as a carrier for the magnesium. The magnesium would tend to settle out of the mixture, requiring frequent mixing. Also, the carrier fluid would need to evaporate before ignition of the magnesium would take place. There may be other carrier fluids that would better than methanol; however, a different approach using a gas as the carrier might work.

A gas would eliminate the problems of evaporation and mixing, as well as the issues associated with the production of the carrier fluid. The ideal gas to use would be the Mars atmosphere itself. It may be possible to devise a mixing chamber on board the vehicle that would be used to mix the magnesium and atmosphere (CO_2) prior to injection into the combustion chamber. The atmosphere could be pumped in at a rate that would stir up the magnesium particles and form a suspension of magnesium power within the tank. The magnesium could be gravity-fed into this mixing chamber at a rate that would maintain the correct concentration of magnesium within the chamber (similar to sand falling through an hourglass). The rate of magnesium power that enters this mixing chamber could be controlled by changing the size of the orifice through which the magnesium power passes. This suspension could then be injected into the combustion chamber. This scheme would not require any gas production and would utilize a fairly simple control scheme of adjusting the atmosphere injector and opening to the magnesium power tank. The mixing chamber would need to be large enough to allow the magnesium to be suspended at the correct mixture ratio prior to being injected into the chamber.

The design and evaluation of a CO_2 burning engine is beyond the scope of this effort; however, the concept has some potential benefits and may be worth evaluating in further detail during any future effort.

3.5.3 Propellant Production and Storage

To evaluate the tradeoff between carrying hydrogen and producing fuel on Mars or just carrying the fuel directly, the overall mass of a system that produces fuel on the surface will be estimated, and this will be compared to the amount of fuel that can be carried directly from Earth utilizing

the same mass. The following system components will be evaluated for producing hydrogen peroxide fuel from the atmospheric gases and stored hydrogen:

- Hydrogen storage system
- Zirconia oxygen generator
- Sorption compressor
- Hydrogen peroxide reactor
- Power source

3.5.3.1 Hydrogen Storage System

Hydrogen is the only component of the potential fuels identified that cannot be obtained from the material found on Mars. Therefore, if fuel is to be produced utilizing the in situ resources available on Mars, hydrogen will need to be brought from Earth. The main issue with storing and using hydrogen is its very low density. At ambient conditions, 1 liter of hydrogen contains only 10.7 KJ of energy. Even in its liquid state, the volumetric energy density of hydrogen (8.4 MJ/liter) is less then half that of other fuels (natural gas 17.8 MJ/liter, gasoline 31.1 MJ/liter). Storing a sufficient amount of it for use requires a large volume. Therefore, to make it practical the storage method must increase the hydrogen density as much as possible.

The first step in evaluating the fuel production system is to determine the best method for storing hydrogen. Conventional methods of storage are as a compressed gas or as a cryogenic liquid. Work is being done in these areas that would make them more applicable to a space mission by reducing storage tank weight (carbon composite tanks) or increasing the density of cryogenic hydrogen (gelled or slush hydrogen). In addition, new storage methods are being devised that may be capable of storing hydrogen without the need for high-pressure tanks or the need to manage a cryogenic liquid (carbon nanotubes, carbon fullerenes, and hydrides).

Hydrogen can be stored as either a gas or liquid. However, the stored hydrogen is only one part of the fuel system. The hydrogen must be reacted with oxygen to form hydrogen peroxide, which is the fuel chosen for production on Mars. The layouts for each of these storage and production systems are given in Figures 3-160 and 3-161. Aside from the storage tank and its associated components, the description and analysis of the remaining components is common to both systems.

3.5.3.1.1 Gaseous Hydrogen Storage

3.5.3.1.1.1 Pressure Tank

High pressure hydrogen storage is the most conventional type of hydrogen storage. As the storage pressure increases, the density of the hydrogen gas will also increase. This relationship is shown in Figure 3-147. This figure represents the change in density (ρ) of hydrogen gas at various temperatures and pressures. This figure is based on the ideal gas law with a compressibility

factor (Z) for the hydrogen gas. [22] Where P and T are the gas pressure and temperature respectively and R is the gas constant for hydrogen (4157 N m/kg °K)

$$\rho = P / ZRT$$ **Equation 3-36**

$$Z = 0.99704 + 6.4149E\text{-}9\ P$$ **Equation 3-37**

The tradeoff with utilizing high density/high pressure storage is the increase in tank mass necessary to withstand the higher pressures. The wall thickness of the tank will increase with the increasing hoop stress due to the higher gas pressure. The calculation of the tank mass for hydrogen gas stored under pressure is a fairly straightforward analysis. This analysis is outlined below.

For this analysis it is assumed that hydrogen will follow the behavior of an ideal gas represented by the equation of state,

$$P\ V_H = nZRT$$ **Equation 3-38**

where R is the gas constant for hydrogen and has a value of 4157.2 (N m/°K kg), P (Pa) is the pressure of the gas, V_H (m^3) is the volume, and T (°K) is its temperature.

Using the gas constant given above, Equation 3-42 can be restated as follows, where m_H is the mass of hydrogen:

$$V_H = 4157.2\ Zm_H\ T / P$$ **Equation 3-39**

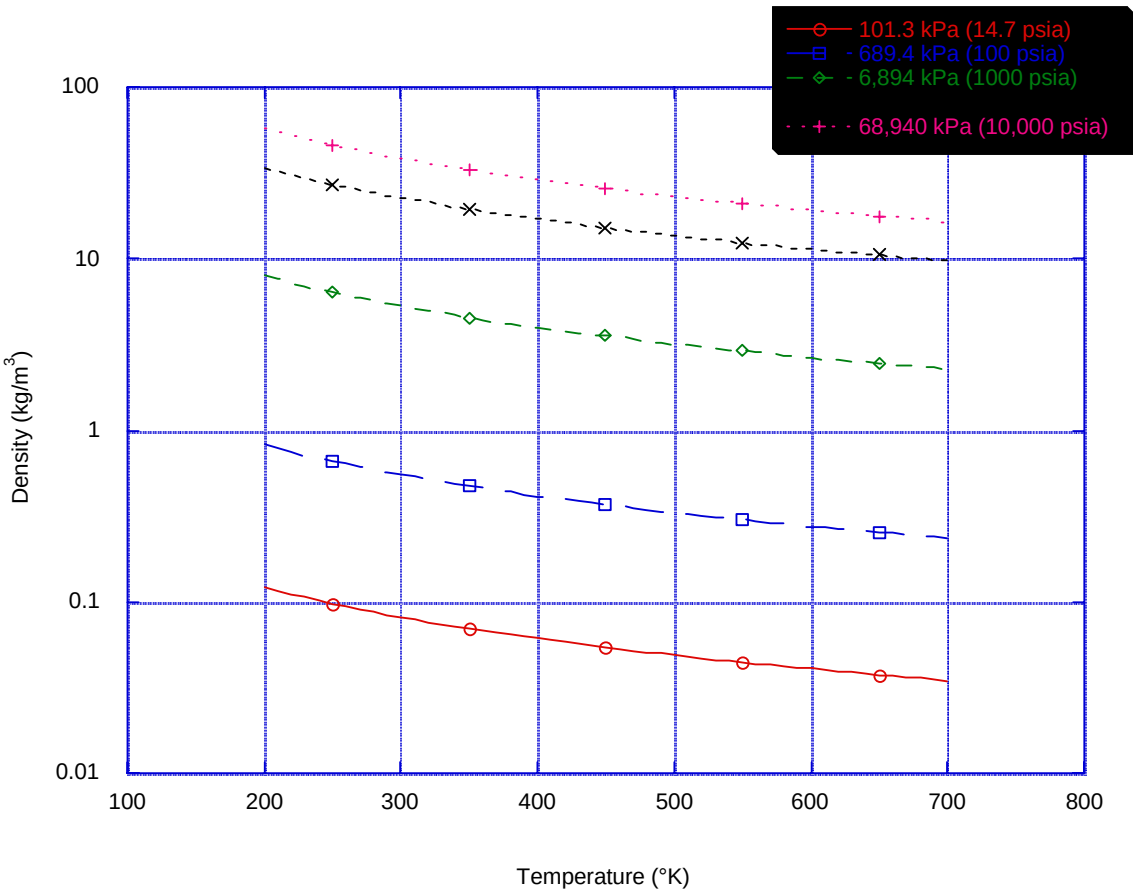

Figure 3-147: Hydrogen Density at Various Pressures and Temperatures

The tank radius (r) can be calculated from the volume determined in Equation 3-39. The tank is assumed to be either a sphere or a cylinder. The sphere is actually a special case of the cylinder in which the length (L) is zero. Equation 3-40 can be solved for r through an iterative process.

$$V_H = 4 \pi r^3 / 3 + \pi r^2 L$$ ***Equation 3-40***

With the radius and tank pressure known, the required wall thickness (t_w) can be determined based on the maximum allowable stress (σ_y) and a factor of safety (FoS). Equations 3-41 and 3-42 represent the wall thickness for a spherical tank and a cylindrical tank with hemispherical end caps, respectively.

$$t_w = P\ r\ FoS / \sigma_y$$ ***Equation 3-41***

$$t_w = P\ r\ FoS / (2\ \sigma_y)$$ ***Equation 3-42***

From the wall thickness and the density of material used to construct the tank (ρt) the mass of the tank (m_t) can be calculated.

$$m_t = \rho_t (4/3) \pi (r + t_w)^3 + \pi (r + tw)^2 L - V_H$$ ***Equation 3-43***

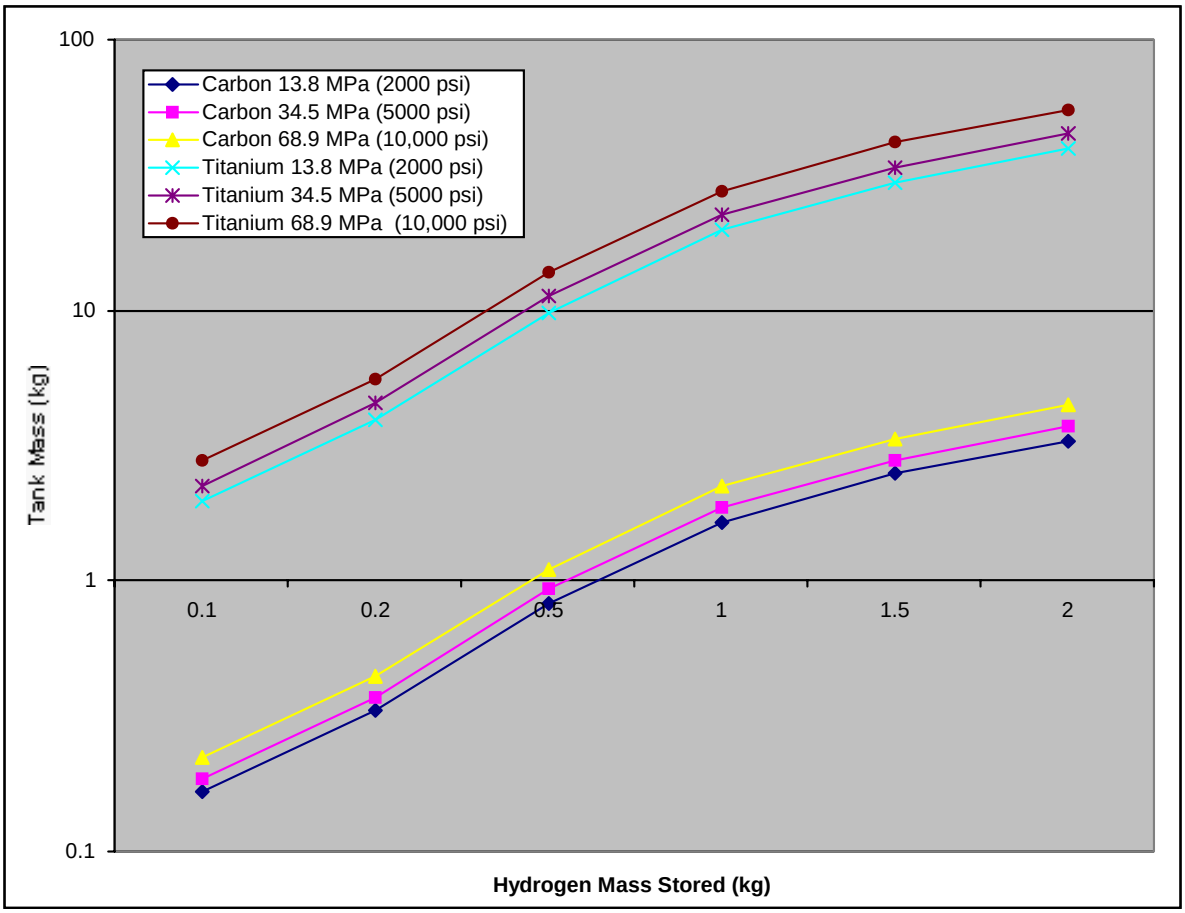

Figure 3-148: Spherical Pressure Tank Mass Constructed of Carbon and Titanium at Various Storage Pressures

Figure 3-148 shows how the mass of the tank will vary with different construction materials. The curves were generated for titanium and carbon over a range of hydrogen storage masses. The effect of storage pressure on the tank mass is due to the compressibility factor, Equation 3-37, that was used. The change in storage pressure also has a significant effect on the volume (or tank radius) as would be expected. This effect is shown in Figure 3-149. This figure represents the same hydrogen storage volumes given in Figure 3-148. This demonstrates that storing hydrogen gas at high pressures will minimize volume with a lesser effect on the overall tank mass.

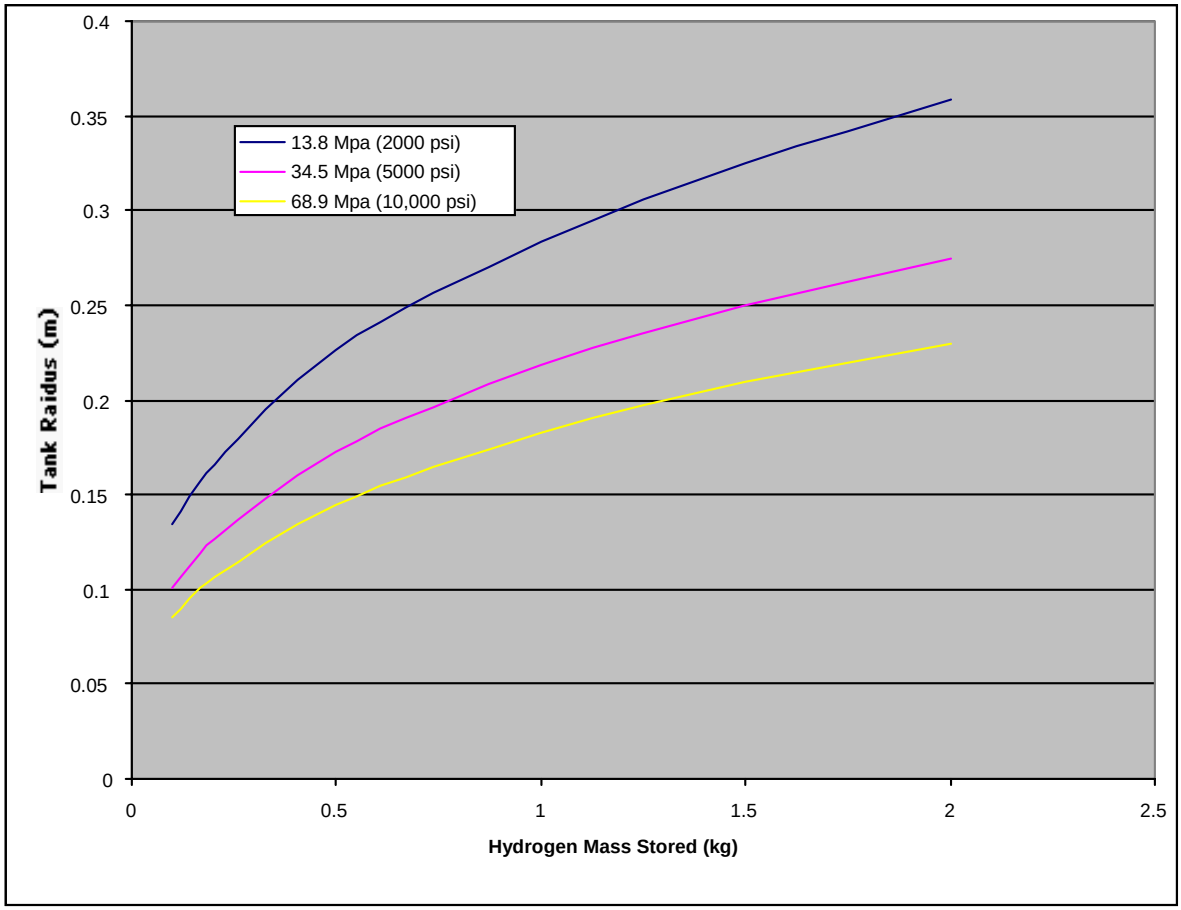

Figure 3-149: Tank Radius as a Function of Storage Pressure for Various Hydrogen Mass

The material utilized in constructing the tank can be either a metal such as steel, titanium, aluminum or a composite. Since most composites are porous to hydrogen, a composite tank will require a liner to prevent the hydrogen from migrating through the tank wall. Liner materials are usually a type of polymer or a metal such as aluminum. Also, coatings are being investigated as a lightweight means of preventing hydrogen penetration through the tank. Composite tanks offer the best weight density of hydrogen. Tanks under development at Quantum Technologies have achieved up to 11.3% hydrogen by weight. However, a more realistic number for composite storage tanks in practical use is between 7.5% and 8.5% weight of hydrogen.

In addition to the stress placed on the tank due to the pressure-loading additional issues will arise when using a high-pressure tank for space applications. These issues include radiation effects, thermal cycling, aging, creep, fatigue, and hydrogen embitterment. Depending on the tank material chosen, the design life and the operating pressure each of these factors would need to be investigated to determine their effects on a particular tank design.

To maximize the storage volume for a given tank placement, the ideal configuration would be to construct a conformal tank. A conformal tank can hold up to 20% more hydrogen in a given envelope and pressure then a cylindrical or spherical tank. This presumes that a conformal tank

can use more than 80% of its envelope volume. This increase in usable storage compared to a conventional cylindrical tank is shown in Figure 3-150.

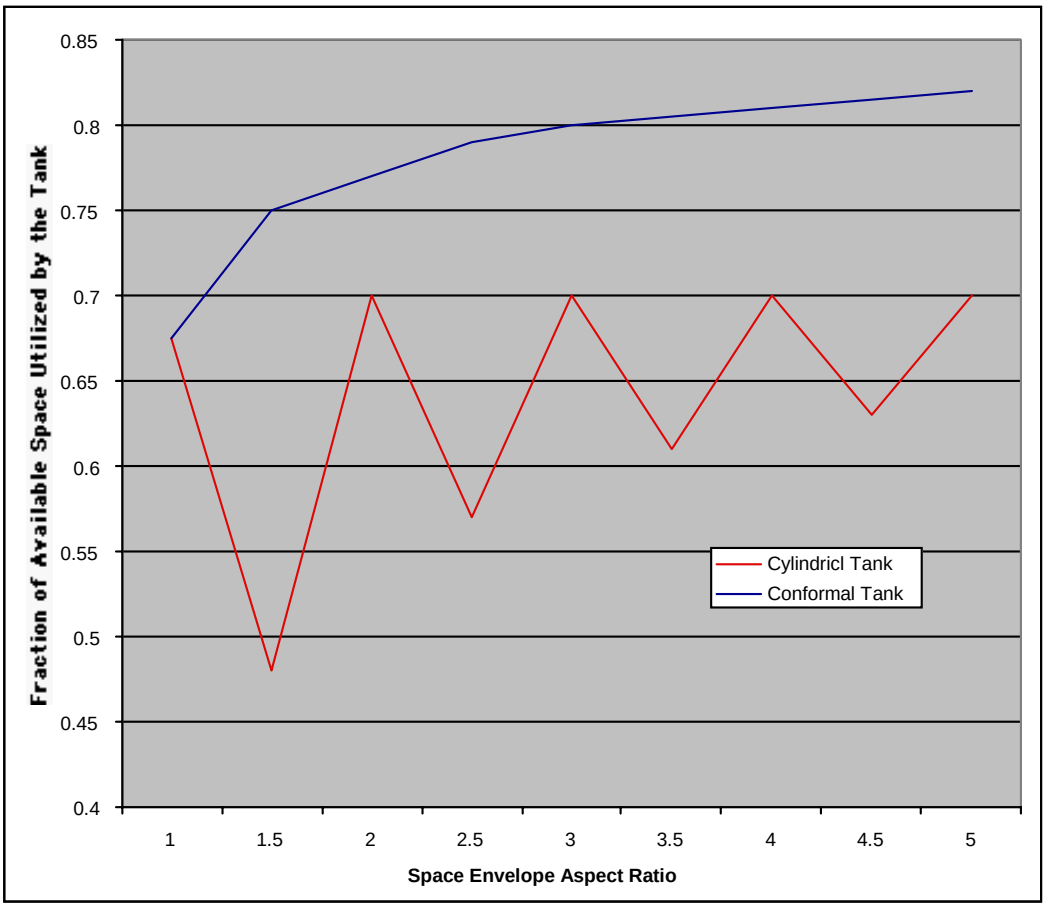

Figure 3-150: Effect of Conformal Tanks on Available Space Utilization [91]

The ability to construct a lightweight, high-pressure conformal tank is presently being investigated by Thiokol Propulsion under a Department of Energy contract. [91]

3.5.3.1.1.2 Metal Hydride

Metal hydrides are metallic alloys that absorb hydrogen. These alloys can be used as a storage mechanism because of their ability to not only absorb hydrogen but also release it. The release of hydrogen is directly related to the temperature of the hydride. Typically, metal hydrides can hold hydrogen equal to approximately 1% to 2% of their weight. If active heating is supplied to remove the hydrogen this can increase to 5% to 7% of the hydride weight. If the temperature is held constant, the hydrogen is released at a constant pressure. The metal hydride tank can be used repeatedly to store and release hydrogen. The limiting factor on its ability to store hydrogen is the accumulation of impurities within the tank. These impurities fill the spaces that would normally store hydrogen, thereby reducing tank capacity.

The key trade off to utilizing a metal hydride storage system is whether there is sufficient heat-generation capability to extract the hydrogen from the hydride. The heat available to the hydride must also address the inefficiencies associated with the heat transfer device used to move the

heat from the source to the hydride. Hydrides constructed of heavy metals, such as vanadium, niobium, and iron-titanium, will release hydrogen at ambient temperatures. This avoids the heating issue, but these hydrides tend to be heavy and reduces the percentage weight of hydrogen carried. Other hydrides constructed of lighter materials will need to be heated from an auxiliary source until the temperature is sufficient to release hydrogen.

Table 3-19 shows a list of potential metal hydride storage materials and the density of the hydrogen stored within the material. It should be noted that the density given in this table is for the hydrogen alone and does not represent the hydride material or any other ancillary components needed for the storage system to operate.

Table 3-19: Metal Hydrides and Hydrogen-density Capability
[4]

Metal Hydride	Hydrogen Density (kg/m^3)
Magnesium (MgH_2)	109
Lithium (LiH)	98.5
Titanium ($TiH_{1.97}$)	150.5
Aluminum (AlH_3)	151.2
Zirconium (ZrH_2)	122.2
Lanthanum ($LaNi_5H_6$)	89

Even though the storage density of hydrogen in a metal hydride is high, the total mass of the system is large. Table 3-20 lists the specifications for commercially available state-of-the-art metal hydride storage tanks.

Table 3-20: Commercially Available Metal Hydride Hydrogen-storage Specifications
[90]

Volume H2 (m2)	Mass H2 (kg)	Metal Hydride Tank Mass (kg)	Percent Mass of H2 of Total Tank Mass
0.042	0.0036	1	0.36%
0.068	0.0058	0.86	0.68%
0.327	0.0273	6.1	0.45%
0.906	0.0767	16.78	0.46%
1.274	0.1078	24	0.45%
2.547	0.214	36	0.59%

Other systems under development can offer higher mass fractions of hydrogen. These systems promise mass fractions up to 5% (6 kg hydrogen storage for a 120-kg system mass). [79]

3.5.3.1.1.3 Carbon Nanotubes

Carbon nanotubes are tubular carbon structures on the order of 2 nm in size. These structures are theoretically capable of storing hydrogen within the tube structure. The storage mechanism is similar to that of metal hydrides, except the hydrogen-storage capability is much greater. It is theorized that carbon nanotubes can store anywhere from 4% to 65% of their weight in hydrogen. This technology is very new and still in the development stage. However, if it can live up to its projected potential, this would by far be the lightest, most efficient way to store hydrogen.

3.5.3.1.1.4 Glass Microspheres

Glass microspheres store hydrogen in tiny hollow spheres of glass. If heated, the spheres' permeability to hydrogen will increase. This provides the ability to fill the spheres by placing the warmed spheres in a high-pressure hydrogen environment. The hoop stresses achievable for glass microspheres can range from 345 Mpa (50,000 psi) to 1,034 Mpa (150,000 psi) [216]. The corresponding maximum pressure sustainable by the micro-sphere is calculated in the same manner as that for any other sphere. This is given by Equation 3-42, which would be solved for P for a given wall thickness (on the order of 0.68 µm). On the high end, this is comparable to the stress achievable with carbon fiber tanks. Once cooled, the spheres lock the hydrogen inside. The hydrogen is released by subsequently increasing the temperature of the spheres. This method of storage provides a safe, contamination-resistant method for storing hydrogen.

The fill rates of microspheres are related to the properties of the glass used to construct the spheres, the temperature at which the gas is absorbed (usually between 150° C and 400° C) and the pressure of the gas during absorption. Fill and purge rates are directly proportional to the permeability of the glass spheres to hydrogen with increases with increasing temperature. At room temperature, the fill/purge rate is on the order of 5,000 hours, at 225° C, it is approximately 1 hour; and at 300° C, it is approximately 15 minutes [216]. This dramatic increase in hydrogen permeability with increasing temperature allows the microspheres to maintain low hydrogen losses at storage conditions while providing sufficient hydrogen flow when needed.

Engineered microspheres provide the greatest advantage for high-density storage of hydrogen. If the engineered microspheres can achieve the high hoop-stress values suggested above, it is estimated that a bed of 50-mm-diameter engineered microspheres can store hydrogen at 62 Mpa (9000 psi) with a safety factor of 1.5 and a hydrogen mass fraction of 10% [216]. This produces a hydrogen density of 20 kg/m^3. There is a trade off between storage pressure and mass fraction of hydrogen stored. At lower storage pressures, the mass fraction of hydrogen stored increases but the overall hydrogen volumetric density decreases. This is caused by the increase in the glass-sphere wall thickness needed to withstand the increase in storage pressure and maintain the same factor of safety. Figure 3-151 shows how the hydrogen mass fraction and volumetric density change for various storage pressures [216].

Although the storage capability of glass microspheres looks impressive there are a number of drawbacks to their use from a system standpoint. The main issue is that, to get the hydrogen into and out of the spheres, they must be heated. This heating takes considerable energy and time to accomplish. The higher the heating, the quicker the hydrogen will purge from the spheres. From a system standpoint, however, this heating, which can be significant, must be accounted for.

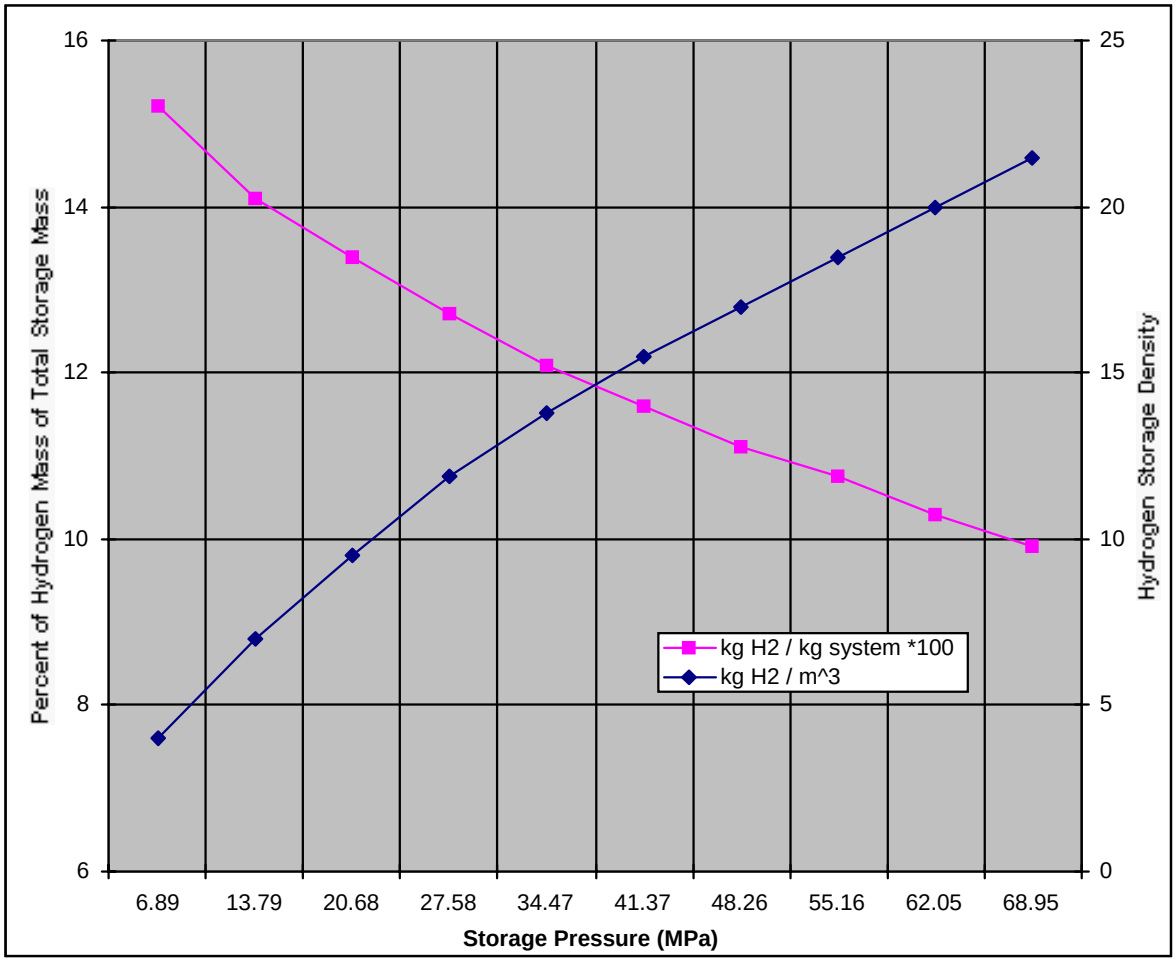

Figure 3-151: Glass Microsphere Hydrogen Storage: Mass Fraction and Density for Various Storage Pressures

3.5.3.1.2 Cryogenic Hydrogen Storage

To reduce tank mass and volume over high-pressure gas storage, cryogenic storage of hydrogen can be used. The properties of liquid hydrogen enable significant increases in density over high-pressure gas storage, as well as reduced tank mass due to lower pressure operation. Liquid hydrogen is around -260° C (-425° F) and has a density (ρLH) of 71 kg/m^3 (4.43 lb/ft^3). To get a further increase in density above that of liquid hydrogen, a mixture of solid and liquid hydrogen can be produced. This mixture is called *slush hydrogen*. For a 50% solid/50% liquid mixture, the hydrogen density is 80.9 kg/m^3.

Cryogenic storage maximizes the density of hydrogen but imposes some significant operational constraints on the fuel system:

1. It requires an airtight insulation system to reduce the boil-off of the liquid hydrogen and maintain it at cryogenic temperatures.

2. Handling liquid hydrogen requires specialized equipment and procedures. Also, the storage of liquid hydrogen is time-limited due to boil-off; Therefore the boil-off must be eliminated for long missions.
3. The fuel tanks need to be maintained at a constant pressure, usually around 1.45E5 Pa (21 psia) to minimize boil-off. This requires a venting system and procedure to be implemented.
4. Liquid hydrogen tanks and lines must be sealed off from the atmosphere. If atmospheric gas enters the tanks, it will freeze solid and can block the flow lines. Only helium can be used as a purge gas.

The main components for storing liquid hydrogen are the tank and insulation. The tank is usually a thin-walled pressure vessel surrounded by a thick layer of insulation. The tank materials must be resistant to hydrogen embrittlement, impermeable to hydrogen gas, and capable of structurally withstanding the temperatures of liquid hydrogen. Also because of the great change in temperature when the tank is fueled or emptied, thermal expansion and contraction is a major concern. Therefore, the attachment points of the tank to any structure must be capable of withstanding this movement as well as the tank structure itself. Because of this it is usually required that the tank be made of one type of material. This also poses a significant problem with regard to lightweight, strong materials, such as carbon, that will require a liner of different material to be impermeable to hydrogen gas.

The storage tank for holding the liquid hydrogen can be sized by the following analysis. The tank volume (V_t) required to hold the hydrogen is given by the following equation, where M_H is the mass of the hydrogen to be stored. There must be space left in the tank to maintain a constant pressure as well as provide space for boil-off. This excess volume is estimated to be around 7.2% (Vi = 0.072) of total tank volume.

$$V_t = M_H \ (1+V_i)/ \rho_{LH}$$ **Equation 3-44**

From this, the tank radius (r) can be calculated by solving Equation 3-45 for r. If the tank is a cylinder this will have to be done iteratively.

$$V_t = 4 \pi r^3 / 3 + \pi r^2 L$$ **Equation 3-45**

The wall thickness for the tank is given by Equations 3-41 and 3-42 for a cylindrical and spherical tank respectively. Utilizing the wall thickness and tank radius, the mass of the tank (m_t) can be calculated.

$$m_t = \rho_t (4/3) \pi (r + t_w)^3 + \pi (r + tw)^2 L - V_t$$ **Equation 3-46**

The next main component of a liquid hydrogen-storage system is the insulation needed surrounding the tank, as well as any fuel lines or handling devices. The insulation serves a few purposes. It is necessary to reduce the amount of boil-off from the storage tanks. Without the insulation, the boil-off rate would make the use of liquid hydrogen completely impracticable. The insulation must be impervious to the atmosphere to eliminate the possibility of frozen CO_2

particles forming, and it must be capable of withstanding the extreme thermal cycling to which it will be subjected.

There are two main categories or types of insulation that can be used. The first is a vacuum-jacketed system consisting of layers of Mylar (or a similar type of low-emissivity, high-reflectivity material), separated by thin fiberglass sheets to maintain spacing, surrounded by an outer container able to maintain a low pressure within the insulation layers. The low-pressure environment minimizes the conductivity between the insulation layers, and the layers act as a radiation barrier keeping heat out of the tank. The pressure within the vacuum-jacketed insulation is typically kept at around 0.1 Torr (Mars surface pressure is approximately 4.5 Torr). The main drawback to the vacuum-jacketed insulation is that if the vacuum is lost, the insulation will fail, causing a large and rapid boil-off of propellant.

The second type of insulation is a rigid, closed-cell foam that can be applied to the outside of the tank. If needed, a thin metal-walled enclosure can be placed outside the foam to maintain its integrity and protect it from damage. The foam type of insulation is much more resistant to catastrophic failure than the vacuum-jacketed type. However, the densities and thermal conductivity of the foam insulation is greater.

Table 3-21 lists a number of different insulation types and the effective conductivity and density [28,126].

Table 3-21: Tank-insulation Properties

Insulation Type	Density (kg/m3)	Thermal Conductivity (W/m ^{o}K)
Rigid closed cell polymethacrylimide	35.3	0.0096
Rigid open cell polyurethane	32.1	0.0112
Rigid closed cell polyvinalchloride	49.8	0.0046
Rigid closed cell polyurethane and chopped glass fiber	64.2	0.0064
Evacuated aluminum foil separated with fluffy glass mats	40	0.00016
Evacuated aluminum foil and glass paper laminate	120	0.000017
Evacuated silica powder	160	0.00017

The amount of insulation needed on the tank will vary depending on the insulation properties, tank size, allowable boil-off rate, and overall allowable weight. To get an estimate of insulation requirements, a brief analysis on the heat flow into the tank needs to be performed. The analysis is a one-dimensional heat flow from the surroundings to the liquid hydrogen. The heat transfer mechanisms are shown in Figure 3-152.

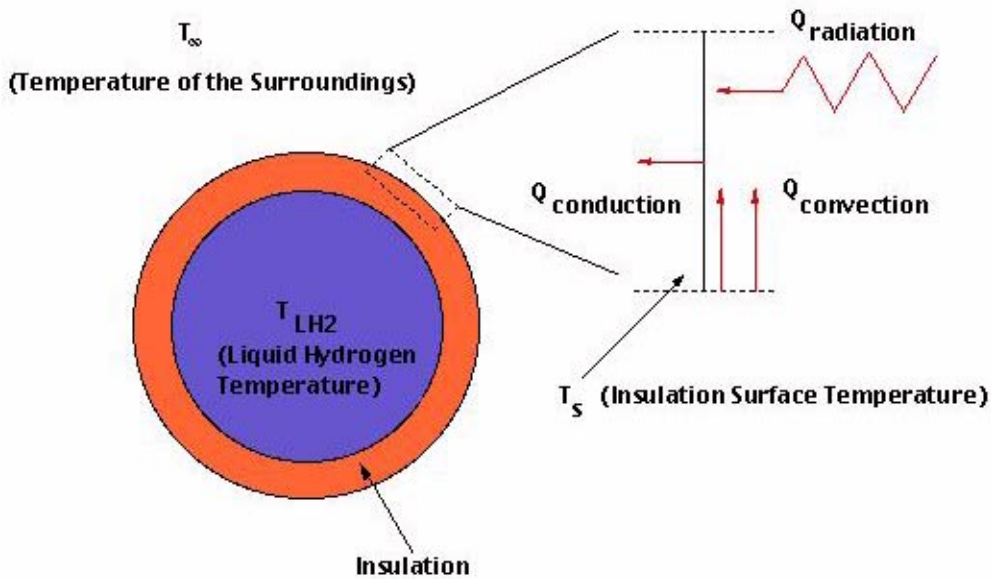

Figure 3-152: One-dimensional Heat Transfer for Liquid Hydrogen Tank

Initially the outside surface temperature of the insulation (T_s) needs to be determined. This wall temperature is based on the heat flow into the insulation from convection and radiation and heat flow to the liquid hydrogen by conduction through the insulation.

$$Q_{in} = Q_{convection} + Q_{radiation} = h(T_8 - T_s) + \varepsilon\sigma(T_8^{\,4} - T_s^{\,4})$$ ***Equation 3-47***

$$Q_{out} = Q_{conduction} = K\,(T_s - T_{LH2})\,/t_i$$ ***Equation 3-48***

Where ε is the emissivity of the insulation surface, σ is the Stefan-Boltzmann constant (5.67E-8 $W/m^{2\circ}K^4$), h is the convection coefficient for the air surrounding the tank, K is the thermal conductivity of the insulation, and t_i is the insulation thickness. It is assumed that the tank is in an isolated environment in which the atmosphere surrounding the tank is still. Therefore, the convection coefficient is based on natural convection of the atmosphere surrounding the tank. This coefficient can be represented by the following equation:

$$h = N_{UD}\,K_g / D$$ ***Equation 3-49***

The thermal conductivity of the carbon dioxide (which composes most of the atmosphere) (K_g) is a property of the fluid at a given temperature and pressure, and D is the tank diameter. The Nusselt number (N_{UD}) is dependent on the geometry of the tank. Expressions for this are listed for spherical and cylindrical tank shapes [205].

For a sphere:

$$N_{UD} = 2 + 0.589\,R_{ad}^{\,1/4} / [1 + (0.469/PR)^{9/16}]^{4/9}$$ ***Equation 3-50***

For a cylinder:

$$N_{UD} = [0.60 + 0.387\ R_{ad}^{\ 1/6} / [1 + (0.559 /PR)^{9/16}]^{8/27}\ ]^{2}$$ ***Equation 3-51***

Where the Rayleigh number is given by the following equation in which g is the gravitational constant.:

$$R_{ad} = g\ \beta\ (T_8 - T_s)\ D^3 / (\nu\ \alpha)$$ ***Equation 3-52***

By assuming an ideal gas, the volumetric thermal expansion coefficient (β) is equal to the inverse of the gas temperature in °K ($\beta = 1/ T_8$).

The gas diffusivity and viscosity can be represented by the following data-curve fits for CO_2.

$$\alpha = -1.2959E\text{-}6 + 8.5377E\text{-}9\ T_8 + 1.0846E\text{-}10\ T_8^{\ 2}$$ ***Equation 3-53***

$$\nu = 4.1273E\text{-}9 + 4.4095E\text{-}9\ T_8 + 7.8266E\text{-}11\ T_8^{\ 2}$$ ***Equation 3-54***

Once the insulation outer surface temperature is known, the boil-off rate (M) in kg/s of the liquid hydrogen can be calculated. This is done through an energy balance between the heat flow through the insulation and the energy taken to boil the liquid hydrogen. The energy to boil the liquid is based on the latent heat of vaporization of liquid hydrogen (h_{fg} = 446592 J/kg):

$$K\ A\ (T_s - T_{LH2})\ /L = M\ h_{fg}$$ ***Equation 3-55***

The above analysis produced an estimate of how long it takes to boil off 50% of the hydrogen and the tank total mass as a function of the insulation thickness. This is shown in Figures 3-153 and 3-154 for various amounts of stored liquid hydrogen. These results are based on using evacuated aluminum foil separated with fluffy glass mats as the insulation material. This insulation, although heavier the most of the others listed, has the lowest thermal conductivity and therefore was deemed the best choice.

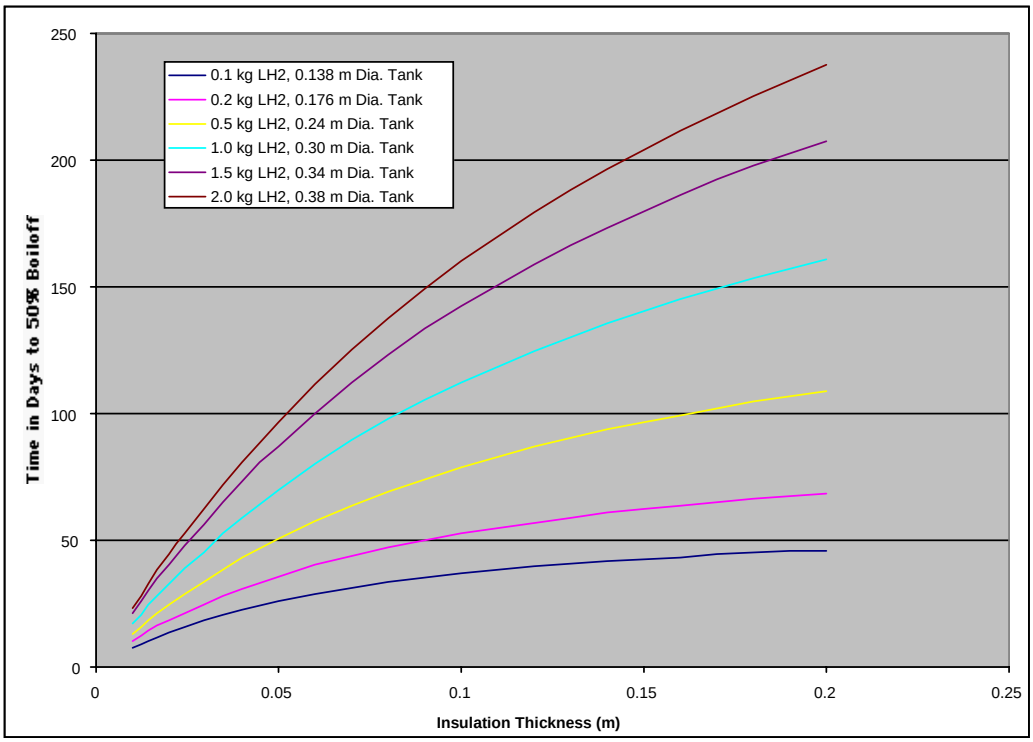

Figure 3-153: Effect of Insulation Thickness on Overall Storage Tank Mass

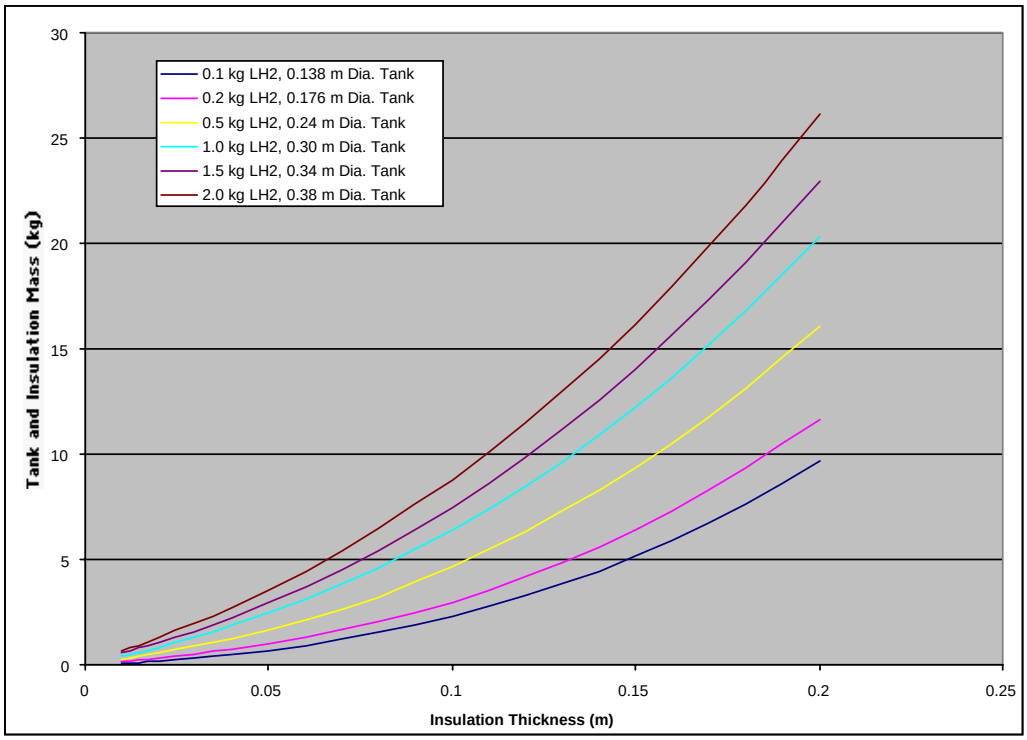

Figure 3-154: Effect of Insulation Thickness on Overall Tank Mass

3.5.3.1.2.1 Gelled Hydrogen

To further increase the density of liquid hydrogen it is possible to produce a gelled liquid hydrogen that produces an increase in density over conventional liquid hydrogen. It is estimated that gelled hydrogen can produce a 10% increase in the density over standard liquid hydrogen.

Gelled hydrogen is produced by introducing a gellant into the liquid hydrogen. This gellant can be either another cryogenic material, such as solid ethane or methane, or silica particles [91]. Gelling agents constructed from other types of hydrocarbons, such as ethyl alkoxides or hexyl alkoxides are also under development [205]. Figure 3-155 shows how the propellant density can increase with increasing gelling agent concentration. This figure is based on data obtained from Reference 289 for methane as the gelling agent.

Gelled hydrogen reduces the boil-off rate by two to three times compared to standard liquid hydrogen. There is also a significant safety benefit to using gelled hydrogen: It has an inherently smaller spill radius due to its higher viscosity than liquid hydrogen, which minimizes its effect if spilled. The increased viscosity reduces the leak potential by making the hydrogen more resistant to seeping through small openings. The higher viscosity also reduces the amount of hydrogen slosh within the storage tank, reducing the chance for instabilities produced by the movement of the hydrogen. [205]

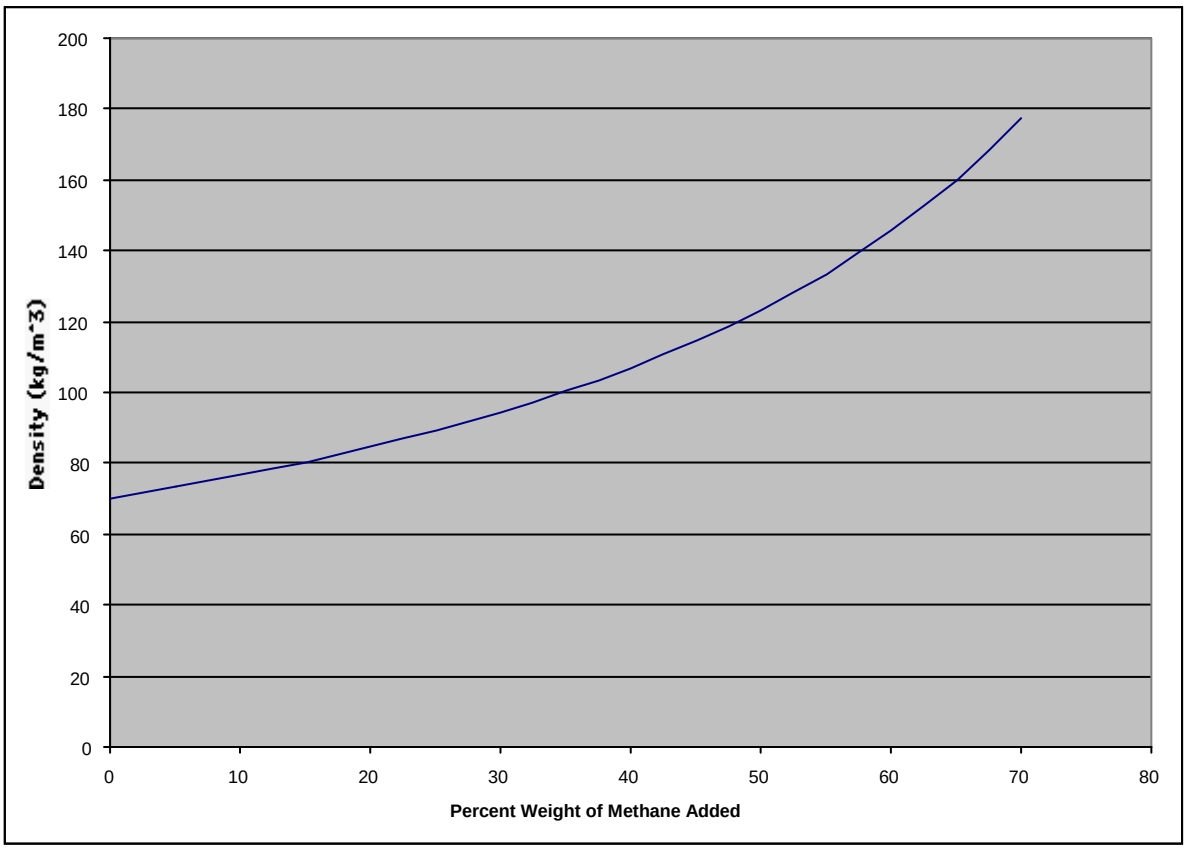

Figure 3-155: Theoretical Increase in Density with the Addition of Methane Gelling Agent [284]

3.5.3.1.2.2 Cryocooler for Boil-off Compensation

Based on the results shown in Figure 3-153, the boil-off rate for the liquid hydrogen is too high to be useful for a mission that can last for more then a year from launch to completion. A way to reduct boil-off therefore must be devised if liquid hydrogen is to be used. Previous work focused on eliminating boil-off in cryogenic systems by incorporating a cryocooler into the storage tank. [210].

The cryocooler is used to condense the hydrogen vapor that forms in the ullage (excess area in the tank not occupied by liquid hydrogen) of the tank. This vapor is generated by heat leakage into the tank through the insulation. By sizing the cryocooler to match the heat leakage, the system effectively can have no boil-off. A typical single-stage cryocooler for reaching liquid hydrogen temperatures is shown in Figure 3-156.

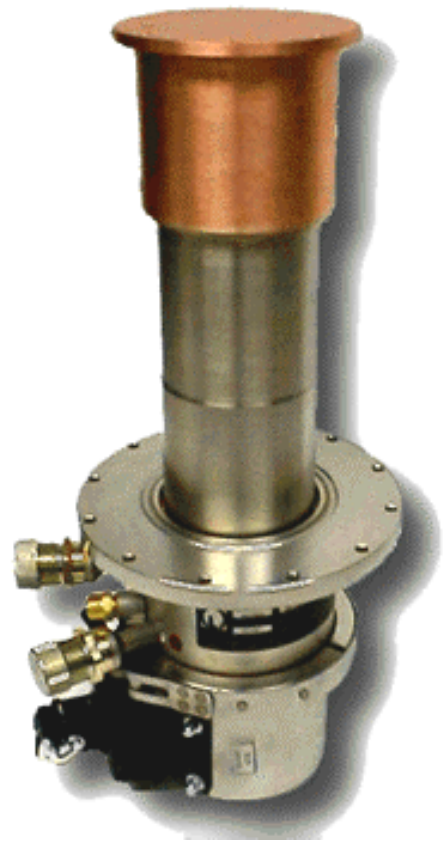

Figure 3-156: Single-stage 20° K Cryocooler
[41]

The energy loss associated with the boil-off rates shown in Figure 3-153 are given below in Figure 3-157. This figure shows the amount of power needed to be supplied by the cryocooler to compensate for the leakage of heat into the tank through the insulation. This power consumption is based on the latent heat of vaporization of hydrogen and the rate of heat flow into the tank, given in Equation 3-55.

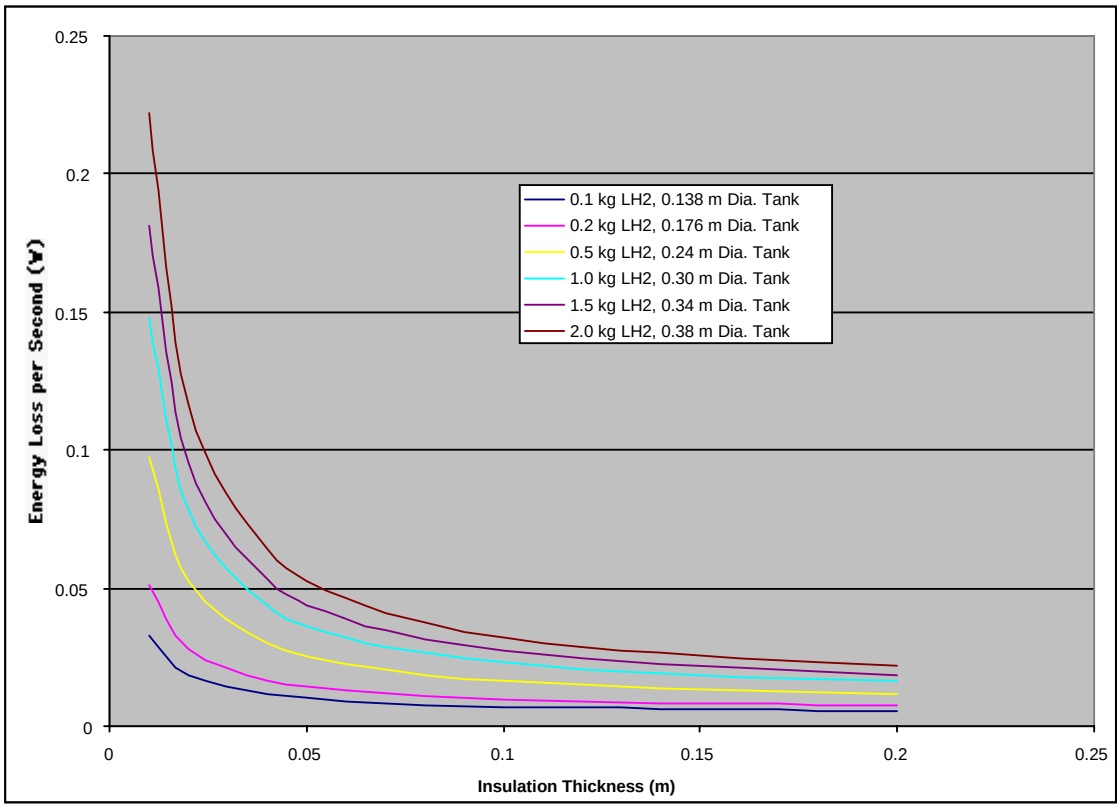

Figure 3-157: Rate of Energy Loss Due to Boil-off of the Liquid Hydrogen

Most cryocoolers in production have capacities that are much greater than that shown in Figure 3-157. The power consumption of these cryocoolers is also much greater than that provided by the proposed Entomopter mission. State-of-the-art cryocoolers require between 2.5 kW to 7.5 kW of power and provide cooling capacities of between 5 W and 18 W at 20°K. This is much more than needed for this application. To get an estimate of the cryocooler power required to meet the power demand shown in Figure 3-157, therefore, the output/power consumption of a number of state-of-the-art cryocoolers was linearly scaled to the range shown in Figure 3-157. This scaling was based on the performance average of all the cryocoolers examined. The resultant cryocooler power requirement is shown in Figure 3-158. These power levels (shown in Figure 3-158) are achievable and realistic for the proposed Entomopter mission and justify the use of liquid hydrogen as a means of storing hydrogen for this mission.

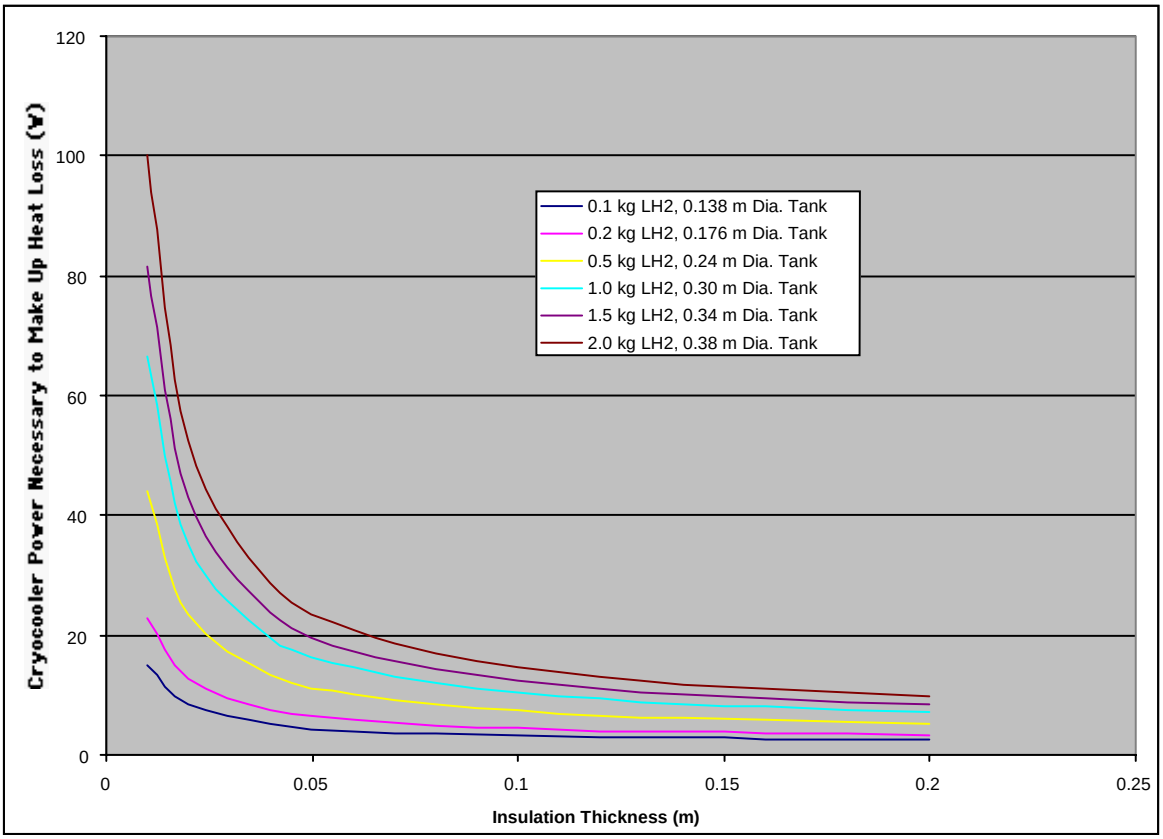

Figure 3-158: Cryocooler Power Requirement to Meet Boil-off Demand

To determine the optimum insulation thickness for a tank that includes the cryocooler, an overall mass estimate of this system has to be made. This mass estimate includes the tank mass, insulation mass, cryocooler mass, and additional power system mass needed to operate the cryocooler. The results of this analysis are shown in Figure 3-159. This figure was generated utilizing a PV battery power system as the power source. The power required to run the cryocooler was based on the heat load shown in Figure 3-157. The mass of the power system was based on the PV/battery system described in the power source section. For all of the liquid hydrogen masses examined, an insulation thickness of 0.04 m was optimal for minimizing the system mass.

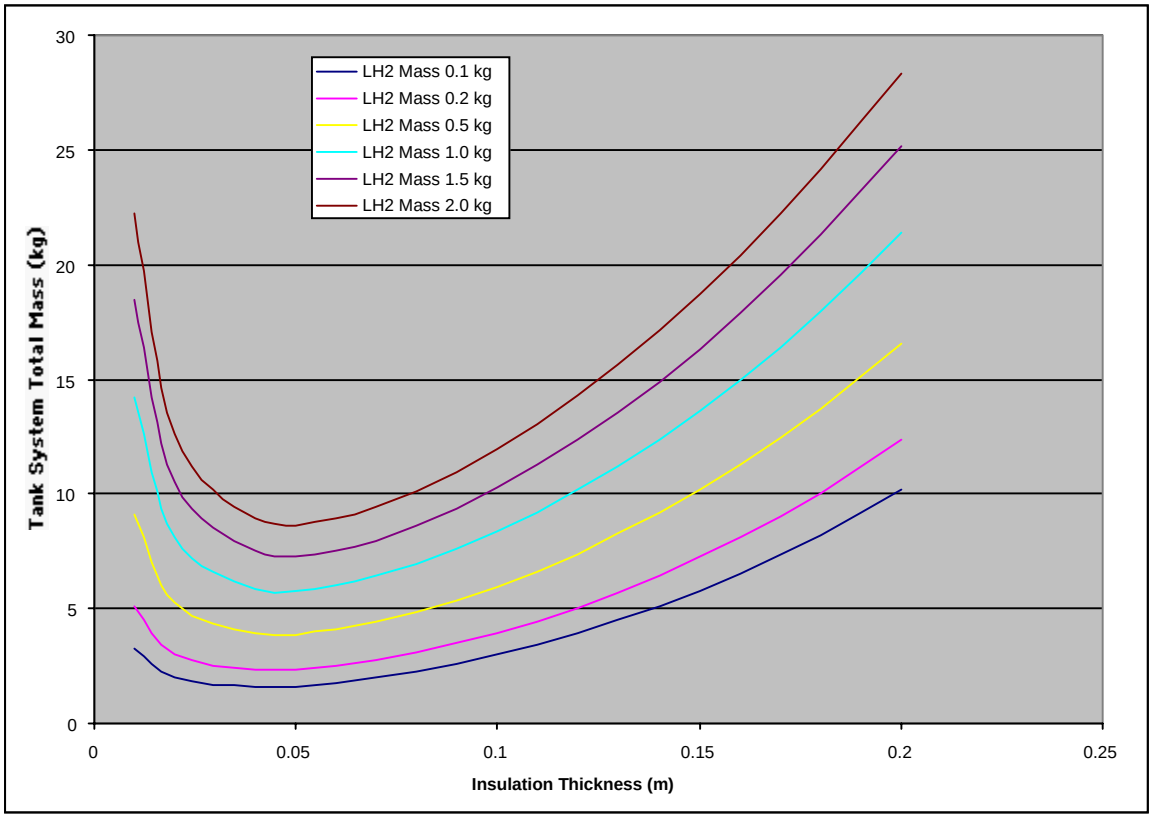

Figure 3-159: Cryogenic Tank System Mass as a Function of Insulation Thickness

3.5.3.2 Zirconia Oxygen Generator

A zirconia solid-oxide oxygen generator is a device that produces oxygen by electrolyzing CO_2, at temperatures up to 750° C, to strip off an oxygen ion from the molecule. Once the oxygen ion has been removed from the CO_2 molecule, the zirconia material acts as an oxygen pump and separator by allowing only the oxygen to pass through its crystal lattice by the process of solid state ionic conduction. This occurs when voltage is applied across the zirconia material. A zirconia oxygen generator was scheduled to be launched on the Mars 2001 Surveyor lander mission and was part of the Mars in situ propellant-processing experiment. The zirconia oxygen generator was sized to produce 0.5 cm^3 of O_2 per minute [138]. The system mass for this device is 1 kg, and the steady state power consumption is 9.5 W.

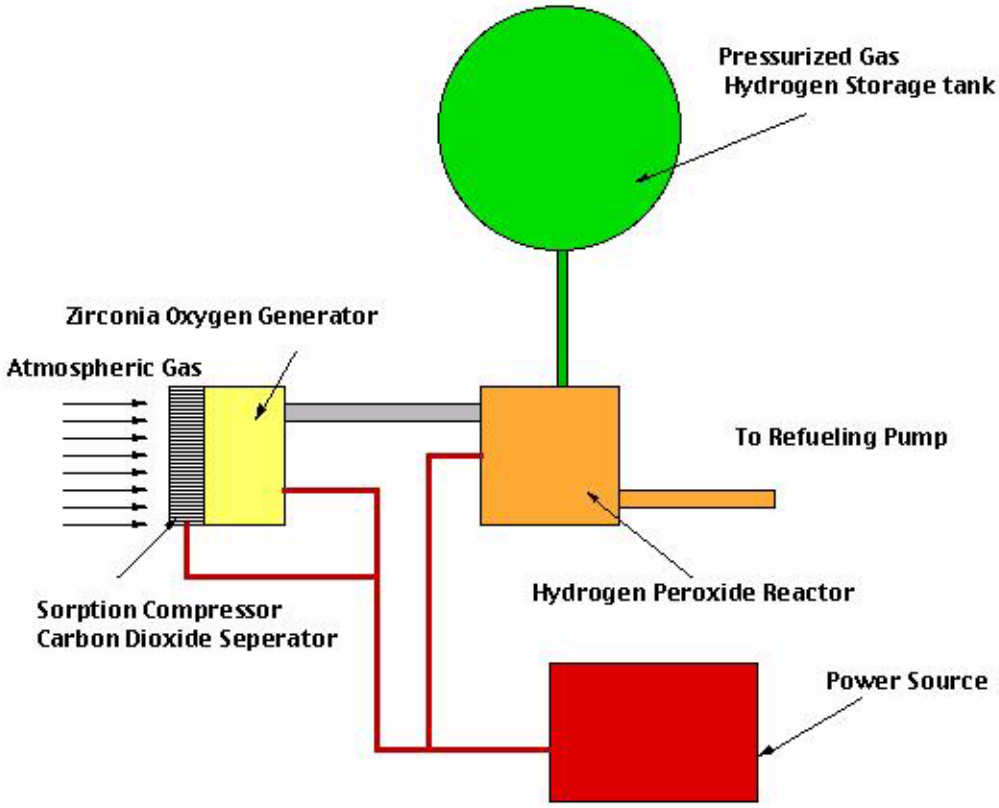

Figure 3-160: Hydrogen Gas Storage System

3.5.3.3 Sorption Compressor

To produce O_2 from the atmosphere, a sorption compressor can be used to separate the CO_2 from the atmosphere and increase its pressure so that it can be used in the zirconia process described previously. A sorption compressor contains virtually no moving parts and achieves its compression by alternately cooling and heating a sorbent bed comprised of materials that absorb low pressure gas at low temperatures and desorb high pressure gas at higher temperatures. The characteristics of the material in the sorption pump define how much gas can be absorbed and which species are more readily absorbed than others. Due to the lack of rotating/moving parts, it has significant potential for long lifetime, reliability, and robustness. Like the zirconia oxygen generator, a sorption compressor was also scheduled to be part of the Mars in suit propellant-processing experiment for the Mars 2001 Surveyor lander. [138].

The sorption material, a zeolite, can adsorb approximately 135 mg/g of material at Mars atmospheric conditions (6 Torr, 200°K). The mass of oxygen produced from the CO_2 is approximately one-third the mass of the CO_2 collected. The amount of energy (E, in Jules) needed to raise the temperature from the initial 200° K to 450° K, where the CO_2 is released at higher pressure, is given by the following equation: where c_p is 1,010 [J/kg °K] for the sorption material, m is the mass in kilograms of the sorption material used and ΔT is the change in temperature in degrees Kelvin [139]:

$$E = m\, c_p\, \Delta T$$ **Equation 3-56**

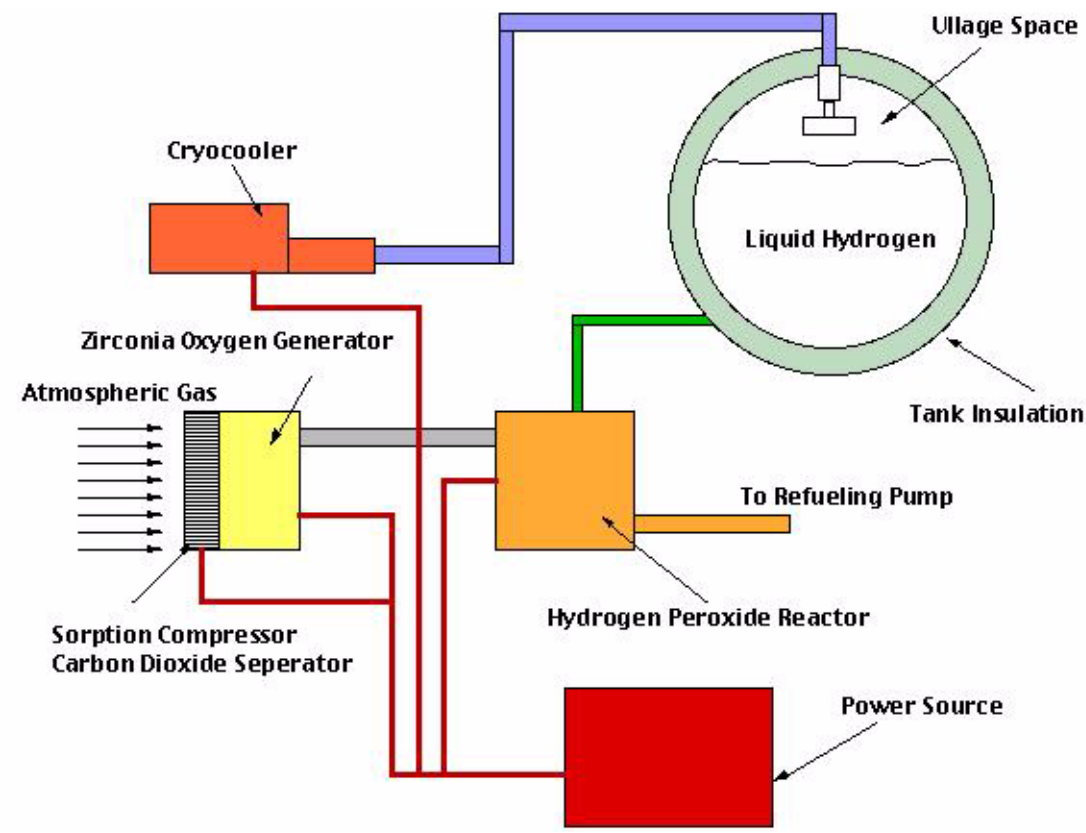

Figure 3-161: Liquid Hydrogen Storage System

3.5.3.4 Hydrogen Peroxide Reactor

Hydrogen peroxide is a clear syrupy liquid in its pure form. It has a density of 1,470 kg/m^3, a boiling point of 424° K, and a freezing point of 261.5° K. Concentrated hydrogen peroxide is a highly reactive substance. It decomposes exothermically in the presence of a catalyst to form water and oxygen gas. Common catalysts are carbon, steel, and copper. To avoid an inadvertent reaction, the reactor and any lines or components that may be in contact with the hydrogen peroxide will need to be manufactured of materials that will not cause decomposition. These materials include aluminum, tin, glass, polyethylene, and coatings such as Teflon and Kel-F. The decomposition reaction for hydrogen peroxide is shown below:

$$2H_2O_2\ (l) \rightarrow 2H_20(l) + O_2\ (g)$$ **Equation 3-57**

Hydrogen peroxide can be generated electrochemically by reacting water and oxygen [155]. Hydrogen peroxide is generated by supplying liquid water to an anode that in turn breaks apart some of the water to form ozone and hydrogen ions, as shown in Equation 3-58. The ozone is released, and the hydrogen ions and water electroosmotically pass through an ionically conduct-

ing membrane. Oxygen introduced through a gas-diffusion layer combines with the hydrogen ion in a cathodic catalyst layer to produce hydrogen peroxide. The reactions that take place at this point are given in Equations 3-59 and 3-60. The hydrogen peroxide and excess water are then released. This process is shown in Figure 3-162.

$$3H_2O\ (l) \rightarrow 6H^+ + 6e^- + O_3\ (g)$$ **Equation 3-58**

$$O_2\ (g) + 4H^+ + 4e^- \rightarrow 2H_20(l)$$ **Equation 3-59**

$$O_2\ (g) + 2H^+ + 2e^- \rightarrow H_2\ O_2\ (l)$$ **Equation 3-60**

This reactor for making hydrogen peroxide is in the development stage; its performance, therefore, is not what would be expected from a production unit. Presently, this unit, operating at 120 W, can produce 9 g of H_2O_2 per day [193]. This rate should scale with power and unit size and improve as further development on the reactor takes place. Because this device operates in a fashion similar to a fuel cell and contains very similar components, its mass can be estimated using state-of-the-art projections for fuel cells. Presently, the near term goal for fuel cell development is 1 kW/kg. Therefore, if this unit is operating at 500 W, an estimate of its mass would be 0.5 kg. The overall hydrogen peroxide reactor mass is then estimated at approximately 2.0 kg, which includes the storage tanks, lines, and other miscellaneous components.

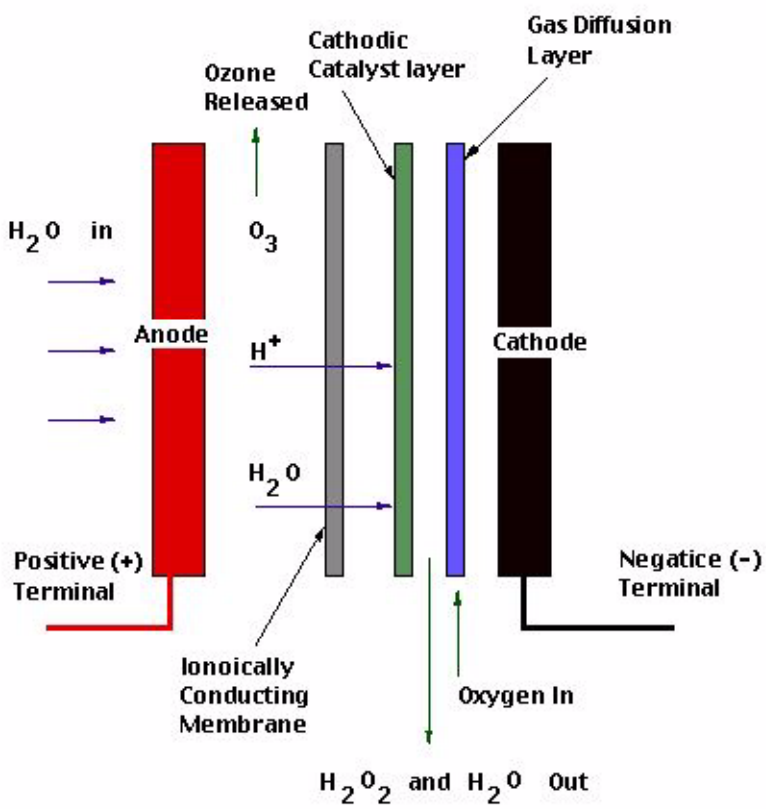

Figure 3-162: Hydrogen Peroxide Generation Method
[16]

3.5.3.5 Power Source

The processes and devices described above require power to produce hydrogen peroxide from the Mars atmosphere, power in addition to what is required by the base lander or rover for normal operation. To determine the impact this increase in power has on the overall system, the increase in mass of the power system must be determined. Because the base-vehicle design has not been established, the two most likely power sources for the vehicle are evaluated here. These are a dynamic isotope power system and a photovoltaic battery power system.

For dynamic isotope systems, there are two main options, a Stirling or Brayton system. These systems have specific power values on the order of 15 W/kg [194]. This system would include either a Brayton of Stirling engine, radiator, and isotope heat source. A diagram of this system is shown in Figure 3-163.

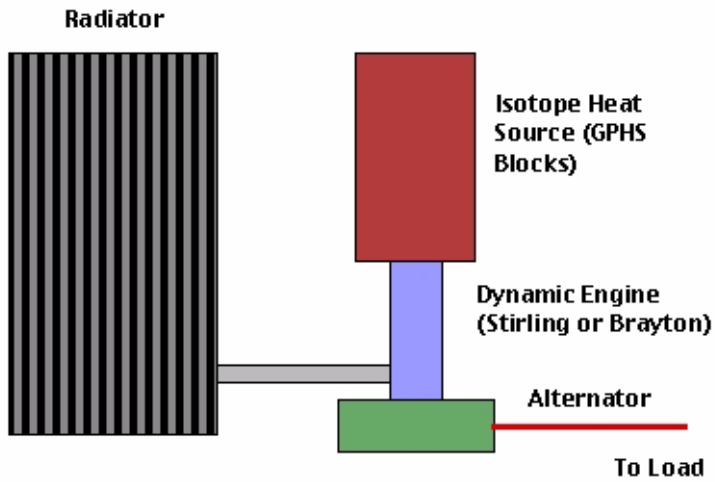

Figure 3-163: Dynamic Heat Engine Power System Diagram

The PV power system has a specific power for the array of 94 W/kg and a specific energy for the battery storage of 300 W-hr/kg. These values are for a GaAs/Ge PV array and lithium ion rechargeable battery [19]. The specific power for the array is an average over the daytime period. Therefore, if the same amount of power is needed throughout the night, the array size will need to double, assuming operation at the equator, where there are equal day and night periods. Because this is a preliminary sizing, no efficiency losses of the battery-charging system were taken into account. A diagram of the PV battery system is shown in Figure 3-164.

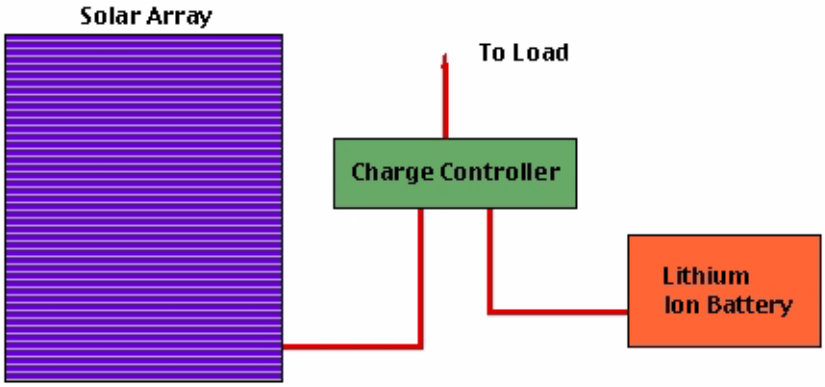

Figure 3-164: PV Battery Power System Diagram

3.5.4 Fuel Storage System

The simplest fuel storage system is to just carry the fuel directly from Earth. Depending on the type of fuel to be stored, certain precautions may be needed. This includes ensuring stability so that the fuel does not react prematurely and maintaining a required temperature to ensure the fuel does not freeze. A diagram of the fuel storage system is shown in Figure 3-165. The mass of this system had to be determined. The analysis was similar to that for the cryogenic tank. An energy balance was set up to determine the heat flow from the tank to the surroundings and the power necessary to maintain a constant temperature within the tank. The hydrogen peroxide temperature was maintained at 270° K. This temperature is above its freezing point of 261.5° K and therefore allows for some margin in the design. The average environment temperature on Mars of 215° K was used as the background temperature. Equations 3-47 through 3-55 were used to calculate the heat transfer from the tank. Because of the relatively low temperature difference between the desired temperature of the fuel and the surroundings, the insulation and power required to maintain the fuel at the desired temperature were minimal. This analysis was performed for various masses of hydrogen peroxide. The masses used corresponded to the total amount that could be made by the various amounts of stored hydrogen used in the pressure and cryogenic storage analysis. The total mass of the fuel storage system, including power production, is shown in Figure 3-165.

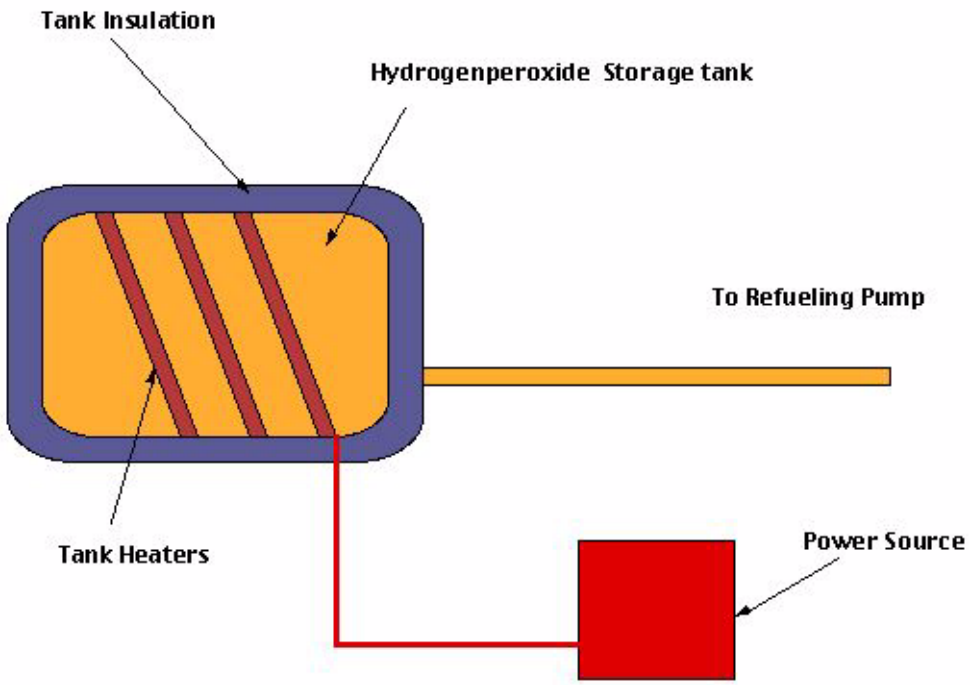

Figure 3-165: Monopropellant Fuel Storage System

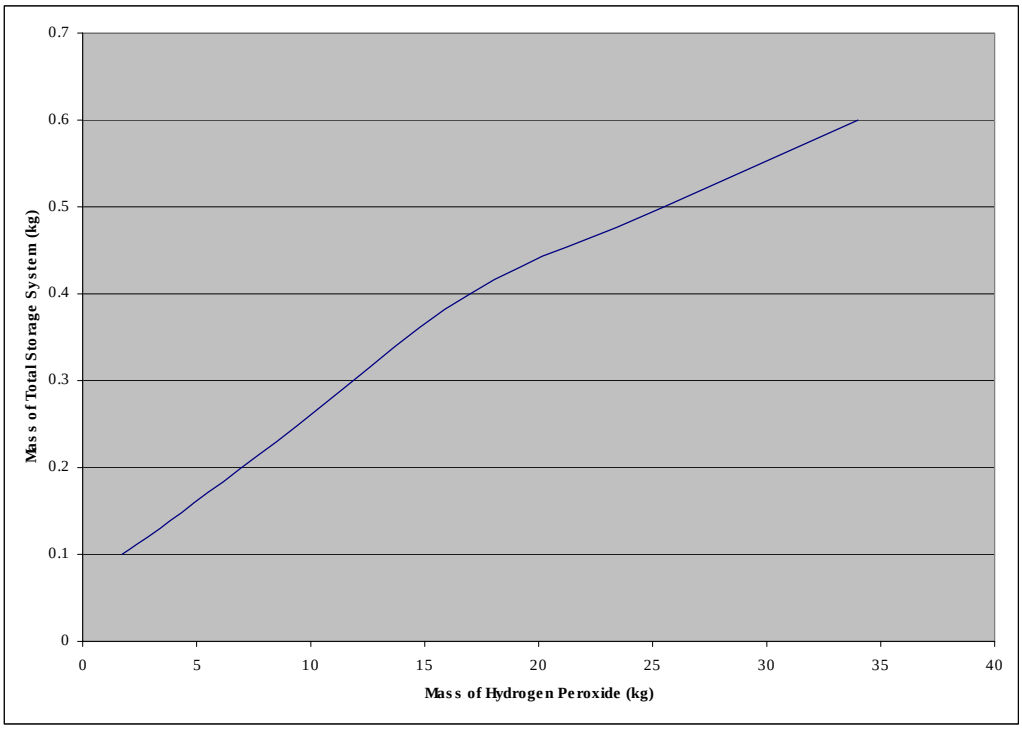

Figure 3-166: Mass of Fuel Storage System Versus Amount of Hydrogen Peroxide Stored

3.5.5 Fuel Systems Comparison

Based on the analysis described above, a comparison was made between the pressure and cryogenic hydrogen storage methods and directly carrying the fuel from Earth. The analysis was performed for both types of power systems, dynamic isotope power and PV battery power. The results of this analysis, shown in Table 3-22 and Figure 3-167, are based on consuming 0.1 kg of hydrogen peroxide per day. This rate was determined through the results of the mission scenarios and vehicle sizing. It is the amount of fuel needed for one round trip mission flight. This consumption number may not be representative of actual usage but was used as a means of comparison in the analysis. This rate represents a conservative mission goal of one Entomopter flight per day. The mass results also include the total storage system, including power production, as well as the amount of hydrogen or hydrogen peroxide carried. The reliability of the systems proposed was not considered in the analysis. It is obvious that the fuel production system would have considerably more risk then the fuel storage method due to the large number of systems and components necessary to produce the fuel.

Table 3-22: Fuel System Mass for Various Mission Durations

Mission Duration (days)	17	34	85	170	255	340
Pressure Storage Dynamic Isotope Power (kg)	124	127	135	149	163	176
Pressure Storage PV/Battery Power (kg)	49	52	61	76	91	105
Cryogenic Storage Dynamic Isotope Power (kg)	121	122	124	126	127	129
Cryogenic Storage PV/Battery Power (kg)	47	48	49	51	53	55
Fuel Storage Tank System (kg)	1.8	3.6	8.8	17.4	26	34.6

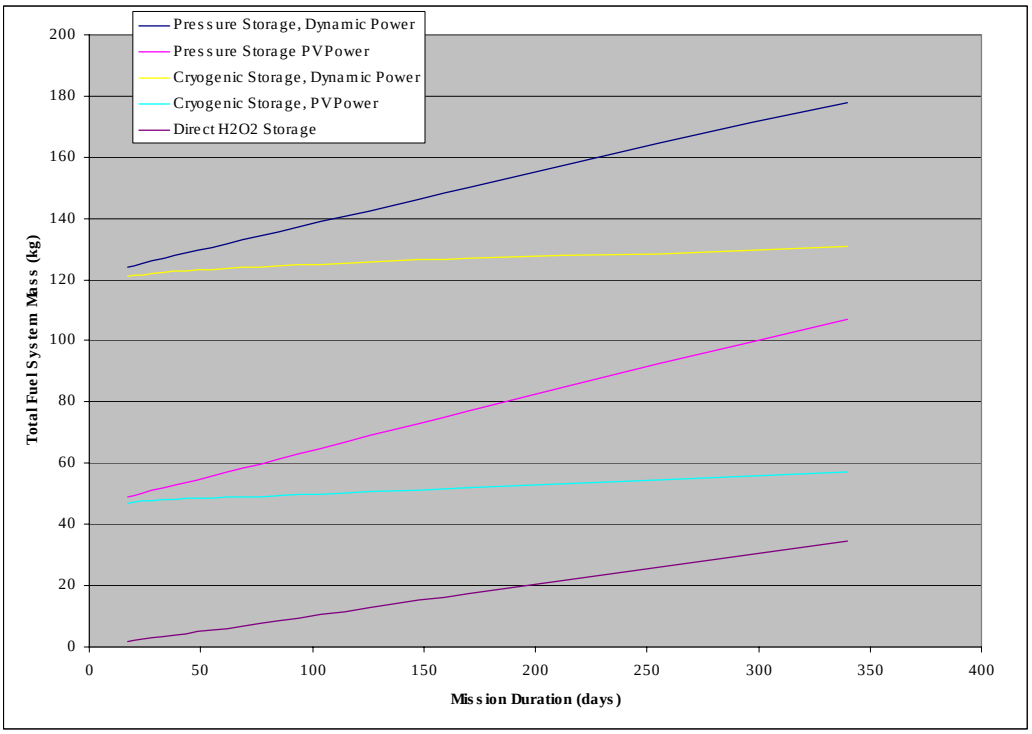

Figure 3-167: Total Fuel System Mass as a Function of Mission Duration

From these results, it is obvious that, for short and moderate mission duration, it is better to carry the fuel directly in a tank instead of trying to manufacture it. If a mission duration of a year or longer is proposed, then producing the fuel on Mars may have an advantage.

If fuel is brought directly from Earth, additional, more energetic fuels too difficult to manufacture on Mars could be considered. This analysis looked only at hydrogen peroxide because it would be one of the easier fuels to manufacture on Mars and the objective of the analysis was to determine if there is an advantage to producing fuel there. By utilizing another type of fuel that provides more energy per volume than hydrogen peroxide, however, the performance of the Entomopter vehicle may be enhanced.

3.6 Power System

Although the Entomopter engine provides the power to propel the vehicle, electric power is still needed to run communications and science equipment. If the vehicle is to be used for repeated missions, this power system would need to be rechargeable or have the ability to produce power for extended periods of time. Systems that may be able to meet this requirement are the following:

- Photovoltaic/Battery System
- Thermoelectric Generator
- Linear Alternator

The key to the evaluation of these systems will be whether they can meet the estimated power-production requirements within the mass and volume constraints of the vehicle. The system will need to power the communications system, science equipment, and onboard computer systems. The overall power system design will depend on the power needs for each of these systems as well as the load profile each requires. For the purposes of comparison, an estimate of the power requirements of each of the systems is given below. These estimates are based on an operational pattern for the Entomopter and the power-required profiles for each of the systems, considered a likely mode of operation for the given system. A typical mission is estimated to last 1 hour. It is estimated that the Entomopter would fly for about 10 minutes total and be on the ground for approximately 50 minutes. While on the ground, the Entomopter would collect and analyze data and transmit information back to the rover. Therefore, the power system will need to operate fully while the vehicle is stationary and the engine is off.

The systems on the Entomopter that require power throughout the mission are:

- Communications
- Science Equipment
- Internal Systems

A description of these systems and estimates of their required power throughout the mission are given in the following sections. The profiles shown for each of the systems is based on an approximation of how the Entomopter will operate for a standard mission. However, unless the energy consumption is significantly changed, a change in the profiles (by staying on the surface longer or making multiple landings) will not have a significant effect on power system requirements or selection.

3.6.1 Communications

The transmitting power for the communications system is estimated to be 0.5 W. The transmission from the communications system will be intermittent and depend greatly on the amount and type of data being transferred. An example of a transmission profile is given in Figure 3-168. Based on this profile, the energy consumption by the communications system through one mission cycle would be 0.3 watthours (W-h).

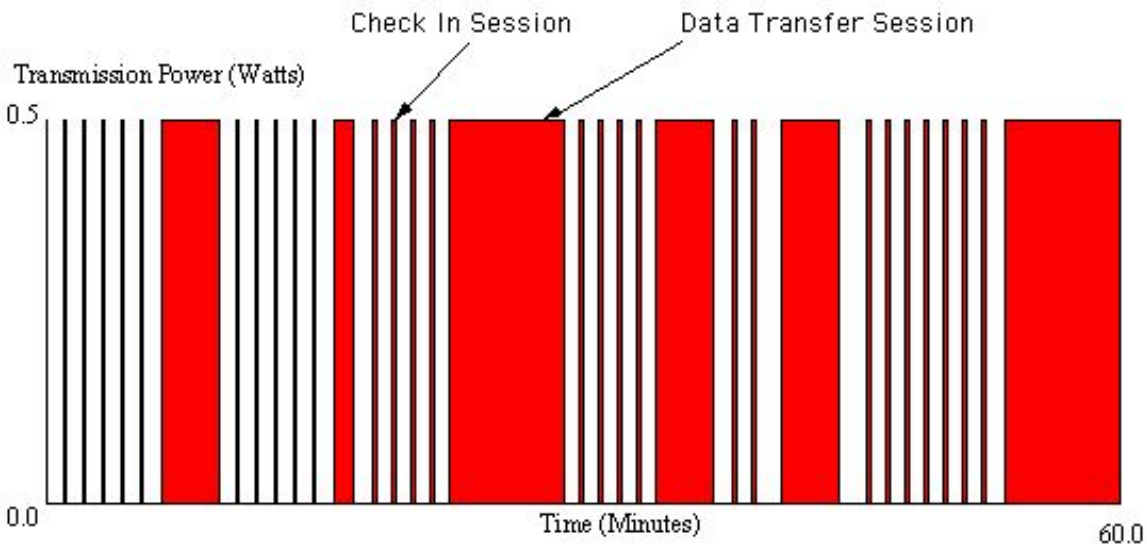

Figure 3-168: Typical Communication Power Profile for One Mission Segment

3.6.2 Science Instruments

The science instrument power requirements will depend on what types of equipment are being used and their duration of use. Also, the ability to store and transmit the data collected will affect the rate of use and therefore power consumption of the science instruments. It is assumed that, while on the ground, soil collection and sampling will require more power than the in-flight instrumentation such as imaging. The energy consumption by the science instruments through one mission cycle would be 1.8 W-h.

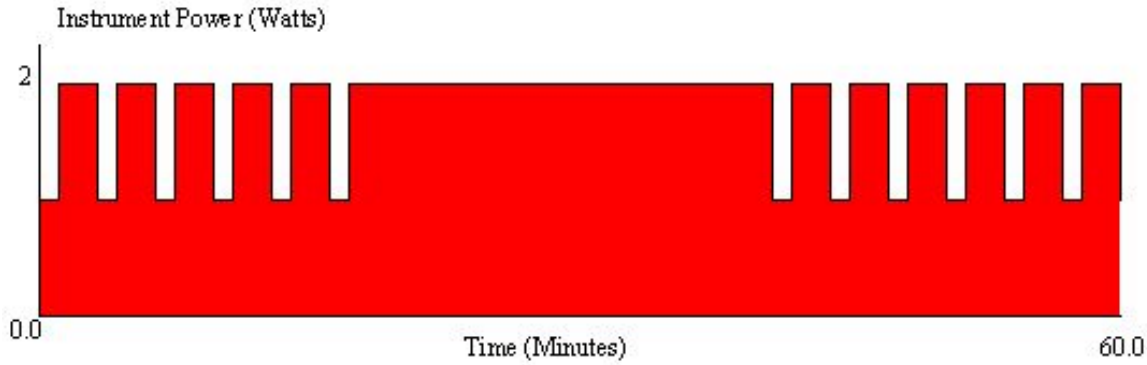

Figure 3-169: Typical Science Instrument Power Profile for One Mission Segment

3.6.3 Internal Systems

The internal systems consist of any onboard computer as well as other internal systems used for vehicle operation. These systems would include health monitoring, avionics, and flight control. Energy consumption by the internal systems through one mission cycle would be 1.0 W-h.

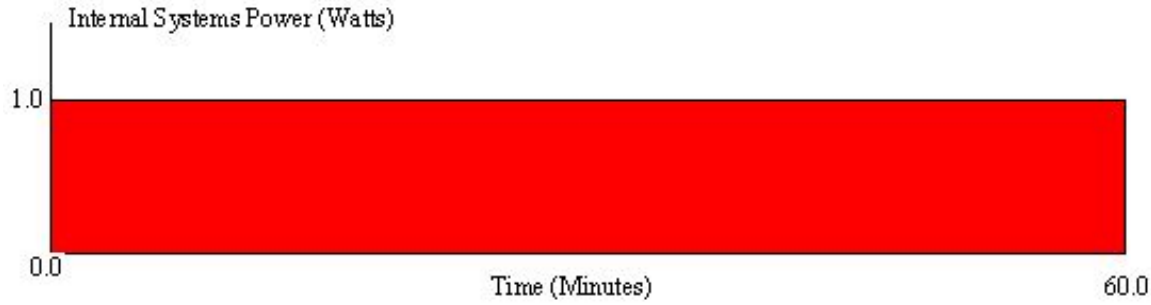

Figure 3-170: Typical Internal Systems Power Profile for One Mission Segment

3.6.4 Photovoltaic/Battery

The photovoltaic (PV) system consists of a flexible thin film array mounted on the wings of the Entomopter with a rechargeable battery and battery-charge controller. The array supplies power directly to the loads and recharging the battery. The battery-charge controller monitors the rate and state of charge of the battery. The battery is used to supply power when either the array is inoperable (such as during the night period) or when the load requirements cannot be met by the array alone. A diagram of the system is shown in Figure 3-171.

The sizing of each of the components depends on the load requirements as well as the available power from the solar array. Some candidate solar arrays and their characteristics are listed in Table 3-23 [293]. The type of PV array best suited for this application is the thin film array. Thin film arrays are very lightweight and flexible. They can be easily molded to the Entomopter's wing and should not affect the aerodynamic performance of the vehicle. Depending on the characteristics of the solar array chosen, it may be possible to use the array as the covering on the wing. This would reduce the structure mass of the vehicle, thereby reducing the impact of the PV array on the system. Thin film PV arrays are also very robust in their construction and present the greatest potential to withstand the acceleration/deceleration loads of the rapidly flapping wing. Because of these characteristics, only thin film PV arrays were considered for this application. Figure 3-172 shows the advancement in performance of thin film solar cells over the last 25 years.

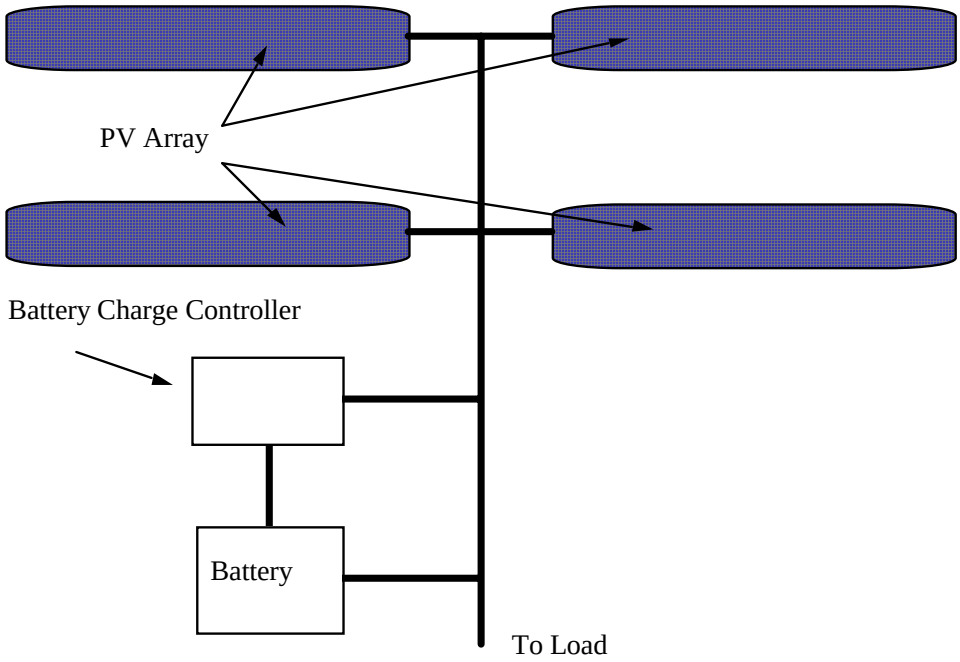

Figure 3-171: PV Array/Battery System Layout

3.6.5 Thin-film Photovoltaics

There have been thin-film PVs since the beginning of PV technology. Thin film arrays are light-weight and highly flexible. The efficiencies of thin film arrays (although not as great as those of other types of solar arrays) has been steadily increasing. The current state-of-the-art thin film solar cells are primarily designed for terrestrial use and have achieved an efficiency in small area cells in excess of 12% AM0. (Efficiency here is defined for Air Mass Zero conditions, that is, for the solar spectrum outside the Earth's atmosphere.) There are four basic areas of research in thin film cells currently being supported in the United States by NASA, DOD, and DOE (i.e., Si-based, CIS-based, CdTe, and thin Si). All of these programs are working to develop a large area thin-film cell on a lightweight flexible polymer substrate or metal foil. Research has achieved respectable efficiency on glass, as well as on stainless steel foil. Progress has also been made toward substrates of Kapton™ or Mylar™, and work is being done on a polymer with high temperature (600° C) capabilities. However, large area thin film cells have yet to achieve 10% AM0 efficiencies.

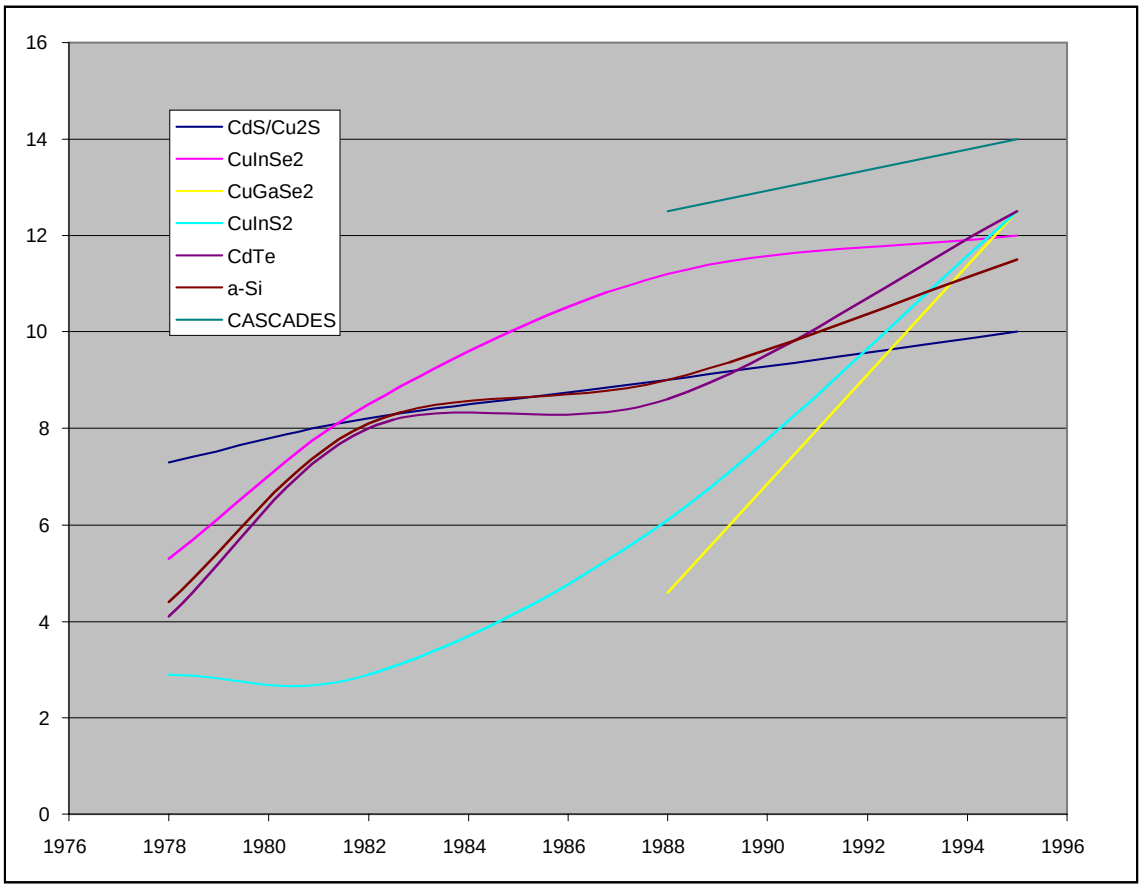

Figure 3-172: Historical Progress of Thin-film Solar Cell Efficiency. Experimentally Achieved Efficiencies (Extrapolated to Air Mass Zero Spectrum, in Percent)
[293]

The Kapton™ or other polymer substrate is capable of serving a double duty as the substrate for the cells and skin for the wing. The thin films are quite flexible and can easily accommodate the curved shape and flapping motion of the wing.

Thin film cells tend to have a high optical absorption constant; therefore, active material may be as thin as 1 to 2 μ, yielding inherently lightweight cells. A very conservative projection of thin-film solar cell technology would be a 5% efficient thinfilm cell fabricated on a 25 μ thick Kapton™ substrate. This yields a PV blanket specific power of 1.7 kW/kg. An optimistic projection might be a 15% thin film cell on a 7 μ thick Kapton™ substrate, leading to a PV blanket specific power of 15 kW/kg. These numbers compare favorably to current state-of-the-art spacecraft solar blankets (e.g., 67 W/kg at the array level for the flight-tested SAFE array) and 130 W/kg at the array level for the experimental APSA array using thin silicon solar cells.

Preliminary results also indicate thin film solar cells may be inherently radiation-tolerant and not require a glass cover for radiation protection. They are highly tolerant of small damage areas from debris impact and any tearing.

Table 3-23: Thin-film Solar Cell Types and Their Characteristics

Solar Cell Type	Efficiency Range	Specific Mass kg/m^2
CuInSe2	11% to 6%	0.286
CdTe	8% to 15%	NA
Si-film	9% to 14%	NA

To determine the available power at the various proposed operational locations on Mars, some assumptions have to be made on the capabilities and geometry of the solar array and its power control system:

- Solar Cell Efficiency (hsc) 10%
- Solar Cell Fill Factor (Sff) 80%
- Power Conditioning Efficiency (hpcon) 95%

Also important in determining the total available power is the orbital and environmental characteristics of the planets where solid-state aircraft might operate. From the environmental section, the data that is important in determining the output of the solar array is given in Table 3-23.

Table 3-24: Environmental Properties for Solar Power Generation

Parameter	Mars
Orbital Eccentricity (e)	0.0934
Maximum Declination Angle (δ_{max})	24°
Mean Orbital Radius (km), (r_m)	228×10^6
Total Days in a Year (d_t)	666
Day Length (hours), (h_l)	24.65
Mean Solar Intensity at Planetary Orbit (W/m^2), (SI_{om})	590
Atmospheric Attenuation (τ)	0.85

The power available (P) per square meter of area is calculated as follows.

$$P = SI_o \, \tau \, \eta_{sc} \, S_{ff} \, (S - C \cos(-a))$$ ***Equation 3-61***

where

$$S = \sin(\phi) \sin(\delta)$$ ***Equation 3-62***

$$C = \cos(\phi) \cos(\delta)$$ ***Equation 3-63***

The latitude (ϕ) and Earth's declination angle (δ) vary with the day of the year (d). This day number (d) is based on the vernal equinox.

$$\delta = \delta_{max} \sin(2 \pi \ d / d_t)$$ **Equation 3-64**

The hour angle (a) is given by the following expression, where i is the instantaneous time of day in hours.

$$a = 2 \pi i / h_l$$ **Equation 3-65**

$$SI_o = SI_{om} (r_m^2 / r^2)$$ **Equation 3-66**

The distance from the flight planet to the sun (r) varies throughout the year. The planet's orbital radius is based on the mean radius (r_m) and is represented by Equations 3-67 and 3-68, where the day number (d_p) is based on the date of perihelion.

$$r = r_m (1 - e^2) / (1 + e \cos(\theta))$$ **Equation 3-67**

$$\theta = 2 \ \pi d_p / d_t$$ **Equation 3-68**

Based on the equations given above, power-available curves were generated. The curves represent the available power at different times of the year and different latitudes. Four times of year were plotted: vernal equinox, summer solstice, autumnal equinox, and winter solstice. These dates represent the maximum and minimum points for the year as well as the times of equal day and night cycle lengths. Figures 3-173 through 3-177 show the power available on Mars.

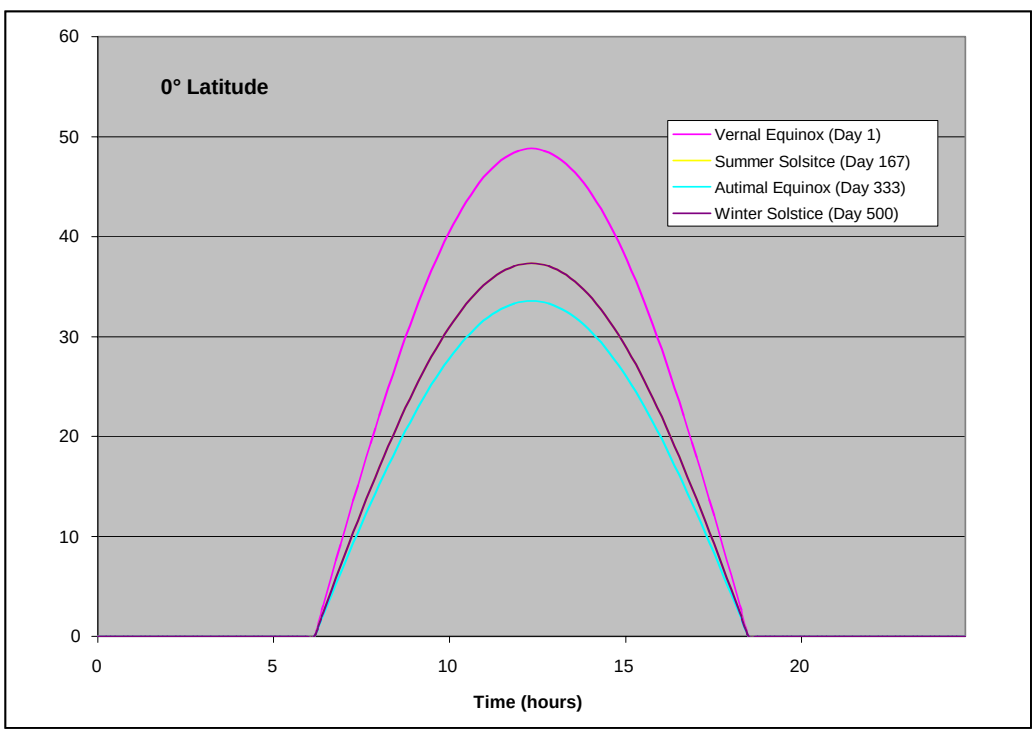

Figure 3-173: Mars: Available Power Throughout the Day at 0° Latitude

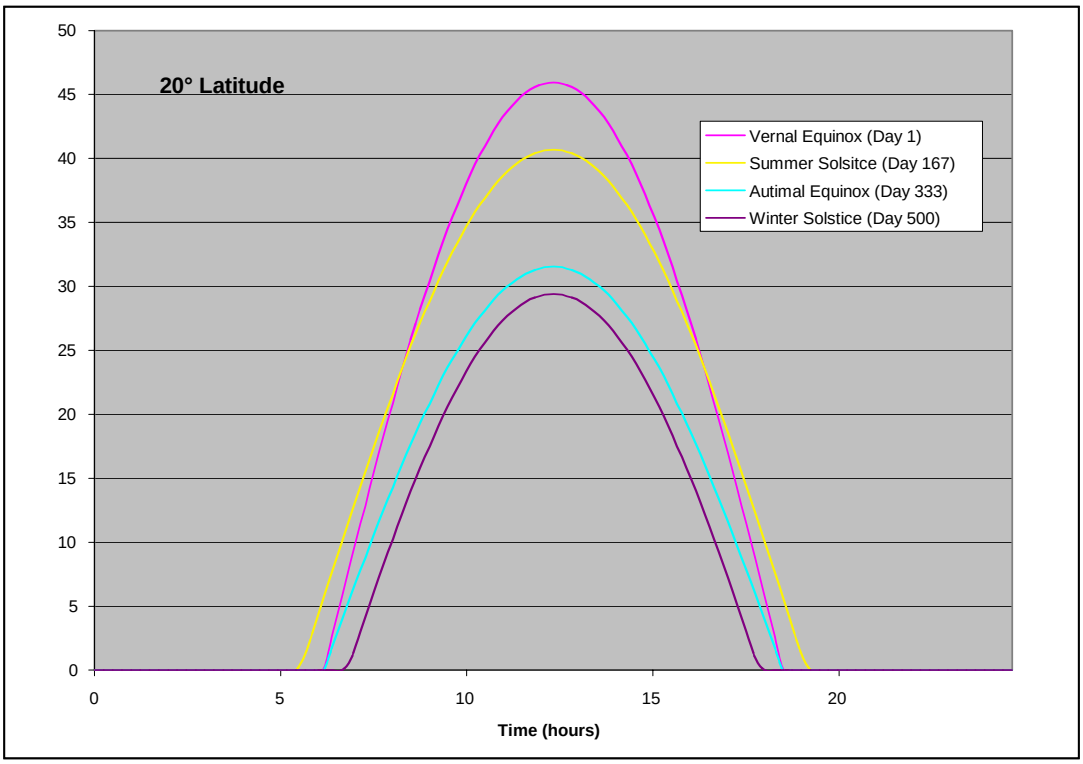

Figure 3-174: Mars: Available Power Throughout the Day at 20° Latitude

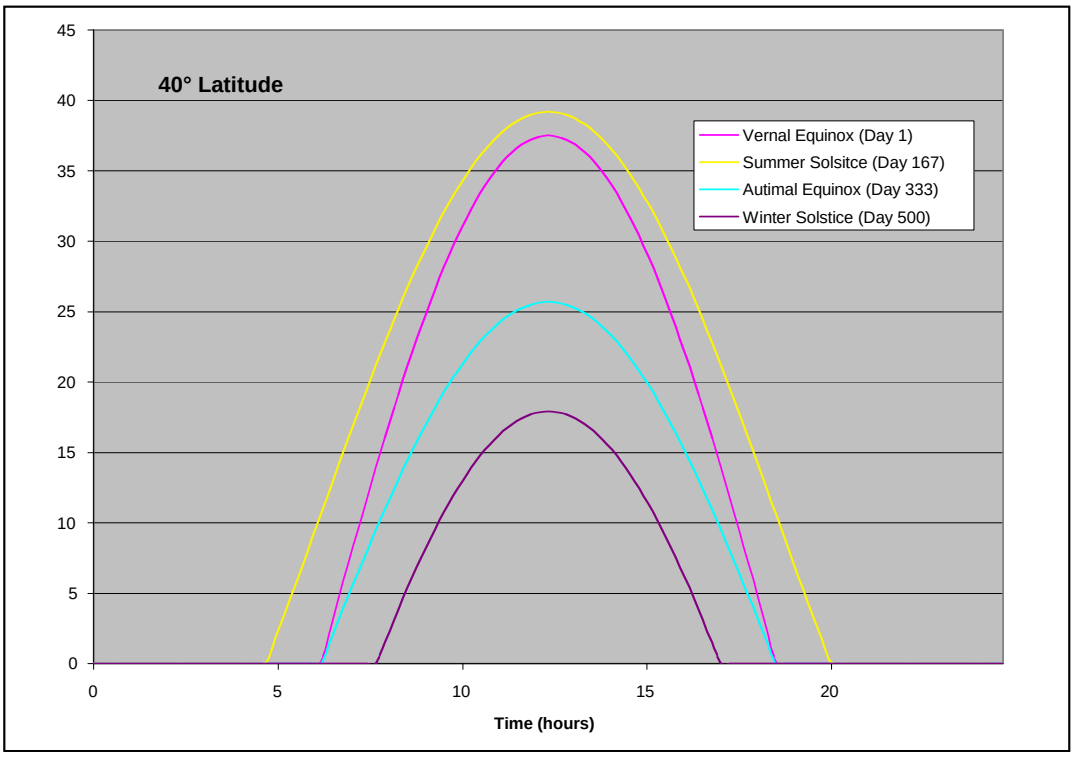

Figure 3-175: Mars: Available Power Throughout the Day at 40° Latitude

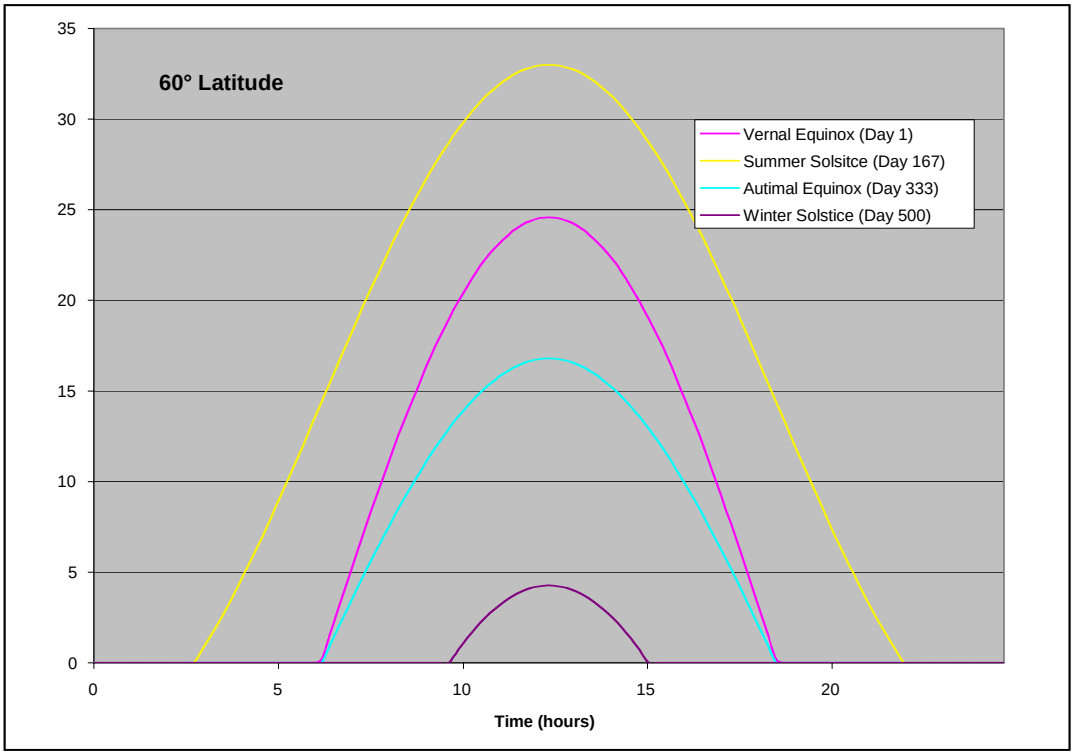

Figure 3-176: Mars: Available Power Throughout the Day at 60° Latitude

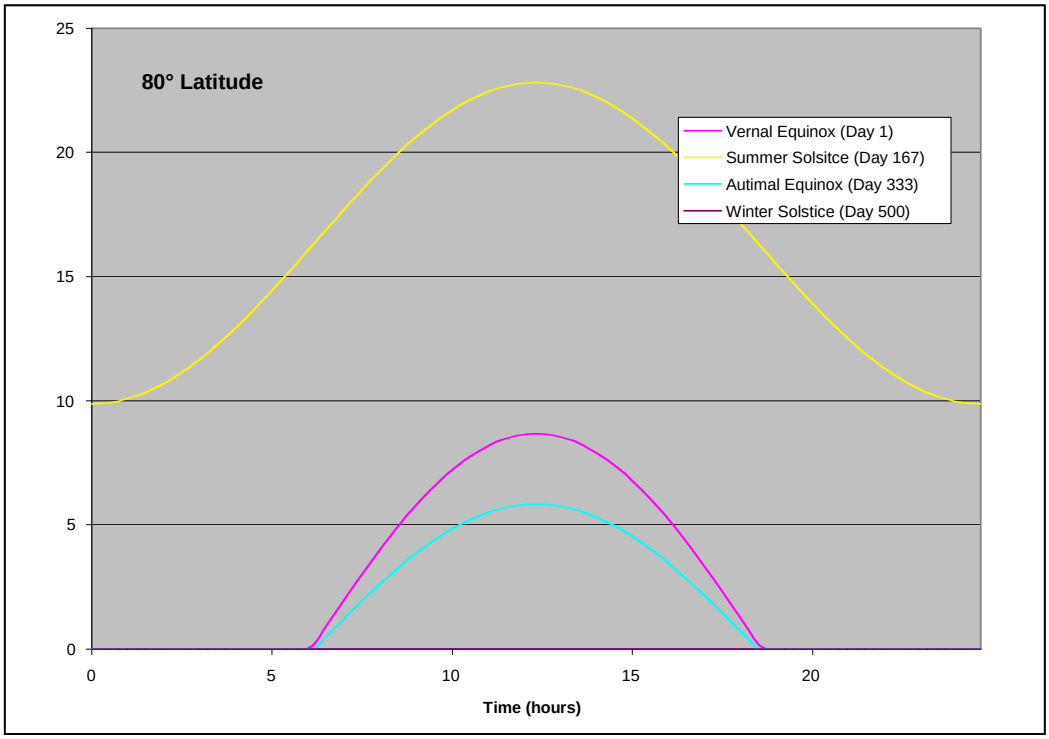

Figure 3-177: Mars: Available Power Throughout the Day at 80° Latitude

Because the wings of the Entomopter are constantly moving during flight, the output of the array will vary continuously. The total wing motion is 150°, +75° (up from the horizontal), and -75° (down from the horizontal). The curves in Figures 3-178 and 3-179 represent the output power of the wing at these three locations. The power output is given as a function of time of day for one complete day cycle. The total usable power available per stroke is given by the average power curve. This curve represents the average power available throughout a wing stroke.

The output power for the total array can be obtained by multiplying the power level on the graphs (11 or 12) by 4. The output is based on a solar intensity of 590 W/m^2 and an atmospheric attenuation of 15%. The mass of the solar array, based on the $CuInSe_2$ array, would be 0.014 kg.

As can be seen from Figures 3-173 through 3-177, the available power changes considerably as the latitude and time of year change. This is due to the inclination of Mars and the change in incident angle on the array due to the change in latitude. For the data shown, it was assumed that the Entomopter was flying east to west.

The average output power per wing stroke for the total array (four panels) is shown in Figure 3-180. The average output power can vary greatly depending on latitude and time of year. Figure 3-180 represents the extremes in average output power, the equator and near the North Pole, at the time of summer solstice. The time of year, especially at higher latitudes, can greatly effect the array output. For example, during the winter at the 85° North latitude there would be no sunlight and therefore no array output for extended periods of time. The watthours provided by the solar array for a day period based on the curves shown in Figure 3-180 are as follows:

- Equator at Solstice 55.71 W-h
- 85° North Latitude at Solstice 107.62 W-h

This is the amount of energy available from the solar array for the given day.

3.6.6 Lithium Batteries

The energy storage component of the system will be used to provide power when the solar array is either obscured from sunlight (either by being shadowed or during nighttime) or when the power demand is greater than what the array can provide. Presently, lithium polymer batteries hold the most promise for a lightweight rechargeable system.

Lithium batteries can be configured in virtually any prismatic shape and can presently be made thinner than 0.039" (1 mm), to fill virtually any space efficiently. This would be a great benefit in entomopter design, because it allows the battery to be placed almost anywhere in the vehicle. It also presents the possibility of making the wing the complete power system by having the batteries within the wing and the solar cells on its surface. One potential lithium battery technology that may address this application are thin film lithium batteries.

Lithium ion thin film batteries are a relatively new technology that is readily finding applications in industry and commercial products, including implantable medical devices, remote sensors, transmitters, smart cards, CMOS-SRAM memory, and other electronic devices. These batteries are rechargeable, lightweight, and flexible. They can be configured in any series/paral-

lel combination to meet power system requirements and they are capable of rapid charging, obtaining 90% of their capacity in less than 20 minutes. For the Entomopter concept, they will be utilized as a means of storing the solar power from the solar arrays. The batteries will be discharged as needed to provide power for any of the onboard electronics and sensors. The batteries have the capability to provide high pulse currents ideal for discrete short duration power loading, such as burst communications transmissions.

There are a number of different types of lithium ion thin film batteries. These differ in the cathode material used (such as magnesium oxides, cobalt oxides and yttrium oxide). The characteristics of thin film lithium ion batteries are well suited for use in the Entomopter power system. The batteries have long cycle lifetimes and can be charged and discharged thousands of times with little loss in capacity. This makes them applicable to long duration flights. They have a long shelf life with little self-discharge over a period of years, allows them to be fully charged and stored during interplanetary transit. In addition, they can operate over a wide range of temperatures, which enables them to operate under a wide range of environmental conditions.

Lithium ion thin film batteries are constructed on a solid substrate material. Common substrates are alumina, glass, silicon, and plastic, but virtually any solid-surface material can serve as the substrate. The layers that make up the battery (current collectors, cathode, electrolyte, and anode) are deposited using standard sputtering or evaporation techniques. Batteries produced today are on the order of 4 mm thick or less. The ability to use different substrate material allows great flexibility in battery design. It may be possible to use the back side of the solar array or the composite wing structure itself as the substrate material for the battery, thereby further integrating the components.

Specifications for present state-of-the-art lithium polymer batteries are given in Table 3-25.

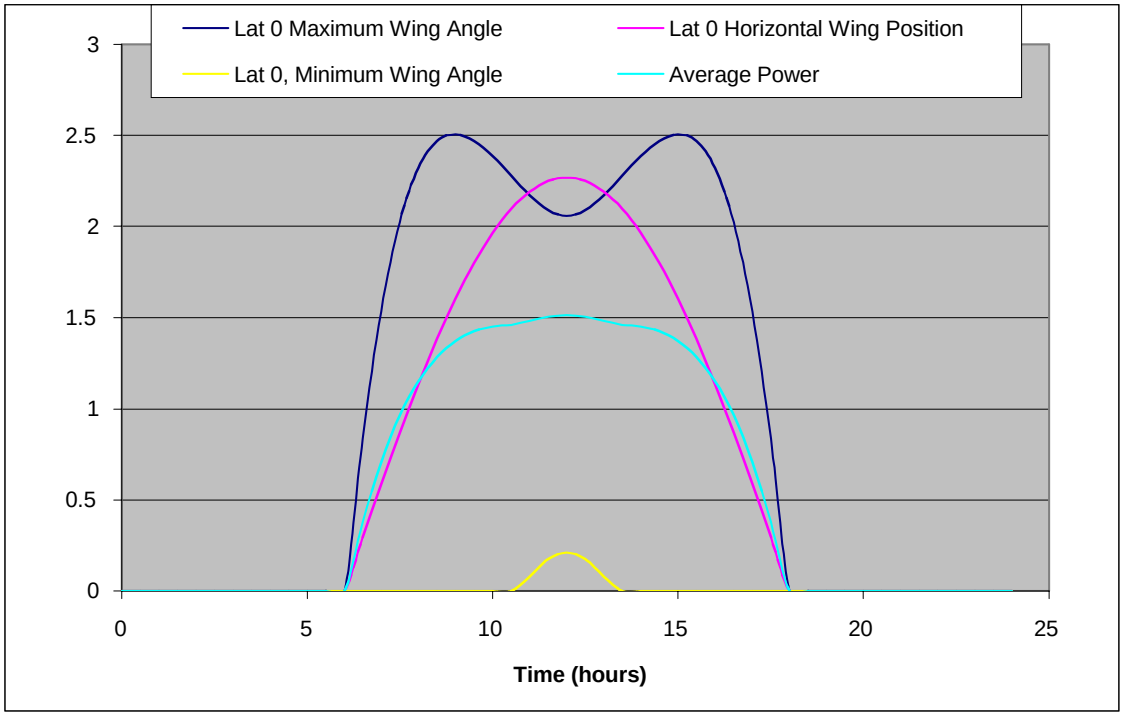

Figure 3-178: Output per Array at the Equator During the Summer Solstice

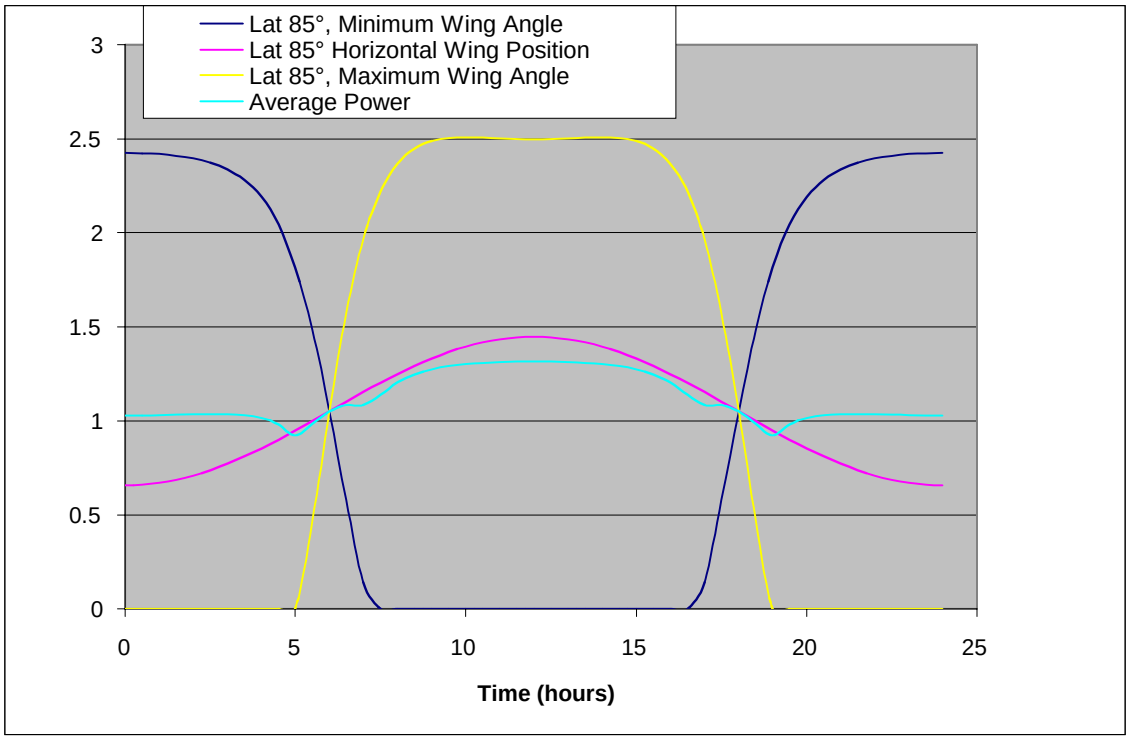

Figure 3-179: Output per Array at 80° North Latitude During the Summer Solstice

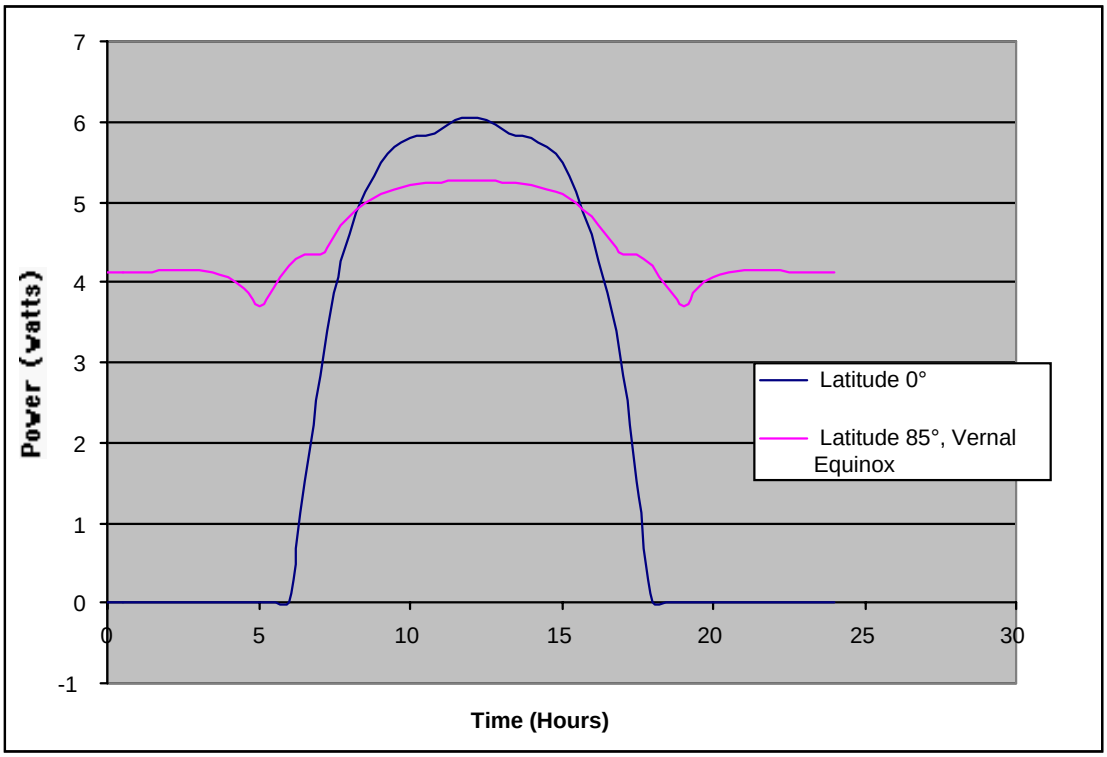

Figure 3-180: Solar Array Average Output Power for the Equator and 85° North Latitude at Day 170 (Summer Solstice, Northern Hemisphere)

Table 3-25: Specifications for Lithium Polymer Batteries, Ultralife Battery Model UBC543483
[264]

Battery Property	Value
Cell Operating Voltage	4.15 V to 3.0 V (3.8 V nominal)
Capacity	930 mAh at C/5 rate*
Maximum Discharge Rate	2C (continuous), 5C (pulse)*
Energy	3.5 Wh
Energy Density	135 Wh/kg, 250 Wh/1
Cycle Life	>300 cycles at C/2 to 80% of initial capacity (no memory effect)*
Operating Temperature	-20°C to 60°C
Charging Temperature	0°C to 45°C
Storage Temperature	-40°C to 60°C
Self Discharge	<10% per month

The C rating is a gauge of the current producing capacity and discharge time of the battery. At 1C the 930 mAh battery would produce 930 mA for 1 hour. At C/5 it would produce 186 mA for 5 hours, and at 2C it would produce 1,860 mA for 0.5 hour. It should be noted that as the discharge time decreases, the overall capacity of the battery will also decrease.

Based on the estimated power consumption of the various systems, shown in Figures 3-168 through 3-170, the maximum power consumption is 3.5 W, and the total energy consumption for a mission cycle is 3.1 W-h. An estimate of the required battery capacity is 100% of the total energy required for the mission. This battery capacity allows the battery to provide power to the systems when the array is offline (shadowed). This also provides a redundancy for supplying sufficient power in the event the array fails. This requires a battery with 3.1 W-h of capacity. Based on the battery data listed in Table 3-25, the battery mass would be 0.023 kg.

The overall system mass estimate for the array/battery system is listed in Table 3-26.

Table 3-26: PV/Battery System Mass Estimate

System Component	Mass (kg)
Solar Array	0.014
Battery	0.023
Contingency (50% for wiring, electronics, etc.)	0.037
Total System Mass	**0.0555**

It should be noted that the system mass shown in Table 3-26 represents values based on state-of-the-art components. With future advancements in these components, this may be significantly reduced. Also any variation in the assumptions used to generate these numbers will also greatly affect these results.

3.6.7 Thermoelectric Power Generation

The basic principle behind a thermoelectric power generator is that if two different metals, semi-metals, or semiconductors are joined at one end and separated along their length, a current will be produced in each metal strip as long as there is a temperature difference between each side of the junction. The configuration of a thermoelectric power generator is shown in Figure 3-181.

The heat source provides a high-temperature source from which heat will flow through the converter. For the Entomopter application, heat can be generated either through the combustion of the propellant or from an isotope heat source. A heat sink must also be used to dissipate the excess heat and maintain the cold side of the thermoelectric generator at a temperature below that of the hot side. It is this temperature difference that produces the direct current electrical power. Thermoelectric generators can be made for power levels ranging anywhere from 10^{-6} W to 10^{2} W. Semiconductor material is by far the best choice for the construction of a thermoelectric generator. These materials can presently achieve efficiencies on the order of 5% to 10%.

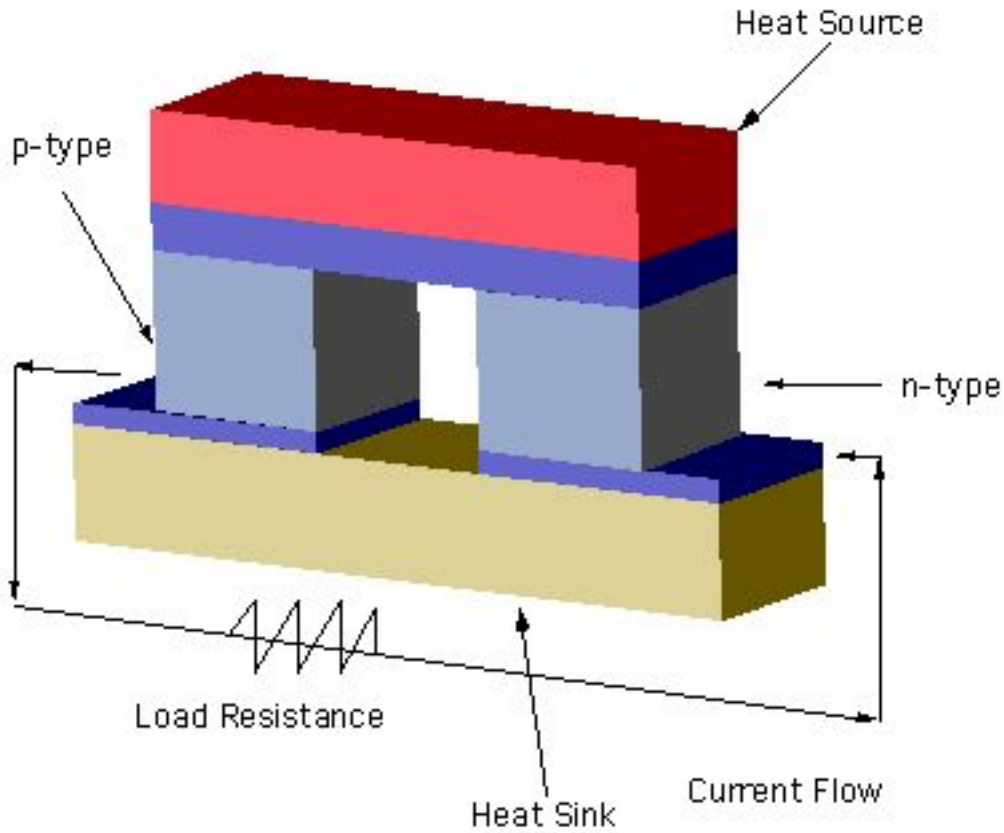

Figure 3-181: Operational Diagram of a Thermoelectric Generator

For use on the Entomopter, the thermoelectric generator would need to be very lightweight and compact. A micro-thin film thermoelectric, under development through DARPA [197], would be the ideal candidate. State-of-the-art thin film thermoelectric devices, shown in Figure 3-182, have efficiencies in the 5% range. However, projections for future efficiencies are up to 20%. These thin film thermoelectric devices can be integrated onto the combustion chamber wall and use the excess heat produced during combustion to produce electricity. Experimental models are capable of generating 20W of power from a 1 cm^3 combustion engine. The specific mass of these devices is on the order of 4 W/gm.

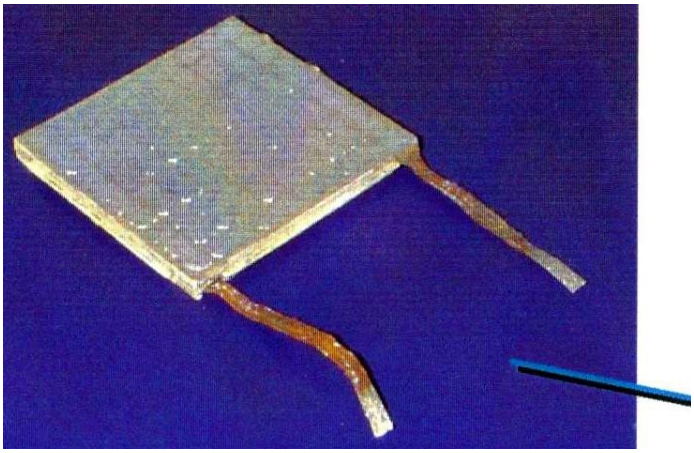

Figure 3-182: Photo of a Thin Film Thermoelectric Device
[27]

From the estimates of the thin film thermoelectric, sufficient power for the Entomopter's systems should be available whenever the engine is operating. However, the engine will not be operating continuously during the mission. In fact, operation time can be a small fraction of the complete mission time. Therefore an auxiliary source of power would be needed. The best choice for this power source is a rechargeable lithium battery similar to that used with the PV system. The operational time of the thermoelectric is limited to 10 minutes over the 1 hour mission. This would provide a total of 3.33 W-h of energy. If 4 W need to be available to the vehicle while the thermoelectric is running, that leaves 16 W or 2.66 W-h available for storage. Therefore, a battery would need to be used with a storage capacity of 2.43 W-h (3.1 W-h for the total mission - 0.66 W-h provided by the thermoelectric and used during flight). Based on the lithium battery specifications given in Table 3-25, the battery mass would be 0.018 kg, and the thermoelectric conversion unit would be 0.02 kg. Also, a cooling system will be needed to keep the back side of the thermoelectric cool in order to maintain the required temperature difference across it. (This temperature difference is usually on the order of 200°C.) However, within the cool atmosphere of Mars, the cooling system may be nothing more than some convective fins. The mass breakdown for the thermoelectric system is given in Table 3-27. Based on these estimates, the thermoelectric system would be about twice as heavy as the battery system. However, if the mission profile is changed, this type of system may look more attractive and should continue to be considered as a viable alternative to the PV system.

Table 3-27: Thermoelectric System Mass Estimate

System Component	Mass (kg)
Thermoelectric Unit	0.020
Battery (based on 100% capacity)	0.023
Cooling Fins	0.010
Contingency (50% for wiring, electronics, etc.)	0.043
Total System Mass	**0.096**

Another approach to using a thermoelectric is to use a radioisotope heat source instead of the combustion-exhaust gasses. This would eliminate the need for a supplemental battery to provide power when the engine is not running. A standard radioisotope heater unit (RHU) can be used as a baseline for the heat source. The specifications of the RHU are given in Table 3-28. [9]

Table 3-28: Specifications for Radioisotope Heater Unit

System Component	Value
Isotope Material	PU-238
Mass (Fuel Source)	3.02 gm
Operating Temperature	310° K
Watts (thermal)	1 Wth

To meet mission requirements, the RHU/thermoelectric system would need to produce 3.5 W to meet maximum power needs plus a 0.5 W contingency. This contingency is needed because there is no backup battery or other power source that could compensate for an unexpected power drain. So the total power to be supplied by the RHU/thermoelectric system is 4 W. Assuming the conversion efficiency of the thermoelectric is 15% (about 200% better then the state of the art), the thermal watts required would be 26.6 W thermal. This translates into an isotope mass of 0.08 kg. This isotope mass alone is greater than the PV/battery system mass. Even eliminating the contingency power, the isotope mass (0.07 kg) is still greater then that of the PV/battery system.

3.6.8 Linear Alternator System

A linear alternator system uses the motion of the engine to generate electricity directly. Because this will extract work from the exhaust gasses by placing an additional load on the engine, however, it will be less efficient overall than the thermoelectric system that provides power by utilizing the waste heat within the exhaust gasses. Also, the alternator will be operating only when the engine is running and would therefore require a supplemental battery similar to the exhaust-powered thermoelectric. Based on these issues, the linear alternator would not be the best choice for the Entomopter vehicle under the mission conditions that were specified.

Chapter 4.0 Entomopter Flight Operations

4.1 Entomopter Navigation and Communications on Mars

There are presently no global navigation systems on Mars to support an Entomopter-based aerial survey mission. Although such a network may be established in the future, it is not really essential to the Entomopter navigation function. Because Entomopters are designed to return to the rover base for refueling, their operations are necessarily rover-centric. For this reason, all navigation cues can (and probably should) be referenced to the refueling rover's position, which from the Entomopter's perspective is decoupled from any Mars coordinate system. All the Entomopters need to know is where they are relative to the refueling rover. The refueling rover, on the other hand, should have an awareness of its global position, but this position is largely irrelevant to the Entomopters. This is particularly true because Entomopter missions are planned to be local to the rover. Due to endurance constraints, the Entomopters are not envisioned as striking out across the Mars landscape to investigate points hundreds of kilometers distant.

This section will present two approaches to Entomopter navigation and communication. The two differ in terms of architecture- basically, where emitters are located. In one case, most of the emitters are carried by the refueling rover, and except for a short distance low-power ranging device to aid in landing, the Entomopters are free from the weight burden of this support equipment. The other option presented places various emitters on the Entomopters, the advantage being that longer range operation is possible and non-line-of-sight flight (relative to the refueling rover) is simplified. The price to be paid for this increase in performance is decreased science payload capacity in terms of weight and volume when both emitters and their supporting energy source are considered. The particular science mission goal will dictate which method is preferred.

4.2 Rover-centric Entomopter Navigation

Because the refueling rover (by definition) is replete with fuel and is therefore not energy constrained to the degree that a flying vehicle would be, it has the luxury of emitting relatively high power radio frequency (RF) radiation (a costly behavior due to emitter inefficiencies). As such, the rover can support a radar system capable of detecting and tracking objects within a hemispherical volume centered about the rover.

The Entomopter has a distinctive radar cross-section (RCS) that involves both high frequency local motions and translational motions. Doppler target acquisition and tracking radar on the rover would easily identify Entomopters in flight based on their motion as distinguished from the stationary Mars landscape. The wingbeat would provide a high frequency (10s of Hz) modulation of the RCS in terms of amplitude, while the flight speed of the Entomopter would provide a Doppler shift of magnitude and sign that depends upon angle of approach or departure. Additionally, the elevation of the Entomopters would be a discriminator most of the time as well, so long as they were operating in the general vicinity of the rover.

Navigation would be accomplished as follows: The refueling rover would maintain a general awareness of its environment through various sensors, including radar. The radar, if configured as a monopulse Doppler system, could provide range, azimuth, elevation, and relative speed of targets within its hemisphere of influence. The rover will be able to determine these parameters for each of the Entomopters as they are launched and fly in the rover's vicinity. This positional information can then be impressed upon the radar signal as a modulation. When an Entomopter is painted by the radar beam, it will receive information about its own position, that of other Entomopters, and the refueling rover. The relative position of looming obstacles can also be communicated.

In addition, radar will serve as a transponder to elicit responses from each Entomopter as it is painted by the radar beam. This response will contain telemetry information identifying the specific Entomopter, its health status, fuel remaining, above-ground-level (AGL) altitude as locally measured by the Entomopter, as well as any other low bandwidth information of import.

One key feature of the transponder signal is that it is passive. Because the radar signal from the rover necessarily has a return that is reflected back to the rover, the Entomopter may use techniques to modulate the radar cross section (RCS) to impress its telemetry information onto the radar return passively. In this way, the Entomopter need not expend any energy in transmission. A property of an omnidirectional retroreflector made of trihedral facets is that it will redirect incident radiation (from the rover) back along its transmission path (regardless of the retroreflector orientation). For this reason, the orientation of the Entomopter need not be tracked or even known. It is completely passive in this regard and even works when illuminated by multiple sources simultaneously. It is independent of flight path and orientation.

The reflectivity of the entire retroreflector can be modulated by changing the RCS of the corner reflector elements electronically. This involves changing the RCS, for example, by ionizing an area that momentarily creates or destroys the corner reflector. To ionize a small region takes high voltage, but essentially no current, so it is very low power. It is also rapid, so it can be used to passively modulate the radar return with amplitude or phase information, or possibly polarization. The U.S. Naval Research Lab (NRL) has demonstrated laser activated quantum well remodulators with data rates of 4.2 Mbits per second from a hovering UAV. They expect to achieve as much as 10 Mbits per second in the future. The power required would be what it takes to light up a small neon bulb. The key is the placement of the remodulator. Upon sensing the signal from the refueling rover as it passes over the Entomopter, an ID code would be impressed upon the reflected signal that tells the rover, “This is Entomopter No. 2 and I am currently at an altitude of four meters, and have nine minutes of fuel remaining.” This method provides wide-area coverage, avoids Entomopter-borne tracking or pointing systems, and avoids frequency interference between Entomopters.

Position updates for the Entomopters will need to be no more than a few times per second (when not in the landing mode), or even less. The rover is not flying the Entomopter (which is fully autonomous) so continual position updates are not necessary. These updates let the rover know only where the Entomopter is relative to itself and the other Entomopter(s). Similarly, health monitoring does not need to occur more than a few times per second. If the Entomopter is self monitoring, it will have a high internal diagnostic bandwidth, but the “I'm OK” signal back to

the refueling rover does not need to be frequent, nor of high bandwidth. Even if there is a problem, there is little that the rover can do to help. The robustness has to be built into the Entomopter.

Without expending energy by radiating signals back to the rover, therefore, the Entomopter can:

- Know where it is relative to the rover,
- Know where other Entomopters are relative to its own rover-referenced position,
- Know where local obstacles are relative to its own rover-referenced position, and
- Exploit the radar beacon to hone in on the rover coordinates when returning to refuel.

This concept can even be extended to gross collision avoidance, wherein the rover warns the Entomopters of surrounding obstacles, although short range onboard systems may be more desirable for last-minute, emergency reactions to avoid collisions.

4.2.1 Minimum Energy Short Range Obstacle Avoidance System

The terrestrial Entomopter with its reciprocating chemical muscle system is capable of emitting short range frequency modulated continuous wave (FMCW) acoustic ranging beams that are swept in a forward hemisphere by the flapping wing action, and this could also be applied to the Mars context. This feature is essentially free in terms of energy expenditure, because it capitalizes on waste gas from the reciprocating chemical muscle that would otherwise be vented into the atmosphere. Using acoustic ranging methods similar to bat navigation, the Entomopter is able to recycle waste products from locomotive respiration to create an FMCW ultrasonic emission for obstacle avoidance and altimetry. A miniature gas-operated ultrasonic transmitter for the Entomopter has been demonstrated as part of the DARPA/DSO Mesomachines for Military Applications program. [186]

Figure 4-1 shows how a tuned resonant cavity can be acoustically excited by a waste gas jet from the reciprocating chemical muscle (used to drive the wing flapping of the Entomopter) to produce an ultrasonic emission (other techniques physically similar to "dog whistles" can also achieve ultrasonic acoustic emissions at scales compatible with the Entomopter and its reciprocating chemical muscle).

By varying the length of the cavity with a mechanical linkage to the reciprocating chemical muscle or Entomopter wing system, the frequency of the ultrasonic emission can be swept as a series of Eigen value frequencies approximating a linear triangle or sinusoidal wave (depending on the linkage used) as shown in Figure 4-2 for the terrestrial Entomopter. A similarly sized system tuned for the speed of sound in the Mars atmosphere would exhibit similar behavior.

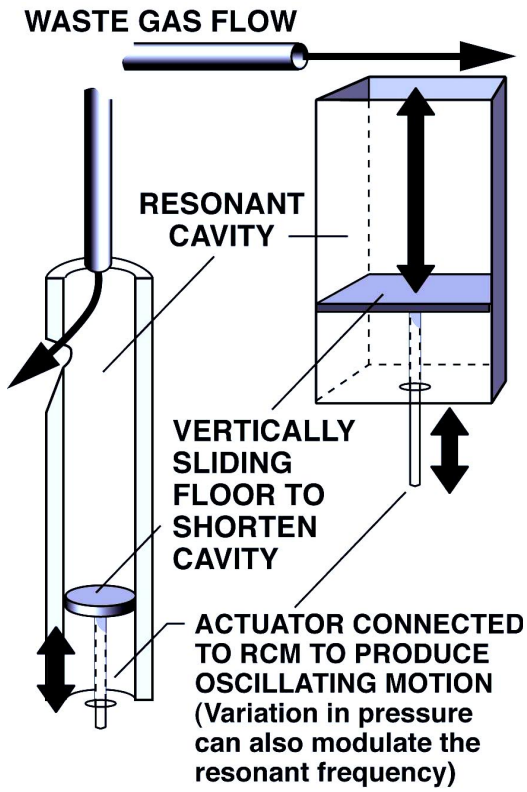

Figure 4-1: Acoustically Excited Tuned Resonant Cavity

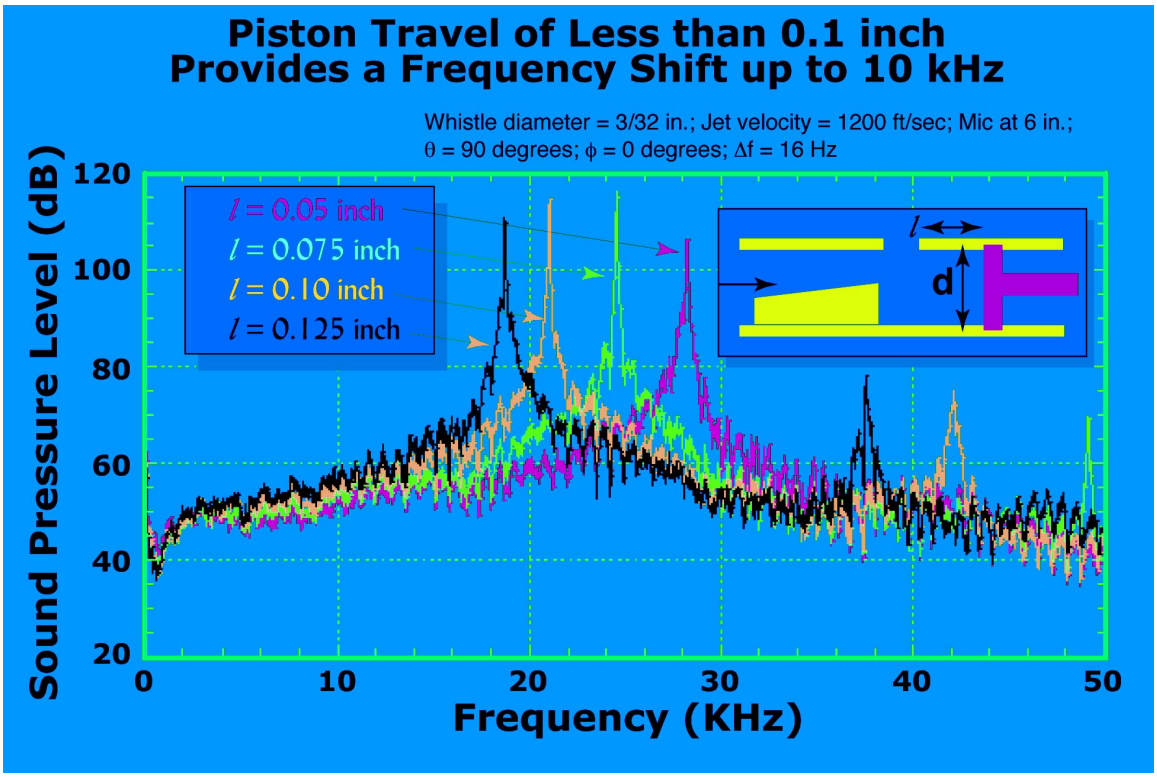

Figure 4-2: Measured Response Data of a Mechanically-modulated FMCW Source Sized for the Terrestrial Entomopter. (Data acquired under GTRI's DARPA/DSO-funded Mesoscaled Aerial Robot Program.)

As shown in Figure 4-3, such an FMCW waveform can be used to generate a ranging solution that resolves Doppler ambiguities.

A single ultrasonic acoustic source can be vectored by the wing flapping mechanism of the Entomopter to illuminate not only the ground for altimetry, but also to each side to detect impending collisions with objects. The same beam can be multiplexed as shown in Figure 4-3 to create a forward looking beam. Response to the received ranging signal would control the lateral flight path of the Entomopter as well as its altitude. Active flow control of the wings would affect lateral maneuvers and can be used to temporarily adjust altitude. An increase or decrease in wing flapping frequency around the resonant point (as controlled by fuel metering) would affect longer term vertical maneuvers.

Processing of these return signals could be discrete in that any range to a side obstacle can be ignored so long as it does not intrude within the Entomopter's safety zone. When an obstacle moves too close (either due to the movement of the obstacle or due to the Entomopter closing in on the obstacle) the behavior could be a simple avoidance response. Such a simple obstacle avoidance algorithm can be implemented with a minimum of onboard processing and can in fact be almost a reflex action, but the resulting flight path could be "zig-zagging" as the vehicle alternately tends toward and avoids opposite obstacles. On the other hand, altitude might be monitored more closely in terms of actual distance to facilitate more coordinated landings.

GTRI has designed and built a mesoscaled ultrasonic ranging transmitter for use on the terrestrial Entomopter, and has performed sound pressure level measurements at reciprocating chemical muscle waste gas pressures in the range of 40 psi. These tests have shown that sensible ranges of three meters are attainable, with greater ranges possible. (See sound pressure levels of Figure 4-3.) Emission patterns have been plotted to show that a directional beam can be created, and an acoustic mirror scheme has been designed into the Entomopter which is capable of scanning the output from a single ultrasonic source ranging from right-horizontal, to head-on, to downlooking (altimetry), to head-on, to left-horizontal on each wing beat. All of these features of the terrestrial Entomopter are transferable to the Mars version.

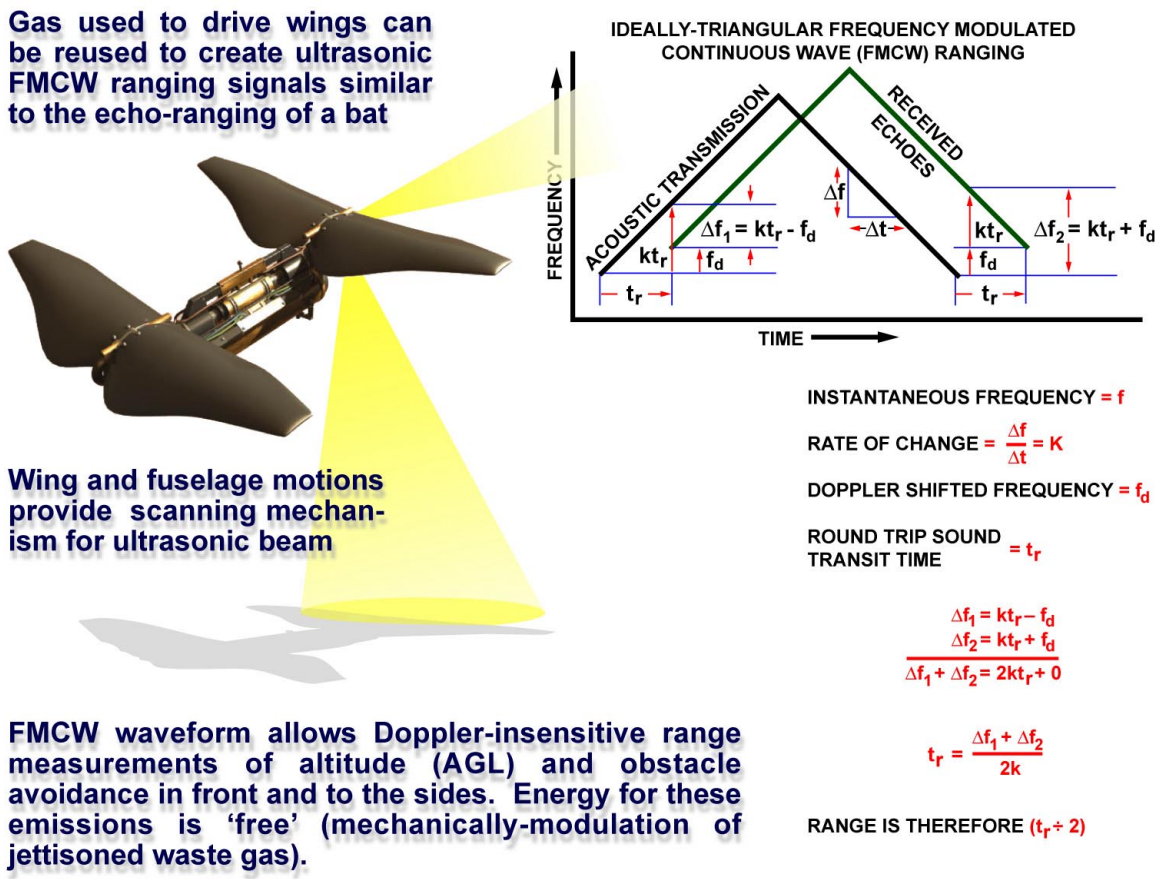

Figure 4-3: Multiplexing of Waste Gas-driven FMCW Ultrasonic Acoustic Ranging Source

The acoustic ranging concept would also be useful during landing in order to give higher resolution short range position updates at a high rate.

Another passive approach would be to observe the optical flow field as the Entomopter approaches either the planet surface or the landing deck on the rover. This is a biologically-inspired approach derived from analysis of honey bees and other insects. Although most insects lack stereo vision, distances to objects are gauged in terms of the apparent speeds of motion of the objects' images. Bees distinguish the presence of objects by sensing the apparent relative motion at the boundary between the object and its background. As demonstrated by research at the Australian National University, even narrow openings are negotiated by balancing the apparent speeds of the images in the two eyes (passive detection). Flight speed is regulated by holding

constant the perceived global image velocity. In doing so, bees landing on a horizontal surface hold constant the image velocity of the surface as they approach it, thus automatically ensuring that flight speed is close to zero at touchdown. This passive close-in navigation technique can be exploited for use in the Entomopter during landing.

The philosophy of minimizing energy expenditures by the Entomopters must be maintained. If there is a function that can be performed by the rover on behalf of the Entomopter, it should be. In doing so, the Entomopter will reap the benefit in either increased endurance, or increased science payload.

4.2.2 Navigation Under the Baseline Mars Scenario

The baseline Mars survey flight scenario has the Entomopter-based Mars surveyors flying in the following way relative to the refueling rover:

1. Entomopter launches from refueling rover and proceeds at an angle of between 80° and 90° from the rover's direction of travel. Launch is to the right side of the rover.
2. The flight path will go out to nearly 200m in a straight line, and then a circular 180° turn to the left will be initiated. At no time will the Entomopter be at a range of greater than 200 m from the rover.
3. The Entomopter will then fly in a straight line back to the rover, which will have progressed along its initial path at an assumed rate of 1 m/s. The diameter of the 180° turn will roughly equal the distance traveled by the rover during the entire flight out and back.
4. The rover launch platform is assumed to be 1m above the surface, and the Entomopter flight altitude is 5m above ground level (AGL).

Under the conditions of this minimal baseline, the maximum rover navigation radar range would be 200 m. A monopulse Doppler radar could identify each Entomopter and track it in range, azimuth, and elevation. A switched scanning array could provide 360° track-while-scan coverage with scan rates of 30 Hz. Each scan would provide not only range, azimuth, and elevation for each of the Entomopters, but also a polar map of obstacles.

The high speed of the Entomopter wing flapping coupled with any radial component of flight will be easily detectable as a Doppler shift in the return signal. The speed of the refueling rover can be easily filtered to remove rover platform motion from the radar data. Ground odometry from the rover will allow a notch filter to be adaptively placed directly over the platform-generated Doppler background impressed on all targets. The Doppler return from the Entomopter, due to its forward flight speed, could fall in the same range as that of the rover, depending on the radial angle of flight relative to the rover's radar and could therefore be filtered out. However, in practice, the low speed of the rover compared to the Entomopter wingbeat frequency will always make discrimination easy, even apart from the Entomopter's fuselage skin return.

Because the atmosphere is rarefied and humidity is low on Mars, high frequency monopulse Doppler radar emissions can be employed. Doppler shift is represented by

$$f_d = 2\nu \div \lambda$$

Equation 4-1

where fd is the radial component of the relative velocity (positive for decreasing range), ν is the radial component of relative velocity, and λ is the radiated wavelength.

For example, were 95 GHz chosen as the radar carrier frequency, the wavelength would be,

$$\lambda = c \div f \qquad \textbf{Equation 4-2}$$
$$= 3E10 \text{ cm/s} \div 95E9 \text{ Hz}$$
$$\sim 0.3 \text{ cm}$$

The Doppler shift resulting from rover platform motion when the rover is traveling at 2 m/s is

$$f_d \text{ (platform)} = 2(2\text{m/s})(100\text{cm/m}) \div 0.3 \text{ cm} \qquad \textbf{Equation 4-3}$$
$$\sim 1.333 \text{ kHz}$$

A low-pass filter with adequate roll-off below 2 kHz will effectively prevent any platform motion from being detected; however, knowing that 1.333 kHz is the offset due to platform motion, the rover can apply the cosine of this value to all Doppler returns depending on their angle relative to the platform motion. In this way, rover platform motion can be completely eliminated from the measurement of the surrounding terrain and Entomopters.

Were the Entomopter to be flying straight and level with one-meter wings (tip-to-tip) flapping at a frequency of 10 Hz over a 180° angle, the returned 95 GHz carrier frequency would be modulated at a 10 Hz rate with the frequency excursion of the Doppler signal depending upon the orientation of the Entomopter to the rover's radar. For example, in the simplest case where the Entomopter is flying parallel to the rover at the moment the radar scans across it, the received Doppler (corrected for rover platform motion) would be:

Wing radial advance distance (m) = 2(0.5)sin (45) = 0.35 m

Assuming a linear acceleration, a distance of 0.35 m would be covered in 0.025 seconds, yielding a radial velocity of 14.142 m/s.

fd (45° downbeat) = 2 (14.142m/s)(100cm/m) ÷ 0.3 cm ~ 9.428 kHz.
fd (midflap) = 2 (0m/s)(100cm/m) ÷ 0.3 cm= 0 Hz.
fd (135° downbeat)= 2 (-14.142m/s)(100cm/m) ÷ 0.3 cm ~ -9.428 kHz.

Note that the negative sign on the 135° case is due to the fact that the wing is moving radially away from the radar, and the Doppler shift will be subtracted from the returned carrier. Since all parts of the wing are moving at different radial rates from the root to the tip, the Doppler signature will range from 0 Hz to a maximum of roughly those shown above (assuming that the wing is accelerating linearly as it flaps).

Therefore, the demodulated and rectified Doppler return from the Entomopter wing under the specified flight conditions would be a unique (for Mars) frequency modulated (FM) signature that varies from 0 to roughly 9 kHz every 0.5 seconds. Such a signal would be unambiguously that of the Entomopter; which Entomopter is being detected is another question, however.

The problem of which Entomopter is detected by the refueling rover's radar is easily resolved by having each Entomopter respond to the rover's radar interrogation signal with a unique code. This code would contain a vehicle-identification code followed by useful information, such as the Entomopter's measured air speed, fuel remaining, vehicle-health monitoring parameters, and altitude above the planet's surface (which would serve both as sanity check for the rover radar, since it already has an estimate of this value, as well as new data were the Entomopter flying over a canyon, the bottom of which is occluded from the view of the rover's radar).

The Entomopter's response to the rover's radar interrogation signal need not be an emission of energy. Rather, the Entomopter can remodulate the radar return by intelligently modulating its own radar cross-section. The choice of frequency for this remodulation must be different than the expected Doppler range presented by the Entomopter (above that expected from the effects of wing-beating) so that the rover can distinguish the Entomopter communication from that of the wing beating. A modulation of the radar cross-section is an amplitude modulation (AM) phenomenon and will not be affected by the Doppler shift. Very low power methods of modulating the radar cross-section of the Entomopter can be achieved by solid state means. A significant advantage to this technique is the obvious frequency deconfliction that results from multiple Entomopters not having to radiate simultaneously.

As shown in Figure 4-4, the information about Entomopter locations, rover range, and obstacle locations can be impressed upon the interrogating radar signal as a frequency that is above the expected Doppler due to the skin return. The flapping-induced Doppler will not enter into this because only the radial closing rate of the Entomopter with the refueling rover will contribute to the Doppler shift seen by the Entomopter.

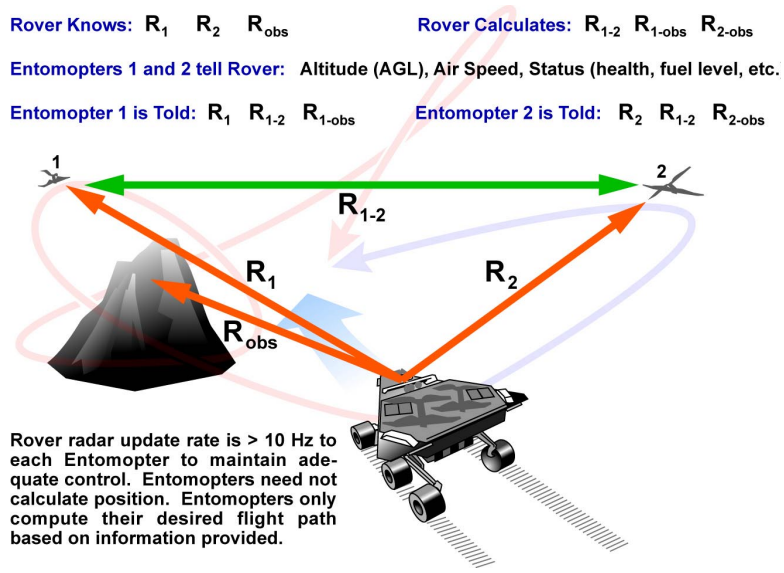

Figure 4-4: Rover-centric Information Paths Used in Navigation

For maximum flight speeds on the order of 30 m/s, the Doppler shift seen on the radar carrier by a painted Entomopter will be

$$f\text{d (platform)} = 2(30\text{ m/s})(100\text{ cm/m}) \div 0.3\text{ cm} = 20\text{ kHz}.$$

Choosing a frequency modulation for the 95 GHz carrier that is ten times this value (200 kHz) would provide adequate FM information bandwidth while at the same time avoiding any corruption due to Doppler shift.

Both the rover information updates and the Entomopter ID and status replies are low bandwidth data and can be exchanged in bursts even with error-correcting code overhead. A refresh rate of 10 Hz for these two-way data bursts even means that not all parameters need to be exchanged upon each radar painting. The highest priority information will be that necessary for obstacle avoidance (the Entomopters themselves being obstacles to each other). Information about fuel remaining is low priority and could be downloaded once every hundred scans (every 10 seconds).

The transmission of high bandwidth data over the navigation link is ill-advised for several reasons. First, the bandwidth and revisit time for this method of information exchange does not support the high bandwidth requirements of video, still-frame pictures, or real-time streaming data. Transmission of color video can consume as much as 75 MHz of bandwidth depending upon the resolution. This is also costly from an energy standpoint, as any onboard emitters carried by the Entomopter will either increase its mission payload weight or reduce mission endurance. Finally, because the projected Entomopter flights will be brief (minutes as opposed to hours), any high bandwidth data can be stored onboard for downloading later during the refueling process.

The need for real-time streaming data is not warranted during early missions prior to manned exploration, because there is no one present to take advantage of the real-time data, and the latency for transmission back to Earth diminishes the timeliness of the data. Data gathered during a 10-minute flight would not be received for 11 minutes, were it able to be transmitted directly back to Earth from the Entomopter. Any reaction to the data received would require a further delay of 11 minutes to be received by the Entomopter due to the 190 million km distance between Earth and Mars--long after the Entomopter would have landed for refueling.

It is assumed that most of the Entomopter science data will be uploaded to the refueling rover when the Entomopter returns for refueling. Continual linking of high bandwidth data is extremely costly from an energy standpoint, and since it is essentially only being archived (as opposed to being used for flight control or real-time viewing), quick-look updates are assumed to be adequate. In the event of a failure or crash, a large amount of data would not be lost since the Entomopter excursions are assumed to be fairly brief (missions of several minutes each, unless the vehicle lands to take data from a stationary location for an extended period). Therefore, only several minutes of stored data would be at risk before it was uploaded to the refueling rover upon return of the Entomopter. Also, because of the low mass of the Entomopter, crashes will not likely disable any of the onboard electronics. Thus, if an Entomopter failed, it might still be able to transmit its data cache back to the rover from its crash site.

The major implication for the use of a rover-centric navigation system is that the Entomopters must remain within the line of sight of the rover to get rapid situational updates. This implies that as range from the rover is increased, due to terrain irregularities, the Entomopters will have to fly at higher altitudes. Because the Entomopters are fully autonomous, however, there is no need for the navigation information to maintain stability of flight.

Therefore, it is entirely reasonable that an Entomopter can consciously break its navigation link and fly below the radar horizon to more closely investigate an item of interest, with the intent of

climbing in altitude a point at which it will be reacquired by the rover radar. Such a maneuver would be negotiated a priori with the rover to assure that the Entomopter is not operating in the vicinity of another Entomopter when it goes out of sight and to alert the rover that it should not expect to see the Entomopter for a brief period.

Were a non-line-of-sight maneuver to be executed, the Entomopter would navigate with only its altimeter and any short range obstacle detection/avoidance system normally used for terminal flight path adjustments during landing (for example, the acoustic FMCW ranger that is inherent to the reciprocating chemical muscle). This would allow emergency obstacle-avoidance maneuvers to prevent a collision with an outcropping or the ground surface. Because there is risk involved in flying without navigation cues, such a maneuver would likely be considered only if the Entomopter were to investigate a large open space on the other side of a masking ridge, or if the Entomopter were to descend into a large chasm or canyon.

Note that were the Entomopter to wander beyond radar detection range due to its own motions or those of the ever-progressing rover, the navigation link would be lost. However, because the rover's radiated signal must be sufficiently strong to elicit a skin return from the Entomopters, the rover transmitter will serve as a useful homing beacon for a much greater range than it can function as a radar. So if an Entomopter were to rise up from behind an obstruction to the point that it is once again in line of sight with the rover, but the rover is unable to acquire the Entomopter, this would immediately be evident to the Entomopter based on the lack of range, azimuth, and elevation information updates sent to it by the rover. Basically, it would still be receiving the “awaiting reacquisition” signal from the rover. The Entomopter would recognize this and change its mode of behavior to one of beacon following. This will lead it back to the rover, even apart from navigation data. At some point it will enter tracking range, and the rover radar will reacquire the Entomopter, whereupon the navigation information stream will be reinitiated and the Entomopter can revert to its mission plan.

Nap-of-the-surface flight is also possible during both line-of-sight and non-line-of-sight operations. The criterion for nap-of-the-surface flight is that the flight speed must not exceed the maneuverability of the Entomopter for its given obstacle-avoidance and altimetry-sensor range.

In summary, navigation can be achieved with a rover-centric scanning radar system that interrogates the environment to detect obstacles as well as flying Entomopters. The distinctive Doppler signature of the Entomopters can be exploited to easily identify and track them against the Mars clutter background. Information gathered by the rover-borne radar, when processed, can be sent to each Entomopter as a frequency modulation of the radar carrier. The center frequency for the uploaded data will be above the maximum expected Doppler shift due to Entomopter radial speed. Each Entomopter, having detected that it is being painted by the radar, will modulate its radar cross-section using techniques similar to quantum well remodulators. This is an amplitude modulation and will not interfere with the already impressed FM data upload, and will not be corrupted by the much lower frequency wing-flapping-induced radar cross-section seen by the rover. This obviates the need for long range emissions by the Entomopter, thereby saving weight and energy. Short range altimetry emissions will require much lower power and will not conflict with the navigation signal cues or responses. High bandwidth payload data will be stored onboard for downloading once the Entomopter has returned to the refueling rover for replenish-

ment. If the acquired payload data needs to be transmitted to Earth, the refueling rover will server as a high power relay once the data has been captured from the Entomopter.

The advantages of the rover-centric navigation approach are thus:

- No a priori knowledge of topography required,
- Rover bears the weight of the system,
- No energy radiated by Entomopter,
- Inherent beacon for homing,
- Extended range, and
- Doubles as communication system.

4.3 Entomopter-borne Active Emitters for Navigation and Communication

A second option was explored in which various emitters are placed on the Entomopters to enable longer range operation and non-line-of-sight flight relative to the refueling rover. There are very strict requirements of low weight, minimum power consumption and small size for the Entomopter onboard system. Given these restrictions, as mentioned above it is beneficial to utilize the rover to perform as much of the required functionality as possible, and to utilize power as efficiently as possible. However, it may not be possible to perform some of the required functions with the rover, making it necessary to utilize a multifunctional communications/control subsystem on-board the Entomopter. In the following sections, the feasibility and required power levels are explored for using onboard active emitters to accomplish communications, positioning, collision avoidance, and altimetry, as well as some remote sensing applications. A conceptual view of Entomopter communications, positioning relative to the rover, obstacle detection and altimetry is shown in Figure 4-5.

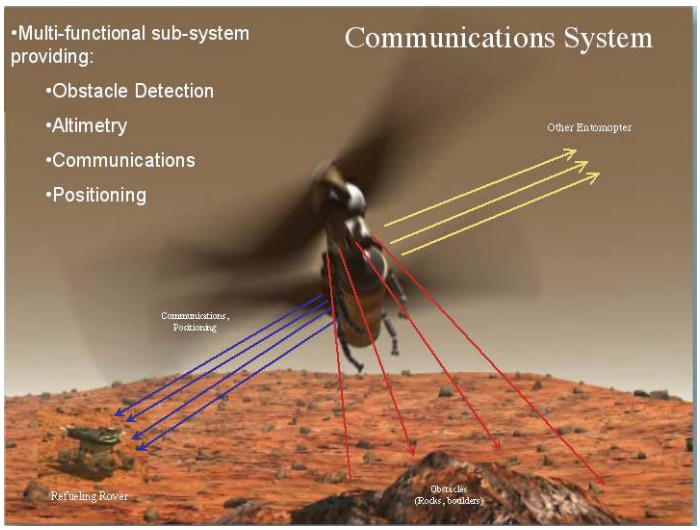

Figure 4-5: Conceptual View of Communications/ Control Subsystem Functionality

4.3.1 Assumptions and Performance Goals

The following assumptions were used as initial performance goals for the communications/control subsystem analyses. Figure 4-6 shows a side view of the Entomopter illustrating the assumed coordinate system.

Altitudes are not expected to exceed 10 m, and distances to the refueling rover are assumed to be within 200 m.

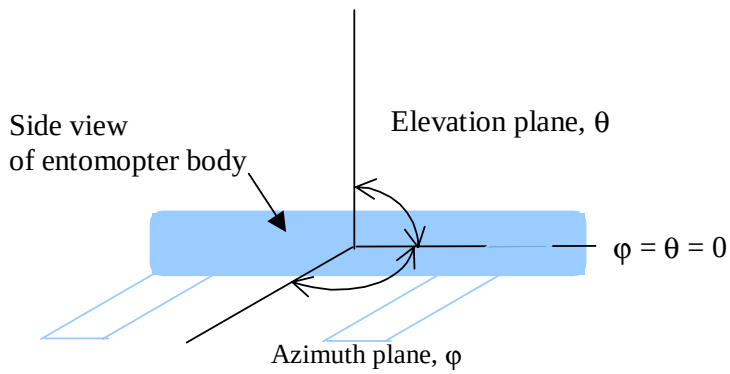

Figure 4-6: Side View of Entomopter Illustrating Assumed Coordinate System

4.3.1.1 Obstacle Detection Assumptions

- Azimuthal coverage: $\varphi = -90^o$ to 90° for front and side coverage
- Elevation angle: $\theta = -90^o$ to 45° for coverage below and in front of the Entomopter
- Minimum range: This minimum range will be determined by the maximum reaction time of the Entomopter. A worst case five-second reaction time will be assumed. At ~14 m/s (cruising speed), this results in a minimum range of 70 m. At ~3 m/s (exploration/inspection speed), this results in a minimum range of 15 m.
- Maximum range: ~ 200 m
- Range resolution: ~ 0.5 m
- Vertical resolution: ~ several meters at maximum range, ~ 25 m at minimum range
- Horizontal resolution: ~ several meters at maximum range, ~50 m at minimum range

The Entomopter will navigate autonomously. It will take off, explore the Mars terrain, and land without human intervention. The multifunctional subsystem investigated here will be capable of detecting objects in the Entomopter flight path, which will eventually be coupled with an onboard auto-routing algorithm and navigational control for a complete collision-avoidance system.

It is unlikely that the Entomopter will fly into enclosed areas, so avoidance of obstacles from above will not be a priority. Fine cross resolutions are not needed because the goal is to avoid obstacles, not to achieve synthetic vision where detailed information is required to identify the detected obstacles. Most obstacles will be terrain features, so the system resolution can be several meters at maximum range. As obstacles get closer, they occupy a greater portion of the field of view, so the ability to avoid smaller things will be enhanced as the Entomopter approaches them. Vertical resolutions (elevation) can be larger than the horizontal (azimuth) resolutions since it is unlikely that the Entomopter will be flying under things or through holes. Since most natural obstacles will not afford a path beneath, obstacle avoidance responses will typically be to

change flight path in azimuth because it takes less energy than climbing over things or having to regain altitude after going under something. Thus, finer azimuthal resolution will be incorporated as opposed to those of elevation.

It is assumed that the Entomopter will be able to look to the front, to the sides, and down with an appropriate antenna. Antenna beams will be scanned in needed directions to conserve power. The frequency of front/side/downward observation will be mission-driven. The desired azimuthal and elevational resolutions can be achieved by designing the antenna to have appropriate beamwidths.

4.3.1.2 Altimetry Assumptions

- Maximum altitude = 10 m
- Minimum range ~ 10 cm
- Range resolution near maximum altitude ~ 1 m
- Range resolution at altitudes < 3 m ~ 6 cm

The Entomopter will have onboard altimetry radar to locate its altitude AGL. This information will be used for the Entomopter to land on the Mars terrain for exploration if the mission so requires. In addition, this information can be used for elevation positioning relative to the rover. Less resolution is needed while the Entomopter is in flight at its nominal altitude, but finer resolution is critical when the Entomopter is flying at low altitudes, as well as for landing. This may drive the design to a multi-sensor solution (radar for long range, FMCW acoustic ranging for low altitude).

4.3.1.3 Communications Assumptions

- Azimuthal coverage = 360°
- Elevation coverage = 360°
- Maximum height = 10 m
- Maximum range = 200 m
- Minimum range = 10 cm
- Acceptable bit error rate (BER) = 10^{-5}
- Required data rates will be based on mission requirements, to be determined.

To conserve power, the multifunctional subsystem can be used simultaneously for communications, positioning, obstacle detection, or altimetry. Again, the Entomopter will be completely autonomous, and its operation need not rely on Earth-bound mission planners nor on the refueling rover. Therefore, continuous, high-data-rate communications are not necessary.

Common science payloads may include sensors onboard the flight vehicles, which make climatic, environmental, and/or magnetospheric readings. In addition, there will be flight monitoring hardware. The lessons learned from the Pathfinder mission, the importance of having an adequate number of telemetry channels to monitor the condition of the radio hardware, and temperature sensors were stressed in order to diagnose problems.

Although the majority of the scientific data will be uploaded directly to the rover, it is assumed that quick-look samples will be communicated back to the rover on a regular basis. These samples will contain only small amounts of data such as health monitoring updates, fuel level and altimetry readings.

4.3.1.4 Positioning Assumptions

- Spherical coverage
- Maximum altitude = 10 m
- Maximum range = 200 m
- Minimum range ~ 10 cm
- Resolution near max range ~ 1 or 2 m
- Resolution at ranges < 2 or 3 m ~ 3 to 6 cm

It is necessary to obtain two-dimensional (2D) positioning information (azimuth and range), because the elevation will be determined by the onboard altimetry information.

Positioning is commonly accomplished by using global positioning satellite (GPS) solutions. In the absence of GPS it is assumed that for this application, the positioning system will be incorporated into the RF functionality of the Entomopter/rover to locate the Entomopters relative to the rover.

4.3.1.4.1 Monopulse Positioning

In an effort to conserve power, the main positioning method will use the “quick look” samples and health monitoring communication signals as described above. To do this, a quick burst encoded with the Entomopter identification, time, and altitude is needed. This can be coded into the header of these quick health monitoring signals sent from the Entomopter to the rover. When the refueling rover or other Entomopters receive the signal, the range can be calculated from the time of flight, and the azimuth can be determined using monopulse techniques where the received signal strength is compared in the azimuthal sectors of the rover’s receiving antenna. Again, an MTI type of radar placed on the refueling rover could easily discriminate between signals returned from ground clutter and the Entomopter. The azimuthal resolution is determined by the antenna beam width of each of the azimuthal sectors. Thus, the resolution could be varied during the mission by using a switching network on the antenna. The altitude can be sent in the reflected signal from the Entomopter by modulating the RCS (as described earlier), or one of the Entomopter emitters can downlink this information to the refueling rover.

4.3.1.4.2 UWB Geolocation System

The Phase I Final Report suggested a positioning scheme based on the ultra wideband (UWB) precision geolocation system presented by Fontana in [96], where N fixed position beacons would be used to determine the 3D position of a mobile ranger--the Entomopter in this case. For this application, the N beacons would be realized by placing N transceivers on the refueling rover.

This system would work as follows:

- The Entomopter sends out a communication signal, which includes a header coded with the Entomopter ID, altimetry, and time. For multiple Entomopters, their transmitted messages will begin with an individual identification code.
- Upon receipt, each beacon determines if the message is from the Entomopter by checking the signal ID.
- If the message is from the Entomopter, each beacon calculates the time it took the signal to reach the beacon ΔtI based on the time of departure from the Entomopter, which was coded in the Entomopter message header.
- The rover signal processing determines the 2D relative position (x,y) by solving N simultaneous equations.

$$c(\Delta t_i - \Delta_i) = 2\{(x - x_i)^2 + (y - y_i)^2 + (z - z_i)^2\}^{1/2}$$ **Equation 4-4**

where c is the speed of light and i = 1, 2, …N, and z_i is the Entomopter altimetry, which is known.

This technique would require additional onboard power from the Entomopter making this method less attractive than the monopulse technique described above. In addition, the size of the rover will limit the distance that the transceivers can be placed from each other. A potential road block to this technique would be that the transceivers located on the refueling rover would be essentially co-located, and as the Entomopter range increases, the baseline for this array becomes more point-like and the elliptical probable error (EPE) increases drastically for the x-y dimension. This is equivalent to bad geometric dilution of precision in the GPS solution. Thus, the concept as proposed in the NIAC Phase I report will not be considered further in this Phase II Final Report.

4.3.2 Propogation Losses

When performing the radio link analysis, propagation losses encountered on the Mars surface must be considered. From a radio wave propagation study for communications on and around Mars, the gaseous atmospheric attenuations by water vapor and oxygen at the Mars surfaces were determined and are compared to those at the Earth's surface versus frequency in Figure 4-7 [123]. As illustrated in the plot, this attenuation is quite low relative to that on Earth, because the Mars atmosphere has very low concentrations of uncondensed H_2O and O_2 [123]. On the contrary, there is a significant amount of CO_2 and N_2, but these gases do not have electric or magnetic dipoles and thus do not absorb electromagnetic energy from the waves. However, Ho and Golshan indicate that these gasses may generate dipoles through collisions and interact with waves under a high-density condition and absorb electromagnetic waves in the infrared and optical bands [123]. For this study, the atmospheric attenuation as plotted in Figure 4-7 is considered, and it is assumed that CO_2 and N_2 gases will not cause attenuation to radio wave propagation. As shown in Figure 4-7, for the short ranges assumed for this mission, propagation attenuation is negligible.

According to the same Mars propagation study, dust storms are considered the most dominant factor in propagation attenuation. There are three supposed types of dust storms. Planet-encircling storms are believed to encircle the planet at some latitudes; regional storms include clouds

and hazes with spatial dimensions greater than 2,000 km, and local dust storms include clouds and hazes with spatial dimensions less than 2,000 km. Reference [123] describes Mars dust as consisting of primarily basalt and montmorillonitic clay. Using a corresponding dielectric constant, it was shown in [123] that at Ka-band, large dust storms can cause as much as 0.3 dB/km or more of loss, with normal dust storms causing about 0.1 dB/km. Most large dust storms occur in the southern hemisphere during later spring and early summer when the southern hemisphere suddenly becomes hot [123]. It is also important to keep in mind that dust attenuation is proportional to operating frequency. Thus, more attenuation will occur at higher operating frequencies. Although it is important to be aware of the potential presence of these dust storms, for the purposes of this analysis Entomopter operations will be curtailed during the presence of dust storms. This is due not only to degraded RF performance, but due to the uncertainties of flight during these storms.

Attenuation will also be caused by scattering of the signal from sharp discontinuities in objects in the communication path. As discussed in [106], a scattering cross-section can be defined for any object as the ratio of the total power scattered by the object and the power-flux density incident on the object. For sharp, long edges (several wavelengths long), the effective scattering cross-section A_s can be described as

$$A_s = K\lambda L \ ,$$

where L is the object edge length, λ is the wavelength, and K is a dimensionless constant less than one, having a magnitude that depends on the scattering object. From this relationship, it is evident that scattering is reduced with higher frequency. Golshan and Ho indicate that signal blockage caused by objects or terrain features on Mars can be a significant problem unless the communications are limited to a small area in a fairly flat terrain with relatively few large rocks. They recommend robust communication protocols or operational procedures to avoid loss of data from such scattering interference, or suggest using Mars orbiting relays to reduce blockage problems. They also suggest positioning the base station on a commanding location to reduce blockage probability and extend line of sight communications.

The baseline scenario used for this study assumes that the ground is flat and there are no obstacles, thus scattering losses will be neglected. However, when considering an operating frequency, the reduced scattering cross-section (and thus reduced scattering losses) with increasing frequency should be considered.

4.3.3 Frequency of Operation

The frequency of operation must be coordinated with those already planned for future Mars missions. This would include the link from the Mars surface to an orbiting relay satellite (UHF) or direct links from the Mars surface to the deep space network (Ka-band and X-band) [70]. When choosing an operating frequency, propagation losses due to oxygen and water vapor are a concern on Earth but are orders of magnitude less on Mars, as shown in Figure 4-7. Because size and weight are important criteria for the Entomopter, it is desirable to operate at higher frequencies so that antenna size is indirectly proportional to frequency. This also has the advantage of reducing scattering losses, as mentioned in the preceding section. One must also consider available hardware, which becomes difficult to realize at higher frequencies. In addition, link budgets

will be performed to determine required power as a function of frequency. The actual frequency must be determined based on available component technology at the time of the actual mission. Based on the above, operation at 18 GHz, or K-band will be assumed in the following analyses.

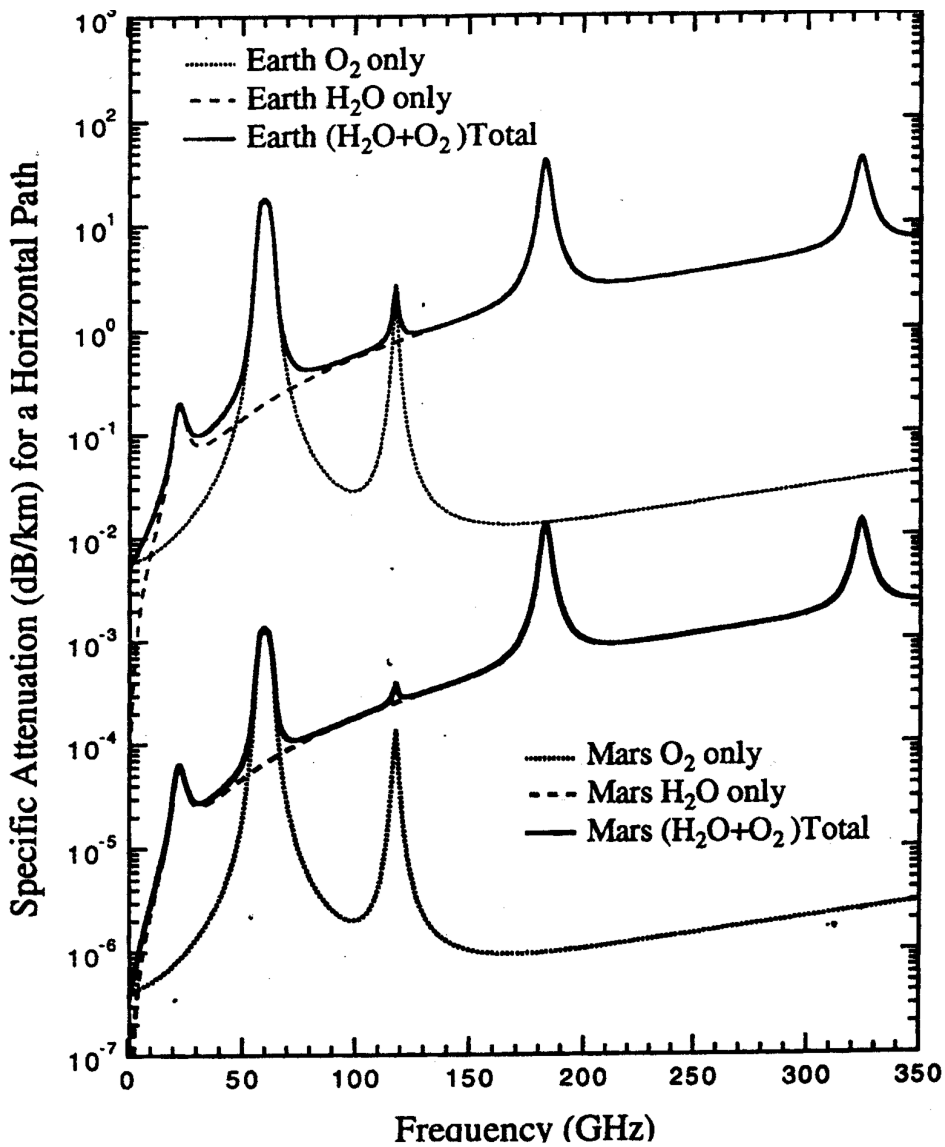

Figure 4-7: Atmospheric Absorption Attenuation by Water Vapor and Oxygen at Earth and Mars Surface

4.3.4 Antennas

The multifunctional antennas used on the Entomopter and rover must provide adequate beam coverage to accomplish the following:

1. Detecting objects in the Entomopter's flight path for collision avoidance. Obstacle detection will be performed in 3D (azimuth, elevation, and range). In this manner, obstacles are detected in front, to the side, as well as up and down so that Entomopter flight is designated by the accurate detection of obstacles instead of trial-and-error flight patterns.
2. Altimetry for the Entomopter must have precise range for detecting the location of the ground for landing and collision avoidance.
3. Communicating between Entomopters and the rover, with spherical coverage around the Entomopter, so that it can communicate with the rover or other Entomopters in any direction.
4. Positioning of the Entomopter in 3D relative to the rover.

Since the Entomopter will typically fly at low altitudes (and hence low angles relative to the rover or other Entomopters), communications will mainly be horizontal. If the Entomopter were flying at its maximum altitude of 10 m and maximum range of 200 m from the rover, this implies an angle of 2.9^{o} with respect to the horizontal. Entomopters communicating with Entomopters overhead will have to look upward, but if the maximum altitude of operation is only 10 m, the antenna gain can be less in the vertical dimension. However, this antenna gain must account for the pitch and roll of the Entomopter during flight or while on an uneven surface. (Assuming an omnidirectional antenna pattern, the design will not have to account for yaw.)

4.3.4.1 The Challenge of Antenna Pointing

Antenna pointing alternatives fall into the following categories: gimbaled, phased arrays, and electronically switched. The main problem with all of these techniques (beyond weight and power) is the necessity to track the aim point to which the energy is to be emitted. For a vehicle flying straight and level, this is less of an issue as transmission angles change slowly, but if the vehicle is changing attitude rapidly, or if the vehicle is interacting with more than one aim point (other Entomopters and the rover), then the onboard inertial system must not only keep track of the aim points based on some external GPS-like reference, but it must factor in its own gyrations as the Entomopter changes altitude.

Gimbaled antennas are too heavy relative to the function that they provide, and based on flight vehicle dynamics, are often too slow in slewing to new positions. When multiple recipients exist (other Entomopters and the rover), the idea of a gimbal is even less attractive.

On the other hand, phased arrays can be much lighter and can redirect multiple simultaneous beams independently, but they can be bulky if both azimuth and elevation beam positioning is required, and the power necessary to run the multiple elements necessary to "bend" the beam is not energy efficient.

Multiple electronically switched antennas (unlike a phased array) orient individual antennas at all angles of interest and emit energy in the desired direction from single or multiple (simultaneous) emitter antennas. Although not phased, and therefore not needing to be contained in an array, electronically switched antennas suffer from the same weight penalty due to the redundant nature of their hardware. The fact that they are discrete directed emitters means that they will be more efficient than a phased array, but will not have the nearly infinite angular coverage of the phased array. As the beamwidth of each switched emitter is decreased to increase gain and direc-

tivity, the number of emitters must increase in order to get adequate angular coverage. In the limit, this will approach the number of emitters found in the phased array, the difference being that one is a conformal array while the other is a more planar array.

4.3.4.2 Requirements Driving the Antenna Design

The goal is to accomplish the described requirements with as much overlap in functionality as possible for power conservation. For this application, the obstacle detection poses the most stringent requirements, so the focus will be on this aspect of the project first. It would be beneficial to use the same antenna to provide front hemispherical coverage for communications as well as obstacle detection. Phased array antennas are commonly used for searching and tracking applications where the 2D or 3D location of an object must be provided. A hemispherical dome-shaped phased array as described in [129] would fulfill all these requirements. However, a large number of antenna elements would be necessary, each requiring a carefully designed signal path to eliminate phase differences between different paths. In addition, each signal path requires a phase shifter and gain-controlled low noise amplifier. The phase and gain are controlled to provide the desired antenna pattern. The complexity of this design may prohibit its use for this application where low power and reliability are critical.

Switched arrays, on the other hand, offer more simplicity, because pattern diversity can be achieved by controlling the state of a number of RF switches but produce a limited number of beam patterns. In this way, beam coverage and resolution can be controlled selectively on a “need only” basis. In this way, power is conserved by illuminating only the required coverage area for the functionality needed at a certain time (obstacle detection, communications, etc.). The linearly tapered slot antenna (LTSA) circular array (sunflower antenna) shown in Figure 4-8 and described in [240 and 154] is one such switched array that could fulfill the Entomopter's multifunctional needs. A photo of an operational K-band sunflower antenna is shown in Figure 4-8. This antenna, proposed for mobile communications, is fed by a 1:16 microstrip line power splitter composed of T junctions and right angle bends. A conventional microstrip-to-slotline transition is used to electromagnetically couple the output ports of the splitter to the slotline of the LTSA. The measured radiation pattern of this endfire antenna is shown in Figure 4-9 at 19.8 GHz when the antenna is placed over a reflecting ground plane. From the figure it is obvious that the antenna beam is omnidirectional in the azimuthal plane and is displaced about 28 degrees above the horizon in the elevation plane. The displacement in the elevation plane is proportional to the distance between the antenna and the ground plane. As shown in Figure 4-10, by removing the ground plane, this displacement above the horizon can be removed and the antenna beam centered about the elevation angle $\phi = 0^o$. The shape of the sunflower elements can be varied to achieve the desired frequency, bandwidth, gain and 3 dB antenna beam bandwidth.

This antenna has advantages of wide bandwidth operation and compact configuration, making it an attractive antenna for this mission where onboard space is limited and very wide band signals are being considered. It resembles a hockey puck that can be mounted easily on the Entomopter body. The diameter of the K-band design shown in Figure 4-8 is approximately 16 cm (6.3"). A potential mounting scenario is shown in Figure 4-11, where half of the LTSA is mounted on the front and half on the back of the Entomopter. In this way, when all elements are illuminated, 360° of azimuthal coverage can be obtained by slightly widening the first and last sunflower pet-

als to provide just over 180° of azimuthal radiation at the front and back antennas. The overlapping patterns would provide full azimuthal coverage for communication as shown in Figure 4-12, where an illustration of the top view of the Entomopter and antenna patterns are shown. The inherent gain variation of this antenna in elevation can be used to provide only the needed gain above and below the Entomopter (where the range is considerably less), and maximum gain in front, back, and to the sides (where range is considerably larger) as shown in Figure 4-13, where a side view of the Entomopter and antenna patterns are shown.

The elements can be switched on and off to achieve narrower beams in azimuth for obstacle detection. The shape and number of elements can be varied to provide adequate gain and horizontal/vertical resolutions. If additional resolution or coverage is needed for obstacle detection in elevation, additional hockey puck halves can be configured above/below the mounting scenario shown in Figure 4-11.

A single element, or sunflower petal, could be configured on the bottom of the Entomopter so that its narrow tip is pointing down for altimetry. This would provide the needed coverage as shown in Figure 4-13. The antenna would be designed so that its beam width is wide enough to maintain ground contact when the vehicle is banking, with maximum expected pitch and roll angles. The distance below would be calculated based on an inertial knowledge of the bank angle and an assumed flat surface beneath. This will require less complexity than steering the beam over small angles to keep it vertical. Altimetry accuracy is not critical at large altitudes, and when the Entomopter is close to the ground, it will probably not be doing high-angle pitch and roll maneuvers (except possibly during flare-out for landing).

The full antenna as shown in Figure 4-8 could be mounted on the refueling rover to provide coverage needed for communications. Monopulse techniques could also be performed using the elements, or sunflower petals, to determine the azimuthal position of the Entomopter relative to the rover. The rover antenna would be mounted on a ground plane to achieve an antenna pattern displaced from the horizon.

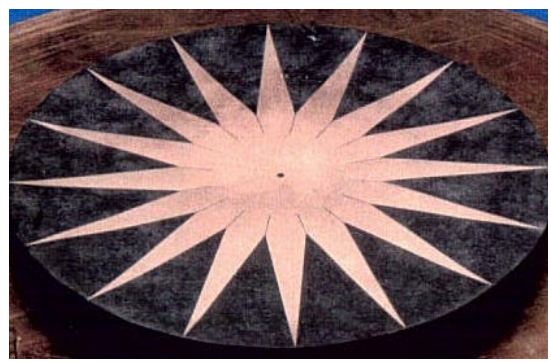

Figure 4-8: Linearly Tapered Slot Antenna (LTSA) Circular Array (Sunflower Antenna)

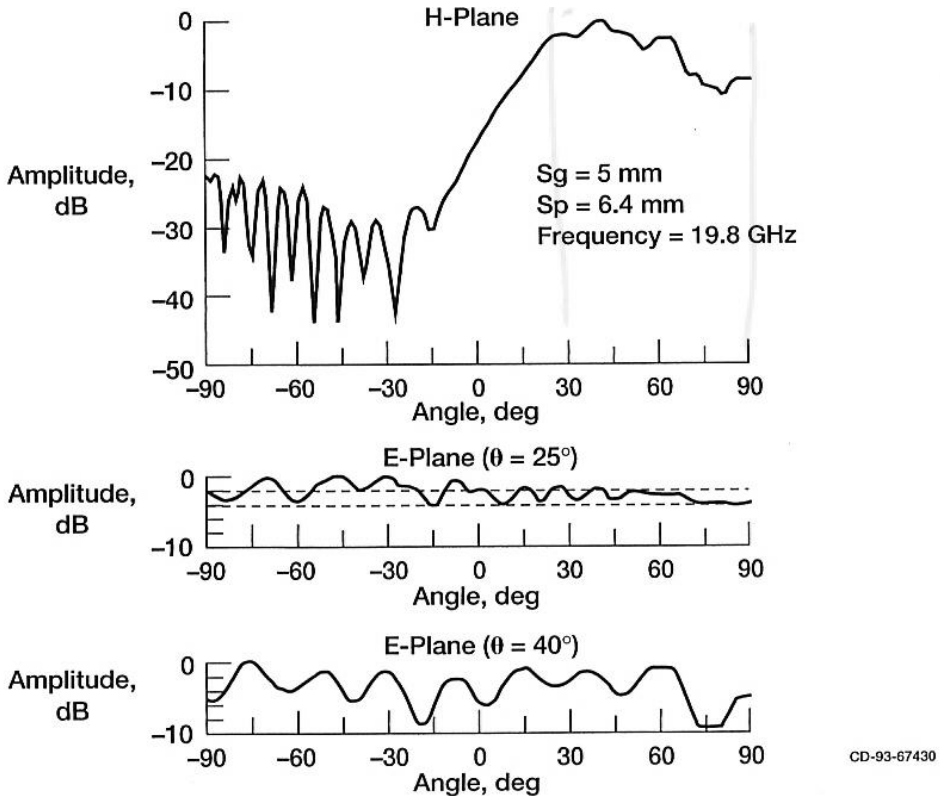

Figure 4-9: Measured Radiation Pattern at 19.8 GHz. H-Plane, and E-Plane at Elevation Angles of 0 = 25° and 40°

[240]

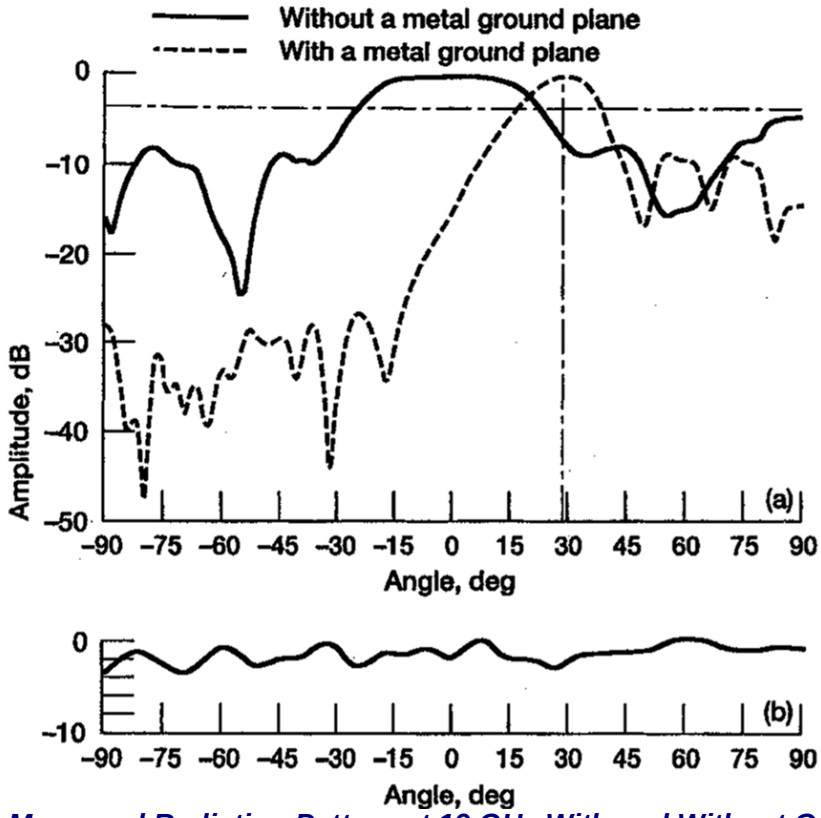

Figure 4-10: Measured Radiation Pattern at 19 GHz With and Without Ground Plane. (a) H-Plane and (b) E-Plane

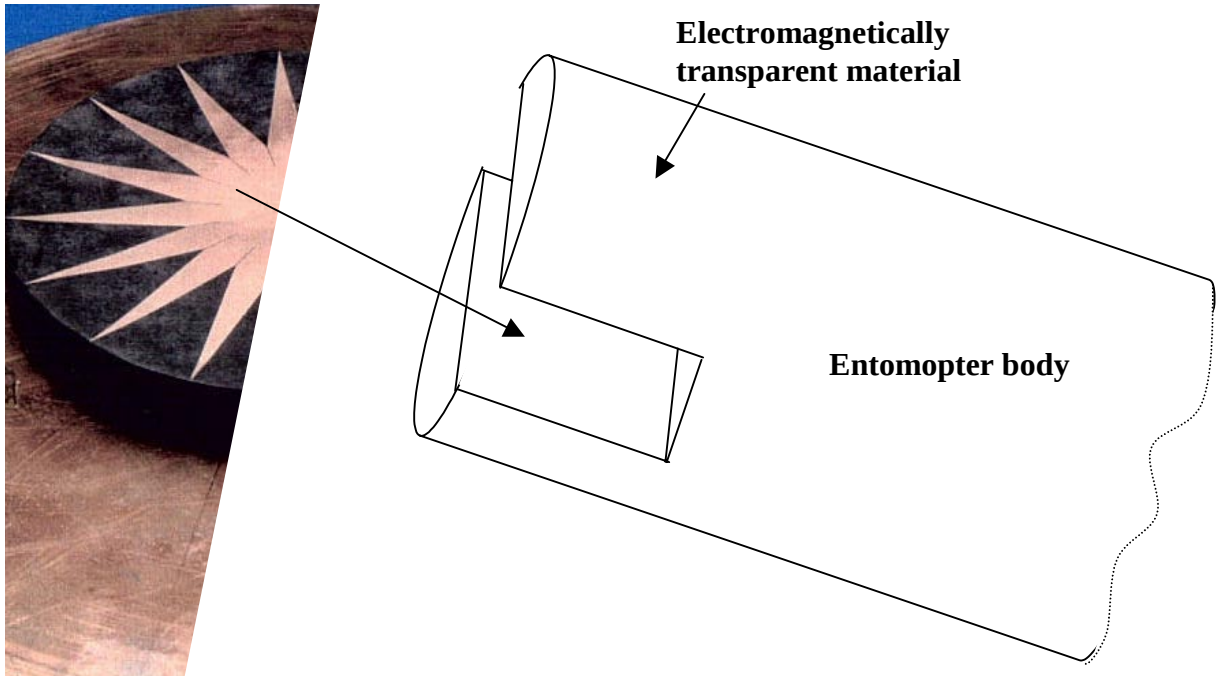

Figure 4-11: Potential Antenna-mounting Scenario for Front and Rear of Entomopter

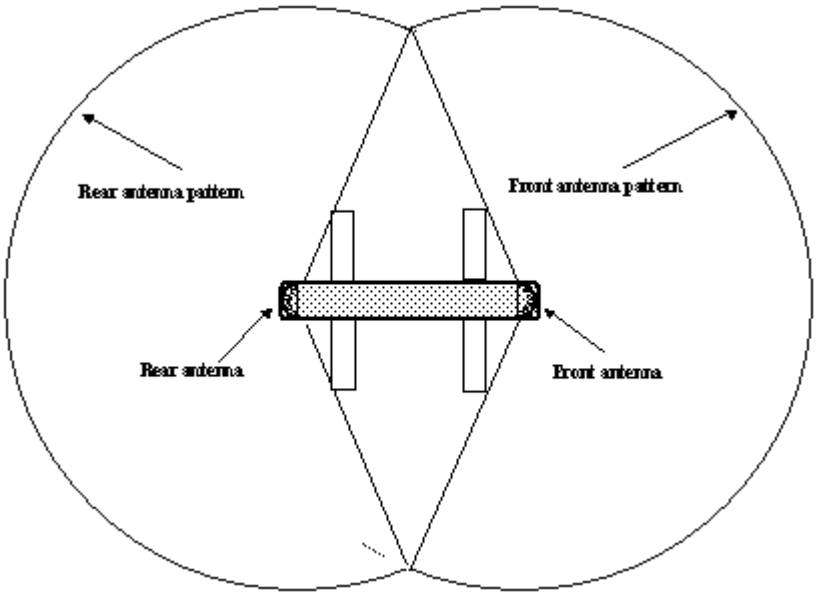

Figure 4-12: Top View of Entomopter Body Showing Illustrative Antenna Patterns from Mounting Scenario of Figure 4-11

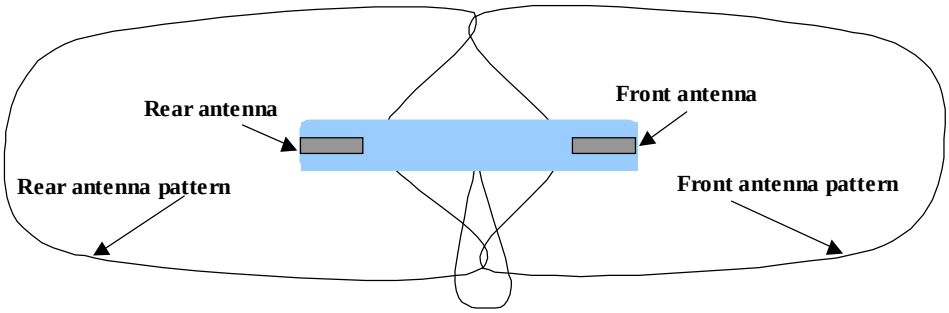

Figure 4-13: Side View of Entomopter Body Showing Illustrative Antenna Patterns from Mounting Scenario of Figure 4-11

4.3.5 Link Budget Analysis

As described in the Phase I report, extremely short, wideband, rapid sequences of RF energy can be used for a host of desired purposes, including communications, obstacle detection, positioning, and altimetry. In this way, a multifunctional subsystem could be fabricated and used by one or more entomopter-type vehicles in a hybrid manner to perform many functions with the single subsystem [229]. Using these wideband pulses is attractive because a single subsystem could be used to perform all of the mentioned functions concurrently using the same hardware, thus conserving mass and stow volume. In addition, these wideband pulses require significantly less

power compared to conventional systems. Lastly, the subsystem could be reconfigured in real time to perform the desired function autonomously by the Entomopter itself.

The radiated waveform is assumed to be a modulated Gaussian waveform (MGW), with its frequency spectrum shifted to the appropriate operating frequency. A time-domain plot of a MGW centered at 18 GHz is shown in Figure 4-14.

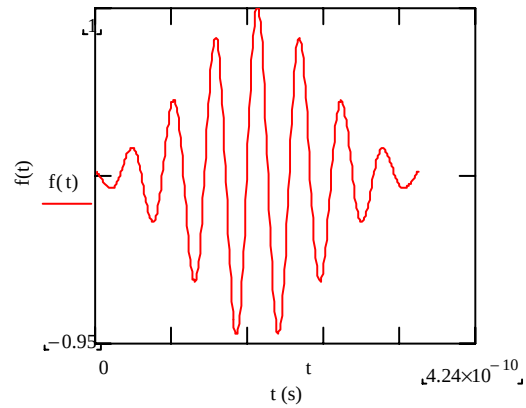

Figure 4-14: Time-domain Plot of Modulated Gaussian Waveform (MGW) Centered at 18 GHz

4.3.5.1 Communications Analysis

An analysis was performed by Volpe National Transportation System Center [291] in which peak powers were calculated for MGW pulses for communication and surveillance applications. For communications, Volpe found that the required peak power is independent of the signal waveform. Thus, for communications, the conventional range equation can be used or

$$P_T = \frac{(4\pi)^2 r^2 k_B T_o \ BW \ SNR \ L_o}{G_T G_R \lambda^2}$$ ***Equation 4-5***

where P_T is the required peak transmitter power; r is the distance from the receiver to the transmitter; k_B is Boltzman's constant; T_o is the effective system noise temperature; SNR is the received signal to noise ratio; G_T and G_R are the gains of the transmitting and receiving antennas, respectively; BW is the signal bandwidth; λ is the wavelength; and L_o is additional losses due to propagation losses, dust, etc. For ultra wideband signals, the time-bandwidth product is given approximately by [95]

$$BW \ T_w \approx 1$$ ***Equation 4-6***

where T_w is the pulse width in time. Assuming all of the received power is in the informational signal, Equation 4-5 also can be expressed in terms of the bit energy to noise ratio E_b/N_o as

$$P_T = \frac{(4\pi)^2 r^2 k_B T_o \ BW \ \frac{E_b}{N_o} \ F \ L_o}{G_T G_R \lambda^2}$$ ***Equation 4-7***

where F is the noise figure. Expressed in this manner, we can relate the required power to achieve bit error rate (BER) performance. Assuming we will use on-off keying (OOK) modulation, the BER can be expressed as [267]

$$BER = Q\left(\sqrt{0.5 * \frac{E_b}{N_o}}\right)$$ **Equation 4-8**

where Q(x) is the complementary error function defined as

$$Q(x) = \frac{1}{\sqrt{2\pi}} \int_x^{\infty} \exp(-u^2/2)\, du$$ **Equation 4-9**

Thus, the required peak power can be related to desired BER. The average power, on the other hand, depends on the data rate R_b. The data rate for OOK can be expressed as one transmitted pulse, or bit, per interpulse period T, or

$$R_b = \frac{1}{T} \quad \text{bits/second.}$$ **Equation 4-10**

It follows that the duty cycle dt can be expressed as

$$dt = \frac{T_w}{T}$$ **Equation 4-11**

and the average transmitter power can be expressed as

$$P_{avg} = dt\ P_T$$ **Equation 4-12**

or in terms of data rate as

$$P_{avg} = T_w R_b\ P_T$$ **Equation 4-13**

4.3.5.2 Radar Analysis

Unlike communications, when using a MGW for radar, the required peak transmitting power is dependent on the waveform [291] and can be expressed as

$$P_T = \frac{SNR\ L_o\ k_B T_o\ 4^3 \pi^4 r^4 c^2\ Tmgw^2}{\sigma^2\ G_T^{\ 2}\ \lambda^2\ T_w\ 3} f_m$$ **Equation 4-14**

In this equation, Tmgw is a time scale parameter, c is the speed of light, σ is the effective radar cross-section of the target, and f_m is a factor introduced by the modulation of the waveform around a carrier frequency f_o.

$$f_m = \frac{3\left[1 + e^{-\frac{w_1^2}{2}}\right]}{1 + w_1^{\ 2} + e^{-\frac{w_1^2}{2}}}$$ **Equation 4-15**

where $w_1 = \omega_o Tmgw$ and $\omega_o = 2\ \pi\ f_o$.

The pulse width was determined from the required range resolution ΔRmin as [174]

$$T_w = \frac{2\ \Delta R\min}{c}$$ **Equation 4-16**

The MGW time constant Tmgw was determined, as suggested in [291], as

$$Tmgw = \frac{T_w}{4}$$ **Equation 4-17**

to include 99.5% coverage of a Gaussian pulse. The pulse-interpulse period T was determined by the application, but must be greater than the value associated with unambiguous range detection. We designate R_u as the required unambiguous range, thus the minimum interpulse period T_{min} is [174]

$$T_{\min} = \frac{2R_u}{c}$$ **Equation 4-18**

The unambiguous range is the maximum range for each application. The corresponding duty cycle and average transmitter power can be expressed as in Equations 4-11 and 4-12, respectively.

The gain of the transmitting antenna can be expressed in terms of its effective area, A_{eff}, as

$$G_T = \frac{4\pi A_{eff}}{\lambda^2}$$ **Equation 4-19**

Equation 4-19 implies that we can take two approaches for frequency variations in our link analyses. The effective area of the antenna can be held constant, which implies the gain will increase with increased frequency, or the gain can be held constant and the antenna physically scaled to operate at the desired frequency. We will take the latter approach and assume the gain will remain fixed with frequency. In this manner, we can take advantage of the reduction in antenna size with increased frequency.

Rewriting Equation 4-14 in terms of the above assumptions to better see how the required peak power varies with system parameters, as follows:

$$P_T = \frac{SNR\ k_B T_o L_o 4^3 \pi^4 r^4 c^2 \left(\frac{2\ \Delta R\min}{4c}\right)^2}{\sigma^2\ G_T^{\ 2} \left(\frac{c}{f}\right)^2 \left(\frac{2\ \Delta R\min}{c}\right) 3} \frac{3\left[1+e^{-\frac{\left(2\pi f \frac{2\ \Delta R\min}{4c}\right)^2}{2}}\right]}{\left[1+\left(2\pi f \frac{2\ \Delta R\min}{4c}\right)^2 + e^{-\frac{\left(2\pi f \frac{2\ \Delta R\min}{4c}\right)^2}{2}}\right]}$$

Equation 4-20

4.3.6 Link Budget Results

The specifications for the radar portions of the system requirements are more stringent compared to the communications requirements. Thus, initially system parameters will be based on radar performance, and communications calculations will be based on these assumptions.

4.3.6.1 Obstacle Detection Results

The following assumptions were made for the radar to perform obstacle detection.

Table 4-1: Parameters for Obstacle-detection Analysis

Effective target cross section, σ (m^2)	1
Temperature of receiver To (Kelvin)	290
Range resolution, ΔRmin (m)	0.5
Isotropic gain of transmitting antenna G_T (dBi)	8
Signal-to-noise ration (dB)	10
Interpulse period, T (ms)	1
Pulse repetition frequency, (kpps)	1

Following the analysis procedure outlined above, the required peak and average transmitter powers are shown in Figure 4-15 for an operating frequency of 18 GHz. It was determined that the minimum and maximum distances for obstacle detection are about 15 m and 200 m, respectively, and range resolution should be held to about 0.5 m. Using the assumptions shown in Table 4-1, the peak and average powers at 18 GHz for a 15-m range are 2.4 µW and 8 pW, respectively. The peak and average powers for a 200-m distance are 76 mW and 254 nW, respectively. The required peak and average powers are plotted as a function of operating frequency in Figures 4-16 and 4-17, respectively. For the chosen parameters, there is little variation in power with frequency. The plots do indicate a savings in required power at frequencies below 0.5 GHz. However, using the chosen pulsewidth, physically realizable operating frequencies are limited to values greater than 0.6 GHz to maintain a bandwidth greater than twice the operating frequency.

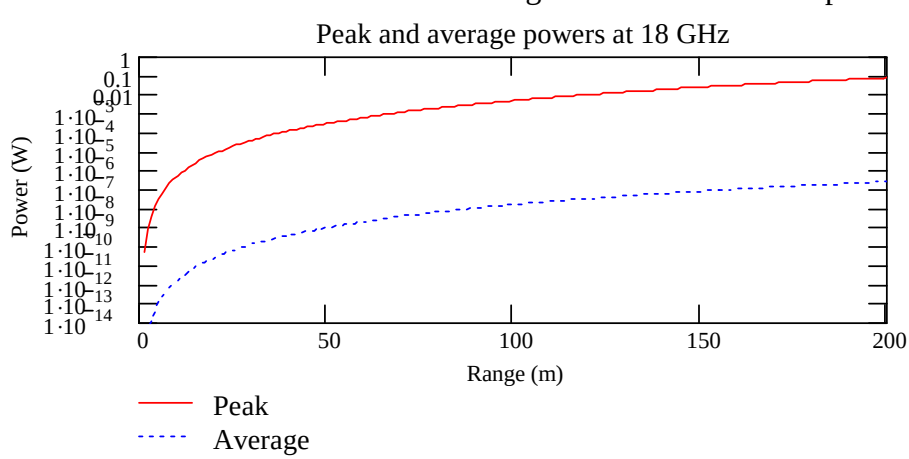

Figure 4-15: Peak and Average Transmitter Power Required for Obstacle Detection at 18 GHz as a Function of Range

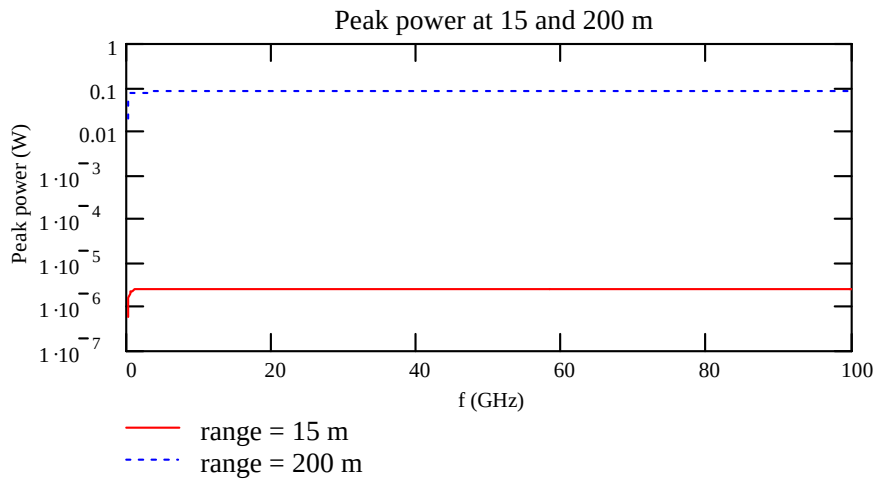

Figure 4-16: Peak Transmitter Power Required for Obstacle Detection at 15 m and 200 m as a Function of Frequency

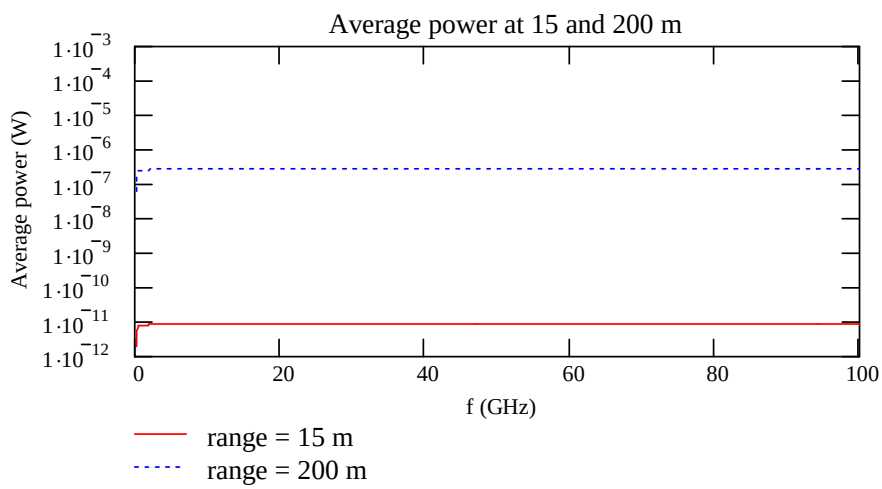

Figure 4-17: Average Transmitter Power Required for Obstacle Detection at 15 m and 200 m as a Function of Frequency

4.3.6.2 Altimetry Results

The altimetry requirements are the most stringent for range resolution because altimetry readings will be used for landing. The minimum-range resolution is 6 cm when the Entomopter is within 3 m of the ground.

The following assumptions were made:

Table 4-2: Parameters for Altimetry Analysis

Effective target cross section, σ (m^2)	1
Temperature of receiver To (Kelvin)	290
Range resolution, ΔRmin (m)	0.06
Isotropic gain of transmitting antenna G_T (dBi)	8

Table 4-2: Parameters for Altimetry Analysis (Continued)

Signal-to-noise ratio (dB)	10
Interpulse period, T (ms)	1
Pulse repetition frequency, (kpps)	1

Following the analysis procedure outlined above, the required peak and average transmitter powers are shown in Figure 4-18 for an operating frequency of 18 GHz. The peak and average powers for a 10-m altitude are 3.9 µW and 1.6 pW, respectively. The peak and average powers for a 200-m altitude are 630 mW and 252 nW, respectively. Note: The required peak power has increased significantly compared to the obstacle-detection results due to the increased range resolution. The required peak and average powers are plotted as a function of operating frequency in Figures 4-19 and 4-20, respectively. These plots show that by decreasing the range resolution, and thus decreasing the pulse width (see Equation 4-16), the frequency dependence is altered compared to the obstacle-detection results. These plots also show that a reduction in required power can be achieved by operating below about 2 GHz. However, using the chosen pulsewidth, physically realizable operating frequencies are limited to values greater than 1.25 GHz to maintain a bandwidth greater than twice the operating frequency.

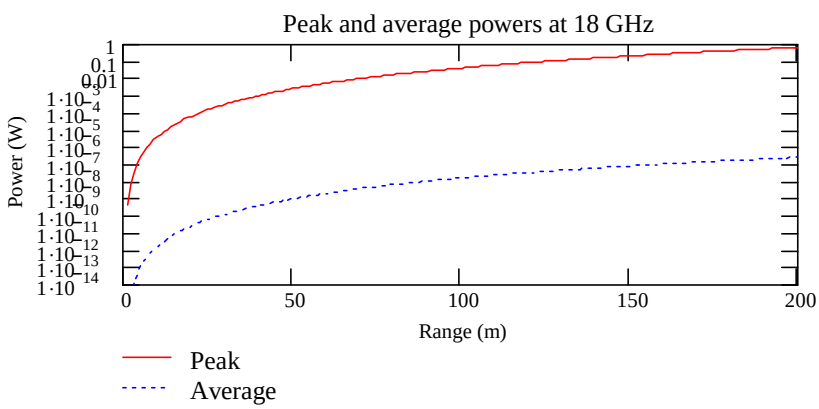

Figure 4-18: Peak and Average Transmitter Power Required for Altimetry at 18 GHz as a function of Altitude

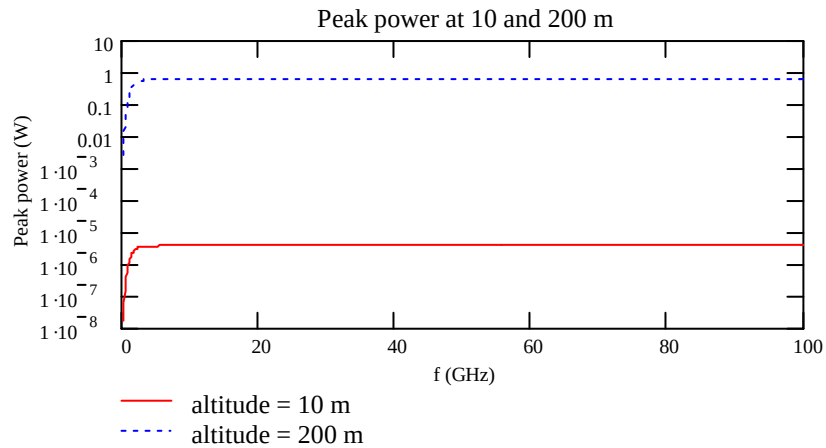

Figure 4-19: Peak Transmitter Power Required for Altimetry at 10 m and 200 m as a Function of Frequency

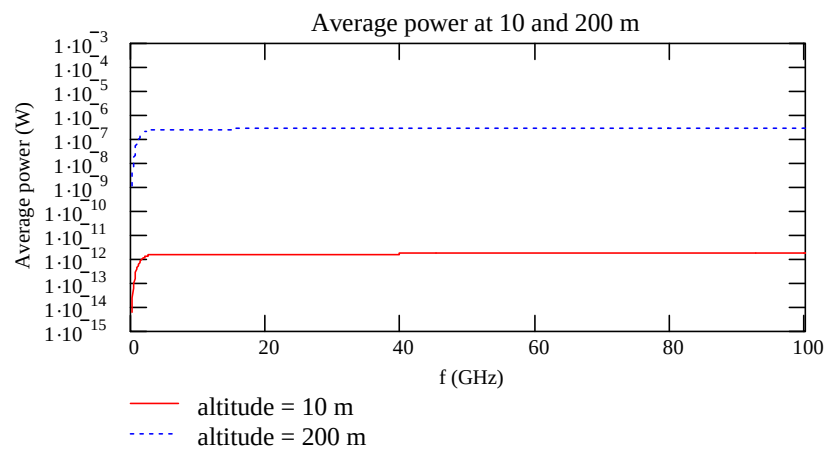

Figure 4-20: Average Transmitter Power Required for Altimetry at 10 m and 200 m as a Function of Frequency

4.3.6.3 Communications Results

Table 4-3: Parameters for Communications Analysis

Temperature of receiver To (Kelvin)	290
Isotropic gain of transmitting antenna G_T (dBi)	8
Isotropic gain of receiving antenna G_R (dBi)	8
Signal-to-noise ratio (dB)	17.6
Noise figure, F (dB)	2
Bit energy to noise ratio, E_b/N_o (dB)	15.6
Bit error rate (BER)	10^{-5}

In the event that the Entomopter must communicate to the rover or other Entomopters, we assume that the obstacle detection subsystem can be used for simultaneous communications and obstacle detection. For the communication link calculations, initially T was fixed at 1 ms to correspond to the assumed interpulse spacing for obstacle detection. This corresponds to a data rate of one kbits/s. With the assumptions listed in Table 4-3, the peak and average powers were calculated and are plotted versus range at 18 GHz in Figure 4-21. The peak average powers at a 200-m range are 39.5 mW and 132 nW, respectively. The peak average powers at a 1000-m range are 986.6 mW and 3.3 µW, respectively. The peak and average powers at 200-m and 1000-m are plotted versus frequency in Figures 4-22 and 4-23, respectively, showing an increase in power with increased frequency for the current assumptions.

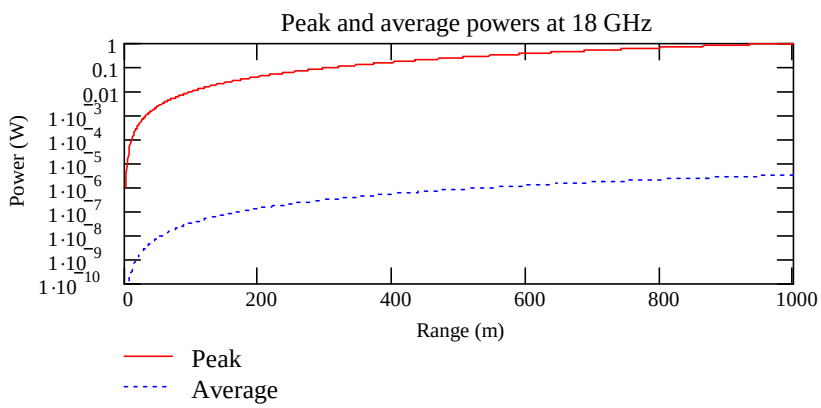

Figure 4-21: Peak and Average Transmitter Power Required for Communications at 18 GHz as a Function of Range

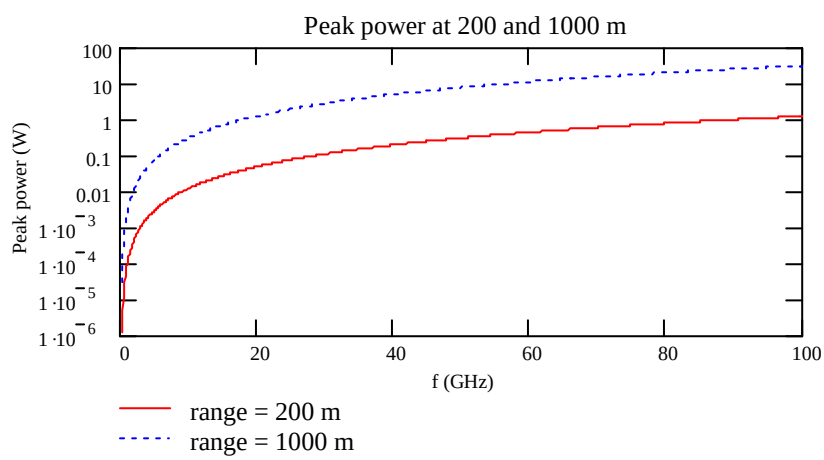

Figure 4-22: Peak Transmitter Power Required for Communications at 200 m and 1,000 m as a Function of Frequency

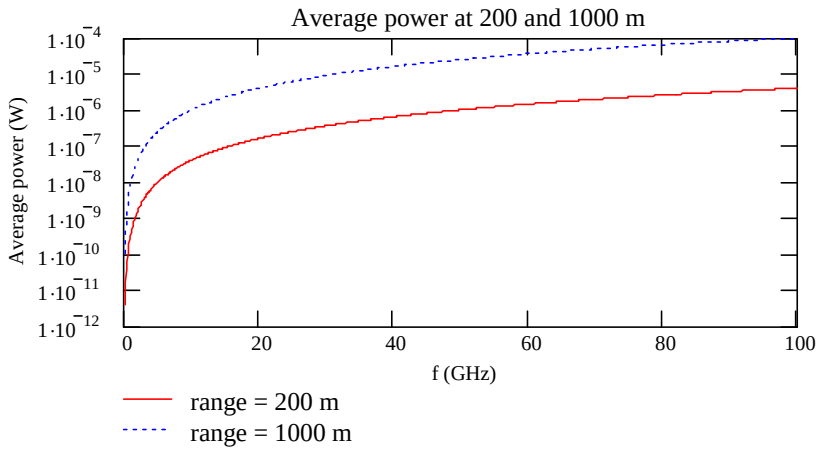

Figure 4-23: Average Transmitter Power Required for Communications at 200 and 1,000 m as a function of Frequency

The peak power will remain constant with bit rate and interpulse period. However, the average power will vary. The required average powers for 200-m and 1,000-m ranges are plotted versus data rate at 18 GHz in Figure 4-24. The range of data rates in Figure 4-24 corresponds to interpulse periods T of 10,000 T_w (dt = 1/10,000) to 100 T_w (dt = 1/100).

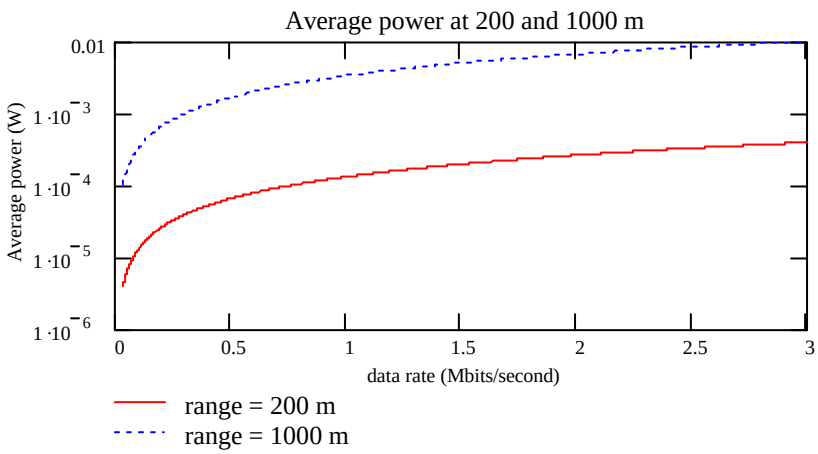

Figure 4-24: Average Transmitter Power Required for Communications at 200-m and 1,000-m as a Function of Data Rate

Power consumption for positioning will not take place on board the Entomopter. It will be performed from the rover.

4.3.7 Future Development Path for the Active Communications Option

In the area of the communications/control subsystem option, future development would include the design and development of the subsystem components including the transmitter, receiver, and antennas. The proposed subsystem uses extremely short, wideband, rapid sequences of RF

energy for a host of desired purposes, including communications, obstacle detection, positioning and altimetry. In this way, a multifunctional subsystem could be fabricated and used by one or more entomopter-type vehicles in a hybrid manner to perform many functions with the single subsystem. There are system design issues that would need to be handled (e.g. synchronizing, and sorting the pulses), however the other functions have been demonstrated. dwell time Size reduction will also be required in the circuitry, antennas/transducers, signal routing, and supporting energy storage, but efforts are already underway by industry in this regard.

The linearly tapered slot antenna (LTSA) circular array (sunflower antenna) was proposed to fulfill the Entomopter's multifunctional needs. Design and development will have to be completed for this antenna to obtain the desired gain, efficiency, and propagation patterns. In addition, the proposed RF communications/control subsystem should be tested on the Entomopter itself to determine exactly how the vehicle body will affect the antenna pattern and system performance. The multifunction antennas used on the Entomopter and rover must provide adequate beam converge to accomplish:

1. Detection of objects in the Entomopter's flight path for obstacle avoidance. Obstacle detection will be performed in 3D (azimuth, elevation and range).
2. Altimetry for the Entomopter must have precise range for detecting the location of the ground for landing and collision avoidance.
3. Communications between Entomopters and the rover with spherical coverage around the Entomopter so that it can communicate with the rover or other Entomopters in any direction.
4. Positioning of the Entomopter in 3D relative to the rover.

Chapter 5.0 Potential Payload Functions Using a Communication/Control Subsystem

5.1 General Science Objectives [228]

The strategy for exploring Mars is to realize a series of spacecraft that carry instruments to answer key questions relating to the origin and evolution of the planet as well as its potential for harboring life. Specific investigations are chosen, in part, based upon the extent to which they address high priority questions. Central to those questions of high priority is whether large quantities of water were ever present on the surface of Mars and therefore whether the planet was ever habitable. Specifically, these questions are:

1. When was water present on the surface of Mars?
2. Did water persist at the surface long enough for life to have developed?
3. How much water was there, and where was it?
4. Where did the water go that formed the fluvial evidence on the surface of modern Mars?

The Mars Expeditions Strategy Group (MESG) was tasked by Goldin in 1996 to create a strategy that would determine whether life had ever existed on Mars. MESG outlined a program consisting of global reconnaissance and in situ measurements of the surface, followed by bringing samples of Mars to Earth. MESG also identified specific classes of surface sites for detailed study:

1. Ancient sites of groundwater.
2. Ancient sites of surface water.
3. Modern sites of ground water.

The Mars Exploration Payload Analysis Group (MEPAG) was tasked to link the goals of the Mars Exploration Program to specific investigations and then to measurements that can be made by science payloads on board spacecraft or conducted in Earth-based laboratories. MEPAG created investigation pathways that linked the program's strategic goals to specific prioritized measurements.

According to the MESG report [228], the study for life on Mars should be directed at locating and investigating, in detail, those environments on the planet that were potentially most favorable to the emergence and persistence of life. This investigation should emphasize sampling at diverse sites and include a range of ancient and modern aqueous environments. These environments should be accessed by exploring ejecta of young craters, investigating material accumulated in outflow channels, and coring.

Preliminary information must be obtained to select the most promising sites for surface studies. The ancient highlands are already known, with reasonable certainty, to be a region with great potential; thus it is recommended that the initial studies be performed there. Surface mineralogy maps will be needed to enhance investigations within the highlands and enable searches in other locations. Additionally, instruments capable of detecting near-surface water, water bound in

rocks, and subsurface ice would greatly accelerate the search for environments suitable for life. NASA's 2001 Mars Odyssey spacecraft's gamma ray spectrometer instrument suite has detected hydrogen in abundance in the upper meter (three feet) of soil in a large region surrounding the planet's south pole [199]. This is indicative of water ice. Now, long range surface exploration is needed.

MEPAG formulated the objectives, investigations, and measurements needed for the exploration of Mars and prioritized them by subgroups of participants focused on the four principal exploration goals. The four goals are:

1. Determine if life ever existed on Mars.
2. Determine climate on Mars.
3. Determine the evolution of the surface and interior of Mars (geology).
4. Prepare for human exploration.

To prepare for human exploration, one of the objectives is to conduct in situ engineering science demonstrations. The investigation involves demonstrating terminal phase hazard avoidance and precision landing, necessary to decrease the risks associated with soft landing, and to enable pinpoint landing. The measurements required include demonstration of a terrain-recognition system [228].

The prolonged lifetime and flight flexibility of the proposed Entomopter aircraft make it ideal to contribute to several of the scientific objectives outlined above. Moreover, the active emitter navigation and communication subsystem alternative with its radar functionality hold the potential for dual use in addressing scientific objectives as described below.

5.2 Imaging and Terrain Mapping

It is reasonable to assume that the Entomopter will be required to perform high-resolution imaging of the Mars terrain to obtain information to select the most promising sites for surface studies. Fine-resolution imaging radars produce images that closely resemble aerial photographs.

Imaging can be accomplished with the Entomopter using the onboard communications/control subsystem coupled with synthetic aperture radar (SAR) to increase the spatial resolution in the along-track direction. SAR is based on the generation of an effectively long linear array antenna to achieve the improved spatial resolutions. In most cases, a single antenna is used and physically translated (such as with the movement of an aircraft) to take up sequential positions along a line [242]. At each position, a signal is transmitted, and the amplitude and phase of the received signals are stored. After processing, these signals strongly resemble the signals that would have been received by the elements of an actual linear array of elements. In airborne ground-mapping systems, the antenna is usually side-looking, and the motion of the aircraft translates the radiating element to each of the positions of the array. These array positions correspond to the location of the antenna at the times of transmission and reception of the radar signals.

Surface topography over a large area can be performed through multiple flight tracks and data combining from each track to create a map of the desired area coverage. Alternatively, a scanning antenna mounted underneath the Entomopter can be used to cover a larger surface, avoiding extraneous (and fuel-intensive) flight paths. Referring to the sunflower antenna configuration mentioned above, instead of a single sunflower petal mounted beneath the Entomopter to perform altimetry, half of the full circular antenna can be mounted and elements switched on and off to scan a larger swath width, S, compared to a single element. The shape and number of elements can be varied to provide adequate gain and along-track and cross-track resolutions, Xa and Xr, respectively. A representative illustration is shown in Figure 5-1. One of the main constraints is that the scan should be completed before the Entomopter moves a distance equal to the along-track resolution, Xa. This imposes a minimum dwell time, t_d, constraint at each position [72] of:

$$t_d < \frac{Xa\ Xr}{S\,v}$$

where n is the Entomopter velocity.

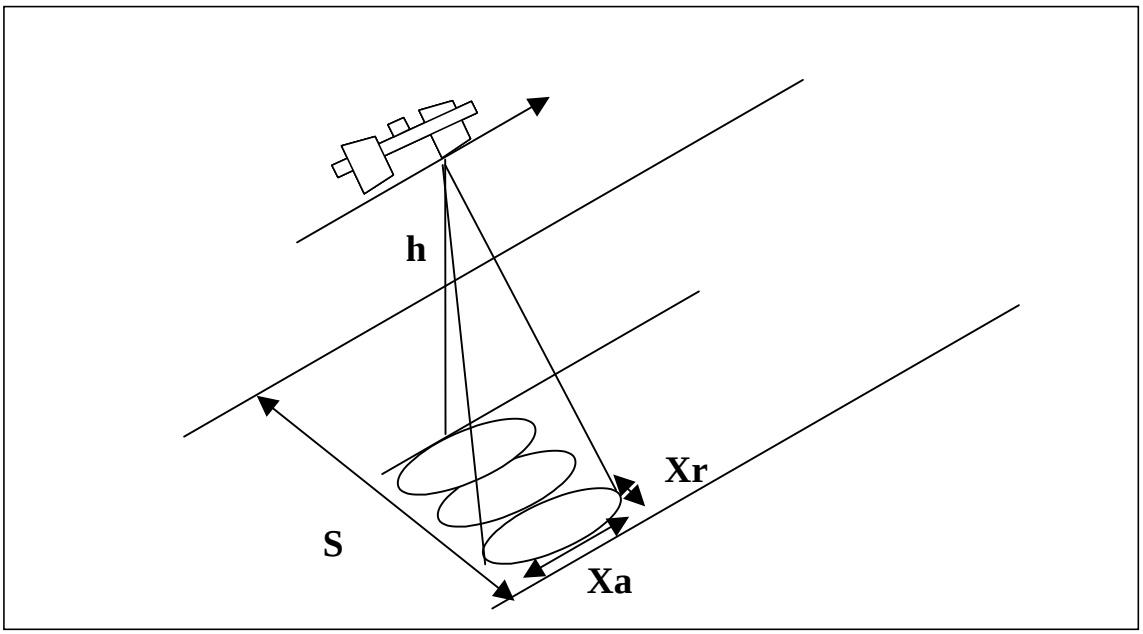

Figure 5-1: Geometry for a Scanning Imaging Radar Altimeter

Three-dimensional mapping can be performed by taking two images of the same area with two different angles of incidence. One method to perform this mapping is to use interferometric synthetic aperture radar (ISAR). Interferometry is based on cross-correlating two SAR images of the same scene with slightly different incidence angles. The 3D position is estimated by measuring the slant range and the phase difference. This could be achieved using a single Entomopter with two antennas offset from each other, or using two Entomopters, each equipped with an antenna, and flying in formation so as to acquire two images of the same surface at different angles, as shown in Figure 5-2. When the SAR images are synthesized, each resolution cell has an amplitude and phase angle between 0 and 2π radians. The phase is an ambiguous measure of the two-way distance, d, between the antenna and a point on the ground.

As an example, two SAR images of the Mars terrain are obtained with antennas displaced along the cross-track direction from one another using one or two Entomopters. The two-way distance from each antenna to a resolution cell on the ground will differ by an amount Δd. By subtracting the phases between the two images, a phase difference map can be produced, and this resolution cell will have a phase corresponding to Δd. Now consider a resolution cell containing a raised structure, such as a rock or other terrain feature. Depending on the height of the feature, the difference in distance from the two antennas to the terrain feature will be some other value Δd´. Thus, the phase difference map encodes information about the third dimension of elevation, which is unobtainable using a single SAR image.

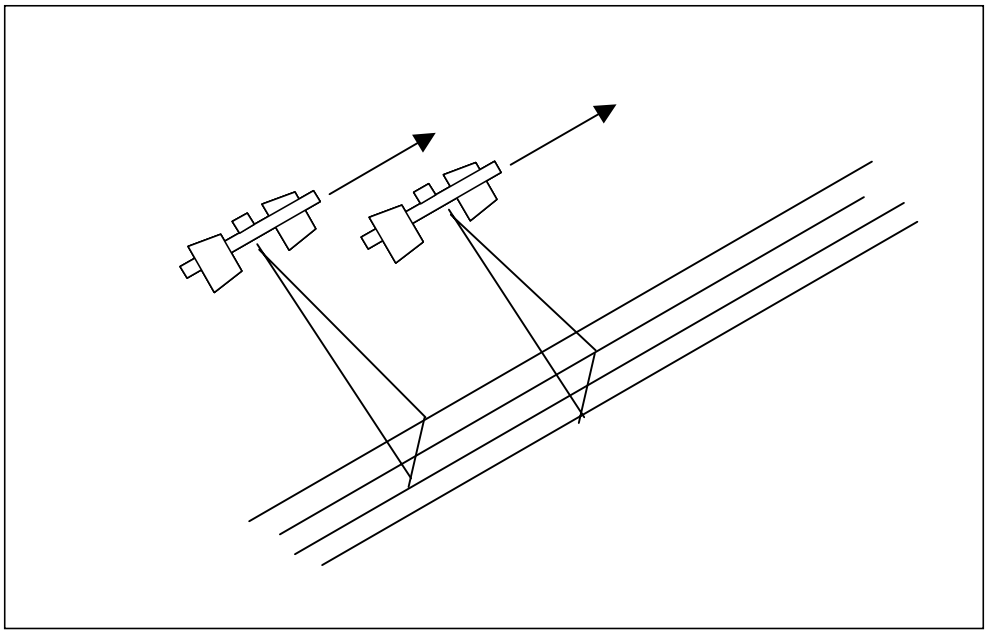

Figure 5-2: Possible Flight Configuration for 3D Mapping

ISAR has all weather capability, allowing functionality in dust storms where the ground would be obscured under theses conditions using laser radar or electro-optic sensors. However, it is sometimes limited in imaging steep slopes and high depression angles [2] such as Mars caverns. ISAR maps can also readily detect change, which shows up as a random mismatch of phases between the before and after ISAR maps. In this manner, changes in the Mars terrain can be monitored over time.

5.3 Digital Terrain System

A digital terrain system (DTS) as described in [97] uses a stored map of terrain elevation with aircraft dynamics and measured height above the ground to provide navigation and terrain reference cues. DTS could provide terrain referenced navigation, terrain following, predictive ground collision avoidance, obstruction warning, and cueing and ranging. If DTS proves to be feasible for the Entomopter mission, a digital terrain system could be used to store a digital map of the terrain for navigation and collision avoidance, potentially resulting in significant savings in

power and flight hardware. Prior knowledge of the exploration terrain could obviate the need for constant radar readings for collision avoidance and provide an optimum flight pattern.

A single Entomopter could be tasked with this digital terrain mapping of a designated area using ISAR as described above. Upon its return to the refueling rover, the digital map could be uploaded to the rover and this information transferred to the other Entomopters. Once the terrain map has been uploaded, it could then be used by the Entomopters to calculate optimum flight patterns. Accurate knowledge of aircraft position relative to the terrain and the terrain ahead will lead to a flight pattern based on the required clearance height and collision avoidance. This terrain-following feature would avoid energy-consuming maneuvers to avoid obstacles and allow the Entomopter to fly at the minimum required clearance height. The reduction in required mass and power on the other Entomopters would allow additional payload functions to be accomplished. This procedure could be repeated for each exploration area. Alternatively, the Entomopters could have modular payload, where the payload is switched for the desired exploratory function. In this manner, each Entomopter would create a digital map of the terrain for a designated area. Upon completion, it would return to the refueling rover and shed its mapping gear to be replaced by additional payload, such as video equipment. The first method seems to be a more realistic alternative. Switching complex payload equipment might sacrifice reliability.

The key capability of a DTS is terrain-referenced navigation. A combination of the stored digital map of terrain elevation and real-time measurements of the aircraft height above the ground allows highly accurate navigation referenced to the terrain without external signals. Typically, this terrain-referenced navigation includes processing and combining data from a dead reckoning system, radar altimetry to give the height above ground, and the digital terrain elevation data map. Generally, there are two modes of operation: Acquisition mode, where the system is initialized by identifying the initial position of the aircraft, and Track mode, where navigation data is provided at a rate of about 2 Hz to 4 Hz. Acquisition mode involves processing a number of altimetry readings to identify aircraft position relative to the terrain map database. This approach relies on the uniqueness of ground profiles within the map. The Acquisition mode will likely be unnecessary for the Entomopter mission, because its initial position relative to the refueling rover will always be known. Thus, the Track mode can immediately be executed.

In Track mode, the aircraft has an estimated position at some point in time (update N). Based on the aircraft dynamics, a Kalman filter is used to propagate ahead (Update N+1) to provide a prediction of the height above ground level from the map database. To account for uncertainties in position, a batch of altimetry measurements can be processed to calculate the location of the aircraft within the map database. The difference between the actual position and the predicted position can be used to correct the Kalman filter estimates. Again, the operation relies upon the uniqueness of the terrain to identify the unique position in the map database. If the Mars terrain is relatively flat, performance will be degraded.

Whether a DTS would be used for the proposed Entomopter mission would be highly dependent on the specific mission goals. Perhaps a terrain map could be uploaded to the rover and transmitted to Earth for review. Based on that information, an Earth-bound mission planner could communicate back to the rover that the Entomopters should explore certain areas.

5.4 Scatterometers and Spectrometers

The communications/control subsystem could also potentially be used as a scatterometer. Radars used to measure ground return are called scatterometers, because the ground return is almost invariably due to scattering. Scatterometers capable of measuring a response over a wide range of frequencies are called spectrometers. Scatterometers are used to measure the surface reflectivity as a function of frequency, polarization, and illumination direction (angle of incidence) of the sensing signal. The depolarization and spectral reflectivity of returned radar echoes from a surface provide information about the roughness structure, geometric structure, morphology, and dielectric constant of the surface and immediate subsurface [72]. The communications/control subsystem and flight configurations could be reconfigured to exploit different polarizations, angles of illumination and center frequencies. Single-frequency, single-polarization radar measurements are useful, but use of multiple polarizations (particularly cross-polarizations) and multiple frequencies significantly increase their value.

Radar ground return is described by σ^0, the differential scattering cross-section, or scattering coefficient (scattering cross-section per unit length), rather than by the total scattering cross-section σ used for discrete targets [242]. Since σ varies with illuminated area and this is determined by geometric radar parameters (pulse width, beam width, etc.), σ^0 was introduced to obtain a coefficient independent of these parameters. Use of σ^0 implies that return from the ground is contributed by a large number of scattering elements whose phases are independent. This is primarily due to differences in distance that are comparable to many wavelengths.

Different wavelengths are sensitive to different elements on the surface. If the geometry of two radar targets is the same, the returns would be stronger from the target with higher complex permittivity, because larger currents (displacement or conduction) would be induced in it. Effective permittivity for ground targets is very strongly influenced by moisture content, because the relative permittivity of liquid water ranges from 60 at X-band to about 80 at S-band and longer wavelengths. Most dry solids have permittivities less than 8 [242]. Attenuation is also strongly influenced by moisture, because wet materials usually have higher conductivity than the same materials dry. Thus, permittivity increases with moisture, and radar return increases with permittivity.

Qualitative information on surface roughness also can be determined. Relatively smooth surfaces tend to reflect radio waves in accordance with Fresnel-reflection direction (angle of reflection = angle of incidence), and so they give strong backscatter only when the look angle is nearly normal to surface. Rough surfaces tend to reradiate almost uniformly in all directions, so they give relatively strong radar returns in any direction. Scattering falls off more rapidly with angle for smooth surfaces than rough.

Variations in amplitude of the returned signal can be converted directly into a scattering coefficient [262]. Scattering coefficient also depends on polarization of transmitted and returned signals, thus significant information about the target is contained in the ratio of the received like-polarized and cross-polarized signals. The variation of scattering coefficient with angle of incidence is different for different classes of targets. Thus, this information can be used for target identification. Scattering versus angle of incidence can be measured with multiple flight passes

along different flight paths at different altitudes using one or more Entomopters. Some radar scatterometers are specifically designed to measure scattering coefficient as a function of angle of incidence, because they have a beam pointed ahead of and behind the aircraft, such that the scattering coefficient can be measured at a variety of angles as the aircraft flies over the target. These can only illuminate along a narrow track, so numerous flights would be needed to get area coverage. Alternatively, the elements of the sunflower antenna could be switched on and off to scan a larger area compared to a single element.

Chapter 6.0 Media Exposure

6.1 Introduction

The amount of press that the Entomopter has received is phenomenal because it demonstrates the topic's allure in a time when few NASA projects are capturing the imagination of the public in the way that the idea of landing a man on the Moon did back in the 1960s. Today Mars is the next frontier in the public eye, eclipsing even larger near-term efforts such as the Space Station. Add to the enthusiasm for Mars exploration the notion of a "robotic bug" being one of the first animated Earthlings to roam the planet, and the media becomes frenetic.

From 1996 forward, the terrestrial Entomopter has received significant attention in the world press, becoming in one particular year the most widely publicized item of research at the Georgia Institute of Technology, where it was conceived. In fact, it was through an April 1999 Scientific American article entitled, "A Bug's Lift," by Phil Scott, that the Entomopter concept first came to the attention of NASA personnel as having potential for Mars exploration.

With the advent of the NIAC Phase I and Phase II Programs to define the role and performance of the Entomopter on Mars, a new dimension in Entomopter public relations dawned. First, the long standing Entomopter website established in 1997 (http://avdil.gtri.gatech.edu/RCM/RCM/Entomopter/EntomopterProject.html) has been a window to the world concerning both the terrestrial and Mars applications for this technology. Although at no time did the design team go out of its way to attract media attention, the nature of the subject soon became a hot topic for the international media as the word spread following a number of scientific presentations made around the world during the Phase II effort.

During the NIAC Phase II effort, the Mars Entomopter was featured in government and industry briefings in the following venues:

3/7/01:	Presented at the Royal Military Academy, Brussels, Belgium, as part of the EuroUVS MAV-Small UAV Conference.
7/31/01 - 8/1/01:	Featured at the GTRI exhibit during AUVSI-2001, Baltimore, Maryland.
9/5/01:	Briefing to Norwegian Ministry of Defense.
9/6/01:	Kongsberg Defense as part of a NATO-sponsored initiative.
10/9/01:	Briefing to Turkish Aircraft Industries as part of a NATO-sponsored initiative.
12/12/01:	Presented as part of the 21st Century Aerial Robotics course at the University of Linkoping, Sweden.
2/14/02:	Presented in conjunction with the IDC-2002 Conference in Adelaide, Australia.
4/26/02:	Invited Presentation, the Notre Dame Aeronautical Seminar Series.
7/9/02 - 7/10/02:	Featured at the GTRI exhibit during AUVSI-2002, Orlando.

Also during the NIAC Phase II effort, the Mars Entomopter was featured in addresses to middle, high, undergraduate, and graduate students in the following venues:

1-17-02:	Georgia Institute of Technology Graduate Design Seminar series presentation.
1-22-02:	Georgia Institute of Technology undergraduate/graduate class, "Micro Air Vehicle Technology" Mars Entomopter class session.
5-27-02:	DeVry-Calgary (Canada) undergraduate presentation.
6-20-02:	Georgia Tech Center for Education Integrating Science, Mathematics, and Computing (CEISMC) Atlanta-area high school presentation.
6-26-02:	Georgia Tech Center for Education Integrating Science, Mathematics, and Computing (CEISMC) Atlanta-area middle school presentation.

6.2 Print Media

The following is a representative list of recent worldwide attention given to the Entomopter-based Mars Surveyor:

1. "Insect-Sized Robots Do Their Part," *Smart Computing*, Cal Clinchard, November 2002, Vol. 13, Issue 11, page 9.
2. "Security in the Air," ATL, Bennett Liles, Vol. 4, No. 139, April 11, 2002, (Cover story for the Hartsfield Atlanta International Airport newspaper), pp. 1-2.
3. "Bugs on Mars," *Science News*, Peter Weiss, May 25, 2002, Vol. 161, 2002, pp. 330-332.
4. "On the Horizon," *Unmanned Systems* (cover story), Ramon Lopez, Vol. 20, No. 3, May/June 2002, pp.8, 40-41.
5. "Mechanical 'Insect' Captures Top Prize," *BUZZwords*, August 1, 2002.
6. "Flying on Mars: Nature's Flight System Could be the Key to Exploring the Newest Frontier," *Research Horizons*, John Toon, Fall 2001, Page 19-24.
7. "INNOVATIONS," *The GTRI Connector*, July 2002.
8. "How it Works: The Entomopter," *Business 2.0*, (scheduled for publication October 2002), Paul Kaihla.
9. "Neurotechnology for Biomimetic Robots," *MIT Press*, August 2002, ISBN 0-262-01193-X (Chapter by Robert Michelson discussing flying robots, including the Entomopter-based Mars surveyor).
10. "Ecco i miei insetti-robot per la Terra e per Marte," *Corriere Della Sera* (Italian magazine), Giovanni Caprara, May 19, 2002, pg. 27.
11. "Gli aerie su Marte faranno il pieno di energia chimica," *Libero*, (Newspaper: Rome, Italy), Futuro, May 18, 2002, pg. 20.
12. "Flugelschlag auf dem Mars," *Computer Zeitung*, Vol. 33, No. 11, March 11, 2002, Rochus Rademacher, pg. 8.
13. "Robotic 'Insect'," *Tech Topics*, Vol. 39, No. 1, Fall 2002 (Georgia Tech Alumni Association magazine) Gary Goettling, pg. 27.
14. "Survey Aircraft on Mars Might Fly as Insects Do," *The Columbus Dispatch*, David Lore, June 23, 2002 (circulation 245,946)
15. "Mars Invasion," *Georgia Tech Alumni Magazine*, Spring 2002, pg. 13.
16. "Robot Bugs Planned for Mars Invasion," *Popular Science*, Etienne Benson, February 8, 2002.
17. "Mars Needs Robo-Bugs!", *International Design*, Gareth Branwyn, June 15, 2002, pg. 85 (circulation, 33,338)

18. "Insectos en Marte," *Mecanica Popular*, John Toon, February 2002(circulation 247,850)
19. "Nature's Flight System Could be the Key to Exploring the Newest Frontier," *The Electron*, June 15, 2002(circulation 25,200).
20. "Bugging the Red Planet," *Georgia Tech BUZZ*, TechLINKS, January/February 2002, pg. 30.
21. "Insect Robot Project Lifts Off to Explore Mars," *Electronic Engineering Times*, R. Colin Johnson, January 21, 2002, pg. 43(circulation 160,310).
22. "Flying on Mars: Nature's Flight System Could be the Key to Exploring the Newest Frontier," *Research Horizons*, John Toon, Fall 2001, Page 19-24.
23. "Faculty Research in the News," *Research Horizons*, pg. 47.
24. "Bot Bits," *Imagine…*, (magazine of the Johns Hopkins University Center for Talented Youth) Vol. 9, No. 5, May/June 2002, pg. 21.
25. *Atlanta Magazine* (8-27-02 interview), publication date estimated during October 2002
26. Flying Robotic Insect Slated to Explore Mars, *EE Times*, Jan. 22, 2002. URL: http://www.eetimes.com/story/OEG20020114S0081, based on telephone interview.

The following publications reference the Entomopter during the NIAC Phase II effort but have not been reviewed:

1. *Baltimore Sun*, July 28, 2002 (Circulation 479,636)
2. *Arkansas Democrat-Gazette*, July 29, 2002 (Circulation 189,213)
3. *Columbus Dispatch*, July 29, 2002 (Circulation 245,946)
4. *Grand Rapids Press*, July 28, 2002 (Circulation 194,048)
5. *Orlando Sentinel*, August 4, 2002 (Circulation 368,333)
6. *Raleigh News & Observer*, July 31, 2002 (Circulation 162,869)
7. *Rocky Mountain News*, August 5, 2002 (Circulation 323,000)
8. *Sacramento Bee*, July 28, 2002 (Circulation 357,999)

6.3 Online Media

1. "Robot Bugs Planned for Mars Invasion", Popular Science, Etienne Benson, February 8, 2002, online at: http://www.popsci.com/popsci/aviation/article/0,12543,201610,00.html.
2. "A Robotic Bug's Life: To Study Mars", March 1, 2002, University of Missouri-Rolla., online at: http://www.umr.edu/~newsinfo/spacebug.html.
3. "INNOVATIONS", The GTRI Connector, July 2002, online at http://webwise.gtri.gatech.edu/corporate/comm/connector.
4. "Bugs on Mars", Science News, Peter Weiss, May 25, 2002, Vol. 161, 2002, pp. 330-332, online at: www.sciencenews.org.
5. "Tiny Flying Robots: Future Masters of Espionage", CNN.com/SCI-TECH, July 27, 2002 (Associated Press story by Andrew Bridges), online at http://www.cnn.com/2002/TECH/science/07/27/flyingmicrobots.ap/index.html.
6. "Flapping Robotic Insects Could Extend Range of Rover Missions," Leonard David, January 11, 2002, online at: http://www.space.com/scienceastronomy.solarsystem/mars_flapper_011205-2.html.
7. "How Spy Flies Will Work", How Stuff Works website, Kevin Bonsor, online at: http://www.howstuffworks.com/spy-fly.htm.

8. "Robotic Moths May Fly Around Mars", ROBOTS.NET, Jim Brown, May 31, 2001, online at: http://www.robots.net/article/147.html.
9. ZZZ Online, Number 71, February 18, 2001, online at: http://zzz.com.ru/71.html.
10. (Japanese text), MyCom pcWEB, February 26, 2001, online at: http://pcweb.mycom.co.jp/news/2001/02/26/08.html.
11. "Entomopter" (Korean text), AeroDavinci (Dachi-Dong,Kangnam-Gu, Seoul, Korea), online at: http://www.flappia.com/viewmypage_3_k.html.
12. "Flying on Mars: Nature's Flight System Could be the Key to Exploring the Newest Frontier", Research Horizons, John Toon, Fall 2001, Page 19-24, online at: http://www.gtresearch-news.gaatech.edu/reshor/rh-f01/mars.html.
13. Russian document (Cyrillic text), December 14, 2001 discusses the Mars Entomopter (online at: http://www.computerra.ru/offline/2001/425/14713/).
14. Ames Research Center, Astobiology Feature: (online at: http://astrobiology.arc.nasa.gov/feature/index.html).

6.4 Television Science Programming, News, and Video Archives

1. TechTV, Peter Barnes, February 2002 (aired on various outlets).
2. 5-15-01 Discovery News.
3. 1-4-02 Wired interview (air date unknown).
4. 5-25-01 KQED interview (air date unknown).
5. 1-7-02 Discovery.ca segment.
6. "Flying on Mars", Breakthroughs in Research, Discovery, April 2002.
7. The Royal Astronomical Society Library maintains a copy of the Entomopter-based Mars Surveyor video in their archives (Royal Astronomical Society, Burlington House, Piccadilly, London W1J 0BQ, UK).
8. Major Minors, a radio interview with the KUMR, April 12, 2002.

6.5 CD Distribution and Live Performances

1. The Smithsonian Institution National Air and Space Museum has included information about the Entomopter-based Mars Surveyor in its Interactive Multimedia CD-ROM entitled, "Solar System Explorer." This CD contains the Mars Entomopter video as well as information for travel, education, virtual tours and exhibits, music, and multi-level games and activities in more than 1,000 photos, two hours of narration, more than 40 videos and animations, an Interactive map of the Mall featuring all Smithsonian museums, and a separate music-only section with the entire score of Gustav Holst's "The Planets." The information on the CD is updatable via the Internet and expandable. The Entomopter-based Mars surveyor is described along with the video of the future NASA exploration mission. This CD is released and distributed through Smithsonian Institution channels. It is anticipated that the Smithsonian Institution will install kiosks within the Air and Space Museum for real-time use by patrons.

2. The San Diego Aerospace Museum CD, “Let the Dream Take Flight,” is similar to the Smithsonian Institute product in that it is an interactive multimedia CD-ROM with more than 1,000 photos, one hour of narration, more than 40 videos and animations, and an interactive multi-layered map of San Diego, including more than 50 museums and attractions in the San Diego area. The Entomopter-based Mars surveyor is described along with the video of the future NASA exploration mission. The release date is October 2002 for use in kiosks within the museum.

3. The Calgary Airport Authority’s “Spaceport” has requested use of the Mars Entomopter video as part of their Mars exploration display. When in place, the video will run in an endless loop near the entrance to the Spaceport.

6.6 Special Recognition and Awards

Pirelli S.p.A. endowed the sixth edition of the “Pirelli International Award” for the diffusion of scientific culture. Two prizes were awarded by the Pirelli Corporation for work on the Entomopter, as described in the multimedia web presentation found at: http://avdil.gtri.gatech.edu/RCM/RCM/Entomopter/EntomopterProject.html. Along with the basic terrestrial Entomopter developmental path, this website includes discussions of the Entomopter-based Mars surveyor, with text, pictures, and video. This website won an international jury prize for the “best multimedia product coming from any educational institution in the world,” as well as the “Top Pirelli Prize,” given to the work considered the best among those winning the various categories. The Entomopter project was considered the best among more than 1,000 projects reviewed by the jury.

Chapter 7.0 Conclusion

The Entomopter was originally conceived as a terrestrial vehicle for operation inside buildings. Unique features such as an anaerobic propulsion system and biologically-inspired wings capable of generating abnormally high coefficients of lift were recognized as having application to slow flight in the lower Mars atmosphere. The Entomopter does not rely on a purely biomimetic paradigm for flight, but goes beyond biomimetics by using a resonantly-tuned circulation-controlled pair of autonomically-beating wings that enable slow flight and landing as well as higher maneuverability than can be achieved with a fixed wing vehicle.

A series of Mars flight scenarios were defined that could take advantage of the unique performance envelope offered by a Mars Entomopter. In particular the ability to launch from a moving rover, conduct nearby aerial surveys, and return for refueling offered, for the first time, the hope that flight missions could be conducted repetitively over extended periods. Various fuels were investigated for use with the Entomopter's Reciprocating Chemical Muscle. These fuels were analyzed for their compatibility with space flight and operation in the Mars environment. An analysis was also performed to determine the trade off between bringing fuel from Earth to Mars, as opposed to the creation of fuel in situ from components found in the Mars Environment. Because most fuels of interest require hydrogen as a constituent, an analysis was conducted to determine the break point beyond which it was more cost-effective to manufacture fuel on Mars rather than supporting the infrastructure for its transport from Earth. This break point was found to be on the order of 300 days. However with the recent discovery of water in the surface layers of Mars, the ability to scavenge a ready source of naturally-occurring hydrogen may make in situ fuel production more attractive.

The most important considerations for Entomopter flight on Mars are weight reduction and wing aerodynamics. Analyses of wing size, wing material, angles of attack, and wing beat frequencies were conducted as an aid in bounding the design space for the sizing of the Mars Entomopter. A design point was chosen as the local optimum based predominantly on power and strength of materials criteria, and although this was used as a basis for other calculations, it does not represent the optimum design point, for all missions or operational conditions.

The leading edge vortex has been shown to be the primary cause of enhanced lift during the wing flap. The LEV is dynamic, changing in diameter and speed as the wing flaps. It rolls along the surface of the wing at an angle (about 45°) and eventually detaches as a shed vortex. The direction of the vortex rotation tends to drive forward velocity air up and over the vortex so that it can reattach to the wing. This is effectively increasing the camber of the wing without inducing the drag that would otherwise be associated with a physical camber of the same size. Blowing of the flapping wing should not only keep this leading edge vortex attached longer, but also enhance the air moving over the vortex. The benefits of this blowing mechanism are essential for Entomopter flight on Mars.

The CFD efforts performed during this NIAC study have attempted to validate the efficacy of blown wing operation under the conditions encountered in the lower Mars atmosphere. Because the notion of blown wing aerodynamics in the unsteady aerodynamic context of the flapping wing is an absolutely new area for research, new codes and techniques have had to be developed

to address this subject. Similarly an analytical solution to blown flapping wing flight does not exist and new formulations for the aerodynamics of the flapping wing have been developed during this NIAC study as a first step toward addressing this deficiency.

In both the CFD and analytical formulations, certain physical properties have yet to be implemented. For example, the analytical formulation correctly characterizes the aerodynamics of the flapping wing and is in agreement with the CFD results, but it has yet to implement those modules that account for the circulation due to the LEV and the effects of blowing. On the other hand, while CFD has been able to show that the effects of a correctly configured and blown flap significantly increase lift, the parameters of the point solution chosen did not yield the optimum levels of performance encountered experimentally in the wind tunnel for other blown wings. The analytical formulation for the flapping wing aerodynamics is designed to be a tool that can allow rapid permutations of these parameters to define the bounds of the design space and also to identify optima within that space. The CFD codes developed can then validate the analytical findings, however the ultimate validation will be future wind tunnel tests that are designed to test the Entomopter wing with the predicted optimal parameter set under Mars atmospheric conditions. This NIAC study has been able to develop the basic tools that will ultimately lead to these validating wind tunnel tests.

The Entomopter's Reciprocating Chemical Muscle was also sized for the Mars flight vehicle. Although torsional resonance is designed into the Entomopter's wing flapping mechanism, this has not been modeled as part of the power calculations used in the design of the propulsion system. Therefore the payload capacity and endurance estimates for a Mars Entomopter with a 1.2 m wing span are conservative.

Having addressed the flight regime and sizing of the Mars Entomopter, the issues of navigation and communication were considered. In particular the issues of Entomopter location and self-awareness amid unbriefed Mars terrain features were addressed. Two approaches were taken, the first of which was "rover-centric" with the philosophy that to reduce Entomopter weight and increased endurance, as much communications and navigation capability as possible should be contained in the Entomopter's refueling rover. The second approach involved a more traditional design in which various sensor systems would be carried by the Entomopter to allow greater self-sufficiency albeit at the cost of greater gross weight and power consumption.

Various science payload packages have been identified as well as Entomopter-enabled missions. Dual use of communications and navigation equipment was explored in support of the science missions so as to reduce the weight of redundant electronics.

Based on the research conducted during this NIAC Phase II study, a design space has been identified in which Mars Entomopter flight is practical. The added capability offered by an Entomopter-based Mars surveyor is significant and will increase the amount of useful science that can be conducted during a Mars mission. The results of this NIAC study indicate that no other Mars surveying vehicle concept is comparable to that of the Entomopter when the combination of mission endurance and surveillance information resolution is considered.

Appendix A: Mars Atmosphere Data

JPL Reference Mars Atmosphere for -20° Latitude

Mars Atmosphere Model

	coxZ	0.7
Lat = -20	Z,deg	41.9298101

H, km	T, K	P, Pa	p, g/m3	μ, Pa*s	v, m2/s	1/v
9.8750	205	273.6	6.968	1.04E-05	0.00150	667
9.6250	206	280.2	7.100	1.05E-05	0.00148	677
9.3750	207	286.8	7.234	1.05E-05	0.00146	687
9.1250	208	293.6	7.369	1.06E-05	0.00144	696
8.8750	209	300.6	7.507	1.06E-05	0.00142	706
8.6250	209	307.6	7.683	1.06E-05	0.00138	723
8.3750	210	314.8	7.826	1.07E-05	0.00136	733
8.1250	211	322.2	7.970	1.07E-05	0.00135	743
7.8750	212	329.7	8.117	1.08E-05	0.00133	753
7.6250	213	337.3	8.266	1.08E-05	0.00131	764
7.3750	214	345.0	8.416	1.09E-05	0.00129	774
7.1250	215	352.9	8.569	1.09E-05	0.00127	785
6.8750	216	361.0	8.724	1.10E-05	0.00126	795
6.6250	217	369.2	8.880	1.10E-05	0.00124	806
6.3750	218	377.5	9.039	1.11E-05	0.00122	817
6.1250	218	386.0	9.243	1.11E-05	0.00120	835
5.8750	219	394.7	9.407	1.11E-05	0.00118	847
5.6250	220	403.5	9.574	1.12E-05	0.00117	858
5.3750	221	412.5	9.743	1.12E-05	0.00115	869
5.1250	222	421.6	9.914	1.13E-05	0.00114	881
4.8750	223	430.9	10.087	1.13E-05	0.00112	892
4.6250	224	440.4	10.262	1.14E-05	0.00111	904
4.3750	224	450.0	10.487	1.14E-05	0.00108	924
4.1250	225	459.9	10.669	1.14E-05	0.00107	936

JPL Reference Mars Atmosphere for -20° Latitude (Continued)

Mars Atmosphere Model

coxZ 0.7

H, km	T, K	P, Pa	p, g/m3	μ, Pa*s	v, m2/s	1/v
3.8750	226	469.9	10.853	1.14E-05	0.00105	948
3.6250	227	480.0	11.039	1.15E-05	0.00104	960
3.3750	227	490.4	11.278	1.15E-05	0.00102	981
3.1250	228	501.0	11.470	1.15E-05	0.00101	994
2.8750	228	511.8	11.717	1.15E-05	0.00099	1015
2.6250	229	522.8	11.917	1.16E-05	0.00097	1028
2.3750	229	534.0	12.172	1.16E-05	0.00095	1050
2.1250	229	545.4	12.433	1.16E-05	0.00093	1073
1.8750	229	557.1	12.699	1.16E-05	0.00091	1095
1.6250	229	569.0	12.971	1.16E-05	0.00089	1119
1.3750	228	581.2	13.308	1.15E-05	0.00087	1153
1.1250	227	593.8	13.655	1.15E-05	0.00084	1188
0.8750	226	606.6	14.012	1.14E-05	0.00082	1224
0.6375	228	619.1	14.174	1.15E-05	0.00081	1228
0.4500	230	629.0	14.276	1.16E-05	0.00082	1226
0.3250	231	635.7	14.365	1.17E-05	0.00081	1229
0.2375	232	640.4	14.408	1.17E-05	0.00081	1228
0.1750	233	643.7	14.422	1.18E-05	0.00082	1224
0.1300	234	646.1	14.414	1.18E-05	0.00082	1218
0.0950	234	648.0	14.456	1.18E-05	0.00082	1222
0.0675	235	649.5	14.427	1.19E-05	0.00082	1214
0.0450	236	650.7	14.393	1.19E-05	0.00083	1207
0.0275	237	651.6	14.353	1.20E-05	0.00083	1198
0.0150	238	652.3	14.307	1.20E-05	0.00084	1190
0.0066	239	652.7	14.257	1.21E-05	0.00085	1181
0.0016	244	653.0	13.970	1.23E-05	0.00088	1135

General Mars Atmosphere Model (NASA Langley)

Altitude(ell), km	Altitude (surf), km	Density (kg/m^3)	Pressure (N/m^2)	Temperature (K°)	Speed of Sound (m/s)
0.00E+00	-5.50E+00	1.44E-02	7.91E+02	2.87E+02	2.68E+02
1.00E+00	-4.50E+00	1.38E-02	7.39E+02	2.81E+02	2.65E+02
2.00E+00	-3.50E+00	1.31E-02	6.88E+02	2.74E+02	2.62E+02
3.00E+00	-2.50E+00	1.25E-02	6.40E+02	2.68E+02	2.59E+02
4.00E+00	-1.50E+00	1.19E-02	5.95E+02	2.62E+02	2.56E+02
5.00E+00	-5.00E-01	1.13E-02	5.52E+02	2.56E+02	2.53E+02
6.00E+00	5.00E-01	1.07E-02	5.11E+02	2.49E+02	2.50E+02
7.00E+00	1.50E+00	1.01E-02	4.72E+02	2.43E+02	2.47E+02
8.00E+00	2.50E+00	9.60E-03	4.35E+02	2.37E+02	2.43E+02
9.00E+00	3.50E+00	9.07E-03	4.00E+02	2.31E+02	2.40E+02
1.00E+01	4.50E+00	8.56E-03	3.68E+02	2.25E+02	2.37E+02
1.10E+01	5.50E+00	7.98E-03	3.37E+02	2.21E+02	2.35E+02
1.20E+01	6.50E+00	7.37E-03	3.08E+02	2.19E+02	2.34E+02
1.30E+01	7.50E+00	6.80E-03	2.82E+02	2.17E+02	2.33E+02
1.40E+01	8.50E+00	6.27E-03	2.58E+02	2.15E+02	2.32E+02
1.50E+01	9.50E+00	5.78E-03	2.35E+02	2.13E+02	2.31E+02
1.60E+01	1.05E+01	5.32E-03	2.15E+02	2.11E+02	2.30E+02
1.70E+01	1.15E+01	4.90E-03	1.96E+02	2.09E+02	2.29E+02
1.80E+01	1.25E+01	4.50E-03	1.78E+02	2.07E+02	2.28E+02
1.90E+01	1.35E+01	4.14E-03	1.63E+02	2.05E+02	2.27E+02
2.00E+01	1.45E+01	3.80E-03	1.48E+02	2.04E+02	2.26E+02
2.10E+01	1.55E+01	3.48E-03	1.34E+02	2.02E+02	2.25E+02
2.20E+01	1.65E+01	3.18E-03	1.22E+02	2.01E+02	2.24E+02
2.30E+01	1.75E+01	2.91E-03	1.11E+02	1.99E+02	2.23E+02
2.40E+01	1.85E+01	2.66E-03	1.01E+02	1.98E+02	2.22E+02
2.50E+01	1.95E+01	2.43E-03	9.12E+01	1.96E+02	2.22E+02
2.60E+01	2.05E+01	2.22E-03	8.26E+01	1.95E+02	2.21E+02
2.70E+01	2.15E+01	2.02E-03	7.48E+01	1.94E+02	2.20E+02
2.80E+01	2.25E+01	1.84E-03	6.77E+01	1.92E+02	2.19E+02

General Mars Atmosphere Model (NASA Langley) (Continued)

Altitude(ell), km	Altitude (surf), km	Density (kg/m^3)	Pressure (N/m^2)	Temperature (K°)	Speed of Sound (m/s)
2.90E+01	2.35E+01	1.68E-03	6.13E+01	1.91E+02	2.18E+02
3.00E+01	2.45E+01	1.53E-03	5.54E+01	1.90E+02	2.18E+02
3.10E+01	2.55E+01	1.39E-03	5.00E+01	1.88E+02	2.17E+02
3.20E+01	2.65E+01	1.26E-03	4.51E+01	1.87E+02	2.16E+02
3.30E+01	2.75E+01	1.15E-03	4.07E+01	1.86E+02	2.15E+02
3.40E+01	2.85E+01	1.04E-03	3.67E+01	1.84E+02	2.15E+02
3.50E+01	2.95E+01	9.46E-04	3.31E+01	1.83E+02	2.14E+02
3.60E+01	3.05E+01	8.58E-04	2.98E+01	1.81E+02	2.13E+02
3.70E+01	3.15E+01	7.77E-04	2.68E+01	1.80E+02	2.12E+02
3.80E+01	3.25E+01	7.03E-04	2.41E+01	1.79E+02	2.12E+02
3.90E+01	3.35E+01	6.36E-04	2.16E+01	1.78E+02	2.11E+02
4.00E+01	3.45E+01	5.75E-04	1.94E+01	1.77E+02	2.10E+02
4.10E+01	3.55E+01	5.19E-04	1.74E+01	1.75E+02	2.09E+02
4.20E+01	3.65E+01	4.69E-04	1.56E+01	1.74E+02	2.09E+02
4.30E+01	3.75E+01	4.23E-04	1.40E+01	1.73E+02	2.08E+02
4.40E+01	3.85E+01	3.81E-04	1.25E+01	1.72E+02	2.07E+02
4.50E+01	3.95E+01	3.43E-04	1.12E+01	1.71E+02	2.06E+02
4.60E+01	4.05E+01	3.09E-04	1.00E+01	1.69E+02	2.06E+02
4.70E+01	4.15E+01	2.78E-04	8.95E+00	1.68E+02	2.05E+02
4.80E+01	4.25E+01	2.50E-04	7.99E+00	1.67E+02	2.04E+02
4.90E+01	4.35E+01	2.25E-04	7.12E+00	1.66E+02	2.04E+02
5.00E+01	4.45E+01	2.02E-04	6.35E+00	1.65E+02	2.03E+02
5.10E+01	4.55E+01	1.81E-04	5.65E+00	1.63E+02	2.02E+02
5.20E+01	4.65E+01	1.62E-04	5.03E+00	1.62E+02	2.01E+02
5.30E+01	4.75E+01	1.45E-04	4.47E+00	1.61E+02	2.01E+02
5.40E+01	4.85E+01	1.30E-04	3.98E+00	1.60E+02	2.00E+02
5.50E+01	4.95E+01	1.16E-04	3.53E+00	1.59E+02	1.99E+02
5.60E+01	5.05E+01	1.04E-04	3.13E+00	1.57E+02	1.98E+02
5.70E+01	5.15E+01	9.26E-05	2.77E+00	1.57E+02	1.98E+02

General Mars Atmosphere Model (NASA Langley) (Continued)

Altitude(ell), km	Altitude (surf), km	Density (kg/m^3)	Pressure (N/m^2)	Temperature (K°)	Speed of Sound (m/s)
5.80E+01	5.25E+01	8.24E-05	2.46E+00	1.56E+02	1.97E+02
5.90E+01	5.35E+01	7.32E-05	2.18E+00	1.56E+02	1.97E+02
6.00E+01	5.45E+01	6.51E-05	1.93E+00	1.55E+02	1.97E+02
6.10E+01	5.55E+01	5.78E-05	1.71E+00	1.54E+02	1.96E+02
6.20E+01	5.65E+01	5.13E-05	1.51E+00	1.54E+02	1.96E+02
6.30E+01	5.75E+01	4.56E-05	1.34E+00	1.53E+02	1.96E+02
6.40E+01	5.85E+01	4.04E-05	1.18E+00	1.53E+02	1.95E+02
6.50E+01	5.95E+01	3.59E-05	1.04E+00	1.52E+02	1.95E+02
6.60E+01	6.05E+01	3.18E-05	9.21E-01	1.52E+02	1.95E+02
6.70E+01	6.15E+01	2.82E-05	8.14E-01	1.51E+02	1.94E+02
6.80E+01	6.25E+01	2.50E-05	7.18E-01	1.50E+02	1.94E+02
6.90E+01	6.35E+01	2.21E-05	6.34E-01	1.50E+02	1.94E+02
7.00E+01	6.45E+01	1.96E-05	5.59E-01	1.49E+02	1.93E+02
7.10E+01	6.55E+01	1.73E-05	4.93E-01	1.49E+02	1.93E+02
7.20E+01	6.65E+01	1.53E-05	4.34E-01	1.48E+02	1.92E+02
7.30E+01	6.75E+01	1.36E-05	3.82E-01	1.48E+02	1.92E+02
7.40E+01	6.85E+01	1.20E-05	3.37E-01	1.47E+02	1.92E+02
7.50E+01	6.95E+01	1.06E-05	2.96E-01	1.46E+02	1.91E+02
7.60E+01	7.05E+01	9.35E-06	2.61E-01	1.46E+02	1.91E+02
7.70E+01	7.15E+01	8.25E-06	2.29E-01	1.45E+02	1.91E+02
7.80E+01	7.25E+01	7.28E-06	2.02E-01	1.45E+02	1.90E+02
7.90E+01	7.35E+01	6.42E-06	1.77E-01	1.44E+02	1.90E+02
8.00E+01	7.45E+01	5.66E-06	1.56E-01	1.44E+02	1.89E+02
8.10E+01	7.55E+01	4.99E-06	1.37E-01	1.43E+02	1.89E+02
8.20E+01	7.65E+01	4.40E-06	1.20E-01	1.43E+02	1.89E+02
8.30E+01	7.75E+01	4.00E-06	1.09E-01	1.42E+02	1.89E+02
8.40E+01	7.85E+01	3.51E-06	9.55E-02	1.43E+02	1.89E+02
8.50E+01	7.95E+01	3.08E-06	8.39E-02	1.43E+02	1.89E+02
8.60E+01	8.05E+01	2.70E-06	7.36E-02	1.43E+02	1.89E+02

General Mars Atmosphere Model (NASA Langley) (Continued)

Altitude(ell), km	Altitude (surf), km	Density (kg/m^3)	Pressure (N/m^2)	Temperature (K°)	Speed of Sound (m/s)
8.70E+01	8.15E+01	2.37E-06	6.47E-02	1.43E+02	1.89E+02
8.80E+01	8.25E+01	2.08E-06	5.68E-02	1.43E+02	1.89E+02
8.90E+01	8.35E+01	1.83E-06	4.99E-02	1.43E+02	1.89E+02
9.00E+01	8.45E+01	1.60E-06	4.38E-02	1.43E+02	1.89E+02
9.10E+01	8.55E+01	1.41E-06	3.85E-02	1.43E+02	1.89E+02
9.20E+01	8.65E+01	1.24E-06	3.38E-02	1.43E+02	1.89E+02
9.30E+01	8.75E+01	1.09E-06	2.97E-02	1.43E+02	1.89E+02
9.40E+01	8.85E+01	9.55E-07	2.61E-02	1.43E+02	1.89E+02
9.50E+01	8.95E+01	8.39E-07	2.30E-02	1.43E+02	1.89E+02
9.60E+01	9.05E+01	7.37E-07	2.02E-02	1.43E+02	1.89E+02
9.70E+01	9.15E+01	6.48E-07	1.78E-02	1.43E+02	1.89E+02
9.80E+01	9.25E+01	5.69E-07	1.56E-02	1.43E+02	1.89E+02
9.90E+01	9.35E+01	5.01E-07	1.37E-02	1.43E+02	1.89E+02
1.00E+02	9.45E+01	4.40E-07	1.21E-02	1.44E+02	1.89E+02
1.01E+02	9.55E+01	3.87E-07	1.06E-02	1.44E+02	1.89E+02
1.02E+02	9.65E+01	3.40E-07	9.35E-03	1.44E+02	1.89E+02
1.03E+02	9.75E+01	2.99E-07	8.22E-03	1.44E+02	1.89E+02
1.04E+02	9.85E+01	2.63E-07	7.24E-03	1.44E+02	1.90E+02
1.05E+02	9.95E+01	2.32E-07	6.37E-03	1.44E+02	1.90E+02
1.06E+02	1.01E+02	2.04E-07	5.61E-03	1.44E+02	1.90E+02
1.07E+02	1.02E+02	1.79E-07	4.94E-03	1.44E+02	1.90E+02
1.08E+02	1.03E+02	1.58E-07	4.35E-03	1.44E+02	1.90E+02
1.09E+02	1.04E+02	1.39E-07	3.83E-03	1.44E+02	1.90E+02
1.10E+02	1.05E+02	1.22E-07	3.37E-03	1.44E+02	1.90E+02
1.11E+02	1.06E+02	1.07E-07	2.97E-03	1.45E+02	1.90E+02
1.12E+02	1.07E+02	9.42E-08	2.62E-03	1.45E+02	1.91E+02
1.13E+02	1.08E+02	8.27E-08	2.31E-03	1.46E+02	1.91E+02
1.14E+02	1.09E+02	7.27E-08	2.04E-03	1.47E+02	1.92E+02
1.15E+02	1.10E+02	6.39E-08	1.80E-03	1.47E+02	1.92E+02

General Mars Atmosphere Model (NASA Langley) (Continued)

Altitude(ell), km	Altitude (surf), km	Density (kg/m^3)	Pressure (N/m^2)	Temperature (K°)	Speed of Sound (m/s)
1.16E+02	1.11E+02	5.62E-08	1.59E-03	1.48E+02	1.92E+02
1.17E+02	1.12E+02	4.95E-08	1.41E-03	1.49E+02	1.93E+02
1.18E+02	1.13E+02	4.36E-08	1.25E-03	1.50E+02	1.93E+02
1.19E+02	1.14E+02	3.84E-08	1.10E-03	1.50E+02	1.94E+02
1.20E+02	1.15E+02	3.39E-08	9.78E-04	1.51E+02	1.94E+02
1.21E+02	1.16E+02	2.99E-08	8.68E-04	1.52E+02	1.95E+02
1.22E+02	1.17E+02	2.64E-08	7.70E-04	1.52E+02	1.95E+02
1.23E+02	1.18E+02	2.34E-08	6.83E-04	1.53E+02	1.96E+02
1.24E+02	1.19E+02	2.07E-08	6.07E-04	1.54E+02	1.96E+02
1.25E+02	1.20E+02	1.83E-08	5.40E-04	1.54E+02	1.96E+02

Mars-GRAM Generated Atmosphere Profile for -25° Latitude, 11° Longitude

Height (km)	Density (kg/ m3)	Temperature (K)	Pressure (Pa)	Speed of Sound (m/s)	Viscosity (kg/m s)
2.38	1.25E-02	252.4	594.8	251.11	1.29E-05
2.5	1.24E-02	251.8	589.2	250.82	1.28E-05
2.75	1.22E-02	250.7	577.9	250.27	1.28E-05
3	1.20E-02	249.7	566.9	249.77	1.27E-05
3.25	1.18E-02	248.6	556	249.22	1.27E-05
3.5	1.17E-02	247.5	545.4	248.66	1.26E-05
3.75	1.15E-02	246.5	534.9	248.16	1.26E-05
4	1.13E-02	245.4	524.7	247.61	1.25E-05
4.25	1.12E-02	244.3	514.6	247.05	1.24E-05
4.5	1.10E-02	243.2	504.8	246.49	1.24E-05
4.75	1.08E-02	242.2	495.1	245.99	1.23E-05
5	1.07E-02	241.1	485.6	245.43	1.23E-05
5.25	1.05E-02	240.5	475.4	245.12	1.22E-05

Mars-GRAM Generated Atmosphere Profile for -25° Latitude, 11° Longitude (Continued)

Height (km)	Density (kg/ m3)	Temperature (K)	Pressure (Pa)	Speed of Sound (m/s)	Viscosity (kg/m s)
5.5	1.03E-02	239.9	465.4	244.82	1.22E-05
5.75	1.01E-02	239.3	455.6	244.51	1.22E-05
6	9.90E-03	238.7	446	244.2	1.22E-05
6.25	9.71E-03	238.1	436.6	243.9	1.21E-05
6.5	9.53E-03	237.6	427.4	243.64	1.21E-05
6.75	9.35E-03	237	418.4	243.33	1.21E-05
7	9.18E-03	236.4	409.6	243.02	1.20E-05
7.25	9.01E-03	235.8	401	242.72	1.20E-05
7.5	8.84E-03	235.2	392.6	242.41	1.20E-05
7.75	8.68E-03	234.6	384.3	242.1	1.19E-05
8	8.51E-03	234	376.2	241.79	1.19E-05
8.25	8.36E-03	233.4	368.3	241.48	1.19E-05
8.5	8.20E-03	232.8	360.5	241.17	1.19E-05
8.75	8.05E-03	232.2	353	240.86	1.18E-05
9	7.90E-03	231.6	345.5	240.54	1.18E-05
9.25	7.75E-03	231	338.3	240.23	1.18E-05
9.5	7.61E-03	230.4	331.1	239.92	1.17E-05
9.75	7.47E-03	229.9	324.2	239.66	1.17E-05
10	7.33E-03	229.3	317.3	239.35	1.17E-05
10.25	7.18E-03	228.8	310.5	239.09	1.16E-05
10.5	7.04E-03	228.4	303.7	238.88	1.16E-05
10.75	6.90E-03	228	297.1	238.67	1.16E-05
11	6.76E-03	227.6	290.7	238.46	1.16E-05
11.25	6.63E-03	227.1	284.4	238.2	1.16E-05
11.5	6.50E-03	226.7	278.2	237.99	1.15E-05
11.75	6.37E-03	226.3	272.2	237.78	1.15E-05
12	6.24E-03	225.9	266.3	237.57	1.15E-05
12.25	6.12E-03	225.4	260.5	237.3	1.15E-05

Mars-GRAM Generated Atmosphere Profile for -25° Latitude, 11° Longitude (Continued)

Height (km)	Density (kg/ m3)	Temperature (K)	Pressure (Pa)	Speed of Sound (m/s)	Viscosity (kg/m s)
12.5	6.00E-03	225	254.9	237.09	1.15E-05
12.75	5.88E-03	224.6	249.3	236.88	1.14E-05
13	5.76E-03	224.2	243.9	236.67	1.14E-05
13.25	5.65E-03	223.8	238.6	236.46	1.14E-05
13.5	5.53E-03	223.3	233.5	236.19	1.14E-05
13.75	5.42E-03	222.9	228.4	235.98	1.13E-05
14	5.32E-03	222.5	223.5	235.77	1.13E-05
14.25	5.21E-03	222.1	218.6	235.56	1.13E-05
14.5	5.11E-03	221.6	213.9	235.29	1.13E-05
14.75	5.01E-03	221.2	209.2	235.08	1.13E-05
15	4.91E-03	220.8	204.7	234.87	1.12E-05
15.25	4.80E-03	220.4	200.1	234.66	1.12E-05
15.5	4.70E-03	219.9	195.6	234.39	1.12E-05
15.75	4.61E-03	219.5	191.1	234.18	1.12E-05
16	4.51E-03	219.1	186.8	233.96	1.11E-05
16.25	4.42E-03	218.7	182.6	233.75	1.11E-05
16.5	4.33E-03	218.3	178.5	233.54	1.11E-05
16.75	4.24E-03	217.8	174.5	233.27	1.11E-05
17	4.15E-03	217.4	170.5	233.05	1.11E-05
17.25	4.06E-03	217	166.7	232.84	1.10E-05
17.5	3.98E-03	216.6	162.9	232.62	1.10E-05
17.75	3.90E-03	216.1	159.2	232.36	1.10E-05
18	3.82E-03	215.7	155.6	232.14	1.10E-05
18.25	3.74E-03	215.3	152.1	231.93	1.09E-05
18.5	3.66E-03	214.9	148.7	231.71	1.09E-05
18.75	3.59E-03	214.5	145.3	231.49	1.09E-05
19	3.51E-03	214	142.1	231.22	1.09E-05
19.25	3.44E-03	213.6	138.8	231.01	1.09E-05

Mars-GRAM Generated Atmosphere Profile for -25° Latitude, 11° Longitude (Continued)

Height (km)	Density (kg/ m3)	Temperature (K)	Pressure (Pa)	Speed of Sound (m/s)	Viscosity (kg/m s)
19.5	3.37E-03	213.2	135.7	230.79	1.08E-05
19.75	3.30E-03	212.8	132.6	230.57	1.08E-05
20	3.23E-03	212.4	129.7	230.36	1.08E-05

Mars-GRAM Generated Atmosphere Profile for 57° Latitude, 2.35^{o} Longitude

Height (km)	Density (kg/ m3)	Temperature (K)	Pressure (Pa)	Speed of Sound (m/s)	Viscosity (kg/m s)
-1.74	2.82E-02	168.3	896.7	205.05	8.44E-06
-1.5	2.72E-02	168.8	865.8	205.36	8.47E-06
-1.25	2.63E-02	169.3	842.1	205.66	8.49E-06
-1	2.55E-02	169.8	819	205.97	8.52E-06
-0.75	2.48E-02	170.3	796.5	206.27	8.55E-06
-0.5	2.40E-02	170.8	774.7	206.57	8.57E-06
-0.25	2.33E-02	171.3	753.4	206.87	8.60E-06
0	2.26E-02	171.7	732.8	207.11	8.62E-06
0.25	2.19E-02	172.2	712.7	207.42	8.65E-06
0.5	2.12E-02	172.7	693.1	207.72	8.68E-06
0.75	2.06E-02	173.2	674.1	208.02	8.71E-06
1	2.00E-02	173.7	655.6	208.32	8.73E-06
1.25	1.94E-02	174.2	637.6	208.62	8.76E-06
1.5	1.88E-02	174.7	620.1	208.92	8.79E-06
1.75	1.82E-02	175.2	603.1	209.21	8.81E-06
2	1.77E-02	175.7	586.6	209.51	8.84E-06
2.25	1.71E-02	176.1	570.5	209.75	8.86E-06
2.5	1.66E-02	176.6	554.8	210.05	8.89E-06
2.75	1.61E-02	177.1	539.6	210.35	8.92E-06

Mars-GRAM Generated Atmosphere Profile for 57° Latitude, 2.35^{o} Longitude (Continued)

Height (km)	Density (kg/ m3)	Temperature (K)	Pressure (Pa)	Speed of Sound (m/s)	Viscosity (kg/m s)
3	1.56E-02	177.6	524.8	210.64	8.94E-06
3.25	1.52E-02	178.1	510.4	210.94	8.97E-06
3.5	1.47E-02	178.6	496.4	211.24	9.00E-06
3.75	1.43E-02	179.1	482.8	211.53	9.02E-06
4	1.38E-02	179.6	469.5	211.83	9.05E-06
4.25	1.34E-02	180.1	456.7	212.12	9.08E-06
4.5	1.30E-02	180.6	444.1	212.41	9.11E-06
4.75	1.26E-02	181	431.9	212.65	9.13E-06
5	1.22E-02	181.5	420.1	212.94	9.15E-06
5.25	1.19E-02	181.8	409	213.12	9.17E-06
5.5	1.16E-02	182.1	398.2	213.3	9.19E-06
5.75	1.12E-02	182.4	387.8	213.47	9.20E-06
6	1.09E-02	182.7	377.5	213.65	9.22E-06
6.25	1.06E-02	183	367.6	213.82	9.24E-06
6.5	1.03E-02	183.3	357.9	214	9.25E-06
6.75	1.00E-02	183.5	348.5	214.11	9.26E-06
7	9.77E-03	183.8	339.3	214.29	9.28E-06
7.25	9.49E-03	184.1	330.3	214.46	9.29E-06
7.5	9.23E-03	184.4	321.6	214.64	9.31E-06
7.75	8.97E-03	184.7	313.2	214.81	9.33E-06
8	8.72E-03	185	304.9	214.99	9.34E-06
8.25	8.48E-03	185.3	296.9	215.16	9.36E-06
8.5	8.24E-03	185.6	289.1	215.34	9.38E-06
8.75	8.01E-03	185.8	281.4	215.45	9.39E-06
9	7.79E-03	186.1	274	215.62	9.40E-06
9.25	7.57E-03	186.4	266.8	215.8	9.42E-06
9.5	7.36E-03	186.7	259.8	215.97	9.43E-06
9.75	7.16E-03	187	252.9	216.15	9.45E-06

Mars-GRAM Generated Atmosphere Profile for 57° Latitude, 2.35^{o} Longitude (Continued)

Height (km)	Density (kg/ m3)	Temperature (K)	Pressure (Pa)	Speed of Sound (m/s)	Viscosity (kg/m s)
10	6.96E-03	187.3	246.3	216.32	9.47E-06
10.25	6.77E-03	187.5	239.9	216.43	9.48E-06
10.5	6.59E-03	187.6	233.8	216.49	9.48E-06
10.75	6.41E-03	187.8	227.8	216.61	9.49E-06
11	6.24E-03	188	221.9	216.72	9.50E-06
11.25	6.08E-03	188.2	216.2	216.84	9.51E-06
11.5	5.92E-03	188.4	210.7	216.95	9.53E-06
11.75	5.76E-03	188.5	205.3	217.01	9.53E-06
12	5.60E-03	188.7	200	217.13	9.54E-06
12.25	5.46E-03	188.9	194.9	217.24	9.55E-06
12.5	5.31E-03	189.1	189.9	217.36	9.56E-06
12.75	5.17E-03	189.3	185	217.47	9.57E-06
13	5.03E-03	189.4	180.2	217.53	9.58E-06
13.25	4.90E-03	189.6	175.6	217.64	9.59E-06
13.5	4.77E-03	189.8	171.1	217.76	9.60E-06
13.75	4.64E-03	190	166.7	217.87	9.61E-06
14	4.52E-03	190.2	162.4	217.99	9.62E-06
14.25	4.40E-03	190.3	158.2	218.04	9.63E-06
14.5	4.28E-03	190.5	154.2	218.16	9.64E-06
14.75	4.16E-03	190.7	150.2	218.27	9.65E-06
15	4.05E-03	190.9	146.4	218.39	9.66E-06
15.25	3.95E-03	190.9	142.7	218.39	9.66E-06
15.5	3.85E-03	191	139	218.45	9.66E-06
15.75	3.75E-03	191	135.5	218.45	9.66E-06
16	3.66E-03	191	132.1	218.45	9.66E-06
16.25	3.56E-03	191.1	128.7	218.5	9.67E-06
16.5	3.47E-03	191.1	125.4	218.5	9.67E-06
16.75	3.38E-03	191.1	122.3	218.5	9.67E-06

Mars-GRAM Generated Atmosphere Profile for 57° Latitude, 2.35^{o} Longitude (Continued)

Height (km)	Density (kg/ m3)	Temperature (K)	Pressure (Pa)	Speed of Sound (m/s)	Viscosity (kg/m s)
17	3.30E-03	191.2	119.2	218.56	9.68E-06
17.25	3.21E-03	191.2	116.1	218.56	9.68E-06
17.5	3.13E-03	191.2	113.2	218.56	9.68E-06
17.75	3.05E-03	191.2	110.3	218.56	9.68E-06
18	2.97E-03	191.3	107.5	218.62	9.68E-06
18.25	2.90E-03	191.3	104.8	218.62	9.68E-06
18.5	2.82E-03	191.3	102.1	218.62	9.68E-06
18.75	2.75E-03	191.4	99.5	218.67	9.69E-06
19	2.68E-03	191.4	97	218.67	9.69E-06
19.25	2.61E-03	191.4	94.5	218.67	9.69E-06
19.5	2.54E-03	191.5	92.1	218.73	9.69E-06
19.75	2.48E-03	191.5	89.8	218.73	9.69E-06
20	2.42E-03	191.5	87.5	218.73	9.69E-06

Appendix B: Sizing Results

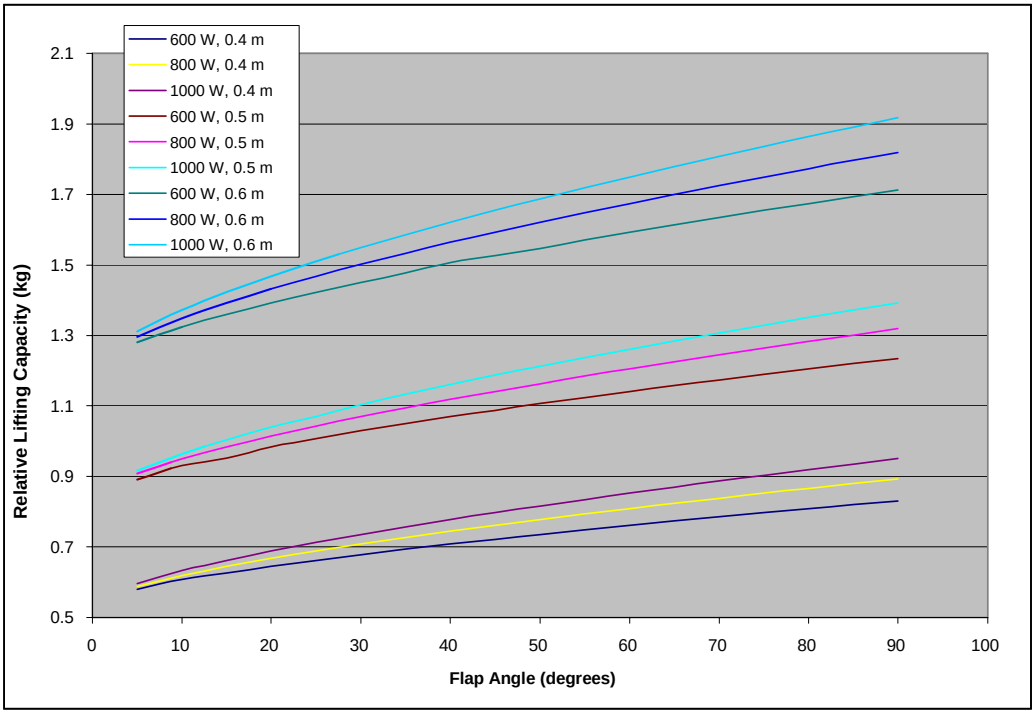

Figure B-1: Relative Lifting Capacity for Various Engine Powers and Wing Lengths at 15 m/s Flight Speed

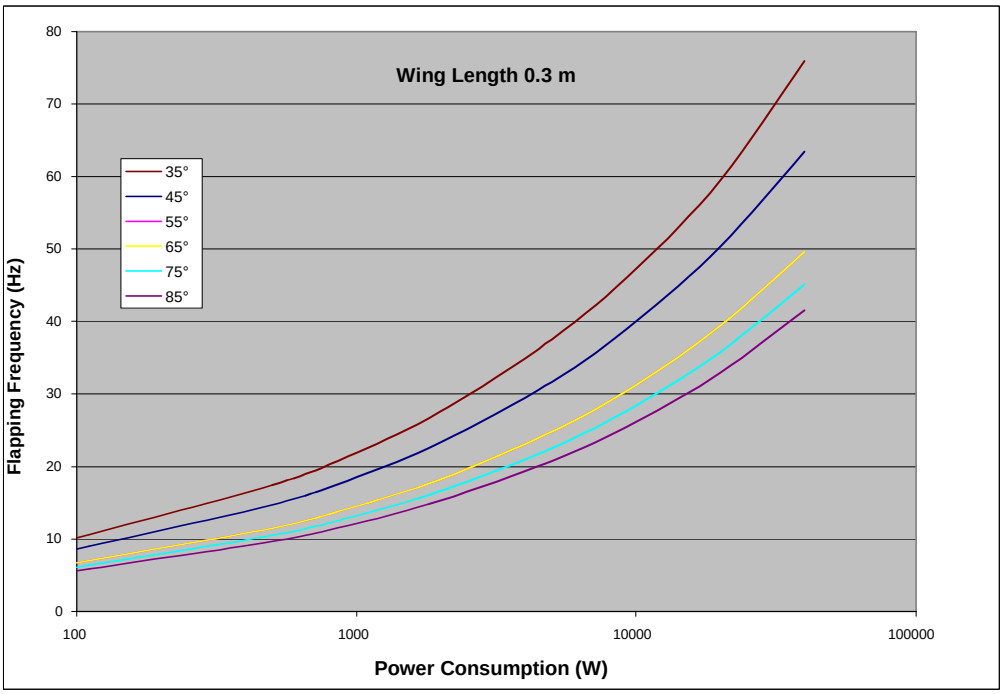

Figure B-2: Flapping Frequency vs. Power Consumption (Watts) for a Wing Length of 0.3 m

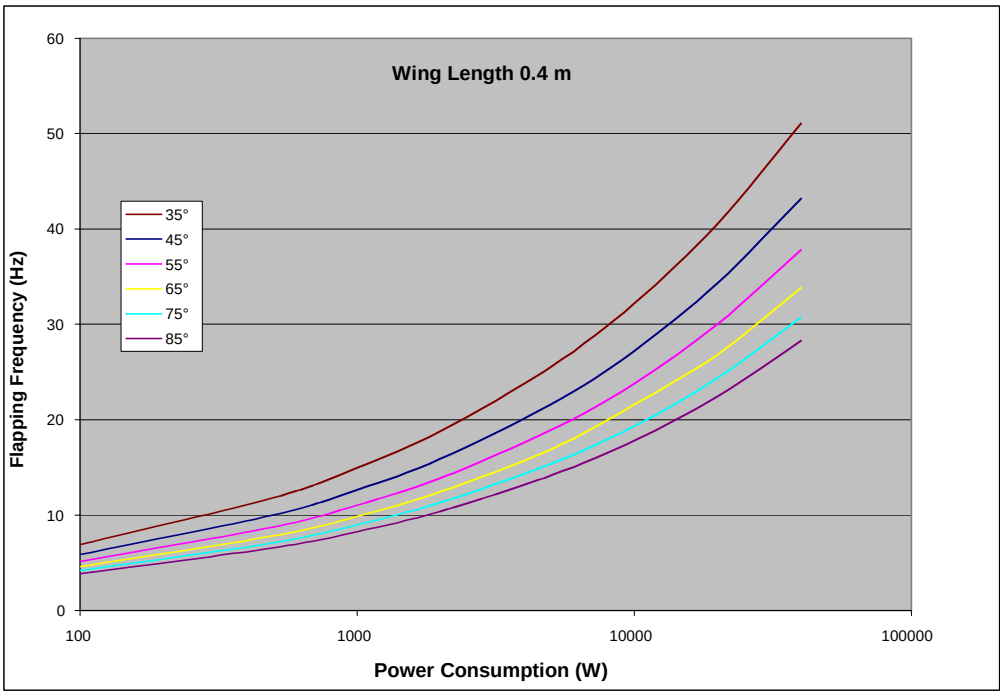

Figure B-3: Flapping Frequency vs. Power Consumption (Watts) for a Wing Length of 0.4 m

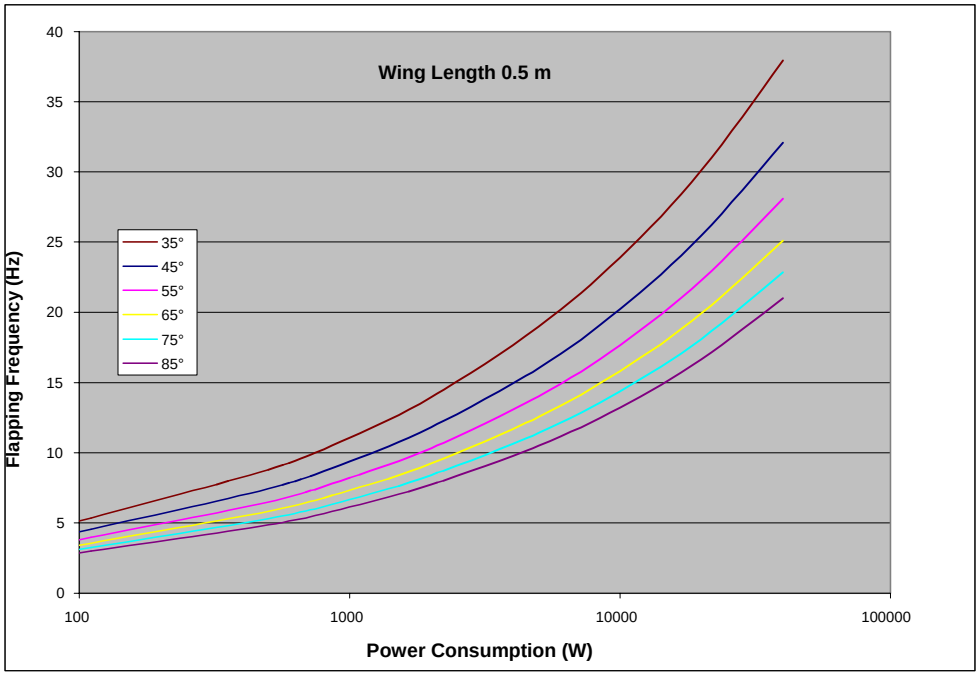

Figure B-4: Flapping Frequency vs. Power Consumption (Watts) for a Wing Length of 0.5 m

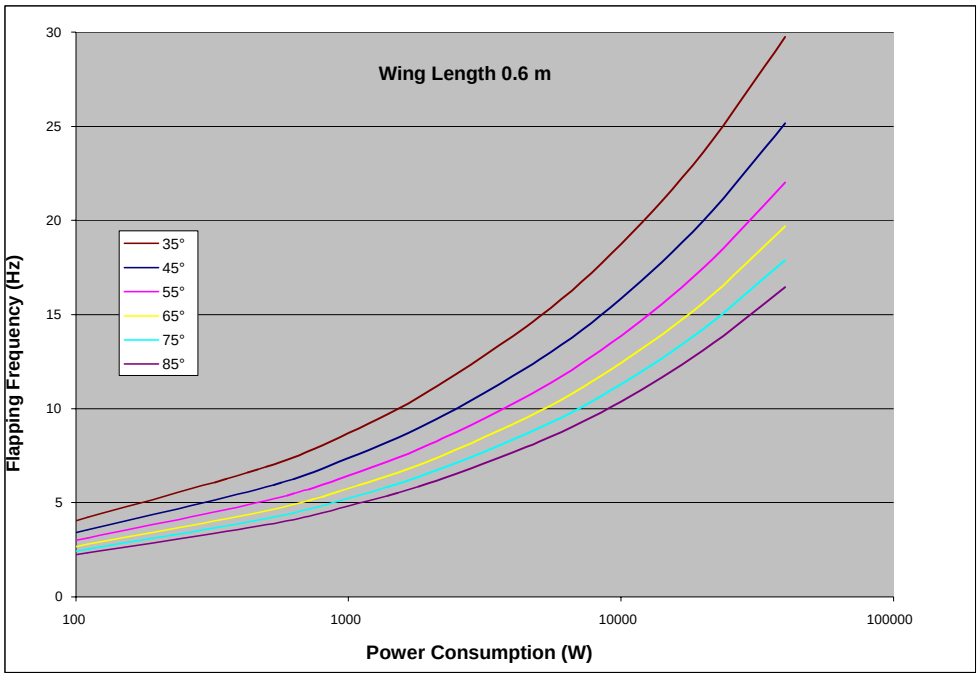

Figure B-5: Flapping Frequency vs. Power Consumption (Watts) for a Wing Length of 0.6 m

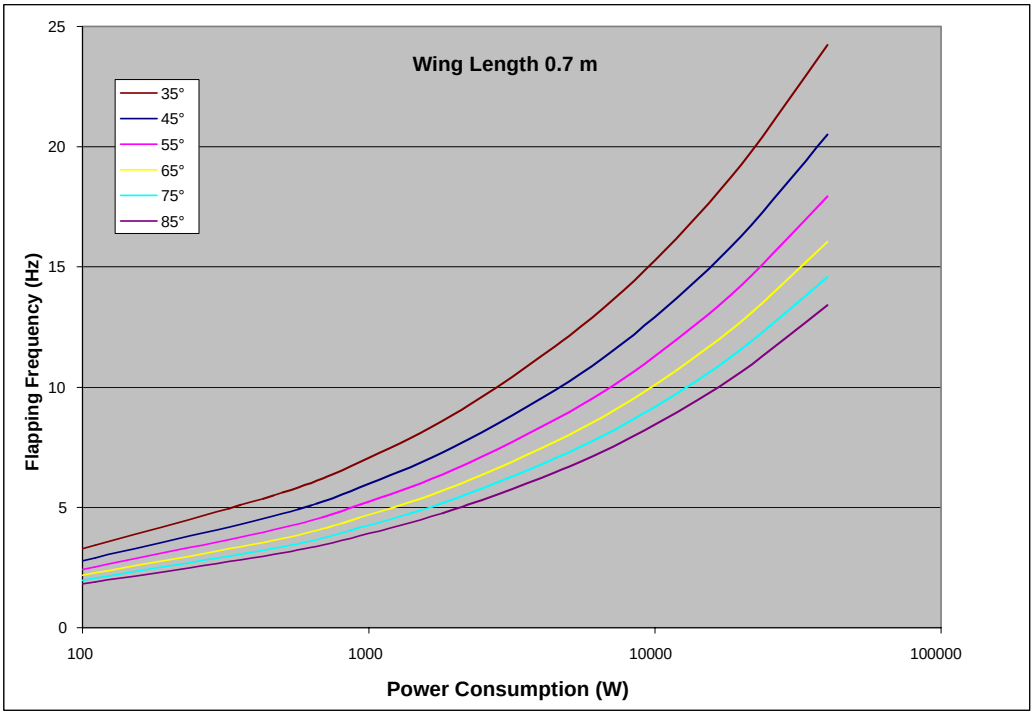

Figure B-6: Flapping Frequency vs. Power Consumption (Watts) for a Wing Length of 0.7 m

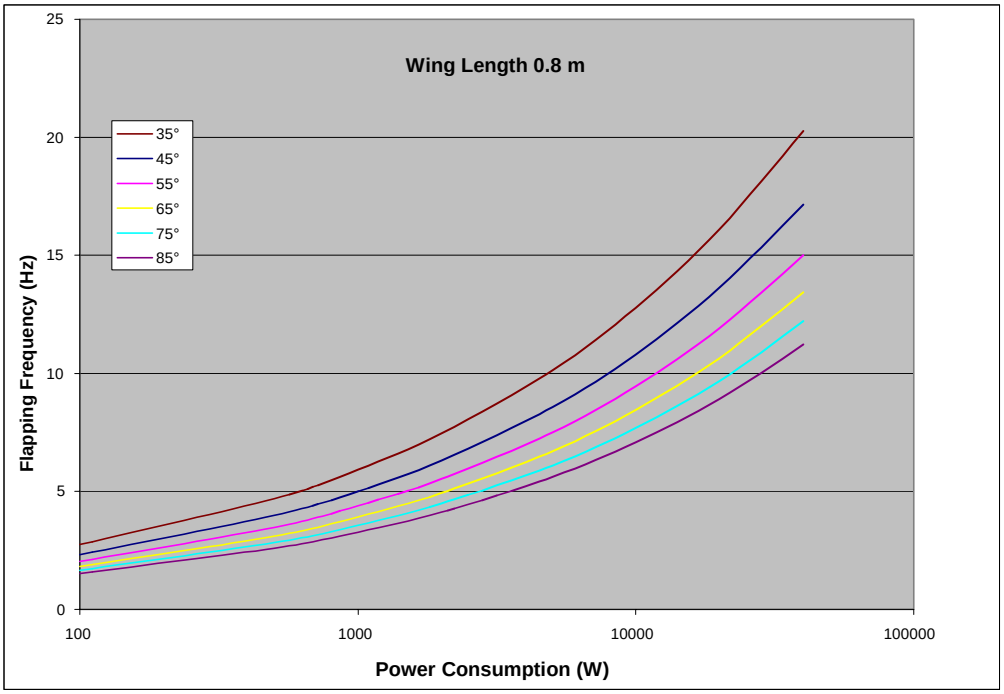

Figure B-7: Flapping Frequency vs. Power Consumption (Watts) for a Wing Length of 0.8 m

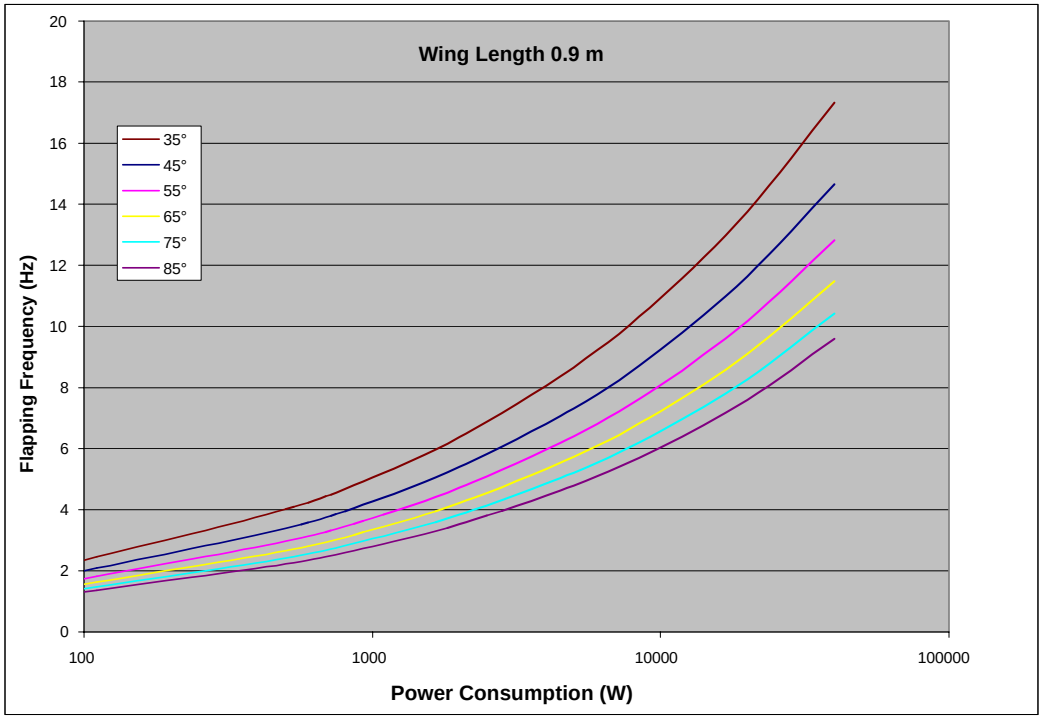

Figure B-8: Flapping Frequency vs. Power Consumption (Watts) for a Wing Length of 0.9 m

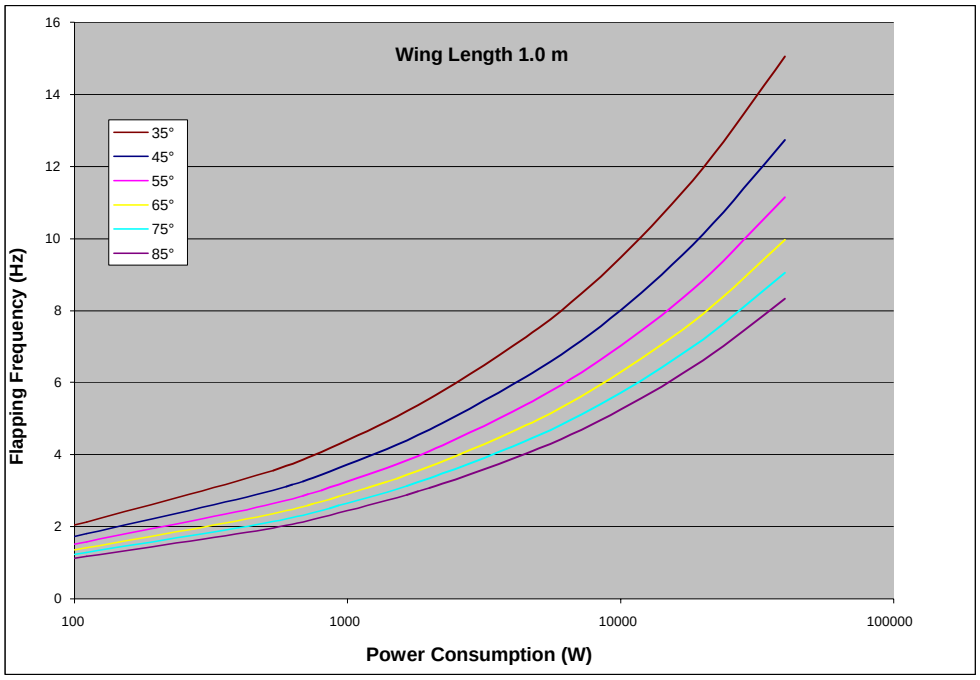

Figure B-9: Flapping Frequency vs. Power Consumption (Watts) for a Wing Length of 1.0 m

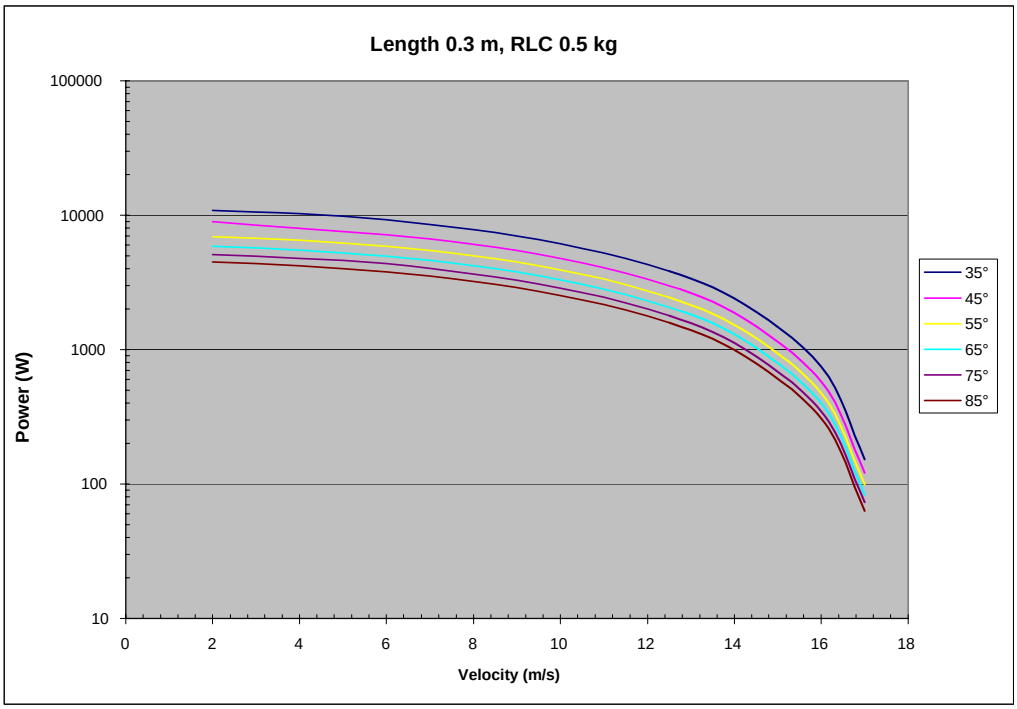

Figure B-10: Flight Power vs. Velocity for a Wing Length of 0.3 m and Relative Lift Capacity of 0.5 kg

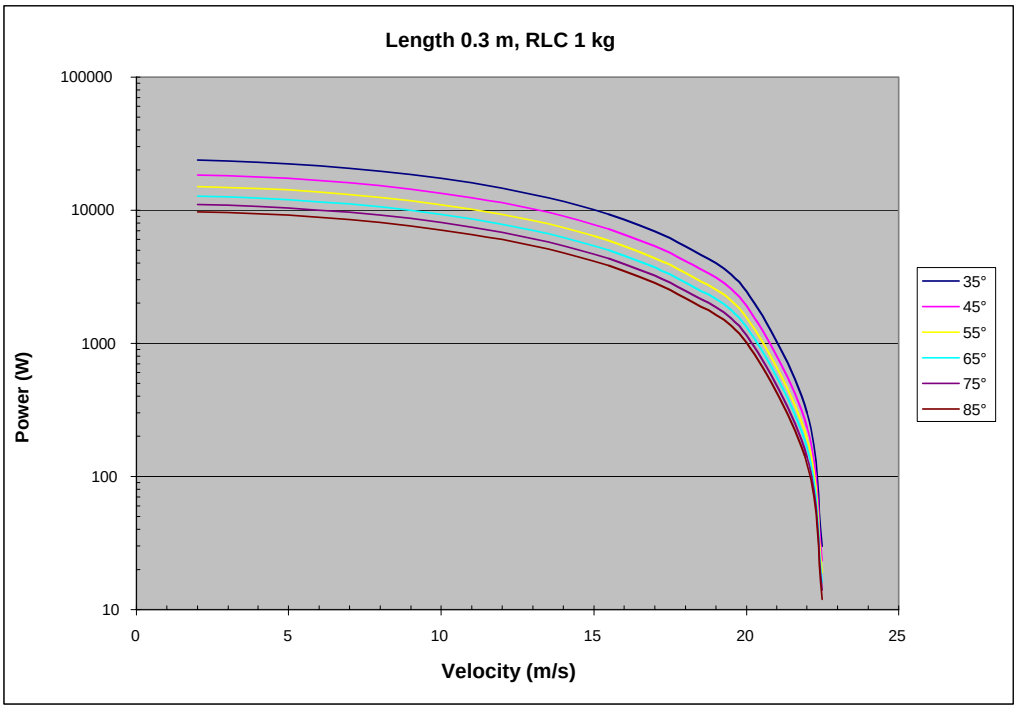

Figure B-11: Flight Power vs. Velocity for a Wing Length of 0.3 m and Relative Lift Capacity of 1.0 kg

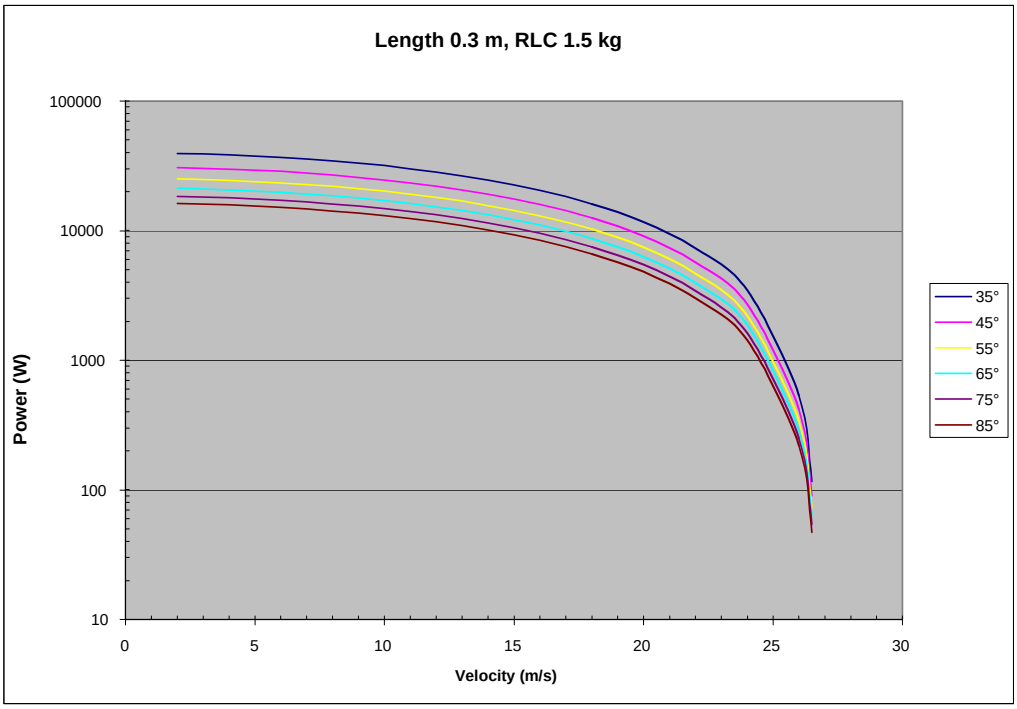

Figure B-12: Flight Power vs. Velocity for a Wing Length of 0.3 m and Relative Lift Capacity of 1.5 kg

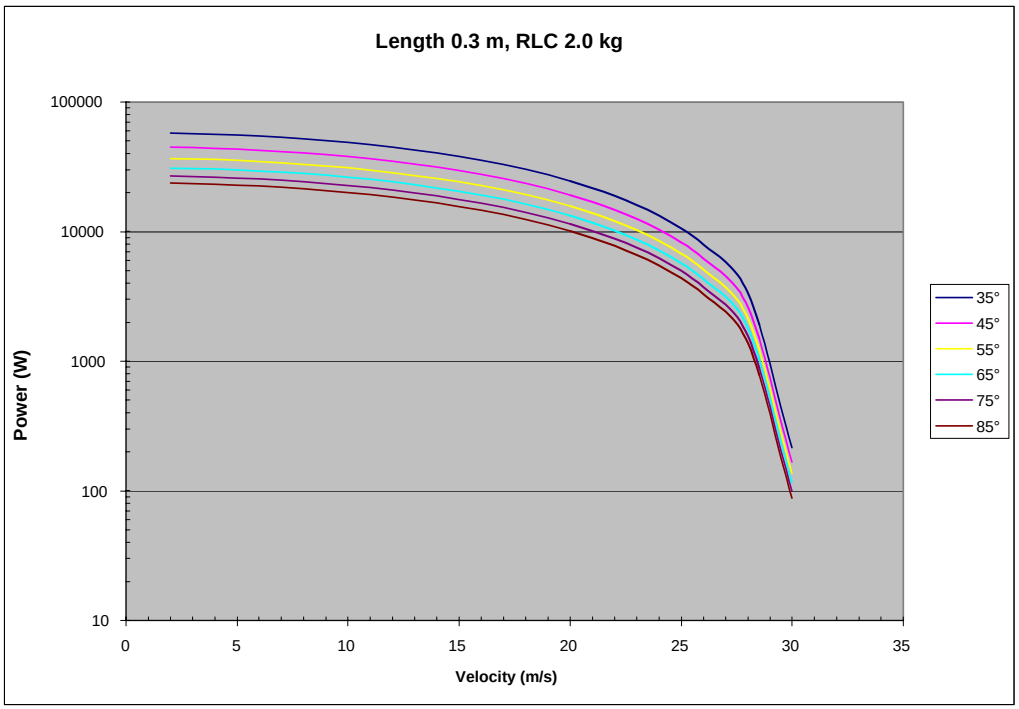

Figure B-13: Flight Power vs. Velocity for a Wing Length of 0.3 m and Relative Lift Capacity of 2.0 kg

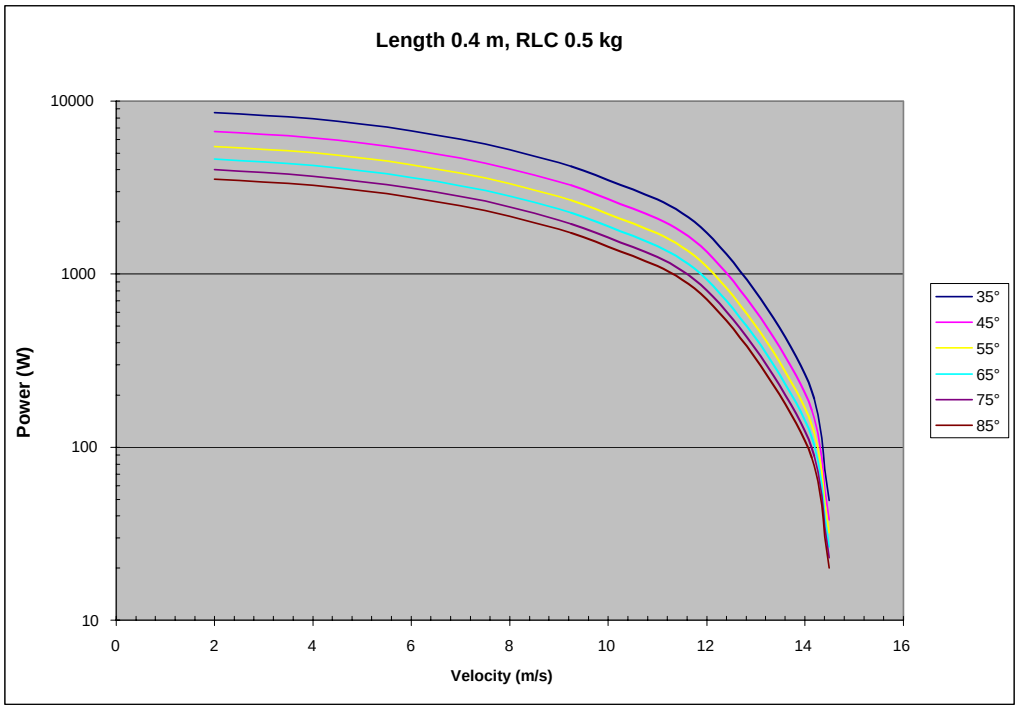

Figure B-14: Flight Power vs. Velocity for a Wing Length of 0.4 m and Relative Lift Capacity of 0.5 kg

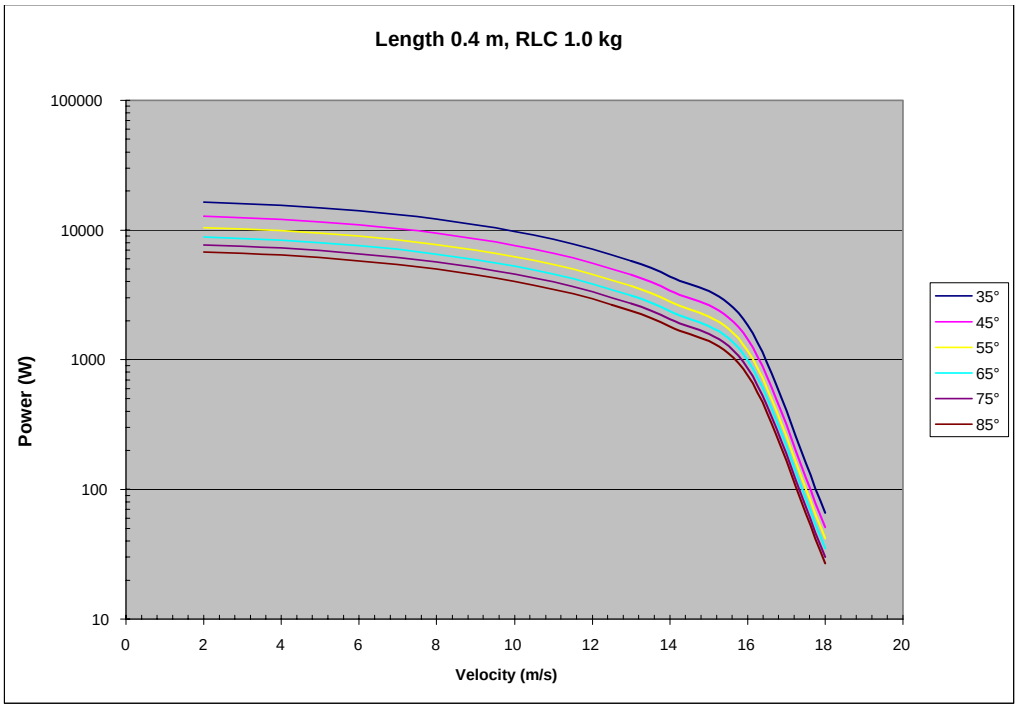

Figure B-15: Flight Power vs. Velocity for a Wing Length of 0.4 m and Relative Lift Capacity of 1.0 kg

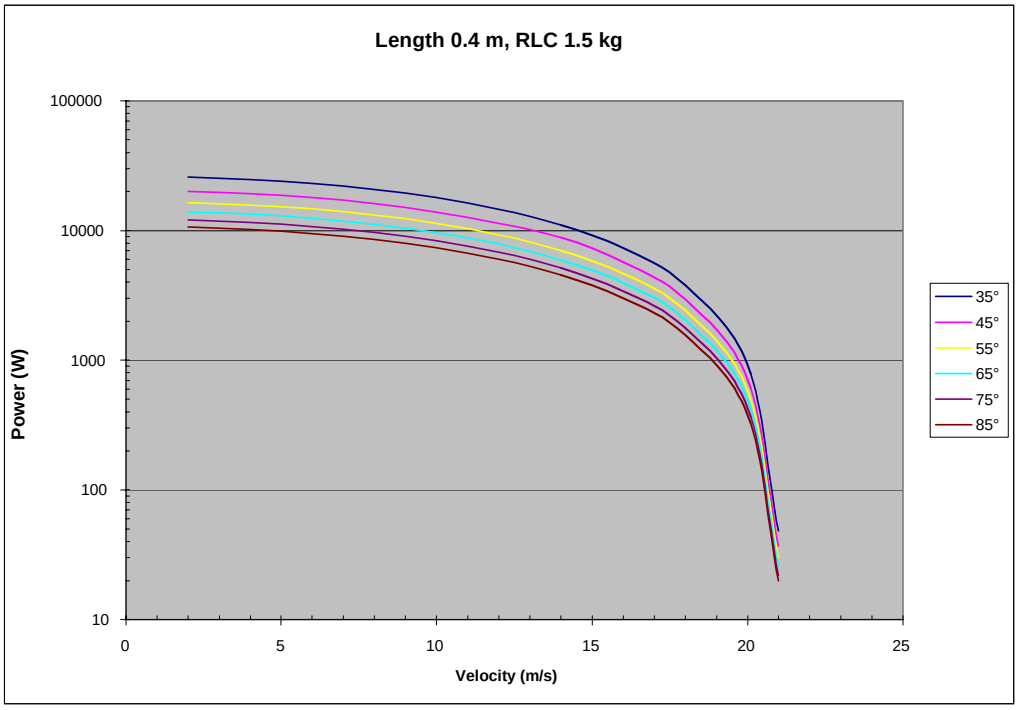

Figure B-16: Flight Power vs. Velocity for a Wing Length of 0.4 m and Relative Lift Capacity of 1.5 kg

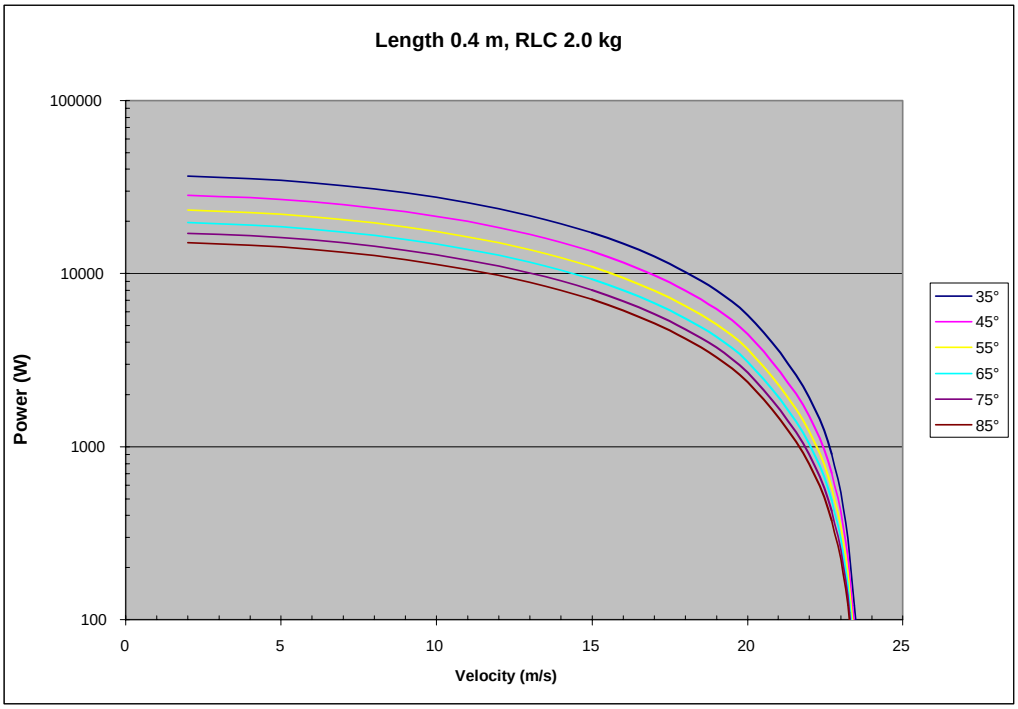

Figure B-17: Flight Power vs. Velocity for a Wing Length of 0.4 m and Relative Lift Capacity of 2.0 kg

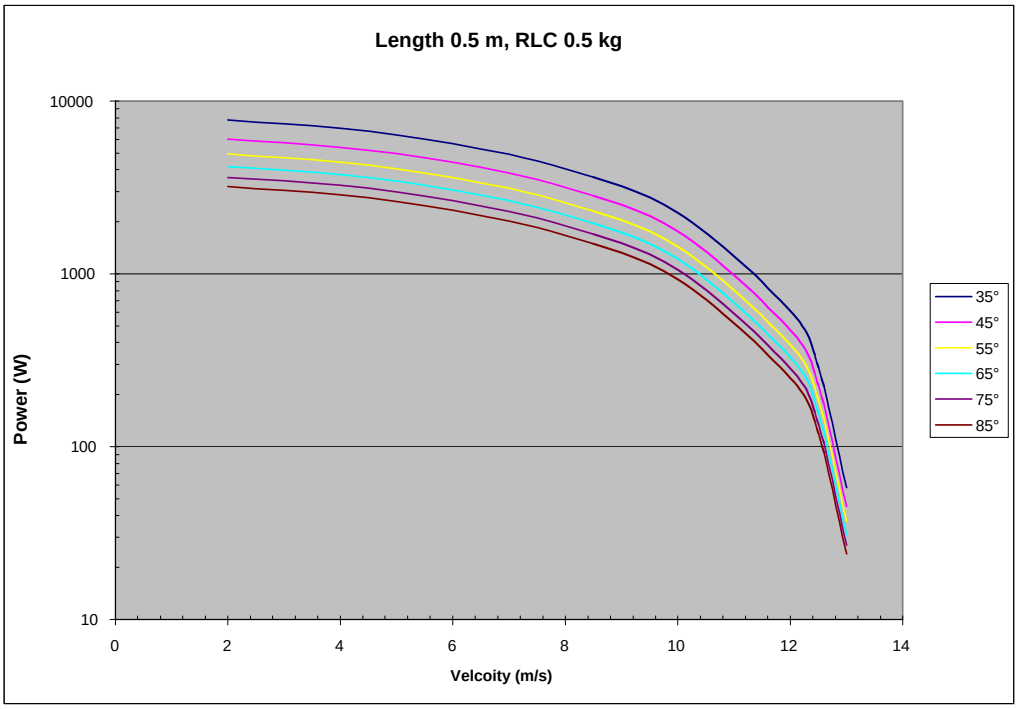

Figure B-18: Flight Power vs. Velocity for a Wing Length of 0.5 m and Relative Lift Capacity of 0.5 kg

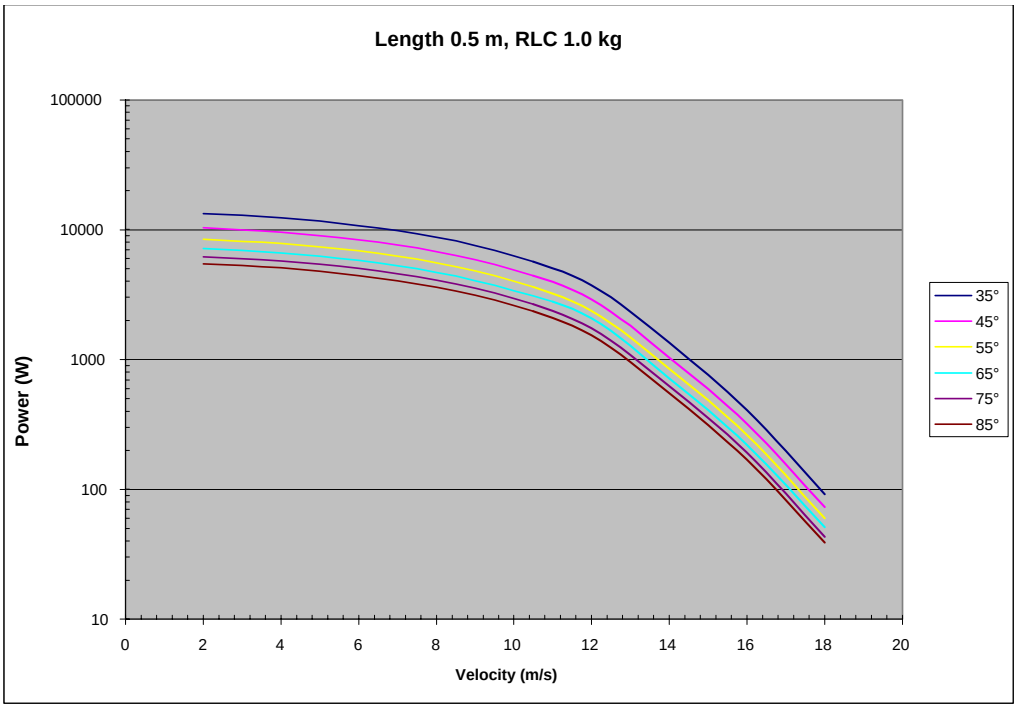

Figure B-19: Flight Power vs. Velocity for a Wing Length of 0.5 m and Relative Lift Capacity of 1.0 kg

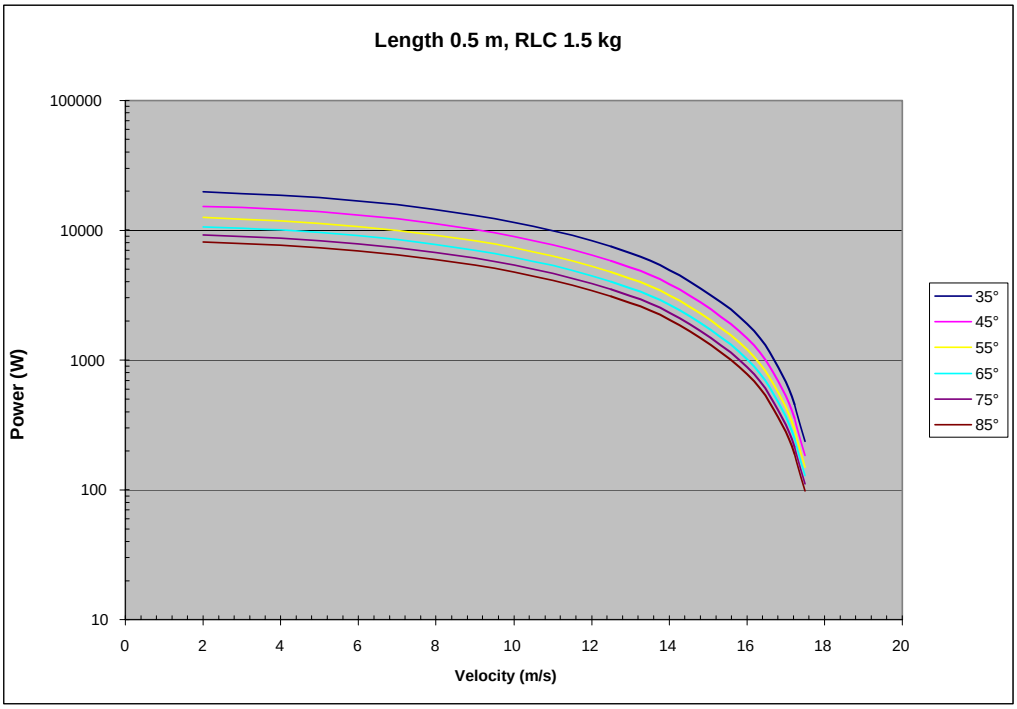

Figure B-20: Flight Power vs. Velocity for a Wing Length of 0.5 m and Relative Lift Capacity of 1.5 kg

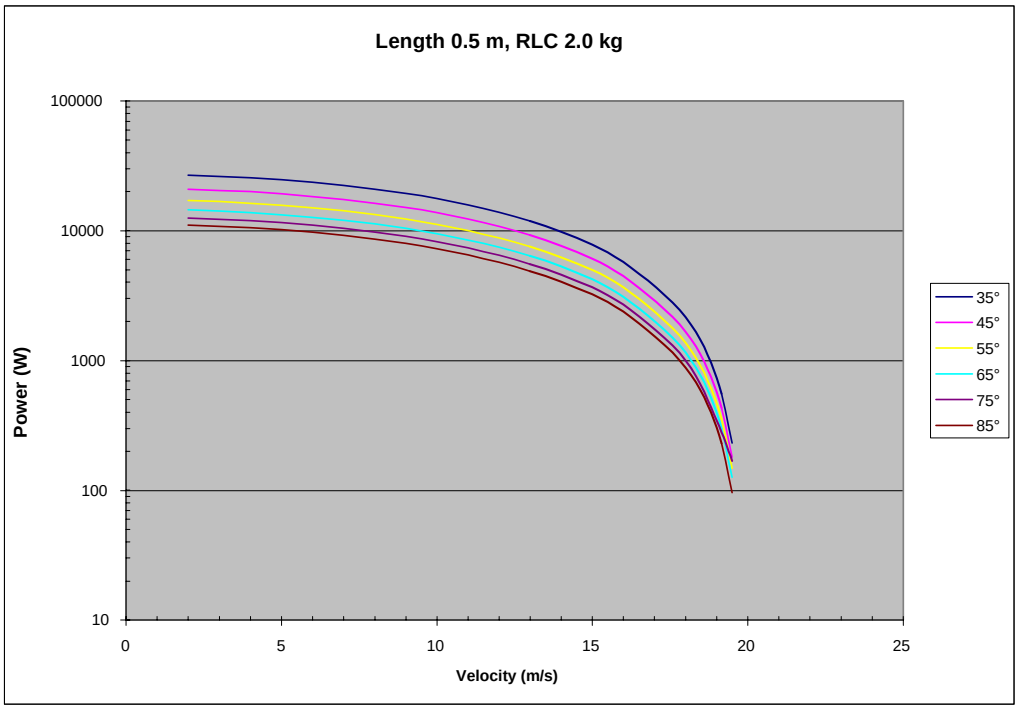

Figure B-21: Flight Power vs. Velocity for a Wing Length of 0.5 m and Relative Lift Capacity of 2.0 kg

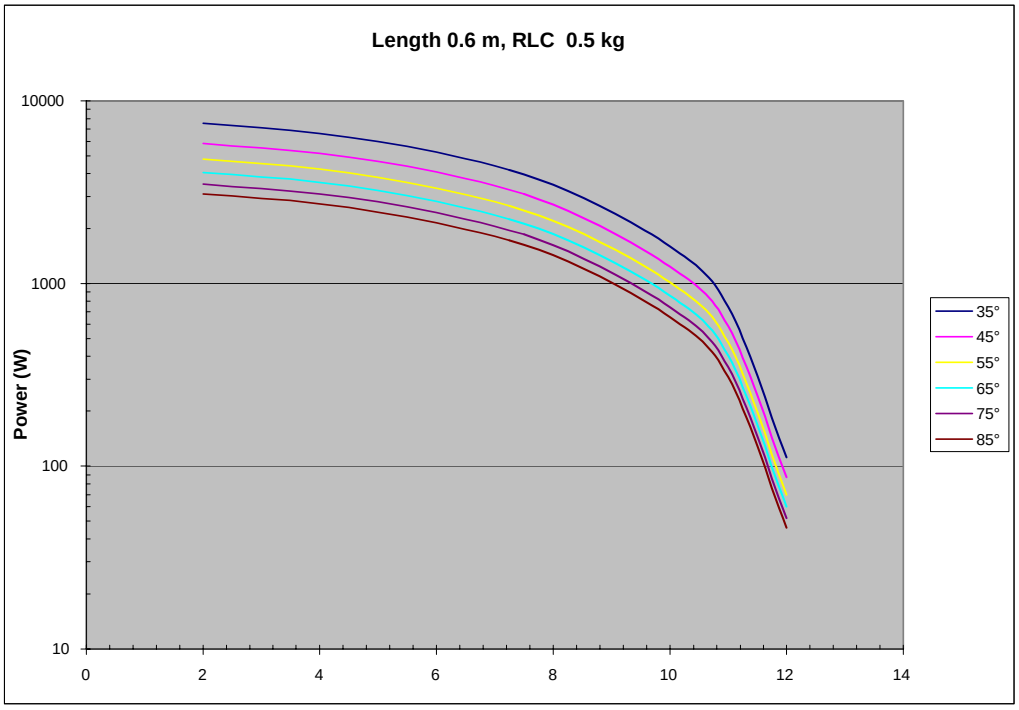

Figure B-22: Flight Power vs. Velocity for a Wing Length of 0.6 m and Relative Lift Capacity of 0.5 kg

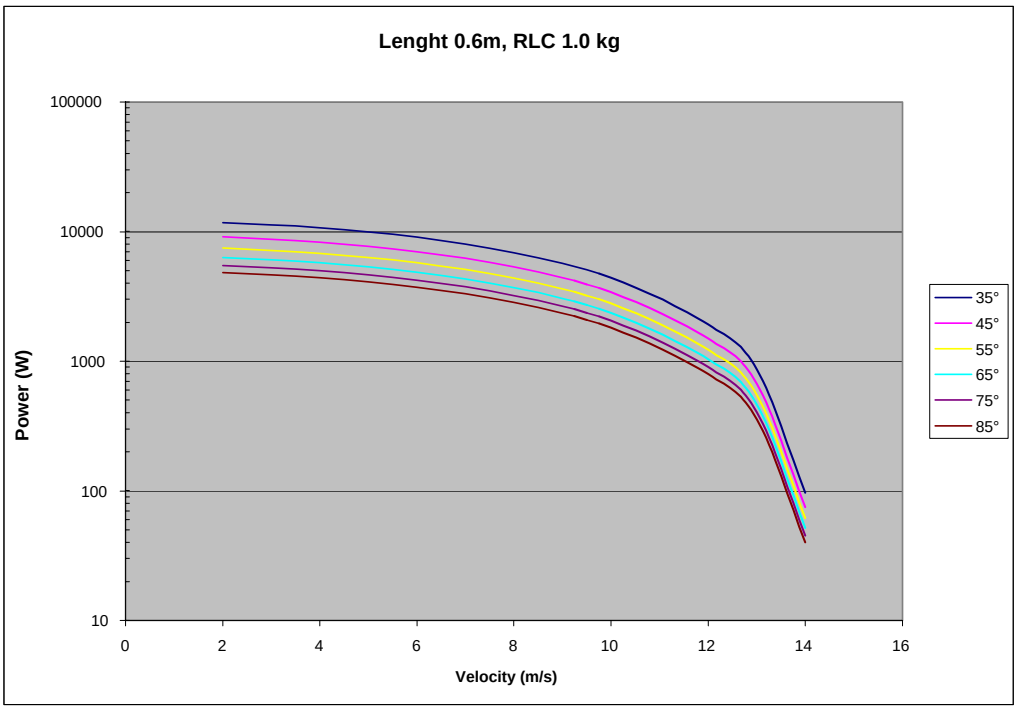

Figure B-23: Flight Power vs. Velocity for a Wing Length of 0.6 m and Relative Lift Capacity of 1.0 kg

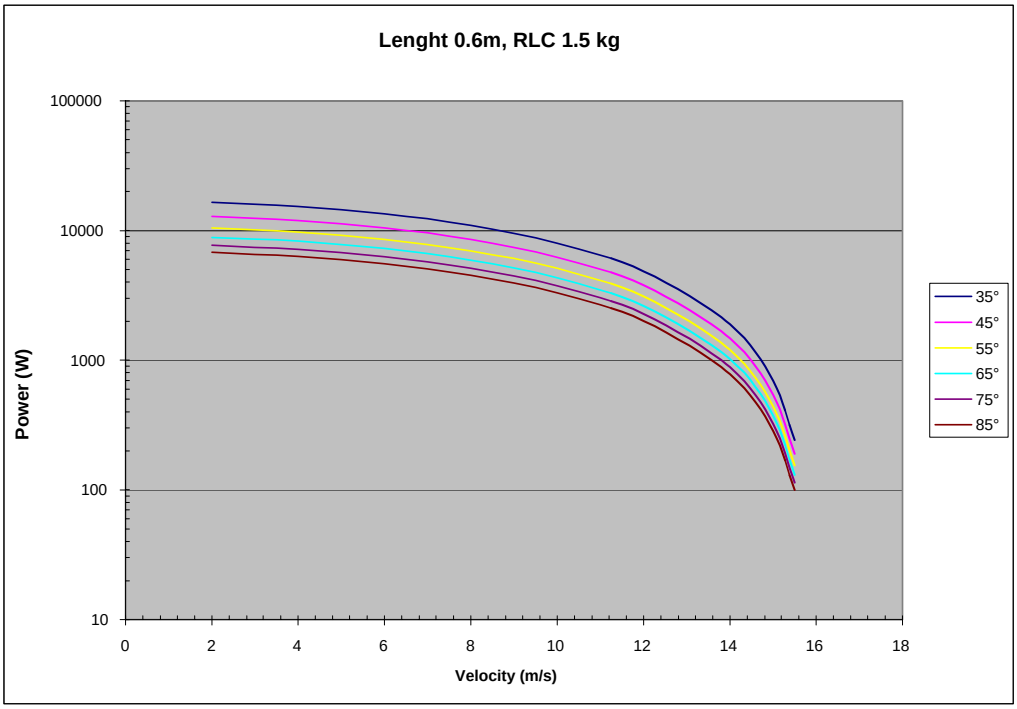

Figure B-24: Flight Power vs. Velocity for a Wing Length of 0.6 m and Relative Lift Capacity of 1.5 kg

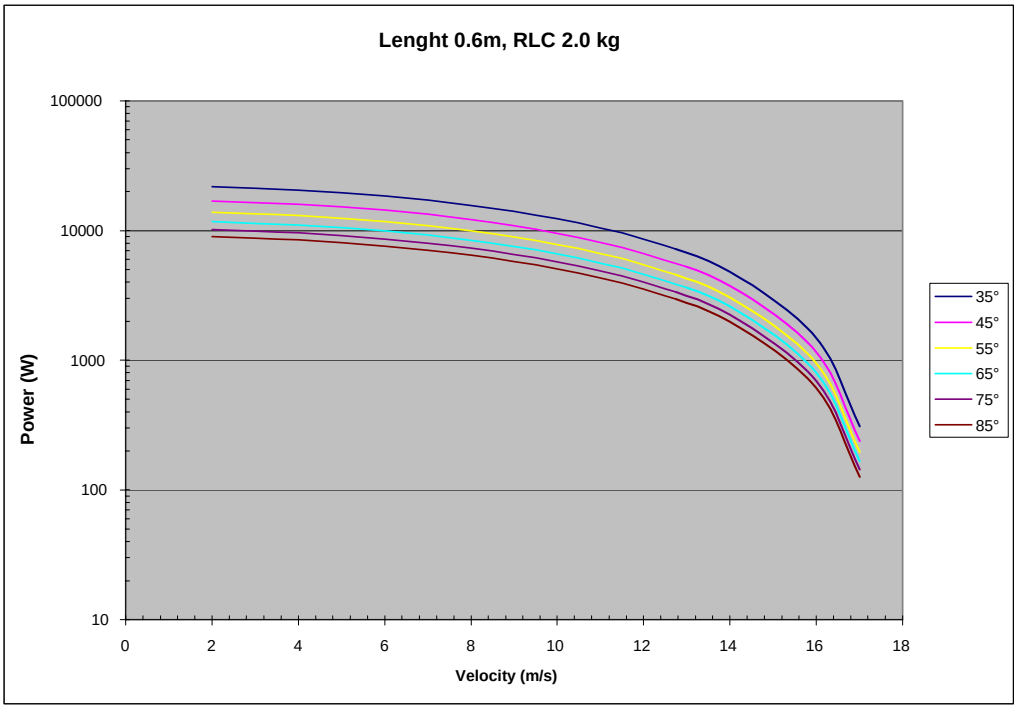

Figure B-25: Flight Power vs. Velocity for a Wing Length of 0.6 m and Relative Lift Capacity of 2.0 kg

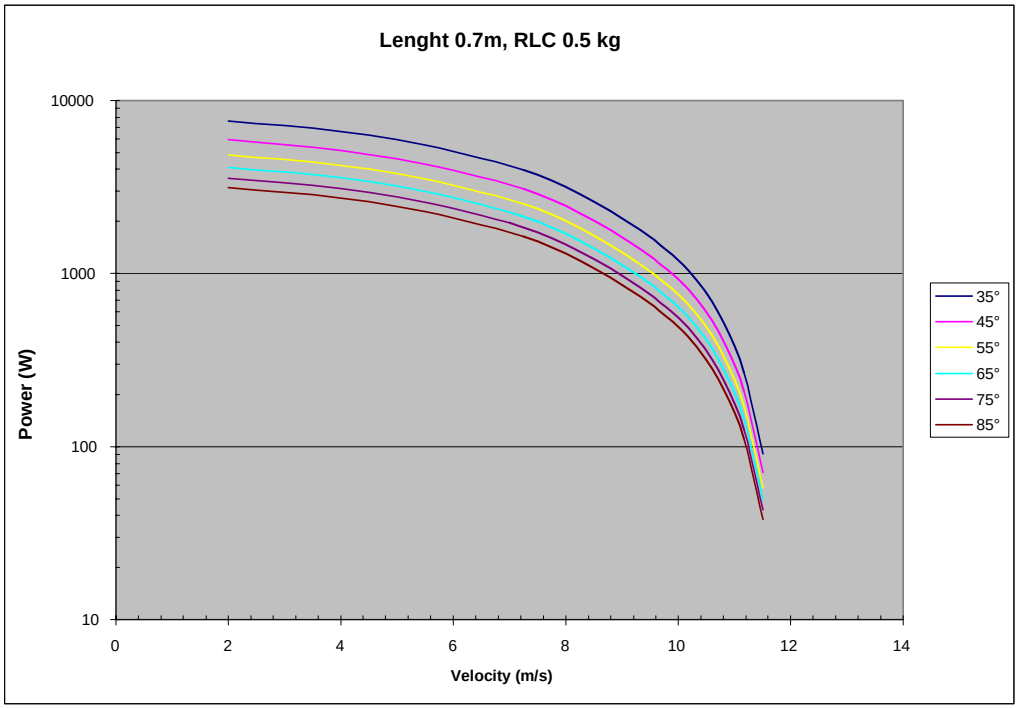

Figure B-26: Flight Power vs. Velocity for a Wing Length of 0.7 m and Relative Lift Capacity of 0.5 kg

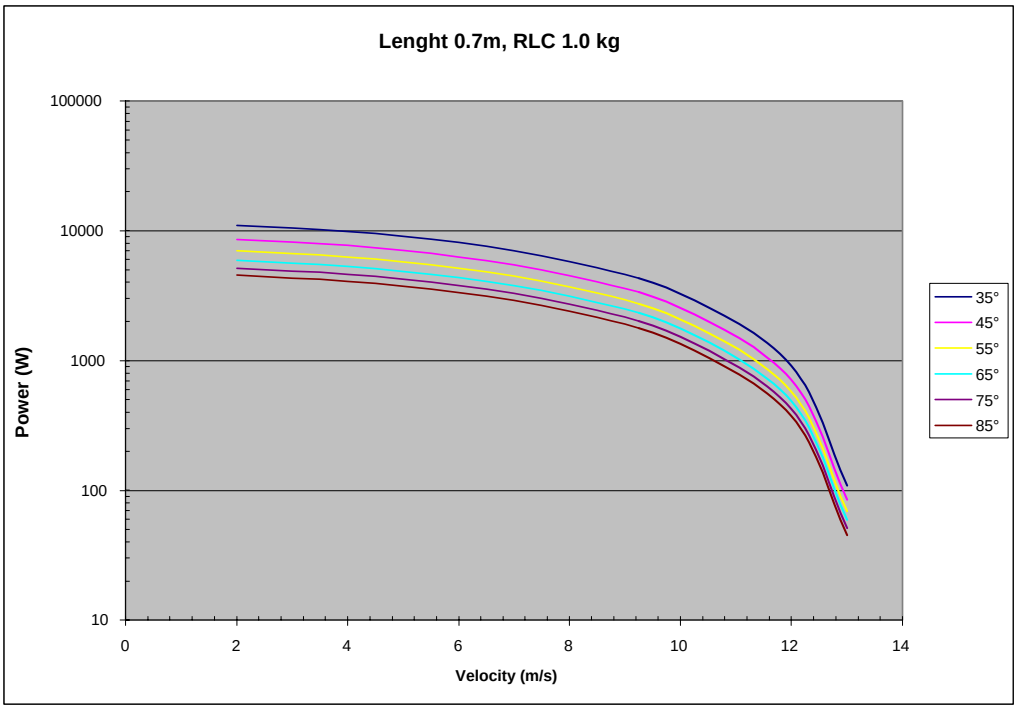

Figure B-27: Flight Power vs. Velocity for a Wing Length of 0.7 m and Relative Lift Capacity of 1.0 kg

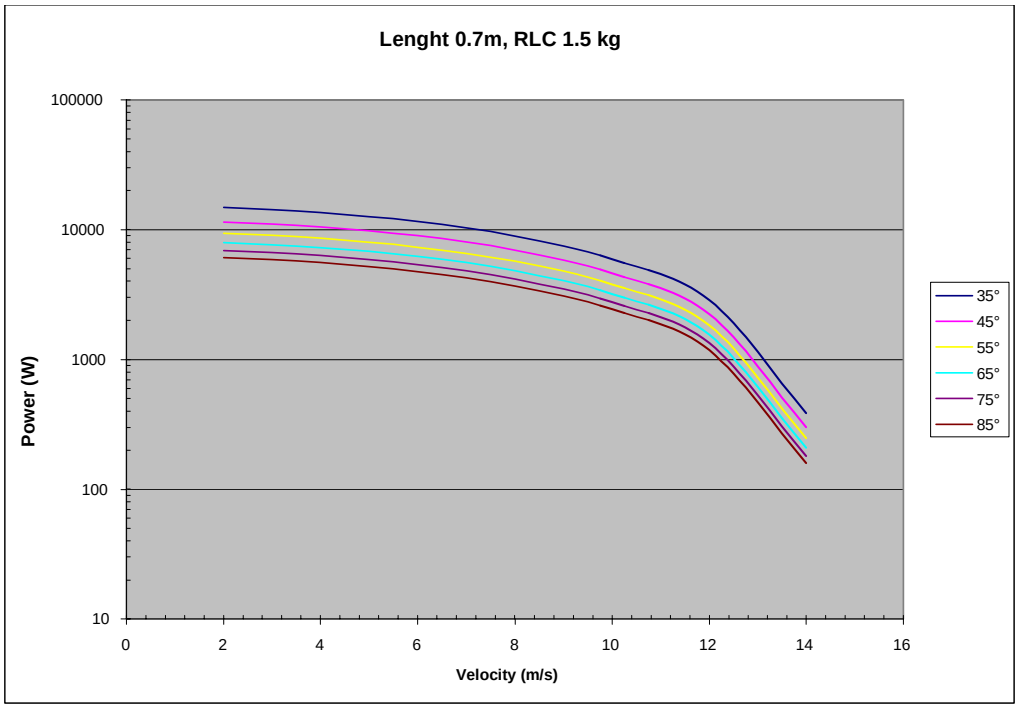

Figure B-28: Flight Power vs. Velocity for a Wing Length of 0.7 m and Relative Lift Capacity of 1.5 kg

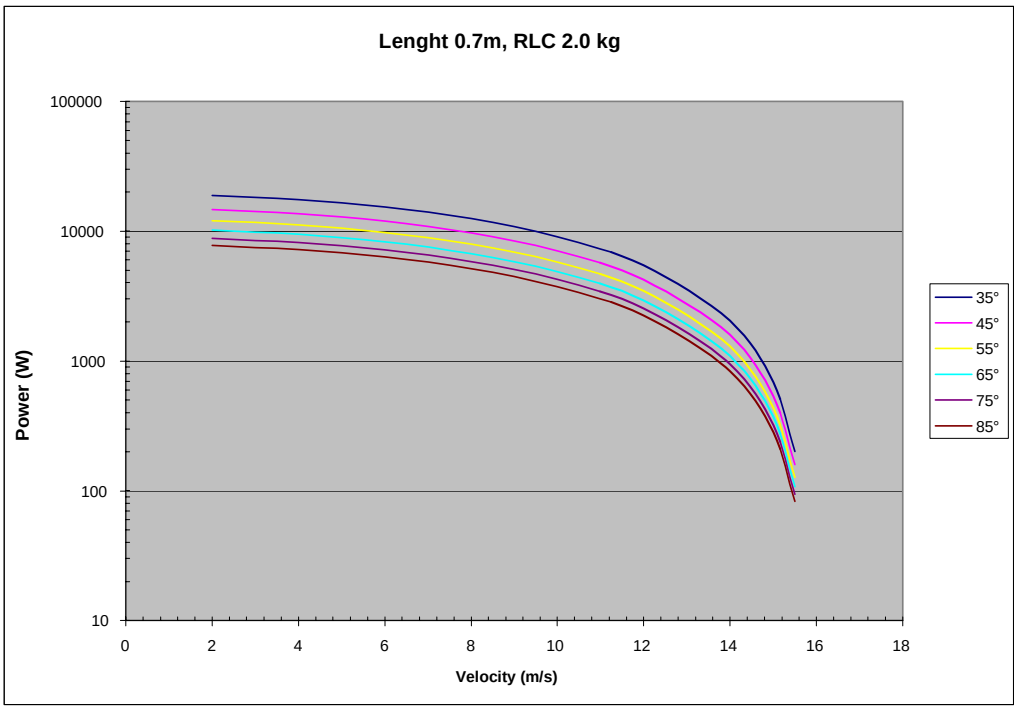

Figure B-29: Flight Power vs. Velocity for a Wing Length of 0.7 m and Relative Lift Capacity of 2.0 kg

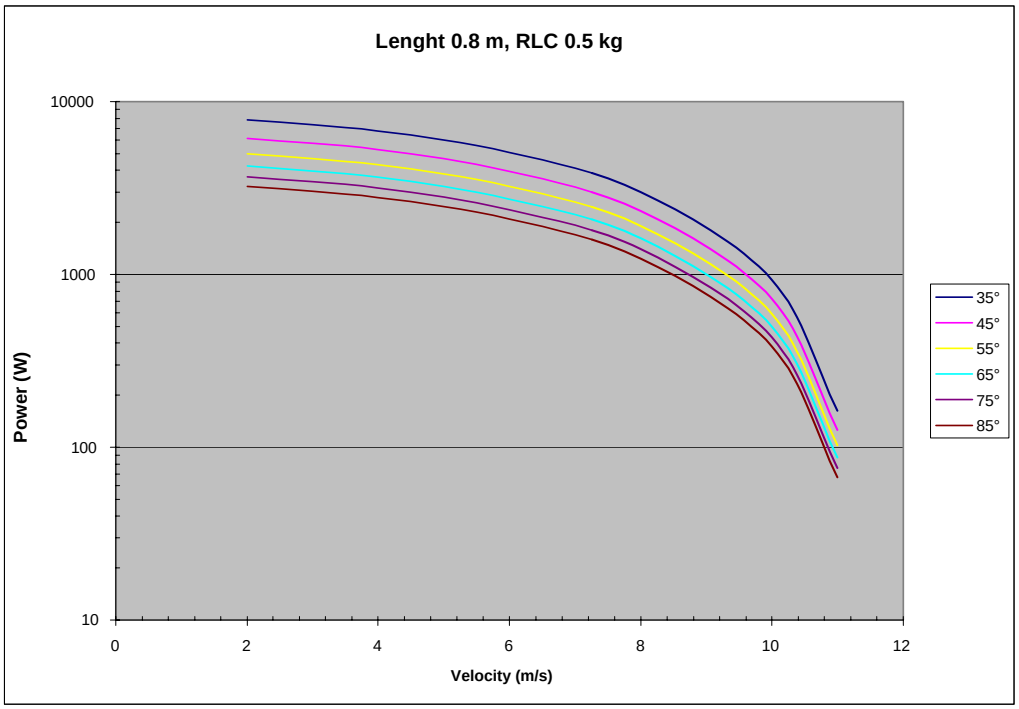

Figure B-30: Flight Power vs. Velocity for a Wing Length of 0.8 m and Relative Lift Capacity of 0.5 kg

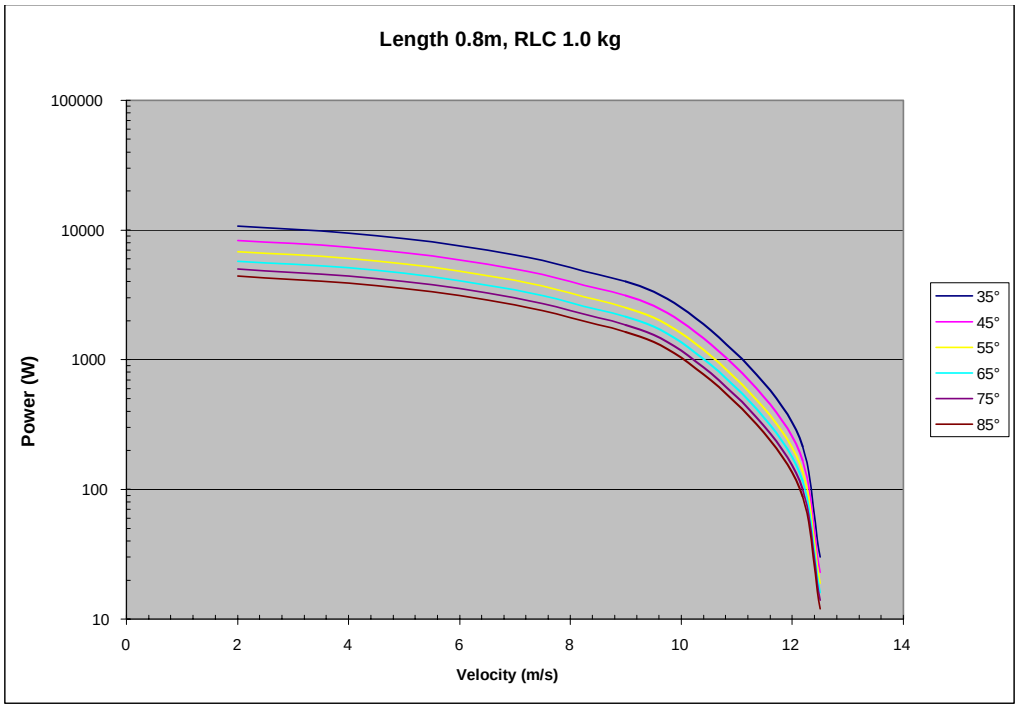

Figure B-31: Flight Power vs. Velocity for a Wing Length of 0.8 m and Relative Lift Capacity of 1.0 kg

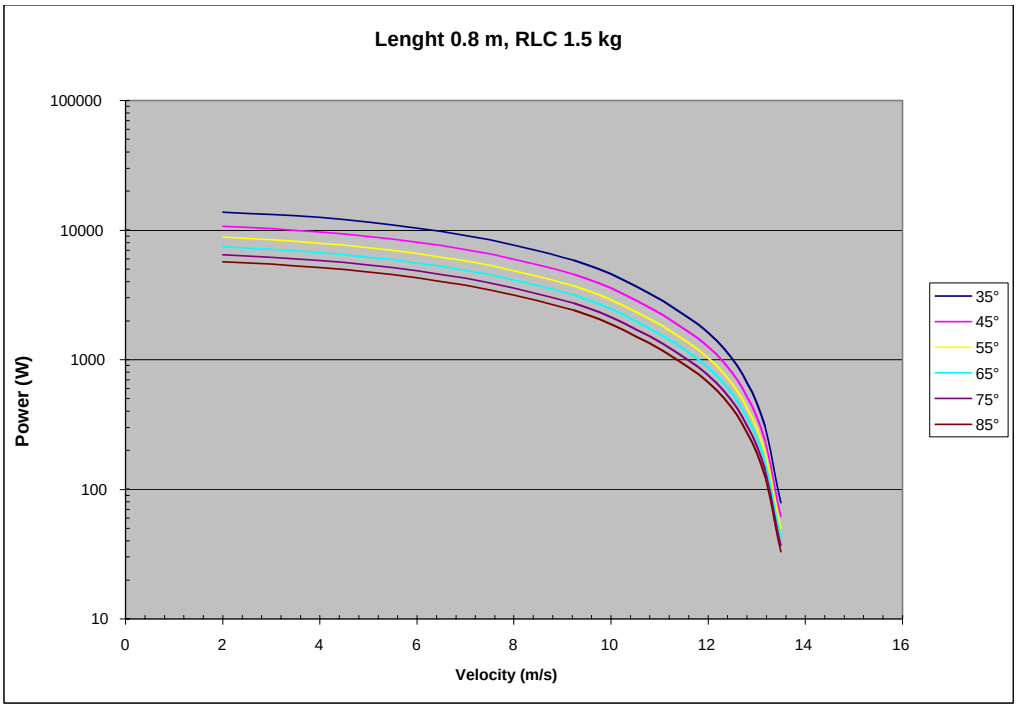

Figure B-32: Flight Power vs. Velocity for a Wing Length of 0.8 m and Relative Lift Capacity of 1.5 kg

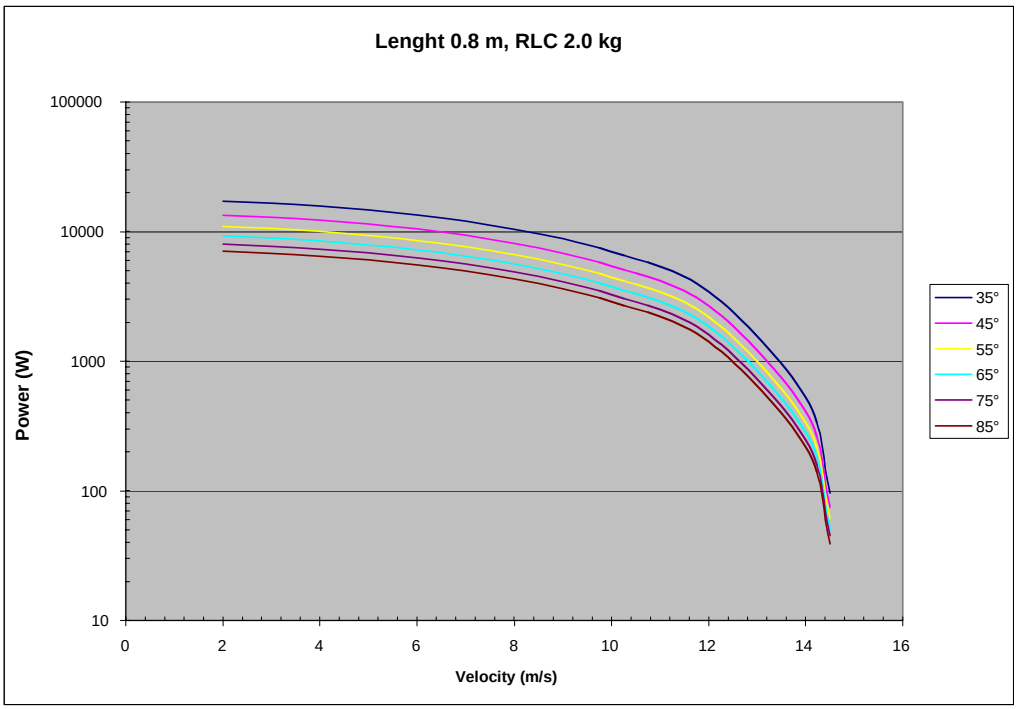

Figure B-33: Flight Power vs. Velocity for a Wing Length of 0.8 m and Relative Lift Capacity of 2.0 kg

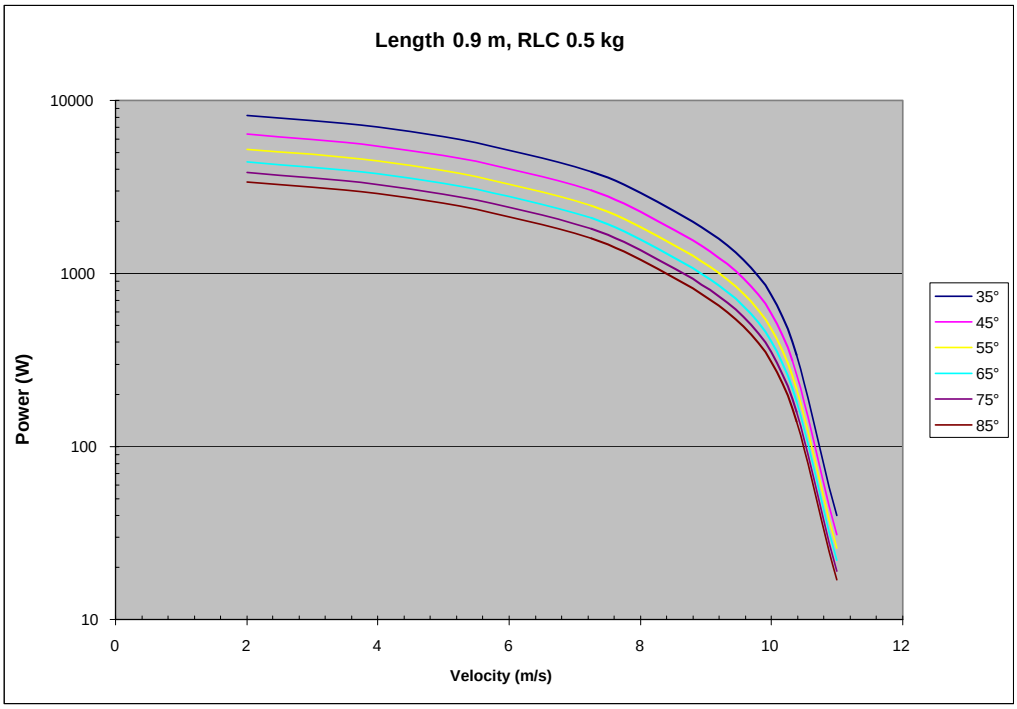

Figure B-34: Flight Power vs. Velocity for a Wing Length of 0.9 m and Relative Lift Capacity of 0.5 kg

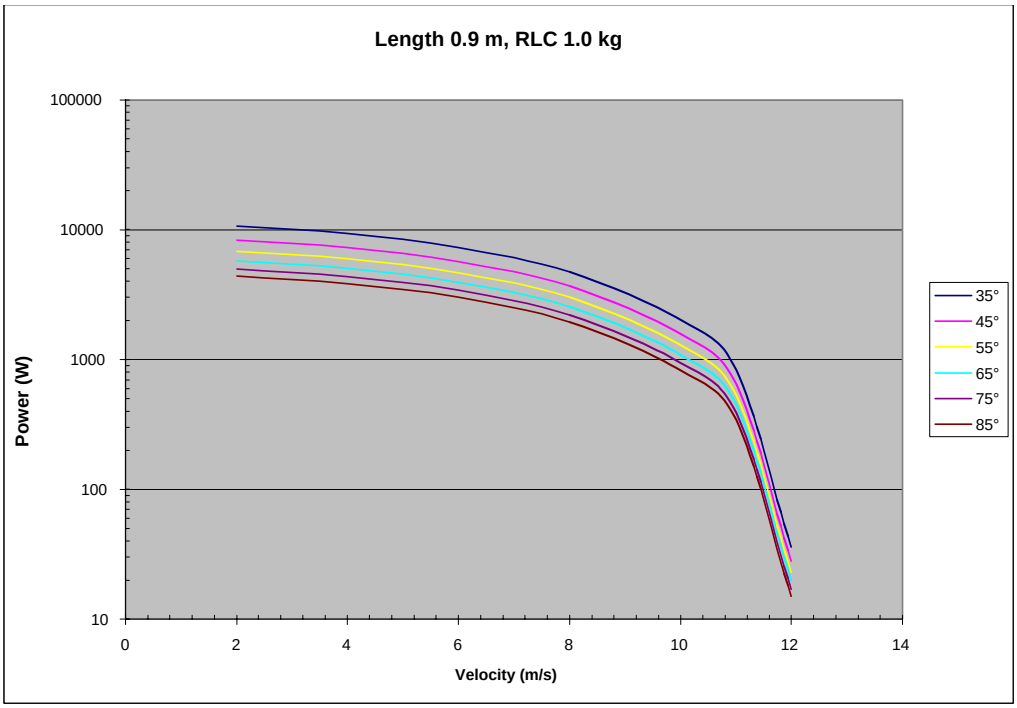

Figure B-35: Flight Power vs. Velocity for a Wing Length of 0.9 m and Relative Lift Capacity of 1.0 kg

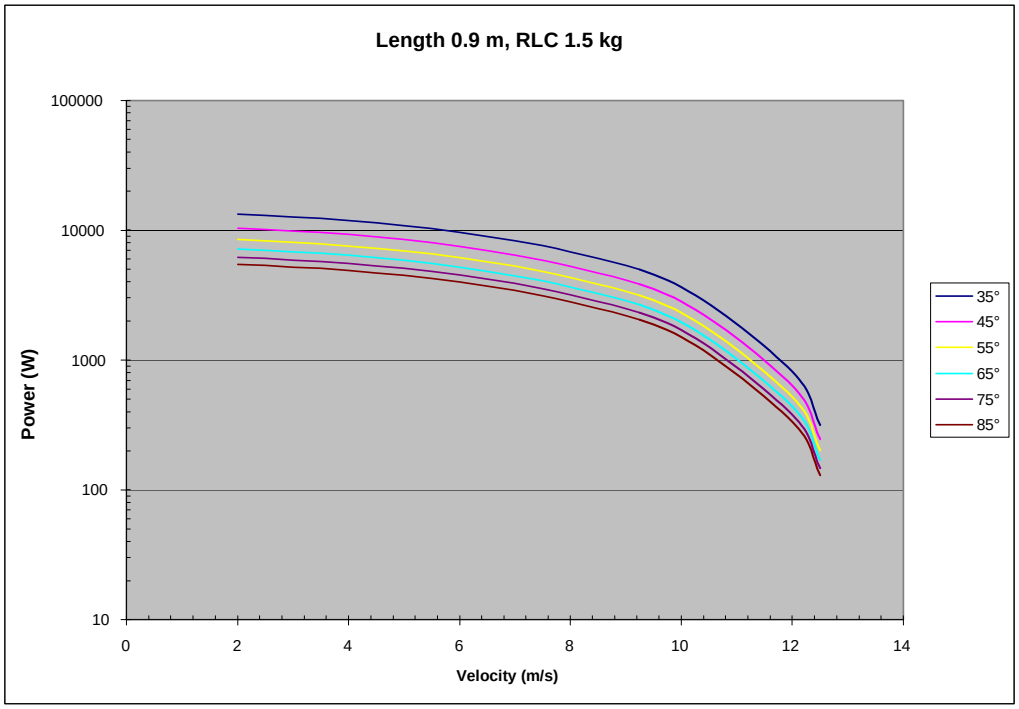

Figure B-36: Flight Power vs. Velocity for a Wing Length of 0.9 m and Relative Lift Capacity of 1.5 kg

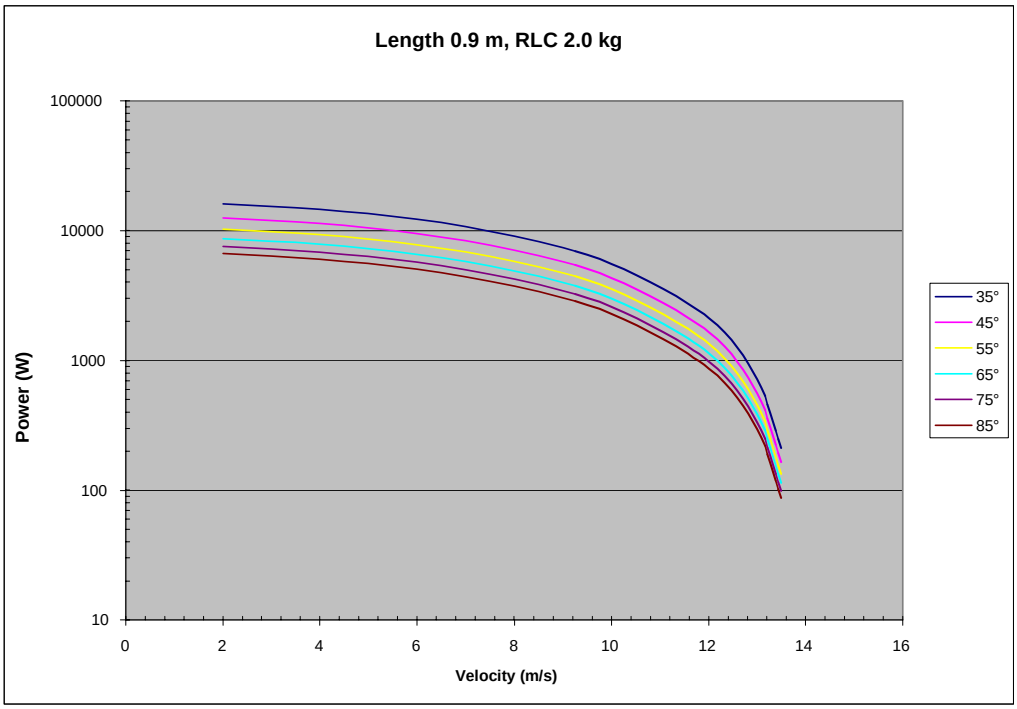

Figure B-37: Flight Power vs. Velocity for a Wing Length of 0.9 m and Relative Lift Capacity of 2.0 kg

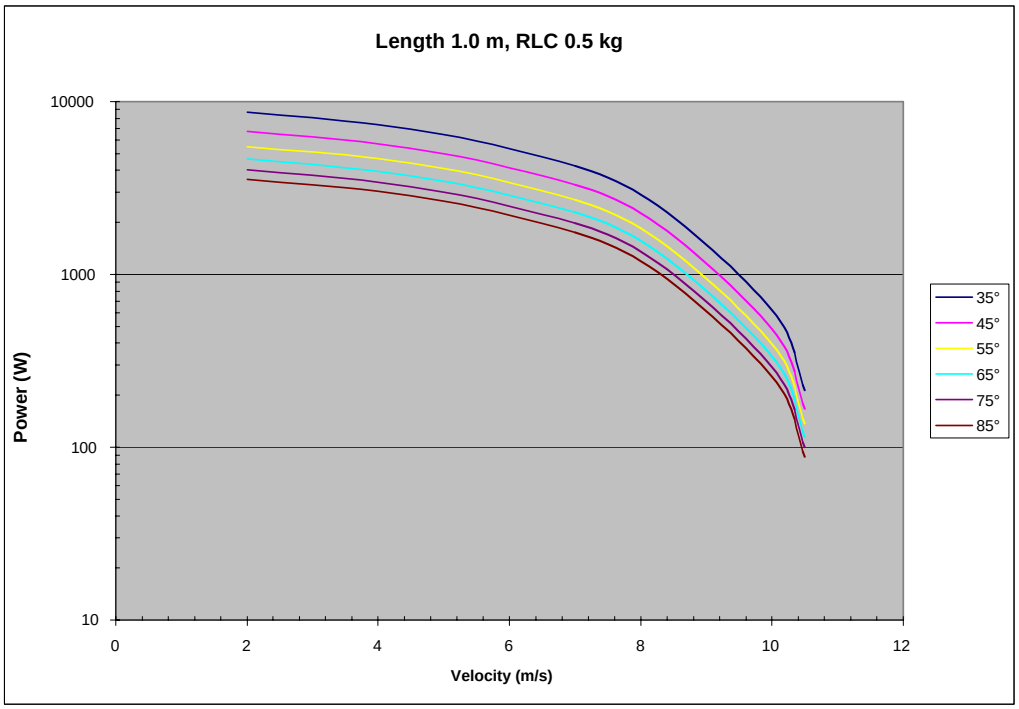

Figure B-38: Flight Power vs. Velocity for a Wing Length of 1.0 m and Relative Lift Capacity of 0.5 kg

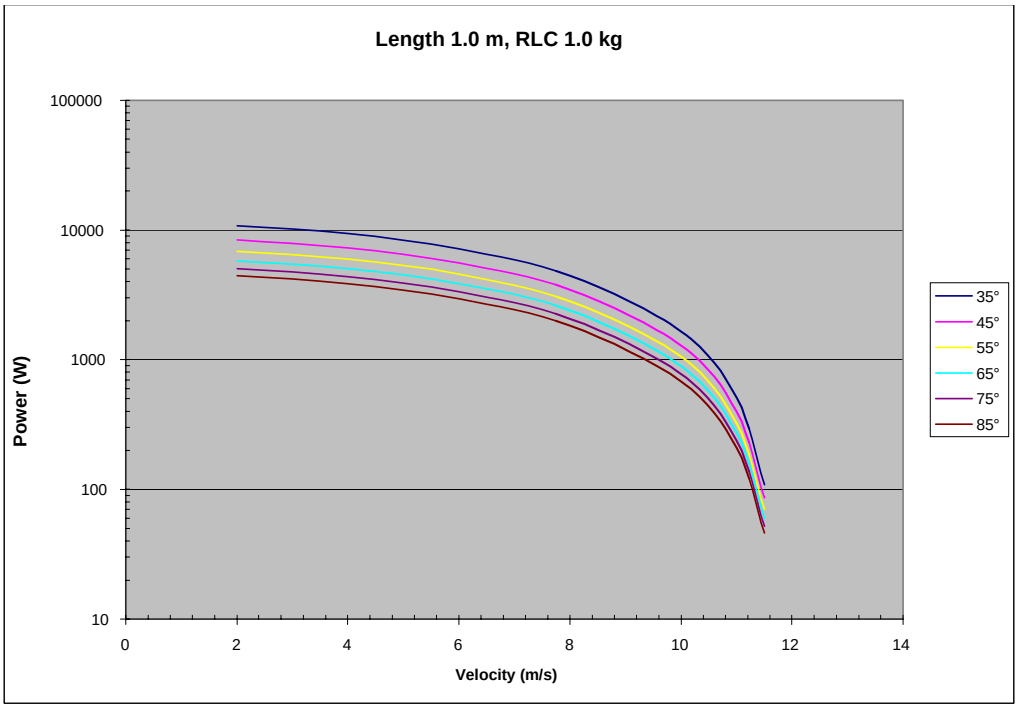

Figure B-39: Flight Power vs. Velocity for a Wing Length of 1.0 m and Relative Lift Capacity of 1.0 kg

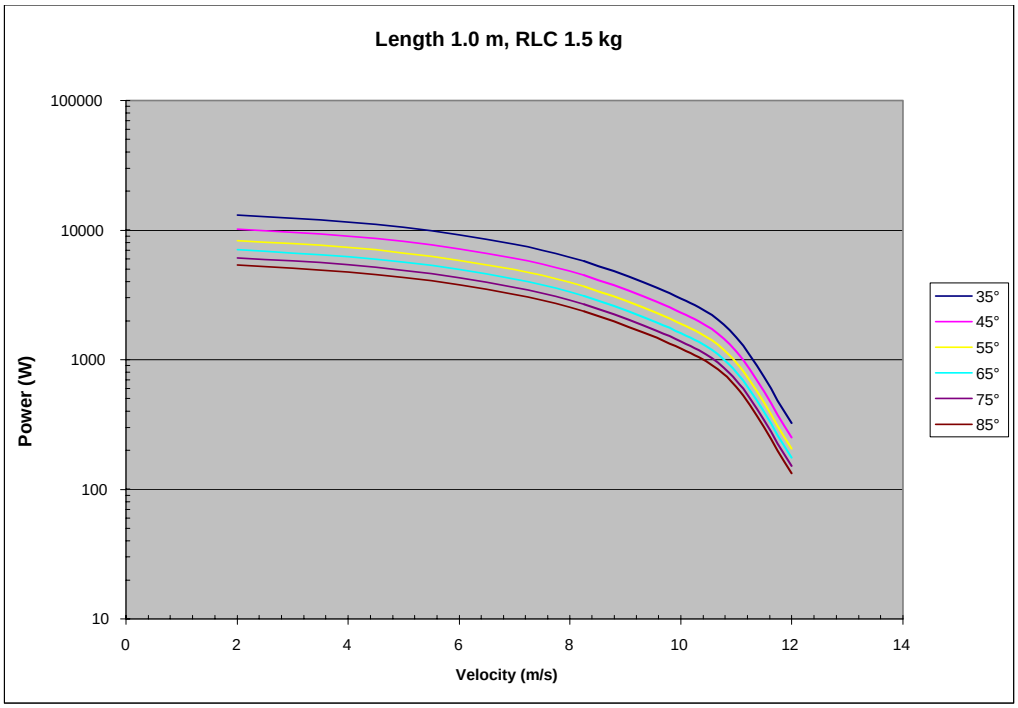

Figure B-40: Flight Power vs. Velocity for a Wing Length of 1.0 m and Relative Lift Capacity of 1.5 kg

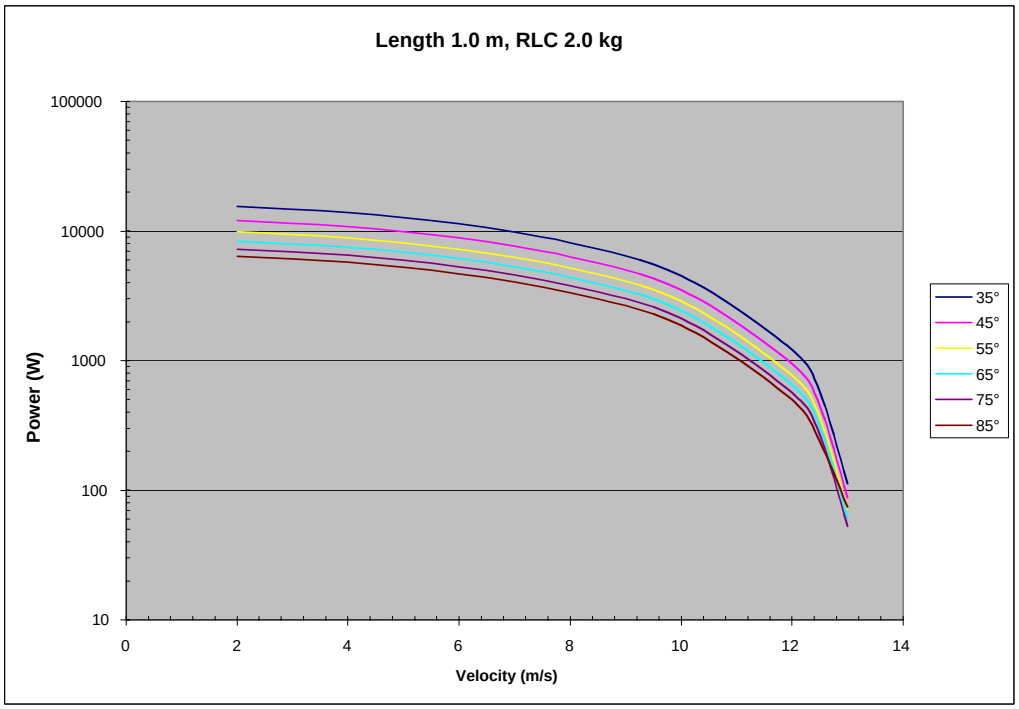

Figure B-41: Flight Power vs. Velocity for a Wing Length of 1.0 m and Relative Lift Capacity of 2.0 kg

Appendix C: List of References

1. Abbott, I. H., von Doenhoff, A. E., and Stivers, L. S. Jr., “Summary of Airfoil Data,” NACA Rept. 824, 1945.
2. Aerospace Operations in Urban Environments, Ch. 6, Enabling Technologies for Urban Aerospace Operations.
3. Ahmadi, A. R., and Widnall, S. E., “Unsteady Lifting-Line Theory as a Singular Perturbation Problem, Journal of Fluid Mechanics,” Vol. 153, April 1985, pp. 59-81.
4. Akyurtlu, A. and Akyurtlu, J.F., “Evaluation of On-Board Hydrogen Storage Methods for High-Speed Aircraft,” NASA-CR-187755, January 1991.
5. Albano, E., and Rodden, W., “A Doublet-Lattice Method for Calculating Lift Distributions on Oscillating Surfaces in Subsonic Flows,” AIAA Journal, Vol. 7, No. 2, 1969, pp. 279-285.
6. Allen, D.H., Haisler, W.E., Introduction to Aerospace Structural Analysis, John Wiley & Sons Publisher 1985.
7. Ames, R., Wong, O. and Komerath, N., “On the Flow Field and Forces Generated by a Flapping Rectangular Wing at Low Reynolds Number,” Fixed and Flapping Wing Aerodynamics for Micro Air Vehicle Applications, T. J. Mueller (Ed.), Prog. in Astronautics and Aeronautics, Vol., 195, 2001.
8. Anderson, J. D. J., Fundamentals of Aerodynamics, McGraw-Hill, New York, 1991.
9. Angelo, J.A. and Buden D., “Space Nuclear Power”, Orbit Book Company, 1985.
10. Ashley, H., and Landahl, M., Aerodynamics of Wings and Bodies, Addison-Wesley, Reading, MA, 1965, pp. 21-50.
11. Augenstein, B.W. (1989), The Mars Airplane Revived-Global Mars Surface Surveys, in: The Case for Mars III: Strategies for Exploration-Technical, pp. 547-556.
12. Azuma, A., Okamoto, M. and Yasuda, K., “Aerodynamic Characteristics of Wings at Low Reynolds Number,” Fixed and Flapping Wing Aerodynamics for Micro Air Vehicle Applications, T. J. Mueller (Ed.), Prog. in Astronautics and Aeronautics, Vol., 195, 2001.
13. Azuma, A., Springer-Verlag, The Biokinetics of Flying and Swimming, Tokyo, 1992, pp. 77 - 154.
14. Balow, F. A., “Effect of an Unsteady Laminar Separation Bubble on the Flow Field over an Airfoil near Stall,” M.S. Thesis, Dept. of Aeronautical and Astronautical Engineering, Univ. of Illinois. Urbana, IL, 1994.
15. Bartlett, G. E., and Vidal, R. J., “Experimental Investigation of Influence of Edge Shape on the Aerodynamic Characteristics of Low Aspect Ratio Wings At Low Speeds,” Journal of the Aeronautical Sciences, Vol. 22, No. 8, 1955, pp. 517-533.
16. Baxter, D. R. J., and East, R. A., “A Survey of Some Fundamental Issues in Micro Air Vehicle Design,” Proceedings of the CAVs Fourteenth International Conference, Univ. of Bristol, U.K., 1999, pp. 34.1-34.13.
17. Beer, F.P. and Johnstor, E.R. Jr, Mechanics of Materials, McGraw Hill Publisher, 1981.
18. Beer, F.P. and Johnstor, E.R. Jr, Vector Mechanics for Engineers, McGraw Hill Publisher, 1984.
19. Bents, D. J., Kohout, L. L., McKissock, B. I., Rodriguez, C. D., Withrow, C. A., Colozza, A. J., Hanlon, J. C. and Schmitz, P. C., “SEI Power Source Alternatives for Rovers and Other Multi-kWe Distributed Surface Applications”, NASA TM- 104359, September 1991.

20. Bisplinghoff, R. L., Ashley, H., and Halfman, R. L., Aeroelasticity, Addison-Wesley, Cambridge, MA, 1955.
21. Bliss, D. B., and Epstein, R. J., "A Novel Approach to Aerodynamic Analysis Using Analytical/Numerical Matching," AIAA Paper 95-1840-CP, 1995.
22. Bolz, R. E., Tuve, G. L. editors , Handbook of Tables for Applied Engineering Science, CRC Press 1973.
23. Bosch, H., "Interfering Airfoils in Two-dimensional Unsteady Incompressible Flow," AGARD CP-227, Paper 7, Sep,. 1977.
24. Bragg, M. B., Heinrich, D. C., and Khodadoust, A., "Low-Frequency Flow Oscillation over Airfoils near Stall," AIAA Journal, Vol. 31, No. 7, July 1993. pp. 1341-1343.
25. Bragg, M. B., Heinrich, D. C., Balow, F. A., and Zaman, K. B. M. Q., "Flow Oscillation over an Airfoil near Stall," AIAA Journal, Vol. 34, No. 1, Jan. 1996, pp. 199-201.
26. Bratt, J. B., "Flow Patterns in the Wake of an Oscillating Airfoil," Aeronautical Research Council. R&M 2773, 1953.
27. Brawn, Robert, NASA Langley Research Center for the Mars Aircraft Micromission program, March 1999.
28. Brewer, D. G., Hydrogen Aircraft technology, CRC Press, 1991.
29. Brodsky, A., The Evolution of Insect Flight, Oxford; New York: Oxford University Press, 1994, pp 35-39.
30. Brodsky, A. K., "Vortex Formulation in the Tethered Flight of the Peacock Butterfly Inachis io L. (Lepidoptera, Nymphalidae) and Some Aspects of Insect Flight Evolution," Journal of Experimental Biology, Vol. 166, 1991, pp. 77-95.
31. Broeren, A. P., "An Experimental Study of Unsteady Flow over Airfoils near Stall," Ph.D. Dissertation, Dept. of Mechanical and Industrial Engineering, Univ. of Illinois, Urbana, IL, 2000.
32. Broeren, A. P., and Bragg, M. B., "Flow Field Measurements over an Airfoil During Natural Low-Frequency Oscillations near Stall," AIAA Journal, Vol. 37, No. 1, Jan. 1999, pp.130-132.
33. Broeren, A. P., and Bragg, M. B., "Low-Frequency Flow Field Unsteadiness during Airfoil Stall and the Influence of Stall Type," AIAA Paper 98-2517-CP, 1998.
34. Broeren A. P. and Bragg, M. B., "Unsteady Stalling Characteristics of Thin Airfoils at Low Reynolds Number," Fixed and Flapping Wing Aerodynamics for Micro Air Vehicle Applications, T. J. Mueller (Ed.), Prog. in Astronautics and Aeronautics, Vol., 195, 2001.
35. Cannor, R.H. Jr, Dynamics of Physical Systems, McGraw Hill Publisher, 1967.
36. Chasman, D. and Chakravarthy, S., "Computational and Experimental Studies of Asymmetric Pitch/Plunge Flapping-the Secret of Biological Flyers," AIAA 39th Aerospace Sciences Meeting, AIAA paper A01-16674.
37. Chen, J. Y., Zhuang, L. X., and Tong, B. G., "Analysis of Swimming Three-Dimensional Waving Plates," Journal of Fluid Mechanics, Vol. 232, 1991, pp. 341-355.
38. Chopra, M. G., "Hydromechanics of Lunate-Tail Swimming Propulsion," Journal of Fluid Mechanics, Vol. 64, 1974, pp. 375-391.
39. Chopra, M. G., "Large Amplitude Lunate Tail Theory of Fish Locomotion," Journal of Fluid Mechanics, Vol. 74, 1976, pp. 161-182.
40. Chopra, M. G., and Kambe, T., "Hydromechanics of Lunate-Tail Swimming Propulsion: Part 2," Journal of Fluid Mechanics, Vol. 79, 1977, pp. 49-69.

41. Clarke, V.C. (1978), Final Report of the Ad Hoc Mars Airplane Science Working Group, NASA CR 158000.
42. Clausen, P. D., Piddington, D. M., and Wood, D. H., “An Experimental Investigation of Blade Element Theory for Wind Turbines, Part 1. Mean Flow Results,” Journal of Wind Engineering and Industrial Aerodynamics, Vol. 25, 1987, pp. 189-206.
43. Coleman, H. W., and Steele, W. G., Experimentation and Uncertainty Analysis for Engineers, Wiley, New York, 1989, pp. 40-118.
44. Colozza, A., Michelson, R.C., et al., “Planetary Exploration Using Biomimetics”, NASA Institute for Advanced Concepts Phase I Final Report, November 30, 2000
45. Colozza, A.J., Miller C., Reed, B., Kohout, L., Loyselle, P.,” Overview of Propulsion Systems for a Mars Aircraft,” NASA report Feburary, 2000.
46. Corrigan, J. J., and Schlichting, H., “Empirical Model for Stall Delay due to Rotation,” Proceedings of the American Helicopter Society Aeromechanics Specialists Conference, San Francisco, CA, 19-21 Jan. 1994.
47. Cruz, J,” Mars Dust Storms”, Mars Airplane Package Document 0807-03-01A. October, 1999.
48. Cruz, J. and Taylor, G., “Mars Airplane Package, Preliminary Baseline Mission Sites”, Document 0867-02-01A, October, 1999.
49. Cutts, J.A., Bauer, J., Blaney, D.L., Lemke, L.G., Smith, S. Jr, Stetson, D.S. and Kerzhanovich, V.V., “Role of Mars Aerial Platforms in Future Exploration of Mars,” Mars Architecture Study, August 1998.
50. Davis, W. R., Jr., Kosicki, B. B., Boroson, D. M., and Kostishack, D. F., “Micro Air Vehicles for Optical Surveillance,” Lincoln Laboratory Journal, Vol. 9, No. 2, 1996, pp. 197-213.
51. de Jong, K., “On the Optimization, Including Viscosity Effects, of Ship Screw Propellers with Optional End Plates (Part I),” International Shipbuilding Progress, Vol. 38, No. 414, 1991, pp. 115-156.
52. de Jong, K., “On the Optimization, Including Viscosity Effects, of Ship Screw Propellers with Optional End Plates (Part II),” International Shipbuilding Progress, Vol. 38, No. 415, 1991, pp. 211-252.
53. De Vries, O., “On the Theory of the Horizontal-Axis Wind Turbine.” Annual Review of Fluid Mechanics, Vol. 15, 1983, pp. 77-96.
54. DeLaurier, J. D., and Harris, J. M., “Experimental Study of Oscillating-Wing Propulsion,” Journal of Aircraft, Vol. 19, No. 5, May, 1982, pp. 368-373.
55. DeLaurier, J. D., “An Aerodynamic Model for Flapping Wing Flight,” Aeronautical Journal, Vol. 97, 1993, pp. 125-130.
56. Dickenson, M. H., Lehmann, F., and Sane, S. P., “Wing Rotation and the Aerodynamic Basis of Insect Flight,” Science, Vol. 284, June 1999, pp. 1954-1960.
57. Dickinson, M., “The Effect of Wing Rotation on Unsteady Aerodynamic Performance at Low Reynolds Numbers,” J. Exp. Biol., Vol. 192, 1994, pp. 179-206.
58. Dickinson, M. and Gotz, K. G., “Unsteady Aerodynamic Performance of Model Wings at Low Reynolds Numbers,” J. Exp. Biol., Vol. 174, 1993, pp. 45-64.
59. Dickinson, M.H., Lighton, J.R.B., “Muscle Efficiency and Elastic Storage in the Flight Motor of Drosophila,” Science, Volume 268, 7 April, 1995, pp. 87-90.

60. Dohring, C. M., Fourier, L., and Platzer, M. F., "Experimental and Numerical Investigation of Flapping Wing Propulsion and Its Application for Boundary Layer Control," ASME Paper 98-GT 46, American Society of Mechanical Engineers, June 1998.
61. Donovan, J. F., and Selig, M. S., "Low Reynolds Number Airfoil Design and Wind Tunnel Testing at Princeton University," Low Reynolds Number Aerodynamics, edited by T. J. Mueller, Vol. 54 of Lecture Notes in Engineering, Springer-Verlag, New York, June 1989, pp. 39-57.
62. Dornheim, M. A., "Tiny Drones May Be Soldier's New Tool," Aviation Week & Space Technology, Vol. 148, No. 23, 8 June 1998, pp. 42-48.
63. Dowell, E. H. (ed.), A Modern Course in Aeroelasticity, 3rd ed., Kluwer Academic, Dordrecht, The Netherlands, 1994.
64. Drela, M., "XFOIL: An Analysis and Design System for Low Reynolds Number Airfoils," Low Reynolds Number Aerodynamics, Springer-Verlag Lecture Notes in Engineering, edited by T. J. Mueller, No. 54, Springer-Verlag, Berlin, 1989.
65. Drela, M., "Low Reynolds-Number Airfoil Design for the M.I.T. Daedalus Prototype: A Case Study," Journal of Aircraft, Vol. 25, No. 8, Aug. 1985, pp. 724-732.
66. Drela, M., "Higher-Order Boundary Layer Formulation and Application to Low Reynolds Number Flows," Fixed and Flapping Wing Aerodynamics for Micro Air Vehicle Applications, T. J. Mueller (Ed.), Prog. in Astronautics and Aeronautics, Vol., 195, 2001.
67. Driver, D. M., Seegmiller, H. L., and Marvin, J., "Time-Dependent Behavior of Reattaching Shear Layers," AIAA Journal, Vol. 25, No. 7, July 1987, pp. 914-919.
68. Dudley, R., and Ellington, C. P., "Mechanics of Forward Flight in Bumblebees. I. Kinematics and Morphology," Journal of Experimental Biology, Vol. 148, 1990, pp. 19-52.
69. Dudley, Robert, The Biomechanics of Insect Flight: Form, Function, Evolution, Princeton University Press, 2000.
70. Edwards, Chad, Mars Communication Architectures, Workshop on Emerging Communications, Networks, and Architectures Technologies for NASA Enterprises, Cleveland, Ohio, August 7-10, 2001.
71. Ekaterinaris, J. A., and Platzer, M. F., "Computational Prediction of the Airfoil Dynamic Stall," Progress in Aerospace Sciences, Vol. 33, 1997, pp. 759-846.
72. Elachi, C., Spaceborne Radar Remote Sensing: Applications and Techniques, IEEE Press, New York, 1988
73. Ellington, C., "The Aerodynamics of Flapping Animal Flight," American Zoology, vol. 24, 1984, pp. 95-105
74. Ellington, C. P., "The Aerodynamics of Hovering Flight," Philosophical Transactions of the Royal Society of London, Vol. 305, No. 1122, 1984, pp. 1-181.
75. Ellington, C. P., "The Aerodynamics of Insect-based Flying Machines."
76. Ellington, C. P., "Unsteady Aerodynamics of Insect Flight," Biological Fluid Dynamics, edited by C. P. Ellington and T. J. Pedley, Symposium of the Society for Experimental Biology, The Company of Biologist Limited, Cambridge, U.K., Vol. 49, 1995, pp. 109-129.
77. Ellington, C. P. and Usherwood, J. R., "Lift and Drag Characteristics of Rotary and Flapping Wings," Fixed and Flapping Wing Aerodynamics for Micro Air Vehicle Applications, T. J. Mueller (Ed.), Prog. in Astronautics and Aeronautics, Vol., 195, 2001.
78. Ellington, C.P., van den Berg, C., Willmott, A.P. and Thomas, A.L.R., "Leading-edge vortices in insect flight," Nature 38:D 1996, pp. 626-630.
79. Energy Conversion Devices Inc., www.ovonics.com, June 2001.

80. Englar, R. J. and Applegate, C. A., "Circulation Control - A Bibliography of DTNSRDC Research and Selected Outside References (January, 1969 through December, 1983)," DTNSRDC-84/052 (September 1984).
81. Englar, Robert J., "Circulation Control Pneumatic Aerodynamics: Blown Force and Moment Augmentation and Modification; Past, Present and Future," AIAA Paper 2000-2541, presented at the AIAA Fluids 2000 Meeting, Denver, CO, June 19-22, 2000.
82. Englar, Robert J., "Experimental Investigation of the High Velocity Coanda Wall Jet Applied to Bluff Trailing Edge Circulation Control Airfoils," published as M. S. Thesis, University of Maryland, Department of Aerospace Engineering, June, 1973.
83. Englar, Robert J., Smith, Marilyn J., Kelley, Sean M., and Rover III, Richard C., "Development of Circulation Control Technology for Application to Advanced Subsonic Transport Aircraft, Part I: Airfoil Development" AIAA Paper No. 93-0644, Log No. C-8057, published in AIAA Journal of Aircraft, Vol. 31, No. 5, pp. 1160-1168, Sept-Oct 1994.
84. Englar, Robert J., Smith, Marilyn J., Kelley, Sean M., and Rover III, Richard C., "Development of Circulation Control Technology for Application to Advanced Subsonic Transport Aircraft, Part II: Transport Application" AIAA Paper No. 93-0644, Log No. C-8058, published in AIAA Journal of Aircraft, Vol. 31, No. 5, pp. 1169-1177, Sept-Oct 1994.
85. Ennos, A. R., "The Importance of Torsion in the Design of Insect Wings," Journal of Experimental Biology, Vol. 140, 1988, pp. 137-160.
86. Ennos, R., "Unconventional Aerodynamics," Nature, Vol. 344, No. 5, 1990, pp. 67-69.
87. Entomopter Video.
88. Eppler, R., Airfoil Design and Data, Springer-Verlag, New York, 1990.
89. Eppler, R. and Somers, D. M., "A Computer Program for the Design and Analysis of Low-Speed Airfoils," NASA TM 80210, Aug. 1980.
90. Ergenics Corporation, Metal Hydride Tank Specifications, www.ergenics.com, June 2001.
91. Euergentics Incorporated, "A Comprehensive Summary of Hydrogen R&D Technologies: Storage," Final Report, US Department of Energy contract DE-FG03-00SF22103, May 2001.
92. Faleschini, G. et al "Ammonia for High Density Hydrogen Storage,"
93. Farren, W. S., "The Reaction on a Wing Whose Angle of Incidence Is Changing Rapidly-Wind-Tunnel Experiments with a Short-Period Recording Balance," Aeronautical Research Council Reports and Memoranda, No. 1648, Jan. 1935.
94. Foch, R. J., "Hero, Propulsion & Planform Considerations for Micro-UAVs," presentation at the Micro-UAV Workshop, 9 Nov. 1995.
95. Fontana, R., On "Range-Bandwidth per Joule" fro Ultra Wideband and Spread Spectrum Waveforms, MultiSpectral Solutions, Inc. July 20, 2000.
96. Fontana, Robert J., Ultra wideband precision geolocation system, US Patent 6054950, January, 1998.
97. Fountain, J. R., Digital Terrain Systems, IEE, Savoy Place, London WC2R OBL, UK, 1997.
98. Frampton, K., Goldfarb, M. and Monopoli, D., "Passive Aeroelastic Tailoring for Optimal Flapping Wings," Fixed and Flapping Wing Aerodynamics for Micro Air Vehicle Applications, T. J. Mueller (Ed.), Prog. in Astronautics and Aeronautics, Vol., 195, 2001.
99. Garrick, I. E., "Propulsion of a Flapping and Oscillating Airfoil," NACA Rept. 567, 1936.
100. Gaster, M., "The Structure and Behavior of Separation Bubbles," Aeronautical Research Council Reports and Memoranda, No. 3595, March 1967.

101. Gault, D. E., "Boundary-Layer and Stalling Characteristics of the NACA 63-009 Airfoil Section," NACA TN 1894, June 1949.
102. Gibbs-Smith, C. H., "Chapter VI, The First Half of The Nineteenth Century," A History of Flying, B. T. Batsford, London, 1953, pp. 108-112.
103. Giguere, P., and Selig, M. S., "New Airfoils for Small Horizontal Axis Wind Turbines," ASME Journal of Solar Energy Engineering, Vol. 120, May 1998, pp. 108-114.
104. Gilmour, K.M., Ellington, C.P., Journal of Experimental Biology, No. 183, pg. 101, 1993.
105. Goldstein, S., "On the Vortex Theory of Screw Propellers," Proceedings of the Royal Society of London, Series A, Vol. 123, 1929, pp. 440-465.
106. Golshan, N., Ho, C., Radiowave Propagation Issues for In-Situ Communications, DESCANSO Symposium, Pasadena, CA, September 21-23, 1999.
107. Gopalarathnam, A., and Selig, M. S., "Low-Speed Natural-Laminar-Flow Airfoils: Case Study in Inverse Airfoil Design," Journal of Aircraft, Vol. 38, No. 1, Jan.-Feb. 2001, pp. 57-63.
108. Grasmeyer, J. M. and Keennon, M. T., "Development of the Black Widow Micro Air Vehicle," Fixed and Flapping Wing Aerodynamics for Micro Air Vehicle Applications, T. J. Mueller (Ed.), Prog. in Astronautics and Aeronautics, Vol., 195, 2001.
109. Gridgen Version 13.3, User Manual, Pointwise Inc., 1998, Bedford, Texas.
110. Grodnitsky, D. L. , Form and Function of Insect Wings: The Evolution of Biological Structures, The John Hopkins University Press, 1999.
111. Guglielmo, J. J., and Selig, M. S., "Spanwise Variations in Profile Drag for Airfoils at Low Reynolds Numbers," Journal of Aircraft, Vol. 33, No. 4, July-Aug. 1996, pp. 699-707.
112. Gursul, L, and Ho, C. M., "High Aerodynamic Loads on an Airfoil Submerged in an Unsteady Stream," AIAA Journal,Vol.30, No.4, 1992, pp. 1117-1120.
113. Hall, K. C., and Hall, S. R., "Minimum Induced Power Requirements for Flapping Flight," Journal of Fluid Mechanics, Vol. 323, Sept. 1996, pp. 285-315.
114. Hall, K. C., Pigott, S. A., and Hall, S. R., "Power Requirements for Large-Amplitude Flapping Flight," Journal of Aircraft, Vol. 35, No. 3, May-June 1998, pp. 352-361.
115. Hall, S. R., "Micro Air Vehicles: Propulsion and Actuation Issues," Defense Science Study Group V.-Study Reports 1996-1997, Volume 1: Papers 1-13, IDA Paper P-3414, Institute for Defense Analyses, Alexandria, VA, February 1998, pp. 193-206.
116. Hall, S. R., Yang, K. Y., and Hall, K. C., "Helicopter Rotor Lift Distributions for Minimum Induced Power Loss," Journal of Aircraft, Vol. 31, No. 4, 1994, pp. 837-845.
117. Hall, K. C., Pigott, S. A., and Hall, S. R., "Power Requirements for Large-Amplitude Flapping Flight," AIAA Paper 97-0827, Jan. 1997.
118. Hall, K. C. and Hall, S. R., "A Rational Engineering Analysis of the Efficiency of Flapping Flight," Fixed and Flapping Wing Aerodynamics for Micro Air Vehicle Applications, T. J. Mueller (Ed.), Prog. in Astronautics and Aeronautics, Vol., 195, 2001.
119. Handbook of Tables for Applied Engineering Science, 2nd Edition CRC press, 1973. Overview of Propulsion Systems for a Mars Aircraft
120. Harris, F. D., "Preliminary Study of Radial Flow Effects on Rotor Blades," Journal of the American Helicopter Society, Vol. 11, No. 3, 1966, pp. 1-21.
121. Heinrich, D. C., "An Experimental Investigation of a Low Frequency Flow Oscillation over a Low Reynolds Number Airfoil near Stall," M. S. Thesis, Dept. of Aeronautical and Astronautical Engineering, Univ. of Illinois, Urbana, IL, 1994.

122. Hemsch, M. J., and Luckring, J. M., "Connection between Leading-Edge Sweep, Vortex Lift, and Vortex Strength for Delta Wings," Journal of Aircraft, Vol. 7, No. 5, 1990, pp. 473-475.
123. Ho, C., Golshan, N., Radio Wave Propagation for Communication on and around Mars, 23rd NASA propagation experiments Meeting (NAPEX XXIII) and ACTS Propagation Studies, Falls Church, VA. June 1999.
124. Hoerner, S. F., and Borst, H. V., Fluid-Dynamic Lift, Hoemer Fluid Dynamics. Brick Town, NJ, 1975.
125. Ikehata, NL, Inoue, T., Ozawa, M., and Matsumoto, S., "Experimental Investigation on Flow Fields of Viscous Fluid around Two-dimensional Wings: Comparison with Computational Results," Journal of Marine Science and Technology, Vol. 2, 1997, pp. 62-76.
126. Incropera, F.P. and DeWitt, D.P., Fundamentals of Heat and Mass Transfer, John Wiley and Sons 1990.
127. Isaac, K. M., "A New Approach to Calculating Internal Compressible Flows," Proceedings of the ASME International Computers in Engineering Conference, Boston, Massachusetts, Vol. 3, Bk. No. G0286C, August 1985.
128. Isogai, K., Shinmoto, Y, and Watanabe, Y., "Effects of Dynamic Stall Phenomena on Propulsive Efficiency and Thrust of a Flapping Airfoil," AIAA Paper 97-1926, June 1997.
129. Johnson, Richard C., Antenna Engineering Handbook, Third Edition, Mc Graw Hill, Inc., New York, 1993, pg. 21-22.
130. Jones, B. M. "An Experimental Study of the Stalling of Wings," Aeronautical Research Council Reports and Memoranda, No. 1588, Dec. 1933, p. 8.
131. Jones, K. D., and Platzer, M. F., "Airfoil Geometry and Flow Compressibility Effects on Wing and Blade Flutter," AIAA Paper 98-0517, Jan. 1998.
132. Jones, K. D., and Platzer, M. F., "Time-Domain Analysis of Low-Speed Airfoil Flutter," AIAA Journal, Vol. 34, No. 5, May 1996.
133. Jones, K. D., Lund, T. C. and Platzer, M. F., "Experimental and Computational Investigation of Flapping Wing Propulsion for Micro Air Vehicles," Fixed and Flapping Wing Aerodynamics for Micro Air Vehicle Applications, T. J. Mueller (Ed.), Prog. in Astronautics and Aeronautics, Vol., 195, 2001.
134. Jones, R. T., "Wing Flapping with Minimum Energy," Aeronautical Journal, Vol. 84, July 1980, pp. 214-217.
135. Jones. K. D., Dohring, C. M., and Platzer, M. F., "Experimental and Computational Investigation of the Knoller-Betz Effect," AIAA Journal, Vol. 36, No. 7, May 1998.
136. Kadlec, R. A., and Davis, S. S., "Visualization of Quasiperiodic Flows" AIAA Journal, Vol. 17, 1979, pp. 1164-1169.
137. Kaplan, D. I. etal, "In-Situ Propellant Production on Mars: The First Flight Demonstration," 30th Lunar and Planetary Science Conference, March 1999.
138. Kaplan,D.I., Ratliff, J.E., Baird, R.S., Sanders, G.B., Johnson, K.R., Karlmann, P.B., Juanero, K.J.,Baraona, C.R., Landis, G.A., Jenkins, P.P. and Scheiman, D.A., "In-Situ Propellant Production on Mars: The First Flight Demonstration," 30th Lunar and Planetary Science Conference, Houston Tx. , March 1999.
139. Karlmann, P., Rapp, D., "Sorption Compressor for Collecting Atmospheric CO2 on Mars," JPL New Technology Report NPO-20353, NASA Technical Support Package October 1998.

140. Katz, J., and Weihs, D., “Behavior of Vortex Wakes from Oscillating Airfoils;” Journal of Aircraft, Vol. 15, No. 12, 1978, pp. 861-863.
141. Katz, J., and Weihs, D., “Wake Rollup and the Kutta Condition for Airfoils Oscillating at High Frequency,” AIAA Journal, Vol. 19, No. 12, 1981, pp. 1604-1606.
142. Kerzhanovich, Victor V., Personal correspondence, JPL, January 2000.
143. Kiya, M., and Sasaki, K., “Structure of a Turbulent Separation Bubble,” Journal of Fluid Mechanics, Vol. 137, 1983, pp. 83-113.
144. Kline, S. J., and McClintock, F. A., “Describing Uncertainties in Single-Sample Experiments,” Mechanical Engineering, Vol. 75, No. 1, 1953, pp. 3-8.
145. Koochesfahani, M. M., “Vortical Patterns in the Wake of an Oscillating Airfoil,” AIAA Journal, Vol. 27, No. 9, Sept. 1989, pp. 1200-1205.
146. Kroo, I. and Kunz, P., “Mesoscale Flight and Miniature Rotorcraft Development,” Fixed and Flapping Wing Aerodynamics for Micro Air Vehicle Applications, T. J. Mueller (Ed.), Prog. in Astronautics and Aeronautics, Vol., 195, 2001.
147. Kuechemann, D., and von Holst, E., “Aerodynamics of Animal Flight,” Luftwissen, Vol. 8, No. 9, Sept. 1941, pp. 277-282; translated by L. J. Baker for the Ministry of Aircraft Production, R. T. P. Translation No. 1672.
148. Kuechemann, D., and Weber, J., “Aerodynamic Propulsion in Nature,” Aerodynamics of Propulsion, McGraw-Hill, New York, 1953, pp. 248-260.
149. Kunz, P. J. and Kroo, I., “Analysis and Design of Airfoils for Use at Ultra-Low Reynolds Numbers,” Fixed and Flapping Wing Aerodynamics for Micro Air Vehicle Applications, T. J. Mueller (Ed.), Prog. in Astronautics and Aeronautics, Vol., 195, 2001.
150. Lai, J. C. S., Yue, J., and Platzer, M. F., “Control of Backward Facing Step Flow Using a Flapping Airfoil,” ASME FEDSM97-3307, June 1997.
151. Lai, J. C. S., and Platzer, M. F., “Jet Characteristics of a Plunging Airfoil,” AIAA Journal, Vol. 37, No. 12, Dec. 1999, pp. 1529-1537.
152. Lan, C. E., “The Unsteady Quasi-Vortex-Lattice Method with Applications to Animal Propulsion;” Journal of Fluid Mechanics, Vol. 93, No. 4, 1979, pp. 747-765.
153. Larijani, R. and DeLaurier, J. D., “A Nonlinear Aeroelastic Model for the Study of Flapping Wing Flight,” Fixed and Flapping Wing Aerodynamics for Micro Air Vehicle Applications, T. J. Mueller (Ed.), Prog. in Astronautics and Aeronautics, Vol., 195, 2001.
154. Lee, K. F., Chen, W., Advances in Microstrip and Printed Antennas, Wiley Series in Microwave and Optical Engineering, Wiley Interscience, New York, 1997.
155. Leybold Cryogenics, www.leyboldcryogenics.com/, July 2001.
156. Liao, J. R., Isaac, K. M., Miles, J. B., and Tsai, B. J. “Navier-Stokes Simulation of Cone-Derived Waverider,” AIAA Journal, Vol. 30, No. 6, June 1992, pp. 1521-1528 .
157. Liao, J. R., Isaac, K. M. and Miles, J. B., “Navier-Stokes Simulation of Waverider Flow Fields,” AIAA-90-3066-CP, AIAA 8th Applied Aerodynamics Conference, Portland, OR, August 1990, pp. 528-538.
158. Lifanov, L. K., and Polonskii,1. E., “Proof of the Numerical Method of `Discrete Vortices' for Solving Singular Integral Equations,” Journal of Applied Mathematics and Mechanics, Vol. 39, No. 4, 1975, pp. 742-746.
159. Lighthill, M. J., “Aquatic Animal Propulsion of High Hydromechanical Efficiency,” Journal of Fluid Mechanics, Vol. 44, 1970, pp. 265-301.

160. Lighthill, M. J., “Some Challenging New Applications for Basic Mathematical Methods in the Mechanics of Fluids That Were Originally Pursued with Aeronautical Aims,” Aeronautical Journal, Vol. 94, No. 932, Feb. 1990, pp. 41-52.
161. Lippisch, A. M., “Man Powered Flight in 1929,” Journal of the Royal Aeronautical Society, Vol. 64, July 1960, pp. 395-398.
162. Liu, H., and Kawachi, K., “A Numerical Study of Insect Flight,” Journal of Computational Physics, Vol. 146, 1998, pp. 1-33.
163. Liu, H. and Kawachi, K., “Leading Edge Vortices of Flapping and Rotary Wings at Low Reynolds Number,” Fixed and Flapping Wing Aerodynamics for Micro Air Vehicle Applications, T. J. Mueller (Ed.), Prog. in Astronautics and Aeronautics, Vol., 195, 2001.
164. Liu, P., “A Time-Domain Panel Method for Oscillating Propulsors with Both Chordwise and Spanwise Flexibility,” Ph.D. Thesis, Univ. of Newfoundland, St. John's, NF, Canada, 1996.
165. Liu, P., “Three-Dimensional Oscillating Foil Propulsion,” M.S. Engineering Thesis, Univ. of Newfoundland, St. John's, NF, Canada, March 1991.
166. Liu. H., Ellington, C.P., Kawachi, K., van den Berg, C. and Willmott, A.P., “A Computational Fluid Dynamic Study of Hawk Moth Hovering,” J. exp. Biol. 201, 1998, pp. 461-477.
167. Lowry, J. G., and Polhamus, E. C., “A Method for Predicting Lift Increments due to Flap Deflection at Low Angles of Attack in Incompressible Flow,” NACA TN 3911, 1957.
168. Lowson, M. V., “Aerodynamics of Airfoils at Low Reynolds Numbers,” Proceedings of the UAVs Fourteenth International Conference, Univ. of Bristol, U.K., 1999, pp. 35.1-35.16.
169. Lund, T. C., “A Computational and Experimental Investigation of Flapping Wing Propulsion,” M.S. Thesis, Dept. of Aeronautics and Astronautics, Naval Postgraduate School, Monterey. CA, March 2000.
170. Lunia, A., Isaac, K. M., Chandrashekhara, K., and Watkins, S., “Wind Tunnel Testing of a Smart Composite Wing using Fiber Optic Strain Sensing and Neural Network,” Smart Materials and Structures, 9, (2000), 767-773.
171. Lyon, C. A., Broeren, A. P., Gigure, P., Gopalarathnam, A., and Selig, M. S., Summary of Low-Speed Airfoil Data, Vol. 3, SoarTech Publications, Virginia Beach, VA, 1998.
172. Lyon, C. A., Selig, M. S., and Broeren, A. P., “Boundary Layer Trips on Airfoils at Low Reynolds Numbers,” AIAA Paper 97-0511, Jan. 1997.
173. Mabey, D. G., “Analysis and Correlation of Data on Pressure Fluctuations in Separated Flow,” Journal of Aircraft, Vol. 9, No. 9, Sept. 1972, pp. 642-645.
174. Mahafza, B. R., Radar Systems Analysis and Design Using Matlab, Chapman and Hall/CRC, New York, 2001.
175. Mars Expedition Strategy Group, NASA, “The Search for Evidence of Life on Mars,” JPL, 1996.
176. Maxworthy, T., “Experiments on the Weis-Fogh Mechanism of Lift Generation by Insects in Hovering Flight. Part 1. Dynamics of the `Fling',” Journal of Fluid Mechanics, Vol. 93, 1979, pp. 47-63.
177. McClaine, A.W., Breault,R.W., Larsen,C., Konduri,R., Rolfe,J. and Becker,F., “Advanced Chemical Hydride Hydrogen-Generation/Storage System for PEM Fuel Cell Vehicles,” Thermo Technologies, DOE 2000 Progress Report Contract No. 98111.
178. McCullough, G. B., and Gault, D. E., “Boundary-Layer and Stalling Characteristics of the NACA 64A006 Airfoil Section,” NACA TN 1923, Aug. 1949.

179. McCullough, G. B., and Gault, D. E., "Examples of Three Representative Types of Airfoil-Section Stall at Low-Speed," NACA TN 2502, Sept. 1951.
180. McCune, J. E., Lam, C. M. G., and Scott, M. T., "Nonlinear Aerodynamics of Two-Dimensional Airfoils in Severe Maneuver," AIAA Journal, Vol. 28, No. 3, 1990, pp. 385-393.
181. McGhee, R. J., Walker, B. S., and Millard, B. F., "Experimental Results for the Eppler 387 Airfoil at Low-Reynolds Numbers in the Langley Low-Turbulence Pressure Tunnel," NASA TM 4062, Oct. 1988.
182. McKay, C.P.,"Mars '03 Airplane Micromission Science Definition Team: Final Report," Document 0907-01-01A, September 1999.
183. McKinney, W., and DeLaurier, J., "The Windmill: An Oscillating Wing Windmill," Journal of Energy, Vol. 5, No. 2, March-April 1981, pp. 109-115.
184. McMasters, J. H., and Henderson, M. L., "Low Speed Single Element Airfoil Synthesis," Technical Soaring, Vol. 2, No. 2, 1980, pp. 1-21.
185. Michelson, R.C., "The Entomopter," Neurotechnology for Biomimetic Robots, ISBN 0-262-01193-X, The MIT Press, 2002.
186. Michelson, R.C., Ahuja, K.K., Amarena, C., Ellington, C. Englar, R.J., "Mesoscaled Aerial Robot" Final Report under Contract Number: DABT63-98-C-0057, DARPA/DSO, February 2000.
187. Michelson, R.C., Amarena, C.S., "4th Generation Reciprocating Chemical Muscle: Reciprocating Chemical Muscle (RCM) for Specialized Micro UAVs and Other Nonelectric Anaerobic Aerospace Actuation Applications", Prepared under Grant No. F086300010007 to the U.S. Air Force Research Laboratories (AFRL/MNGN), October 15, 2001.
188. Michelson, R.C., Reece, S., "Update on Flapping Wing Micro Air Vehicle Research - Ongoing work to develop a flapping wing, crawling Entomopter," 13th Bristol International RPV/UAV Systems Conference Proceedings, Bristol England, 30 March 1998 - 1 April 1998, pp. 30.1-30.1
189. Monttinen, J. T., Shortridge, R. R., Latek, B. S., Reed, H. L., and Saric, W. S., "Adaptive, Unstructured Meshes for Solving the Navier-Stokes Equations for Low-Chord-Reynolds Number Flows," Fixed and Flapping Wing Aerodynamics for Micro Air Vehicle Applications, T. J. Mueller (Ed.), Prog. in Astronautics and Aeronautics, Vol., 195, 2001.
190. Mueller, T. J., "Low Reynolds Number Vehicles," AGARD monograph No. 288, 1985.
191. Mueller, T. J., Fluid Mechanics Measurements, edited by R. J. Goldstein, Taylor & Francis, Washington DC, 1996, pp. 367-450.
192. Mulloy, Robert, Personal communication, MulitSpectral Solutions, Inc., July 2002.
193. Murphy,O.J. and Hitchens,G.D., "Electrochemical Production of Ozone and Hydrogen Peroxide," United States patent 5,972,196, October 26, 1999.
194. NASA Glenn Research Center, Dynamic Power Conversion Web Site, http://www.grc.nasa.gov/WWW/tmsb/dynamicpower.html, July 2001.
195. Neace, K. S., "A Computational and Experimental Investigation of the Propulsive and Lifting Characteristics of Oscillating Airfoils and Airfoil Combinations in Incompressible Flow," M.S. Thesis, Dept. of Aeronautics and Astronautics, Naval Postgraduate School, Monterey, CA, Sept. 1992.
196. Neef, M. F. and Hummel, D., "Euler Solutions for the Finite Span Flapping Wing," Fixed and Flapping Wing Aerodynamics for Micro Air Vehicle Applications, T. J. Mueller (Ed.), Prog. in Astronautics and Aeronautics, Vol., 195, 2001.

197. Ng, Wing Fai, “Thermoelectric-Based Micro-Air-Vehicles”, Mechanical Engineering Department, Virginia Tech, 1998.
198. Nyborg, U. M., Vertebrate Flight: Mechanics, Physiology, Morphology, Ecology and Evolution, Springer-Verlag, New York, 1990.
199. Odyssey Finds Water Ice in Abundance Under Mars’ Surface, Media Relations Office, Jet Propulsion Laboratory, http://mars.jpl.nasa.gov/odyssey/newsroom/pressreleases/20020528a.html, May 28, 2002
200. Ohashi, H., and Ishikawa, N., “Visualization Study of a Flow near the Trailing Edge of an Oscillating Airfoil,” Bulletin of the Japanese Society of Mechanical Engineers, Vol. 15, 1972, pp. 840-845.
201. Osborne, M. F. M., “Aerodynamics of Flapping Flight with Application to Insects,” Journal of Experimental Biology, Vol. 28, 1951, pp. 221-245.
202. Pang, C. K., “A Computer Code for Unsteady Incompressible Flow past Two Airfoils,” Aeronautical Engineer's Thesis, Dept. of Aeronautics and Astronautics, Naval Postgraduate School, Monterey, CA, Sept. 1988.
203. Pankhurst, R. C., and Holder, D. W., Wind-Tunnel Technique, Pitman, London, 1952.
204. Paulsen, P. E., Mars Airplane Package Communication System Design Trades, NASA Glenn Research Center Document 0806-02-01A, 2000.
205. Pelaccio, D.G., Palaszewski, B. and O'Leary R., “Preliminary Assessment of Using Gelled and Hybrid Propellant Propulsion for VTOL/SSTO Launch Systems,” NASA TM-1998-206306, February 1998.
206. Pelletier, A., and Mueller, T. J., “Low Reynolds Number Aerodynamics of Low-Aspect Ratio, Thin/Flat/Cambered-Plate Wings,” Journal of Aircraft, Vol. 37, No. 5, Sept.-Oct. 2000, pp. 825-832.
207. Pfenninger, W., and Vermuru, C. S., “Design of Low-Reynolds Number Airfoils-I,” AIAA Paper 88-2572-CP, 1988.
208. Pfenninger, W., Vermuru, C. S., Mangalam, S. M., and Evangelista, R., “Design of Low-Reynolds Number Airfoils-II,” AIAA Paper 88-3764-CP, 1988.
209. Phlips. P. J., East, R. A., and Pratt, N. H., “An Unsteady Lifting Line Theory of Flapping Wings with Application to the Forward Flight of Birds,” Journal of Fluid Mechanics, Vol. 112. Nov. 19 81, pp. 97-125.
210. Plachta, D.W., “Hybrid Thermal Control Testing of a Cryogenic Propellant Tank,” NASA TM-1999-209389, August 1999.
211. Platzer, M. F., Neace, K. S., and Pang, C. K., “Aerodynamic Analysis of Flapping Wing Propulsion,” AIAA Paper 93-0484, Jan. 1993.
212. Polhamus, E. C., “A Concept of the Vortex Lift of Sharp-Edge Delta Wings Based on a Leading-Edge-Suction Analogy,” NASA TN D-3767, 1966.
213. Polhamus, E. C., “Predictions of Vortex-Lift Characteristics by a Leading-Edge Suction Analogy,” Journal of Aircraft, Vol. 8, 1971, pp. 193-199.
214. Rae, W. H., Jr. and Pope, A., Low-Speed Wind Tunnel Testing, Wiley, New York, 1984.
215. Ramamurthi, R. and Sandberg, W., “Computation of Aerodynamic Characteristics of a Micro Air Vehicle,” Fixed and Flapping Wing Aerodynamics for Micro Air Vehicle Applications, T. J. Mueller (Ed.), Prog. in Astronautics and Aeronautics, Vol., 195, 2001.
216. Rambach, G.D., “Hydrogen Transport and Storage in Engineered Glass Microspheres,” Lawrence Livermore National Laboratory, April 1994.

217. Rayner, J. M. V., "On Aerodynamics and the Energetics of Vertebrate Flapping Flight," Fluid Dynamics in Biology, edited by A. Y Cheer and C. P. van Dam, Vol. 141, Contemporary Mathematics, American Mathematical Society, Providence, RI, 1993, pp. 351-400.
218. Rayner, J. M. V., Jones, G., and Thomas, A., "Vortex Flow Visualizations Reveal Change in Upstroke Function with Flight Speed in Bats," Nature, Vol. 321, 8 May 1986, pp. 162-164.
219. Rayner, J., "A Vortex Theory of Animal Flight. Part 2. The Forward Flight of Birds," Journal of Fluid Mechanics, Vol. 91, Part 4, 1979, pp. 731-763.
220. Rayner, J., "Thrust and Drag in Flying Birds: Applications to Birdlike Micro Air Vehicles," Fixed and Flapping Wing Aerodynamics for Micro Air Vehicle Applications, T. J. Mueller (Ed.), Prog. in Astronautics and Aeronautics, Vol., 195, 2001.
221. Rediniotis, O. K. and Lagoudas, D. C., "Shape Memory Alloy Actuators as Locomotor Muscles," Fixed and Flapping Wing Aerodynamics for Micro Air Vehicle Applications, T. J. Mueller (Ed.), Prog. in Astronautics and Aeronautics, Vol., 195, 2001.
222. Reissner, E., and Stevens, J. E., NACA TN 1194 & 1195 "Effect of Finite Span on the Airload Distributions for Oscillating Wings."
223. Rieder, R, et.al., "The Chemical Composition of the Martian Soil and Rocks Returned by the Mobil Alpha Proton X-Ray Spectrometer: Preliminary Results form the X-Ray Mode," Science 278: 1771-1774, 1997.
224. Riester. P. J., "A Computational and Experimental Investigation of Incompressible Oscillatory Airfoil Flow and Flutter Problems," M.S. Thesis, Naval Postgraduate School, Monterey, CA, June 1993.
225. Roell, M. M., Mars Airplane Package 2003 Micromission/Mars Airplane Package Mission and Interface Description, NASA Langley Research Center Document 0300-1B, 1999.
226. Schlichting, H., Boundary Layer Theory, 7th ed., McGraw-Hill, New York, 1979.
227. Schofield, J.T., Barnes, J.R., Crisp, D., Haberle, R.M., Larsen, S., Magalhaes, J.A., Murphy, J.R., Seiff, A., Wilson, G., "The Mars Pathfinder Atmospheric Structure Investigation/Meteorology (ASI/MET) Experiment."
228. Science Planning for Exploring Mars, NASA, Jet Propulsion Laboratory Publication 01-7, July 2001.
229. Seibert, M., Multifunction Ultra-Wideband (UWB) Subsystem for Entomopter Simultaneous Communications, Positioning, Collision-Avoidance and Radar, Personal Communications, 2001.
230. Selig, M. S., "The Design of Airfoils at Low Reynolds Numbers," AIAA Paper 85-0074, Jan. 1985.
231. Selig., M. S., Lyon, C. A., Giguere, P., Ninham, C. N., and Guglielmo, J. J., Summary of Low-Speed Airfoil Data, Vol. 2, SoarTech Publications, Virginia Beach, VA, 1996.
232. Selig, M. S., and Maughmer, M. D., "Generalized Multipoint Inverse Airfoil Design," AIAA Journal, Vol. 30, No. 11, Nov. 1992, pp. 2618-2625.
233. Selig, M., Gopalarathnam, A., Giguere, P. and Lyon, C. A., "Systematic Airfoil Design Studies at Low Reynolds Numbers," Fixed and Flapping Wing Aerodynamics for Micro Air Vehicle Applications, T. J. Mueller (Ed.), Prog. in Astronautics and Aeronautics, Vol., 195, 2001.
234. Send, W., "Otto Lilienthal and der Mechanismus des Schwingenfiugs," DGLR-JT96030, German Aerospace Congress, Dresden, Sept. 1996.
235. Shevell, R. S., Fundamentals of Flight, Prentice-Hall, Englewood Cliffs, NJ, 1989.

236. Shi, Y.-J., Miles, J. R. and Isaac, K. M., "Computational Fluid Dynamic Simulation of Inviscid and Viscous Waverider Flowfields with Sideslip," AIAA Journal of Spacecraft and Rockets Vol. 34, No. 1, Jan.-Feb. 1997, pp. 76-82.
237. Shi, Y. J., Tsai, B.-J., Miles, J. B. and Isaac, K. M., "Cone-Derived Waverider Flow field Simulation Including Turbulence and Off-Design Conditions," AIAA Journal of Spacecraft and Rockets, Vol. 33, No. 2, March-April 1996, pp. 185-190.
238. Shyy, W., Berg, M., and Ljungqvist, D., "Flapping and Flexible Wings for Biological and Micro Air Vehicles," Progress in Aerospace Sciences, Vol. 35, No. 5, 1999, pp. 455-506.
239. Shyy, W., Klevebring, F., Nilsson, M., Sloan, J., Carroll, B., and Fuentes, C., "Rigid and Flexible Low Reynolds Number Airfoils," Journal of Aircraft, Vol. 36, No. 3, May-June 1999, pp. 523-529.
240. Simons, R. N., Kelly, E., Lee, R. Q., Taub, S. R. Linearly Tapered Slot Antenna Circular Array for Mobile Communications, NASA Technical Memorandum 106441, January 1994.
241. Simpson, R. L., "Turbulent Boundary-Layer Separation," Annual Review of Fluid Mechanics, Vol. 21, 1989, pp. 205-234.
242. Skolnik, M. Radar Handbook, Second Edition, McGraw Hill, New York, 1990.
243. "Space and Planetary Environment Criteria Guidelines for Use In Space Vehicle Development 1982 Revision (Volume 1)," NASA TM-82478, January 1983.
244. Space Studies Board, National Research Council, "A Scientific Rationale for Mobility in Planetary Environments," National Academy Press, Washington, D.C., 1999.
245. Space Studies Board, National Research Council, "An Integrated Strategy for the Planetary Sciences: 1995-2010," National Academy Press, Washington, D.C., 1994.
246. Space Studies Board, National Research Council, "Review of NASA's Planned Mars Program," National Academy Press, Washington, D.C., 1996.
247. Sparenberg, J. A., Hydrodynamic Propulsion and Its Optimization: Analytic Theory, Kluwer Academic, Boston, 1995, pp. 216-217.
248. Spedding, G. R., "The Aerodynamics of Flight," Mechanics of Animal Locomotion, edited by R. McNeill Alexander, Advanced Comparative Environmental Physiology, Vol. 11, Springer-Verlag, Berlin, 1992.
249. Spedding, G. R., Rayner, J. M. V, and Pennycuick, C. J., "Momentum and Energy in the Wake of a Pigeon (Columba livia) in Slow Flight," Journal of Experimental Biology, Vol. 111. 1984, pp. 81-102.
250. Srinivasan, M.V., "Principals of Insect Vision and Navigation, and Applications to Autonomous Vehicles," Proceedings of the Information, Decision, and Control 2002 Symposium, Adelaide Australia, February 11-13, 2002, (CD ROM proceedings).
251. Sunada, S., and Ellington, C. P., "An Approximate Added Mass Method for Estimating Induced Power for Flapping Flight," AIAA Journal, Vol. 38, 2000, pp. 1313-1321.
252. Sunada, S., Sakaguchi, A., and Kawachi, K., "Airfoil Section Characteristics at a Low Reynolds Number," Journal of Fluid Engineering, Vol. 119, 1997, pp. 129-135.
253. Tani, I., "Low-Speed Flows Involving Separation Bubbles," Progress in Aeronautical Sciences, Vol. 5, 1964, pp. 70-103.
254. Theodorsen, T., "General Theory of Aerodynamic Instability and the Mechanism of Flutter," NACA Rept. 496, 1935.
255. Theodorson, T., "The Theory of Propellers- Determination of the Circulation Function and the Mass Coefficient for Dual Rotating Propellers."

256. Thomas, G. "Overview of Storage Development DOE Hydrogen Program," Presentation-US DOE Hydrogen Program 2000 Annual Review, May 2000.
257. Torres, G. E., and Mueller, T. J., "Aerodynamics Characteristics of Low Aspect Ratio Wings at Low Reynolds Numbers," Fixed and Flapping Wing Aerodynamics for Micro Air Vehicle Applications, T. J. Mueller (Ed.), Prog. in Astronautics and Aeronautics, Vol., 195, 2001.
258. Triantafyllou, G. S., Triantafyllou, M. S., and Grosenbaugh, M. A., "Optimal Thrust Development in Oscillating Foils with Application to Fish Propulsion;" Journal of Fluids and Structures, Vol. 7, 1993, pp. 205-224.
259. Tuncer, I.H., Platzer, M. F., and Ekaterinaris, J. A., "Computational Analysis of Flapping Airfoil Aerodynamics," American Society of Mechanical Engineers Fluids Engineering Division, Summer Meeting, June 1994.
260. Tuncer, I. H., and Platzer, M. F., "Thrust Generation due to Airfoil Flapping," AIAA Journal, Vol. 34, No. 2, 1996, pp. 324-331.
261. Tuncer, I. H., Lai, J., Ortiz, M. A., and Platzer, M. F., "Unsteady Aerodynamics of Stationary/Flapping Airfoil Combination in Tandem," AIAA Paper 97-0659, Jan. 1997.
262. Ulaby, F. T., Moore, R., K., Fung, A. K., Microwave Remote Sensing, Active and Passive, Volume II. Radar Remote Sensing and Surface Scattering and Emission Theory, Artech House, Inc. Norwood, MA, 1982.
263. Ulander, L. M. H., Ultra-wideband and low-frequency SAR interferometry, IEEE 1996.
264. Ultralife Batteries Inc., Lithium Polymer Specifications, July 2000.
265. van den Berg, C. and Ellington, C.P., "The Vortex Wake of a 'Hovering' Model Hawk Moth," Phil. Trans. R. Soc. Lond. B, 352, 1997, pp. 317-328.
266. van den Berg, C., and Ellington, C.P., "The Three-Dimensional Leading Edge Vortex of a 'Hovering' Model Hawk Moth," Philosophical Transactions of the Royal Society B, Vol 352, 1997, pp. 329-340.
267. Van Trees, H. L., Detection, Estimation and Modulation Theory, Vol. 1, Chapter 4, Wiley, NY, 1968.
268. Vest, M. S., and Katz, J., "Unsteady Aerodynamic Model of Flapping Wings," AIAA Journal, Vol. 34, No. 7, 1996, pp. 1435-1440.
269. Vogel. S., "Flight in Drosophila II. Variations in Stroke Parameters and Wing Contour," Journal of Experimental Biology, Vol. 46, 1967, pp. 383-392.
270. von Karman, T., and Burgers, J. M., "General Aerodynamic Theory-Perfect Fluids," Aerodynamic Theory, Division E, Vol. II, edited by W. F. Durand, Julius Springer, Berlin, 1934, p. 308.
271. von Karman, T., and Burgers, J. M., "Problems of Non-Uniform and Curvilinear Motion," Aerodynamic Theory, W. F. Durand, Editor-in-Chief, Vol. Il, Division E, Julius Springer, Berlin, 1934, pp. 304-310.
272. Wakeling, J. M., and Ellington, C. P., "Dragonfly Flight I. Gliding Flight and Steady State Aerodynamic Forces," Journal of Experimental Biology, Vol. 200, 1997, pp. 543-556.
273. Wang, J. "Vortex Shedding and Frequency Selection in Flapping Flight," Journal of Fluid Mechanics, Vol. 410, 2000, pp. 323-341.
274. Weinig, F., "Lift and Drag of Wings with Small Span," NACA TM 1151, 1947.
275. Weis-Fogh, T., "Energetics of Hovering Flight in Hummingbirds and in Drosophila," Journal of Experimental Biology, Vol. 56, 1972, pp. 79-104.

276. Weis-Fogh, T., “Quick Estimates of Flight Fitness in Hovering Animals, Including Novel Mechanisms for Lift Production,” Journal of Experimental Biology, Vol. 59, 1973, pp. 169-230.
277. Weis-Fogh, T., “Unusual Mechanisms for the Generation of Lift in Flying Animals,” Scientific American, Vol, 233, No. 5, 1975, pp. 80-87.
278. Wickman, J. H., “In-Situ Mars Rocket and Jet Engines Burning Carbon Dioxide,” AIAA 99-2409, 35th Joint Propulsion Conference, June 1999.
279. Wickman, J. H., “In Situ Martian Rocket and ‘Air Breathing’ Jet Engines”, NASA SBIR Phase II Final Report, Contract NAS8-97048, November, 1998
280. Willmott, A.P. and Ellington, C.P., “The Mechanics of Flight in the Hawk Moth Manduca *Sexta*. I. Kinematics of Hovering and Forward Flight,” J. exp. Biol. 200, 1997, pp. 2705-2722.
281. Wilmott, A.P., Ellington, C.P., and Thomas, A.L.R., “Flow Visualization and Unsteady Aerodynamics in the Flight of the Hawk Moth Manduca *Sexta*,” Philosophical Transactions of the Royal Society B, Vol 352, 1997, pp. 303-316.
282. Wilmott, P., “Unsteady Lifting-Line Theory by the Method of Matched Asymptotic Expansions,” Journal of Fluid Mechanics, Vol. 186, Jan. 1988, pp. 303-320.
283. The Wind User's Guide Version 3, User Manual, The NPARC Alliance, July 7, 2000, Cleveland, Ohio.
284. Wong, W., Starkovich, J., Adams, S. and Palaszewski, B., “Cryogenic Gellant and Fuel Formation for Metallized Gelled Propellants: Hydrocarbons and Hydrogen with Aluminum”, NASA TM-106698 June 1994.
285. Wonmann, F. X., “Progress in the Design of Low Drag Airfoils,” Boundary Layer and Flow Control, edited by G. V. Lachmann, Pergamon, London, 1961, pp. 748-770.
286. Wooton, R. J., “The Mechanical Design of Insect Wings,” Scientific American, Vol. 263, No. 5, Nov. 1990, pp. 114-120.
287. Wu J. Z., Vakili, A. D., and Wu, J. M., “Review of the Physics of Enhancing Vortex Lift by Unsteady Excitation,” Progress in Aerospace Science, Vol. 28, 1991, pp. 73-131.
288. Wu, T. Y, “Swimming of a Waving Plate,” Journal of Fluid Mechanics, Vol. 10, No. 3, 1961, pp. 321-344.
289. Yuasa, S. and Isoda, H., “Carbon Dioxide Propulsion for a Mars Airplane,” AIAA-89-2863, 25th Joint Propulsion Conference,1989.
290. Zaman, K. B. M. Q., McKinzie, D. J., and Rumsey, C. L., “A Natural Low-Frequency Oscillation over Airfoils near Stalling Conditions,” Journal of Fluid Mechanics, Vol. 202, 1989, pp. 403-442.
291. Zhang, Y., Geyer, M. E., Primeggia, C., Transmitter Power Requirements for Ultra-Wideband and Wideband Short Pulses in Radar and Communication Applications, NASA Glenn Research Center Contract C-79275-J , Final Report, March, 2000.
292. Zimmerman, C. H., “Characteristics of Clark Y Airfoils of Small Aspect Ratios,” NACA TR 431, 1932.
293. Zweibel,K. “Thin Films: Past, Present, Future”, National Renewable Energy Laboratory Document, April, 1997.